WRDC-TR-90-4096
VOLUME 1

AD-A243 219

DTIC
ELECTE
NOV 2 5 1991
S C D

DETERMINATION OF THE TRIBOLOGICAL FUNDAMENTALS OF SOLID LUBRICATED CERAMICS VOLUME 1: SUMMARY

M.N. Gardos
Hughes Aircraft Company
El Segundo, CA 90245

November 1990

Final Report for Period 09 September 1985 to 16 September 1989

91-16286

Approved for public release, distribution is unlimited

91 1122 019

MATERIALS LABORATORY
WRIGHT RESEARCH AND DEVELOPMENT CENTER
AIR FORCE SYSTEMS COMMAND
WRIGHT-PATTERSON AIR FORCE BASE, OHIO 45433-6533

NOTICE

When Government drawings, specifications, or other data are used for any purpose other than in connection with a definitely Government-related procurement, the United States Government incurs no responsibility nor any obligation whatsoever. The fact that the government may have formulated, or in any way supplied the said drawings, specifications, or other data, is not to be regarded by implication or otherwise in any manner construed, as licensing the holder or any other person or corporation, or as conveying any rights or permission to manufacture, use, or sell any patented invention that may in any way be related thereto.

This report is releasable to the National Technical Information Service (NTIS). At NTIS, it will be available to the general public, including foreign nations.

This technical report has been reviewed and is approved for publication.

Bobby D. McConnell, Chief
Nonstructural Materials Branch
Nonmetallic Materials Division

FOR THE COMMANDER

Merrill L. Minges, Director
Nonmetallic Materials Division

If your address has changed, if you wish to be removed from our mailing list, or if the addressee is no longer employed by your organization, please notify WL/____, Wright-Patterson AFB, OH 45433-____ to help us maintain a current mailing list.

Copies of this report should not be returned unless return is required by security considerations, contractual obligations, or notice on a specific document.

UNCLASSIFIED

SECURITY CLASSIFICATION OF THIS PAGE

REPORT DOCUMENT PAGE

Form Approved
OMB No. 0704-0188

1a. REPORT SECURITY CLASSIFICATION UNCLASSIFIED	1b. RESTRICTIVE MARKINGS
2a. SECURITY CLASSIFICATION AUTHORITY EDSG Document	3. DISTRIBUTION / AVAILABILITY OF REPORT Approved for public release; distribution is unlimited
2b. DECLASSIFICATION / DOWNGRADING SCHEDULE	
4. PERFORMING ORGANIZATION REPORT NUMBER(S)	5. MONITORING ORGANIZATION REPORT NUMBER(S) WRDC-TR-90-4096, Vol. I
6a. NAME OF PERFORMING ORGANIZATION Hughes Aircraft Company Electro-Optical & Data Systems Group 6b. OFFICE SYMBOL (If applicable) EDSG	7a. NAME OF MONITORING ORGANIZATION Materials Laboratory (WRDC/MLBT) Wright Research and Development Center, AFSC
6c. ADDRESS (City, State, and ZIP Code) P.O. Box 902 El Segundo, CA 90245	7b. ADDRESS (City, State, and ZIP Code) Wright-Patterson AFB OH 45433-65333
8a. NAME OF FUNDING / SPONSORING ORGANIZATION 8b. OFFICE SYMBOL (If applicable)	9. PROCUREMENT INSTRUMENT IDENTIFICATION NUMBER F33615-85-C-5087
8c. ADDRESS (City, State, and ZIP Code)	10. SOURCE OF FUNDING NUMBERS PROGRAM ELEMENT NO. 61101E; PROJECT NO. 5177; TASK NO. 00; WORK UNIT ACCESSION NO. 01

11. TITLE (Include Security Classification)

Determination of the Tribological Fundamentals of Solid Lubricated Ceramics
Volume I: Summary

12. PERSONAL AUTHOR(S)

Michael N. Gardos

13a. TYPE OF REPORT	13b. TIME COVERED	14. DATE OF REPORT (Year, Month, Day)	15. PAGE COUNT
Final	FROM 09-85 TO 09-89	November 1990	496

16. SUPPLEMENTARY NOTATION

a scanning electron microscope; molybdenum disulfides; barium fluorides

17. COSATI CODES		
FIELD	GROUP	SUB-GROUP

18. SUBJECT TERMS (Continue on reverse if necessary and identify by block number)

Ceramics	Ab-initio	Solid Lubricants
Diamond	Molecular Dynamics	Extreme Environments
Tribology	Analytical Tribometry	Friction/Wear Testing

19. ABSTRACT (Continue on reverse if necessary and identify by block number)

calcium fluorides; silicon nitride

The goals, structure and highlights of a recently completed multiyear/multinational research program are described. The main driving force behind this effort was the aim to advance the technology base so engineers can successfully and confidentially design, build and operate solid lubricated ceramic tribocomponents in extreme environments. Specially designed friction and wear testers were employed to perform well-defined model experiments on single crystal and polycrystalline ceramics and solid lubricants. The research led to discoveries such as (1) a lubricious oxide with the shear strength of MoS_2 in vacuum, (2) CVD diamond films with low friction and extraordinarily low wear, (3) intercalated graphites with high tribothermal resistance in vacuum and in air, and (4) a wear equation for Si_3N_4 ceramics. The fundamental nature of the research was exemplified by ab-initio predictions of the friction coefficient of single crystal (111) diamond sliding against its mating $(\bar{1}\bar{1}\bar{1})$ diamond plane, and molecular dynamics calculations on single crystal CaF_2 and BaF_2 (111) $[\bar{1}10]$ interface shear forces. The test equipment developed for completing the model experiments included an Auger/ESCA tribometer capable of unidirectional and oscillatory sliding at room temperature, a SEM tribometer designed for oscillatory sliding to 1000°C in vacuum and in partial pressures of reactive gases, an 850°C + dual-rubshoe friction and wear tester employing a rolling contact fatigue rod as one of the sliding specimens, and 850°C + friction/traction apparatus capable of operating to extraordinarily high PV limits.

The fundamental nature of the research notwithstanding, the main goals were directed towards finding potential solutions and applications useful to practicing tribologists and lubrication engineers.

20. DISTRIBUTION / AVAILABILITY OF ABSTRACT	21. ABSTRACT SECURITY CLASSIFICATION	
☒ UNCLASSIFIED/UNLIMITED ☐ SAME AS RPT. ☐ DTIC USERS	UNCLASSIFIED	
22a. NAME OF RESPONSIBLE INDIVIDUAL KARL R. MECKLENBURG	22b. TELEPHONE (Include Area Code) (513) 255-2465	22c. OFFICE SYMBOL WRDC/MLBT

DD Form 1473, JUN 86 — Previous editions are obsolete. — SECURITY CLASSIFICATION OF THIS PAGE

UNCLASSIFIED

FOREWORD

The overall objective of this 48-month interdisciplinary program was to investigate fundamental microscopic, macroscopic and continuum phenomena which occur between bare and solid lubricated ceramic surfaces exposed to a variety of extreme, triboenvironmental conditions. The title of the program is "Determination of Tribological Fundamentals", DARPA Order No. 5177, WRDC Contract No. F33615-85-C-5087.

Key government personnel monitoring the program included: Lt. Col. Steven G. Wax, Dr. Kay Rhyne and Dr. Benjamin A. Wilcox as the DARPA Program Managers and Bobby D. McConnell as the WRDC/MLBT Project Engineer. Dr. Larry L. Fehrenbacher (TA&T, Inc., Annapolis, MD) was a consultant to DARPA, assisting in the programmatic oversight and guidance of the technical efforts.

Various aspects of research were performed within the Technology Support Division of the Electro-Optical and Data Systems Group (EDSG) of Hughes Aircraft Company, under the direction of Dr. Michael N. Gardos as the Principal Investigator. The Hughes Program Managers were Dr. Gardos, Robert W. Seibold, Dr. Arthur B. Naselow and Earl B. Holst in chronological order of service. The research activities were conducted by personnel at EDSG and other Hughes groups, ably assisted by expert subcontractors from academia and industry located in this country and Western Europe.

Hughes personnel performing various technical tasks included Bonnie L. Soriano, Bruce W. Buller, Patrick S. Davis, Gerald L. Meldrum and Phil M. Magallanes (tribotesting and data reduction), Leo Fiderer, Dr. Stuart S. Gassel, Larry Czichola, Hans D. Metzler and Jim J. Erickson (tribotester design), Crawford R. Meeks, Ahn A. Tran, John P. Harrell and Rick Williams (mechanical and thermal analyses by computer methods), Dr. Norman H. Harris, Dr. Daniel A. Demeo and Phyllis J. Kelleghan (ceramic science and chemical analysis), as well as Dr. Mort Robinson, Mr. Kevin W. Kirby and Dr. John A. Roth (CaF_2/BaF_2 single crystal growth, polishing and analysis). Special recognition is given to Dora A. Monteiro (technical publications).

The Hughes subcontractors and the DoD scientists which closely cooperated within the confines of the program are properly recognized in the INTRODUCTION AND EXECUTIVE SUMMARY section.

Accession For
NTIS GRA&I ☒
DTIC TAB ☐
Unannounced ☐
Justification
By
Distribution/
Availability Codes
Dist | Avail and/or Special
A-1

CONTENTS

		Page
1.0	INTRODUCTION AND EXECUTIVE SUMMARY	1
1.1	Background	1
1.2	Program Philosophy	2
1.3	Critical Technical Issues	4
1.4	General Program Structure	6
1.4.1	Hughes In-house Research	6
1.4.2	Subcontractor Activities	8
1.4.3	Cooperative Research with Selected DoD Laboratories	15
1.5	Most Significant Achievements	17
1.5.1	Lubricious Oxides	17
1.5.2	CVD Diamond Films	17
1.5.3	Metal Chloride Intercalated Graphites	18
1.5.4	Predicting the Wear of Silicon-based Ceramics in a Wide Environmental Regime	18
1.5.5	Measurement of Coating Delamination and Surface Shear Interaction by Microscopic Tribometry	19
1.5.6	Intangible Benefits	20
2.0	THEORETICAL PREDICTIONS AND SPECIAL TEST EQUIPMENT	21
2.1	Theoretical Predictions	21
2.1.1	Quantum Dynamics and Suggested Experiments	22
2.1.2	Molecular Dynamics and Suggested Experiments	30
2.1.3	Ball Bearing Dynamics	36
2.2	Special Test Equipment	37
2.2.1	Auger/XPS Tribometer [Room Temperature (R.T.)]	42
2.2.2	SEM Tribometers (from -173° to 1000°C)	46
2.2.3	Dual Rubshoe Tester (R.T. to 850°C)	70
2.2.4	High PV Friction/Traction Testers (R.T. to 850°C)	111
3.0	TRIBOLOGICAL PROPERTIES OF SELECTED CERAMICS, HARDCOATS AND SOLID LUBRICANTS IN EXTREME ENVIRONMENTS	123
3.1	Bare and Modified α-SiC and Si_3N_4	126
3.1.1	The Effect of Preparation Method and Sintering Aid on the Friction and Wear of Polycrystalline α-SiC	126
3.1.2	The Effect of Preparation Method, Sintering Aid and Lubricant Additives on the Friction and Wear of Polycrystalline Si_3N_4	172
3.2	Layered Hexagonal Solid Lubricants	236
3.2.1	Single Crystals and Sputtered Films of MoS_2	236
3.2.2	Metal-Chloride Intercalated Graphites	256
3.2.3	CVD-deposited h-BN	298

CONTENTS (Concluded)

Page

3.3 Rutile (TiO_{2-x}) as a Lubricious Oxide 304

3.3.1 Anion Vacancy Effects on Shear Strength (Single Crystal Rutile) 304
3.3.2 Anion Vacancy Effects on Shear Strength (Polycrystalline Rutile) 307
3.3.3 Oxidation of Rutile-Forming TiC and TiN Substrates 334

3.4 CaF_2 and BaF_2 as Wide Temperature Range Lubricants 348

3.4.1 Surface Shear Strength of Ultrapure CaF_2 and BaF_2 (111)[$1\bar{1}0$] by SEM Tribometry 348
3.4.2 Surface Shear Strength of Commercial Purity CaF_2 (111) and BaF_2 (111) Single Crystal Surfaces Against (0001) Sapphire in a Wide Environmental Regime, by SEM Tribometry 373

3.5 The Tribological Behavior of Polycrystalline, CVD Diamond Films 386

3.5.1 Environmental and Purity Effects 386
3.5.2 Large Area Deposition and Polishability of Thick Films 420
3.5.3 Fluorination of CVD Diamond Films 428
3.5.4 Overall Conclusions and Recommended Future Work 447

4.0 CONCLUSIONS 453

5.0 REFERENCES 455

APPENDICES (ATTACHED SEPARATELY IN VOLUME 2)

APPENDIX A – W.A. Goddard III, "Atomic Level Modeling of the Chemical and Tribological Properties of Ceramic Surfaces," Final Report, California Institute of Technology, Pasadena, CA, 17 February 1988; Hughes P.O. S9-225147-237, Rev. A A1-A33

APPENDIX B – U. Landman, "Microscopic Modeling of Tribological Phenomena," Final Report, Georgia Institute of Technology, Atlanta, GA, Hughes P.O. S9-512917-SKG B1-B35

APPENDIX C – S. Granick, "Assessment of the Usefulness of Direct Force Methods to Elucidate the Adhesion and Tribology of Solid Lubricated Ceramics," Final Report, U. of Illinois, Urbana-Champaign, IL, October 23, 1989; Hughes P.O. M9-515286-Z6L C1-C25

APPENDIX D – J.-M. Martin, and Th. Le Mogne, "Friction of Hexagonal Boron Nitride in Various Environments," Final Report, Ecole Centrale de Lyon/SORETRIB, Lyon, France, Feb. 1990; Hughes P.O. S9-317657-SKD D1-D154

APPENDIX E – J.-M Martin, Th. Le Mogne, H. Montes, and M.N. Gardos, "Tribochemistry of Alpha Silicon Carbide Under Oxygen Partial Pressure," Proc. 5th Int. Congress on Tribology, EUROTRIB '89, Paper S2. 5/5, June 12-15, 1989, Helsinki, Finland E1-E6

APPENDICES (ATTACHED SEPARATELY IN VOLUME 2) (Concluded)

		Page
APPENDIX F	– J.J. Erickson, "Meeting at MRL Re: SEM Cryogenic Tribotester,: Hughes Interdepartmental Correspondence No. 7641.20/1076, 30 November 1987	F1-F4
APPENDIX G	– L. Fiderer, "Unique Friction and Wear Tester for Fundamental Tribology Research," Hughes Technical Internal Correspondence No. 867282.00/920, 22 September 1986	G1-G44
APPENDIX H	– J.P. Harrel, "Tribotester Structural Analysis," Hughes Interdepartmental Correspondence No. 867282.20/930, 29 October 1986	H1-H15
APPENDIX I	– R. Williams, "Thermal Analysis of the Tribotester Test Fixture," Hughes Interdepartmental Correspondence No. 7735.10/234, 09 September 1986	I1-I12
APPENDIX J	– B.L. Soriano, "Room Temperature Friction and Wear Testing for Bare Ceramic Contacts," Hughes Interdepartmental Correspondence No. 7621.12/121.87, 02 November 1987	J1-J35
APPENDIX K	– H. Kaplan, "Summary Report on Infrared Pyrometer Selection," Honeyhill Technical Co., Norwalk, CT, 01 August 1986, Hughes P.O. S9-245763-Z6X	K1-K5
APPENDIX L	– PYROLASER Description and Specifications, Pyrometer Instrument Co., Inc., Northvale, NJ, Tech. Bulletin	L1-L3
APPENDIX M	– W.O. Winer, "Tester 2A," technical letter to M.N. Gardos (Hughes) from the Georgia Institute of Technology, 13 April 1987	M1-M5
APPENDIX N	– H. Heshmat, "Rotor and Structural Dynamic Analysis and Assessment of Hughes Tribotester 2A," Technical Report, Mechanical Technology, Inc., Latham, NY, Hughes P.O. S9-266415-S7H	N1-N87
APPENDIX O	– H. Heshmat, P. Albrecht, and J.F. Dill, "Friction and Wear Testing of Ceramic Materials," Final Report, MTI Report No. 90TR1, Mechanical Technology, Inc., Latham, NY, Hughes P.O. S9-316055-SAC	01-087

APPENDICES (ATTACHED SEPARATELY IN VOLUME 3)

APPENDIX P	– N.H. Harris, "Phase Equilibria Relevant to the Tribological Fundamentals of Solid Lubricated Ceramics," Hughes Materials Science Dept. Report (Div. 76), Hughes Aircraft Co., El Segundo, CA, 13 March 1986	P1-P28
APPENDIX Q	– J.-M. Martin, Th. Le Mogne and M.N. Gardos, "Friction of Alpha Silicon Carbide Under Oxygen Partial Pressure: High Resolution Analysis of Interface Films," Proc. Jap. Int. Tribology Conf., Oct. 29 – Nov. 1, 1990, Nagoya, Japan	Q1-Q6
APPENDIX R	– J.-M. Martin, and Th. Le Mogne, selected Monthly Reports on α-SiC, ranging from Feb. 1988 to June 1988, Ecole Centrale de Lyon/SORETRIB, Lyon, France, Hughes P.O. S9-507874-SRW	R1-R50

APPENDICES (ATTACHED SEPARATELY IN VOLUME 3) (Continued)

Page

APPENDIX S – J.-M. Martin, "AES/XPS Analysis of Silicon Carbide Tribofilms," Progress Report, Ecole Centrale de Lyon/SORETRIB, Lyon, France, 27 October 1989, Hughes P.O. S9-507874-SRW..... S1-S17

APPENDIX T – B. Wong, "Assessment of Sharp and Spherical Indentation Techniques," Hughes Avoid Verbal Orders (AVO) Memo, 25 July 1986..... T1-T11

and

B. Wong, "Indentation for Tribocontact Fracture Characterization and Analysis," Hughes Interdepartmental Correspondence No. 7641.20/770, 06 January 1987..... T12-T35

APPENDIX U – B. Wong, "High-Speed Contact Failure and Microindentation," Hughes Interdepartmental Correspondence No. 7641.20/804, 27 February 1987..... U1-U26

APPENDIX V – G.D. Eisenbrand, "Status Report: Hertzian Cone Cracking Apparatus," Hughes Interdepartmental Correspondence No. 7621.13, 27 June 1986..... V1-V15

and

B. Billington, "Hertzian Stresses," Hughes Avoid Verbal Orders (AVO) Memo. 31 October 1986..... V16-V23

APPENDIX W – R.G. Hardistry, "Materials Removal Rate; Silicon Nitride Materials; Base-Data," Final Report, Spheric Special Products Report No. 1.015, Spheric, Inc., W. Sussex, England, 04 September 1989; Hughes P.O. M9-317643-KKD..... W1-W11

APPENDIX X – J.-M. Martin, and Th. Le Mogne, selected Monthly Reports on α-SiC, ranging from Dec. 1987 to March 1989, Ecole Centrale de Lyon/SORETRIB, Lyon, France, Hughes P.O. S9-317657-SKD... X1-X43

APPENDIX Y – H. Heshmat, "High Temperature Solid Lubricated Bearing Development - Dry Powder Lubricated Traction Testing," Proc. 26th Joint AIAA/SAE/ASME Propulsion Conf. Paper No. 90-2047, 16-18 July 1990, Orlando, FL..... Y1-Y8

APPENDIX Z – C. Schmutz, "Characterization of TiO_{2-x} Layers," CSEM Technical Report No. 232, Project No. 51.312, CSEM, Neuchatel, Switzerland, Hughes P.O. S9-507875-SRW. Nov, 1988..... Z1-Z30

and

H. Boving, "Generation of TiO_2-Rutile Coatings and their Tribological Characterization," CSEM Technical Report No. 307, Project No. 51.207, CSEM, Neuchatel, Switzerland, Hughes P.O. S9-318804-SAC, November, 1988..... Z31-Z82

APPENDICES (ATTACHED SEPARATELY IN VOLUME 3) (Concluded)

Page

APPENDIX AA – B.G. Bovard, S. Chiao, and H. Angus Macleod, "Deposition of Titanium Oxide Films of Controlled Stoichiometries," Final Report, U. of Arizona Optical Sciences Center; Tucson, AZ, Hughes P.O. M9-315734-KKD..... AA1-AA18

APPENDIX BB – K.V. Ravi, et al. "Thin Film Diamond Deposition on Silicon Wafers for Tribological Testing," Final Report (Phase I), Crystallume, Palo Alto, CA, 29 December 1987, Hughes P.O. P9-519308-SLX..... BB1-BB37

APPENDIX CC – L.S. Plano, S. Yokota, and K.V. Ravi, "Thin Film Diamond Deposition on Sapphire and Silicon Carbide for Tribological Testing", Crystallume, Menlo Park, CA, 30 June 1988, Hughes P.O. P9-519308-SLX..... CC1-CC16

APPENDIX DD – L.S. Plano, S. Yokota, and K.V. Ravi, "Thin Film Diamond Deposition on Silicon Carbide," Crystallume, Menlo Park, CA, 12 September 1988..... DD1-DD12

APPENDIX EE – R.W. Seibold, Hughes technical letter to Dr. K.V. Ravi of Crystallume, with data package on surface evaluation of HAC-GLAS disc prior to diamond coating, 8 August 1988..... EE1-EE26

APPENDIX FF – B.L. Soriano, and B. Buller, "HAC-GLAS 13-2 Optical Diamond Coating – Characterization and Polishing," Hughes Technical Internal Correspondence No. 7621.12/13, 21 February 1989..... FF1-FF30

APPENDIX GG – M.N. Gardos, "Graphite Fiber Reinforced Glass-Ceramic Composite Materials – Program Summary and Status Report".... GG1-GG14*

and

B.L. Soriano, "HAC-GLAS 13-2 Substrate-Diamond Coating Characterization and Polishing"; viewgraph handouts of presentations given at the Diamond Initiative Planning Meeting, U. of A Optical Sciences Center, Tucson, AZ, 23 February 1989..... GG1-GG29

APPENDIX HH – P.G. Magallanes, "Crystallume Diamond Films—Analysis by FTIR," Hughes Analytical Chemistry Laboratory Memo, Materials Science Dept. (Div. 76), Hughes Aircraft Co., El Segundo, CA, 18 December 1988..... HH1-HH5

and

P.G. Magallanes, "Wide Wavelength Spectrum of Diamond Film" Hughes Analytical Chemistry Laboratory Memo, Materials Science Dept. (Div. 76), Hughes Aircraft Co., El Segundo, CA 02 March 1989..... HH6-HH12

APPENDIX II – J.L. Margrave, R.H. Hauge, and R.B. Badachhape, "Oxidation and Fluorination Studies of Diamond," Program Report, Rice

* Pages GG2 through GG14 are deleted due to ITAR regulations.

FIGURES

Figure		Page
1	Hierarchy of tribology models in the space-time continuum (after Professor W.W. Goddard III, California Institute of Technology)	3
2	Model of contacting, solid lubricated ceramic surfaces under normal load, tangential shear and environmental stresses	5
3	Program structure and activities	7
4	Sheared slabs of hydrogen-terminated (111) vs. ($\bar{1}\bar{1}\bar{1}$) diamond surfaces displaced against each other; (a) the periodic boundary conditions of each slab; (b) schematic representation of the sheared system under load (lengths of interplanar sp^3 bonds are exaggerated for clarity)	26
5	Static and dynamic energy surfaces of diamond (111) vs. ($\bar{1}\bar{1}\bar{1}$); (a) no normal load; (b) minimum energy path (see text for explanations)	27
6	Schematic of the MD calculational cell. N_{LA} is the number of layers in the A (hard) material and N_{LB} the number of layers in the B (soft) material. The interface is between N_{LA} and $N_{LA}+1$. The directions of the applied load and shear stresses are indicated. Three dimensional periodic boundary conditions are employed in the simulations	31
7	Critical issues associated with the adhesion of solid lubricant films	39
8	Critical issues of friction provided by solid lubricant films	39
9	Critical issues of solid lubricant film and ceramic substrate wear	41
10	Load-speed map of commonly used bearing elements (1000 psi = 6.8948 MPa; 1 in $\cdot s^{-1} = 2.54 \times 10^{-2}$ m$\cdot s^{-1}$)	43
11	The schematic of the Ecole Centrale de Lyon/SORETRIB Auger(AES)/XPS tribometer; (a) the rotating/oscillating pin-flat combination; (b) overall view	44
12	Engineering drawings of the Ecole Centrale de Lyon/SORETRIB Auger(AES)/XPS tribometer pin and disc/flat specimens	45
13	MRL, Inc., high temperature SEM Knudsen cell-like enclosures for controlled atmosphere reactions (courtesy of Dr. Jack R. Alonzo, MRL, Inc., North Branch, NJ))	47
14	Schematic representations of the Hughes high-temperature SEM (HT-SEM) tribometer; (a) overall view with Knudsen cell lid in place; (b) 3-D cutaway view with lid removed	48

FIGURES (Continued)

Figure		Page
15	Schematics of HT-SEM pin and flat specimen combinations and their specimen holders; (a) pin assembly; (b) flat installed in thermally isolated heater block; (c) stationary pin vs. oscillating flat assembly with gas inlet near the contact zone.....	50
16	Engineering drawings of the HT-SEM pin and flat specimens.....	52
17	Polished, single crystal sapphire pins (90°; pin axes normal to (0001) basal plane) and as-cut (unpolished) flats (0°; 5 mm x 7 mm plane is cut on (0001) basal plane).....	53
18	Schematics of the normal load/friction force transfer arm of, and typical friction data provided by, the HT-SEM tribometer; (a) the double-parallel-springs transducer with the installed pin; (b) typical friction trace and method to calculate average friction force.....	54
19	Photograph of the HT-SEM tribometer with the lid removed (for description of parts, refer to Figures 14 through 18 and the text).....	56
20	The HT-SEM tribometer with the Knudsen cell lid removed, attached to a removable SEM chamber door.....	57
21	The HT-SEM tribometer with the Knudsen cell lid installed, attached to a removable SEM chamber door.....	58
22	HT-SEM tribometer specimen alignment, transducer calibration and equipment check-out, before test.....	59
23	Fully assembled HT-SEM tribometer in differentially pumped/gas backbleed mode, attached to auxiliary support cart housing the tribostage electronics, temperature/normal load/friction force chart recorder, and vacuum pump for evacuation of the differentially pumped, partial gas pressure-containing Knudsen cell (computerized data acquisition system not shown).....	60
24	Data logging and analysis scheme.....	61
25	Data acquisition by computer and chart recorder; (a) computer-logged, real-time trace of oscillatory friction force also showing automatic friction averaging calculation technique, (b) the identical trace taken from the recorder chart, along with temperature and normal load data.....	62
26	Sample mounting configuration of a liquid helium-cooled stationary SEM stage: 1, electron beam; 2, sample; 3, sample holder; 4, clamping screw; 5, copper ring for wire heat sinking; 6, thermal shield; 7, LHe tank; 8, clamping ring; 9, indium seal; 10, LHe tubes; from (47).....	65
27	The Hexland CT 1000A cryostage with modification for housing the 7 mm x 5 mm x 2 mm triboflat.....	65
28	Schematic of the Cryo-SEM tribometer.....	66

FIGURES (Continued)

Figure		Page
29	Sideview photographs of (a) the transducer/friction transfer arm assembly housing the insulated pin holder and the orthogonal strain gage flex plates (normal load and friction force transducers) -- motor and sliding weight assembly not shown, and (b) the oscillating cryostage and drive/sample positioning systems -- LN_2 transfer lines not shown	67
30	Photographs of the cryogenic SEM tribometer in various stages of assembly: (a) bottom of the Knudsen cell subchamber, (b) the pin-flat mechanical assembly (see 29) installed into the Knudsen cell bottom and onto the door bracket; and (c) the SEM door assembly (Knudsen cell chamber attached to the other side of the door is hidden from view) with the cryogenic LN_2 Dewar	69
31	Specimen contact schematics of (a) the NTN-Bower RCF-tester, and (b) the Tester 2A	72
32	Overall layout of the Tester 2A: (a) top view, (b) side view of the portable test stand	73
33	Photographs of the Tester 2A: (a) oblique side view; (b) data logging and analysis computer	75
34	Rubshoe and holder schematics; (a) different types of rubshoes and a metallic rubshoe holder for room temperature tests, and (b) thermally insulating ceramic (MACOR®) rubshoe holder with metallic holding fixture for high temperature tests	76
35	Engineering drawing of regular size and undersized RCF rods	77
36	Engineering drawings of flat and cylindrically convex rubshoes	78
37	Engineering drawing of simplified flat rubshoes	79
38	Engineering drawings of spherical and cylindrically concave rubshoes	80
39	Brassboard set-up of a Tester 2A friction transfer arm: (a) steady-state loading spring only, (b) loading spring and vibratory load transducer	82
40	Engineering drawing of the Tester 2A spindle	83
41	Mechanism details of the Tester 2A: (a) top view, (b) side view	84
42	Typical friction and wear traces of a room temperature Tester 2A experiment: (a) normal applied load (F_y), friction force (F_x), and the calculated coefficient olf kinetic friction (F_x/F_y), measured as a function of test duration	86
43	Typical friction and wear traces of a high temperature Tester 2A experiment: (a) normal load applied load (F_y), friction force (F_x) and the calculated coefficient of kinetic friction (F_x/F_y), measured as a function of test duration	89

FIGURES (Continued)

Figure		Page
44	Typical rubshoe thermocouple and Vanzetti pyrometer temperature read-out traces of a high temperature Tester 2A experiment	90
45	Surface temperature as the function of emissivity with the Vanzetti I.R. pyrometer: (a) computer-generated data analysis plots at 60% lamp power, (b) emissivity vs. temperature function at 60% power	93
46	Analyzed normal total emittance of silicon monocarbide (63)	94
47	Calibration and surface temperature measurement schematics with a laser pyrometer; from (64)	95
48	The PRYOLASER®installed into the Tester 2A	97
49	The average emissivity of α-SiC at λ= 0.865 μm; from (63)	99
50	The new antireflection aperture plate for the Tester 2A	101
51	Basic loading mechanism concepts of the Tester 2A: (a) candidate designs; (b) selected concept	104
52	Tester 2A-induced frictional variations: (a) as estimated by Professor Ward O. Winer (Georgia Tech), (b) as refuted by Mr. Leo Fiderer (Hughes), the designer of Tester 2A, with hypothesized contact force vectors	105
53	Run-out-caused friction variations: (a) maximum dynamic friction force [{f_d(max.)] as a function of (sin ωt) orbital motion	107
54	Overall sideview layouts of the MTI (a) high PVT pin-on-disc sliding (friction) tester, and (b) high PVT disc-on-disc rolling (traction) tester (83)	114
55	Engineering drawings of the MTI high PVT pin-on-disc tester specimens: (a) pin, (b) disc (83)	115
56	The effect of speed on the sliding velocity pattern in the Hertzian contact zone of a radial ball bearing, after (85)	117
57	Conceptual schematics of (a) perpendicular, and (b) parallel shaft traction test designs; self-lubricating composite specimens shaded	119
58	The Battelle Ball Bearing Simulator (89, 90)	119
59	Schematics of slip velocity gradients or disc-on-disc traction test configurations, as compared to those of a ball bearing	120
60	Size and shape of the traction coefficient as a function of pure rolling vs. rolling-spinning in a ball bearing, from (86)	120

FIGURES (Continued)

Figure		Page
61	Stacking sequence of 6H polytype of α-SiC; (a) side view; (b) top view (94)	127
62	Pieces of α-SiC reactor core aggregate formed by the Acheson process: (a) from ESK, W. Germany, and (b) from Carborundum, in the U.S	129
63	Single crystal α-SiC pieces removed from the ESK reactor core aggregate shown in Figure 62a, by diamond saw cutting	132
64	SiC processing by the Acheson process, from (97)	133
65	A ball-spoke model of the (hexagonal) α-SiC basal planes depicting dangling bonds on the Si (0001) and C (000$\bar{1}$) sides	135
66	SORETRIB Auger (AES)/XPS tribometer friction traces of α-SiC vs. itself in (a) vacuum, and (b) 50 Pa P_{O_2}	137
67	AES spectra of the α-SiC at the end of the P_{O_2} test, from (a) inside the wear scar, and (b) outside the wear scar (also see 66)	137
68	Pin and flat wear scars associated with the data in Figures 66 and 67	138
69	Test tracks of 2 ea. vacuum tests and 2 ea. P_{air} tests with the Hughes SEM Tribometer; for the associated test data, see Figures 70 and 71	139
70	SEM tribometer coefficient of friction (COF) data with α-SiC vs. itself as a function of temperature in a vacuum (1.33×10^{-2} Pa = 1×10^{-5} torr) environment: (a) Test track No. 1 (Figure 69), (b) Test track No. 2 (Figure 69)	140
71	SEM tribometer coefficient of friction (COF) data with α-SiC vs. itself, as a function of temperature, in a P_{air} (13.3 Pa = 0.1 torr) environment. Test track No. 4 (Figure 69), compared with the vacuum data in Figure 70a	141
72	Microstructure of sinter-HIP and fully can-HIP Ekasic® α-SiC by ESK	145
73	Microstructure of pressureless-sintered Hexoloy® SA-80T α-SiC by Carborundum (formerly SOHIO Engineered Materials)	146
74	Normalized mean wear rates of the α-SiC materials at R.T. and H.T.; Tester 2A	150
75	Rod/rubshoe wear scars, starting average Hertz stress and volume wear of an ESK α-SiC (fully can-HIP) R.T. test, Tester 2A	151
76	Rod/rubshoe wear scars, starting average Hertz stress and volume wear of an ESK α-SiC (fully can-HIP) H.T. Test; Tester 2A	152

FIGURES (Continued)

Figure		Page
77	Mean flexural strength of fine and coarse grain α-SiC as a function of test temperature (109)	156
78	Oxidation of the ternary system Al-Si-C: a schematic quarternary phase diagram (courtesy of Dr. Irwin L. Singer, NRL)	158
79	Various ceramic powder consolidation processes (also used for α-SiC), involving hot-isostatic pressing (HIP); (119).	160
80	The effect of temperature on the flexural strength of variously prepared, α-SiC, 4-point bending strength specimens (120)	161
81	The effect of consolidation methods on the thermal conductivity of α-SiC (120)	161
82	The oxidation kinetics of SiC and Si_3N_4 (136,137)	164
83	Oxidative weight gain vs. time functions of various ceramic materials (139)	165
84	Weight loss of B_4C/graphite and B_4C/SiC/graphite (3 hours exposure, flowing steam-saturated argon); from (139)	165
85	SEM photomicrographs of as-polished, α-SiC Tester 2A rubshoe surfaces: (a) ESK fully can-HIP (rubshoe No. ESKF-H1), (b) ESK sinter-HIP (rubshoe No. ESKF-P1), and (c) Hexoloy SA-80T (rubshoe No. SASCF-2)	167
86	SEM photomicrographs of the used (R.T.) 85a (ESK-HIP) rubshoe wear scar: (a) the wear scar, with arrows indicating the direction of sliding, (b) middle of wear scar, (c) and (d) edge of wear scar at the outlet region, depicting cracked glassy layer	168
87	SEM photomicrographs of the used (R.T.) 85b (ESK-HIP) rubshoe wear scar: (a) the wear scar, with arrows indicating the direction of sliding, (b) unused portion adjacent to wear scar with little evidence of accumulated glassy layer, (c) and (d) middle of wear scar	169
88	SEM photomicrographs of the used (R.T.) 85c (Hexoloy) rubshoe wear scar: (a) the wear scar, with arrows indicating the direction of sliding, (b) middle of wear scar, (c) and (d) edge of wear scar at the outlet region, depicting cracked glassy layer	170
89	The elastic moduli of fused quartz as a function of hydrostatic pressure; C_{11} = longitudinal, G = transverse (shear) and K = bulk moduli (147)	171
90	Decrease in the magnitude of the applied load needed for surface crack initiation as a function of silica glass scale thickness on Al_2O_3-SiC composite (151)	171
91	Time-to-failure predictions of NC-132 HPSN tribocontacts containing various initial surface cracks, under high speed motion; assumed operating temperature = 617°C	176

FIGURES (Continued)

Figure		Page
92	Selected physical properties of the Cercomp® h-BN/Si_3N_4 composites as a function of h-BN content (184)	182
93	Selected physical properties of the Cercomp® h-BN/Si_3N_4 composites as a function of temperature (184)	183
94	Strength vs. orientation of hot-pressing direction, with HPSN (data from the Norton Co.)	185
95	The validity of the Evans-Wilshaw wear relationship with a variety of HP/HIP Si_3N_4 ceramics	190
96	Selected properties of CVD h-BN by Atomergic Chemetals Corp., Plainview, N.Y., from (204)	195
97	Shapes of CVD h-BN molds obtained from Atomergic Chemetals Corp	196
98	Close-up of a fractured CVD h-BN disc, indicating layered, onionskin-like structure	197
99	Directionally machined pins and flats from the anisotropic Combat® BN and Cercomp® h-BN/Si_3N_4 compositions	200
100	Selected area (electron) diffraction (SAD) pattern of the CVD h-BN plate with the electron beam normal to the mold surface, with the corresponding bright field image, indicating random crystallite orientation	202
101	Electron diffraction patterns from the CVD h-BN plate's sample flake: (a) large volume sample showing more-less random orientation, and (b) lattice fringes of flake portion with the flake crystallite's c-axis parallel with the surface, (i.e., the basal planes are normal to the mold surface); notice excellent resolution of the 3.3Å lattice spacings of the h-BN layers	203
102	The friction behavior of variously treated, Combat® "flat" (=) and "edge" (⊥) samples in various atmospheric environments, at room temperature (XPS/AES tribometry, computer-averaging f_k data as a function of the number of oscillatory passes):	210
102 (a)	Rinsed vs. annealed (=) specimens in 10^{-8} Pa UHV;	210
102 (b)	Rinsed vs. annealed (⊥) specimens in 10^{-8} Pa UHV;	211
102 (c)	"Flat" (=) vs. "edge" (⊥) specimens in 10^{-8} Pa UHV;	212
102 (d)	"Flat" (=) vs. "edge" (⊥) and "flat" (=) vs "flat" (=) combinations in 10^{-8} Pa UHV and atmospheric air;	213
102 (e)	"Flat" (=) vs. "flat" (=) in 10^{-8} Pa UHV, 1.33 x 10^{-3} Pa H_2O and 13.3 Pa N_2;	214

FIGURES (Continued)

Figure		Page
102 (f)	"Flat" (=) vs. "flat" (=) in 10^{-8} Pa UHV, 13.3 Pa O_2 as well as 1.33 x 10^{-3} Pa and atmospheric air;	215
102 (g)	"Flat" (=) vs. "flat" (=) in 10^{-8} Pa UHV, 1.33 x 10^{-3} Pa and 13.3 Pa CO and 1.33 x 10^{-3} Pa and 13.3 Pa C_3H_8	216
103	Tester 2A test matrix and data of the 40% h-BN containing Cercomp® and 100% h-BN Combat ® BN; two white blocks (h-BN vs. h-BN) signify single transfer h-BN wear; one white/one black (h-BN vs. α-SiC vs. α-SiC; bold-face number on the bottom of each set is the wear rate in $m^3/N•m$; the plain-face number on top is t he apparent shear strength in MPa, calculated on the basis of the projected wear scar area on each rubshoe block	221
104	Wear rate differences between single transfer, 40% vs. ~100% h-BN rubshoe wear; R.T. (=) tests	222
105	Coefficient of friction (COF) charts for the R.T. single-transfer tests in Figure 103 (Test Nos. CBNP-1/BNFB-1)	223
106	Room temperature (R.T.) double-transfer of ~100% h-BN (Combat® BN) to α-SiC	225
107	Room temperature (=) double transfer friction traces for ~100% h-BN and α-SiC	226
108	Room temperature, time-dependent wear rates of the (=) single and double-transfer ~100% h-BN blocks	227
109	Appearance of (=) h-BN-containing Si_3N_4 and mating α-SiC rubshoes after R.T. and high temperature double-transfer tests	228
110	Appearance of (⊥) h-BN-containing Si_3N_4 and mating α-SiC rubshoes after high temperature double-transfer test	229
111	Coefficients of friction (COF) charts for the high temperature (=) vs. (⊥) double-transfer film tests	230
112	Coefficients of friction (COF) charts for R.T. vs. high temperature (=) double-transfer film tests	232
113	Hardness and thermal conductivity comparison of α-SiC and Si_3N_4	237
114	SEM photomicrograph of natural molybdenite crystal edge sites (211)	239
115	Gänsheimer's schematic on the lubrication properties of partially oxidized MoS_2 film (214)	240
116	Large, natural molybdenite crystal (provided by Mr. Thomas J. Risdon of AMAX/Climax, Ann Arbor, MI), cleaved in liquid nitrogen at Hughes	242

FIGURES (Continued)

Figure		Page
117	SEM photomicrographs of natural molybdenite flake (a) before and (b) after oxidation for 5 minutes, in 133 Pa = 1.0 torr O_2 at 850°C, on the hot-stage of the MRL, Inc. environmental-SEM Knudsen-cell (see Figure 13)	243
118	Salient features of the oxidized flake in 117 by SEM photomicrography: (a) close-up of MoS_2 flake (see arrow) entirely converted to molybdenum oxides, in layers; (b) preferential oxidation at basal plane scratches, step-sites and point defects	244
119	High magnification SEM photomicrographs of oxidized basal plane edge sites from Figure 117 (a) before and (b) after exposure to 1.33 x 10^{-3} Pa = 1x10^{-5} torr/850°C, for 10 seconds	245
120	Room temperature and elevated-temperature-ramped friction traces for The Aerospace Corporation's 200 nm thick AT/MoS_2 film on α-SiC sliding against a XTL sapphire pin	249
121	Room temperature friction traces for The Aerospace Corporation's 200 nm thick AT/MoS_2 film on α-SiC with and without a Mo underlayer, sliding against a XTL sapphire pin	250
122	Room temperature and elevated-temperature-ramped friction traces for The Aerospace Corporation's 200 nm thick AT/MoS_2 film on 17-4 PH(H900) steel (R_C40), sliding against a XTL sapphire pin	251
123	Thermograms of MoS_2 powder/Ni and MoS_2 powder/Ag composites in high temperature air (223)	255
124	Room temperature and elevated-temperature-ramped friction traces for the NRL 240 nm thick IBAD-MoS_2 film on α-SiC, sliding against a XTL sapphire pin	257
125	SEM photomicrographs of the Aerospace Corporation's 200 nm RF-AT MoS_2 film with Mo underlayer (higher mag. photos of Wear Track No. 4, R.T. test)	258
126	SEM photomicrographs of the used, NRL 240 nm IBAD-MoS_2 film with BN underlayer (higher mag. photo of Wear Track No. 1, R.T. test, also see 124)	259
127	SEM photomicrographs of the used, NRL 240 nm IBAD-MoS_2 film with BN underlayer (higher mag. photos of Wear Track No. 4, H.T. test, also see 124)	260
128	SEM photomicrographs of the new, NRL 240 nm IBAD-MoS_2 film with BN underlayer, depicting blistering and silver globules on the triboflat edges	261
129	TGA of $NiCl_2$-intercalated graphite powders (also see Table 31)	265
130	TGA of $CrCl_3$-intercalated graphite powders (also see Table 31)	266
131	TGA of $CdCl_2$ and $CuCl_2$ intercalated graphite powders and TGA of such powders mixed with Cu powder (also, see Table 31)	267

FIGURES (Continued)

Figure		Page
132	Expanded TGA of selected, metal chloride intercalated graphite powders in the low weight loss regime (also see Table 31)	268
133	DSC of $NiCl_2$-intercalated graphite powders (also see Table 31)	270
134	DSC of $CrCl_3$-intercalated graphite powders (also see Table 31)	271
135	DSC of $CdCl_2$ and $CuCl_2$ intercalated graphite powders and DTA of such powders mixed with Cu powder (also see Table 31)	272
136	Schematic of staging in intercalated graphites; interlayer stacking of adjacent graphite planes remains AB AB as in pure graphite, although the stacking order can change across the intercalated layers, as indicated	273
137	Mechanism for transition between stages according to the Daumas-Herold domain model (230)	275
138	TGA of $NiCl_2$-intercalated graphite mold sites and starting powder (p = powder; ms = mold surface; mc = mold center)	278
139	TGA of $CrCl_3$-intercalated graphite mold sites and starting powder (p = powder; ms = mold surface; mc = mold center)	279
140	TGA of $CdCl_2$-intercalated graphite mold sites and starting powder (p = powder; ms = mold surface; mc = mold center)	280
141	DSC of $NiCl_2$-intercalated graphite mold sites and starting powder (p = powder; ms = mold surface; mc = mold center)	281
142	DSC of $CrCl_3$-intercalated graphite mold sites and starting powder (p = powder; ms = mold surface; mc = mold center)	282
143	TGA of $CrCl_3$-intercalated graphite mold sites and starting powder (p = powder; ms = mold surface; mc = mold center)	283
144	SEM photomicrographs of the used $CdCl_2/NiCl_2$-intercalated HOPG triboflats; numbers refer to Test and/or Test Track (Wear Scar) number	285
145	Wear scar width development on $CdCl_2/NiCl_2$-intercalated HOPG triboflats during the respective second tests (see Track No. 2's in Figure 144)	286
146	Average coefficients of friction (COF) of $CdCl_2/NiCl_2$-intercalated HOPG triboflats during the respective second tests (see Track No. 2's in Figures 144 and 145)	287
147	Average coefficients of friction (COF) and apparent surface shear strength (τ_S) of $CdCl_2/NiCl_2$ intercalated HOPG triboflats during the respective (R.T.) first tests (see Track No. 1's in Figure 144)	288

FIGURES (Continued)

Figure		Page
148	Average coefficients of friction (COF) and apparent surface shear strength (τ_S) of $CdCl_2/NiCl_2$-intercalated HOPG triboflats during the respective heated second tests (see Track No. 2's in 144)	289
149	Average coefficients of friction (COF) and apparent surface shear strength (τ_S) of $CdCl_2/NiCl_2$-intercalated HOPG triboflats during the respective (R.T.) first tests (see Track No. 3's in 144)	290
150	SEM photomicrographs of $CdCl_2$/HOPG transferred to the tip of the XTL sapphire pin, after all three tests	292
151	SEM photomicrographs of the Test No. 1/2/3 $CdCl_2$/HOPG wear tracks (from Figure 144), at 75x to 100x magnifications	293
152	SEM photomicrographs of the Test No. 1/2/3 $CdCl_2$/HOPG wear tracks (from Figures 144 and 151), at 200x magnification	294
153	SEM photomicrographs of the $CdCl_2$/HOPG Test Track No. 3 at 1000x magnification, showing run-in alignment of the flat crystallites	295
154	SEM photomicrographs of the Test No. 1/2/3 $NiCl_2$/HOPG wear tracks (from Figure 144), at 100x to 200x magnifications	296
155	SEM photomicrographs of the $NiCl_2$/HOPG Test Track No. 3 at 200x to 500x magnifications	297
156	EDX spectra of used $CdCl_2$/HOPG triboflat sites on Test Track No. 3	299
157	SEM photomicrographs and EDX spectra of new $NiCl_2$/HOPG triboflat showing contamination with $CrCl_3$	300
158	EDX spectra of used $NiCl_2$/HOPG triboflat sites on Test Track No. 3, showing contamination with $CrCl_3$	301
159	SEM photomicrographs depicting the topography of a small flake of h-BN cleaved from the broken mold shown in 98	302
160	SEM photomicrographs of the flake shown in 159, exposed to 650°/850°C/0.1 torr environments in the MRL Inc. environmental SEM cell previously shown in 13	303
161	The effects of oxygen vacancies on the shear strength, electrical conductivity and weight loss of rutile (TiO_{2-x}): (a) shear strength (τ_S) of rutile, changing with oxygen stoichiometry and the consequent formation of Magnèli phases (13); and (b) electrical conductivity and weight loss, changing with oxygen stoichiometry and the consequent formation of Magnèli phases (233, 234)	305

Figure		Page
162	Close-packed billiard-ball model of the (100) plane of rutile: (a) the (011)1/2[011], stoichiometric antiphase boundary (APB); (b) lamellae of α-PbO_2-type and rutile microtwin produced by repeating the APB operation on every second or every (011) oxygen plane; and (c) a family of Ti_nO_{2n-1} crystallographic shear (CS) planes aka. Magnèli phases (n=5), derived by the operation (132)1/2[011]; from (235)	308
163	High resolution electron microscopy (HREM) of TiO_{2-x}: (a) a 500 kV [111] HREM image of (132) CS plane in $TiO_{1.9965}$; note single (S) and pairs (P) of CS planes; associated pairs are labeled 1 through 5, in order of increasing separation, and (b) 500 kV image of $TiO_{1.9965}$ showing lamellar (132) CS planes (A); also note hairpin defects (B and C); from (236)	309
164	Schematic representations of CS plane structures: (a) interconversion of [100] and (132) [010]-type CS-plane-pair linear defects, and (b) bounded projection along [010] for the rutile structure containing a pair of (121), and pairs of (253), (132) and (143) CS planes; from (236)	310
165	Average coefficients of kinetic friction (COF) of (001) [110] rutile as a function of SEM tribometer test cycles, temperature and atmosphere during the three tests reported in (14)	312
166	Estimation method for τ_S as a function of single crystal (XTL) rutile stoichiometry, using the F_k values of Test No. 3 in 165 and $A_{app.} \cong A_r$ as reported in (14), also see Figure 168	313
167	Average coefficients of kinetic friction (COF) of polycrystalline (poly-XTL) rutile as a function of SEM tribometer test cycles, temperature and atmosphere during three test runs identical to the ones described in Figure165, per the methodology reported in (14)	314
168	SEM photomicrographs of identically SEM-tribotested portions of the single crystal (XTL) and polycrystalline (poly-XTL) rutile flats, at various magnifications	316
169	Linear wear scar width increase of the polycrystalline (poly-XTL) rutile flat during Test No. 3 (measured by video), with corrections incorporated by post-test SEM photomicrography, also see Figure 168	319
170	Estimation method for τ_S as a function of polycrystalline (poly-XTL) rutile stoichiometry, using the Fk values of Test No. 3 in 167 and the wear scar widths from Figure 169	320
171	Theoretically dense, centrifugal rutile compact produced after approximately 4 hrs at 1000°C. The grain size is about 1.9 μm or ≥5 times the original particle size; from (237)	321
172	X-ray diffractograms of (a) Kyocera's TiO_2, (fired), (b) Cercom's TiO_2 (as-pressed), and (c) Cercom's TiO_2 (fired), indicating that all three samples consist of rutile	323

FIGURES (Continued)

Figure		Page
173	SEM photomicrographs of the fired (a) Cercom rutile and (b) Kyocera rutile fracture surfaces at 200x and 500x magnifications	324
174	EDX spectra of the fired (a) Cercom rutile and (b) Kyocera rutile, indicating no sintering aid in the former and Al_2O_3/SiO_2 sintering aids in the latter	325
175	Tester 2A friction traces of a rutile rubshoe tested against an α-SiC RCF rod, under standard load/speed conditions, in various atmospheres (Test No. RUTF-1/2, Rubshoe No. 2), also see Figure 176	327
176	Appearance of used Tester 2A rutile rubshoes tested against an α-SiC RCF rod, under standard load/speed conditions, in various atmospheres (Test No. RUTF-1/2), also see Figure 175 for the friction traces associated with the Rubshoe No. 2. contact	328
177	Tester 2A friction traces of rutile rubshoes tested against an α-SiC RCF rod, under standard load/speed conditions, in various atmospheres (Test No. RUTF-3/4, duplicates of Test No. RUTF-1/2, see Figure 175)	329
178	Appearance of used Tester 2A rutile rubshoes tested against an α-SiC RCF rod, under standard load/speed conditions, in various atmospheres (Test No. RUTF-3/4, duplicates of Test No. RUTF-1/2, see Figure 176)	330
179	Correlation of volume wear rate of various ceramics (TiO_2 included), as functions of hardness and fracture toughness; from (239)	331
180	Tester 2A friction traces of Hexoloy-SA80T α-SiC rubshoes tested against a Kyocera rutile RCF rod, under standard load/speed conditions, in various atmospheres, also see Figure 181	332
181	Appearance of used Tester 2A α-SiC rubshoes tested against a rutile RCF rod, under standard load/speed conditions, in various atmospheres, also see Figure 180	333
182	Schematic of rutile film preparation on CVD-TiC-coated AISI 440C steel specimens	336
183	SEM photomicrograph (at 360x) of scratch test wear path of rutile formed on TiC by wet oxidation at 850°C (Type I), at the critical load (L_C in Table 33), where delamination of the oxide began; arrows indicate areas where the layered nature of the smeared and delaminating oxide is evident	338
184	Photographs of IBAD TiN-coated NBD-100 HPSN Tester 2A specimens before tests: (a) stripe-coated RCF rod with coated (1 through 4) and bare (5,6) conforming rubshoes; (b) stripe-coated RCF rod with coated (1 through 4) and bare (5,6) flat rubshoes	341

FIGURES (Continued)

Figure		Page
185	Tester 2A test matrix and data of bare and TiN-coated NBD-100 specimens, at R.T. and H.T., compared with the data associated with Hexoloy SA-80T α-SiC specimens; two white blocks under "bare NBD 100" signify all-Si_3N_4 rubbing combinations and two black blocks under "bare sint. α-SiC" mean all-SiC rubbing combinations; under "TiN-coated NBD-100", one white and one black blocks signify one uncoated and one TiN coated rubshoe sliding against a TiN-coated NBD-100 RCF rod, while two black blocks indicate an all-TiN-coated NBD-100 combination	343
186	Tester 2A average coefficient of friction (COF) data with NBD-100 HPSN vs. itself as a function of temperature (baseline data)	344
187	Tester 2A average coefficient of friction (COF) data at high temperature, with an all-bare-NBD-100 and an NBD-100 system IBAD-TiN coated	345
188	Optical photomicrographs of used NBD-100 HPSN Tester 2A rubshoes operated against a bare, NBD-100 HPSN RCF rod at various temperatures (baseline data)	346
189	Optical photomicrographs of used, bare and IBAD-TiN-coated NBD-100 HPSN rubshoes operated against an IBAD-TiN-coated NBD-100 HPSN RCF rod, at various temperatures	347
190	Schematic representation of the permanent deformation of a crystal by shear force-induced interplanar slip (252)	349
191	Conventional measurement of the critical resolved shear stress (S_{cr}, aka τ_{cr}), by compression of a XTL boule (252)	349
192	Orientation of the CaF_2 (111) tribopin sliding against the CaF_2 (111) triboflat in the [$1\bar{1}0$] direction	351
193	Crystal orientation goniometer used for aligning the tribopin and triboflat for Laue-reflection-aided cutting and polishing; the barrel holder is adjusted in the goniometer, then transferred to a polishing wheel	352
194	Side view of the brass polishing jig for the tribopin	354
195	The 3-cycle, once-over test track pattern on the fluoride triboflats (thin lines) followed by 100 cycles in the same track (heavy line)	356
196	Computer friction traces and method of averaging the coefficients of friction during oscillatory sliding, shown with the corresponding chart recorder friction traces combined with temperature and normal load recording	356
197	The coefficients of friction of the 3-cycle (once-over) and 100-cycle (repeated) test with a CaF_2 pin vs. a CaF_2 flat in the (111)[$1\bar{1}0$] sliding combination	358

Figure		Page
198	The coefficients of friction of the 3-cycle (once-over) and 100-cycle (repeated) test with a BaF_2 pin vs. a BaF_2 flat in the (111)[$1\bar{1}0$]sliding combination	358
199	The coefficients of friction of the 3-cycle (once-over) and 100-cycle (repeated) test with a BaF_2 pin vs. a CaF_2 flat in the (111)[$1\bar{1}0$] sliding combination	359
200	SEM photomicrographs of the 100-cycle wear track of the BaF_2 (pin) vs. CaF_2 (flat) combination, at various magnifications; arrows indicate the boundaries of the wear scar; debris was shown to be transferred BaF_2 particles	360
201	Correlation lines for metals and ionic crystals, relating hardness numbers and yield stresses (254)	362
202	Micro-hardness of XTL (a) CaF_2 and (b) CaF_2, along with poly-XTL silver, as a function of temperature (255)	363
203	Temperature dependence of yield point of CaF_2 single crystals. 1) natural fluorite, 2,3,4) synthetic fluorite containing Sm^{3+}, Sm^{2+}, and Nd, respectively (256)	364
204	Yield point of single crystal CaF_2 as a function of hardness for various temperatures; after (255 and 256)	365
205	Stress-strain curves of as-cleaved CaF_2 XTL in which the (111) and the (110) planes were normal to the applied compressive stress (258)	367
206	Yield strength and hardness as a function of temperature. The data are estimated to be in the form Y=B exp (k/T) and curve fit by the straight line ln y = ln b + k(1/T)	368
207	The generation of the CaF_2, La_2O and NaCl structure types from the α-UO_3-type by CS plane formation; note that CS operation is ... a (α) → b(β) → c(δ) → a (α) → b(β); ↓ = an eliminated anion layer; on the bottom the respective planes of cations parallel to (100) and the projected anion environments are depicted, idealized so that the [MX_8] is a perfect cube, from (267)	375
208	The coefficients of friction (COF) of CaF_2 (15° off 111) [$10\bar{1}/11\bar{2}$] in vacuum (1.33×10^{-3} Pa = 1×10^{-5} torr), with or without impingement of the imaging SEM beam, at various temperatures (90° XTL sapphire pin)	376
209	The coefficients of friction (COF) of CaF_2 (15° off 111) [$10\bar{1}/11\bar{2}$] in P_{air} (13.3 Pa = 0.1 torr) at various temperatures; SEM beam on (90 XTL sapphire pin)	377
210	Optical photomicrographs of the CaF_2 wear tracks associated with the tests described in Figures 208 and 209	379
211	The coefficients of friction (COF) of BaF_2 (111) [$01\bar{1}/01\bar{1}$] in vacuum (1.33×10^{-3} Pa = 1×10^{-5} torr), with or without impingement of the imaging SEM beam, at various temperatures (90° XTL sapphire pin)	380

Figure		Page
212	The coefficients of friction (COF) of BaF_2 (111) [$01\bar{1}/01\bar{1}$] in P_{air} (13.3 Pa = 0.1 torr) at various temperatures; SEM beam on (90° XTL sapphire pin).....	381
213	The effect of wear track width on the coefficients of friction (COF) of BaF_2, during the tests described in Figures 211 and 212.....	382
214	Optical photomicrographs of the BaF_2 wear tracks formed during the imaged vacuum and P_{air} tests described in Figures 211 and 212.....	383
215	Sample maps of two diced, 4 in. dia. silicon wafers with CVD diamond films deposited by Crystallume.....	387
216	Discontinuous portion of CVD diamond film, showing island-like nucleation; EASI-20-K, Sample No. 73 (also see Figure 215).....	389
217	Faceted growth of a thin, but continuous CVD diamond film; EASI-20-K, Sample No. 71 (also see Figure 215); parallel white borders indicate film thickness.....	390
218	Cauliflower growth of EASI-20-K, Sample No. 76 (also see Figure 215); parallel white borders indicate film thickness.....	391
219	Nodular coning of a thicker EASI-36-I, Sample No. 11 (also see Figure 215); parallel white borders indicate film thickness.....	392
220	High and low tilt angle SEM photomicrographs of cauliflowered, ~400 nm thick CVD diamond film, EASI-36-I, Sample No. 27 (also see Figure 215); parallel white borders indicate film thickness.....	393
221	The faceted appearance of EASI-36-I, Sample No. 27 (same as Figure 220), under ultrahigh (53,200 x) SEM magnification, typical of {111} texturing.....	394
222	Raman spectra of (a) EASI-20-K film portion, showing characteristic sp^3 diamond peak (1331-1335 cm^{-1}) and mixed $sp^2 - sp^3$ bonding (1340-1360 and 1490-1580 cm^{-1}) on Sample No. 64 (see 215); and (b) EASI-36-I film portion (Sample No. 33, see 215), showing the same 1331 cm^{-1} sp^3 diamond peak and a complex $sp^2 - sp^3$ peaks in the 1490-1520 cm^{-1} range.....	395
223	Schematics of test combinations for first round of SEM tribotests.....	396
224	Coefficients of kinetic friction (COF) of (a), (b), "sp^3" vs. α-SiC and (c) "$sp^2 + sp^3$" vs. α-SiC, as a function of temperature, in 1.33 x 10^{-3} Pa = 1 x 10^{-5} torr vacuum.....	397
225	Coefficients of friction (COF) of (a) "sp^3" vs. α-SiC and (b) "$sp^2 + sp^3$" vs. α-SiC, as a function of P_{air}, at various temperatures.....	398
226	Appearance and surface topography of a HIP α-SiC tribopin coated with ~1.5 μm CVD diamond film; SEM photomicrographs at various magnifications.....	405

FIGURES (Continued)

Figure		Page
227	Coefficients of friction (COF) of diamond vs. diamond in 1.33 x 10^{-3} Pa (1 x 10^{-5} torr), at various temperatures: (a) Pin No. 1/Test No. 1 (Wear Track No. 1); (b) Pin No. 1/ Test No. 2 (Wear Track No. 2); (c) Pin No. 2/Test No. 1 (Wear Track No. 3); and (d) Pin No. 2/Test No. 2 (Wear Track No. 4)	407
228	Coefficients of friction (COF) of diamond-on-α-SiC pin vs. diamond-on-Si(100) in 1.33 x 10^{-3} Pa (1 x 10^{-5} torr), at various temperatures, before and after diamond film delamination from the Si(100) flat (17)	409
229	Mixed pyramidal and prism-edge model of (111) planes of diamond comprising pseudo-(100) surfaces, forming the preferentially {111} textured surface	411
230	Post-test appearance of the worn, but undelaminated diamond film on the triboflat, in the wear track associated with 227b; double-headed arrows indicate direction of oscillatory sliding	412
231	Coefficients of friction (COF) of diamond vs. diamond in 13.3 Pa (1 x 10^{-1} torr) P_{air}, at various temperatures; Pin No. 1/Test No. 3 (Wear Track No. 5)	414
232	Post-test SEM photomicrograph of the five wear tracks referred to in 227 and 231, along with optical photomicrographs of the pin tip wear scars employed to calculate the wear rate of diamond in vacuum and in P_{air} (Table 41); double-headed arrow indicates direction of oscillatory sliding	416
233	Post-test SEM photomicrographs of the edge of the wear track associated with Figure 227a (also see 232), showing interfacial delamination of the diamond film from its α-SiC substrate	418
234	Low magnification, shallow-angle SEM photomicrograph of Crystallume's broken X-ray window; indicated areas are clear or hazy in terms of visual transparency	422
235	High magnification SEM photomicrographs of Crystallume's broken X-ray window, at a clear area; note poor nucleation of drop-like diamond crystallites on DLC underlayer	423
236	High magnification SEM photomicrographs of Crystallume's broken X-ray window, at a hazy area; note better, but still incomplete nucleation and coverage of more faceted diamond crystallites on the DLC underlayer	424
237	Optical photomicrograph of one of Crystallume's unbroken, hazy X-ray windows, at 200x magnification	426
238	Optical photomicrographs of Crystallume's unbroken, clear X-ray window, at various magnifications (a = 250x; b = 625x; c = 500x; d = 625x, under reflected light)	427
239	IR transmittance and absorbance of Crystallume's 6-8 μm thick X-ray window	429

FIGURES (Concluded)

Figure		Page
240	The fluorination of graphite fiber weaves; (a) original weave; (b) after brief reaction, and (c) halfway to complete decomposition (reaction) to graphite fluoride ($CF_{1.1}$).....	431
241	The appearance of fluorinated, poly-XTL CVD diamond films on sapphire and poly-XTL α-SiC substrates.....	433
242	XPS spectrum of fluorinated diamond (unpolished) on α-SiC triboflat (see Table 43)...	435
243	XPS curve-fit for carbon (same specimen as in Figure 242).....	436
244	XPS curve-fit for carbon, after a 15 sec. Ar ion etch (same specimen as in Figures 242 and 243).....	437
245	XPS spectrum of fluorinated diamond (polished) on α-SiC triboflat (see Table 43).....	439
246	XPS curve-fit for carbon (same specimen as in Figure 245).....	440
247	XPS curve-fit for carbon, after a 1x15 sec. Ar ion etch (same specimen as in Figures 245 and 246).....	441
248	XPS curve-fit for carbon, after a 2x15 sec. Ar ion etch (same specimen as in Figures 245 and 246).....	442
249	Coefficients of friction (COF) of fluorinated-unpolished diamond on α-SiC pin vs. fluorinated-polished diamond on α-SiC flat, in 1.33×10^{-3} Pa = 1×10^{-5} torr vacuum and in 13.3 Pa = 0.1 torr P_{air}, at various temperatures.....	445
250	The appearance of the used SEM tribometer counterfaces at various SEM magnifications, associated with the tests described in 249; double headed arrow indicates direction of oscillation.....	446
251	Coefficients of friction (COF) of fluorinated-unpolished diamond on α-SiC pin vs. fluorinated-unpolished diamond on Si(100) flat, in 1.33×10^{-3} Pa = 1×10^{-5} torr vacuum and in 13.3 Pa = 0.1 torr P_{air}, at various temperatures.....	448
252	The appearance of the used SEM tribometer counterfaces at various SEM magnifications, associated with the tests described in Figure 251; double headed arrow indicates direction of oscillation.....	449

TABLES

Table		Page
1	Model triboexperiments suggested by Prof. W.W. Goddard III (Caltech)	25
2	Selected properties of Group IIA fluorides	34
3	The shear strength of (111) [$1\bar{1}0$] CaF_2 vs. CaF_2, BaF_2 vs. BaF_2 and BaF_2 vs. CaF_2 couples—experimental data by SEM tribometry; predicted τ_S values are near 100 MPa, see APPENDIX B: (a) calculated by τ_S (app.) = $f_k \cdot P_y$; (b) calculated by τ_S (app.) $\cong F_k/A_H$	35
4	Test conditions for Tester 2A experiments	87
5	Statistical analysis of duplicate Tester 2A experiments (4 ea rubshoe vs. RCF rod contacts) with selected materials combinations: (a) surface shear strength ($\tau_{app.}$) data analysis; (b) wear data analysis	110
6	Notation, stacking sequence and hexagonal fraction of SiC polytypes (94)	127
7	Semi-quantitative emission spectroscopy of various α-SiC single crystal samples (percent elemental contents indicated)	131
8	Tester 2A and MTI's tribometer specimen materials fabricated from α-SiC	144
9	Modulus, hardness and fracture toughness data on α-SiC at R.T. (as-received) and H.T.-tested (HTT)	148
10	Coefficient of friction (COF) and apparent surface shear strength (τ_S) data on α-SiC at R.T. and H.T.	149
11	Normalized mean wear rates of a variety of ceramic couples, ESK α-SiC included, at H.T. and high V; MTI pin-on-disc tester	153
12	Speed-controlled friction (a) and mean τ_S values (b) with selected ceramic couples from Table 11	154
13	Selected mechanical properties of Norton Noralide NC-132 HPSN, as measured by the Vickers indentation method at Hughes Aircraft Company	178
14	Selected physical properties of the Cercom PAD-1 HPSN	184
15	Selected physical properties of (a) Toshiba TSN-03H, and (b) UBE HIPSN materials subjected to ball polishing at Spheric	187
16	Ball/grinding/polishing data for precision bearing balls fabricated from selected HP/HIP-Si_3N_4 materials	189
17	Properties of Combat® BN solids; from (203)	198

TABLES (Continued)

Table		Page
18	XPS analysis of h-BN and h-BN-related standards at SORETRIB (all energies in eV)	205
19	XPS analysis of propanol-cleaned Combat® BN (=)/(⊥) specimens (all energies in eV)	206
20	XPS analysis of propanol-cleaned and argon-ion-etched Combat® BN (=)/(⊥) specimens (all energies in eV)	207
21	XPS analysis of propanol-cleaned and 450°C-heat-treated Combat® BN (=)/(⊥) specimens (all energies in eV)	208
22	The friction of Combat® BN as the function of test atmosphere	218
23	The most significant friction and wear findings with Combat® BN, using XPS/AES tribometry	219
24	MTI pin-on-disc test matrix and summary of the results	233
25	Normalized surface shear strength (τ_s) values of the MTI pin-on-disc test matrix, in units of $N \cdot m^{-2}$ (Pa)	235
26	Disc-on-disc traction test conditions at MTI	238
27	Substrates and preparation techniques for The Aerospace Corporation's 200 nm thick AT/HT sputtered MoS_2 films	247
28	Room temperature, SEM tribometer friction data for The Aerospace Corporation's 200 nm thick AT/HT sputtered MoS_2 films	252
29	SEM tribometer wear life data for The Aerospace Corporation's 200 nm thick AT/HT sputtered MoS_2 films	253
30	Intercalated graphite powders formerly available from the Intercal Co., Port Huron, MI	263
31	Intercalated graphite powder samples (from Intercal) for TGA/DSC analyses	264
32	Pressed flat molds (~10 mm x 5 mm x 3 mm) of selected, intercalated graphite powders (from Intercal)	276
33	Physical-chemical-mechanical characterization of rutile films grown by the processes described in Figure 182; σ = oxide film stress, (-) indicates compressive and (+) tensile stresses; L_C = scratch test critical load, indicating degree of oxide adhesion to TiC; and H_V = Vickers micro-hardness of oxide film under 1 g load	337
34	Room temperature friction and wear of rutile films grown by the processes described in Figure 182, at high and low humidities	339

Table		Page
35	The shear strength (τ_s) of CaF_2 (111) and BaF_2 (111), as estimated by their yield strength (σ_y) and the equation $\tau_y = f_k \cdot \sigma_y$	371
36	The shear strength (τ_s) of CaF_2 (111) and BaF_2 (111), as estimated by their Hertzian/apparent areas ($A_r/A_{app.}$) of contact and the equation $\tau_y = F_k/A_r$	372
37	Selected thermodynamic data on the oxidation of CaF_2 and BaF_2, after (268)	384
38	SEM tribometer-measured surface shear strength of CaF_2 and BaF_2 as a function of temperature and atmosphere, using uncorrected (U) and corrected (C) values of P_y in estimating $\tau_s = f_k \cdot P_y$	385
39	Thin CVD diamond films on sapphire wafers (from APPENDIX CC)	401
40	Thin CVD diamond films on sinter-HIP/HIP ESK α-SiC and XTL β-SiC films on Si(111) SEM triboflats, and on sinter-HIP/HIP ESK α-SiC SEM tribopins (from APPENDIX CC)	404
41	The wear rate of α-SiC and diamond versus diamond in various environments	479
42	Thick CVD diamond films on sinter-HIP/HIP ESK α-SiC SEM triboflats and tribopins, on XTL β-SiC films, on Si(111) SEM triboflats and on HAC-GLAS billet coated with polished CVD β-SiC (polycrystalline) film (from APPENDIX DD)	419
43	Fluorination parameters of poly-XTL CVD diamond film-coated, ceramic SEM tribometer specimens	434
44	Atomic concentration for the unpolished diamond-on-SiC triboflat side (see Figures 242, 243, and 244), by XPS	438
45	Atomic concentration for the polished diamond-on-SiC triboflat side (see Figures 245 through 248), by XPS	443

1. INTRODUCTION AND EXECUTIVE SUMMARY

1.1 BACKGROUND

This program came to fruition, because the main findings of a November 1984 U.S. Government-funded study (1, 2) coincided with the premises of a Hughes proposal submitted to DARPA in March 1984: (a) an overwhelming number of extreme environment moving mechanical assemblies (MMA's), which must operate at very high or very low temperatures in a variety of atmospheres, required solid lubrication of ceramic triboelements (bearings, gears, seals, cams, bushings, etc), and (b) the technical/scientific community has not been capable of producing such elements with the needed wear lives, due mainly to poor understanding of the related tribological fundamentals.

Prior to this program, efforts on the solid lubrication of ceramics were sporadic and limited in scope. The absence of wide-spread interest stemmed mainly from failure to recognize that a general need existed. The available few, limited capability friction and wear testers that were originally designed with certain narrow aspects of extreme environments in mind (i.e., high and cryogenic temperature use in air, vacuum or in inert gases) generated mostly insufficient or inappropriate data, marginal in terms of volume or in general usefulness. Emphasis had been historically placed on "materials screening" rather than on elucidation of dynamic surface interactions under realistic (MMA) conditions and the determination of well-defined friction and wear mechanisms. To further exacerbate matters, tribologists were (and still are) forced to appropriate structural ceramics for bearings, because purposely designed triboceramics are not yet available. Unfortunately, even the strongest of the most commonly used materials (e.g., SiC and Si_3N_4) are largely inert (covalent-bonded). Without some surface activation, they exhibit no tendency of adhering to the also covalently bonded basal planes of conventional, layered-hexagonal solid lubricants such as MoS_2, graphite or hexagonal (h)-BN, even under the mildest operational conditions. First and foremost, a solid lubricant must stick to its substrate to claim the title. In air, at temperatures to 850°C (and higher), not only do these initially adherent lubricants delaminate, degrade or decompose, but their oxidation/ decomposition products tend to combine with the surface oxides of the ceramics to create complex and often unfortunate tribocatalytic surface reactions.

These types of unproductive surface interactions, exacerbated by the brittle, impure, low fracture toughness and tensile strength nature of the available structural ceramics, have repeatedly led to costly MMA failures during extreme environment testing. By and large, known rules of thumb and guidelines governing the solid lubrication of metals are inapplicable to ceramics. As a consequence, "brute force" engineering has continually and consistently failed to produce the desired results, despite the enormous sums spent.

Before the onset of the present program, the participants of a variety of topical workshops repeatedly arrived at a consensus that the main cause of this state of affairs was a lack of fundamental understanding of tribological phenomena. Unfortunately, there was no consensus on a unified, rational approach to attaining the necessary knowledge. Even an agreement on such basics as the type of experimental tools

(i.e., the most realistic and useful friction and wear tester designs and the attendant analytical techniques needed to examine environment tribological behavior) remained elusive.

1.2 PROGRAM PHILOSOPHY

Figure 1 (prepared by Professor William A. Goddard III from Caltech) is an appropriate guide to how this program had to overcome traditional barriers to fundamental research:

1. Historically, lubrication engineers have only been comfortable with testing engineering designs of MMA's, as aided by materials screening/bench-test-type-friction and wear experiments in the continuum mechanical* regime. They did not reach down into the more fundamentals-oriented, smaller distance and temporal scale regions of the space-time continuum, most likely because of a lack of sufficient training in the basic sciences. Ironically, as the traditional engineering approaches failed to solve extreme environment lubrication problems, the only hope of solution lays in clarifying the uncertainties of atomic-molecular level phenomena governing the friction and wear of solid lubricated ceramics.

2. Those academicians who could take steps toward such atomic-level understanding and, in turn, develop at least qualitative methods useful for selecting new or improved ceramics and better solid lubricants, were generally not interested in such unusual endeavors. There was neither sufficient prestige nor enough funding associated with the problem to encourage interest.

3. Fundamental models were needed to consider selected ceramic and lubricant molecules in contact, by initially carrying out first principles quantum mechanical calculations of the wave functions in order to define complete potential surfaces. Force fields could be extracted from these surface potentials, which then could further be used in large scale atomic-molecular level simulations (e.g., molecular dynamics calculations) of a finite piece of the ceramic/lubricant interface represented by a friction couple. Moreover, predictions as to the adhesion, friction, wear, transfer etc. of the interacting surfaces had to be confirmed by highly controlled experiments. Neither the calculation methods nor the microscopic tribometers and the associated test methodology existed to address these important issues.

The following major program objectives were set to overcome these barriers:

1. Define the fundamental principles through which the friction and wear mechanisms of environmentally stressed, bare and solid lubricated ceramics can be elucidated.

2. Modify solid lubricated tribosystems based on an understanding of fundamental principles to attain controlled friction and wear responses under given thermomechanical and atmospheric conditions.

3. Advance the technology so that engineers can successfully and confidently begin to design, build and operate solid lubricated ceramic machine components for extreme environments.

---

* In continuum mechanics, a continuous medium is regarded as a set of structured particles, each possessing individual mass, velocity, translation, rotation or deformation. The behavior of the macrovolume is determined by the summed behavior of the microvolumes or "particles".

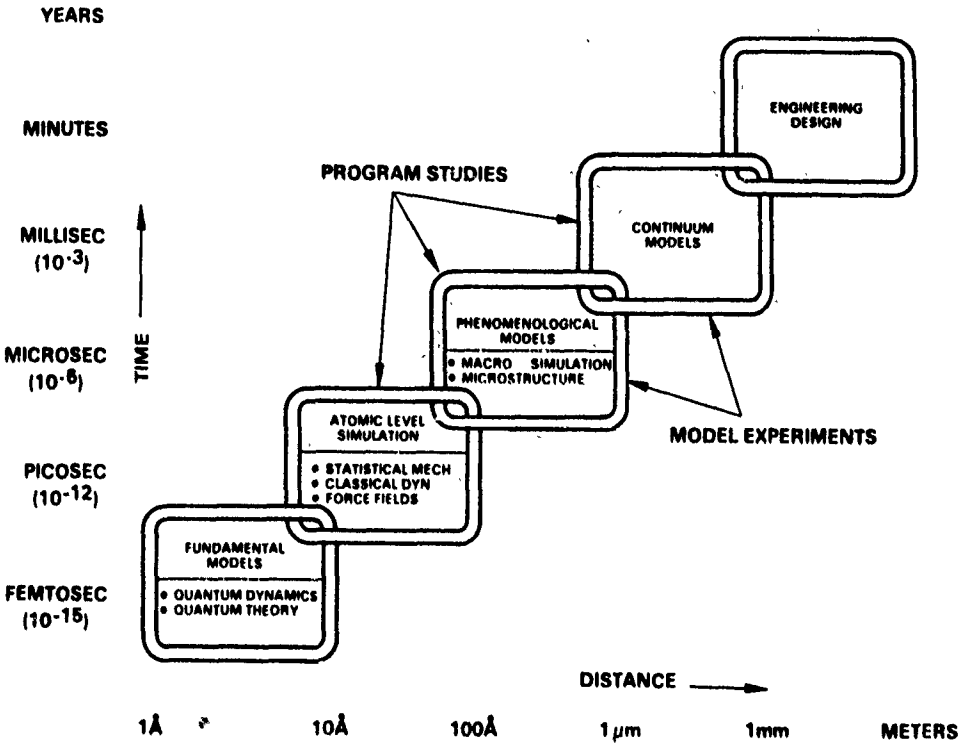

Figure 1. Hierarchy of tribology models in the space-time continuum (after Professor W.W. Goddard III, California Institute of Technology).

Although it was the third of these objectives which gave impetus to the program, our work mainly involved (a) atomic and molecular (microscopic) modeling and testing of ceramic/solid lubricant interface bonding effects, and (b) elucidating the thermodynamics of selected solid lubricant films and model ceramic tribosystems in the microscopic, macroscopic and continuum mechanical regimes by specially developed tribometers and friction and wear test methods. However, the fundamental nature of the research notwithstanding, the main goals were directed towards finding potential solutions and applications useful to practicing tribologists and lubrication engineers.

1.3 CRITICAL TECHNICAL ISSUES

Before any of the laboratory work commenced, however, the critical technical issues had to be defined and addressed first. These issues needed to be identified and prioritized, because their relative importance helped determine (a) the type and the number of model experiments, and (b) the apparatus/techniques required for the completion of these experiments. If these apparatus and methodology were not available, they had to be constructed in time to complete both the test machine shake-down and the model experiments within the allotted four-year program period.

Having examined the schematic representation of two idealized, solid lubricated surfaces under normal load and tangential shear and further subjected these surfaces to extreme environmental conditions (Figure 2), the following axiomatic assumptions were set forth to comprise the basis for the experimental models:

1. A stepwise reduction in shear strength exists, as one traverses the path normal to the plane of shear, from the ceramic substrate to the sliding interface.

2. The solid lubricant layer must first adhere to its substrate but not adhere to itself before it can serve as an effective lubricant.

3. The solid lubricant film's chemistry and crystal structure must be engineered not only to resist *adhesive delamination*, but also to exhibit a low net interfacial shear force interaction at the countersurface. At the same time, the film itself must contain a graded, progressively decreasing shear strength region going toward the sliding surface to prevent premature, *cohesive delamination* within the film, which also causes rapid wear. The low net interfacial shear may be attained by solid lubrication of both surfaces in an identical manner. Alternatively, one may be solid lubricated along with providing a low-surface-energy-producing treatment of the other (countersurface) simultaneously, e.g., fluorination to render it inert and *non-adherent* to the solid lubricated counterface. The key objective must always be to preferentially wear the low shear, but long wear life (most likely replenished) solid lubricant film. The ultimate goal is to prevent wear of the ceramic substrate to the critical point of losing MMA tolerances. Crystal structure engineering of a graded solid lubricant film is a difficult proposition.

4. Low shear strength surfaces produce low coefficients of kinetic friction (f_k <0.3). Although low f_k places the region of *maximum* octahedral stresses *below* the ceramic substrate's surface, the stresses on the surface are still high even at $f_k = 0.20$ (a value generally considered low with

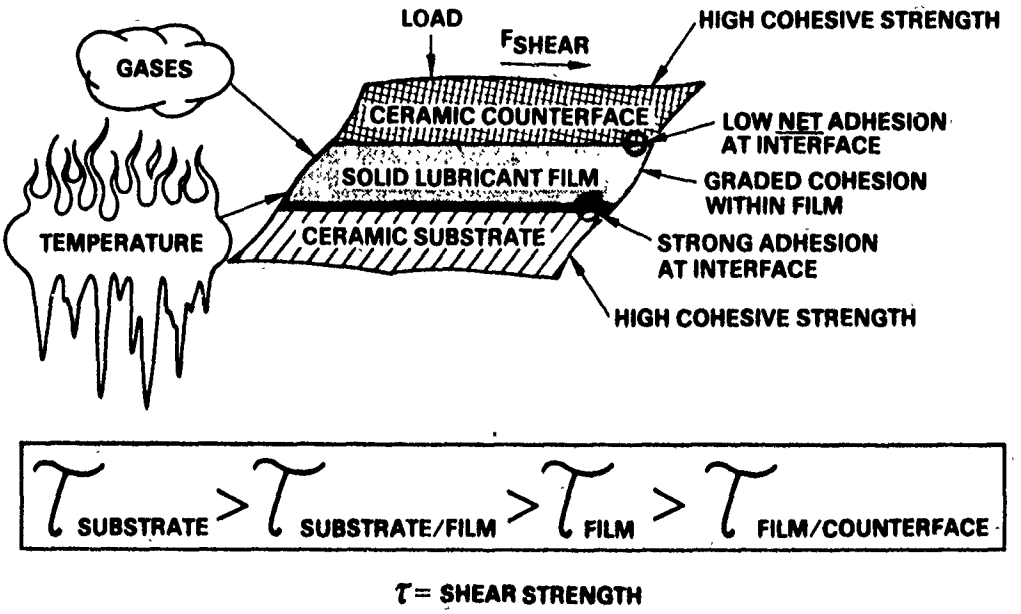

Figure 2. Model of contacting, solid lubricated ceramic surfaces under normal load, tangential shear and environmental stresses.

solid lubricated ceramics). As a consequent, the ceramic must exhibit high structural integrity to prevent crack-induced generation of (a) wear particles, and (b) initiation sites for the delamination of the solid lubricant coating.

The importance of some of these key technical issues and the associated philosophy were discussed more comprehensively in (3, 4).

1.4 GENERAL PROGRAM STRUCTURE

The structure of the program, grouped into essentially four sets of activities as well as the associated interactions are depicted in Figure 3.

The first group consisted of the prime agency (DARPA) funding the Hughes program, working in concert with U.S. Government-related program management and oversight representatives (Bobby D. McConnell of WRDC/MLBT and Dr. Larry L. Fehrenbacher of TA&T, Inc., see FOREWORD).

The second and the third groups were comprised of research activities at Hughes, supplemented by selected Hughes subcontractors, respectively.

The fourth group, consisting mainly of two DoD laboratories (NRL and the Aerospace Corporation), was funded separately by DARPA to address key issues important to the overall effort. Expert scientists, such as Dr. Irvin L. Singer (NRL) and Dr. Paul D. Fleischauer (The Aerospace Corporation) and their staff, injected fundamental knowledge characteristically unique to both organizations. This research group also included the recently started AFOSR Tribology Initiative, which was created after the onset, and with the help of, the DARPA/Hughes program. According to plan, a few promising aspects of our research were to be transitioned into the AFOSR initiative. The transition of selected activities did indeed begin during the course of the present program; selected former Hughes subcontractors and WRDC/MLBT scientists are now funded by AFOSR along promising lines of research associated with tribological fundamentals of solid and liquid lubrication.

1.4.1 Hughes In-house Research

In addition to providing overall direction to the program, Hughes elected to retain and perform certain portions of the research in-house. Most notable of these efforts consisted of:

(a) establishing the basic design for two scanning electron microscope (SEM) tribometers capable of traversing a –173°C to 1000°C temperature range (both constructed by Microscopy Research Labs, Inc., North Branch, NJ, with the close cooperation of Hughes designers and SEM technologists),

(b) completing the design and construction of an 850°C dual-rubshoe tribotester (Tester 2A) capable of using a ceramic *rolling* contact fatigue (RCF) rod as one of the *sliding* friction and wear specimens,

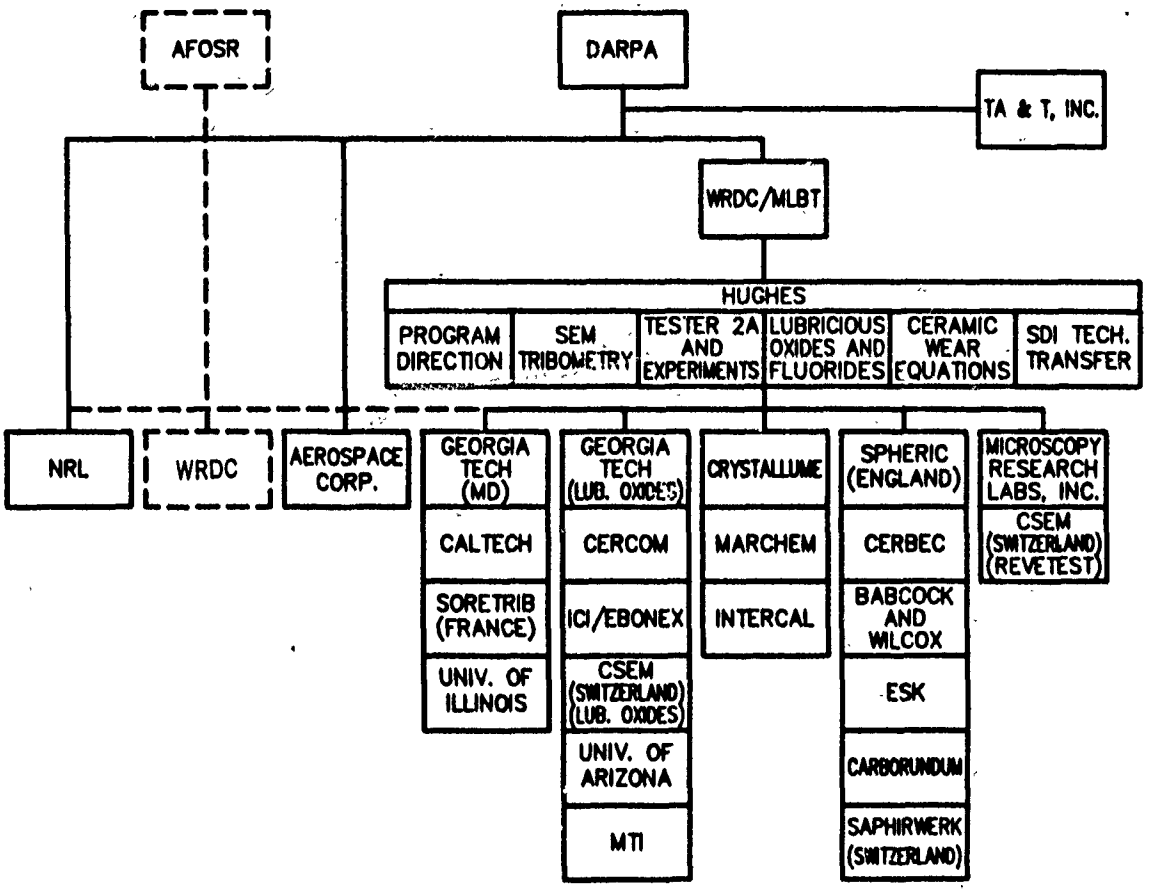

Figure 3. Program structure and activities.

(c) completing a large number of model experiments performed with the high temperature SEM tribometer and the Tester 2A on a variety of model ceramics and solid lubricants,

(d) establishing the basic hypotheses and their proof as to the tribological fundamentals controlling the friction and wear of substoichiometric rutile (TiO_{2-x}), stoichiometric CaF_2 and BaF_2, as well as the behavior of hot-pressed (HP) and hot-isostatically pressed (HIP) Si_3N_4 and α-SiC, and

(e) completing the six-degrees-of-freedom computer program SEPDYN, predicting the fully dynamic behavior of ball bearing components in an operating bearing. The data were meant to provide property design windows for advanced tribomaterials and establish realistic test parameters for tribometers.

Approximately half-way through the Tribological Fundamentals Program (designated hereafter as Part I), the original scope was restructured to accelerate basic and applied research on the area of cryogenic lubrication. In particular, an SDI-funded add-on effort was started under the title of "Determination of Tribological Fundamentals of Solid Lubricated Ceramics, Part II: Formulation of Improved Tribomaterials for Advanced Cryogenic Turbopump Applications". The objective of this 53-month, currently ongoing addition to the basic Part I program is to provide the technology base needed for the development of better hydrostatic bearings, hydrodynamic bearings and seals, as well as self-lubricating separators mated with their specially designed countersurfaces and ceramic rolling elements for use in advanced cryogenic turbopumps. These pumps will feed liquid hydrogen and/or hydrocarbons and oxygen to Advanced Launch System (ALS) rocket engines. Since reporting of the Part II portion is governed by International Traffic in Arms Regulation (ITAR) rules and regulations, data on Part II are restricted and are not included in the present report.

1.4.2 Subcontractor Activities

1.4.2.1 Atomic-Molecular Level Research (First Subcontractor Column, Figure 3). The first Hughes subcontractor column on the left in Figure 3 contains academic participants, who were involved in basic research kept at the atomic-molecular level.

Prof. William A. Goddard III (Caltech) fulfilled two roles. In addition to helping establish the program's philosophy and directions toward selecting model compounds and experiments, he demonstrated the type of ab-initio calculations needed to predict the likely outcome of these closely controlled experiments by a specific example. He and his students performed computer-aided quantum chemical calculations of two, hydrogen-terminated, (111) and ($\bar{1}\bar{1}\bar{1}$) diamond (mating) planes under load, moving tangentially relative to each other. A maximum coefficient of kinetic friction (f_k) = 0.132 was predicted for this idealized system. Literature data on equivalent single crystals, as well as program results on polycrystalline diamond films with a largely (111) faceted orientation on the mating, sliding surfaces found f_k values close to 0.10. Prof. Goddard's work has been one of the activities transitioned

into the AFOSR Tribology Initiative, where he is now performing calculations on the energetics involved with idealized ceramic and polymer surface interactions.

Prof. Uzi Landman (Georgia Tech) and his coworkers used larger scale molecular dynamics (MD) simulations by specially developed computer methods. The dynamic response on a microscopic scale, i.e. deformation and stress relief mechanisms, were modeled at equally idealized, single crystal interfaces subjected to external perturbations, such as constant tension, strain rate and isoexternal stress. The (111) plane of one model FCC material with twice the cohesive energy density (i.e., twice as hard, twice the surface energy) of another, weaker FCC (111) were tangentially sheared against one another in the [1$\bar{1}$0] direction. This shear was modeled via pairwise 6-12 Lennard-Jones potentials to (a) identify the mechanisms for deformation, stress accumulation and relief, as well as the dynamic response to external perturbation, and (b) show the dependence of the above phenomena on interface bonding, crystallography, atomic sites of the respective interfaces and ambient conditions (adiabatic or isothermal). The MD calculation results seemed sufficiently promising that pair potentials and many-body potentials of real molecules were substituted into the calculations. These interacting surfaces were amorphous and crystalline silicon (examples of covalent bonding), as well as CaF_2 and BaF_2 (examples of ionic bonding). The results of the predictions involving CaF_2 vs. itself, BaF_2 vs. itself and BaF_2 vs. CaF_2 were checked with highly controlled SEM tribotests performed with ultrapure fluoride (111) [1$\bar{1}$0] sliding combinations, at low loads and speeds, at room temperature. The experiments indicated only fair correlation with the MD calculations, as described in more detail in para. 2.1.2 herein. Prof. Landman's work is also being continued under AFOSR's sponsorship.

Ecole Centrale de Lyon (Ecully, France) and selected personnel of its subsidiary *SORETRIB* (an acronym for the *So*ciety for the *Re*search of *Trib*ology), under the direction of ***Prof. Jean-Michel Martin***, combined a wide variety of surface analytical instrumentation with in-situ friction and wear testing of ceramics and solid lubricants. In particular, the uniqueness of *SORETRIB*'s work stemmed from the use of a specialized (room temperature) Auger/ESCA tribometer, and an ability to fully analyze wear debris by other, additional methods such as STEM, EFEM, EXAFS, EXELFS, EELS and PEELS. (It is assumed that the reader is familiar or can become familiar with these standard analytical methods without any further description of the acronyms here). By detailed understanding of the spectra associated with the chemical building blocks of their candidate ceramics (e.g., α-SiC) and the solid lubricants of interest (e.g., graphite and h-BN), our French colleagues were able to shed light on previously unelucidated tribological phenomena. They refined debris analysis into a highly efficient technique, whereby the local chemical environment of the atoms and the symmetry of the atomic sites, as well as the chemical bonding within the wear debris particles could be unambiguously translated into a wear mechanism. It was shown that h-BN is basically a poor lubricant for ceramics in vacuum and only a marginal-to-acceptable one for high temperature air applications. This finding was confirmed by Hughes and Mechanical Technology, Inc. (MTI, Latham, NY) tribotests in a wide pressure-velocity-temperature (PVT) range. Boron

carbonitride was predicted to be a more promising candidate, the elucidation of which should comprise the basis for similar future work.

Inasmuch as atomic force microscopy and molecular tribometry are the only currently known atomic-level techniques for high-sensitivity, experimental confirmation of ab-initio and MD calculations of sheared systems, ***Prof. Steve Granick's (U. of Illinois)*** already ongoing NSF grant was supplemented to review the available atomic-molecular force balance techniques, which might be capable of such confirmatory work. His findings indicated that the use of these techniques would be premature with solid lubricated surfaces. There would be too many technical difficulties involved with knowing and controlling the real area of contact between an atomic force microscope tip and its mating flat, or that between flat or curved single crystal surfaces of ceramic/solid lubricant combinations. These combinations do not lend themselves to test specimen substrate as useful as contacting (or nearly contacting), atomically smooth basal planes of flexible mica lubricated with monolayers of model fluids. (Mica is typically used as flat or cylindrically-curved counterfaces in atomic force balances.) For these reasons, these microscopic techniques were better suited for longer-termed development under AFOSR auspices than pursuit within the more immediate confines (and requirements) of our program. As a result, tribometry in the micro-macroscopic regimes was restricted to tests with SORETRIB's Auger/ESCA room temperature apparatus and the Hughes, high-temperature (room temperature to 1000°C) SEM tribometer.

1.4.2.2 Lubricious Oxides (Second Subcontractor Column, Figure 3). One of the major thrusts of the Part I program was the establishment and confirmation of the Hughes hypothesis on the effects of anion (oxygen) vacancies on the tribological properties of the rutile polymorph of titanium dioxide (TiO_{2-x}). The subcontractors grouped in this column were instrumental in preparing specimens or performing friction and wear tests supplementing the Hughes in-house theoretical and experimental efforts.

Under the direction of ***Prof. Ward O. Winer***, his able assistant ***Dr. Hyun-Soo Hong (Georgia Tech***, now employed by The Lubrizol Corp., Wickliffe, OH) used high temperature pin-on-disc tester specimens fabricated from single crystal rutile and polycrystalline rutile films generated from oxidized titanium pins to help confirm the Hughes hypothesis. They showed independently from the Hughes SEM tribometer and Tester 2A experiments that the shear strength of rutile indeed depends on the alteration of its oxygen stoichiometry. The Georgia Tech tests supplemented the Hughes results in verifying that two specific substoichiometric compositions ($TiO_{1.98}$ and $TiO_{1.70}$) produced shear strength values in the range of sputtered MoS_2 films in vacuum (10-15 MPa). Additional Georgia Tech pin-on-disc tests compared the results of oxidized titanium with the effectiveness of molybdenum oxide films generated in-situ on pure molybdenum surfaces in 400°C air, sliding against a $(1\bar{1}20)$ sapphire counterface. The softer molybdenum oxides formed not only lowered the f_k level from ~0.7 in the case of the severely reduced, abrasive titanium oxides to ~0.3 with the softer molybdenum oxides, but also retained (and further lowered) the already low wear rate previously experienced with the abrasive-oxidized titanium surfaces.

CERCOM, Inc. (Vista, CA), under the direction of ***Drs. Richard Palicka and Adre Ezis*** provided a source for hot-pressed (HP), polycrystalline bodies and Tester 2A tribospecimens machined from molds hot-pressed from ultra-pure rutile power at CERCOM and at Kyocera. A hot-isostatically pressed (HIP)-version of Y_2O_3-Al_2O_3 sintering-aid-containing Si_3N_4 was also prepared by thermal nitriding of silicon powder, followed by an attempt to at least partially devitrify the glassy grain boundaries. This material, as well as its commercially available, HP precursor served as two of the six Si_3N_4 ceramics used in the ball polishing wear study commissioned by Hughes at Spheric, Inc. (England; see fourth column and later discussion herein).

Dr. Kevin Kendall (ICI, Runcorn, England) and ***Dr. Robert L. Clarke of EBONEX (a U.S. subsidiary of ICI, located in Emeryville, CA)*** supplied SEM tribometer specimens from their version of hot-pressed, substoichiometric rutile, commonly utilized as an electrode material in various electrochemical applications. Their expertise in fabrication of high structural integrity parts from TiO_{2-x} rutile with some measure of control of the oxygen stoichiometry was utilized to obtain specimens kept within five different substoichiometric ranges. SEM tribotests with two of these polycrystalline flats ($TiO_{2.00}$ and $TiO_{1.95-1.98}$) further confirmed the Hughes hypothesis previously found true for single crystals of rutile. The rest of the substoichiometric specimens are being saved for future research activities.

Lubricious oxides were also generated by in-situ oxidation of rutile-forming substrates, e.g., TiC and TiN. ***CSEM (Neuchatel, Switzerland)***, under the direction of ***Dr. Hans Boving*** and with the able participation of ***Mr. Werner Hänni,*** devised various methods of converting CVD TiC layers deposited on 440C steel into stoichiometric and substoichiometric rutile. While the conversion into rutile was successful, keeping the oxygen stoichiometries in the desirable ranges was not. This lack of success was confirmed by various analytical techniques, combined with room temperature friction and wear tests. Holding the oxygen content within specific boundaries by simple oxidation of TiC was shown to be extremely difficult, if not impossible.

Another approach was tried by ***Dr. Bertrand G. Bovard (U. of Arizona, Optical Sciences Center).*** Since thin (~1 μm) films of mostly amorphous (and low index of refraction) $TiO_{2.0}$ are conventionally used as anti-reflection coatings on optical surfaces, it made sense to look for a vacuum deposition technique amenable to controlling the oxygen stoichiometry of thin TiO_{2-x} films. This work was attempted even though the ability to deposit the oxide layers in the rutile morphology was questionable. While the reactive evaporation technique used appeared successful in controlling the stoichiometry to a surprising degree, the films suffered from surface cracking. Lowering the film thickness to 200 nm was finally successful in preventing extensive checkerboard fracture. Since the substrate was unreactive (it was fused silica), the formation of the crack networks may be attributed to a combination of factors, such as volume changes associated with polymorph alteration (e.g., anatase ⟶ rutile) substrate/coating thermal expansion differences, moisture absorption in air and possible hydrogen inclusion in the lattice.

Drs. James F. Dill and Hooshang Heshmat from Mechanical Technology, Inc. (MTI, Latham, NY) fulfilled two important roles in the program. First, they designed and built a high temperature friction and wear tester under their own internal funding. This apparatus exceeds the PVT capabilities of the Hughes Tester 2A by using larger specimens and a higher speed test spindle. Furthermore, their tribotester can be operated both in the sliding (friction) and rolling (traction) mode. As such, they extended the surface speed limit of the Tester 2A operating with the small-diameter RCF rod and enabled expanded correlation runs elucidating the friction and wear of α-SiC, Si_3N_4 and h-BN/Si_3N_4 composites in a much wider environmental stress regime and operational modes. Their work also included the measurement of traction coefficients of powder-lubricated ceramic interfaces to temperatures as high as 1000°C, using potential high temperature lubricants such as pulverized, stoichiometric rutile, h-BN and MoS_2.

By virtue of their renowned expertise in tribotester design, MTI was also engaged to double-check the mechanical and thermal modal computer analyses and experimental verification originally performed at Hughes on the Tester 2A friction transfer arm, drive mechanism and support structure prior to apparatus construction. We had to be sure that the measured tribological behavior of bare and lubricated ceramics was largely materials-dependent, influenced only minimally by test machine dynamics. The MTI analysis indicated only negligible machine effects at spindle/test rod run-outs of 2.54×20^{-6} m (1×10^{-4} in) or less, at or below rotational speeds of 4000 rpm = 2 m • s^{-1} = 393 ft • min^{-1}. Inasmuch as the operational velocity of the Tester 2A was held to a standard 700 rpm = 0.35 m • s^{-1} = 69 ft • min^{-1} speed and a total indicted runout (TIR) of 1.8×10^{-6} m (7×10^{-5} in.) or less throughout the present program, the Tester 2A friction and wear data generated at Hughes are considered highly reliable.

1.4.2.3 Diamond and Graphite Compounds (Third Subcontractor Column, Figure 3). Another important portion of the Part I program consisted of identifying the friction and wear mechanisms controlling the tribological behavior of polycrystalline, CVD diamond films. ***Crystallume (Menlo Park, CA)***, under the direction of ***Drs. K.V. Ravi and Mike Pinneo***, deposited thin layers (0.8 μm to 8 μm) of diamond on a variety of ceramic substrates by plasma-assisted CVD methods. SEM tribometry of the polycrystalline diamond films at Hughes demonstrated that in vacuum, friction is controlled by thermal desorption-resorption of gases with the attendant generation and annihilation of dangling bonds, whereas in partial pressures of air, friction is controlled by high temperature oxidation and graphitization effects. High friction leads to surface cracking of the low tensile strength and fracture toughness diamond films (especially those with sp^2 bonding contamination in the grain boundaries), causing higher wear. On the whole, attempts to lower both the friction and the wear using post-deposition fluorination of the diamond surfaces, devised by ***Prof. John Margrave (Rice University, Houston, TX)*** and his associates, were not successful. Fluorine did not react with diamond to form polytetrafluoroethylene-like bonds, even when subjected to high temperature fluorination. Although the reduction of friction was possible under certain deposition and test (temperature) conditions, post-growth fluorination did not seem to be effective for reducing the surface shear strength and wear of diamond films. Furthermore, the treatment techniques

caused severe attack of the diamond/substrate interfaces, resulting in large-scale delamination of the films.

On the one hand, π-bonding-generated chains of reconstructed (111) and (100) diamond (and silicon) facets, combined with occasional oxidation-graphitization of selected sites, provide low friction (~0.10 - 0.15) of the sliding surfaces, even at elevated temperatures. On the other hand, the friction of bulk graphite itself is known to be high in vacuum, especially at high temperatures. Desorption of the water (atmospheric moisture) normally intercalated within the layers reduces the van der Waals gap (i.e., the length of the C-axis), leading to increased critical resolved shear stress/surface shear strength of the polycrystalline graphite and, consequently, to high wear. One method of extending the thermal and atmospheric-environmental range of graphite is by intercalation with selected donor or acceptor species more thermally stable than water. ***Prof. F. Lincoln ("Linc") Vogel of Intercal (Port Huron, MI),*** provided powders and pressed SEM triboflats of selected metal-chloride-intercalated graphites to the program. For the first time, DSC/TGA of powders combined with wide environmental range SEM tribometry at Hughes demonstrated the general usefulness of such acceptor-intercalated graphites both in air and in vacuum, to temperatures as high as 700°C. Although partial deintercalation at elevated temperatures and in vacuum led to increased wear of the flats, the surface shear strength remained low under all test conditions.

1.4.2.4 Ceramic Research and Specimen Sources (Fourth Subcontractor Column, Figure 3). Messrs. Robert Hardisty and Julian R. Pratt of Spheric Special Products (West Sussex, England), cooperating with ***Mr. Robin Cundill of the SKF Engineering & Research Center (Neuwegein, The Netherlands)*** ground and polished six different kinds of HP/HIP Si_3N_4 ceramics into 1.27 cm = 0.5 in. dia., precision bearing balls. Precision of Grade 5 to Grade 25 was achieved, depending on the degree of isotropic nature of the base stocks. Holding all grinding/polishing parameters constant, the volume removed from the ball blanks as a function of time was measured. Then, the data were fitted to the Evans-Wilshaw wear relationship, which states that the volume removed by grinding and polishing is inversely proportional to the $(K_{Ic}^{3/4} \cdot H_v^{1/2})$ factor, where K_{Ic} is the critical stress intensity factor (a measure of fracture toughness — a higher K_{Ic} signifies a tougher material) and H_v is the Vickers hardness number measured at a given indentation load. Both H_v and K_{Ic} were first measured at SKF on each base stock followed by ball polishing at Spheric. The inverse-linear Evans-Wilshaw relationship was shown to hold for all of the two-phase Si_3N_4 ceramics (i.e., containing Si_3N_4 grains and glassy grain boundaries). It was surprisingly accurate even where the second phase was improperly engineered or where a third phase (e.g., some h-BN) was purposely included in the sample.

CERBEC (East Granby, CT) provided NBD-100 HIP Si_3N_4 spherical preforms and ***Babcock & Wilcox (Lynchburg, VA)*** supplied us with HP (3.5% h-BN + Si_3N_4) ceramic composite rods, which were eventually ground into spherical preforms at SKF. These and the two other types of HP/HIP Si_3N_4 ceramic rods by CERCOM, Inc. comprised the US-made samples of the study, complementing the HIP equivalent ones received from Japan through Spheric (Toshiba TSN-03H and UBE-SN).

The α–SiC ceramics of interest were furnished by ***Electroschmelzwerk Kempten GMBH (ESK, Kempten, W. Germany)*** providing HIP and sinter-HIP versions of their α–SiC (graphite + Al_2O_3 as sintering aids), and by the ***Carborundum Co. (Niagara Falls, NY),*** offering their pressureless-sintered Hexoloy SA-80T (graphite + B_4C as sintering aids) as basestocks for specimens. These materials were specially selected for their characteristically different grain structures and sintering agents. As such, they comprised ideal model compounds of engineering ceramics for the SORETRIB/Hughes/MTI joint friction and wear studies of α–SiC conducted in a wide triboenvironmental regime.

As during the previous 1978-1984 DARPA/Hughes program entitled: "Solid Lubricated Rolling Element Bearings", ***Saphirwerk (Biel/Bienne, Switzerland)*** continued to utilize their world-renowned expertise at fabricating precision specimens from hard ceramics (sapphire, SiC, Si_3N_4, etc.) as well as from soft solid lubricant materials (e.g., the hot-pressed Combat® h-BN from The Carborundum Co., and various Cercomp® (h-BN + Si_3N_4) composites from Babcock & Wilcox). Since the h-BN-containing materials were anisotropic (i.e, the hexagonal basal planes of the fused crystallites were arranged more-or-less perpendicular to the direction of hot-pressing), special expertise and care were needed to fabricate tribospecimens with the basal planes arranged mostly parallel or normal to the plane of sliding. Saphirwerk's extraordinarily careful efforts were complemented by CERCOM in the U.S. by machining similar specimens with well-defined crystallite orientations.

1.4.2.5 Specialized Test Equipment (Fifth Subcontractor Column, Figure 3). As previously mentioned, ***Microscopy Research labs, Inc., (North Branch, NJ),*** under the direction of ***Dr. Jack R. Alonzo,*** undertook the job of first constructing the high temperature version (to 1000°C), then later a cryogenic version of a small, controlled-environment tribometer, which fit the stage of the Hughes Cambridge Stereoscan 250 Mk. 3 SEM. The high temperature version can operate in the column vacuum of the SEM (1.33×10^{-3} Pa = 1×10^{-5} torr), or in a Knudsen-cell-like, differentially pumped configuration to gases pressures as high as 13.3 Pa = 1×10^{-1} torr, with real time imaging of the sliding interfaces. The in-situ measurement of the wear scar width, friction force, normal load and specimen temperature permits the calculation of the temperature-dependent, apparent surface shear strength. The basis for this value is the apparent area of contact between the small, hemispherical pin and the triboflat estimated from the video data and after-test SEM photomicrographs. Video imaging of the sliding interface, in real time, also gives clues as to debris generation, coating delamination and the formation of unusual tribochemical compounds. Successful and reliable operation of the high temperature SEM tribometer prompted the design and construction of the cryogenic version where the triboflat can be cooled down to –173°C = 100K. The latter apparatus is intended for use during Part II of the program. It will aid in the development of cryogenic tribomaterials. At the time of this writing, the cryotester is being debugged in preparation for future research.

The ability to measure the adhesion of coatings to a variety of substrates under tribothermal conditions using the SEM tribometer was complemented by a similar, but more limited capability

instrument. A REVETEST® was purchased from ***CSEM (Switzerland)***, capable of quantifying the adhesive and cohesive delamination of hard and brittle coatings deposited by a variety of methods. With this apparatus, the surface of a coated flat is scratched with a hemispherical diamond indenter under progressively increasing or steady-state loads at room temperature, in air. Delamination of the coating is sensed with an acoustic emission pick-up (a piezoelectric accelerometer). The analysis of the load vs. acoustic emission signal yields qualitative and quantitative information on the adhesion and mechanical strength of the coating. The adhesion and delamination of soft layers (e.g., sputtered MoS_2) may also be measured with the REVETEST®, even though the accelerometer there does not give a sufficiently strong acoustic signal. Post-test microscopic analysis of the wear path and the scratch distance to delamination can, however, be correlated with the load at which the delamination occurred. The REVETEST® will be used mainly in Part II of the program, measuring the adhesion of hard and soft coatings applied to physically and chemically stabilized cryogenic bearing surfaces.

1.4.3 Cooperative Research with Selected DoD Laboratories. ***Dr. Paul D. Fleischauer's*** in-house activities at ***The Aerospace Corp.***, separately funded by DARPA, dealt with the enhancement of adhesion between sputtered MoS_2 films and ceramic substrates (5). The greatest significance of his and his staff's research lies in showing that active sites on the surface of carbon-contaminated or thin oxide-hydroxide covered ceramics cause orientation of the MoS_2 lamellae/crystallites perpendicular to the substrate. Removal of such sites (e.g., by chemical etching of the surface layer) results in the deposition of the MoS_2 basal planes parallel to the substrate. A perpendicular alignment leads to higher adhesion than a parallel alignment. Precursor work by Bertrand (6), using methanol-rinsed and HF-etched Si (111) surfaces as substrates for RF-sputtered MoS_2, has helped to confirm this hypothesis.

Our program interacted with The Aerospace Corp. by utilizing the SEM tribometer to measure the adhesion, friction and wear of ambient substrate temperature-deposited (AT) and high substrate temperature-deposited (HT) RF-MoS_2 layers sputtered onto methanol-rinsed or HF-etched α–SiC, as well as on solvent-rinsed, steel triboflats (7).

The tests did show that the wear life of films, regardless of the substrate temperature, was measurably greater on the methanol-rinsed α–SiC still containing reactive surface species (e.g., carbon contaminants) than on the acid-etched equivalent substrate. The wear life of the sputtered MoS_2 was defined as the number of cycles to complete delamination (clearly observable by video), coinciding with a catastrophic increase of f_k from the steady-state values of 0.03 - 0.05 to 0.10+. However, even the best films on the ceramics did not last nearly as long as the identical films on steel. It is noteworthy that Swiss REVETEST® scratch test experiments with RF-MoS_2 on various substrates showed the same mode (appearance) of the adhesive delamination sites as the ones we observed on the SEM flats.

Inasmuch as the SEM tribometer was shown eminently capable of measuring the adhesion-related wear life of MoS_2 films (as indicated by friction and real-time video data), we were encouraged to further determine the wear life of sputtered MoS_2 films coated onto the type of previously used, unetched α–SiC

substrate by ion-beam-assisted-deposition (IBAD), see (8). This new process was performed in the laboratories of ***Dr. Irvin L. Singer (NRL) by Robert N. Bolster***. This coating is in fact the replication of a Japanese method (9), whereby the IBAD-MoS_2 is sputtered onto thin (~40 nm) BN interlayer-coated ceramics, yielding extraordinary wear lives. Ultra-low friction and frictional insensitivity to atmospheric moisture (a ubiquitous problem with other types of sputtered MoS_2 films) were added benefits of this coating system.

Our SEM tribotests found the IBAD-MoS_2 far superior to those of the RF-MoS_2 versions, equivalent to the long wear life of RF-MoS_2 on steel. However, with both the RF/IBAD films, thermal cycling triboflats during sliding to 200°C (max., or lower) and back to room temperature significantly decreased wear life.

As a result of these experiments, the SEM tribometer will be employed to select the best available sputtered MoS_2 candidate(s) for the immediately forthcoming SDI/WRDC/Hughes Solid Lubricated Gimbal Bearing Demonstration Program ball bearing tests.

Another avenue of cooperation with NRL scientists covered the area of in-situ lubricious oxide generation on ceramic surfaces. In particular, one of Dr. Singer's DARPA-funded tasks consisted of predicting likely methods to produce highly adherent TiN on HP/HIP Si_3N_4 bearing surfaces. By invoking the Si-N-Ti ternary phase diagram and the use of special deposition processes (10 and 11), he predicted that the best-adhering TiN films will form on nitrogen-deficient Si_3N_4. His hypothesis, combined with another by Gardos (12) on generating lubricious rutile by oxidizing TiN substrates, led to IBAD-deposition of TiN onto NBD-100 HIP-Si_3N_4 Tester 2A specimens. This deposition process was performed by ***Dr. Richard A. Kant of NRL***. The coated specimens were then subjected to room temperature and ~850°C Tester 2A friction and wear experiments, in air.

The data showed that the thin (~200 nm) TiN films were rapidly removed from the ceramic surfaces. The IBAD-TiN process appeared to weaken the NBD-100 surface, causing higher than normal wear rates (i.e., wear in the uncoated mode), at any temperature. Although the TiN converted to TiO_{2-x} (rutile) by oxidation did cause measurable decrease of the frictional forces, this shear strength lowering may also have been assisted by the tribochemically generated, SiO_2-based, glassy oxide layers also formed on the Si_3N_4 substrate.

With respect to any programmatic interaction with the AFOSR Tribology Initiative and the WRDC in-house research spin-off therefrom, the previously described program ties may well be supplemented in the future by newly started WRDC work. As the DARPA/Hughes program results receive progressively more scrutiny and recognition with respect to new research possibilities, WRDC will gradually phase-in promising aspects of our accomplishments.

1.5 MOST SIGNIFICANT ACHIEVEMENTS

1.5.1 Lubricious Oxides

Stable oxides would be ideal high temperature lubricants for the critical, Integrated High Performance Turbine Engine Technology (IHPTET) applications, were it not for their highly abrasive (high friction) nature. Note that the IHPTET initiative's main goal is to double propulsion performance. This will be achieved through innovative designs attaining higher cycle temperatures through the use of advanced materials.

Our high temperature (to 1000°C) tribotests confirmed the hypothesis, showing that the shear strength of the rutile polymorph of titanium dioxide (TiO_{2-x}) may be tailored by altering its oxygen stoichiometry. The shear strength (τ_s) of rutile is ~10 MPa at $TiO_{1.98}$ and ~15 MPa near $TiO_{1.70}$, equivalent to the shear strength range of sputtered MoS_2 films in vacuum. At all other stoichiometries, rutile is hard, brittle and abrasive (although low in wear rate). This research laid the groundwork for future work, a plan to stabilize the low friction phases by doping in order to prevent environment-induced compositional changes. There are other transition metal oxides which could complement rutile as likely model compounds that behave similarly. For the most significant publications on this subject already available in the open literature, see (12 through 16).

1.5.2 CVD Diamond Films

Our program was the first to comprehensively examine the fundamental aspects of wide environmental range tribological behavior of polycrystalline diamond films deposited by plasma-assisted CVD techniques.

It was hypothesized from the data that the friction of CVD diamond films grown in methane-hydrogen atmospheres is controlled by the surface chemistry of the exposed grains. Desorption of gases (mainly hydrogen) upon heating in vacuum created dangling bonds on the surface, just as it does with single crystals of diamond. If these bonds do not reconstruct or are not satisfied (capped) by a stable adsorbate, they will then interact with the sliding counterface to generate high friction forces. Enhanced resorption of selected gases on cooling annihilates the unreconstructed dangling bonds, lowering the friction. Some lowering of the friction at high temperatures can also be achieved, if the rubbed diamond surface undergoes a phase change to graphite. This change is catalyzed even by very small amounts of oxygen, enhanced by the act of shearing under load.

In partial pressures of air and in the absence of carbonaceous surface contaminants or moisture, the generation of oxidation products (CO, CO_2, the hexagonal-planar graphite oxide solid) and shear-temperature-induced phase transformation to graphite commensurately lead to lower surface shear strengths and thus, lower friction.

Wear of the diamond films appears to be directly proportional to the friction forces. These forces cause tensile cracking of the low tensile strength and low fracture toughness diamond films in the wake of the tribocontact. Films which contain sp^2-bonding-contaminated (graphitic-bonded) grain boundary phases tend to wear more due to the generally weaker nature of the graphitic regions. Wear rates of pure, polycrystalline diamond range from ~4 x 10^{-16} $m^3/N \cdot m$ in vacuum to 1 x 10^{-15} $m^3/N \cdot m$ in 13.3 Pa (0.1 torr) air.

We were not successful in lowering the friction and wear of diamond by high temperature fluorination of the diamond film surfaces, because no PTFE-like C-F bonding occurred. Furthermore, most of the fluorination processes were harsh enough to debond the diamond films from their ceramic substrates. The diamond films tended to delaminate even from polycrystalline α–SiC, where the bond strength otherwise is excellent.

For the most significant publications in the open literature on this subject to date, see (17 and 18).

1.5.3 Metal Chloride Intercalated Graphites

For the first time, it was shown that $CdCl_2$ and $NiCl_2$ -intercalated graphites may be considered as a new class of solid lubricants for space applications. At the same time, these materials appear to be equally useful for service in low-humidity air environments. Both compounds exhibit low shear strength properties in air and in vacuum, even after heating to 700°C. Low shear strength is retained despite mass sublimation of $CdCl_2$ during thermally-induced deintercalation, or decomposition of the $NiCl_2$ to Cl_2 and a non-volatile residue, in vacuum.

The strength of molded bodies prepared by warm isostatic pressing of the intercalated graphite powders may not be sufficiently high for use as monolithic bearing parts. These powders are recommended as lubricant pigment additives blended into self-lubricating composites formed mainly from polymeric matrices, for use in low-moisture environments. At high humidities, the chloride salts decompose and tend to become corrosive.

1.5.4 Predicting the Wear of Silicon-based Ceramics in a Wide Environmental Regime

Our research showed that at room ambient temperatures the abrasive wear of silicon nitride ceramics (and to some extent, that of α–SiC) may be predicted by the ceramics' fracture toughness and hardness (the Evans-Wilshaw wear relationship). Even though these parameters are not fundamental properties, because hardness depends both on the elastic and plastic response of the material while K_{Ic} is highly dependent on the residual stresses in the ceramic and the surface flaws left behind by the grinding/polishing/sliding wear, the usefulness of H_v and K_{Ic} is both intellectually and practically appealing. Simple Vickers hardness indentations and the attendant crack-tip-extension-indicated K_{Ic} measurements offer convenient means of quality control for ceramic bearing blanks prior to subjecting them to the time-consuming and expensive grinding and polishing process.

In high temperature air, wear of the ceramics is determined less by the K_{Ic}/H_v factors and more by their oxidation resistance (i.e., the tendency to form more or less glassy oxide layers on the sliding/rolling surfaces). While these high temperature glassy layers do reduce the apparent surface shear strength of otherwise unlubricated α–SiC by about two orders of magnitude (from ~2 MPa to 0.5 MPa at moderate PV and to as low as 0.01 MPa at high PV), the wear increases from the low temperature, moderate PV value of 1×10^{-15} $m^3/N \cdot m$ to as high as 1×10^{-12} $m^3/N \cdot m$ at high PVT. It appears that these glassy layers do not have the same load carrying capacity as elasto-hydrodynamic films generated from lubricating oils. This would be expected from the high compressibility of silica-silicate materials. They are also easily removed from the contact zone by tribological action. More work needs to be done to determine the relative contribution of toughness-hardness-induced and oxidation-generated wear of Si_3N_4 and SiC ceramics at temperatures intermediate to room ambient and ~850°C.

It was shown, however, that due to the molar volume reduction occurring on formation of the glassy SiO_2-based layers generated from Si_3N_4 and SiC, the vitrified surface film will be under tension. As such, thermal-cycled ceramic surfaces will wear more at room temperature than ceramics which have never been heated and oxidized. There is increased wear because the fracture toughness of glass-covered (tensile-stressed and usually cracked) surfaces is significantly lower than those of the unoxidized versions.

1.5.5 *Measurement of Coating Delamination and Surface Shear Interaction by Microscopic Tribometry*

The high temperature SEM tribometer is a highly efficient apparatus capable of determining the dynamic adhesion of lubricant films (hard or soft) by correlating friction changes in extreme environments with video-monitored delamination. In fact, this apparatus is the only one in existence today capable of measuring the dynamic delamination of CVD diamond films by tangential sliding, at temperatures to 1000°C. The REVETEST® diamond stylus or a Vickers hardness tip, for example, wears flat after a few traverses over a polycrystalline, faceted (extremely abrasive) diamond surface, even at room temperature.

Also for the first time, highly controlled SEM tribotests at low loads, low speeds and room temperature using ultrapure single crystals of CaF_2 and BaF_2 sliding against themselves and each other in the $(111)[1\bar{1}0]$ surface configuration served to produce unusually precise and accurate surface shear strength results. The generated data are considered more meaningful to a tribologist than those provided by other τ_s-determining techniques currently available.

1.5.6 Intangible Benefits

In addition to these and the rest of the technical results described in the present report, attention is called to the intangible benefits of the program:

1. Interest in microscopic modeling of interfaces was kindled among highly respected academicians. Graduate students following in their footsteps are sure to appear on the horizon.
2. Our results also generated wide-spread interest in constructing microscopic/macroscopic tribometers equipped with in-situ surface analytical instrumentation. The advent of increased utilization of such friction and wear testers challenges the ingenuity of experimentalists to confirm or modify the theoretical predictions or generate new ones.
3. The program data have been widely disseminated through periodic semiannual reports and yearly technical exchange conferences. We thus exposed ourselves to the arduous process of continued peer review. Valuable ideas were promptly incorporated, while blind alleys were avoided through the constructive criticism of colleagues.
4. No disciplinary provincialism was permitted and no national boundaries were recognized in search of the scientific principles.

The role of any DARPA-funded program is to sow the seeds of science and point the way for future work. The number and the size of the mosaic pieces put in place by the present program were intended to solve present problems and to establish the pattern of solid lubrication research for years to come.

2.0 THEORETICAL PREDICTIONS AND SPECIAL TEST EQUIPMENT

2.1 THEORETICAL PREDICTIONS

The complexities of materials-related interactions on sliding/rolling ceramic surfaces, especially when lubricated with a variety of solid lubricants, reduces the probability of constructing meaningful statistical test matrices. The large number of tests, the impure nature of engineering ceramics and the cost involved in completing such matrices dictated an approach employing carefully designed model experiments with high purity specimens. The ideal samples consist of highest purity versions of single crystals. The experiments had to eventually define the chemical and microstructural aspects of the solid lubricated ceramics which influence the strength, toughness and surface shear behavior of the lubricated interfaces. First, however, theoretical predictions are needed to be established with idealized couples.

At the most fundamental level, all tribology is chemistry, in that making and breaking chemical bonds at the interface (friction) and within each counterface (wear) are the controlling factors. Bonding ranges from the weak van der Waals, to the stronger ionic and strongest covalent interactions; implying progressively higher friction at the interface but progressively lower wear within the contacting surfaces.

As previously depicted in Figure 1 and in (19), theoretical predictive techniques can range from the microscopic (atomic level) to the continuum. The most basic methods are the ab-initio type, molecular orbital (MO) and valence bond (VB) theories [also see (20)].

In the MO, electrons are paired up in their orbitals and these orbitals are delocalized over the entire system. The VB takes only one electron per orbital into account, and the orbitals are pretty much localized over one or two atoms. Both MO and VB can be used to calculate such fundamental parameters as bond energy, electron density and dipole moment. The VB is, however, more suited to elucidating bond directionality, thermodynamic quantities related to the breaking of bonds and reconstruction of surfaces. (*Note:* During *reconstruction* (an important concept for friction reduction, already discussed in this report), change in the two-dimensional periodicity of the surface occurs.)

Alteration in the surface structure is caused by the self-arrangement (collapse) of the dangling bonds into well-defined unit cells (domains) of given configuration and size along specific mesh vectors. This concept is different from surface *relaxation* , where the freshly cleaved surface also results in a two-dimensional-perodic structure of the atoms, but this new surface structure retains the periodicity of the bulk. The bond lengths and angles here are simply self-adjusted to minimize a potential energy function. In addition, the VB method was shown successful for ionic bonded surfaces, whereas the MO is most often used for systems with multiple bonding, such as aromatic compounds with conjugated bonds (e.g., polymers).

Unfortunately, the powerful nature of these quantum mechanical methods is overshadowed by their inability to handle much more than ~20 particle (atom) systems. The limitations lie in the fact that even

the fastest computational techniques offered by the most modern and expensive supercomputers take too long with clusters larger than that number.

To predict the bulk properties of matter, techniques capable of much larger ensembles of particles must be employed. Stochastic approaches such as the (a) semiempirical, (b) bond structure, (c) density functional and (d) quantum Monte Carlo methods all have their own advantages and disadvantages in handling larger systems. Although their use can lead to periodic potentials in perfect crystals developed by their own particular model of electronic wave functions, they are not considered suitable for predicting the bulk mechanical properties of realistically defective materials, e.g., real ceramics or solid lubricants.

As a consequence, in addition to the VB, the molecular dynamics (MD) method was selected as an avenue of approach to calculate equilibrium properties of an atomic system consisting of hundreds-to-thousands of particles. In MD, the interatomic potential(s) derived ab-initio-quantum-mechanically (or semi-empirically) are utilized in classical integration of the equations of motion for the positions and velocities of a large group of atoms (viz., $F=m \cdot a$). It works best for ionic-bonded systems where pair potentials and many–body potentials work well. In spite of its own shortcomings (e.g., inability to handle greater than ~160,000 particles), MD demonstrated promise to model atomic motion and interaction on the idealized microasperity level, as discussed later in this section.

2.1.1 Quantum Dynamics and Suggested Experiments

There are a number of difficulties involved with elucidating the microscopic details of the electronic states at surfaces and interfaces by the most basic quantum chemistry techniques, as shown by the recently released IDA report (19). The first step should be to determine the electronic structure at the interface, but this is difficult experimentally even for a clean and ordered ceramic or solid lubricant surface. It is also extremely difficult where impurity atoms are present, even for cases as simple as nonordered oxide layers. Nevertheless, procedures are available which consist of treating a finite piece of the surface or interface as a small, perfect cluster of molecules. Ab-initio calculations are then carried out on these molecules using the generalized valence bond (GVB) method with additional configuration interaction (i.e., beyond just using pair potentials), thereby incorporating the dominant many-body effects (20).

As previously discussed, methods have been developed over the last two decades for accurate first-principles-calculations of the wavefunctions of molecules. These methods can be used to obtain complete surface potentials and activation barriers for the interaction (reactions) of molecules.

Since the quantum chemical methods deal with evaluation of the explicit wavefunctions, they are amenable to direct, sequential inclusion of two- and three-body effects. Similar calculations showed that an increasing number of occupied metal-sapphire (Al_2O_3) antibonding molecular orbitals explains qualitatively the observed decrease of contact shear strength through the series Fe, Ni, Cu and Ag (21). Such calculations are equally essential to the understanding of solid lubricant adhesion to ceramics. As a

consequence, we started a broadbased theoretical program with Prof. Goddard of Caltech, aimed at providing the fundamentals for constructing such an atomic-level (microscopic) model of the chemical, tribological, physical and mechanical properties of ceramic surfaces and interfaces. The approach was:

- to start a series of quantum chemical studies to establish the dominant surface species for clusters of atoms modeling various ceramics and solid lubricants, and to elucidate the thermochemistry and detailed mechanistic steps involved in surface reactions of such systems;
- to use the energy surfaces for clusters to develop theoretical force fields which allow predictions of the energies and geometries for surfaces and interfaces first on the atomic-molecular level, then eventually in the continuum;
- to develop procedures for subsequent MD simulations which, in conjunction with the force fields, could be used to predict the rates for various diffusive and chemical processes relevant to tribology and materials synthesis processes; and to interface the results of these simulations onto appropriate computer graphics systems, allowing the designer to follow a three-dimensional image of the evolving system while interactively changing conditions and characteristics of the system.

Through simultaneous examination of all properties of the surface (chemical, physical, and tribological) with the same theory, there is the possibility for strong tests of different aspects of the theory. In addition, such a central theory would provide new connections between these properties serving to correlate the large number of experiments in huge test matrices, which may still appear largely disconnected and disjointed especially if improperly constructed in the first place, i.e., without the help of theoretical methods. These theoretical developments of experimentally relevant systems should offer a level of understanding useful in designing new materials with desired tribological properties. In addition, the computer-aided materials simulations should provide tools allowing many of the design concepts to be tested on the computer, before difficult syntheses and characterizations are attempted in the laboratory.

The necessarily short nature of a DARPA program dictated that Prof. Goddard's involvement would start under the auspices of the Part I effort and transition into the AFOSR Tribology Initiative. His Part I work is summarized in APPENDIX A. The essential general findings are as follows:

1. Due to the expensive and time-consuming nature of quantum chemical calculations, only a few systems have been studied. The extraction of force fields from such calculations (needed to describe bond breaking processes important for the prediction of wear) is still in its infancy.
2. In order to describe making and breaking of chemical bonds or describe surfaces containing broken (dangling) bonds or other active sites, one must carry out high-level calculations including electron correlation (i.e., many-body) effects. The GVB theory seems to be ideal for this purpose. However, for passivated surfaces where radical (active) sites are not present, the less sophisticated stochastic methods are still reasonably useful.
3. By combining quantum chemistry, force fields and atomic/molecular dynamics, the adhesion of various adsorbates or solid lubricants to a surface can be studied. However, the simulation of wear processes (which requires the description of bond breaking) has yet to be implemented.

Clearly, a theory specifying the configuration of the valence electron orbitals would have great significance in predicting the bulk properties of matter which, in turn, depend on the nature of the interatomic bonds. Since theoretical calculation methods employ small ensembles of atoms/molecules of idealized structure, any experiment designed to check the theory must, by definition, use the most perfect single crystals of ceramics and solid lubricants as specimens in the most inert environment possible (in nearly all cases, ultrahigh vacuum). As shown in Table 1, Prof. Goddard recommended several ceramic and solid lubricant systems for model experiments. He stressed the importance of surface analytical instrumentation in elucidating the nature of the rubbing interfaces prior to test, and the development of experimental procedures for measuring friction , wear, hardness, etc. under well-defined (read: ultrahigh vacuum and ultrapure gases) conditions.

After extended discussions on the dearth of readily available, ultrahigh vacuum tribometers combined with in-situ surface analytical instrumentation at the beginning of the program (SORETRIB's apparatus was not yet finished), two types of experimental systems appeared to be acceptable to suit the capabilities of the SEM tribometer (1.33×10^{-3} Pa = 1×10^{-5} torr vacuum, no in in-situ surface and analytical instrumentation) providing the shortest, most realistic lead-time. One consisted of rubbing interfaces of CaF_2 and BaF_2, which in their purest single crystal form are less sensitive to surface contamination by atmospheric species (e.g., oxygen and moisture) than most other solid lubricants. As such, the relatively low-grade vacuum of the SEM column would minimally influence the outcome of tribotests run with properly prepared single crystals. The other type of system was comprised of two materials, where thermally desorbed and resorbed species in the SEM tribometer chamber(s) can predictably increase or decrease friction (and therefore, friction-induced surface cracking and, perhaps wear) due to the generation or annihilation of dangling bonds or other active sites on the rubbing surfaces. The two model compounds of interest were single crystal and polycrystalline rutile (TiO_{2-x}), and polycrystalline diamond (single crystals of diamond large enough for SEM triboflats were prohibitively expensive).

In order to provide some insight on using calculated microscopic quantities as a tool for predicting friction, Prof. Goddard and his students carried out a series of calculations, simulating the hydrogen-terminated (111) surface of diamond sliding against the equally passivated ($\bar{1}\bar{1}\bar{1}$) mating plane (Figure 4). The space between the slabs was optimized to obtain equilibrium. Then, equilibrium structures were calculated by treating the lateral displacement as a shear in the fundamental unit cell of the three-dimensional system under an external load, as shown schematically in Figure 4b. Note that in the diamond cubic lattice, layers of six-membered rings in the chair configuration are separated by staggered bonds. The stacking sequence in each [111] direction is ABC/ABC/. . . . . (not completely shown in Figure 4b, because only two layers per slab are depicted), and each exposed carbon atom on the (111) or ($\bar{1}\bar{1}\bar{1}$) is bonded to one hydrogen atom.

The results are shown in Figure 5. Figure 5a depicts the (111) energy surface under no normal load, superimposed on the atomic position of the lower ($\bar{1}\bar{1}\bar{1}$) surface. The minimum position (i.e., 0.000 in Figure 5b) has the C-H bond of the upper surface symmetrically between the three C-H

Table 1. Model triboexperiments suggested by Prof. W.W. Goddard III (Caltech).

Model Compound	Suggested Triboexperiments
Diamond and Silicon (Single crystal, polycrystalline and amorphous)	• Freshly cleaved; • Surface saturated with hydrogen or fluorine; • Dry or wet oxidized
SiC and Si_3N_4 (Single crystal or CVD, and polycrystalline)	• As cleaved/grown/pressed; • Wet and dry oxidized; • Surface modified by doping
Metals (Au, Ag, Ni) and metal oxides (Al_2O_3, CoO, MoO_3), various forms	• Clean; • Surface modified by doping
Layered hexagonal materials (graphite, MoS_2, h-BN), various forms	• As cleaved/grown/pressed; • Oxidized

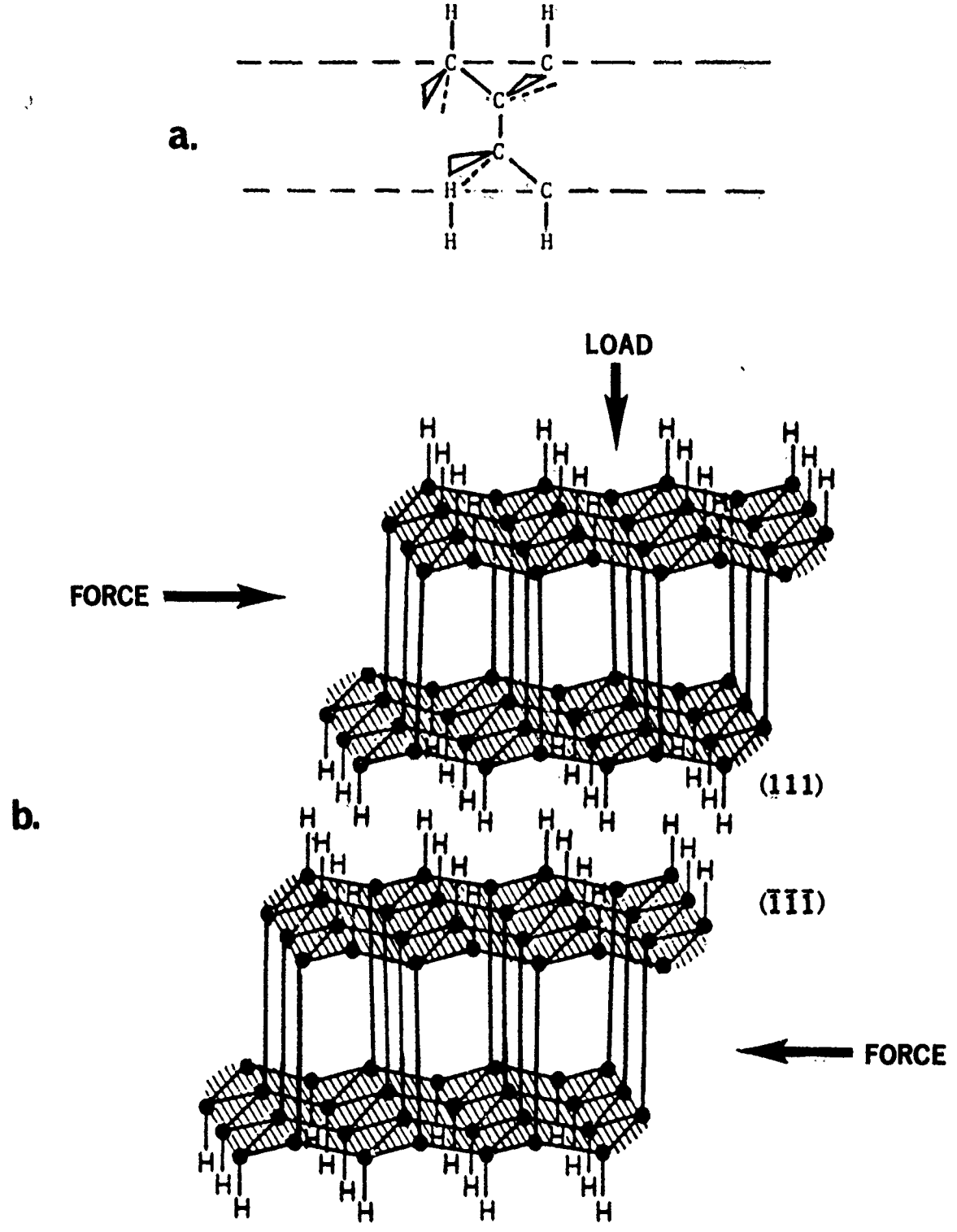

Figure 4. Sheared slabs of hydrogen-terminated (111) vs. ($\bar{1}\bar{1}\bar{1}$) diamond surfaces displaced against each other; (a) the periodic boundary conditions of each slab; (b) schematic representation of the sheared system under load (lengths of interplanar sp^3 bonds are exaggerated for clarity).

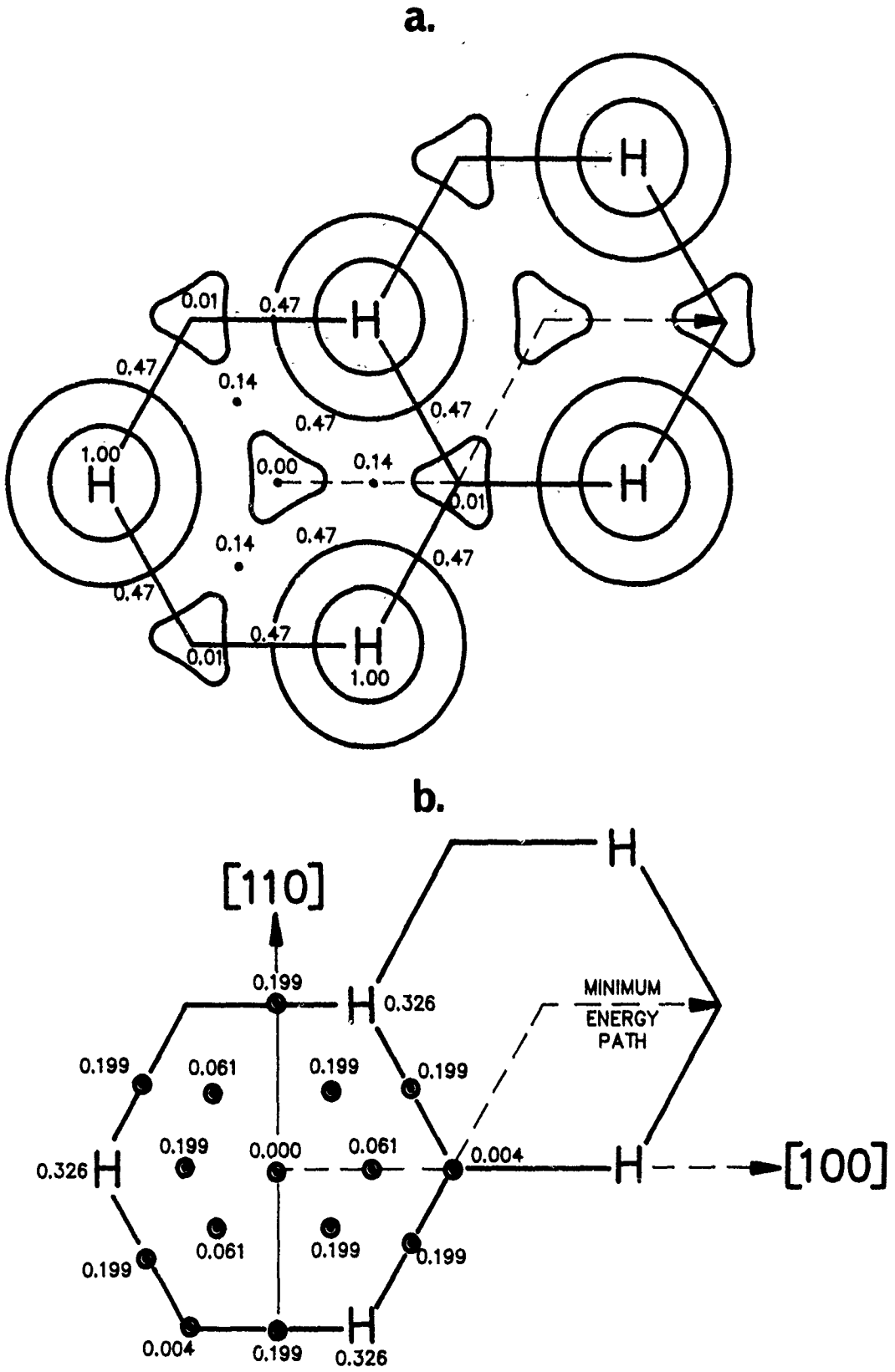

Figure 5. Static and dynamic energy surfaces of diamond (111) vs. ($\bar{1}\bar{1}\bar{1}$); (a) no normal load; (b) minimum energy path (see text for explanations).

bonds of the lower surface. The minimum energy path for displacement is where the C-H of the upper surface slides over to the right (in the [100] direction), moving over an energy barrier of 0.14 kcal/mole to a new position. There, the energy is only 0.01 kcal/mole higher than the original equilibrium position. To continue on the minimum energy path, a zig-zag motion must be followed. If not, i.e., if motion were forced in a straight line, the lowest energy path would be over a 0.47 kcal/mole or worse, an even larger 1.0 kcal/mole barrier.

As shown in Figure 5b, the optimum energy path can be converted to a coefficient of friction (f_k) by considering the 0.000 Å $\longrightarrow$ 0.004 Å $\longrightarrow$ 0.061 Å $\longrightarrow$ 0.000 Å vertical displacements between the diamond slabs necessary for the system to move along the minimum energy path. Note that the horizontal displacement during going over the first 0.000 Å $\longrightarrow$ 0.061 Å $\longrightarrow$ 0.004 Å energy hill is 1.456 Å. The rest can be explained best by Prof. Goddard's own words:

> "If there is an external load on the system, we must do work against this bond to displace it back 0.06 Å to go over the first hill, but the bond can do work on the system as we go down the hill again. If this process were carried out with no energy transfer, there would be no friction. That is, the energy cost in going up one hill is returned upon going down and is then available to go up the next hill. However, if the energy is dissipated from the surface as it goes down one hill, it cannot be returned to climb the next and there is friction. To get an idea whether there is time for such dissipation, consider that a velocity of 2 meters/sec converts to 0.02 Å per picosec. Thus, at this velocity, it takes 35 picosec for the system to go back down hill. One the other hand, the characteristic time for energy transfer from the C-C-H bending modes at the surface is likely to be ~1 psec. Thus the energy should be dissipated. .... We can thus estimate the maximum coefficient of friction as the maximum slope of the displacement curve or

$$f_k = \frac{0.061}{1.456} = 0.132.$$

> "It is interesting that this value is in the ballpark of experimental measurements of the coefficient of friction in diamond by Tabor[31*] who reports $f_{(k)} = 0.1$ for diamond (111). This does not prove our simple model. The experiments on diamond were carried out with a metal probe in a normal atmosphere. We now know that a well polished diamond surface is covered with C-H bonds. Hence these experiments should be repeated in an inert atmosphere with a diamond probe so that one does not have to worry about the surface H on the diamond being transferred to the metal."

---

* Ref. 31 (APPENDIX A) = Tabor, D., "Adhesion and Friction", Chapter 10 in *Properties of Diamond*, Ed. Field, J.E., Academic Press, London, 1979.

"It is also not clear that the coefficient of friction for a completely flat surface is relevant for friction studies where even for a single crystal there will be steps and other imperfections that may keep parts of the surface from interacting. . . . . That is, the experiments on the best quality single crystal surface may be dominated by what happens when two steps come together rather than by the sliding of two surfaces with respect to each other. Of course, similar theoretical calculations can be carried out at the steps; however, there are new questions. Are the step atoms also completely saturated with C-H bonds? We could assume this in the calculations, but this should be tested with appropriate surface science experiments. Using these theoretical approaches, one should be able to examine systems modeling (such) system. . . . . and provide simulations of friction and wear for these systems."

In one of his previous publications (22) and during his many program lectures listed in APPENDIX A, Prof. Goddard expanded on Pepper's results (23) with respect to dangling bond generation on diamond surfaces. Pepper showed that the appearance of unoccupied states in the band gap (i.e., dangling bonds) on diamond surfaces heated in high vacuum (and thus dehydrogenated) was accompanied by drastically increased friction of a diamond-metal couple. Capping the active sites with hydrogen brings the friction down to its original value. The hydrogen-saturated surface of diamond (sliding against itself, e.g., see Figure 4b) is now stable at near room temperatures (no electron can be added or removed), assuming the surface properties of a paraffinic lubricating oil.

As pointed out in (22), each dangling bond orbital on diamond spin-pairs with another electron donated from a contacting surface, leading to the formation of a Schottky barrier. The size of the barrier height is one measure of this interaction and thus, adhesion and friction.

Indeed, Mishina and Buckley (24) previously demonstrated that the friction of (110)[[11$\bar{2}$] Si and (100)[011] GaAs single crystals in contact with pure metals depended on the Schottky barrier height (ϕ_b) formed at the metal-semiconductor interface. Metals with a higher barrier height on semiconductors gave lower friction, and the lower friction may be explained in terms of weaker adhesion at the interface. From Ti (ϕ_b = 0.50 eV) to platinum (ϕ_b = 0.81 eV) sliding on Si, the coefficient of friction (f_k) decreased linearly with ϕ_b (1 eV = 23.05 kcal • mole^{-1}). The effect of ϕ_b on f_k was more specific for freshly cleaved surfaces than for surfaces containing surface films in room air. Similar trends were found for GaAs in contact with other selected metals. Recent work by Stepien, et al (25) came to the dramatic conclusion that intrinsic Schottky barriers are due to dangling-bond resonances.

It appears, therefore, that the ease of surface defect creation during diamond sliding against itself or metals (22, 23), combined with the willingness of the metallic counterface to form carbidic-type bonds, are the controlling factors of adhesion and friction. For example, the relative strength of the carbidic bond is often estimated by the size of the (negative) free energy of formation (ΔG_f°) of a given metal carbide.

As also pointed out by Prof. Goddard in (22), diamond cleaved in vacuum has the tendency to decompose, forming graphitic regions. Carbon in bulk diamond is bonded to four atoms arranged in a

tetrahedron. A surface carbon is bonded to only three other carbons, leaving a dangling bond orbital. In its new state, this small cluster now prefers a planar configuration (e.g.,CH_3^+ is planar). Thus each carbon in the top row of the diamond lattice wants to move down to the next row to become planar-oriented (use Figure 4b for better understanding of this concept). If a second row carbon atom moves up to the first row to bond to the dangling orbital (forming π-bonds) and this process repeats itself layer-by-layer, surface graphitization occurs. Energy input conducive to the formation of dangling bonds (e.g., heating, ion bombardment, electron beam impingement or tangential shear under load) accelerates this process.

Cleaving diamond in air causes the surface to react with the oxygen by linking the singly occupied orbital of the dangling bond to one oxygen. Singly occupied orbitals are needed to bond to one oxygen, thereby weakening the O-O bond before combustion can occur. The (a) higher stability of the diamond (100) plane to oxidation [where each surface carbon is bonded to two hydrogens, as opposed to that of the less oxidatively stable (111) where one hydrogen per carbon is attached (26)], (b) the increased reactivity of the diamond (111) to water vapor and oxygen resulting in hydrophilic surfaces (27, 28) and (c) the planarity of the "graphite oxide" solid (29) all appear to be the manifestations of the same quantum chemical behavior.

The models brought forth here were instrumental to the establishment of experimental and data-analytical protocols employed in elucidating the tribological behavior of polycrystalline, CVD diamond films with the high temperature SEM tribometer (see Section 3.5). Similar quantum chemical and thermodynamic models were used in (12) for explaining the differences between the oxidation resistance of TiC and TiN hardcoats (see Section 3.3).

2.1.2 Molecular Dynamics and Suggested Experiments

As previously stated, an ab-initio cluster calculation method is not feasible for a number of particles (atoms or molecules) larger than 15 to 20, because there is excessive super-computer time required to complete the large number of computational steps needed for clusters beyond that size.

Molecular dynamics (MD) calculation methods are applicable to a much larger number (thousands) of particles by (a) utilizing interatomic potentials already derived from ab-initio or semi-empirical calculations, and (b) classically integrating the equations of motion for the positions and velocities of a group of many particles by computer. The basic equation is essentially related to the well-known F=ma.

One of the applications for which MD works best is in ionic-bonded systems, where pair and many-body potentials are tractable. Examples are cubic (FCC or BBC) structures such as CaF_2, or other ionic structures such as the rhombohedral Al_2O_3.

The initial set of MD calculations was completed with a sheared (111)[1$\bar{1}$0] interface of two hypothetical materials, see Figure 6 and (30, 31, and 32). The system consists of 1200 interacting particles in an FCC structure, with the bottom half of the system having an interaction (surface) potential

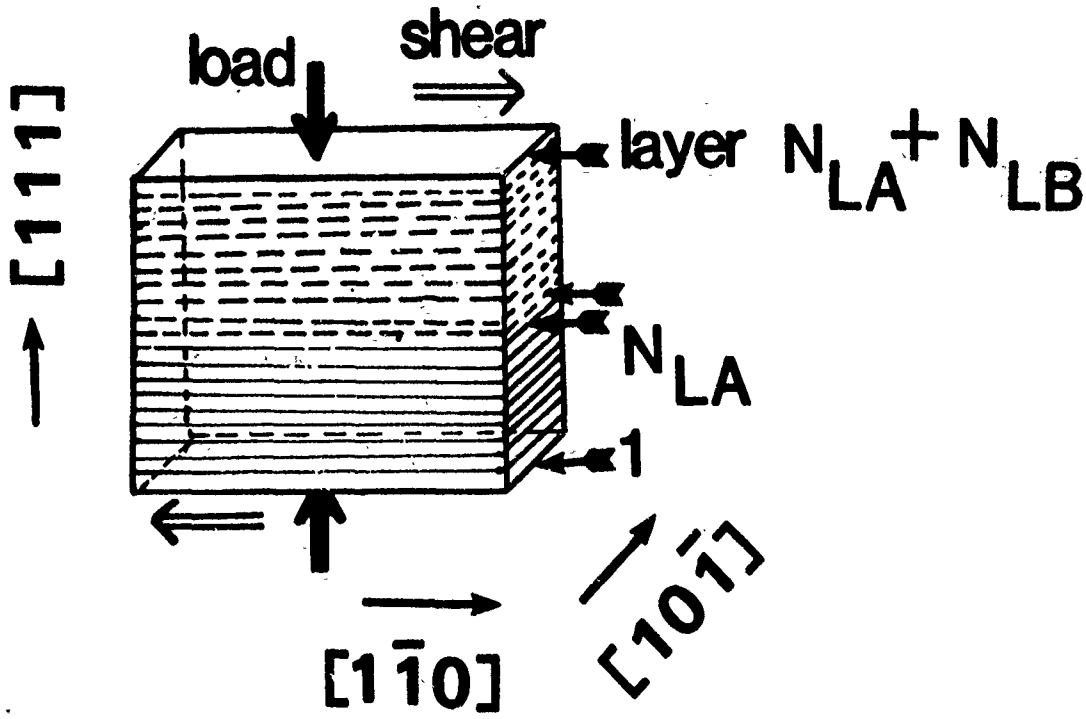

Figure 6. Schematic of the MD calculational cell. N_{LA} is the number of layers in the A (hard) material and N_{LB} the number of layers in the B (soft) material. The interface is between N_{LA} and N_{LA} +1. The directions of the applied load and shear stresses are indicated. Three dimensional periodic boundary conditions are employed in the simulations.

twice the strength of the potential for the top half. The interaction strength between species at the interface is the geometric mean of the top and bottom strengths and thus falls between them. The system was first equilibrated at a temperature about one-sixth of the melting temperature (corresponding to room temperature for a system that melts at about 1800 K). Then, a normal load was added corresponding to a typical pressure on the real area of contact for a system such as that between two steel plates. Shear forces were next applied to the system in stages, until it failed. A wealth of information came from this study.

Some highlights are that the system fails in the top (weaker) half (however, the layer next to the interface remains in its original configuration), and at failure the temperature of the top half very quickly approaches melting. Also, dislocations appear clearly in the top half of the system near failure. The system tears in the region between the third and fifth planes above the interface, but clear slip directions do not emerge until the sixth plane. The coefficient of friction $f_k \cong 4$, a value of the same order as the coefficient of static friction (f_s) for clean metals in contact in ultrahigh vacuum. Still, stress relief and the associated structural transformations in the soft material are accompanied by an accumulation of stress in the interfacial region of the hard material.

Where there is a mismatch in the atomic sizes (i.e., the atoms of the soft (B) material in Figure 6 are characterized as having a larger size), the critical yield value for the thermodynamic tension for this system is considerably lower than that for the system with equally sized atoms. Furthermore, unlike the previous system, the soft layer slipped in unison, without exhibiting plastic behavior prior to tearing/shearing. As explained in (31), . . . "These observations can be understood when considering that as a consequence of the larger atomic size the atoms of the soft material at the interface coverage over the corrugation of the potential due to the substrate, resulting in an effective potential surface which exhibits smaller variations for lateral displacements parallel to the interface plane, and consequently a reduced resistance to shear."

It is appropriate to summarize Prof. Landman et al's extensive investigations on this idealized system with their own words, from (32):

1. "For interfacial systems which are characterized by differing interatomic interaction strengths (i.e., the interface is between a hard and soft material), the system responds to an applied nonisotropic perturbation (applied shear or strain) first elastically and then via stress relief mechanisms which involve structural transformations (stacking fault formation and interlayer slip). For larger values of the external forces, eventual yield occurs.

2. Critical values of the external perturbation required in order to bring about inelastic response (structural transformations and yield) have been determined. Our simulations demonstrate that the critical values are smaller for a system under isothermal conditions, which necessitates larger values of the external perturbations in order to overcome potential barriers for structural modifications and eventual yield.

3. The cohesive interatomic interactions at the interface between a hard substrate and a soft material result in "pinning" of the soft material at the interface (1-3 atomic layers). As a result, the response of the system to the transformations occurs in a "shear band" consisting of a few atomic layers inside the soft material, which for our model system are located at about 1-3 layers away from the original (unstressed) interface. The stress relief in the soft material is accompanied by stress accumulation in the hard substrate.

4. MD simulations for interfacing hard and soft materials, which in addition are characterized by differing atomic sizes, reveal the important role played by atomic size mismatch in determining the atomic-scale mechanism of response. For such systems it was found that no adhesive "pinning" occurs at the interface, and that the soft (and larger atomic size) material responds as a whole with no distinct structural transformations preceding the yield point. The critical yield stress value for this system is significantly lower than that found for the corresponding equal-atomic-size system.

5. Comparison of our results in this study for the [100] interface with our previous investigations of the [100] interface [26]* demonstrates the dependence of the critical values of the shear stresses on the crystallographic-orientation of the interface, as well as of certain details of the stress relief mechanisms."

Although they also investigated, under the auspices of the Part I program, atomic force microscope tip/flat interactions and bounded thin liquid films in preparation for the transitions into the AFOSR Tribology Initiative (31, 32), the results are not summarized here. These data did not impact our experimental protocol aimed at confirming the MD calculations with real material models, because neither atomic force microscopy nor molecular tribometry were performed during Part I for reasons explained in Section 1.0.

Inasmuch as (a) ultrapure (99.99%), oxide-hydroxide-free single crystals of CaF_2 and BaF_2 were available at Hughes [grown by the Bridgman method in a reactive atmosphere by Dr. Mort Robinson and his colleagues at the Hughes Malibu Research laboratories, see (33 through 37)], (b) CaF_2 and BaF_2 SEM triboflats and hemispherical pins could be fabricated with well-controlled crystallographic planes and directions on the sliding surfaces, (c) CaF_2 and BaF_2 appeared to be ideal model compounds with respect to hardness, surface energy and size differences of the particles used in the MD calculations (see Table 2), and (d) their chemical inertness made SEM tribometry possible, Prof. Landman embarked on predicting the τ_s of idealized CaF_2 vs. CaF_2 [and BaF_2 vs. BaF_2 (111)[$1\bar{1}0$] surfaces by MD calculations. His prediction with an idealized system of CaF_2 vs. CaF_2 was about an order-of-magnitude higher than measured by SEM tribometry (Table 3). His report on the subject is attached here as APPENDIX B.

---

* Ref. 26 in (32): Ribarsky, M. W., and Landman, U., in *Approaches to Modeling of Friction and Wear*, Eds. Ling, F.F., and Pan, C.H.T., Springer-Verlag, NY, p. 159 (1988).

Table 2. Selected properties of Group IIA fluorides.

Property	CaF_2	SrF_2	BaF_2
Cation Radius (Å)	1.06	1.27	1.43
Lattice Constant (Å)	5.46	5.80	6.20
Knoop Hardness (kg/mm^2)	163	140	82
Surface Energy (dynes/cm)	450	340	280

Table 3. The shear strength of (111) [$1\bar{1}0$] CaF_2 vs. CaF_2, BaF_2 vs. BaF_2 and BaF_2 vs. CaF_2 couples—experimental data by SEM tribometry; predicted τ_S values are near 100 MPa, see APPENDIX B: (a) calculated by τ_S (app.) = $f_k \cdot P_y$; (b) calculated by τ_S (app.) $\cong \frac{F_k}{A_H}$

a.

	P_y kg / mm^2	f_k avg.	τ_s kg / mm^2 (MPa)
CaF_2 / CaF_2	26.86	0.042	1.13 (11.06)
BaF_2 / CaF_2	7.14	0.080	0.57 (5.60)
BaF_2 / BaF_2	7.14	0.077	0.55 (5.39)

b.

	F_k x 10^{-3} kg	A_H x 10^{-4} mm^2	τ_s kg / mm^2 (MPa)
CaF_2 / CaF_2	0.26	2.50	1.04 (10.21)
BaF_2 / CaF_2	0.52	3.09	1.68 ⇒ 0.78* (16.52) (7.67)
BaF_2 / BaF_2	0.52	3.62	1.44 (14.07)

* Measured apparent area of 8.73 x 10^{-4} mm^2

2.1.3 Ball Bearing Dynamics

As more thoroughly described in (4), materials system requirements in terms of property design windows can be defined by computerized analysis of MMA kinematics. Trade-off studies of mechanism design configurations minimize the demands on the materials scientist, because the best possible contact stress reduction has already been realized by design optimization of component dynamics.

Since a rolling element bearing is one of the most difficult MMAs to solid lubricate for extreme environment applications, we began computer simulation of (a) the dynamics of a bearing separator (aka cage or retainer) and (b) the ball motions by employing the unique, six-degrees-of-freedom model SEPDYN initially developed during a previous DARPA/Hughes program (38, 39, 40). Under the auspices of the present program, we teamed with the WRDC Aero Propulsion and Power Laboratory (WRDC/POSL) in funding the completion of SEPDYN to the point of making it user-friendly and available to qualified technologists and programs. This work is now finished (41) and the Final Report may be obtained from WRDC/POSL under certain distribution restrictions.

Essentially, SEPDYN can now simulate all the kinematics and dynamics of a double-row bearing pair, one row at a time, with any combination of axial, radial and moment loads. The model was designed for solid lubricated bearings and requires empirical data on the coefficients of friction (traction) between the ball-to-raceway contacts. With these experimental data, which must be generated under the most realistic MMA-like conditions, the vector sum of the ball integrations can be computed at all ball and separator-raceway contacts.

The program is in PL/I language for high calculational efficiency and ease of vector manipulation, and all equations are in polar coordinates. The simultaneous six-degree-of-freedom vector matrix equations are solved in a cage coordinate system to simplify the equations of motion and to drastically reduce computing time.

Maximum bearing operating time in a computer run is made possible by varying the integration step size. The program automatically selects the integration time step size. Both advanced Runge-Kutta-Fehlberg and predictor-corrector algorithms are incorporated and can be selected as appropriate for a specific design problem. Integration step size and truncation error limits can be set to obtain the required level of accuracy.

The results can be plotted in conventional abscissa/ordinate time plots for identification of characteristic cage frequencies and amplitudes of motions as well as impact force magnitude and direction. SEPDYN also computes heating rates, friction torque noise due to all collisions and friction losses, and the ball skid of each ball. The position of each ball is also tracked.

Since the most frequent failure mode of solid lubricated rolling element bearings is the destruction of the self-lubricating composite separator by (a) excessive wear of the ball pockets due to high ball-to-

pocket loads, and (b) excessively high impact loads which fatigue and fracture the separator webs, one of SEPDYN's most valuable contributions lies in predicting these loads as a function of bearing material properties (e.g., density and elastic constants) and design variables (e.g., ball-to-pocket and separator-to-land clearances). Then, depending on the type of bearing and the circumstances of use, the separator wear characteristics and durability properties of the separator can be optimized.

The completion of SEPDYN enhanced our modeling capabilities, which now range from the atomic-level to the continuum regime (see Figure 1).

2.2 SPECIAL TEST EQUIPMENT

The ability of solid lubricated ceramics to withstand tribostresses depends a great deal on the magnitude and location of the maximum Hertzian compressive, shear and tensile stresses which exist in a given contact situation. It is well-known that at friction/traction coefficients less than 0.3, the region of maximum stresses is located below the surface. As previously shown by oil-lubricated rolling contact fatigue (RCF) tests, there are ceramics (e.g., the Norton Noralide NC-132 HPSN or its HIP-ed version NBD-100) which must be loaded to over 6.9 GPa (1 Msi) to initiate a subsurface-generated fatigue spall within a reasonable amount of time. Although most ceramics currently considered for friction and wear applications have lower RCF resistance, the artificially high load levels used in accelerated RCF testing are still much higher than the actual stresses found in real bearings. It appears that progress to improve subsurface integrity (where RCF crack initiation and propagation occurs) can still be made. Nevertheless, some current ceramics are already good enough to fulfill a practical role in ceramic tribology.

On the other hand, friction/traction coefficients (f_k/f_t) of 0.3 or more find the region of the maximum stresses on the surface. In view of the inherently poor tensile and shear properties of ceramics, the tensile and Hertzian cone-type surface and substrate cracking of these materials is especially accelerated under high-load, high tangential shear force conditions. Such conditions are far more harmful than those existing at low f_k/f_t values.

Unfortunately, it has been repeatedly demonstrated that the f_k/f_t for *unlubricated* ceramics is considerably higher than 0.3, at any test temperature. Furthermore, the meager data that existed on *solid lubricated* ceramics at the onset of the program all indicated that friction/traction seldom falls below 0.3. At high temperatures in air where solid lubricants oxidize, these oxides can react with the oxidized ceramic surface under enhanced, tribocatalytic conditions to create complex and, more often than not, unfortunate tribological surface reactions. Such reactions can lead either to high or low friction/traction coefficients. At room or especially at cryogenic temperatures where thermodynamics-driven surface reactions are minimized, the dominating effects are the fundamental willingness for mutual attraction or repulsion of the solid lubricated ceramic surfaces, surface roughness-induced friction variations, and abrasive wear.

One major thesis of the program professed the inability of *unlubricated* ceramics to serve in extreme environment MMAs (4). Their friction/traction coefficient often exceeds 0.5 and unless the triboconditions are unrealistically mild, the wear is unacceptably high. This has now been described in reports and papers too numerous to list here. The myth of high wear resistance of unlubricated ceramics is usually based on their high indentation hardness. The effects of the excessively high shear forces and the inelastic strain caused by the tribocontacts fabricated from low tensile strength, high modulus (brittle) and low fracture toughness ceramics are overpowering, yet often ignored.

In support of this thesis, the critical solid lubricant film adhesion, friction and ceramic substrate wear issues were addressed from the microscopic, macroscopic and continuum mechanical viewpoints to cover all interacting factors responsible for the degradation of solid lubricated ceramic surfaces. To resolve these issues, the proper test techniques had to be chosen.

Ideally, the experimental tools should be selected by the nature of experiments predetermined by theoretical models of adhesion, friction and wear. More often than not, the opposite is true: it is the nature of the available testers that limits the kind of experiments and models.

Initial evaluation of the causes and effects of adhesion, friction and wear (see Figures 6, 7, 8 and 9) indicated the all-pervasive need for surface analytical and tangential shear techniques. The tribotests themselves had to be performed in a wide variety of thermal and atmospheric specimen environments. A thorough survey of the needed vs. available instrumentation revealed the following shortcomings and their most likely solutions capable of satisfying both the intent and the available resources of the program:

1. It was concluded in APPENDIX C (prepared by Prof. Steve Granick, U. of Illinois) that atomic force microscopy (AFM) and molecular tribometry (MT) are complementary and not competing approaches. AFM studies substrate-tip tribology; MT involves substrate-lubricant-substrate-tribology, closer to our object of interest. The chief virtues of MT are a well-defined contact area, the ease of studying boundary layer lubrication, and control over the surface chemistry of the substrates. The latter is easier to obtain in high vacuum than in air. The substrate surfaces must, however, be atomically smooth over the characteristically small contact area (~100 μm^2 in Steve's apparatus). As such, going beyond liquid molecular species sorbed on cleaved mica surfaces to all-solid-lubricant systems is no simple matter. Translucency of the thin solid lubricant layer and the substrate is required for optical interferometer interrogation of the interface contact. Cross-cylinders geometry is needed to alleviate alignment problems. As a consequence, the use of AFM or MT was found premature for elucidating the microscopic interaction of solid lubricated ceramic counterfaces.

2. Although a wide variety of highly sophisticated, ultra-high vacuum surface analytical apparatus and techniques were available in industry and academia, the samples were small, highly polished flats and the analysis involved static specimens only. This specimen configuration is more useful to those investigating the electronic properties of surfaces and interfaces than to tribologists dealing with wear scars. Analysis of worn, rough surfaces is not a routine endeavor.

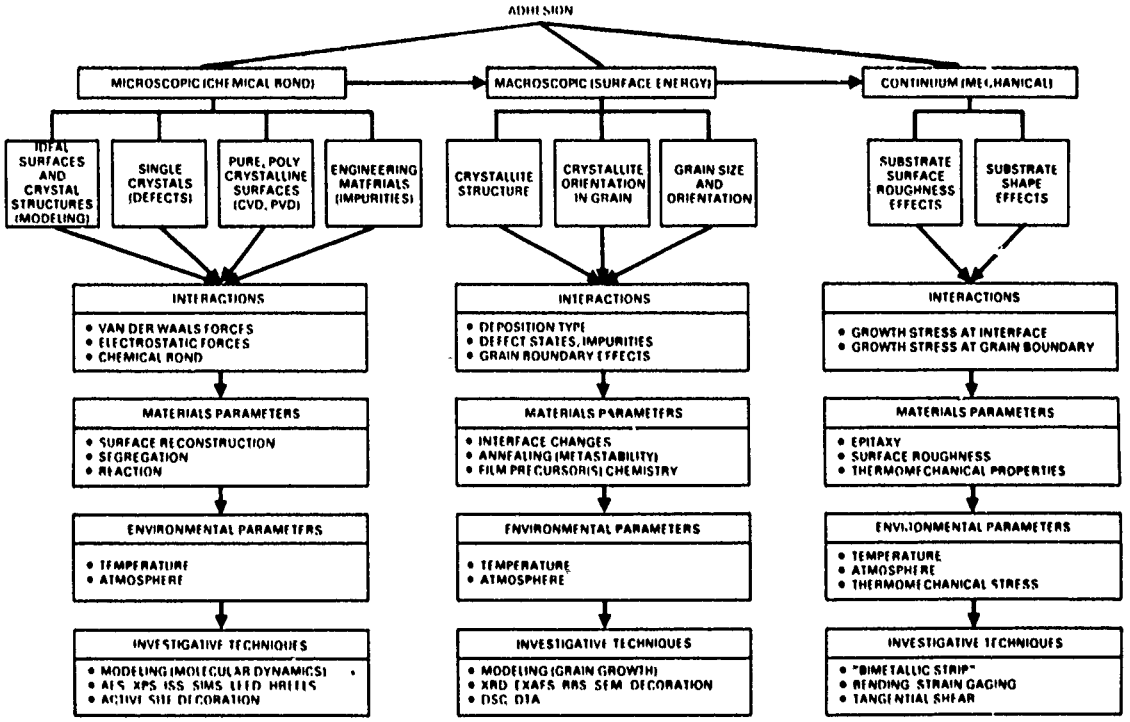

Figure 7. Critical issues associated with the adhesion of solid lubricant films.

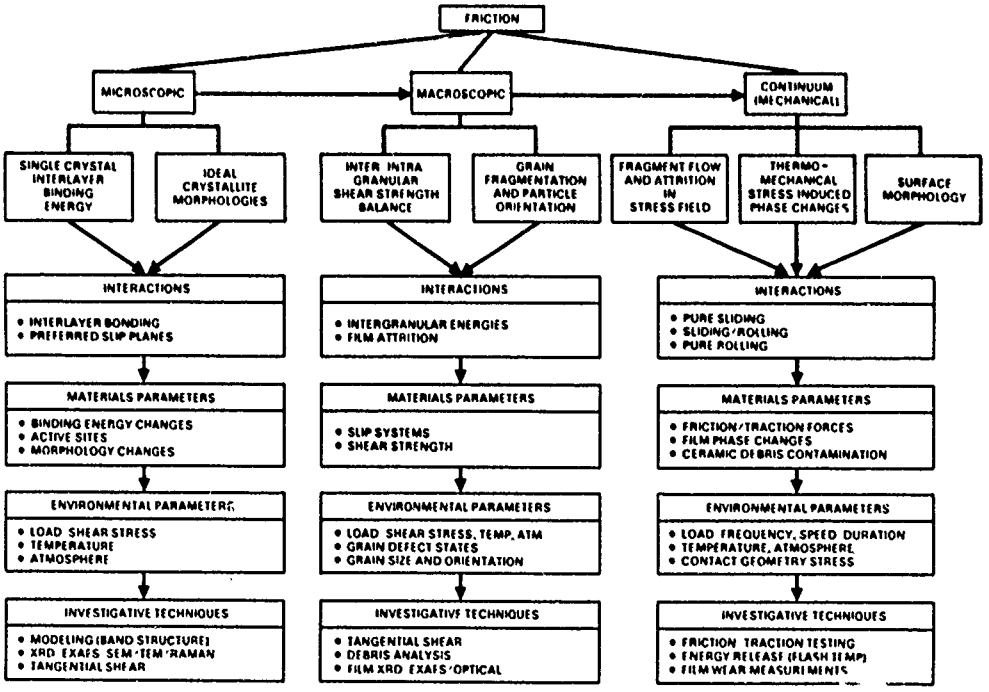

Figure 8. Critical issues of friction provided by solid lubricant films.

3. Auger/ESCA tribometers which have been used previously by pioneers in the field (21, 23, 25) are operated in one single, ultrahigh vacuum chamber. An ultrahigh vacuum environment needed to fulfill the analytical needs can be attained only where the tribotest chamber is isolated from the analysis chamber (e.g., by a load-lock mechanism), or by complex pump-down and backfill procedures which are both expensive and time-consuming. Furthermore, an additional surface treatment chamber, also attached to the test/analytical chamber, would be desirable. Lubricant coatings could be deposited and pretreated there under controlled conditions, prior to tribotesting and surface analyses. Such multi-purpose testers were not available at the start of our work. The lead time between design and data generation with such complex apparatus would have been longer, and the associated costs higher, than the duration and available funding of the program. Therefore, we selected the best (room temperature) Auger/ESCA tribometer that was still under construction, presumed to satisfy our needs as closely as possible. Fortunately, the near-availability of such an apparatus was also commensurate with the associated laboratory expertise by highly talented personnel at the Ecole Centrale de Lyon/SORETRIB (Ecully, France).

4. An extreme environment, microscopic/macroscopic tribometer, capable of operating at temperatures up to 1000°C and in a variety of gaseous atmospheres, still had to be constructed. The specimens needed to be small enough to (a) accommodate fabrication from small boules of single crystals, (b) lend themselves to before-after test surface analysis and (c) allow their placement on small substrate tables of experimental PVD chambers and CVD reactors during the various surface treatment and coating processes. The test apparatus itself had to be rugged and reasonably simple to operate. In view of (a) past successes with the observation of sliding interface in scanning electron or Auger microscopes under high magnifications (42 through 46), and (b) the existence of a differentially-pumped, high partial gas pressure, Knudsen cell-like hot-stage available at the Microscopy Research Laboratories (MRL), Inc., the construction of a high temperature SEM tribometer appeared to be the best compromise of all the options considered. As soon as promising results began to come forth with the high temperature apparatus, the design and construction of a cryogenic version was started. The new design was similarly based on prior work with cold SEM stages (47, 48, 49).

5. Continuum-mechanical sliding and rolling tribotests are meaningful only if the load, speed, frequency of contact and equilibrium contact temperatures are measurable and reflect realistic MMA conditions. Inappropriate extrapolation of friction and wear data obtained with nonrepresentative laboratory rigs to industrial problems has been repeatedly deplored in the literature (50, 51, 52). Our approach was especially unique in that the mechanical engineer/MMA computer diagnostician participated in what was essentially a materials science program. He predetermined the load, loading rate and speed of the tribotesters purchased or specially contracted for the program (see Figure 10). There were more than one continuum-mechanical test machines slated for use, because no single apparatus can traverse all PVT regimes, atmospheric environments and contact conditions relevant to our program goals. These machines were (a) the Georgia Tech pin-on-disc tribometer, a well-established apparatus useful to 400°C, (b) the commercially available, room temperature NTN-Bower RCF tester, (c) the Tester 2A specially designed and constructed at Hughes (a dual rubshoe tester capable of

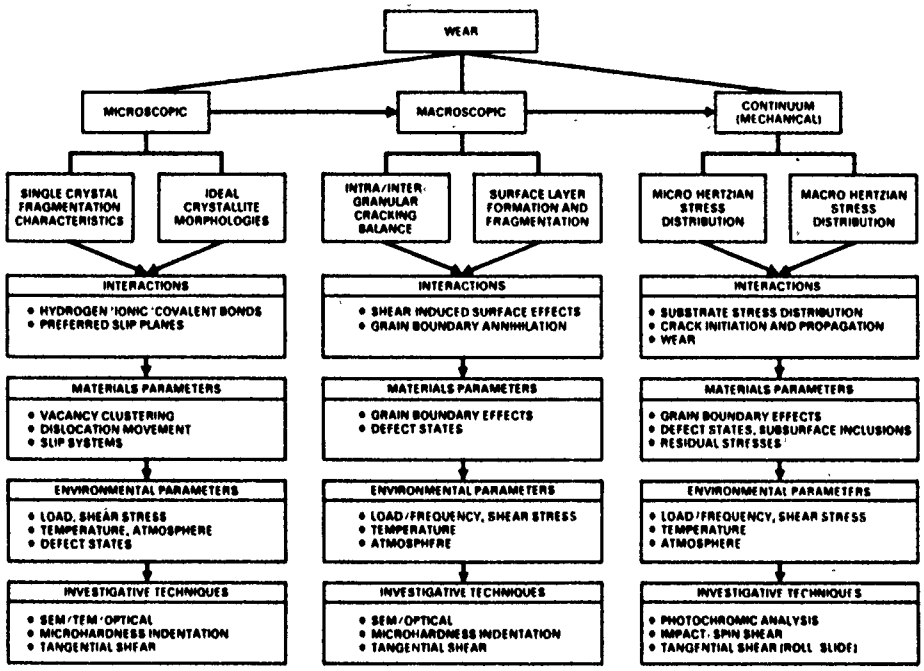

Figure 9. Critical issues of solid lubricant film and ceramic substrate wear.

operation to ~850°C), and (d) the specially designed and constructed, high PVT MTI friction/traction testers (to ~850°C).

Since the Georgia Tech pin-on-disc tester (14, 15, 16, 53) and the NTN-Bower RCF apparatus (58) have been adequately described elsewhere, no further description of them is given here. All of the other tribometers are described below.

2.2.1 Auger/XPS Tribometer [Room Temperature (R.T.)]

The existence of the precursor version of this apparatus was discovered in early 1986, during a Hughes/WRDC/TA&T, Inc. W. European survey trip, taken mainly to identify centers of tribological excellence capable and willing to support our program. The Ecole Centrale de Lyon's Laboratoire de Technologie des Surfaces (Ecully, France), under the leadership of Prof. Jean-Marie Georges, accumulated an outstanding collection of knowledgeable researchers addressing the type of fundamental tribology problems our program was called upon to solve. One highlight of the survey was the unusual capabilities of a then recently-constructed Auger/XPS (ESCA) tribometer, coupled with the ability of a work team, under the leadership of Prof. Jean-Michel Martin, to unravel complex friction and wear mechanisms using data generated by this apparatus.

As a consequence, they were invited to participate in the program, mainly to elucidate the tribochemical fundamentals related to the usefulness of hexagonal boron nitride (h-BN) as an extreme environment lubricant for ceramic surfaces. It is appropriate to describe this unusual apparatus here, before presenting the results of their overall research, both described here more thoroughly in APPENDICES D and E. Note that the Auger/XPS tribometer has undergone considerable improvements during the course of the present study. The schematic of the current version is shown in Figure 11. The engineering sketches of the disc (rotational motion), the flat (oscillatory motion), and the mating pin are included in Figure 12.

As depicted in Figure 11, both the pin and the disc/flat holders have their own XYZ manipulator arms. The unusual ability to expose not only the wear scar(s) and debris on the disc/flat, but also the worn pin tip to surface analysis is attributed to the rotational capability of the pin translator (see Figure 11a). A disc can be either rotated, or a flat oscillated, under the stationary pin under load. The test/surface analysis chamber also contains an SEM detector (for in-situ observation of the sliding interfaces) and an ion gun for sputter etching the surfaces during the analytical phase.

The disc/flat may be transferred into a differentially-pumped preparation chamber, without breaking vacuum. There, it can be infra-red-heated, along with ion-bombardment-assisted cleaning and reactive-gas-deposition of various surface films by vacuum evaporation or other PVD techniques. The gaseous atmosphere may be sampled with a residual gas analyzer (RGA). The deposited layers can then be tribotested and surface-analyzed by returning the flat into the test/analysis chamber (Figure 11b).

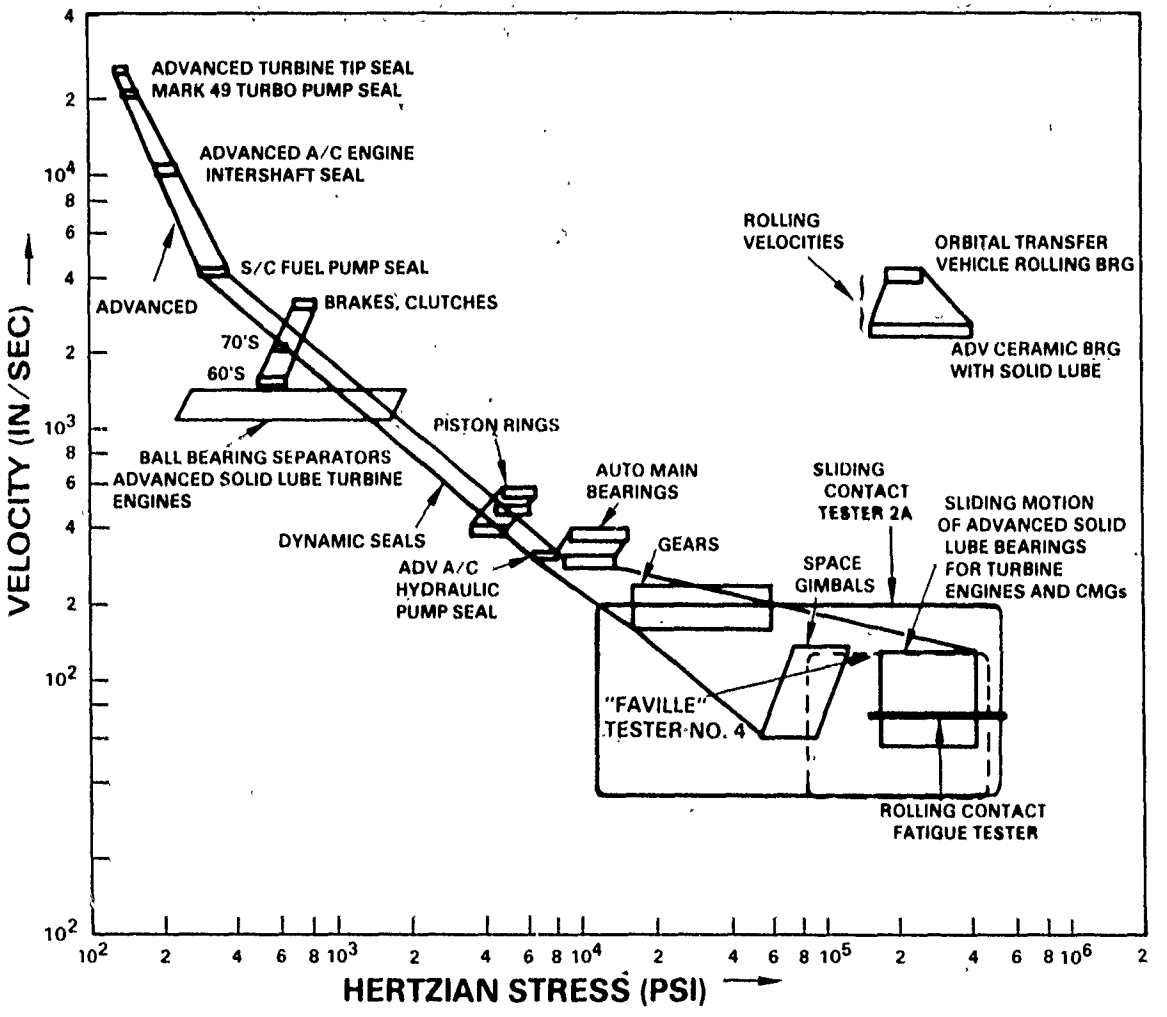

Figure 10. Load-speed map of commonly used bearing elements (1000 psi = 6.8948 MPa; 1 in $\cdot s^{-1} = 2.54 \times 10^{-2}$ m$\cdot s^{-1}$).

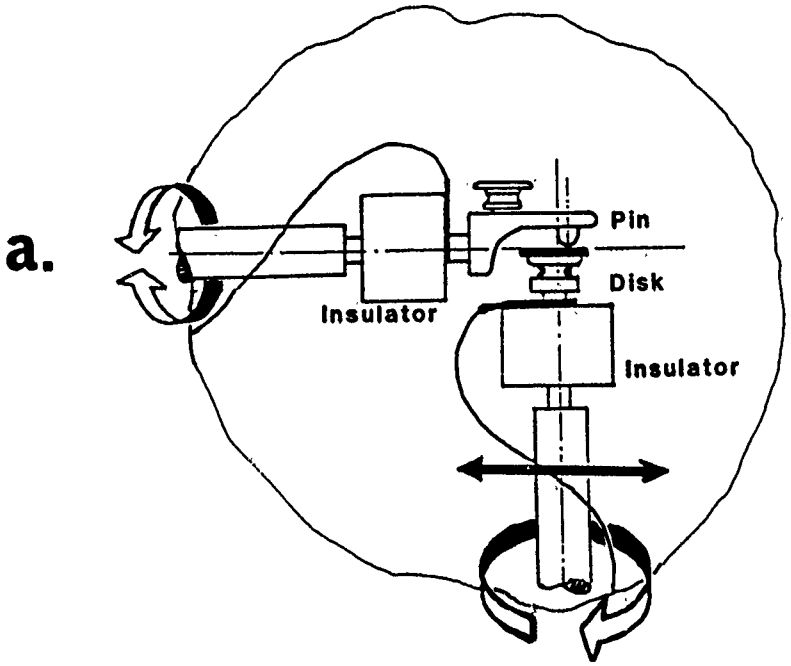

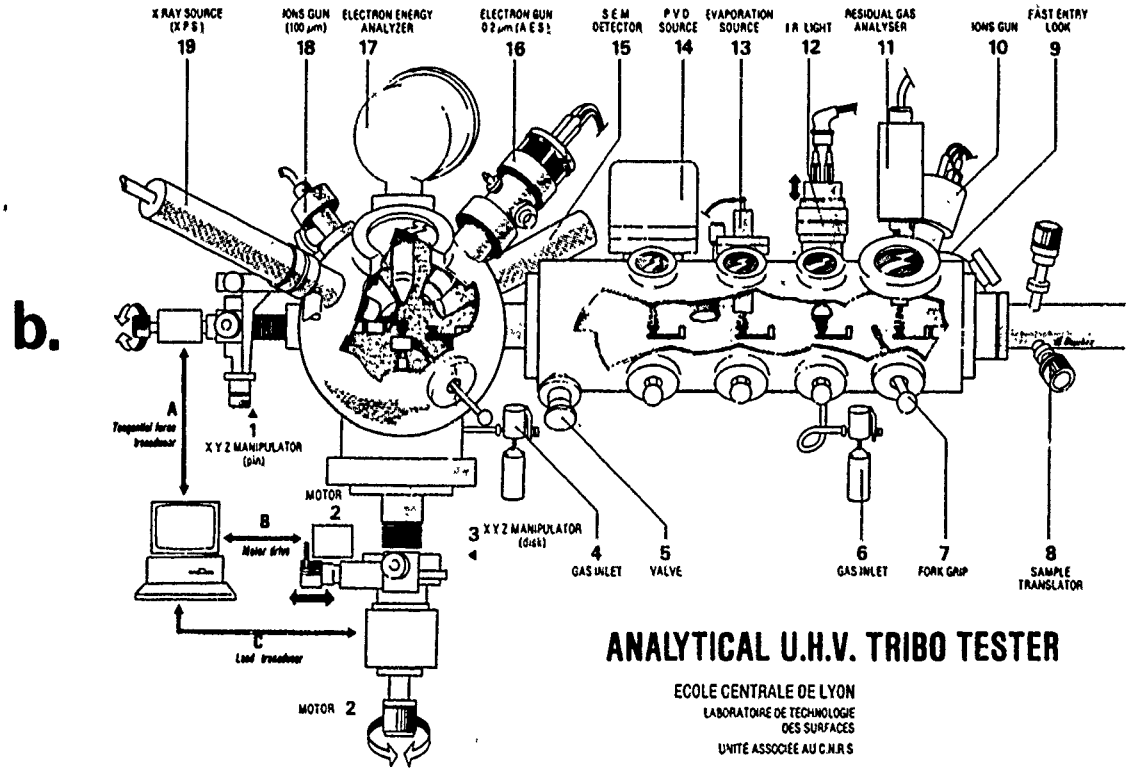

Figure 11. The schematic of the Ecole Centrale de Lyon/SORETRIB Auger(AES)/XPS tribometer; (a) the rotating/oscillating pin-flat combination; (b) overall view.

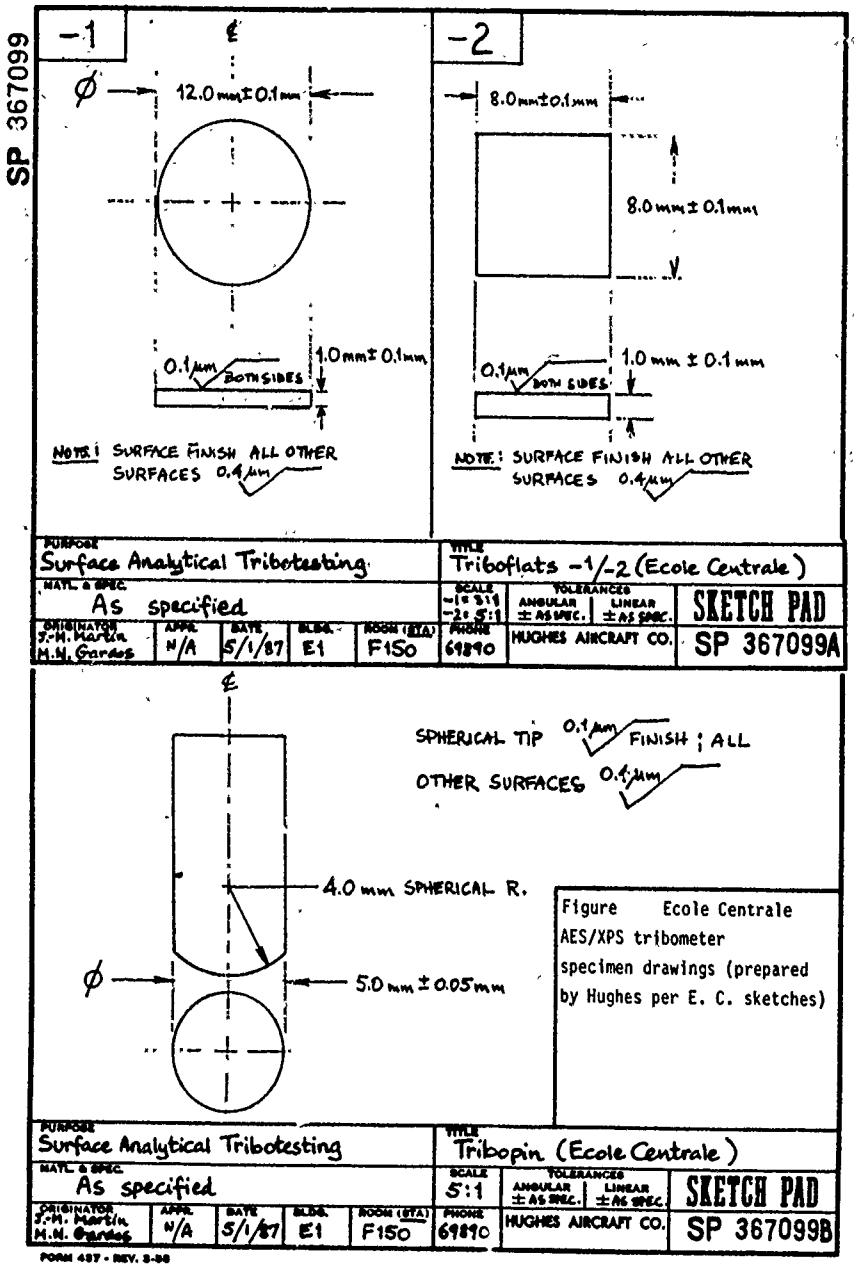

Figure Ecole Centrale AES/XPS tribometer specimen drawings (prepared by Hughes per E. C. sketches)

Figure 12. Engineering drawings of the Ecole Centrale de Lyon/SORETRIB Auger(AES)/XPS tribometer pin and disc/flat specimens.

Results generated with this apparatus will be presented in Section 3.1 based on the information in APPENDICES D and E.

2.2.2 SEM Tribometers (from –173° to 1000°C)

2.2.2.1 The High Temperature (HT SEM Tribometer (R.T. to 1000°C))

2.2.2.1.1 General Design Features. Evaluation of the causes and effects of adhesion, friction and wear at the onset of the program indicated the all-pervasive need for highly controlled surface analytical and tangential shear techniques which can traverse the space-time continuum range of interest as much as possible (Figure 1). The model experiments themselves had to be performed in a wide variety of thermal and atmospheric specimen environments. The key tasks, therefore, appeared to be establishing the ability to (a) perform in-situ measurements of surface chemical changes during sliding, (b) measure coating adhesion (i.e., delamination) by real-time, microscopic-macroscopic tribometry and associate these events with friction and wear changes, and (c) determine friction and wear in air from cryogenic temperature to 850°C with realistic specimen contact configurations.

In view of the relatively short (4-year) duration of the program, available tribometers that already fulfilled specific needs in the range of requirements had to be located. Where suitable apparatus did not exist, we were compelled to design and construct new ones.

The first step towards microscopic-macroscopic adhesion, friction and wear testing in extreme environments was taken by designing and constructing a high temperature SEM (HT-SEM) tribometer which fits the stage of the Hughes Cambridge Stereoscan 250 MK. 3 SEM. The HT-SEM (to 1000°C) version was based on a unique SEM accessory, available at MRL, Inc. This accessory (see Figure 13) is a heated stage enclosed in a differentially pumped Knudsen cell. The sample is placed in a metal support boat, heated in partial pressures of reactive gases to 665 pa (5 torr), and imaged in the SEM through the Knudsen orifice. Viewing the images on a TV monitor, in real time, and recording them on videotape, gives some indication of surface reactions through visible sample phase, shape or volume changes.

As shown in Figure 14, the HT-SEM tribometer is a dynamic-stage version of the static-stage precursor. This apparatus is the result of a joint design and construction effort between MRL, Inc. and Hughes Aircraft Company.

Essentially, the apparatus contains an oscillating, 7 mm x 5 mm x 2 mm flat sliding against a 10 mm long, 2 mm dia., hemispherically tipped pin, at speeds ranging from 9.5 cpm (1 cycle = 2 x 3.5 mm wear scar length) equal to 1.1 mm • s^{-1} to 40 cpm = 4.66 mm • s^{-1}, under normal loads varying from 8 to 50 g. This specimen combination is housed in a differentially pumped and pressurized, Knudsen-cell-like subchamber affixed to the x-y SEM stage. The developing wear scar on the flat can be imaged, in real time, with or without a hermetically sealed lid covering the cell. With the lid on, the scar is imaged through the small (~0.5 mm dia.) Knudsen orifice drilled into the part of the lid positioned immediately

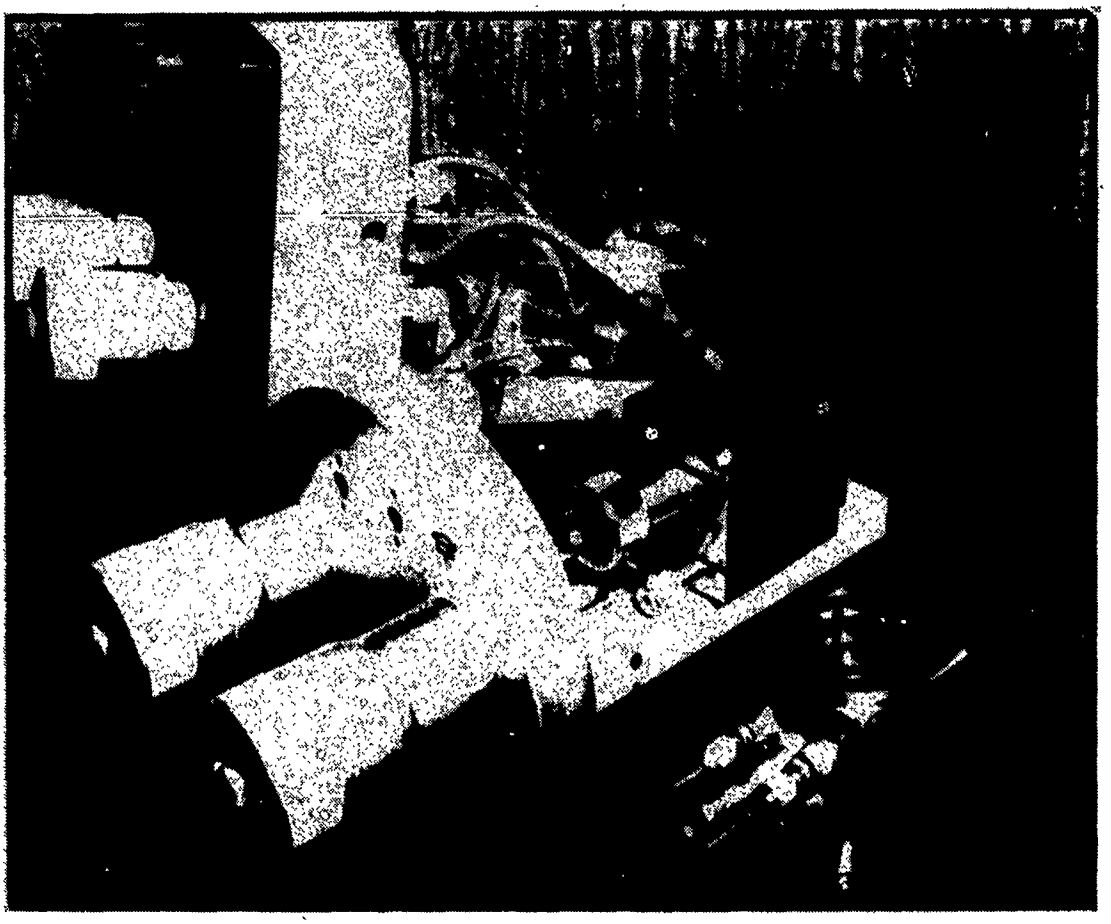

Figure 13. MRL, Inc., high temperature SEM Knudsen cell-like enclosures for controlled atmosphere reactions (courtesy of Dr. Jack R. Alonzo, MRL, Inc., North Branch, NJ).

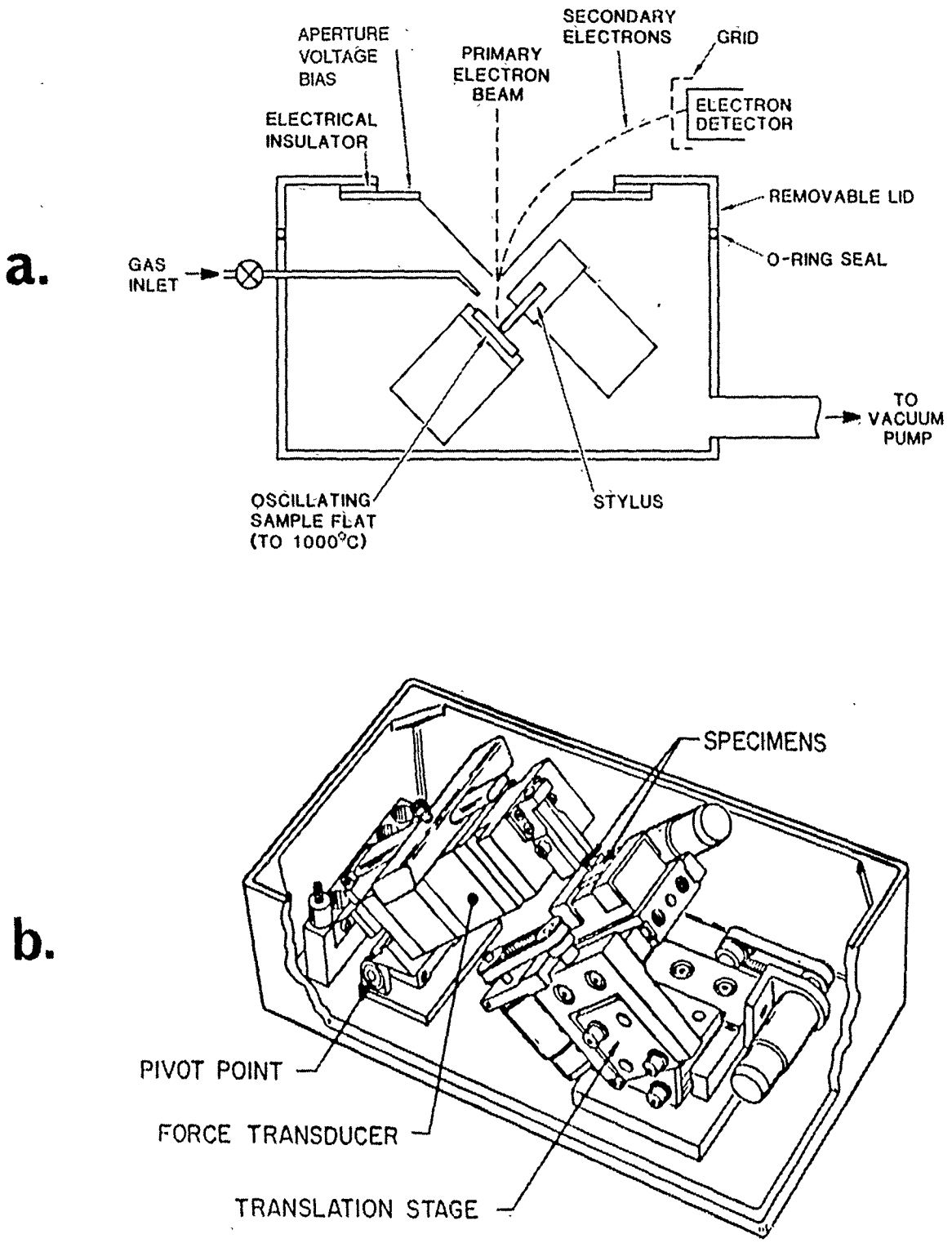

Figure 14. Schematic representations of the Hughes high-temperature SEM (HT-SEM) tribometer; (a) overall view with Knudsen cell lid in place; (b) 3-D cutaway view with lid removed.

over the specimen combination. The moving flat may be tested several times with the same pin, by generating parallel wear scars. These scars can be observed during tests on a TV screen and by videotaping at magnifications up to 200X. The scars may be imaged at subchamber partial pressures not exceeding 13.3 Pa (0.1 torr), or in the typical atmosphere (1.33×10^{-3} Pa = 1×10^{-5} torr) of the lidless subchamber fully exposed to the turbomolecularly pumped SEM column. The thermally isolated flat can be resistively heated to 1000°C in vacuum or in various, selected gas atmospheres.

2.2.2.1.2 Specimen Fixturing and Environment. The schematics of the tribospecimens and their receptacles in Figure 15 depict that the pin is secured by a tuning fork-like, insulated MACOR® part (a machinable ceramic, with a thermal conductivity $k = 1.8\ W \cdot m^{-1} \cdot K^{-1}$), squeezed within a similar, stainless steel clamp tightened with a screw (Figure 15a). The test flat is clamped onto the platinum (Pt) heater strip by beveled, gold-plated stainless steel edges in front and back. The heater strip is draped over a low thermal conductivity zirconia ceramic ($k = 2.3\ W \cdot m^{-1} \cdot K^{-1}$) heater platform, in contact with a water-cooled, copper heat sink block (Figure 15b). The large amount of power going through the Pt heater strip at temperatures up to 1000°C requires cooling with a chilled water circuit (T~15°C) to prevent premature warm-up of the neighboring assemblies. Additional zirconia thermal isolation blocks separate the heated zone from other contacting metal parts to reduce unwanted heat transfer.

The thermocouple sensing the heater strip temperature is a very thin (30-gage, 2.54×10^{-4} m = 0.01 in dia.) Pt - Pt/Rh wire couple, with the bead embedded into a small wire-conduit-containing well drilled into the middle of the zirconia heater block. To assure no shift in its position, it was bonded with an α–SiC powder-containing, high temperature ceramic glass adhesive. In spite of these precautions, the temperature of the triboflat's surface is only approximately measured (it is lower than the true surface temperature) by this thermal sensing arrangement. The thermal gradient between the measured and the true triboflat surface temperature is nevertheless estimated to be less than 10° to 20°C due to the close tolerance mounting practices and the thinness (2 mm or less) of the triboflats (low thermal conductivity of most ceramics notwithstanding). A 2 mm thickness is preferred, imparting sufficient structural integrity to the flat to force the underlying Pt heater strip to be in intimate thermal contact with the thermocouple bead, when clamped to the zirconia base.

The pin is thoroughly insulated, so it would not act as a heat pipe, conducting heat away from the contact zone. Efficient conduction of heat away from the hot flat's rubbing surface would result in larger disparities between the measured and the actual temperature of the tribocontact. Simultaneous heating of the pin imposed formidable experimental challenges and therefore, it could not be accomplished successfully.

The assembled pin/flat assembly is shown in Figure 15c. The oscillating stage supporting the heated flat is moved back and forth by a specially designed version of an optical platform operated on guide rails by a sputtered MoS_2 (solid)-lubricated, 304 stainless steel jackscrew. Actually, there are three orthogonally arranged stages, driven by three, hermetically sealed drive motors. One oscillates the

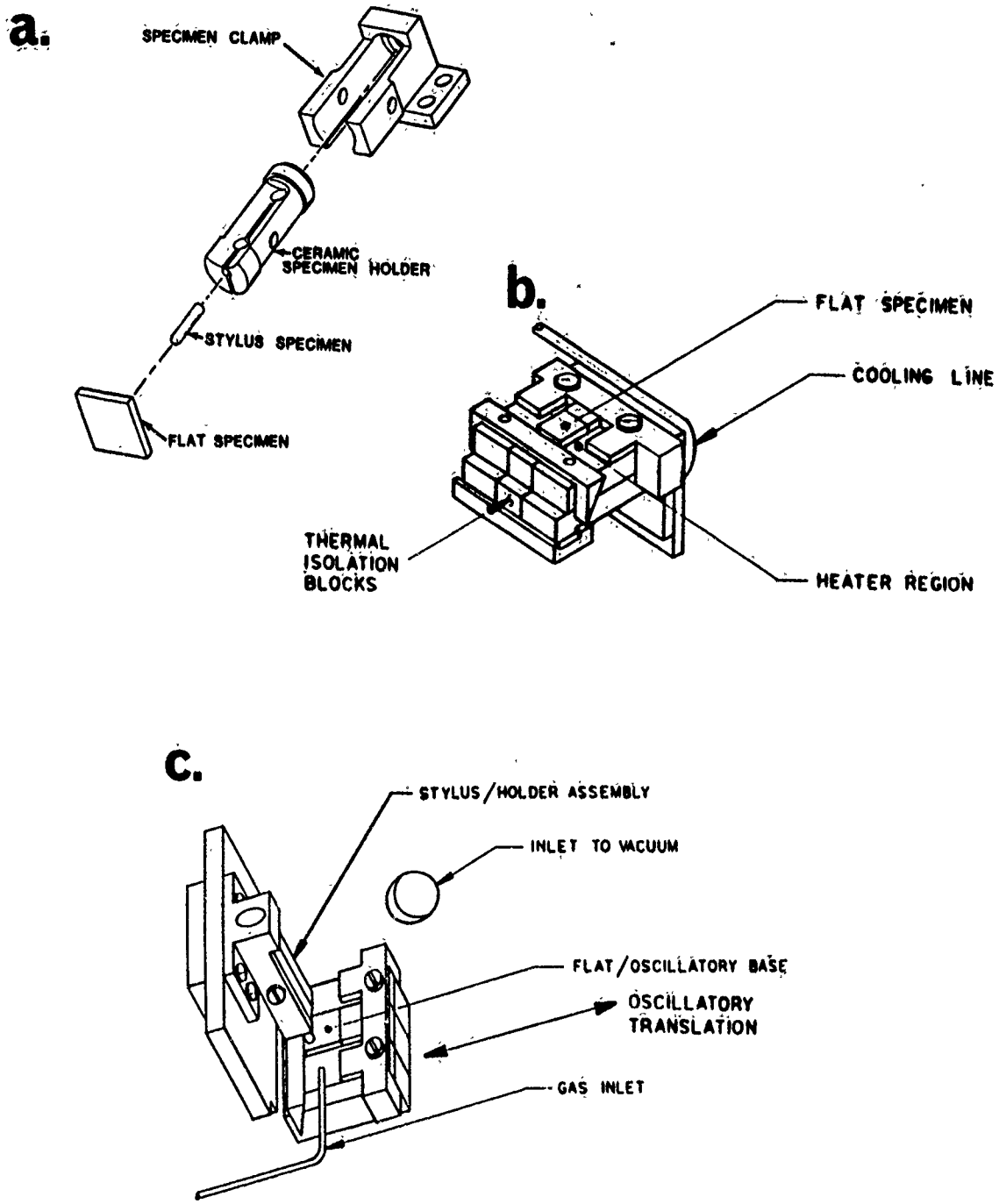

Figure 15. Schematics of HT-SEM pin and flat specimen combinations and their specimen holders; (a) pin assembly; (b) flat installed in thermally isolated heater block; (c) stationary pin vs. oscillating flat assembly with gas inlet near the contact zone.

triboflat in the x-axis, the second translates the flat sideways (the y-axis) under the pin to expose fresh wear track(s) to the used pin, and the third (used very seldom) adjusts the flat-to-Knudsen orifice distance for optimal imaging (the z-axis). The motors move the stages through the clockwise and/or counter-clockwise-rotated jackscrews driven by bicycle-type, stainless steel chains powder-burnished with $CdCl_2$-intercalated graphite (a good vacuum lubricant, see Section 3.2.2). The chains are cogged onto MoS_2-sputtered, 304 stainless gears. Note that these solid lubricated sliding assemblies have routinely operated for millions of cycles before requiring relubrication, general maintenance or replacement. Also note that all other components of the HT-SEM tribometer are fabricated from equally non-outgassing materials to reduce the possibility of internal contamination of the tribocontact, especially in the closed-lid mode. The motor shafts themselves are painted with an extremely thin (~20 to 50 nm) fluorocarbon barrier coating, often used in vacuum technology to prevent out-migration of lubricating oils from hermetically sealed enclosures and evaporation of the oil from wetted motor shafts.

As also depicted in Figure 15c, low partial pressure of gasses are metered into the Knudsen-cell subchamber through a variable leak valve. These can be laboratory air or high purity gasses stored in lecture bottles. The gas inlet is in line with the pumping port, so the sample is constantly bathed in freshly flowing (and progressively removed) gas at ~0.1 torr partial pressures. These pressures can be attained by a highly efficient mechanical pump, as measured by a Baratron® pressure gage capable of ranging to 10 torr.

Without the cell lid, the specimens are in the typical vacuum environment of the turbomolecular-pumped SEM column (1.33×10^{-3} Pa = 1×10^{-5} torr). This relatively low grade vacuum stems mostly from an inability to vacuum-bake the otherwise pre-cleaned and inherently non-outgassing cell components. Pump-down at room temperature cannot remove the adsorbed atmospheric moisture and gasses all at once. Consequently, overnight evacuation of the assembled HT-SEM tribometer, without the cell lid, always provides the most rarified test atmosphere. Normally, a 15 to 20 minutes long pump-down sequence is sufficient to achieve the standard column pressure.

The engineering drawings (Figure 16) and photographs of typical tribopins and triboflats (Figure 17) are included in the respective, referenced illustrations. Due to the importance of the friction transfer arm, its design details are attached separately below.

2.2.2.1.3 Load Sensing and General Instrumentation. The pin holding fixture in Figure 15a is part of a dead-weight-loaded, record player tone arm-like loading and friction transfer arm equipped with two orthogonal sets of parallel leaf springs (Figure 18a). These flat springs, with SR-4 strain gages bonded to them with a non-outgassing adhesive, serve as the normal load and friction force transducer. Similar friction and load sensing arm designs were previously described in (51 and 53).

The pivot of the loading arm consists of a pair of spring-preloaded 440C steel R-3 ball bearings lubricated with burnished MoS_2 powder. Spring preloading prevents any sideways-misaligned movement

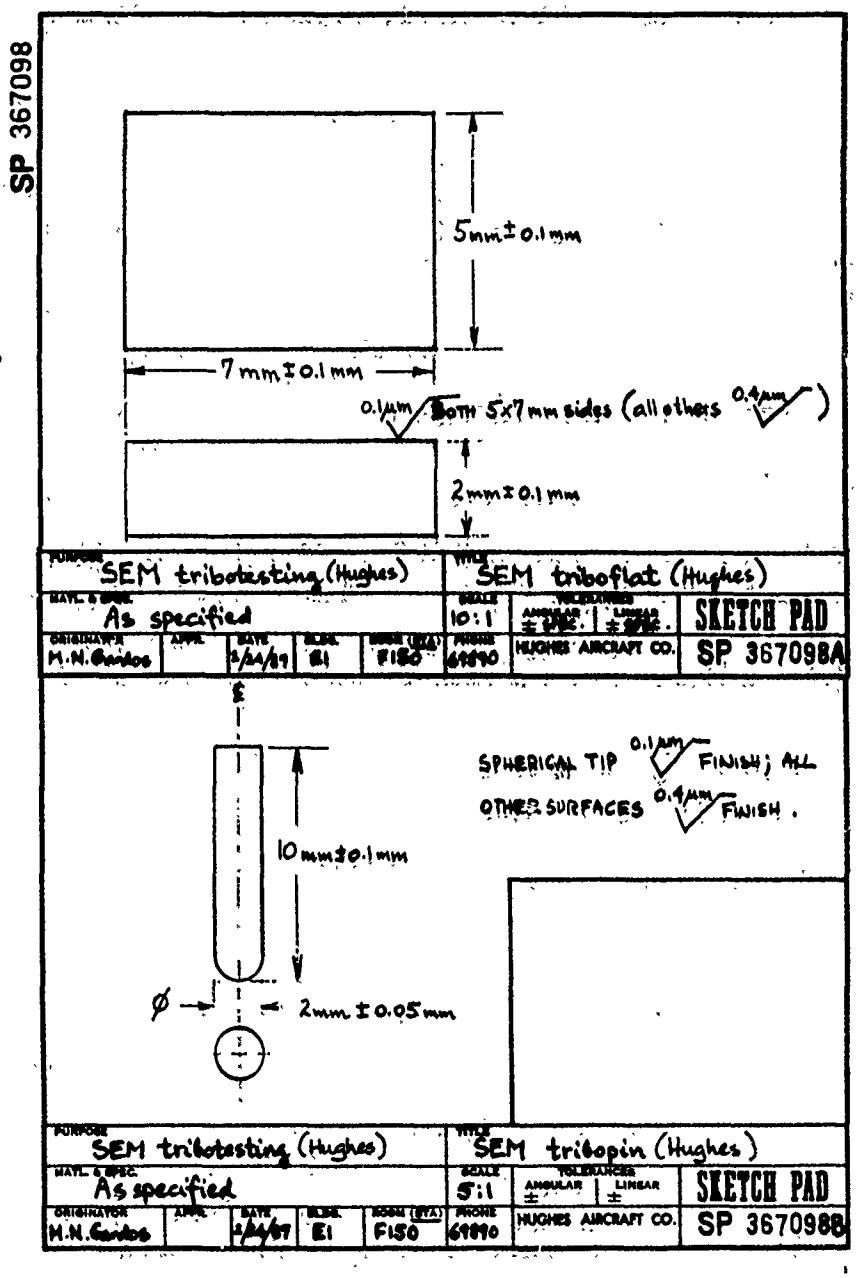

Figure 16. Engineering drawings of the HT-SEM pin and flat specimens.

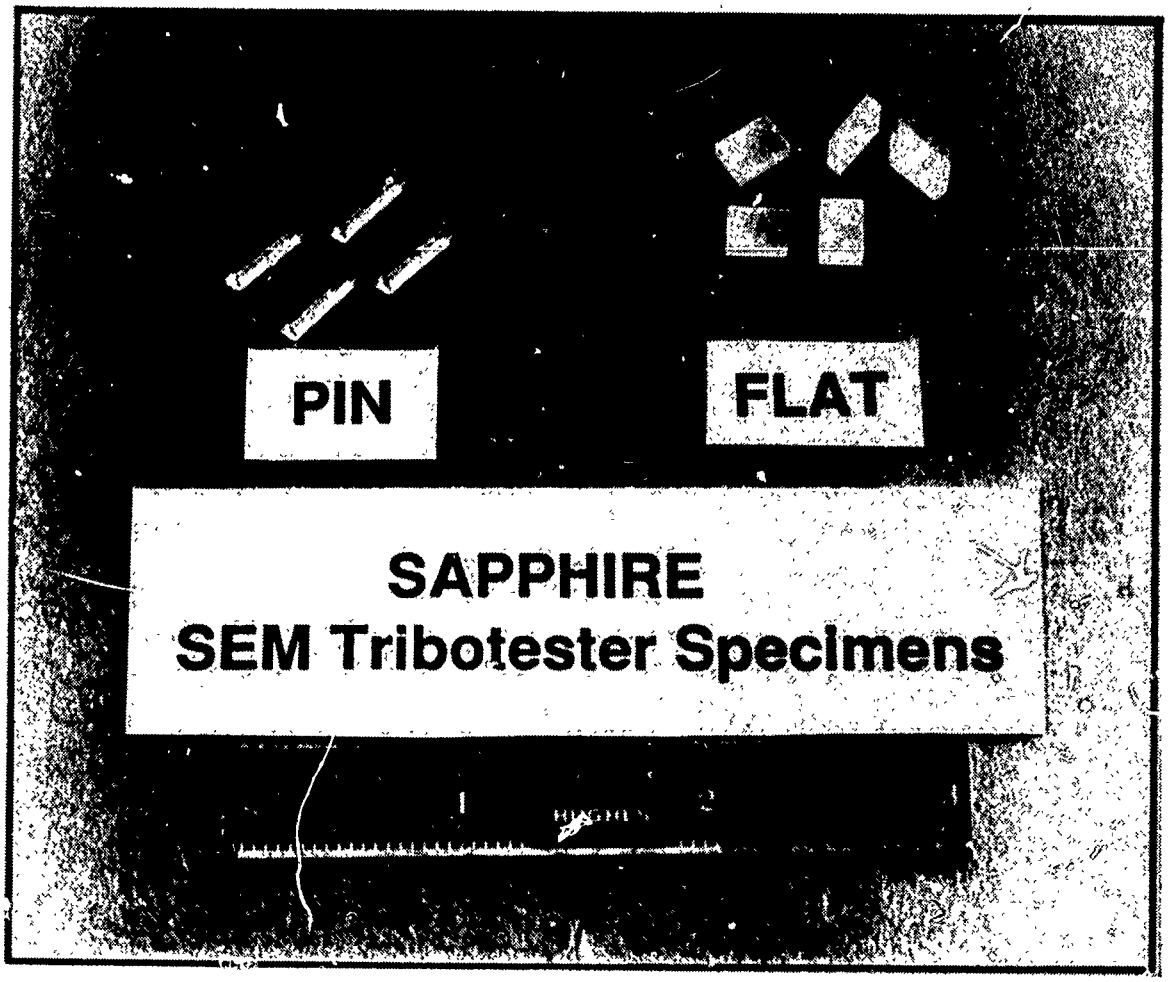

Figure 17. Polished, single crystal sapphire pins (90°; pin axes normal to (0001) basal plane) and as-cut (unpolished) flats (0°; 5 mm x 7 mm plane is cut on (0001) basal plane).

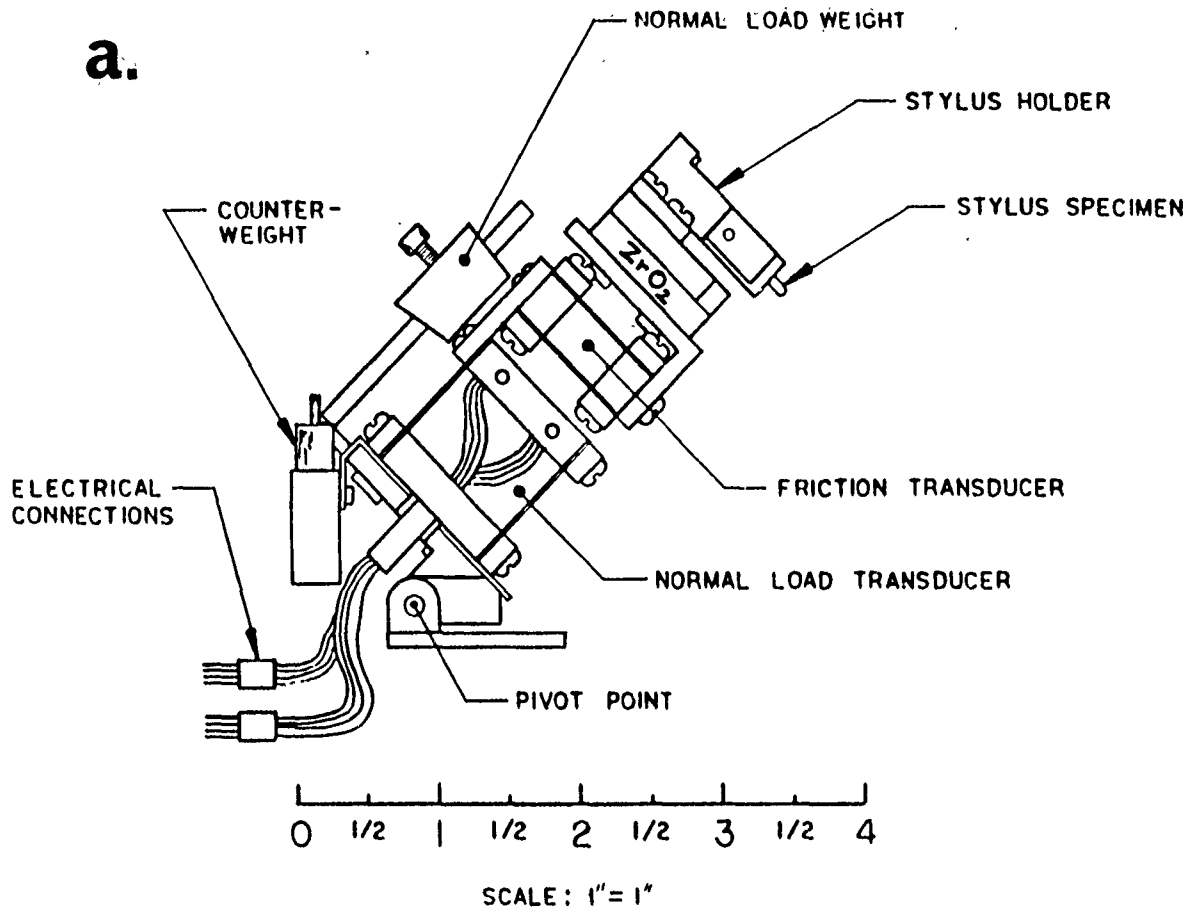

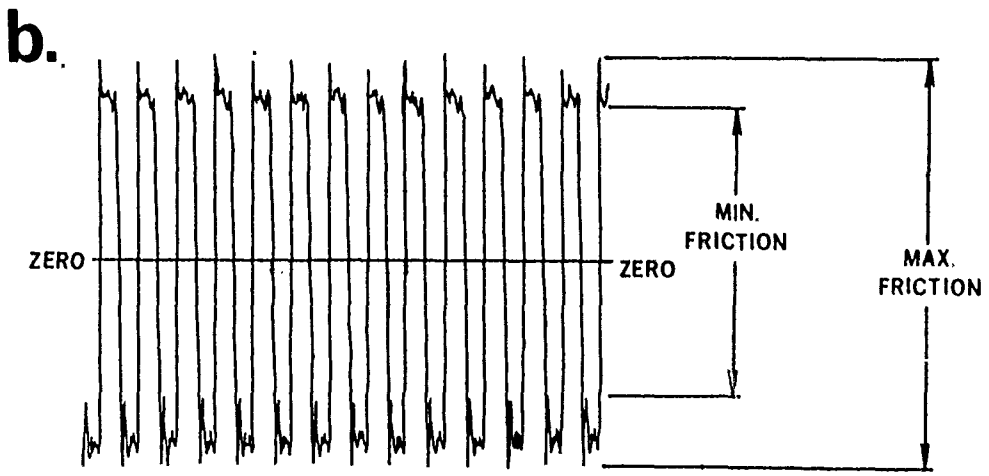

$$\text{AVE. FRICTION} = \frac{1}{2}\left(\frac{\text{MAX.+MIN.}}{2}\right) \text{ GMS.}$$

$$\text{AVE. COF.} = \frac{\text{AVE. FRICTION LOAD}}{\text{AVE. NORMAL LOAD}}$$

Figure 18. Schematics of the normal load/friction force transfer arm of, and typical friction data provided by, the HT-SEM tribometer; (a) the double-parallel-springs transducer with the installed pin; (b) typical friction trace and method to calculate average friction force.

of the pin during test: an absolutely steady and well-defined position of the pin tip is essential for its precision alignment under the Knudsen orifice during gas-partial-pressure tests. Alignment is attained by a long-focal-length microscope looking through the lid orifice, where the assembled specimens (with the lid on and fastened) are illuminated through a removable side port on the lower part of the Knudsen-cell chamber with fiber-optics lighting.

An apparatus was constructed to calibrate the friction force transducers before and after each test. This simple mechanism pulls the loading arm parallel to one direction of sliding, through a string-on-pulley arrangement loaded with dead weights. The normal load transducers are calibrated by placing nickel-plated, lead counterweight(s) of different sizes into their well-like receptacles (also see Figure 18a). Then, the main weight is moved until the force transducers register no normal load (i.e., until the "tone-arm" assembly is perfectly balanced). As the counterweight(s) is (are) removed, their total weight is equal to the normal load; this load is now registered by the appropriate transducer.

The strain gages bonded to the leaf springs are temperature sensitive. The number of cycles heating to high temperatures is therefore limited, because of eventual overheating of the force transducers. To prevent overheating and thermal drift (i.e., higher friction force read-out than actual), a thermocouple was placed behind a zirconia (ZrO_2) thermal dam (see Figure 18a). Once this sensor placed up-stream of the thermal flux registers ~40°C, the test is terminated. Note that in oscillatory motion zero is automatically taken as the average of the friction traces (Figure 18b). This averaging is completely valid only if the reciprocal sliding motion and the force balance are isotropic. In the present case, the small error introduced by sliding on an incline (i.e., working against or with vector components of mass x gravity) is neglected.

The photographs of the HT-SEM tribometer fully assembled for test are shown in Figures 19 and 20 (lid removed) and Figures 21 and 22 (lid assembled). The lid is fastened to the body of the Knudsen cell by two clamps (one of the unfastened clamps is clearly visible in Figure 21), providing a vacuum-tight seal with a Viton O-ring embedded in the cell rim (see Figure 20). The tribometer fully assembled into the SEM, operating in the partial gas pressure mode, is depicted in Figure 23.

2.2.2.1.4 Data Logging and Analysis System. The data logging and analysis scheme is described by the flow-chart in Figure 24. The various force and temperature sensor signals are sensed on a chart recorder, further downloaded through a Metrabyte Dash-8® A/D-D/A board to a 640K RAM, 20 MB hard disc/1.2 MB floppy disc in an IBM-compatible PC-AT, equipped with enhanced graphics, color monitor, an 80287 co-processor, a printer and a multi-pen (color) plotter. The Dash-8 board has 16 channels A/D (4000/sec) with 12 bit resolution, capable of measuring low-level (0-100 mV) and high level (0-10V) signals. It has high versatility in terms of speed and channel changes, can monitor multiple channels, and has ample data storage capacity. It is backed with the chart recorder as a precaution.

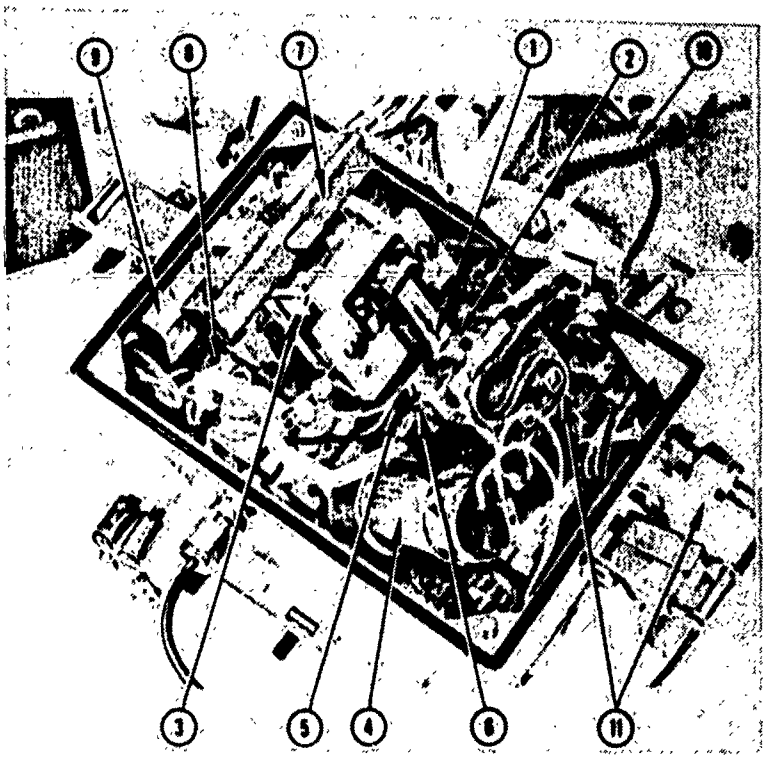

1. PIN HOLDER WITH TRIBOPIN
2. TRIBOFLAT
3. NORMAL LOAD/FRICTION FORCE TRANSDUCER ARM
4. DRIVE MOTOR
5. GAS INLET
6. HEATER CONNECTION
7. NORMAL LOAD WEIGHT
8. TRANSDUCER ARM FULCRUM BEARINGS
9. COUNTERWEIGHT SLOTS
10. PUMPDOWN PORT
11. COOLING LINES

Figure 19. Photograph of the HT-SEM tribometer with the lid removed (for description of parts, refer to Figures 14 through 18 and the text).

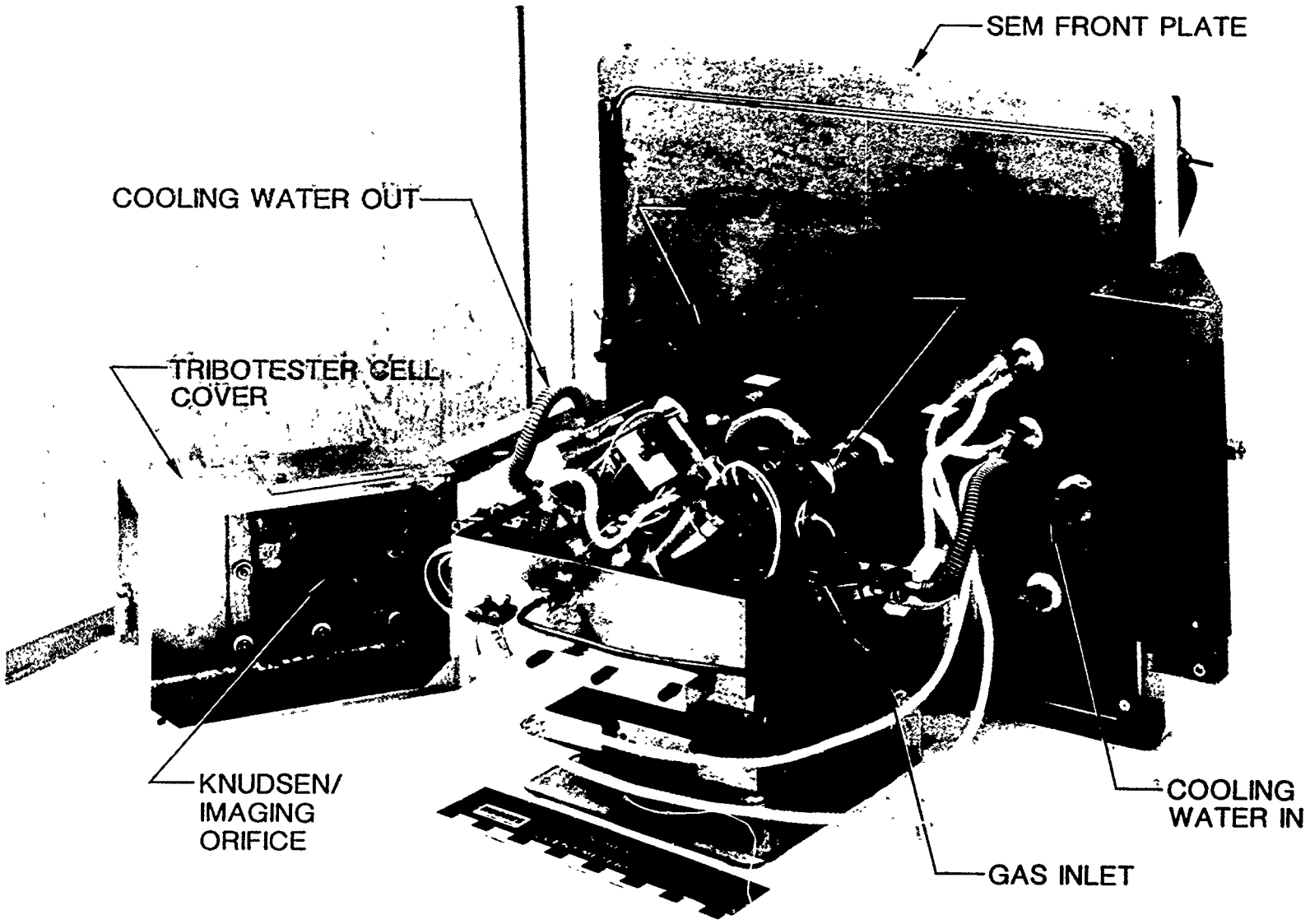

Figure 20. The HT-SEM tribometer with the Knudsen cell lid removed, attached to a removable SEM chamber door.

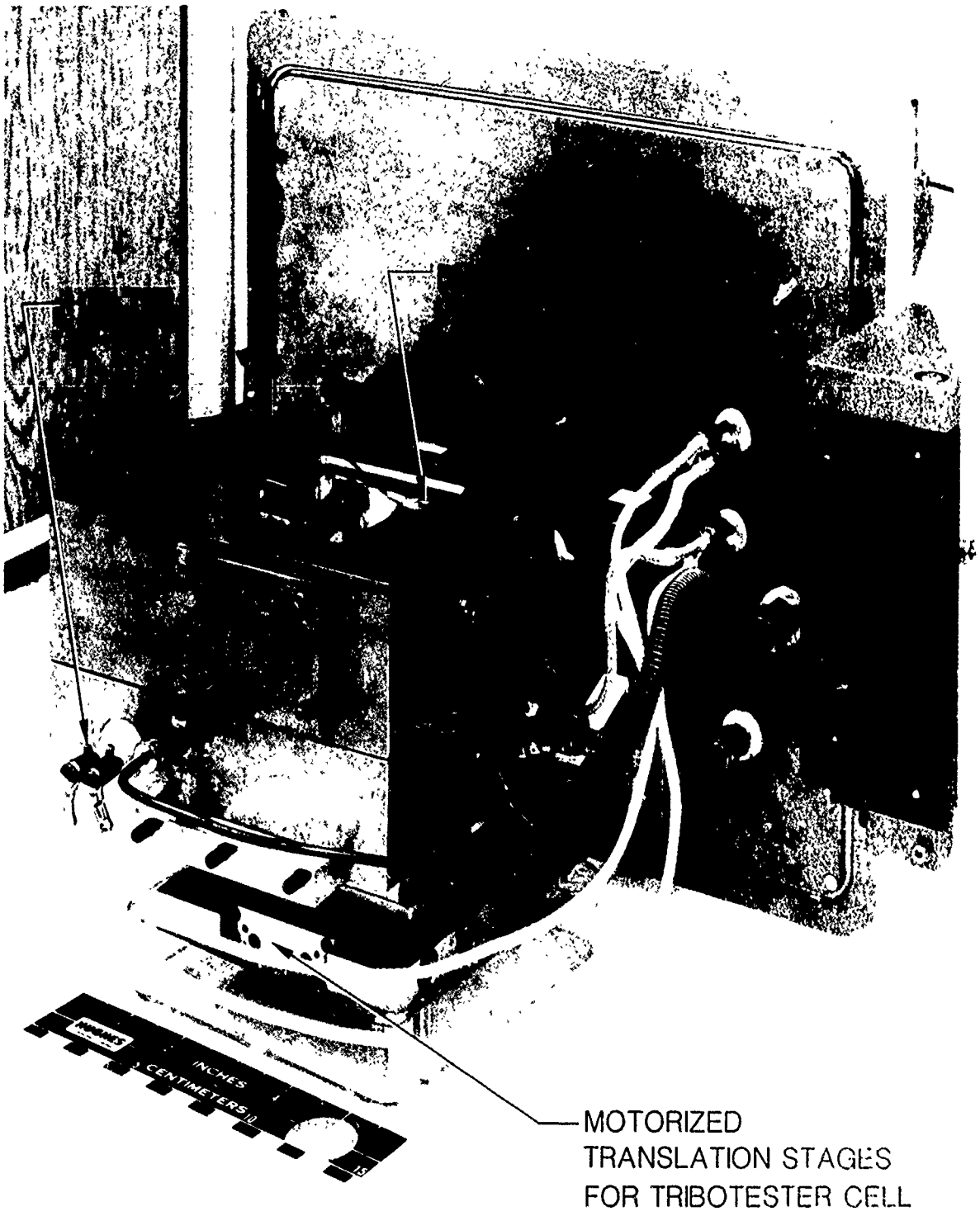

Figure 21. The HT-SEM tribometer with the Knudsen cell lid installed, attached to a removable SEM chamber door.

Figure 22. HT-SEM tribometer specimen alignment, transducer calibration and equipment check-out, before test.

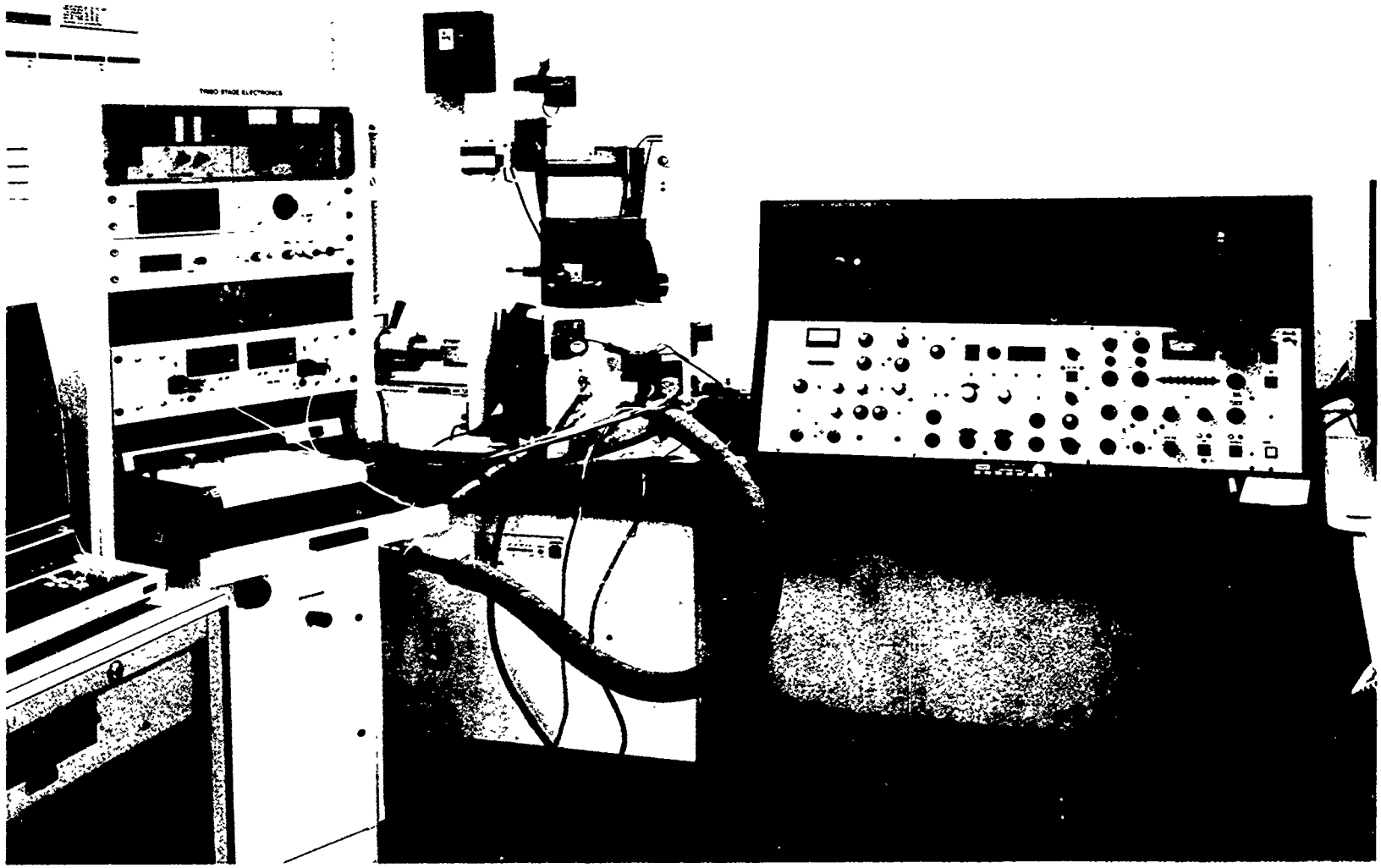

Figure 23. Fully assembled HT-SEM tribometer in differentially pumped/gas backbleed mode, attached to auxiliary support cart housing the tribostage electronics, temperature/normal load/friction force chart recorder, and vacuum pump for evacuation of the differentially pumped, partial gas pressure-containing Knudsen cell (computerized data acquisition system not shown).

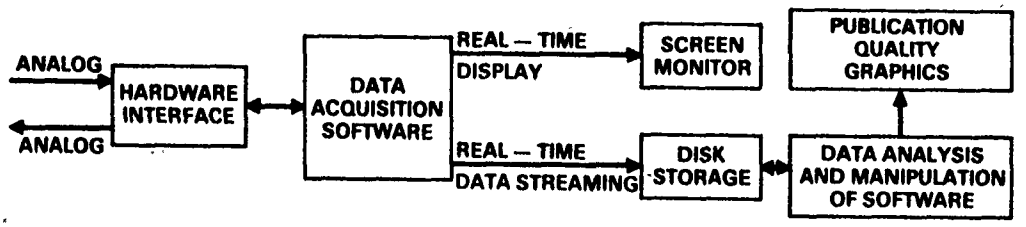

Figure 24. Data logging and analysis scheme.

Logging of all data was accomplished by the widely utilized Labtech Notebook® computer program (Laboratory Technology Corp, Wilmington, MA). The data were manipulated by the extremely powerful RS/1® (BNN Software Products, Cambridge, MA 02238) software capable of curve fitting, statistical analysis, analytical model development, extended graphics – in other words, complete data analysis.

Figure 25a depicts the methodology of computer-logging, then calculating the average friction previously schematized in Figure 18b, by a simple program. Figure 25b represents the identical friction trace simultaneously recorded on chart paper, along with those for the normal load and the triboflat's temperature.

With respect to the computer analysis of the coefficient of friction (f_k), all data are acquired through the Dash-8 A/D board installed in the PC-AT desktop computer. The data are stored in two files, using the Labtech Notebook®. Each file contains various parametric measurements sampled at a different rate. One file, sampled at 40 Hz, contains the friction force (F_k) values and motor direction (i.e., forward sliding or reverse sliding). The other file, sampled at the lower rate of 4 Hz, contains the normal load (N), triboflat temperature, elapsed time and motor direction. Counting motor direction changes from the beginning of each file, sampled at the lower rate, gives the number of oscillatory sliding cycles and serves as a kind of internal clock for each test. Note that a lower rate of sampling is sufficient for the latter parameters, because these do not vary nearly as much (and as fast) as F_k.

After each test the data are reduced by a special computer program written in BASIC. This program averages (ranks) 40 ea., randomly selected but equally spaced F_k points from the mechanically most reliable portion of each half cycle associated with a given motor direction signal (see Figure 25a). This step is repeated with the next (reversed) motor direction-associated F_k data, again as shown in Figure 25. These half-cycle friction force data are averaged again to result in one single F_k value per full cycle. Then, by utilizing the well-known equation f_k (or COF) = F_k/F_n, the f_k (COF) values are calculated.

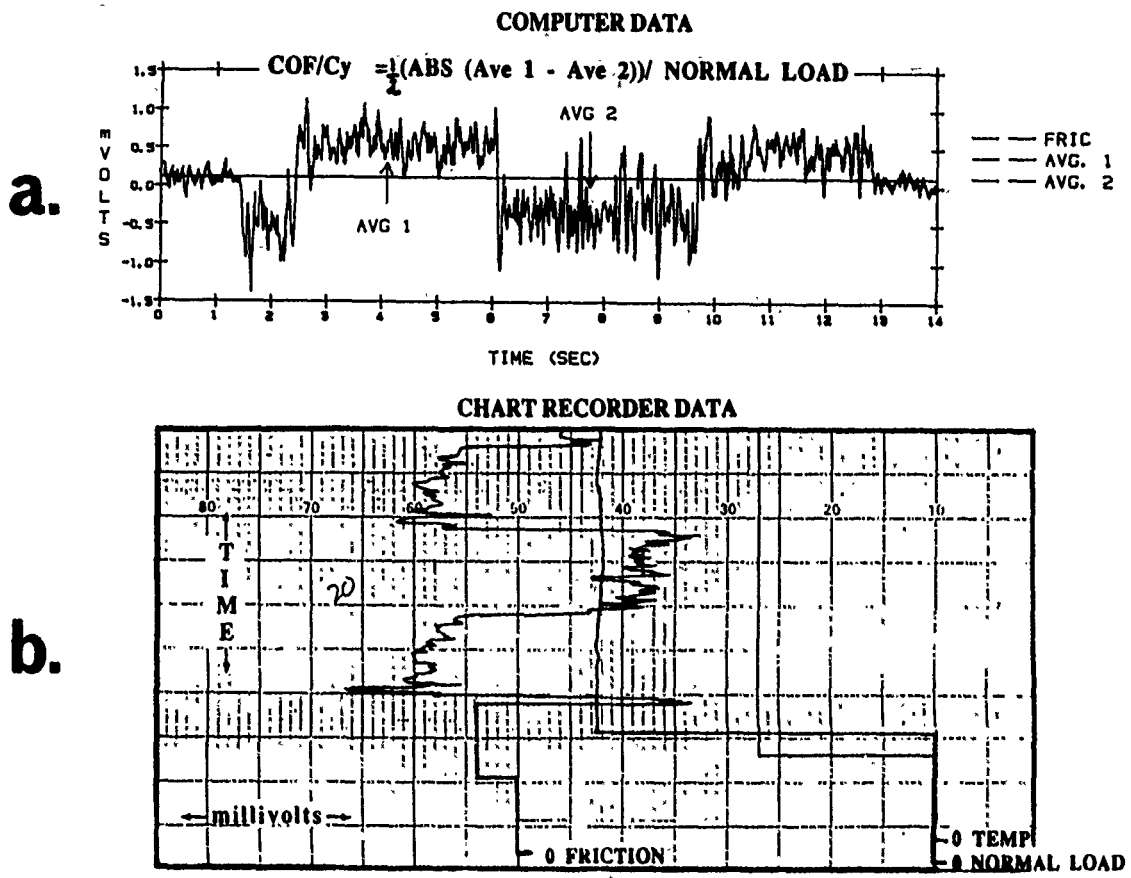

Figure 25. Data acquisition by computer and chart recorder; (a) computer-logged, real-time trace of oscillatory friction force also showing automatic friction averaging calculation technique, (b) the identical trace taken from the recorder chart, along with temperature and normal load data.

The data are thus averaged ("filtered") to reduce the noise ("hash") within each cycle. Unfortunately, the "hash"-associated F_k differences from cycle-to-cycle must also be accounted for. For example, the HT SEM tribometer's strain gages are only marginally sensitive to measure very low friction (f_k = 0.01 - 0.03). In such cases, the computer-generated friction curves are somewhat noisy (see Section 3.2.1).

The developing (i.e., progressively widening) wear scar and its general appearance on the triboflat are observed in real-time by high magnification imaging and videotape recording.

The in-situ measurement of the wear scar width, friction force, normal load and the heated triboflat's temperature permits the calculation of the PVT-and-time-dependent, apparent surface shear strength ($\tau_{app.}$). The basis for this value is the apparent (or a closely estimated real) area of contact between the small, hemispherical pin and the flat. This area is routinely measured from the video data with dynamic alphanumeric labeling of PVT, magnification and voice-recorded time with observations, and by after-test SEM photomicrography. Video imaging of the sliding interface thus gives information on debris generation, coating adhesion or delamination and the formation of unusual tribochemical compounds.

When the wear path on the triboflat is perfectly aligned under the cell orifice (with the lid on; partial pressure mode) and exactly in the path of the rastered electron beam, its further development (e.g., debris generation and morphology, possible substrate cracking, scar width increase, etc.) can still be imaged and recorded on videotape by the SEM electronics. Imaging under any circumstance is possible to a specimen temperature ≅700°C. Beyond that temperature, the emitted thermal electrons tend to degrade picture resolution. With the cell lid on or off, the scar on the oscillating flat can be observed and videotaped in real time at magnifications up to 200 X. With the lid on, it is possible only if the partial pressure of various gases does not exceed 13.3 Pa = 0.1 torr (i.e., the mean-free-path of the electrons is not reduced below the imaging limit). Positive biasing of the lid (see Figure 14a and 21) helps clarify "snowy" images under such partial pressure conditions somewhat by attracting the emitted secondary electrons to the SEM detector. The clarity of the image is also strongly dependent on the flat's position relative to the orifice (the contact zone-to-orifice distance).

2.2.2.1.5 General Utility. The HT-SEM tribometer was shown to be a highly effective apparatus capable of determining the dynamic adhesion of lubricant films (hard or soft) by correlating friction changes in extreme environments with video-monitored delamination. In fact, this apparatus is the only one known to be in existence today capable of measuring the dynamic, real-time delamination of sputtered MoS_2 films to 200°C (see Section 3.2.1) and CVD diamond films at temperatures to 1000°C

(see Section 3.5). The diamond stylus or a Vickers hardness tip of conventional scratch testers, for example, wear flat after a few traverses over a polycrystalline, faceted (extremely abrasive) diamond surface, even at room temperature.

Also for the first time, highly controlled SEM tribotests at low loads, low speeds, from room temperature to 800°C and using single crystals of CaF_2 and BaF_2 sliding against themselves, each other, and sapphire, produced accurate and self-consistent surface shear strength results. The data are considered to be τ_s values that are more meaningful to a tribologist than those provided by conventional τ_s-determining techniques (see Section 3.4). Similar tests with pressed flats of metal chloride-intercalated graphites helped determine the shear strength and tribothermal stability of these materials (see Section 3.2.2).

2.2.2.2 The Cryogenic (CRYO) SEM Tribometer (R.T. to -173°C). Successful and reliable operation of the HT-SEM tribometer prompted the design and construction of a cryogenic version, where the test flat can be cooled to -173°C = 100K. The later apparatus is intended for use during the separately funded, and now ongoing Part II effort of the program: it will aid in the development of improved cryogenic tribomaterials.

The CRYO-SEM tribometer was based on static SEM cold stage designs just as the high temperature equivalent was patterned after MRL, Inc.'s hot stage. One example of a liquid-helium-cooled stage is depicted in Figure 26, taken from (47). The sample chamber resembles a Knudsen cell, except that the coverplate with the orifice is intended as a thermal shield/baffle rather than the hermetic lid for a differentially-pumped Knudsen cell. To the best of our knowledge, CRYO-SEM tribometers based on the same cryogenic liquid-gas cooling principle have not been described in the literature.

The main difference here lies in cooling instead of heating the triboflat. The initial plans called for incorporating a commercially available, but modified cryostage (Figure 27) to chill the flat. The installation and operation schematic of the modified stage is shown in Figure 28. As it turned out, the purchased system was too large to fit the space allocated for the tribometer. A new, more compact cryostage had to be constructed by MRL, Inc. The newly designed stage (Figure 29) is continuously cooled by LN_2-GN_2 via gently flexing PTFE tubing, with a lowest flat temperature design goal of 100K. There is a heater built into the stage also, enabling control of the temperature of the flat anywhere between 100K and 373K (100°C). This ability to heat the flat, combined with a Knudsen cell cold finger positioned near the sliding interface which is chilled before the cryostage is cooled, was purposefully designed to prevent gas/vapor contamination of the flat during cryogenic temperature tribotests.

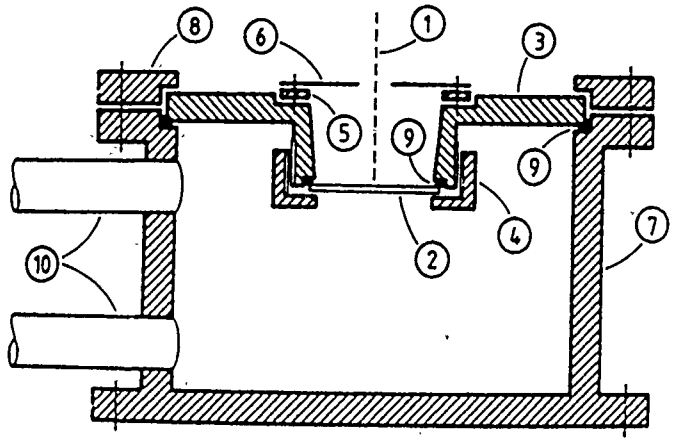

Figure 26. Sample mounting configuration of a liquid helium-cooled stationary SEM stage: 1, electron beam; 2, sample; 3, sample holder; 4, clamping screw; 5, copper ring for wire heat sinking; 6, thermal shield; 7, LHe tank; 8, clamping ring; 9, indium seal; 10, LHe tubes; from (47).

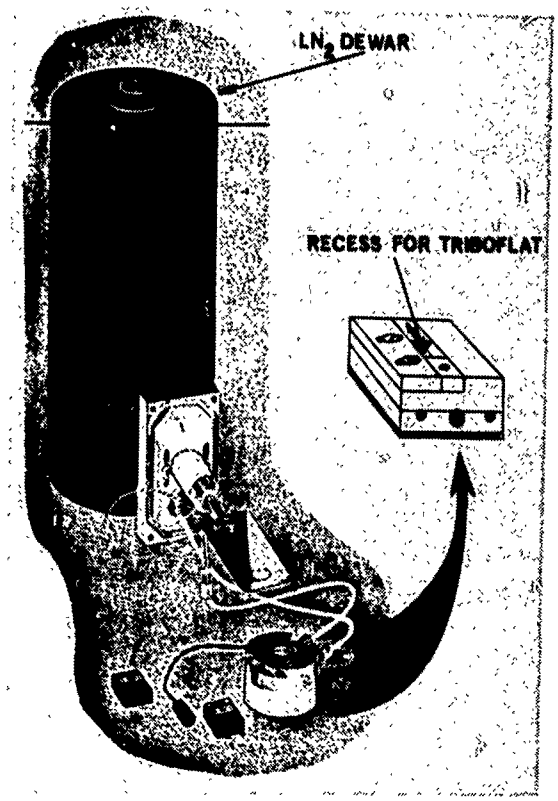

Figure 27. The Hexland CT 1000A cryostage with modification for housing the 7 mm x 5 mm x 2 mm triboflat.

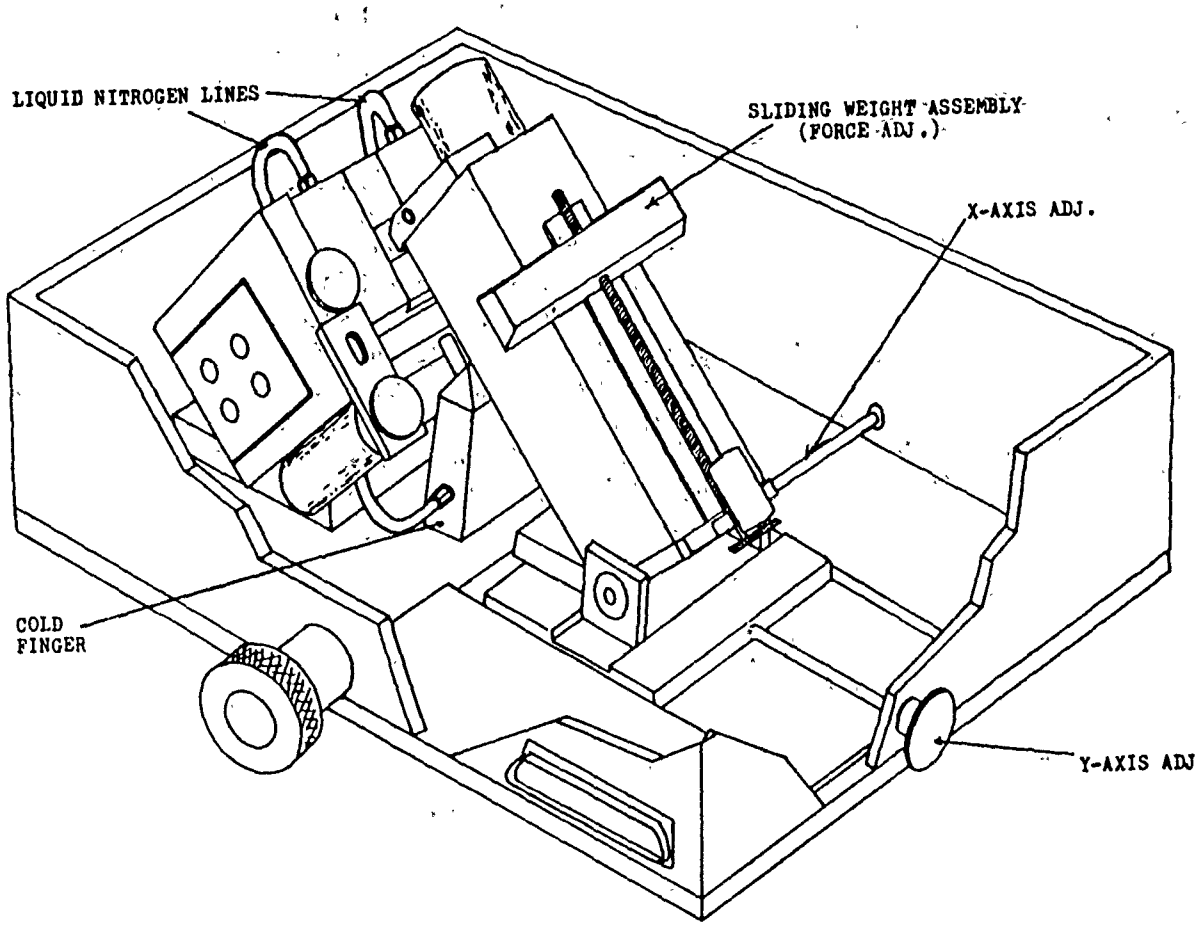

Figure 28. Schematic of the Cryo-SEM tribometer.

a.

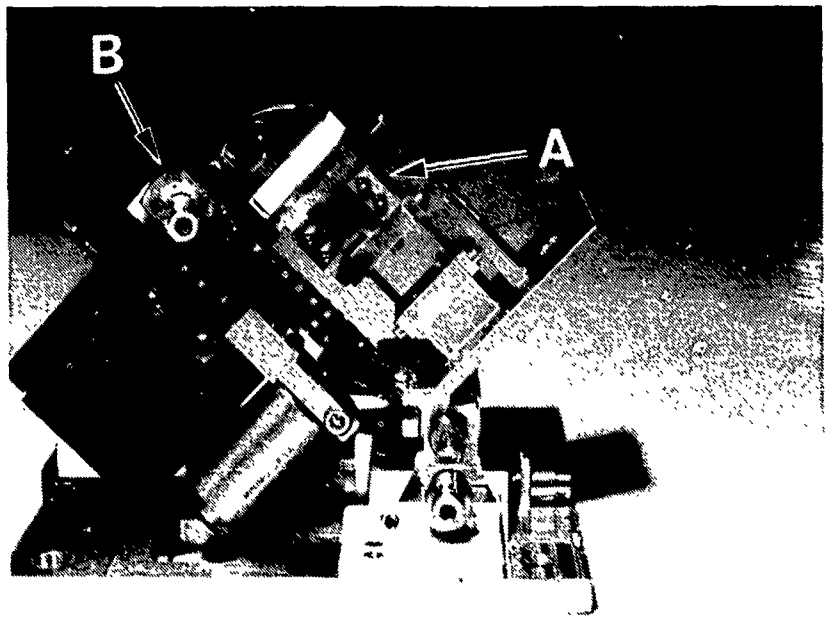

b.

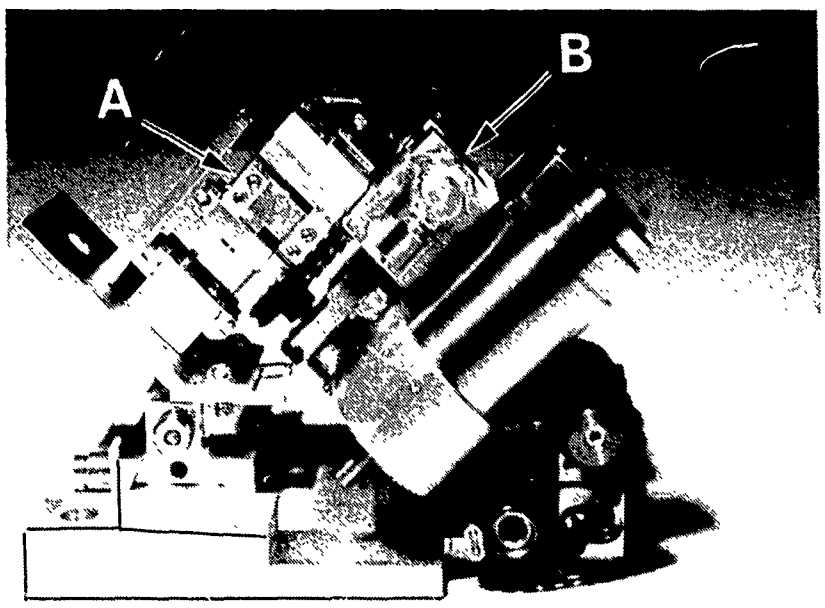

Figure 29. Sideview photographs of (a) the transducer/friction transfer arm assembly housing the insulated pin holder and the orthogonal strain gage flex plates (normal load and friction force transducers) -- motor and sliding weight assembly not shown, and (b) the oscillating cryostage and drive/sample positioning systems -- LN_2 transfer lines not shown.

The schematic of the CRYO-SEM is presented in Figure 28. Since it closely resembles the high temperature (HT) version, the lessons learned from the HT prototype (in terms of workmanship, setup, alignment and repairability) have all been incorporated into the new design. Each subsystem, i.e., the SEM door, the Knudsen cell, the positioning and oscillating stages and the friction transfer/transducer arm have all been modified accordingly. For example, the friction transfer/transducer arm (Figure 29) was thoroughly modified. Most importantly, it now rides on a small, precision X-Y stage that can be positioned manually from outside the Knudsen cell and the vacuum chamber. This design should reduce the time and trouble involved in aligning the stylus with respect to the cell aperture. The arm pivot was machined with closer tolerances to reduce the side-to-side play in the arm. The size of the arm was reduced to increase the clearance around it. The tribopin holder is smaller and no longer has a ceramic insert. Thermal management was also improved. The insulation between the pin holder and the arm was increased. To insure that the strain gauges on the arm's flex plates remain at a constant temperature, a heater was placed behind this insulating thermal barrier. An attempt was made to add a motor (not shown in Figure 30) to move the weight that sets the normal load on the pin, as depicted in the Figure 28 schematic. Unfortunately, there was no room to add this motor and thus the load still cannot be changed from outside the vacuum chamber while a test is running.

The stages which move the sample (also shown in Figure 29) remained unchanged. The oscillating stage was modified to accept ball bearings on both ends of the jackscrew. All of the moving parts (jackscrews, gears, chains, disassembled bearings) were sputtered with a thin layer of MoS_2. The new stages and their moving mechanical assemblies should exhibit lower friction/traction and longer wear lives, while operating with a non-contaminating lubricant system.

The design of the Knudsen cell (see Figure 30) was equally and significantly improved. Electrical signals are routed through flange-mounted connectors. The cooling gas for the cryogenic stage goes through a flange with screw-on hose connectors on both sides. The X-Y stage, which positions the Knudsen cell, is mechanically controlled from outside the vacuum chamber using the mechanical feedthroughs in the door. The stage is much more substantial in mass and strength than the HT equivalent. The door (Figure 30c) now has all electrical feedthroughs mounted on flanges with O-rings. The vacuum inlet uses a standard, quick-disconnect vacuum flange, which mates to a new stainless steel vacuum hose, replacing the rubber hose shown in Figure 23. A high vacuum valve was added so that the external mechanical pump (preferentially pumping the Knudsen cell during partial pressure operation) can be disconnected without venting the SEM chamber. This will allow us to pump the Knudsen cell overnight in the SEM without causing backstreaming of the oil from the mechanical pump. The maximum flow rate of the gas metering valve was increased to 133 Pa = 1.0 torr.

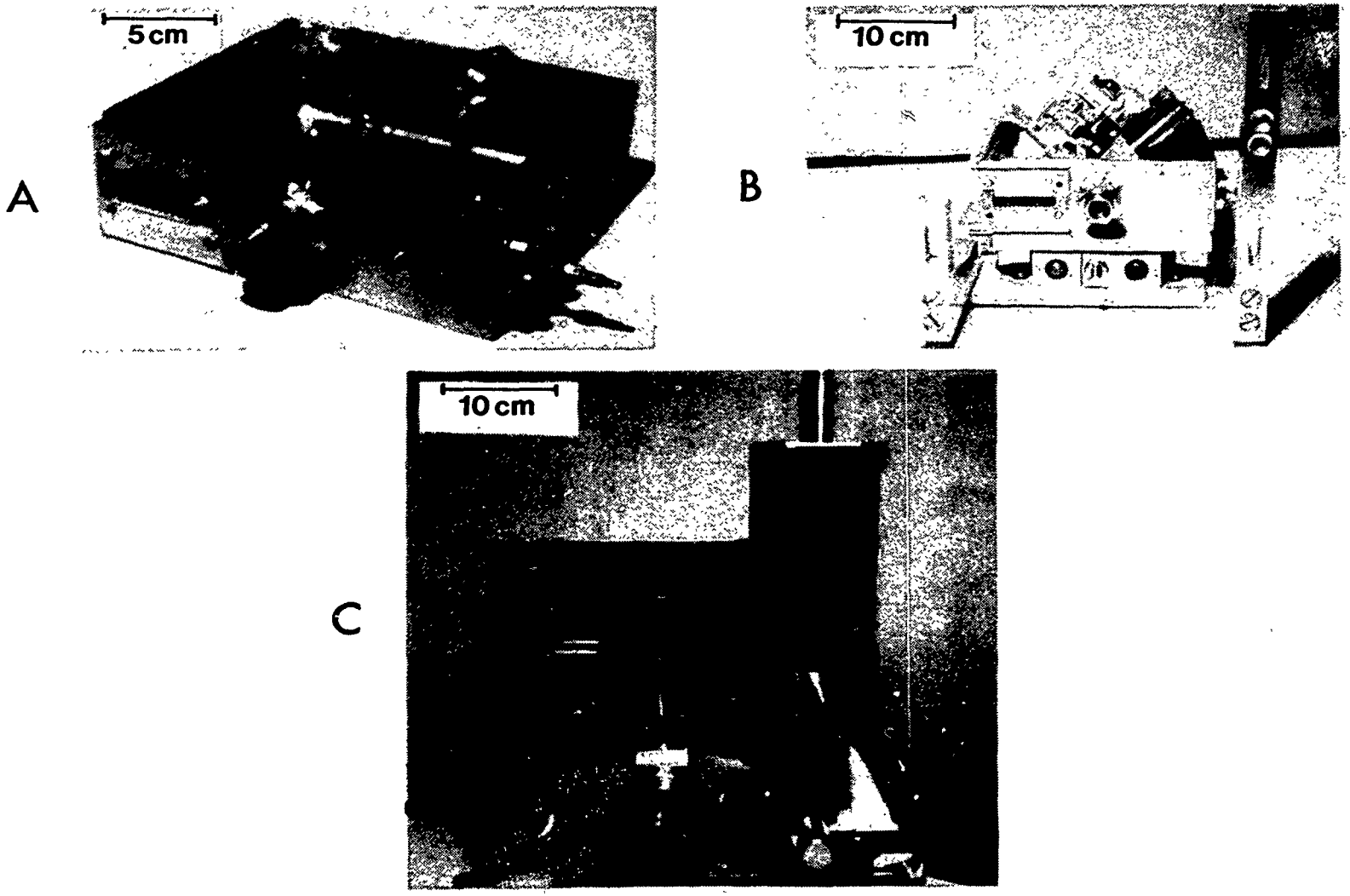

Figure 30. Photographs of the cryogenic SEM tribometer in various stages of assembly: (a) bottom of the Knudsen cell subchamber, (b) the pin-flat mechanical assembly (see Figure 29) installed into the Knudsen cell bottom and onto the door bracket; and (c) the SEM door assembly (Knudsen cell chamber attached to the other side of the door is hidden from view) with the cryogenic LN_2 Dewar.

These improvements were incorporated through a joint effort between Hughes and MRL, Inc., as exemplified by the minutes of a design review in APPENDIX F. The main concern remaining, not to be resolved until the shakedown of the CRYO-SEM tribometer in mid-1990, is that imaging ceramics (insulators) at very low temperatures will be extremely difficult due to charging effects.

Several solutions to this problem which could either neutralize or dissipate the accumulated surface charge were discussed. Two of the more exotic and difficult-to-affect solutions were the use of a "proton gun" or a positive ion beam to neutralize the charge, or the use of metal "brushes" outside of the area being examined to "sweep" the charges from the surface previously bombarded by the electron beam. Again, experiments will have to be performed first to determine the severity of the charging problem. Corrective actions will then be taken as necessary, as assisted by some recent experience in the field (49).

2.2.3 Dual Rubshoe Tester (R.T. to 850°C)

2.2.3.1 General Design Philosophy. It is well established that in rolling contacts, the effect of shear as well as normal forces at the surfaces is to increase the magnitude of the maximum shear stress and to raise its region of occurrence closer to the contact surface (4, 54 through 57). Under marginally- or non-lubricated condition, the tangential shear is higher and the region of the peak octahedral shear stress moves toward the surface. Progressively larger traction coefficients (f_t) commensurably increase the peak stresses. At an $F_t = 0.3$, these stresses are on the surface. Under pure sliding where the coefficient of kinetic friction (f_k) is 0.3 or more, these stresses are always on the surface.

The way in which the inherent structural integrity of the ceramic reacts to these stresses and to the superimposed environmental conditions will determine the tribological behavior of bare and solid lubricated ceramics.

Insofar as (a) f_k (in pure sliding) is always larger than f_t (under sliding-rolling) in either bare or lubricated contacts and (b) the f_k or f_t of solid lubricated contacts (≥ 0.3) is always considerably larger than the equivalent values for liquid lubricated contacts under oil-lubricated, rolling contact fatigue (RCF) testing conditions, the maximum shear stresses occur in the subsurface of the ceramic. As a consequence, under oil lubrication, the chemistry, crystal structure and the elasto-plastic properties of the bulk are the controlling factors for fatigue crack initiation and propagation forming a conventional fatigue spall.

In the case of bare, or even some solid lubricated ceramics under pure sliding, the values of f_k nearly always exceed 0.3. Consequently, shear-induced mechanical alloying, shock-load-induced phase transformations and hot-spot-induced chemical reactions causing the high-friction conditions on the surface are the controlling factors of the friction and wear mechanism(s). They come especially into play at high temperatures, in air, where surface reactions generate secondary structures distinctly different from the bulk (e.g., glassy layers, brittle and non-lubricious oxides, etc.)

It follows that a ceramic specimen which can be tested for both RCF resistance in the oil-lubricated, rolling condition (low f_t) and for wear resistance and friction behavior in the bare and solid lubricated sliding condition (high f_k) can serve as a universal specimen in determining the usefulness of a ceramic under the stresses induced by the two main modes of tribological (i.e., rolling and sliding) use. Ideally, one would have to do RCF testing at the same elevated temperatures as the high temperature sliding tests to account for both the creep and plastic components of the inelastic strain. At this time, only oil lubricants can provide the low f_t needed to place the region of maximum shear stress below the surface. Unfortunately, oil-lubricated RCF tests are currently done at room temperature only.

With these stipulations, the RCF rod appears to be an ideal, universal test specimen for the wide triboenvironmental evaluation of bare and solid lubricated ceramics. Since the greatest amount of surface damage by wear occurs under pure sliding in high temperature air, at high loads and high speeds (3), tribotesting in that environmental regime becomes an early object of concern.

The room temperature RCF tester of interest was developed by the NTN-Bower Corporation (formerly Federal Mogul), (58). It was originally designed for the rolling mode testing of bearing steel RCF rods with steel balls. However, it can also be used in conjunction with ceramic material samples of the same dimensions and geometries. In fact, for ceramics and hard-metal-coated steel or cermet specimens, this apparatus is now used exclusively (58, 59, 60), even though its ultra high-load, empirical use with ceramics has yet to be justified theoretically.

The RCF rod specimen is clamped in the collet of a vertically mounted drive spindle, with a portion of the rod protruding above the spindle nose. Three rolling balls are forced against the protruding segment via two axially loaded cones (Figure 31a). In the Tribotester 2A (referred to hereafter with the Hughes designation "Tester 2A", the RCF rod specimen is also clamped in a vertically mounted spindle with a portion protruding above the spindle nose and the other material samples forced against it radially (Figure 31b). But this is where the similarity ends.

2.2.3.2 Tester 2A Capabilities and Design Features. The final design of Tester 2A, as thoroughly described in APPENDIX G and (61), depicts a unique, wide temperature range friction and wear tester. It was developed to test the sliding friction and wear characteristics of various bare and solid lubricated ceramic and other high temperature bearing material combinations under a wide spectrum of environmental conditions.

The Tester 2A (for overall layout and appearance, see Figures 32 and 33) has several unique features, which are not found in other tribotesters:

1. The friction contact surfaces can be heated to temperatures ranging from 25°C (77°F) to ~850°C ≅1500°F.
2. Sliding contact speeds can be varied from 0.5 to 5.0 $m \cdot s^{-1}$.
3. Normal contact forces can be adjusted up to 200 N (45 lbs.).

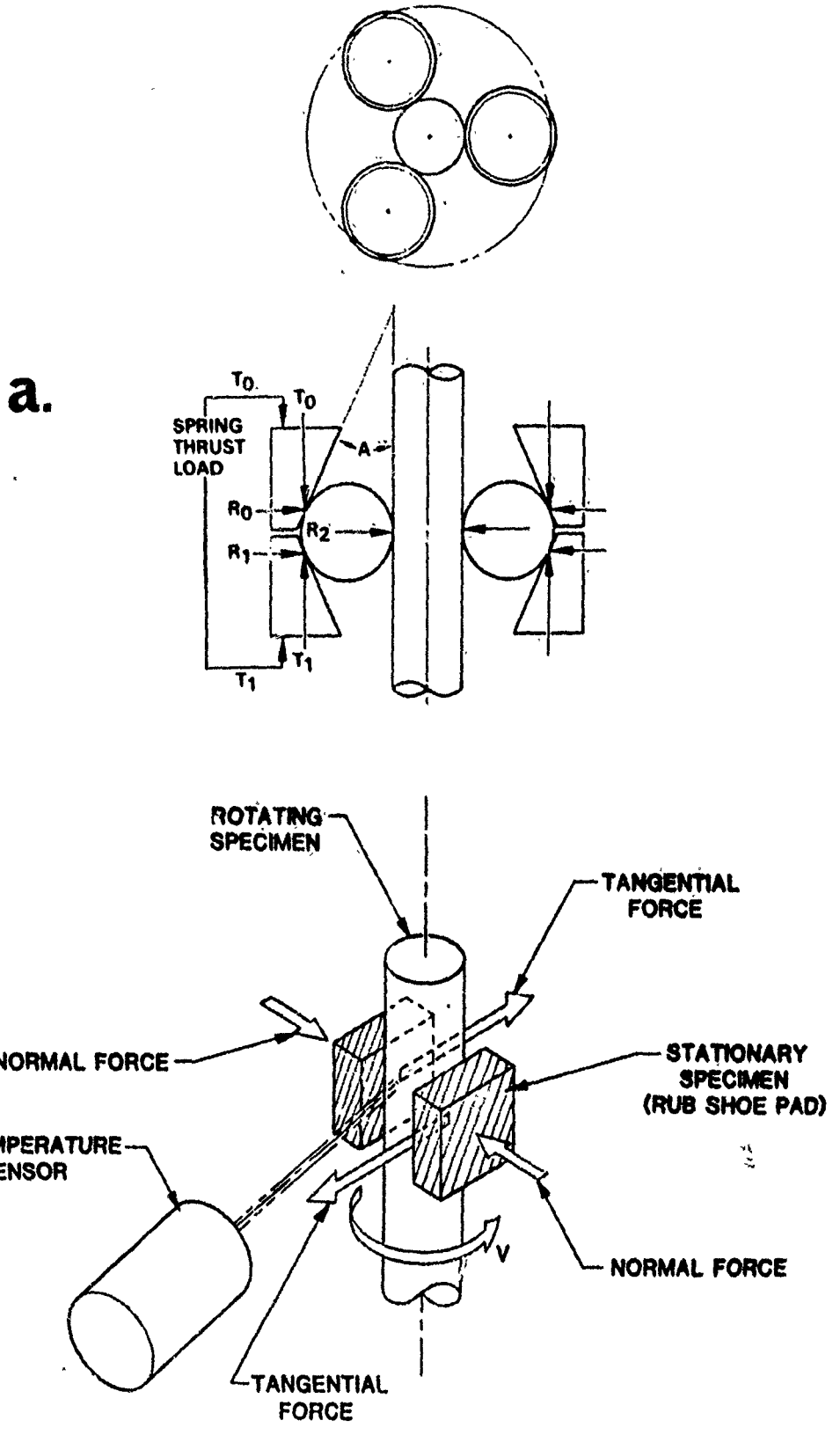

Figure 31. Specimen contact schematics of (a) the NTN-Bower RCF-tester, and (b) the Tester 2A.

a.

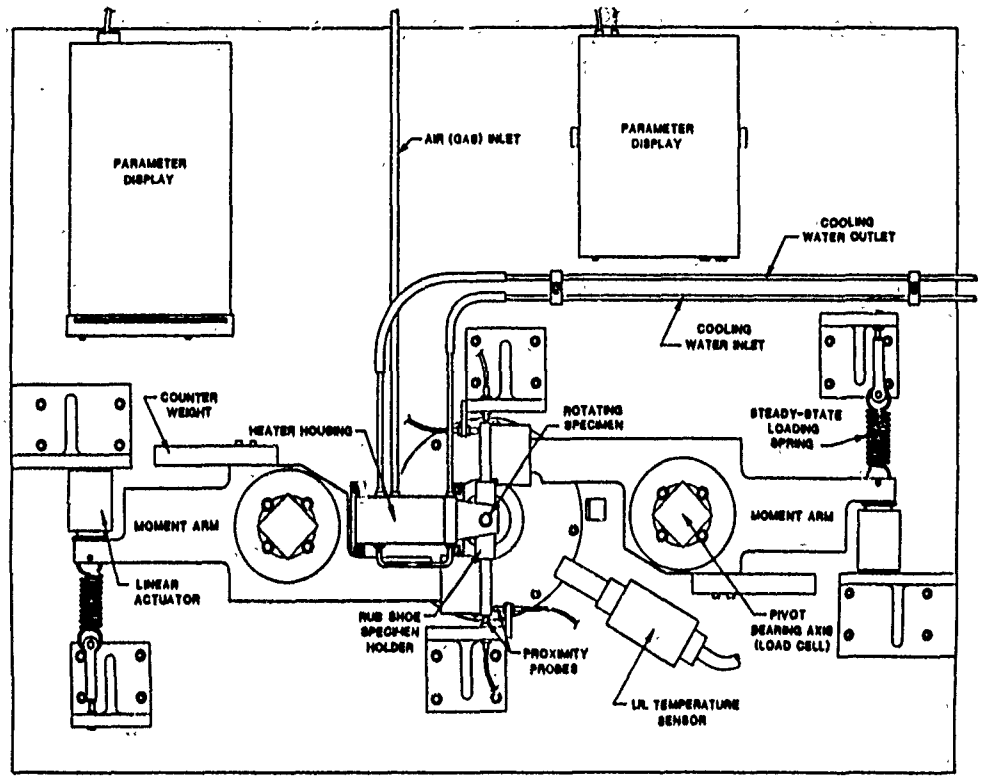

b.

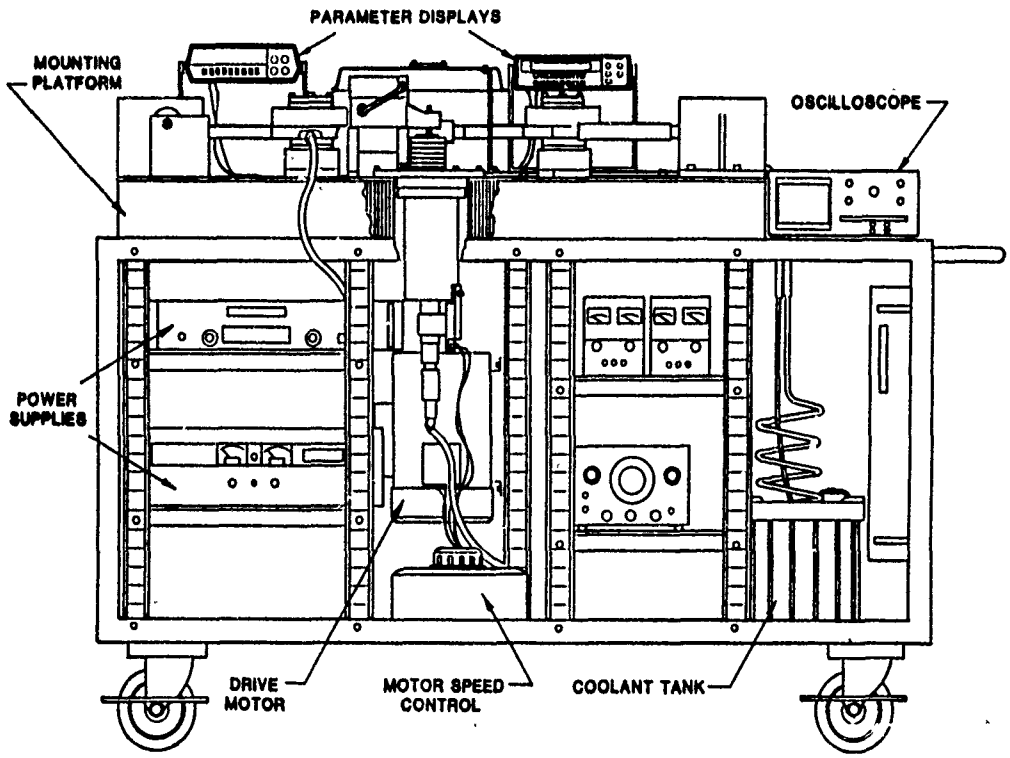

Figure 32. Overall layout of the Tester 2A: (a) top view, (b) side view of the portable test stand.

4. The applied load can be either a constant steady-state force or that superimposed by a repetitive function (sinusoidal or other) with frequencies up to 50 Hz, thus simulating the actual variable loading conditions found in many types of machinery.

5. Each stationery specimen can be readily changed to permit tests with flat, concave or convex cylindrical and spherical contact surfaces.

6. The atmosphere surrounding the co ntact areas can be purged either with standard air or an inert gas, such as dry nitrogen, helium or argon.

7. Unlike other high temperature testers, it does not require a large furnace, but uses a compact I.R. quartz lamp heater (the approximate furnace volume is only ~500 cm^3).

The apparatus has instrumentation to monitor: (a) the temperature near the contact points, (b) tangential and normal loads, (c) rotational speeds, and (d) the combined wear depth on the stationary and rotating surfaces. The tester is constructed with readily available state-of-the-art components and is easily operated.

In essence, a vertically spinning, regular-sized or slightly longer than normal ceramic RCF rod is squeezed, in a nutcracker fashion, by two rubshoes or point, line or area contact configurations (Figures 33b and 34). The line and area contact rubshoe designs are based on regular RCF rod dimensions (Figure 35; -1/-2), modified by two parallel planes ground into the RCF rod on opposite sides of its diameter (Figure 36). Then, the rod can be sliced up (like bread), providing uniform pieces with one flat surface for a line sliding contact and another flat surface which fits into a machinable ceramic (MACOR®), standard specimen holder. The truncated circle of the contact face provides for an ideal wear scar length, enabling the placement of a predetermined number of friction paths with a predetermined number of RCF tests on the same rod which can follow the sliding tests. Where flat rubshoes had to be fabricated from anisotropic base stock, a simpler block geometry was used (Figure 37).

The same rubshoe piece can also be ground concave, [0.64 cm (0.25 in) radius] for a conforming area contact, or convex for a cylinder-to-cylinder parallel axis line contact or a cross-cylinders point contact; for specimen drawings, see Figures 36 and 38.

By taking a commercially available, 1.28 cm (0.5 in) dia. ceramic ball, followed by grinding a cylindrical surface about one axis then slicing the hemispherically-tipped cylinders in two pieces, provides two of the highest-unit-load-providing, sphere-to-RCF-rod (cylinder) point contacts are provided (also see Figure 38). This configuration completes the rubshoe series. All rubshoes contain a thermocouple hole penetrating as near to the sliding surface as practicable and they all fit into the same, tuning-fork-like MACOR® specimen holder housed in a clampable steel or superalloy jacket.

a.

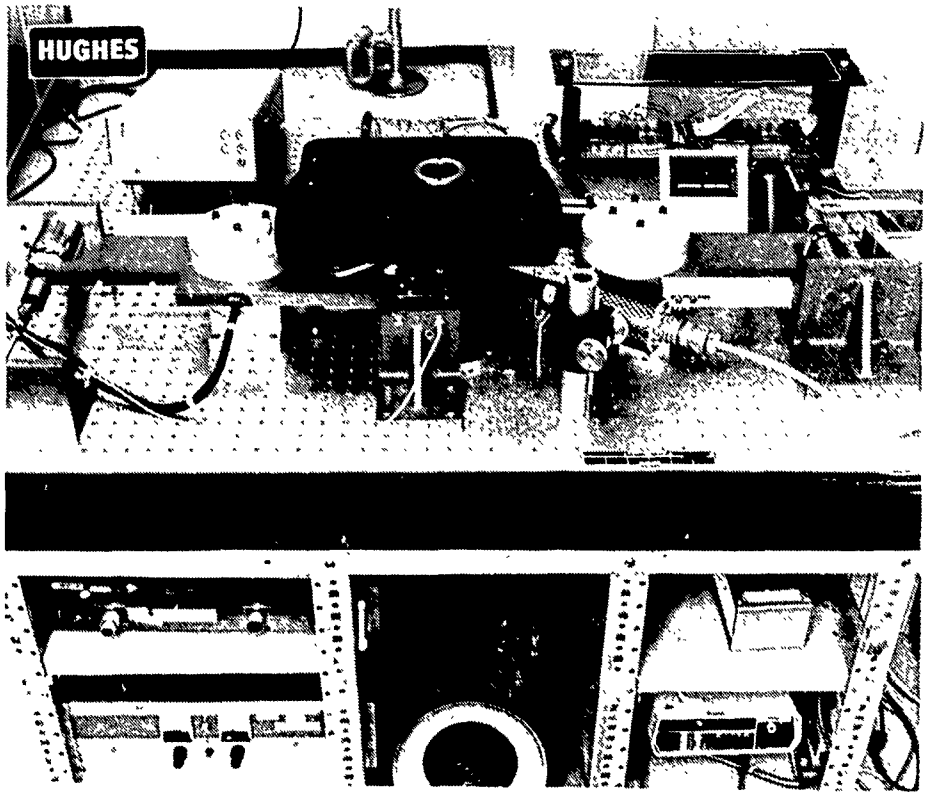

b.

Figure 33. Photographs of the Tester 2A: (a) oblique side view; (b) data logging and analysis computer.

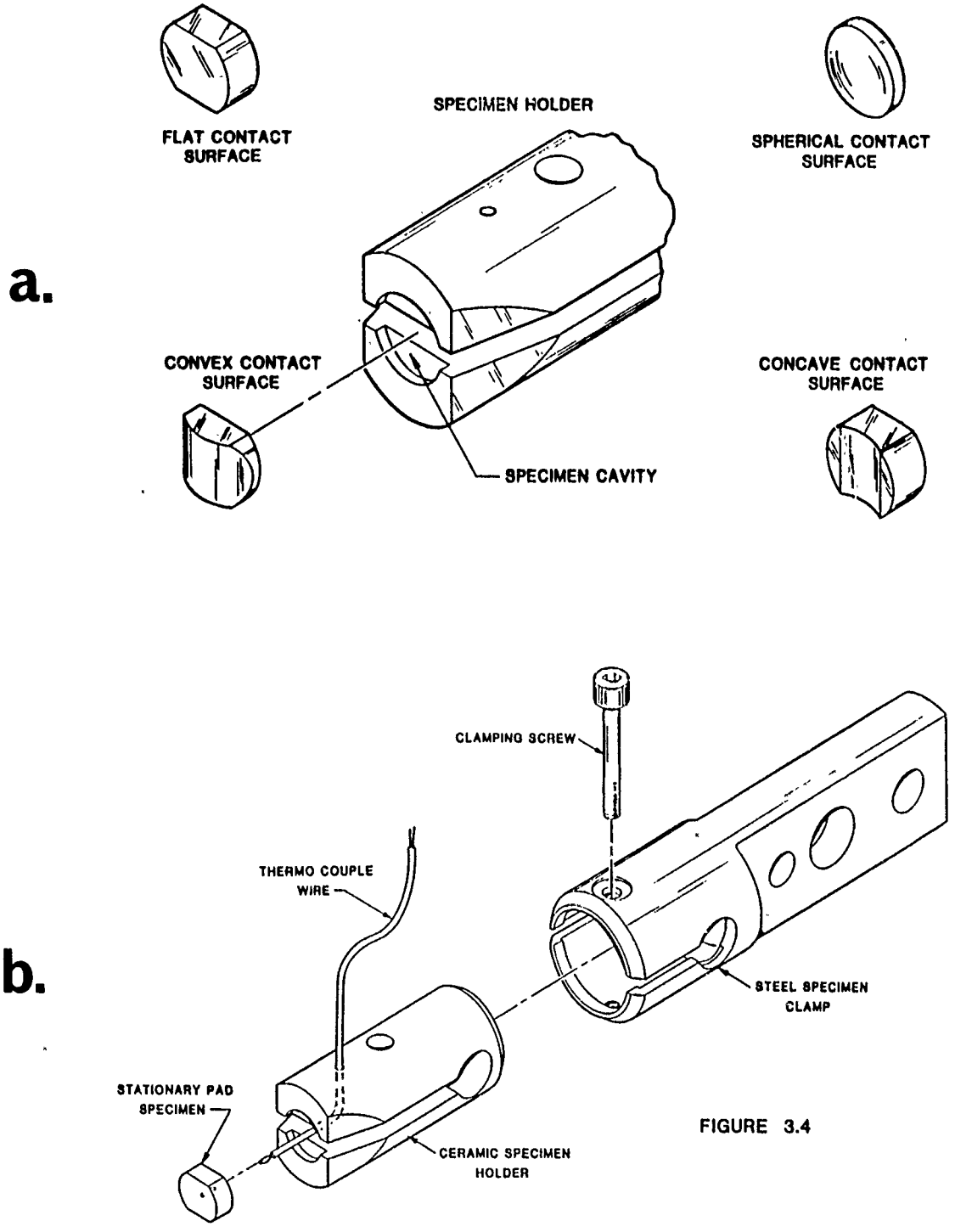

Figure 34. Rubshoe and holder schematics; (a) different types of rubshoes and a metallic rubshoe holder for room temperature tests, and (b) thermally insulating ceramic (MACOR®) rubshoe holder with metallic holding fixture for high temperature tests.

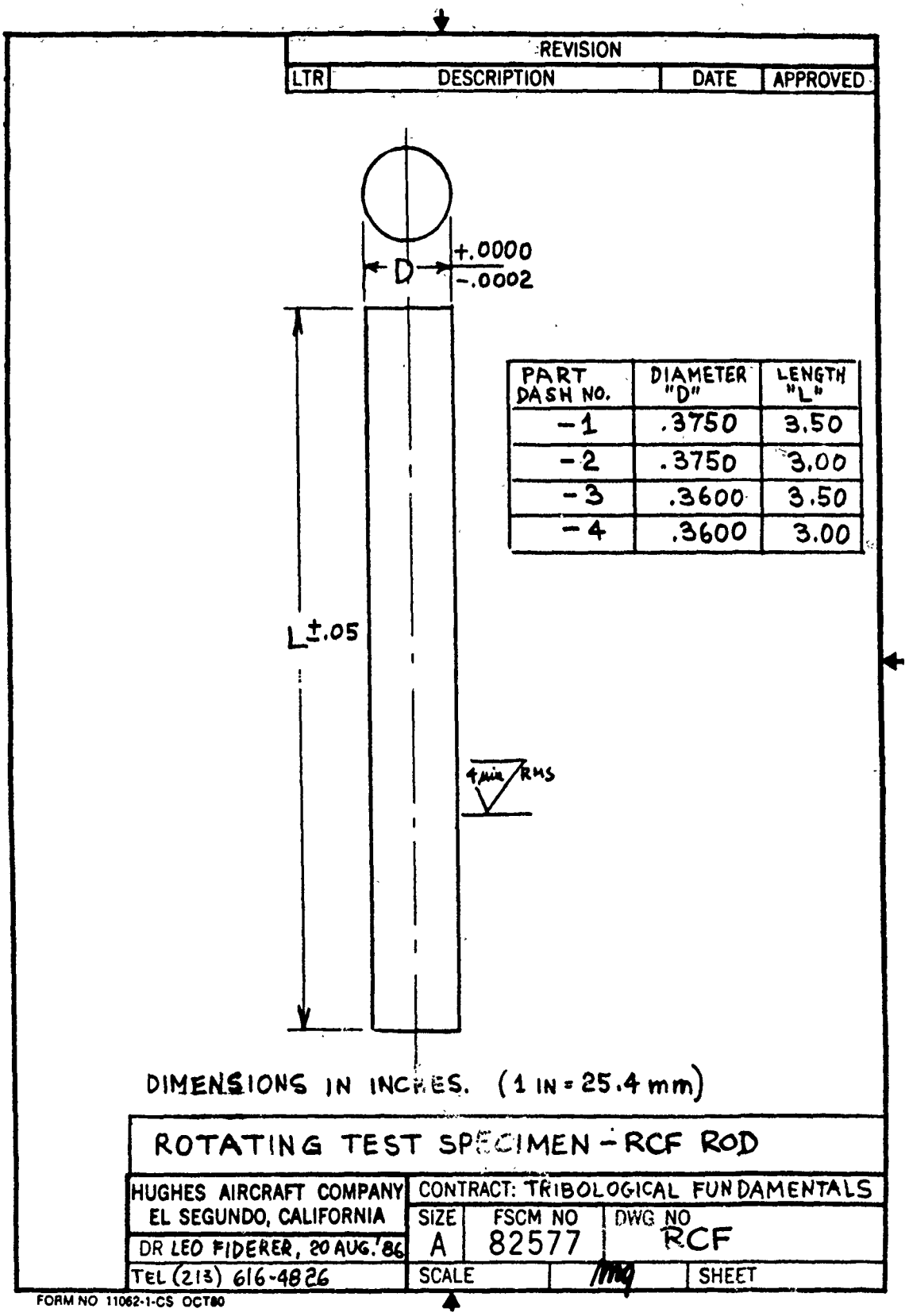

Figure 35. Engineering drawing of regular size and undersized RCF rods.

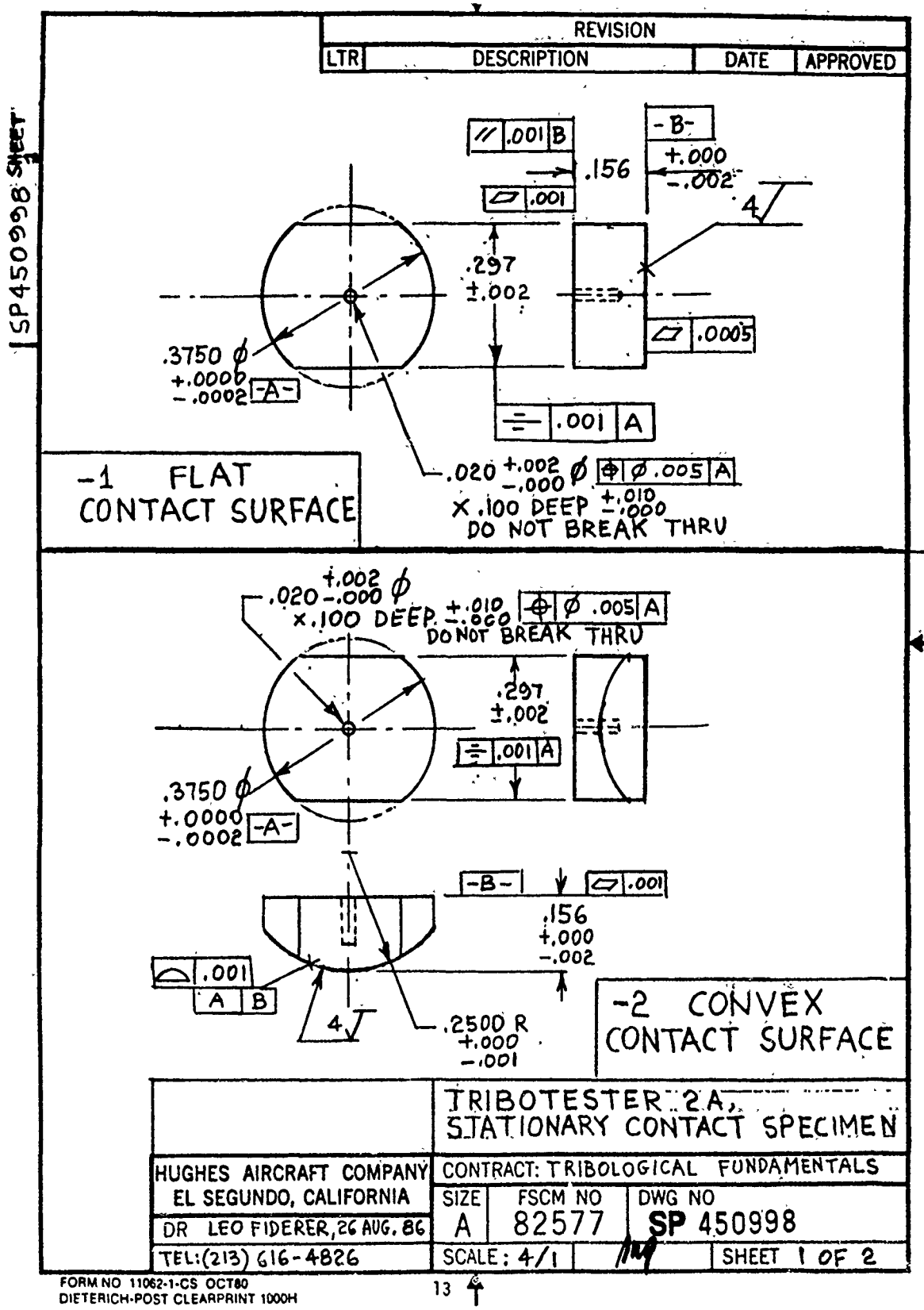

Figure 36. Engineering drawings of flat and cylindrically convex rubshoes.

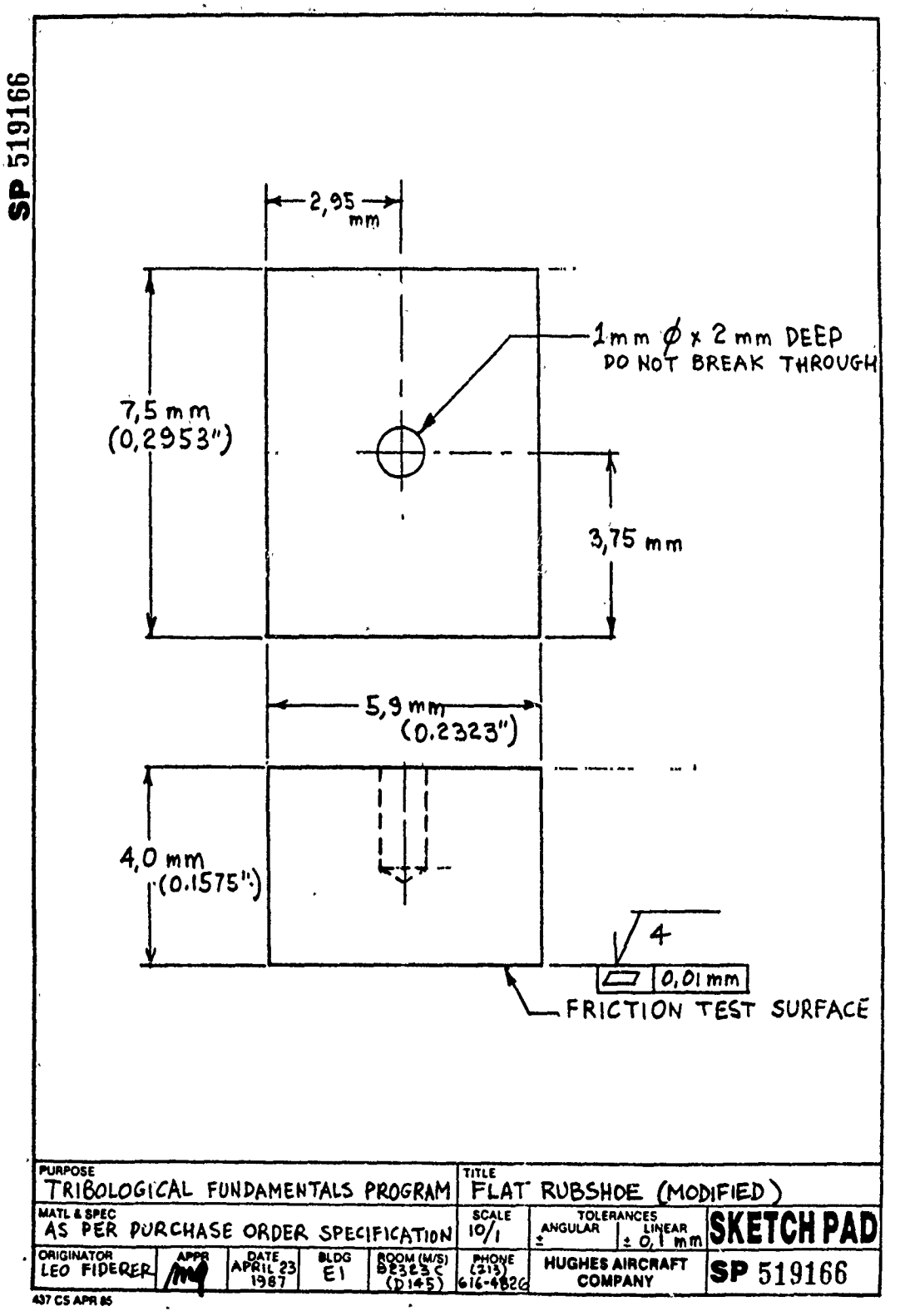

Figure 37. Engineering drawing of simplified flat rubshoes.

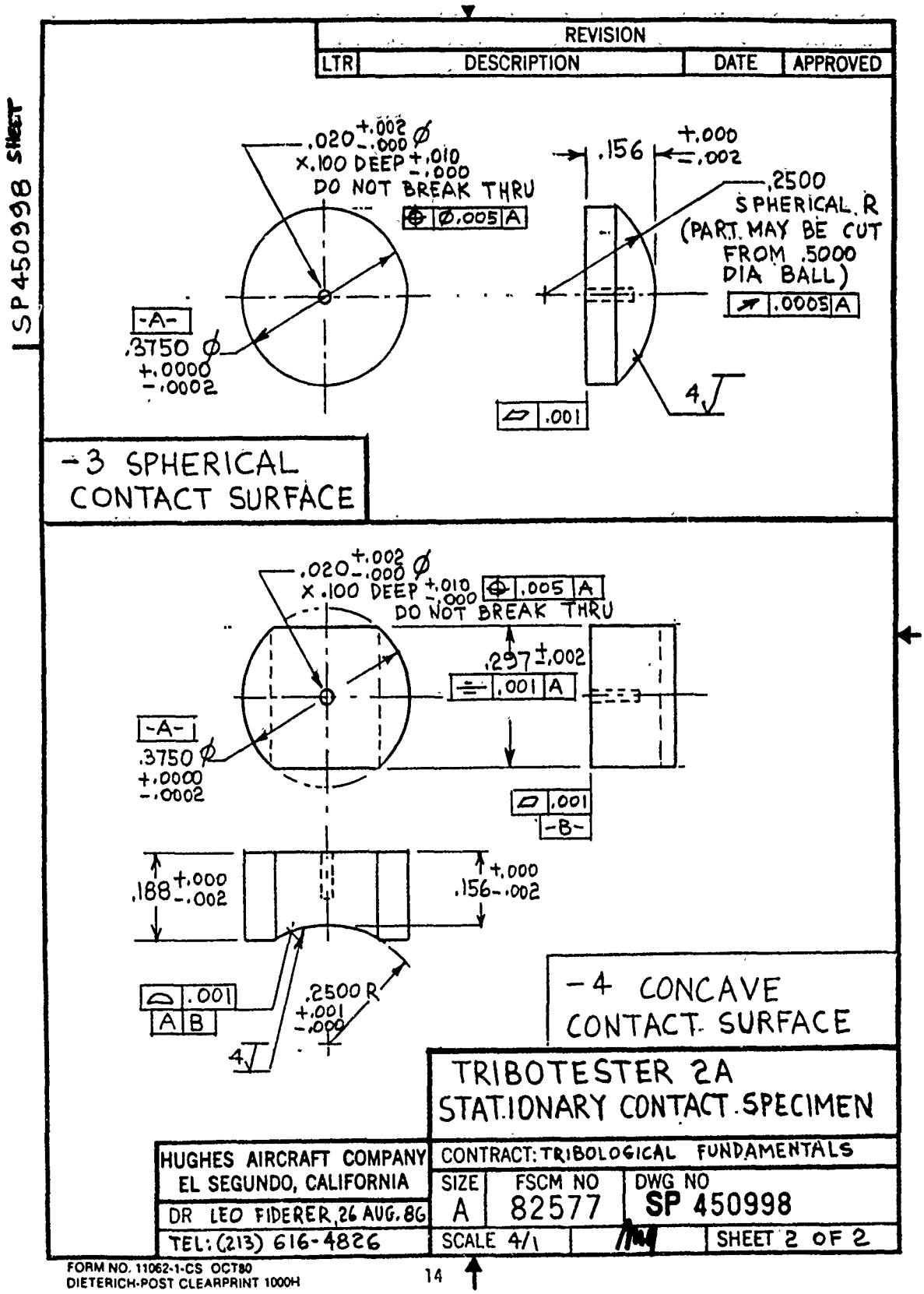

Figure 38. Engineering drawings of spherical and cylindrically concave rubshoes.

The rubshoes are pressed against the RCF rod through rigidly constructed, very stiff moment arm/pressure bar combinations pivoted around their own triaxial transducer. These six-degrees-of-freedom A.M.T.I. transducers are capable of measuring the normal load and the friction force, along with any misalignment loads, simultaneously. Steady-state loads of appropriate magnitude are applied through adjustable tension springs. Cyclic, sinusoidal or other wave form loads can be superimposed through moving coil, linear actuators ("vibrators"). The actuators far exceed the capacity to deliver the planned 50 Hz (max.) vibratory loads approximately 5 kg (~10 lbs) in magnitude. An in-house mechanical-nodal, finite element computer analysis (see APPENDIX H) of the moment arm/pressure bar combination's characteristic frequencies preceded the finalization of the design. Dynamic breadboard tests with a closely-simulated friction transfer arm (see Figure 39) confirmed the computer predictions that the resonance peaks of the moment arm occurred at approximately 140 and 170 Hz, well above the 50 Hz value of interest.

The tribocontacts are heated by a single, water-cooled quartz lamp equipped with special reflectors to heat the rod/rubshoes contact region only. This concentration of heat, combined with the special design to minimize heat conduction away from the contact region, enables the size of the specimen furnace to be somewhat smaller than one-half of a 10 cm cube. A metal safety cover was installed on top of the heated region, containing a quartz observation window and an orifice for the I.R. temperature sensor beam. The beam further passes through an inner aperture heat shield. There are gas cooling passages through the spindle, exhausting the warmed-up cooling gas around the sliding couple. This feature permitted the running of tribotests in filtered air or in argon/nitrogen, without substantial cooling of the specimen region.

There was no detrimental specimen cooling effects from these gases, so no other venting arrangements were needed. Another, in-house thermal-nodal computer analysis (see APPENDIX I) helped decide the final specimen heating and spindle cooling designs. Based on this analysis, the final Hughes spindle design was fabricated by the Emhart Corp., Whitnon Spindle Division, Farmington, CT (Figure 40).

The mechanism details of the Tester 2A, incorporating the design particulars described above, are included in Figure 41.

2.2.3.3 Data Logging and Analysis System. The data logging and analysis system is similar to the one used with the SEM tribometer (see para. 2.2.2.1.4), including the Labtech Notebook® and the RS/1® software packages. The sampling rates for this measurement system are limited by the constraints of the real time display software. Consequently, the critical measurements (load, friction force, wear, rubshoe and tribocontact temperatures, see Figures 42, 43 and 44) were sampled more frequently than the secondary monitors sensing heater and spindle bearing temperatures and power sources (see APPENDIX J).

a.

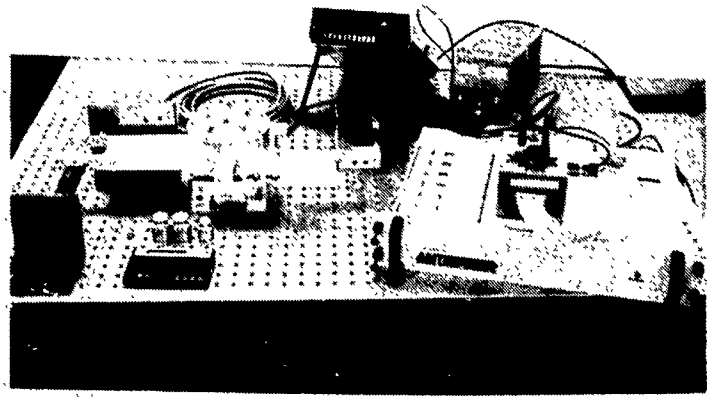

b.

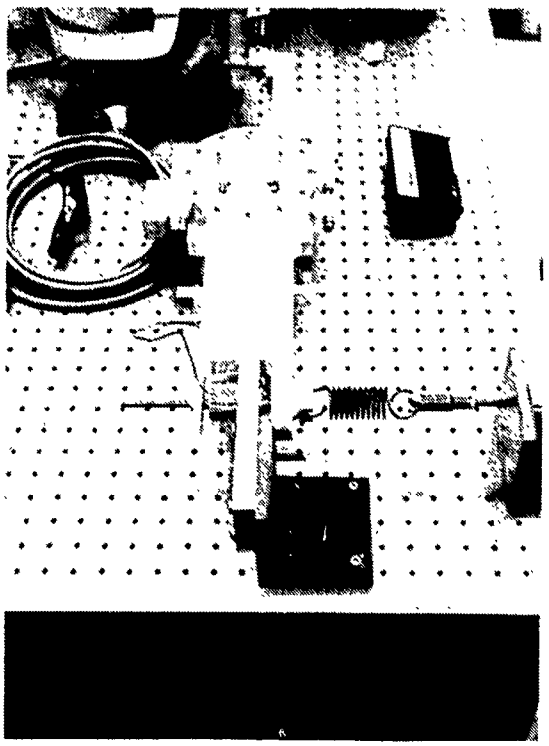

Figure 39. Brassboard set-up of a Tester 2A friction transfer arm: (a) steady-state loading spring only, (b) loading spring and vibratory load transducer.

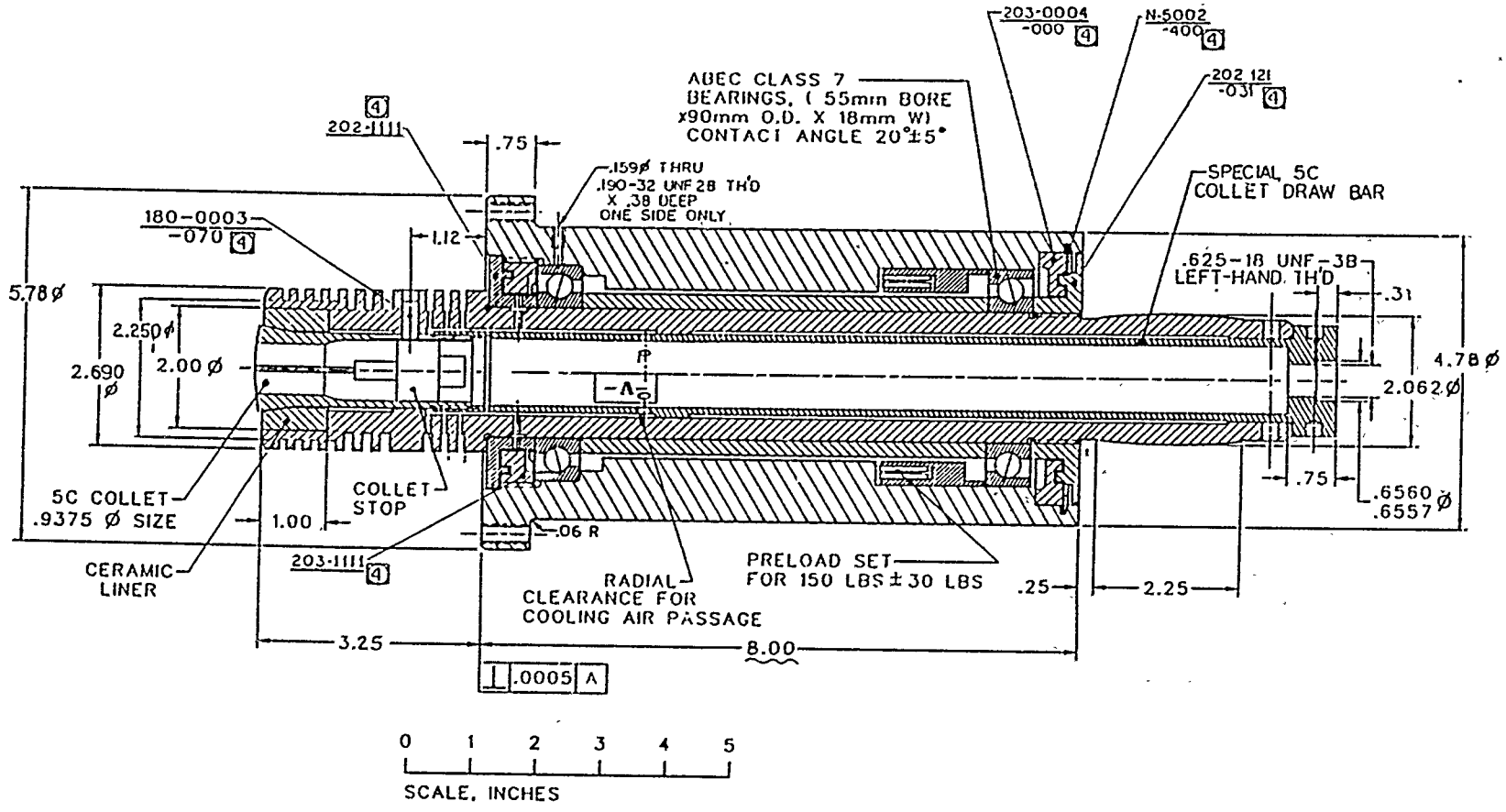

Figure 40. Engineering drawing of the Tester 2A spindle.

a.

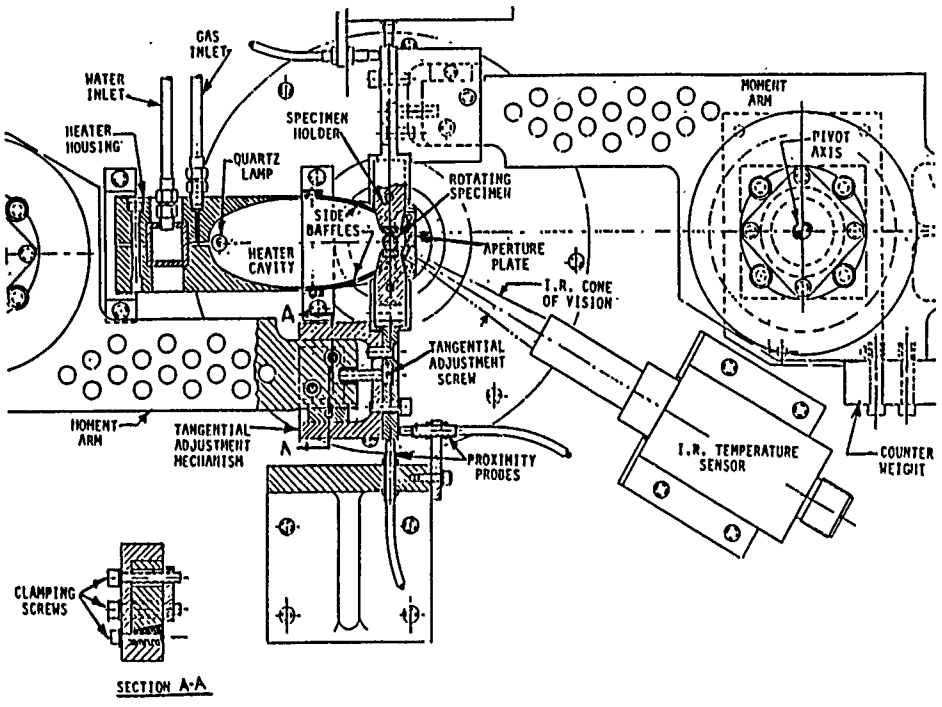

b.

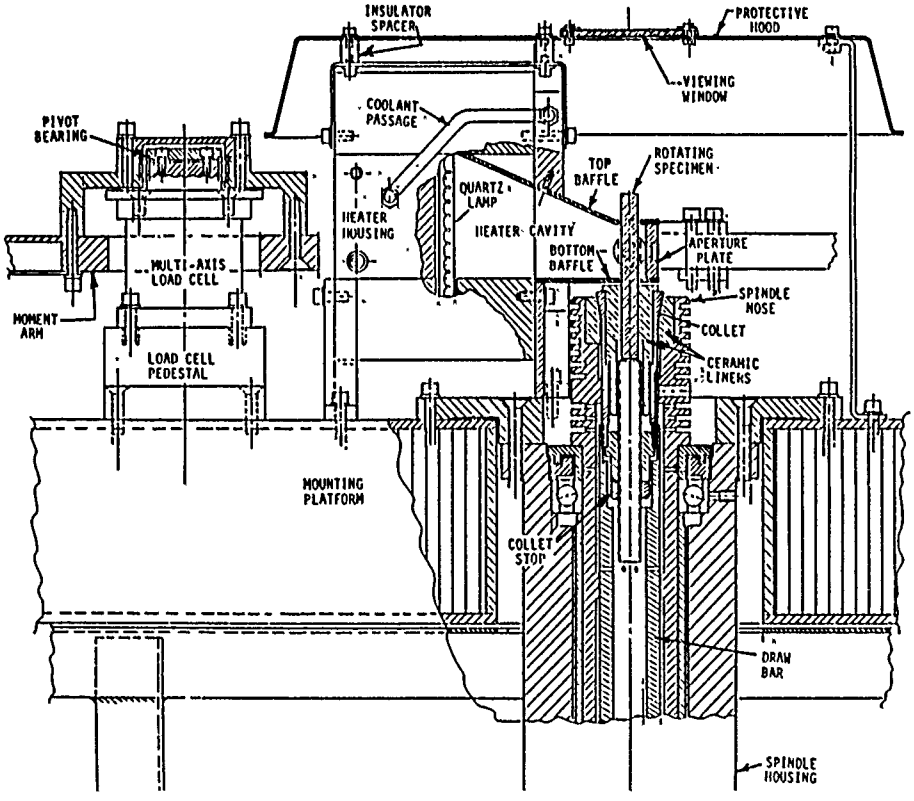

Figure 41. Mechanism details of the Tester 2A: (a) top view, (b) side view.

2.2.3.4 General Test Procedures. The procedure for the room temperature tests is included in APPENDIX J and also see Figure 42. Essentially, the procedure consisted of applying the preset, steady-state spring load and then removing the spring load with the linear actuators, while still maintaining contact between the rod and rubshoes. This ensures that there is no impact loading upon start-up: use of the actuators to reapply the load allows ramp-loading of the rubshoes against the rod. The rod is then rotated at a fraction of the steady-state speed, while the steady-state normal load was reapplied by decreasing the offsetting actuator load component. The actuator voltage source and power supply are then turned off, because the switching amplifier of the actuator drive system is still a verified electronic noise source in spite of EMI shielding. Therefore, the recorded data are more reliable with this system disengaged. Upon disengaging the actuators, the rotational speed is then increased to 700 rpm and maintained for approximately a 20 minute test duration. At the end of the test the actuators are engaged to provide ramp-unloading the rubshoes from the rod and the rotation is stopped. Throughout the duration of the test, the spindle and the test region are purged with a slow flow rate of dry, filtered air or inert gas. All tests in this program were run under a 1.36 kg = 13.34 N (3.0 lbs) steady state coil spring load. The actuators were not used to superimpose an AC (vibratory) signal over the DC (steady-state) load; as mentioned here they were employed to offset the tension-spring-induced normal load and to apply/remove this load upon test start-up as gently and gradually as possible. The standard test speed was held to 700 rpm = 0.35 $m \cdot s^{-1}$, with a general test duration of 20 to 30 minutes, depending on the degree of rubshoe wear. These general conditions are listed in Table 4.

During high temperature testing, a large error manifested itself in the combined rubshoe/RCF rod wear rate as a result of expansion and contraction of each friction transfer/load arm during heating and cooling. The heating and loading procedure was modified for this test in an effort to isolate the effects of the errors in the observed wear rate. The modified test procedure was as follows:

1. Preset the steady-state spring load (no rotation of the RCF rod).
2. Remove two-thirds of the 1.36 kgf (3.0 lbs) steady-state load with the actuators, leaving a 4.54 x 10^{-1} kgf (1.0 lb) contact load.
3. Rotate the rod at a fraction (400 rpm) of the steady-state (700 rpm) speed. (These first three steps are per the usual procedure followed during room temperature tests.)
4. Heat the rod to the maximum temperature at the slow speed with only the 4.54 x 10^{-1} kgf (1.0 lb) contact load.
5. After the rod's surface temperature has stabilized, load the rubshoes against the rod with the full 1.36 kgf (3.0 lbs) steady-state load and turn off the actuators.
6. Increase the rotational speed from 400 rpm to 700 rpm.
7. Run the test for 20 to 30 minutes under these steady-state conditions.
8. Cool the sample, remove the load and stop the RCF rod rotation.

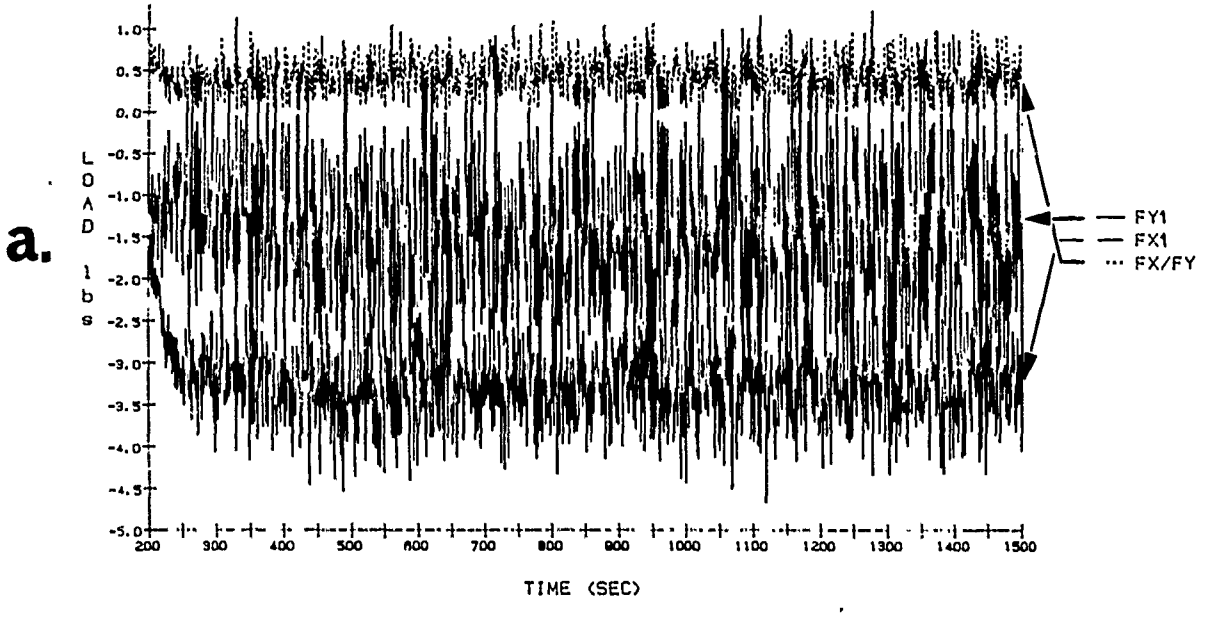

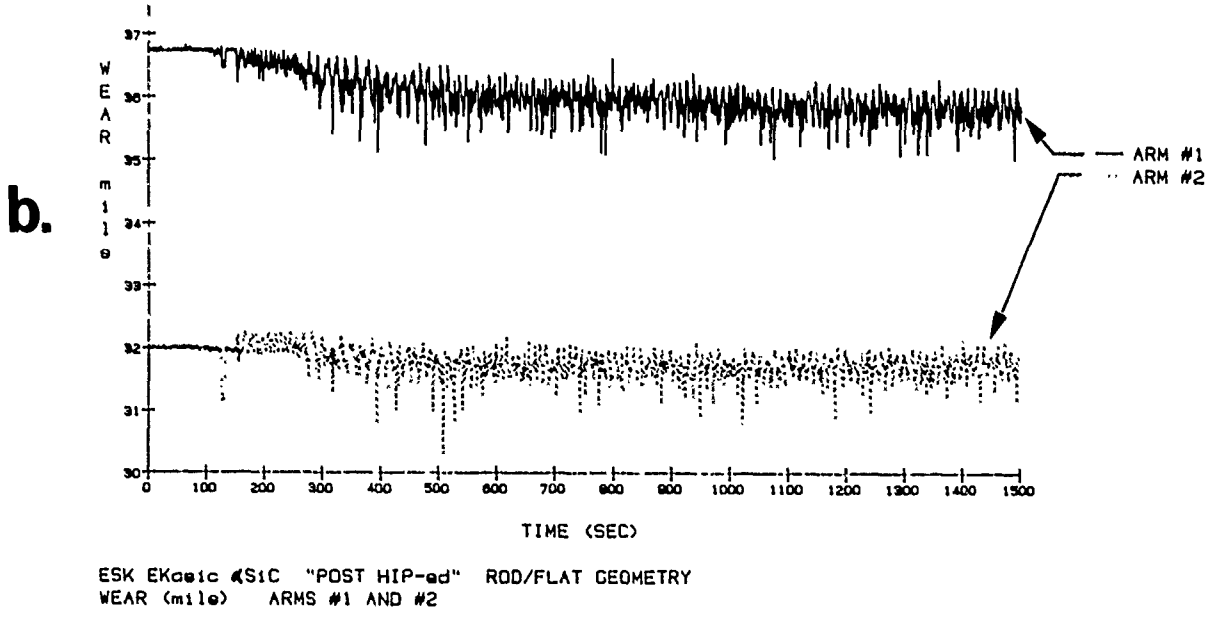

Figure 42. Typical friction and wear traces of a room temperature Tester 2A experiment: (a) normal applied load (F_y), friction force (F_x), and the calculated coefficient of kinetic friction (F_x/F_y), measured as a function of test duration.

Table 4. Test conditions for Tester 2A experiments.

Test Parameters	Magnitude
Normal Load (Steady-State)	1.36 kgf = 13.34 N (3.0 lbs)*
Speed: • during loading • steady-state	~ 400 rpm = 0.20 $m \cdot s^{-1}$ (0.66 fps) 700 rpm = 0.35 $m \cdot s^{-1}$ (1.16 fps)
Duration: • time • sliding distance	20 - 30 minutes 420 - 630 m (1378 to 2067 ft)
Data Sampling Rates: • Wear • Load • Friction Force • Rubshoe Temperature • Pyrometer Temperature Output • Heater Temperature • Bearing Temperature • Proximity Probes Power • L.C. Power	 1 Hz 1 Hz 1 Hz 1 Hz 1 Hz 0.5 Hz 0.5 Hz 0.5 Hz 0.5 Hz
Test Atmosphere	Dry, Filtered Air or Inert Gas
Test Temperatures	R.T. (No Heat Added) or ~ 850°C (Pyrometer temperature)
*Equivalent to a unit load of 125 MPa ≅ 18 Ksi with α-SiC versus α-SiC (see APPENDIX J).	

The time-dependent responses have been plotted for each of the load, temperature and wear variables to show the effects of this new heating and loading procedure (see Figure 43b):

1. Expansion of the friction transfer/load arm as a result of heating before full loading resulted in a decrease of the proximeter-measured wear gap of approximately 4.08×10^{-5} m (0.002 in). Observe that the wear rate (slope of the curves) is almost linear in the steady-state load and temperature region (600 to 1900 seconds). The rate then apparently (and falsely) increases after 1900 seconds as a result of arm contraction on cool-down. This new test method isolates the expansion and contraction of the test arm outside of the full-scale loading range of interest. The disturbing effects of expansion and contraction occur before and after the true wear curves are thus established. Note that the examination of numerous test specimens indicated that in every case, over 95% of the wear occurred on the rubshoes (forming the wear scars). The material removal rates during scar formation are, therefore, valid measures of the rubshoe material's wear rate.

2. The decrease in the applied load throughout the duration of the test here is only 2.22×10^{-1} kg (0.5 lbs). With higher wearing materials (e.g., h-BN, see para. 3.1.2), the test was terminated when the wear-induced relaxation of the steady-state spring load reached 4.44×10^{-1} kg (1.0 lb), and the test load was taken as an average of 8.88×10^{-1} kg (2.0 lbs).

3. The steady-state-portion of the heated and fully loaded test region is longer in duration because the total test time at the elevated temperatures did not include the heat-up period. It takes approximately 300 seconds (6 minutes) to reach the top test temperature. The improved procedure provides an extended steady-state region in which to determine accurate wear rates (Figure 44). The data in this illustration also indicate that the thermocouple-measured bulk temperatures of the rubshoes are far below the surface temperatures measured with the pyrometer. Even finite difference analysis of heat flow invoked to correct for the distant positioning of the thermocouple from the rubbing surface of the rubshoes (see Reference 62 for an example of such work) may be prone to large errors compared to actual pyrometer measurements. The differences in the thermocouple-measured temperature values in the steady-state region may have been made worse by the varying insertion depths or contact conditions of the thermocouples loosely inserted in the rubshoe thermocouple wells.

2.2.3.5 Pyrometry of the Tribocontacts. The basic equation of I.R. pyrometry is:

$$R + A + T = 1.0$$

where R = fraction of reflected energy;

A = fraction of absorbed energy;

T = fraction of transmitted energy.

An I.R. pyrometer detects both the reflected and absorbed energy without distinguishing between them. It stands to reason that the design of a tribospecimen heating device should avoid reflected energy as much as possible to minimize reading errors.

a.

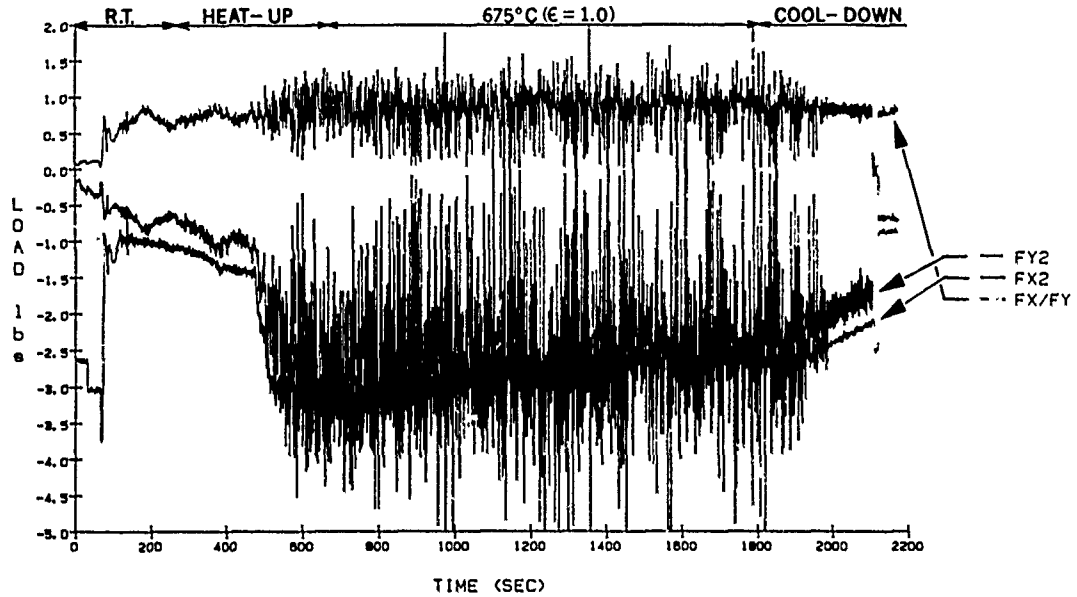

TEST #5, 13.3 N (3.0 lbe), 700 RPM
ESK EKASIC SiC "POST HIP-ed" ROD/FLAT GEOMETRY
LOAD VALUES ARM #2, HIGH TEMPERATURE

Figure 2. Combined rod and rubshoe wear as a function of time, test #5; arms #1 and #2 (initial values are set arbitrarily).

b.

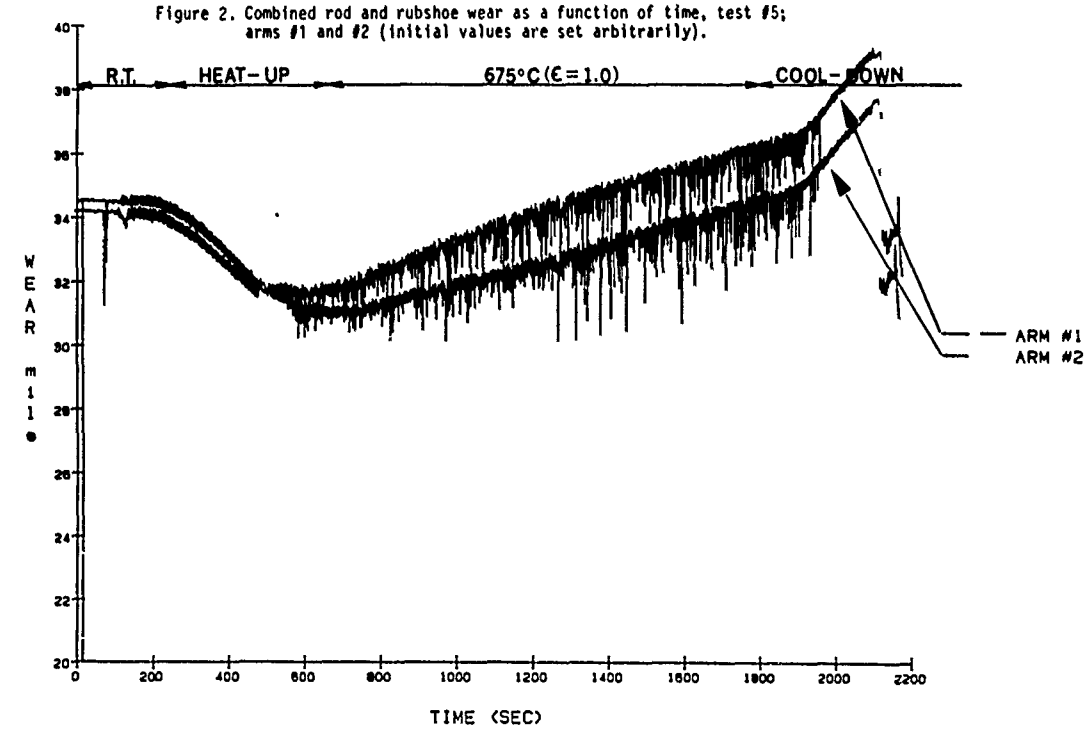

TEST #5, 13.3 N (3.0 lbe), 700 RPM
ESK EKASIC SiC "POST HIP-ed", ROD/FLAT GEOMETRY
WEAR VALUES ARMS #1 AND #2, HIGH TEMPERATURE

Figure 43. Typical friction and wear traces of a high temperature Tester 2A experiment: (a) normal load applied load (F_y), friction force (F_x) and the calculated coefficient of kinetic friction (F_x/F_y), measured as a function of test duration.

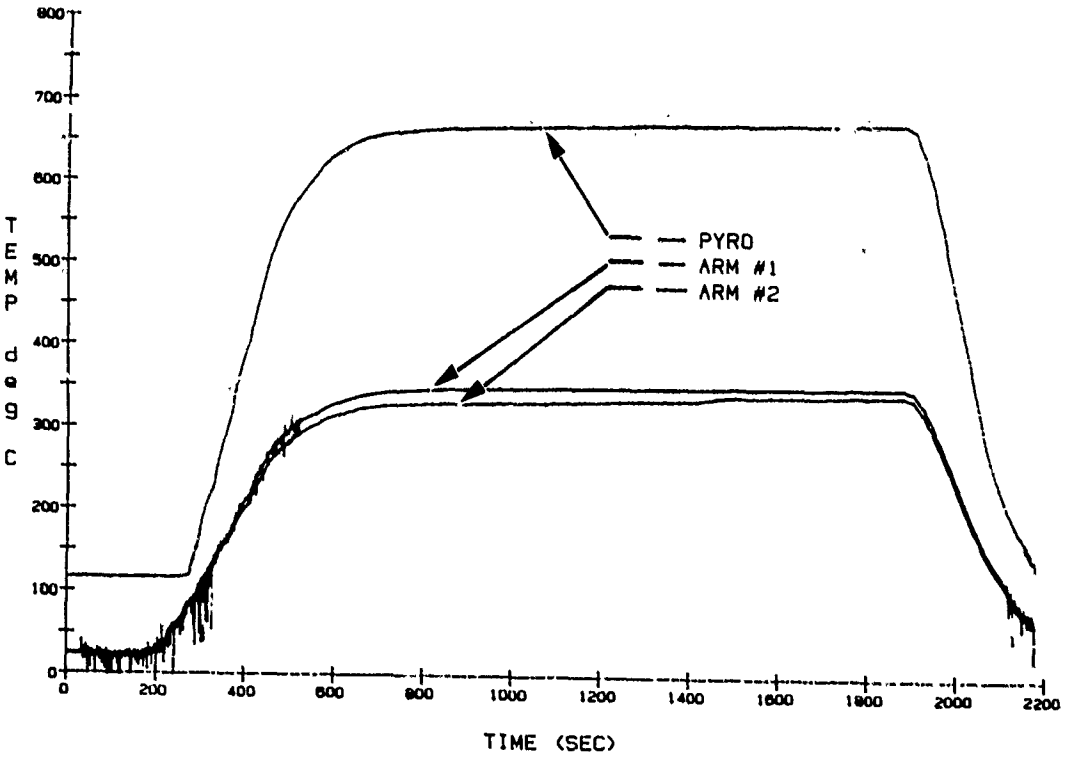

TEST #5, 13.3 N (3.0 lbs), 700 RPM
ESK EKASIC SiC "POST HIP-ed" ROD/FLAT GEOMETRY
TEMPERATURE VALUES, HIGH TEMPERATURE, EMISSIVITY=1.0

Figure 44. Typical rubshoe thermocouple and Vanzetti pyrometer temperature read-out traces of a high temperature Tester 2A experiment.

Most ceramic compounds have low emissivity at short wavelengths and high emissivity at longer wavelengths. The cross-over regions are usually between 2 and 5 μm. Each instrument model is designed to accommodate a certain range of wavelengths. Instruments designed for the longer wavelengths with high emissivities have larger minimum target spot size, whereas in our application the smallest target spot size was desirable. When selecting the instrument model, trade-offs had to consider applicability to a wide range of ceramic compounds.

Each instrument control panel has adjustments for the emissivity of the target. Wrong settings of the emissivity designation will produce errors in the temperature readings. Therefore, emissivity of the target material must be ascertained as accurately as possible before the test is conducted.

When focusing in the tangential path of the outlet region on the RCF rod specimen, the location of the focal plane is optimum at a point where the width of the target spot is equal to the distance between the rotating and the stationary specimen surfaces.

A method of concentrated heating the specimen in the area surrounding the rubbing contact only, such as the use of quartz lamps, is preferable to the heating of the entire environmental chamber for the following reasons:

1. With the chamber walls acting as a heat source, these walls will have to be kept at temperatures higher than the maximum 816°C specimen temperature. Reflections from the background heat sources will cause erroneous readings from the pyrometers.
2. A protective sight tube with a large amount of coolant flow must be constructed for an I.R. lens assembly to reduce the errors caused by background radiation. This is quite an expensive proposition.

Based on a Hughes-funded study and report by Mr. Herb Kaplan (Honeyhill Technical Co., Norwalk, CT), see APPENDIX K, a Vanzetti pyrometer with a backlighting source and fiber optics projector was selected from five candidates as the main component of the I.R. sensing and sliding surface temperature measuring instrumentation. As mentioned before, this method of sliding temperature measurement is deemed more accurate than the use of thermocouples positioned at some significant distance away from the sliding interfaces. Then I.R. beam spot size is 1.3 mm (~0.5 in.) in diameter and at a 10 cm (~4 in.) focal distance is compatible with the 4 mm (0.156 in.) heat shield aperture. Note that the spot size is generally understood to mean that 85 to 90% of the energy at the target (i.e., the heated and rubbed RCF rod's surface) within the spot reaches the instrument. With the Vanzetti pyrometer it is anticipated that at least 90% of the energy in a larger 2.54 mm (0.1 in.) spot (twice as large as our design size) at the target would reach the instrument. This assures that the 4 mm (0.156 in.) aperture size is large enough not to shield any of the returning energy, resulting in no detectable aiming error.

The compact sensing head is an advantage, because the Tester 2A platform size (see Figures 32 and 33) is only 1.2 m x 0.9 m (48 in. x 36 in.). The 4.5 μm spectral range is far enough into the infrared to assure no interference from the quartz heater or from visible light sources such as the projected aiming spot.

The deciding factor to select the Vanzetti pyrometer was the aiming system, which no other candidate instrument offers. Here, a high intensity light beam is projected, along with a darkened cross-hair, onto the target surface. The combination allows aiming and reaiming without having to sight through the instrument's optics. It enables us to observe if, for any reason, the instrument lost its aim or focus on the target. Fortunately, reaiming was shown not to be necessary when the Tester 2A was operating; it would have been difficult where the RCF rod glowed red-hot.

None of these advantages, however, eliminate the need to dial-in a known surface emissivity on its instrument panel to obtain an accurate surface temperature measurement ($E = \alpha\varepsilon T^4$, therefore $T = (E/\alpha\varepsilon)^{1/4}$). An example of this problem is given in Figure 45, where flat α-SiC rubshoes were sliding against an α-SiC RCF rod, at 60% power amplified to the heater lamp. At progressively decreased emissivity values ranging from $\varepsilon = 1.0$ to $\varepsilon = 0.5$, respective temperatures increased from 540° to ~750°C.

If we now take the average literature value of the emissivity $\varepsilon = 0.865$ for α-SiC (see Figure 46 taken from Reference 63) either with the Vanzetti pyrometer-measured 675°C (984K) = 1247°F at $\varepsilon = 1.0$ or the emissivity-corrected 780°C (1053K) = 1436°F, ε does not change significantly between these two temperatures. Therefore, the best estimated sliding surface (mean) temperature (not corrected for oxidation at the present time) is 780°C (1436°F). An inverse-linear relationship between ε and temperature was assumed for the 0.8 to 1.0 ε regime for this estimate, a reasonable assumption per the data in Figure 45b. If we, on the other hand, parallel-extrapolate the 60% lamp power curve here to 100% lamp power in Figure 44 (675°C @ $\varepsilon = 1.0$), the surface temperature estimated by this method is only ~725°C (~1337°F). It appears that the corrected temperatures cannot be calculated using the simple equation $E = \alpha\varepsilon T^4$, with no other terms involved.

Further error is introduced by not accounting for surface tribo-oxidation. As shown in Figure 46, an SiO_2-covered α-SiC would have about one-half of the emissivity of pure α-SiC, with an attendant, substantial increase in temperature.

Since a recently available, laser pyrometer (the PYROLASER®, see APPENDIX L) measures the emissivity as an integral part of the overall temperature sensing process, considerable effort was expended to incorporate this improved I.R. pyrometer into the Tester 2A.

A laser pyrometer (see Figure 47) passively measures the radiation emitted by a spot on the target. It is calibrated by a smaller, passive measurement on a blackbody of known temperature. The laser beam is turned on for active measurements of the reflectances of the target spot and of a reflectance standard. The temperature of the target spot is inferred from these measurements.

The PYROLASER® includes a laser with a wavelength (λ) and a photodetector that has a highly linear response and is equipped with a band-pass filter at that wavelength. The laser and the photodetector are mounted with the appropriate optical hardware so they both focus on the same target spot.

a.

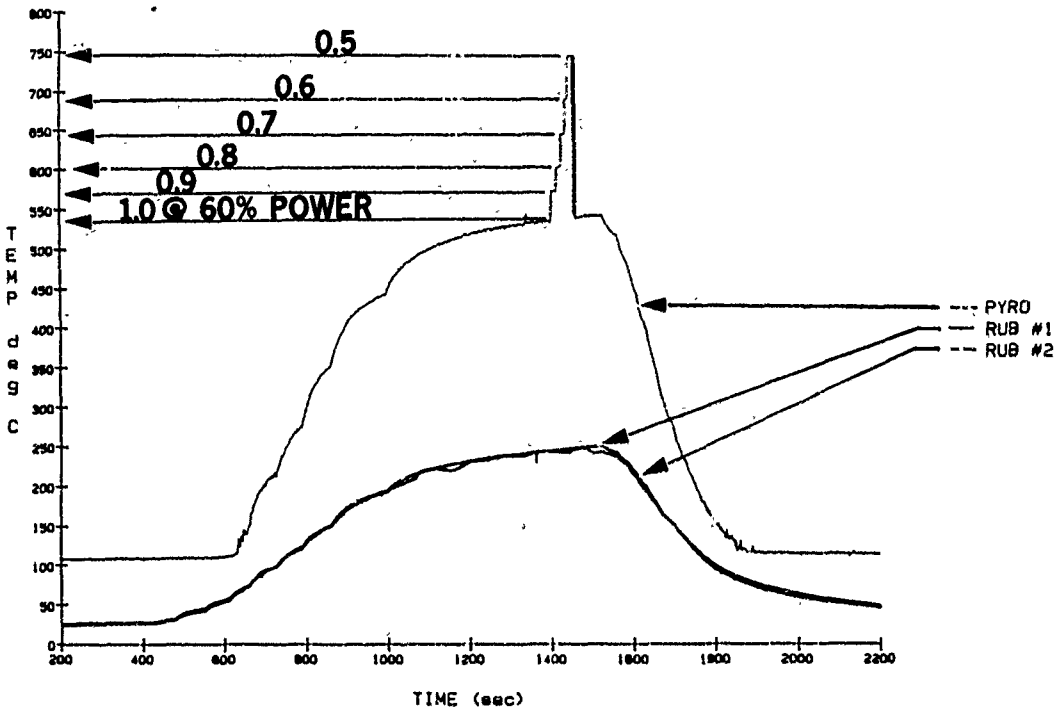

TEST #3, 13.3 N (3.0 lbs), 700 RPM
ESK EKASIC SiC "POST HIP-ed", ROD/FLAT GEOMETRY
TEMPERATURE VALUES, EMISSIVITY=1.0

b.

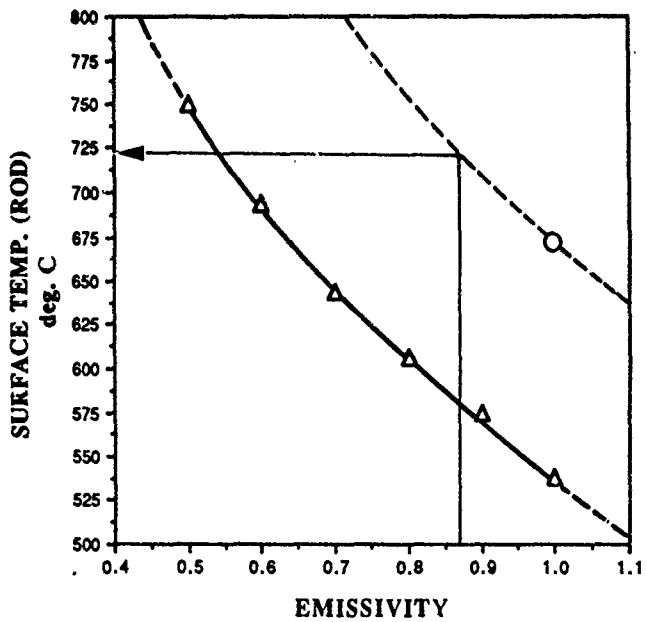

Figure 45. Surface temperature as the function of emissivity with the Vanzetti I.R. pyrometer: (a) computer-generated data analysis plots at 60% lamp power, (b) emissivity vs. temperature function at 60% power.

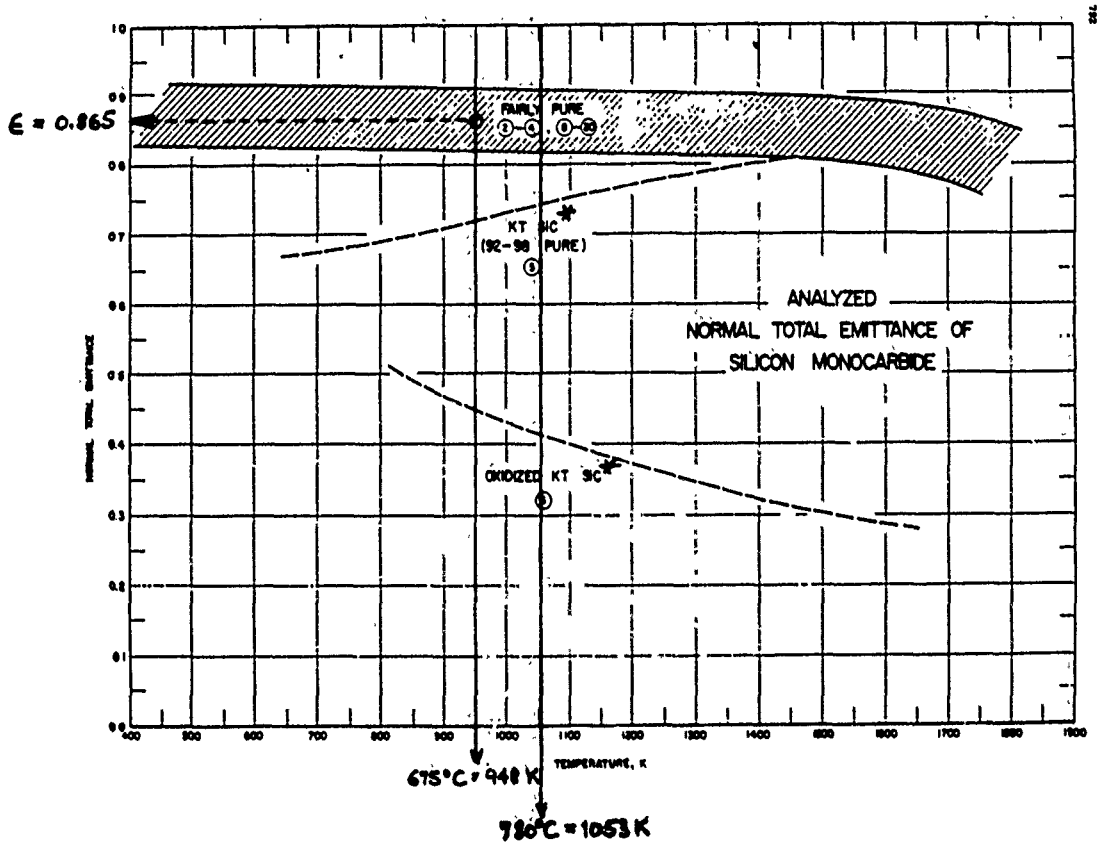

*KT-SiC is reaction - bonded, containing a considerable amount of residual silcon. The SiO_2 formed on the surface is thicker here than SiO_2 on the surface of sintered α-SiC containing no free Si.

Figure 46. Analyzed normal total emittance of silicon monocarbide (63).

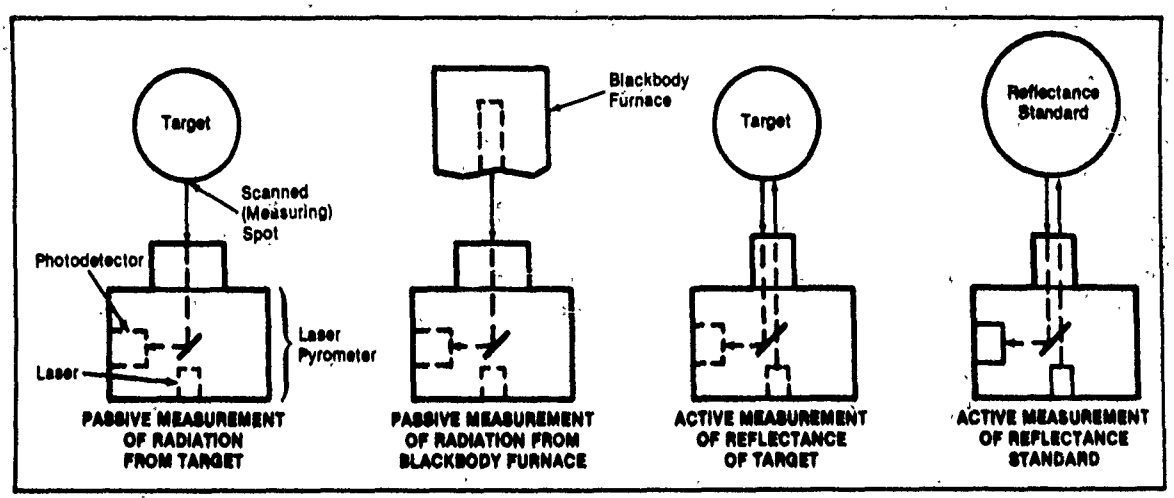

Figure 47. Calibration and surface temperature measurement schematics with a laser pyrometer; from (64).

From Planck's Law of Radiation, the absolute temperature (T) of the target spot is given by: $T = [T_b^{-1} + (\lambda/C_2)\ln(\varepsilon R_b/R_t)]^{-1}$, where T_b is the temperature of a blackbody furnace used as radiation standard, C_2 is a constant from the Planck radiation law, ε is the spectral emissivity of the target, R_b is the radiance of the blackbody at wavelength λ, and R_t is the radiance of the target at wavelength λ.

Because of the linear photodetector response, an absolute calibration of the photodetector is not required; it suffices to use $R_b/R_t = V_b/V_t$, where V_b and V_t are the photodetector output voltage when observing the blackbody furnace and the target, respectively. The emissivity of the target is obtained from the response of the photodetector to the laser radiation reflected from the target (V_{lt}) and to the laser radiation reflected from a gold object (V_{lg}) that is shaped like the target and has a known reflectance r_g. Then the emissivity is give by $\varepsilon = 1 - r_g (V_{lt}/V_{lg})$.

When the reflectivity is high (such as with highly specular surfaces), small inaccuracies in resolving r_g can lead to large errors of ε. Also, the reflectance from wear scar (rarely specular) is changing with time of sliding and may or may not approach an equilibrium value. The value of emissivity itself changes with the environmental temperature. Our efforts, therefore, centered mainly around the PYROLASER®'s promising but unproven usefulness for the Tester 2A, mainly in terms of these pressing issues.

Tests of a laboratory model PYROLASER®were conducted with separate lenses, as follows:

- 1000 mm target distance, 5 mm target diameter, *results satisfactory*;
- 400 to 500 mm distance, 2 mm target diameter, *results marginal*;
- 200 to 250 mm distance, 1 mm target diameter, *results unsatisfactory*.

Sources of deficient performance at the close distances needed for the Tester 2A were traced to excessive reflected energy of the laser beam from the target, and to degree and surface distortions caused by the lenses. Several approaches were investigated to counteract these problems.

One approach used filter coatings at the center portion of the lens to cut down the transmitted and reflected laser energy. It did not show promising results. Next, a special lens with the center portion completely removed ("doughnut lens") was designed, whereby the outer rim of the lens was to collect only the radiant energy, while the laser energy in the center beam was attenuated by other means. This approach appeared more promising, but not quite satisfactory.

Parallel work concentrated on the feasibility of accommodating the PYROLASER® by reversing the mounting position, so that the lenses and the viewing aperture could be at the bottom and the connectors at the top. A special mounting bracket was fabricated with provisions for line-of-sight adjustments, and the pyrometer was installed on the Tester 2A (see Figure 48). After mounting, it was focused on a new, ESK sinter + HIP α-SiC RCF rod (the kind used in the high temperature tests described in this report).

The focal distance was only 241 mm. Room temperature emissivity readings were taken with the

Figure 48. The PRYOLASER®installed into the Tester 2A.

stationary and the rotating rod. No RPM effect was noted (ε remained at the steady-state value of 0.86). Since this instrument utilized an IR band-width centered at 0.865 microns (normally found effective in industrial applications, see the description of the PYROLASER® in APPENDIX L), Ref. (63) was consulted for the reasonableness of the ε = 0.86 (R.T.) @ 0.865 microns for α-SiC. As shown in Figure 49, the average value of the best accepted measurement error band is ε = 0.885 (between 873-1375K). Inasmuch as ε seems to change little with temperature (see Figure 46), the ε = 0.86 value for sintered α-SiC measured with the PYROLASER® was sufficiently accurate, *at room temperature.* As discussed later, the main problems arose at high temperatures.

At that time, Pyrometer Instrument Co. personnel visited Hughes to teach us how to use this pyrometer and obtain output. We were also supplied with a barium sulfate emissivity standard and a serial printer to calibrate and print out the α-SiC emissivity measurement data. The data link to our data logging and analysis computer was to be established at some later date.

Our main concern with the Tester 2A design was that the aluminum aperture, through which the IR beam penetrates the heating chamber, would cause unwanted reflected energy from the lamp and test chamber to reach the PYROLASER® lens. Unfortunately, the lamp emits at 0.865 μm (the center of the PYROLASER's IR bandwidth). Any stray radiation sensed will produce anomalously high temperature readings during elevated temperature friction tests.

During high temperature tests, we indeed found that the unit picked up reflected energy from the quartz heater. The sensing of the stray radiation resulted in erroneous temperature readings. This problem became the limiting factor in whether or not we could incorporate the PYROLASER® into our tribometric system. The aperture configuration that we have used with the Vanzetti pyrometer did not work with the other unit, even after anodizing all reflective surfaces on the aperture plate and aperture opening. We designed several different types of aperture plates, as suggested by the Pyrometer Instrument Company. Because the diameter of the aperture (2 mm) is not much larger than our target size (1 mm), the PYROLASER® became inherently more difficult to align and focus.

Although alignment and focusing may seem like a trivial problem, it is not. During our limited use of the unit, we have already seen that the aperture geometry seems to have an effect on the emissivity readings, although we have gone to great lengths to ensure that the aperture is not in the targeted area. Also, this unit is aligned and focused entirely by eye. The presently used Vanzetti pyrometer has a light source, which pinpoints the target area for the use with a small spot of light. The PYROLASER® must be focused much the same as one would a camera, but without the same sharp images a camera viewfinder would offer. This means that focusing through the aperture onto the dark, curved surface of the RCF rod is difficult and extremely operator-dependent. We have also found that the emissivity values changed as the focus changed. Therefore, we were not confident enough that our alignment and focusing techniques are sufficient to ensure accurate and precise temperature readings on a consistent basis.

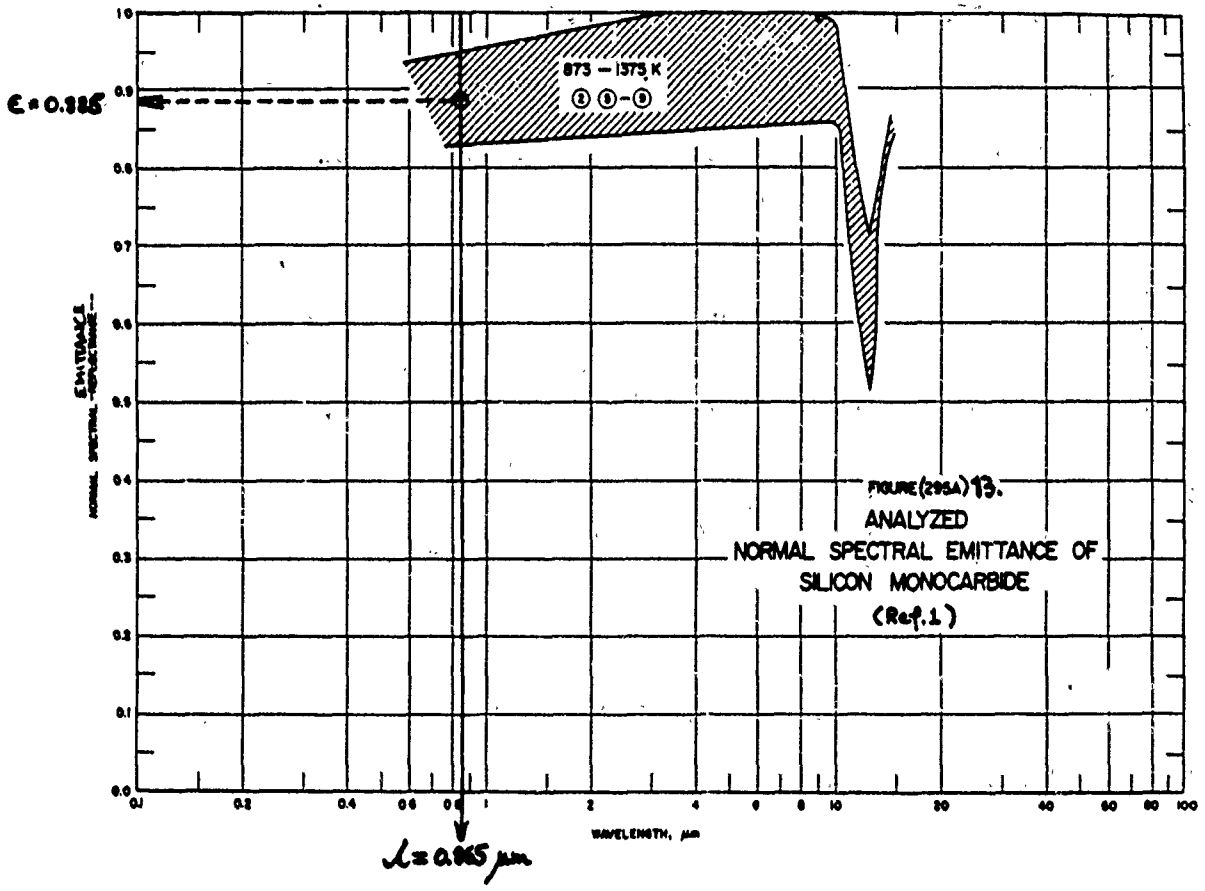

Figure 49. The average emissivity of α-SiC at λ= 0.865 μm; from (63).

During the months of December 1988 and January 1989, we made further modifications to the test chamber, trying to further isolate the target area on the RCF rod from the radiant energy emanating from the heater.

The additional modifications of the original sample chamber included a redesigned front plate with a viewing tube which we positioned as close to the rod as possible, depending on rod run-out. The second modification was to add a back plate (heater side) which is polished on the heater side and black-anodized on the chamber side. Finally, we added a skirt around the back plate to further reduce the amount of light which could leak around the rubshoe holder arms and into the target region. As a result of these changes, we did not measure instantaneous heater background until approximately 50 to 60% of full heater power. Without the modifications we already measured the heater background near 20% of full power. From these results, we defined the remaining problem areas that had to be resolved before we could routinely use this pyrometer for dynamic surface temperature measurements. These issues to be resolved were as follows:

1. We needed to measure the background levels as a function of the heater power. We also had to know if the temperature background profile was dependent on the specific material and surface finish of the rod (differences in reflectance and emissivity). If practical, we wanted to periodically monitor and change the background corrections values if we determined that they were dependent on certain test parameters.
2. We needed to know if the heater radiance introduced errors into the emissivity measurements. If so, we needed to consider the same effects listed for the temperature corrections.
3. Did our fixturing result in any interference in the target region, which would introduce further error into the measurement?
4. We needed to develop a calibration technique so that we could periodically calibrate the background levels, corrected temperature and emissivity measurements.
5. For our computer data system, we would need analog outputs for both corrected temperature and emissivity. To measure background levels, we may also need additional signal outputs.
6. Because we could not separate the background and true temperature levels yet, we were not sure that with all the additional fixturing we could still reach temperatures above the PYROLASER®'s current, realistic threshold (650°C).

After extensive, cooperative work between personnel from the Pyrometer Instrument Co., Inc. and Hughes, it was found that the technical problems listed above could not be overcome in time to serve the Tester 2A for the remaining part of the program (to Sept. 30, 1989). In spite of our extensive "optical housekeeping efforts" (e.g., see Figure 50), the signal-to-noise ratio was far too small to constitute reliable rubbing surface temperature measurements.

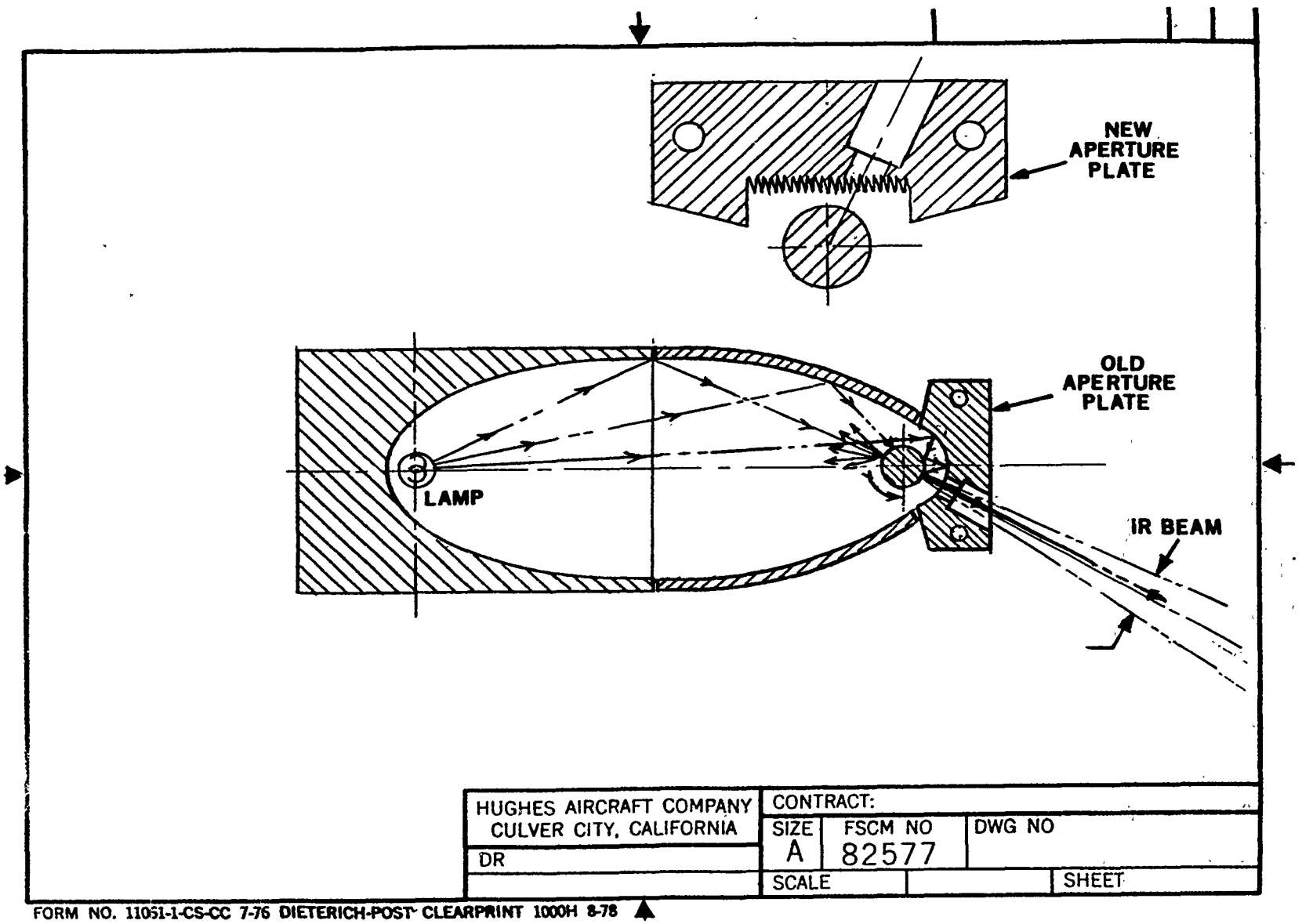

Figure 50. The new antireflection aperture plate for the Tester 2A.

Our efforts to locate a heat lamp operating at a wavelength different from 0.865 μm met with failure. Such lamps are simply not being manufactured. As a result, further work with the current PYROLASER® design was postponed to some future date, when the current technical problems might become solvable.

It should be noted, however, that a similar prototype of another laser pyrometer built at Caltech for NASA's Jet Propulsion Laboratory (64) was tested with a laser at $\lambda = 0.904$ μm, stainless-steel and carbon spherical targets heated in a vacuum bell jar by radio-frequency induction, and a gold sphere of 0.99 reflectance. This system can attain a temperature resolution of about 5°C at 1,300°C. It is anticipated that with the use of a laser wavelength at 1.3 μm, a signal-to-noise ratio of 10, and a scanning rate of 10^5 picture elements per second, an imaging pyrometer will provide a temperature resolution of 1°C at 1,300°C and a spatial resolution of 10 μm.

As for further, high temperature tribometry with the Tester 2A, we had to depend on published emissivity measurements of our ceramic materials to calibrate the Vanzetti pyrometer. All such measurements were, therefore, made at $\varepsilon = 1.0$ and all data are reported as such.

2.2.3.6 Evolution and Independent Critique of the Tester 2A Design. Preliminary brainstorming and investigation of different approaches, including examination of then already existing friction testers, was started in December 1985. We found that there was no equipment available to meet all our requirements. Gradually, after several exhaustive design reviews and breadboard tests, several alternate concepts were discarded and the existing concept was agreed upon in August 1986.

A special effort was made to avoid the conventional pin-on-disc geometry unless it was thoroughly characterized for thermal and mechanical response at high temperatures, in air. This sliding geometry is beset with inherent problems, such as inadequate thermal mapping (65), severe unit load reduction due to rapid growth of the wear scar on the tip of a hemispherically tipped pin (66), and wear results clouded by the specific stiffness of the pin used in the various apparatus designs (67, 68, 69).

As reported by Sakurai (70), Japanese workers also studied the influence of vibrational amplitude under a fixed frequency of 22 kHz on friction and wear using a pin-on-disc apparatus. They revealed that aspects of friction and wear varied with changes in vibrational amplitude and that a critical amplitude existed. At small amplitudes, the amount of wear and the value of the torque were large and increased rapidly with time and closely agreed with those at no vibration. An increase in the amplitude reduced the amount of wear and the torque up to the critical amplitude of around 4-6 μm. Above this, a marked decrease in wear was observed and the frictional torque was also reduced and its time dependence disappeared. Surface roughness in the low wear region was low and waviness due to vibration was observed; meanwhile, in the high wear region the surface roughness was high and scratch flaws were visible.

Although it is understood that certain experimental designs occasionally force the need for the pin-on-disc or sphere-on-plane configuration, our philosophy of test machine design was based more on the desire to create realistic contact configurations, which represent at least some semblance of real tribomachinery contacts.

Preliminary structural analysis led to the selection of one out of the three likely RCF rod/dual rubshoe configurations, as shown in Figure 51. The MSC/PAL finite element analysis computer program (APPENDIX H) was utilized to guide the detailed design in Figure 51b by a 30-node analysis:

1. The initial idea of having the friction transfer/load (moment) arm supported by flexure columns was discarded. These columns were to be stiff in the vertical plane, but very soft horizontally to permit relatively free motion of the arm in the horizontal plane. Instead, the six-degrees-of-freedom A.M.T.I. "Multi-Platform Dynamometer", affixed at the pivot point of the arm with a DF-duplex bearing pair, comprised the load transfer and measuring mechanism's key sensor. The bearing renders the assembly radially stiff, but compliant in the moment direction.

2. The pressure bar, which extended into the heated environmental chamber, appeared to be the weakest link in the structure. It had to be stiffened in the plane common to the load cell axes. The moment arm stiffness also had to be increased in that plane as much as possible, without excessive added weight. The stiffness-to-weight ratio was maximized by milling out a substantial portion of the moment arm and affixing an outer "skin" of reinforcing plates perforated for further weight savings (see Figure 33a). The resonant frequency of this high specific strength moment arm was above 100 Hz, as checked with a piezoelectric impact hammer connected to a frequency analyzer. Therefore, an actuating force frequency of up to 50 Hz is permitted (about one-half of the lowest resonance), equivalent to spindle speeds of up to 3000 rpm. Inasmuch as the standard speed (700 rpm) of all Tester 2A experiments performed during the program was well below the 3000 rpm limit, erroneous "hash" was not transmitted to the Type 363, high stiffness force transducer.

3. The moment arm and the pressure/load arm end were proportioned so that the mass center was at the pivot point of the load cell. As such, the loading forces are applied through the pivoting moment arm by the spring and the vibrator, instead of directly in line with the normal force.

After the computer analyses but prior to cutting metal, we consulted Georgia Tech and MTI personnel to double-check our calculations and the state of the final design for errors. Prof. Ward Winer of Georgia Tech expanded on certain anticipated friction measurement and IR pyrometry problems associated with the Tester 2A. Essentially, his calculations in APPENDIX M (also see Figure 52a) indicated that due to the characteristic formation of a wear scar in the flat or conforming rubshoes, coupled with an inherent inability to define the real point of contact, there is no way of knowing the actual coefficient of friction. His analysis also predicted that these problems would be aggravated by using mating cylinders of progressively smaller diameters, because the wear scars become too deep too quickly. The relatively small diameter of the RCF rod would make the flat rubshoes vs. RCF rod specimen combination especially vulnerable to this problem. These dire predictions notwithstanding, all program data indicated that such drastic increases in f_k did not occur (e.g., see Figure 42a and 43a). Of course, the rubshoe wear

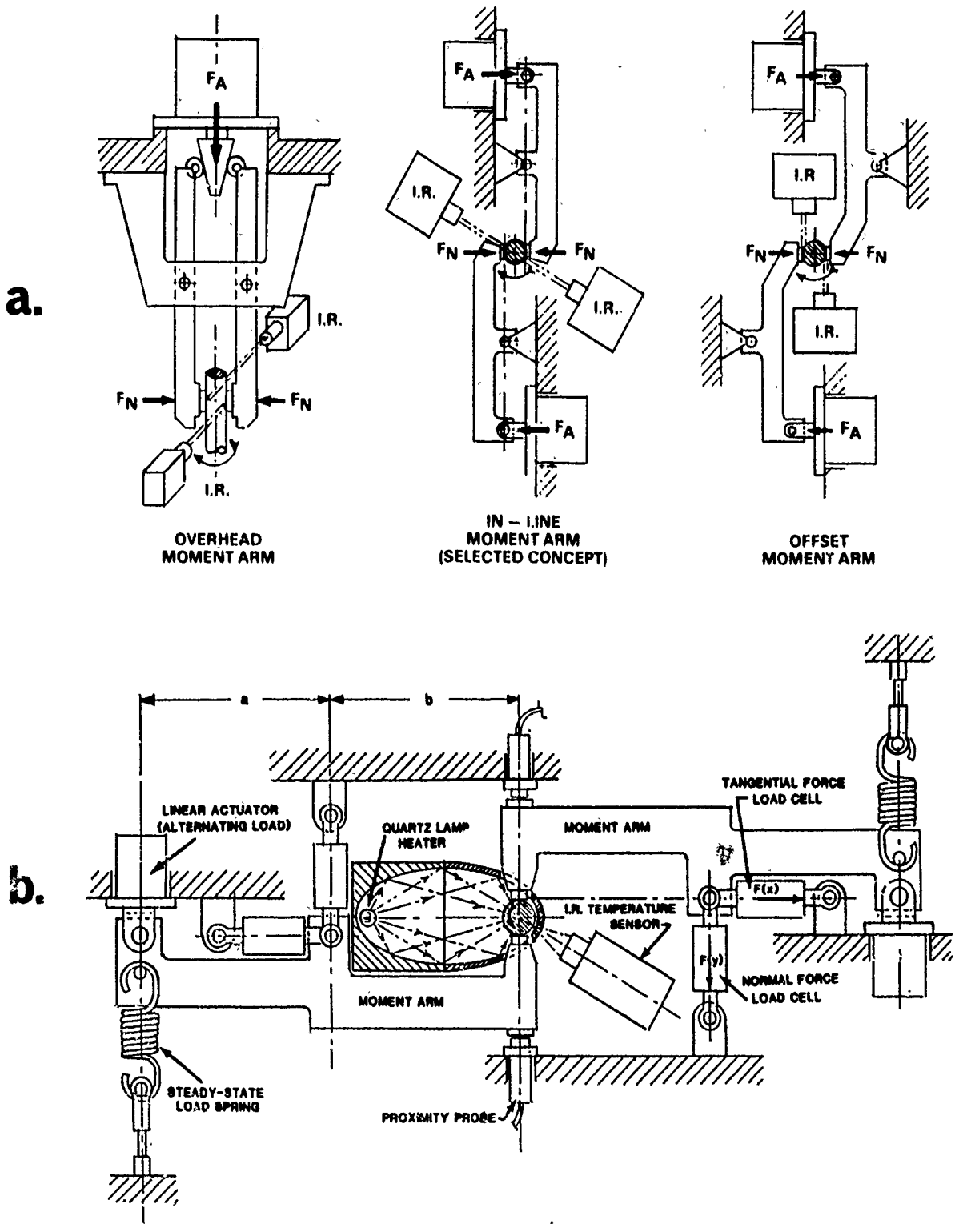

Figure 51. Basic loading mechanism concepts of the Tester 2A: (a) candidate designs; (b) selected concept.

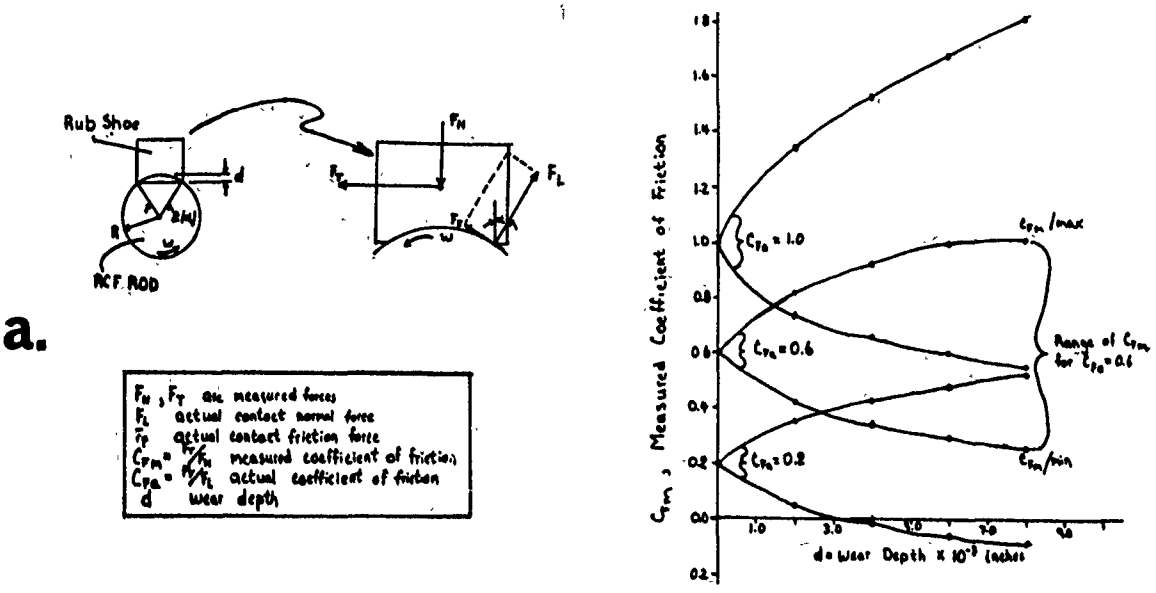

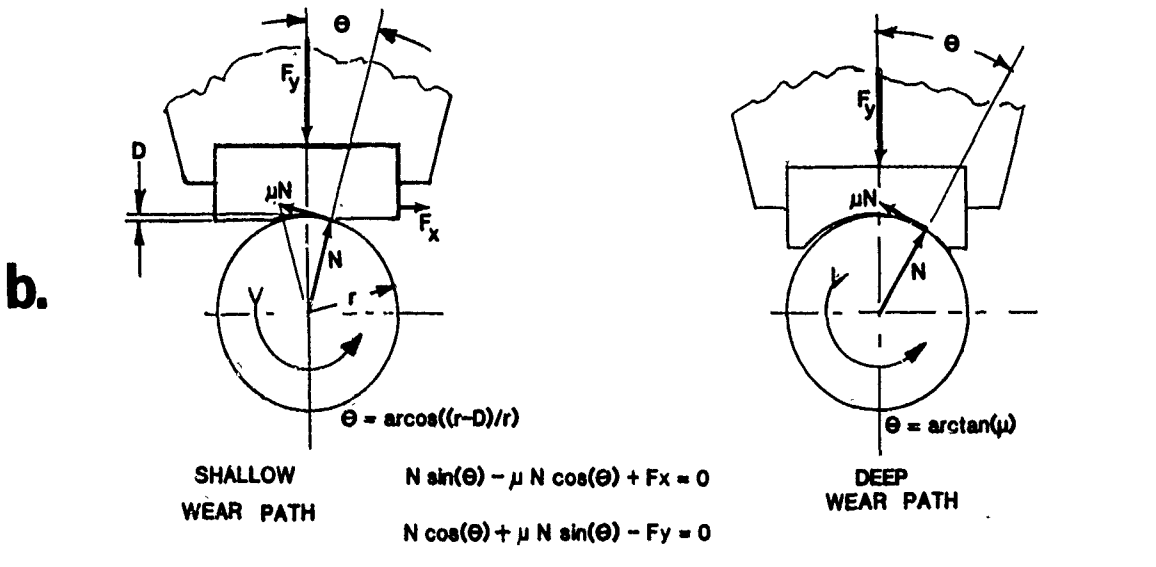

Figure 52. Tester 2A-induced frictional variations: (a) as estimated by Professor Ward O. Winer (Georgia Tech), (b) as refuted by Mr. Leo Fiderer (Hughes), the designer of Tester 2A, with hypothesized contact force vectors.

scars associated with these tests were very shallow, around only 2.54×10^{-5} m (0.001 in.). However, as shown later in this report, such increases in friction did not manifest themselves, even where the scars were larger and deeper. We at Hughes believe there was no increase, because even in the case of a deep scar, the μN vector component in Figure 52b remained small due to some inescapable misalignment. This misalignment is caused by the fact that even a stiff force transducer is not infinitely stiff. Even though the angle θ is larger with a deeper scar, the (slightly) misaligned direction and small size of μN is not substantially greater than in the case of a shallow scar.

Prof. Winer also felt that the PYROLASER® (with the in-situ emissivity calibration at any temperature and automatic feedback compensation of the readout) will do no more than measure the bulk temperature of the ceramic RCF rod's surface, because of the small size, number and lifetime-at-a-location of the hot-spots. He recommended the use of a simple thermocouple inserted into a hole (black-body-cavity) drilled into the rotating RCF rod instead as a sufficient and inexpensive substitute.

These points were seriously considered at Hughes. APPENDIX M was forwarded to MTI, then already under contract to review and critique the Tester 2A design. The papers and report attached to APPENDIX M (see 71 through 75) were also carefully considered. After thorough assessment of all the data, it was decided to continue measuring the average surface temperature of the sliding surfaces with both the rubshoe thermocouples and the IR pyrometer, because there was ample evidence that the temperature measured by thermocouples alone was significantly lower.

MTI's analysis (see APPENDIX N) concentrated mainly on three items:

1. Dynamic forces due to runout of the rapidly spinning rod specimen;
2. Load and coefficient of friction measurements and their interlocking relationship with 1. above; and
3. Wear measurements, their accuracy and interlocking relationship with 1. above.

The significance of MTI's analysis lies in predicting the shaft-run-out caused cyclic loading of the rubshoe-rod interface. Since the inertia of the loading/friction transfer arm will prevent the force transducers from sensing these run-out induced loads (these transducers can only measure the spring-applied (stead-state) and linear actuator-superimposed (cyclic wave-form) loads in the normal load-sensing mode), the coefficient of friction values would contain a certain degree of error. As shown in Figure 53, at 700 rpm and at the anticipated runout of substantially less than 1.27×10^{-4} m (0.005 in.), the cyclic load error at a nominal, steady-state normal spring load of 1.36 kgf (3.0 lbs) or less is negligible. However, at higher speeds (where we did not run tests), these errors progressively multiply and must be accounted for by actual measurement of the dynamic runout.

With respect to wear data measured by the Tester 2A proximity sensors, their "noise band" may actually indicate some materials-related dynamic effects and this noise should not be (and was not) filtered out.

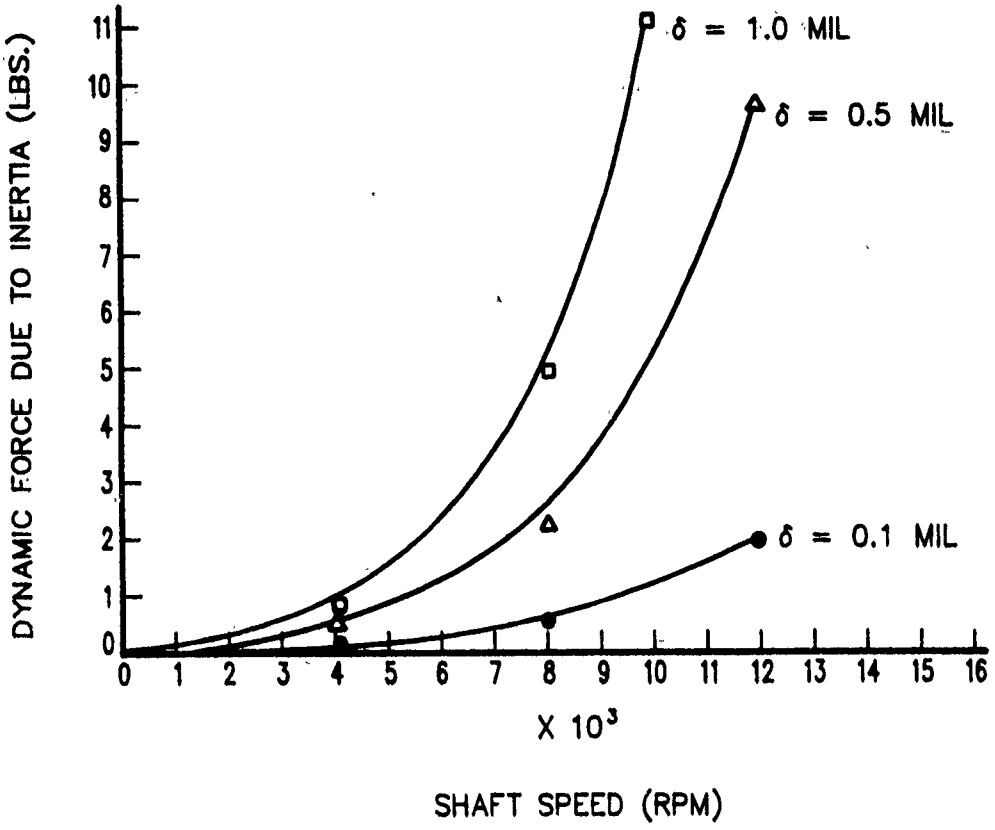

Figure 53. Run-out-caused friction variations: (a) maximum dynamic friction force [(f_d(max.)] as a function of (sin ωt) orbital motion..

In fact, each friction trace (for examples see Figures 42a and 43a) is broken down into two components: The mean level and the superimposed oscillatory values. The mean level appears to be a function of the inherent frictional behavior of the contact materials. The oscillating component appears to be a function of the materials' frictional behavior combined with speed and runout-dependent variables.

We have shown, for example, that the mean value of the coefficient of friction can be constant for two different experiments with the same specimen types, while the amplitude of the alternating component was different. The amplitude of the alternating portion measured in the first test, which had larger runout and was tested at a higher speed, was much larger than that of the second test. Also note that the magnitude of the alternating portion of the tangential load for each test was approximately equal. The most interesting observation is that the range of COF (f_k) values in each test is noticeably smaller than that of the tangential load. This result substantiates the conclusion that the alternating components of the applied load and the friction force are in phase to some degree, see, for example Figures 42a and 43a. Note, however, that our speed vs. runout values [worst case = (700 rpm) (1.77×10^{-5} m = 0.0007 in.)] were, therefore, predicted to be much too small to be significant by the MTI analysis in Figure 53a, as mentioned before.

These analyses were commissioned by Hughes to compensate for the well-known, but notoriously uncharacterized relationship between the coefficient of friction, wear and sliding velocity as functions of a tribotester's global dynamic properties: its mass, stiffness, damping, transducer "ringing" etc. Although various theoretical treatise on these subjects are available in the open literature, e.g., (76) and (77), we have yet to see coefficients of friction or wear values reported in the literature corrected for the mechanical characteristics of a test system. Therefore, friction and wear data attributed solely to materials properties do not reflect reality and should not be accepted as absolute values.

It follows that Rakowski's cry for appropriate materials friction standards which are insensitive to machine dynamics (78) will remain unanswered until tribologists thoroughly characterize (a) their friction and wear testers for machine dynamics and accurately compensate for undesirable (and often not totally avoidable) dynamic inputs and specimen shape factors, as well as (b) the surface/subsurface chemistry and physics of the used specimens for any alteration in composition and microstructure, which would signal materials-related causes of friction (and wear) changes as a function of carefully measured environmental parameters (P, V, T and atmosphere). Without completing item (a) first, item (b) is difficult to realize.

We believe that our thermal/mechanical computer analyses of the Tester 2A design prior to cutting any metal, followed by thorough instrumentation (e.g., with thermocouples and accelerometers) during all stages of the shake-down tests were necessary. We can now confidently state that the friction and wear data of the Tester 2A experiments presented in the following sections can be attributed largely to test specimen materials characteristics. The good repeatability of the test data (see next paragraph) only confirmed the validity of our test machine design philosophy and the reliability of the tester.

2.2.3.7 Statistical Analysis of Tester 2A Data. Duplicate Tester 2A data were collected from forthcoming sections (i.e., apparent surface shear strength and wear scar volume loss results at four (4 ea) rubshoe vs. RCF rod contacts, using selected materials combinations) and statistically analyzed in Table 5. The analysis indicates good repeatability, except in the case of early tests (ESK sinter-HIP α-SiC, at R.T.) and a high-wearing material (100% h-BN at high temperature).

The data in Table 5a also indicate the range of apparent surface shear strengths ($\tau_{app.} = F_n/A_{app.}$, where A_{app} is calculated from the projected wear scar area on the flat rubshoe), varying from $\tau_{app.} = 2.57$ MPa (highest, with unlubricated α-SiC at R.T.) to the $\tau_{app.} = 0.06$ MPa (lowest with 100% h-BN at high temperatures). The volume wear rates in Table 5b range from ~2 x 10^{-12} $m^3/N \cdot m$ (highest, with the low-shear 100% h-BN at high temperatures) to ~8 x 10^{-16} $m^3/N \cdot m$ (lowest, with the high shear strength α-SiC at R.T.). There is no surprise in the fact that low shear strength materials are also weak and exhibit high wear rates.

Our wear scar measurements and the reported units are standard and widely accepted [e.g., see (79, 81)].

2.2.3.8 Documentation for Tester 2A. In the interest of economy, it was decided at the start of the design phase not to generate a full-fledged set of Level-3 Production Drawings. Also, some items, such as the arrangement of the electronic power and control boxes and the shelving of the support cart under the operating table top were improvised with convenience in mind, without formal drawings. We presumed that if anyone decided to build another Tester 2A, some flexibility in the arrangement of the auxiliary devices would be desirable.

A drawings and information package was submitted to WRDC/MLBT, covering the fabrication and assembly of the loading mechanism, which is the essential ingredient of the Tester 2A. The package included the following:

1. Copy of Hughes Technical Internal Correspondence, Ref. 86-7282.00/920, (APPENDIX G), which contains the theoretical basis, historical background, and a detailed description of the device, prepared during the final design phase and initial construction stage of the tribotester.
2. Copy of ASTM Technical Paper, ASTM STP 1010, May 13, 1987, UNIQUE FRICTION AND WEAR TESTER FOR FUNDAMENTAL TRIBOLOGY RESEARCH. This paper is an abbreviated and updated version of the above T.I.C. (61).
3. Hughes Drawing No. SP 519152, 3 Sheets, TRIBOTESTER 2A, LOADING MECHANISM SUBASSEMBLY.
4. Parts Lists SP 519152-PL, which covers the Loading Mechanism portion of the Tribotester, and a set of detail drawings, Level 1 and Level 2, for the fabricated components on that list. The status list was compiled during the fabrication and assembly of the Loading Mechanism at Winter Engineering (a precision machine shop, Santa Monica, CA, used by us to fabricate key parts) to facilitate the tracking of the status of individual parts. The parts identified with balloon numbers on the assembly drawing are included in that list.

Table 5. Statistical analysis of duplicate Tester 2A experiments (4 each rubshoe versus RCF rod contacts) with selected materials combinations: (a) surface shear strength ($\tau_{app.}$) data analysis; (b) wear data analysis.

a.

Materials Groups / Data	NBD-100 HIP-Si_3N_4 (R.T.)	ESK α-SIC SINTER+HIP (R.T.)	ESK α-SIC SINTER+HIP (H.T.)	POLY-XTL RUTILE (H.T.)	~100% h-BN (H.T.)
Test Numbers	NBDF-1 and NBDF-15	ESKFP-1 and ESKFP-3	ESKFP-7 and ESKFP-9	RUTF-1 and RUTF-3	BNFP-4 and BNFP-6
No. of Data Points (n) (MPa)	0.70/1.51	1.80	0.53	0.62	0.06*
	0.75/1.60	1.85	0.54	0.57	0.06*
	1.19	3.38	0.56	0.54	0.05
	1.24	3.24	0.62	0.56	0.05
Arithmatic Mean (MPa)	0.97/1.39	2.57	0.56	0.57	0.0550
SAMPLE Std. Deviation (σ_{n-1})	0.28/0.20	0.86	0.04	0.03	0.0057
Population Std. Deviation (σ_n)	0.25/0.17	0.74	0.03	0.03	0.0050

* BNFE-4 SHEAR DATA

b.

Material Groups / Data	NBD-100 HIP-Si_3N_4 (R.T.)	ESK α-SIC SINTER+HIP (R.T.)	ESK α-SIC SINTER+HIP (H.T.)	POLY-XTL RUTILE (H.T.)	~100% h-BN (H.T.)
Test Numbers	NBDF-1 and NBDF-15	ESKFP-1 and ESKFP-3	ESKFP-7 and ESKFP-9	RUTF-1 and RUTF-3	BNFP-4 and BNFP-6
No. of Data Points (n) (m^3/N m)	7.66×10^{-15}	1.38×10^{-15}	1.87×10^{-13}	4.62×10^{-14}	4.71×10^{-12}
	6.48×10^{-15}	1.25×10^{-15}	1.76×10^{-13}	5.85×10^{-14}	1.73×10^{-12}
	8.98×10^{-15}	3.31×10^{-16}	2.06×10^{-13}	5.69×10^{-14}	9.56×10^{-13}
	8.08×10^{-15}	3.84×10^{-16}	1.55×10^{-13}	5.29×10^{-14}	8.59×10^{-13}
Arithmetic Mean (m^3/N m)	7.80×10^{-15}	8.36×10^{-16}	1.81×10^{-13}	5.36×10^{-14}	2.06×10^{-12}
Sample Std. Deviation (σ_{n-1})	1.04×10^{-15}	5.56×10^{-16}	2.13×10^{-14}	5.48×10^{-15}	1.81×10^{-12}
Population Std. Deviation (σ_n)	8.99×10^{-16}	4.81×10^{-16}	1.85×10^{-14}	4.75×10^{-15}	1.56×10^{-12}

5. Supplementary drawings and sketches generated after the fabrication of the Loading Mechanism, which are not included in the above part list. They are for parts and modifications made as a result of our initial experience with the operation of the device.

6. Two photographs of the Tester 2A with labels for the key components. One shows a close-up view of the loading mechanism with the protective hood and the Plexiglass shield removed (Figure 33a). The other photo illustrates the overall arrangement, including the computer for data acquisition (Figure 33b).

For the benefit of anyone attempting to build a similar tribotester, the following additional comments are made:

1. Catalog information for many of the employed instruments and auxiliary devices is contained in the T.I.C. (Appendix G). This information was edited out of the ASTM paper as being non-essential to the device itself. Besides, the Tester 2A was designed for maximum flexibility and expansion capability of auxiliary components and electronic monitoring devices. The optical bench which serves as the operating table has a grid of threaded holes at one inch centers, to permit attachment of the auxiliary components in any convenient location.

2. The items used for shelving and shelf support, shown on page 33 of the T.I.C. (Appendix G), were obtained from a supplier in Los Angeles. Similar devices can be obtained from local suppliers in any part of the country. They permit adjustment of height and location of the auxiliary devices in the cart, by drilling attachment holes in the frame of the cart wherever convenient. Therefore, it would not have been cost effective to generate formal drawings for every shelf and support location.

3. Experience with the operation of the Tester 2A for almost two years has shown that it would have been more convenient to mount most of the electronic components and amplifiers in a standard equipment rack instead of on the cart. It would have made the problem with EMI shielding much less severe. Once the location for the operation of the apparatus has been selected, there is very little chance that it will be moved again at frequent intervals, and the emphasis on mobility of the entire equipment is not required any more.

To summarize, the documentation forwarded to WRDC/MLBT is as complete as necessary to build another Tester 2A for any organization competent in the field.

2.2.4 High PV Friction/Traction Testers (R.T. to 850°C)

During high-load and high-speed MMA applications, there is a considerable loss of mechanical (i.e., frictional) energy. As before, some of this energy is expended in moving dislocations, generating new surfaces by cracking as well as forming wear debris or wear particles. However, the largest percentage is transformed into heat through much heavier plastic deformation of the surface. Superimposed environmental temperatures which may themselves be high, coupled with atmospheric influences (e.g., oxidation in high temperature air), only complicate this already complex situation. As a consequence, the greatest amount of wear damage is generated under pure sliding, at high PVT conditions.

The heat (Q) generated per unit area per second (in SI units of $J \cdot m^{-2} \cdot s^{-1}$) is $Q = (f_k) \cdot PV$ (65).

A fraction of the heat diffuses into a rubshoe or a pin, the rest goes into the RCF rod or a disc. Some of the heat entering both types of specimens is lost as radiation, and the rest diffuses through the body of the specimen and is absorbed by the specimen holder and loading mechanism.

In the case of rolling element bearing the situation is similar, but not identical.

The bearing designer also needs the following sliding and rolling contact friction and traction data:

- $f_k = f(P, T, V)$
- $f_t = f(P, T, V)$

where,

f_k = friction coefficient between rolling element and separator, as well as separator versus the race land contact areas;

f_t = traction coefficient between the rolling element and raceway;

P = contact pressure(i.e., Hertz stress);

T = contact temperature;

V = sliding speed (V is usually replaced by creep = V_{slip}/V_{roll}).

These data are critical to an understanding of bearing heat generation, dynamics and ultimately, the functional performance of the bearing.

In the case of the race contacts, pressures are high (on the order of 1.7 GPa≅250 Ksi) but slip speeds are low. The contact stresses at the cage/rolling element and cage/land are small, but sliding speeds are high. The sliding speed of the cage/rolling element interface in a high speed bearing could easily be in the range of 90 $m \cdot s^{-1} \cong 200$ mph. These extremes in operating conditions demand test apparatus and test machines higher in PV capacity than the Tester 2A (see Figure 10).

In addition, friction and wear under high PVT conditions are best accelerated when the contacting specimens are insulated and have unequal size and mass. An example of this combination is a pin relatively small in size compared to a large diameter mating disc spinning rapidly in an oven.

If the steady-state temperature distribution were established in both pin and disc or rolling element contacts, frictional heat would be divided equally between them. But a point on the disc (or larger rolling contact) surface has heat injected into it only for the interaction time (the time taken for the point to slide across the diameter of the pin) whereas the pin (or smaller rolling contact) has heat injected into it all the time. The steady state is established in the smaller specimen, but it may not be established in the larger one: that depends on whether the interaction time is bigger or smaller than the heat diffusion time. In the case of the equal-sized specimens and low relative sliding speeds (as in traction testers), the oven must be

capable of raising the environment temperature, so the total contact temperature ($T_{total} = T_{environmental} + T_{flash}$) is appropriately high.

With these general requirements in mind, MTI's high PVT pin-on-disc (sliding) and disc-on-disc (rolling) tribotesters were selected (see Figure 54) to complement the lower PV capacity Tester 2A.

2.2.4.1 The MTI High PVT Pin-on-Disc Sliding Tester. This sliding friction and wear tester (Figure 54a) has been used by MTI for approximately 15 years and is a well-proven test rig. It was utilized during the previous DARPA/Hughes program (38). NASA-Lewis Research Center has been using a similar rig built by MTI, with considerable success. The apparatus is capable of operating in an up-to-850°C test specimen environment. A water-cooled support spindle minimizes test disc overhang and the attendant flexure and resonance problems. The purpose of this design is to permit the shaft to operate at speeds up to 50,000 rpm. Friction and wear studies have been conducted at rotor speeds up to 30,000 rpm, at an equivalent rotating disc vs. stationary pin (see Figure 55) surface speed of 76 $m \cdot s^{-1}$ (250 $ft \cdot s^{-1}$), see APPENDIX O (the test results pertaining to this program are also described in this APPENDIX and will be abstracted in Section 3.1).

An important point to note is that the MTI sliding tester is adjusted to a disc surface (O.D.) run-out of 2.54×10^{-6} m (1×10^{-4} in.) during operation. This small dynamic motion is maintained essentially up to the maximum operating speed of 50,000 rpm. The precision spindle, combined with such high specimen and assembly tolerances, is very important for reliable friction and wear testing. They insure minimum runout and dynamic motion of the test disc at high speeds (see previous discussion). If testing is done to investigate dynamic loading conditions by simulating the impulsive interaction between rolling element and the retainer in a bearing, for example, a precision spindle like that found in the MTI tester is especially desirable. Contact loading due to runout or dynamic spindle motion could easily be comparable to externally applied dynamic loads in a poorly designed system, making results difficult to interpret. The modal analysis-assisted design (83) of this precision spindle is well established (38) and has been used for a number of years with great reliability. It has been found, similar to the case of Tester 2A, that the f_k varies due to the inherent materials characteristics of the ceramic specimens, and not to variations related to rig vibrations (84).

2.2.4.2 The MTI High PVT Ball-on-Disc Rolling Tester. The design of machine elements such as rolling element bearings, gears, cams and continuously variable traction drives requires quantitative understanding of the concentrated contacts which they embody. These contact zones are formed when two surfaces with low geometrical conformity are brought together under load, and exhibit extremely small areas of interference which are very highly stressed. Due to the high concentrated contacts, the presence of a lubricant film becomes crucial for satisfactory operation.

The lubricant film, referred to as a liquid-elastohydrodynamic (EHD) or a solid lubricant film, is generated by the viscous or solid traction resulting from the relative motion at the contact interface. The film can vary in thickness from a fully developed film to a thin boundary film. In the latter case,

a.

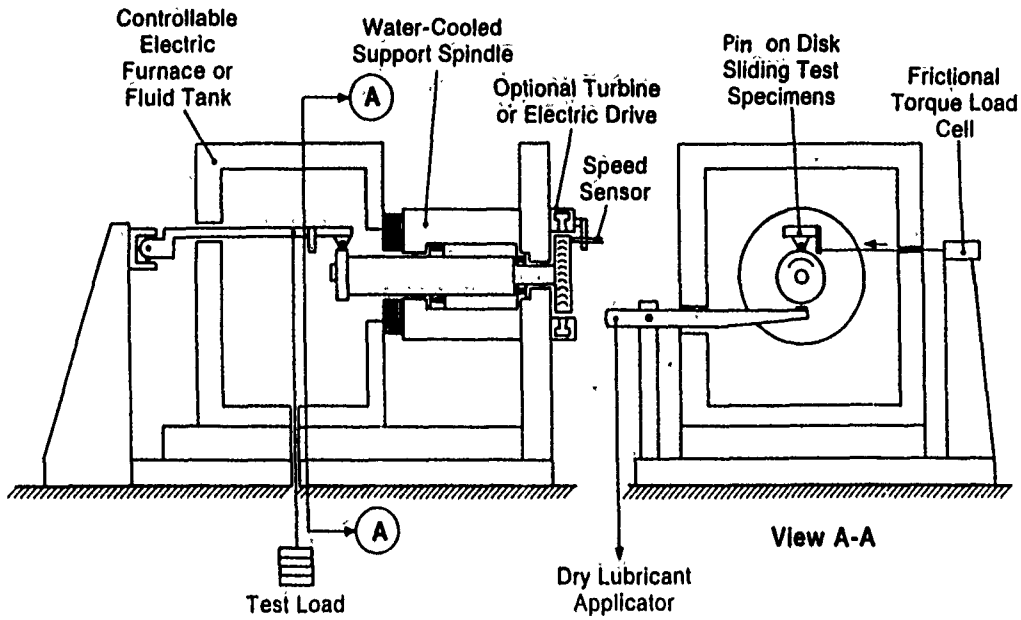

b.

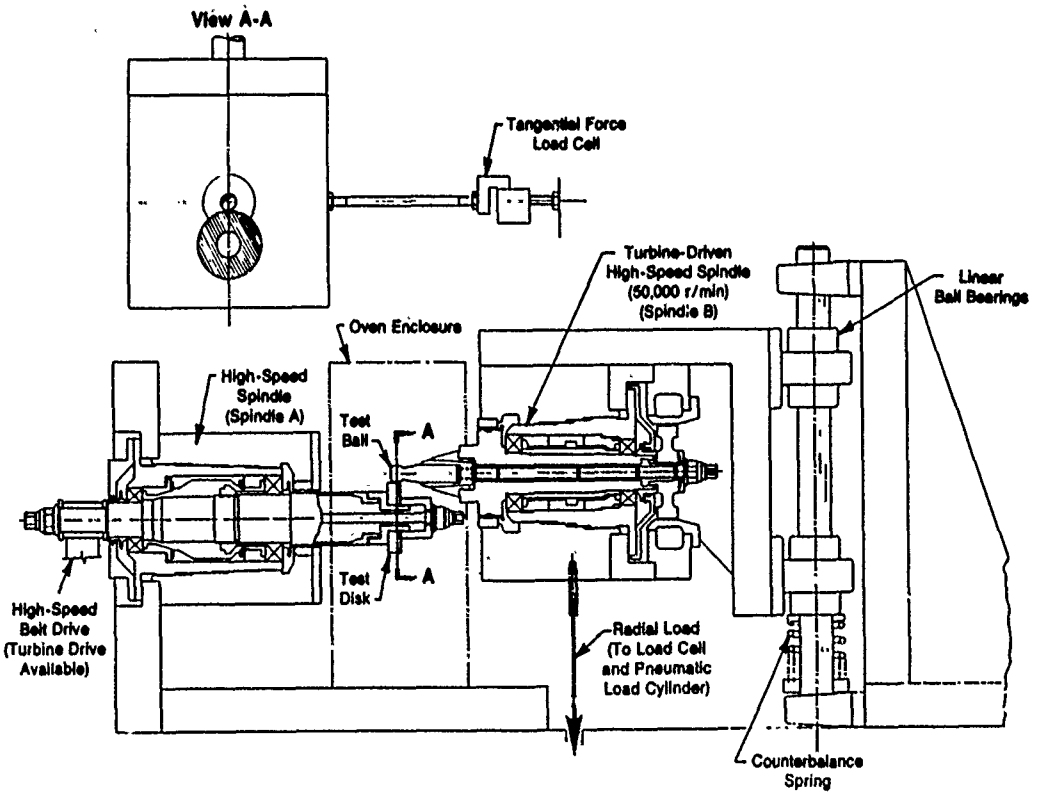

Figure 54. Overall sideview layouts of the MTI (a) high PVT pin-on-disc sliding (friction) tester, and (b) high PVT disc-on-disc rolling (traction) tester (83).

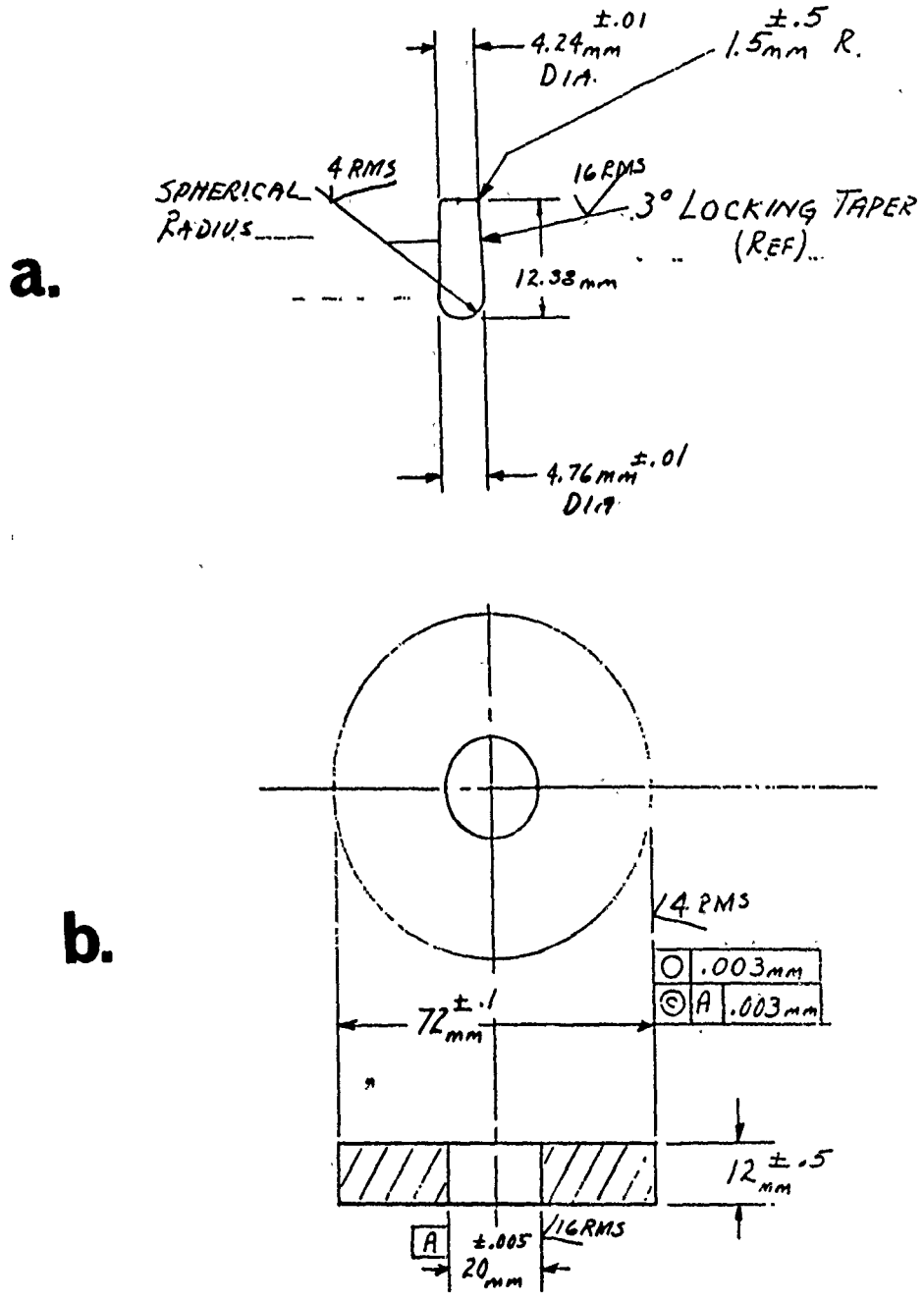

Figure 55. Engineering drawings of the MTI high PVT pin-on-disc tester specimens: (a) pin, (b) disc (83).

asperities of the solid surfaces will come into contact and will transmit even larger tangential tresses. The traction forces that result are therefore strongly coupled to the film thickness, shear strength and surface geometry of the mating materials and the lubricant film.

Since the traction behavior is governed by the relative slip in the contact, the kinematics of complex machine elements like rolling element bearings also control their friction behavior. The dramatic impact of operating speed alone on the sliding velocity pattern in a radial ball bearing is illustrated in the sequence of Figure 56a through 56d, taken from Harris (85). Figure 56a shows the classical sliding velocity pattern in an elliptical contact for zero spin and negligible gyroscopic motion. There are two points of pure rolling which define symmetry zones of slip in and against the rolling direction. As the bearing speed increases, the effect of spin and lateral sliding (gyroscopic motion) change the pattern as illustrated in Figure 56b and 56c. The situation is even more complex for angular contact bearings where the center of sliding is not in the center of the contact, resulting in asymmetric slip patterns (Figure 56d).

Further complication arises due to thermal effects. Any frictional energy is dissipated as heat ($Q = f_t \cdot PV$), which results in increased temperatures at the interface. The viscosity or shear strength of the lubricant is highly dependent on both temperature and pressure. Therefore, interface temperatures, pressures and, especially, velocity have significant influence on the film formation and traction in the contact. Finally, the significance of dynamic effects on contact performance must be addressed. Components experience time-dependent loads, and the importance of loading frequency and amplitude needs to be thoroughly studied.

Understanding of traction in bearings and other mechanical components therefore requires a concurrent knowledge based on film thickness, pressure and temperature as a function of the contact kinematics and kinetics for different mating materials and lubricants. As such, several questions therefore arise concerning the state-of-the-art in measuring traction and in utilizing that data to optimally design bearings (our major interest here) and other power transmission devices:

- What is the adequacy of existing traction machines to quantify contact performance for ball bearings?
- What are the tradeoffs between similitude and experimental accuracy with regard to contact kinematics?
- What is the best way to measure film thickness? Is more than one technique configuration needed for a given tester?
- What analytical models are available to screen experimental results or to define component level performance, and how is their integrity verified?
- Is it possible to design a universal traction machine, or should several (presumably less complex) "bench-rigs" be designed?

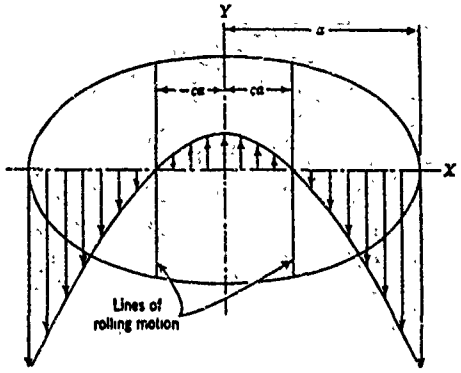

a. SLIDING VELOCITY ON ELLIPTICAL CONTACT FOR ZERO SPIN AND GYROSCOPIC MOTION

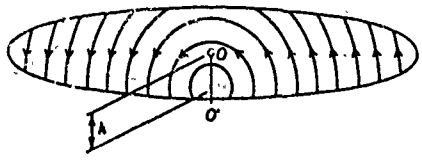

b. SLIDING LINES FOR ROLLING, SPINNING AND GYROSCOPIC MOTION-LOW SPEED

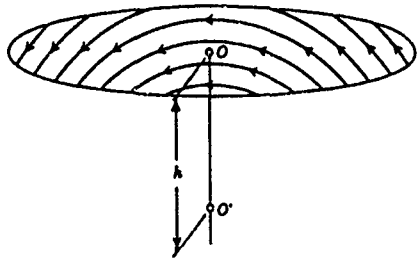

c. SLIDING LINES FOR ROLLING, SPINNING AND GYROSCOFIC MOTION-HIGH SPEED

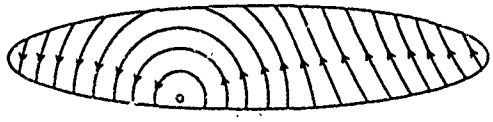

d. SLIP PATTERN-HIGH SPEED ANGULAR CONTACT BALL BEARING

Figure 56. The effect of speed on the sliding velocity pattern in the Hertzian contact zone of a radial ball bearing, after (85).

Since the mid-fifties, a large number of experiments have been conducted to measure film thickness, traction, pressure and temperature in EHD contacts. The effects have been too numerous to list here. It suffices to say the test geometries used for these studies have been either (a) a rolling disc (two or four) or a rolling element (ball or roller) against a rotating, flat part of a disc (Figure 57), or (b) a freely spinning ball squeezed between two inner races in a nutcracker fashion (Figure 58).

The specific contact configuration of a given traction tester and the distribution of velocity gradients in the Hertzian contact zone heavily influence the magnitude and the slope of the traction curve. In view of the high modulus nature of ceramics and hardcoated bearing components as well as the fine design line that has to be drawn between the desired close conformity between the ball and the race and the consequently larger Heathcote slip in the Hertzian contact, it is of the utmost importance that a traction test contact closely approximates that in a real bearing. These conditions include: ball/roller and raceway geometry, materials and surface finishes, contact stresses, kinematics (roll, slip, spin and lateral sliding), temperature and lubrication system.

A single-contact traction machine is a logical candidate, but the configuration of the tester must be amenable to the above requirements. In the past, single-contact traction rigs have taken the shape of either a cross-axis (e.g. ball against a flat plate) or parallel-axis (e.g. twin disc) arrangement. Examples of these types of test machines are shown in Figure 57. The general approach adopted is to develop traction curves, and via analytical predictions of contact kinematics, infer the traction conditions in an operating bearing.

In this regard, note that for such an approach the parallel axis machine (Figure 57b), with uniform slip velocity across the contact, is much preferable to a cross-axis arrangement (Figure 57a). The latter design evolved mainly to accommodate optical interferometric measurements of oil film thickness. However, parallel axis machines will themselves provide unrealistic data, if the contact specimen configuration is inappropriate (Figure 59). Even if one disc is replaced by a ball and the other disc is ground to contain a toroidal ball path, the fact that the ball-on-shaft is uniaxially rotating will provide the wrong traction slope as a function of slip (aka, creep).

As demonstrated by Hewko (86), see Figure 60, both the contact geometries of a ball bearing and a roller bearing, as well as the unit load, affect the traction coefficient. Therefore, deciding the relative validity of the solid lubricated traction coefficients generated by (a) a perpendicular shaft, crowned roller versus flat, spinning disc apparatus (87, 88) or (b) a rig like the Battelle Ball Bearing Simulator working with a freely-spinning ball squeezed between two inner races (Figure 58) see (89, 90), is a function of analysis of the problem depicted in Figures 56, 59 and 60. The disc-on-disc results resemble more the high slope/high magnitude function (91, 92), while the Battelle simulator data (89, 90) resemble the lower slope/lower magnitude function (attributed to the spinning ball). Superimposed is the problem that in ball bearings, balls tend to run on a single path on their outside surface, or at the most, two or three (ball

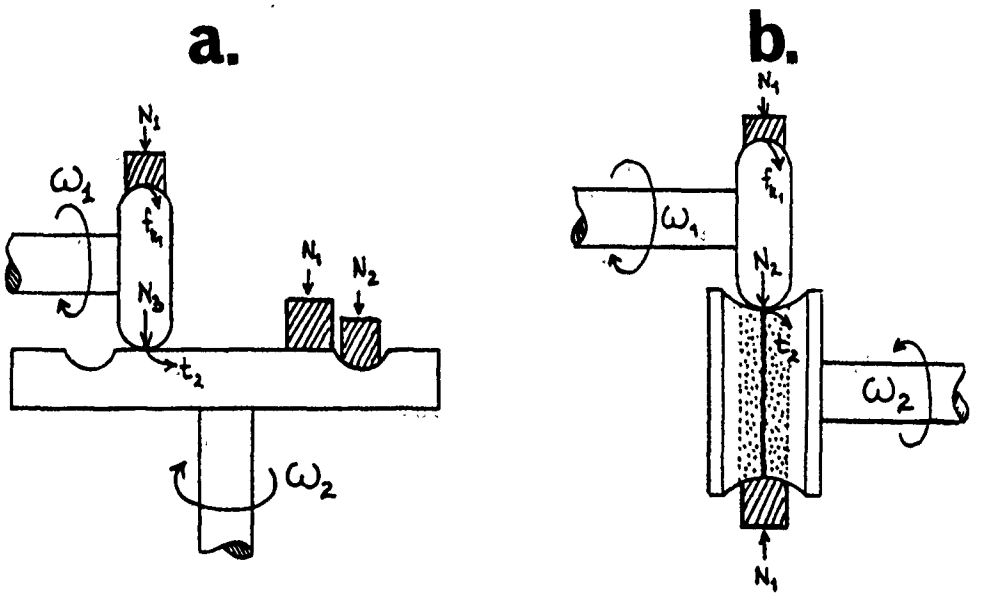

Figure 57. Conceptual schematics of (a) perpendicular, and (b) parallel shaft traction test designs: self-lubricating composite specimens shaded.

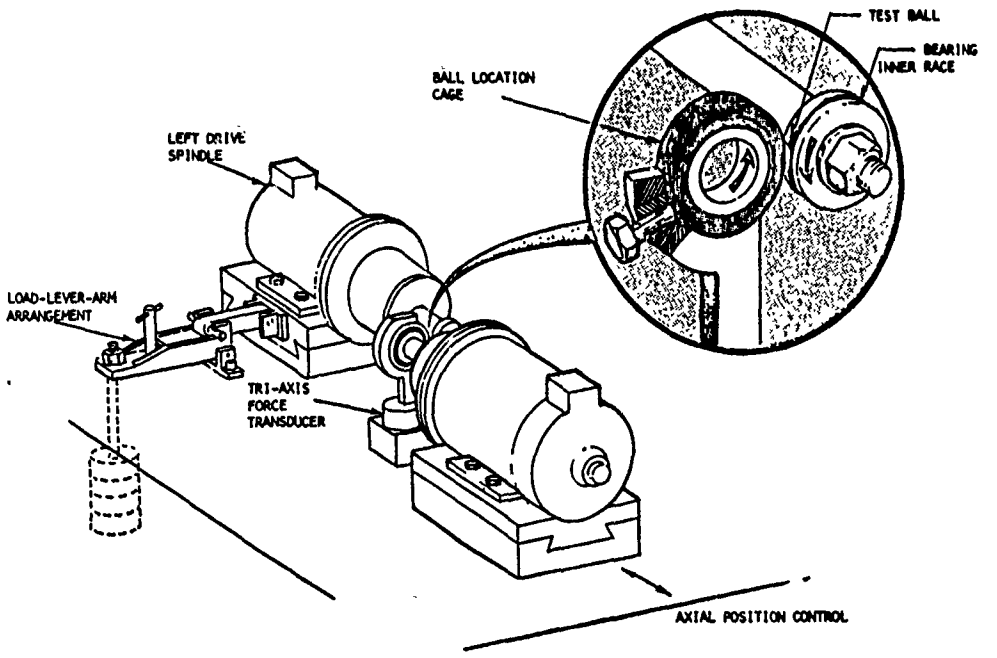

Figure 58. The Battelle Ball Bearing Simulator (89, 90).

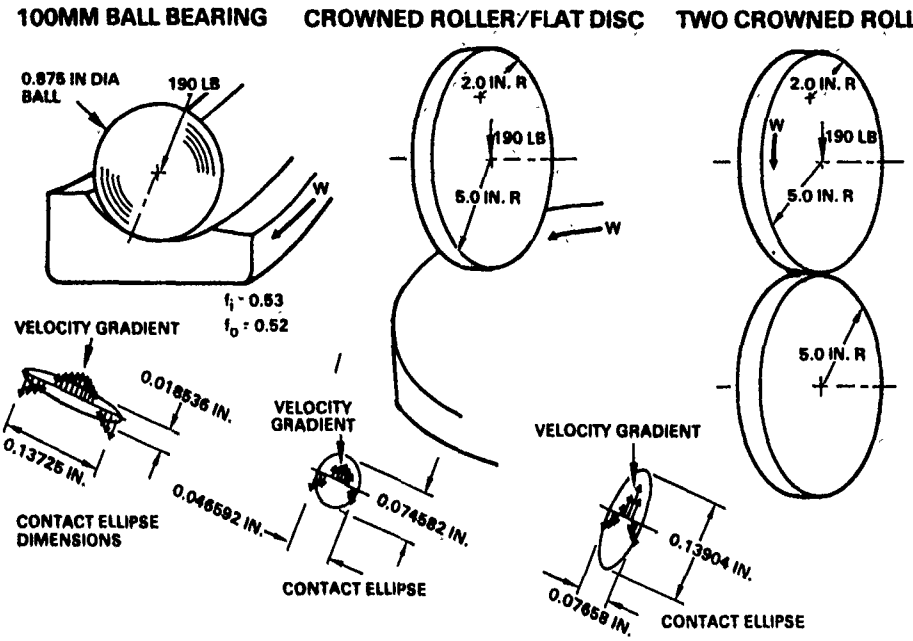

Figure 59. Schematics of slip velocity gradients or disc-on-disc traction test configurations, as compared to those of a ball bearing.

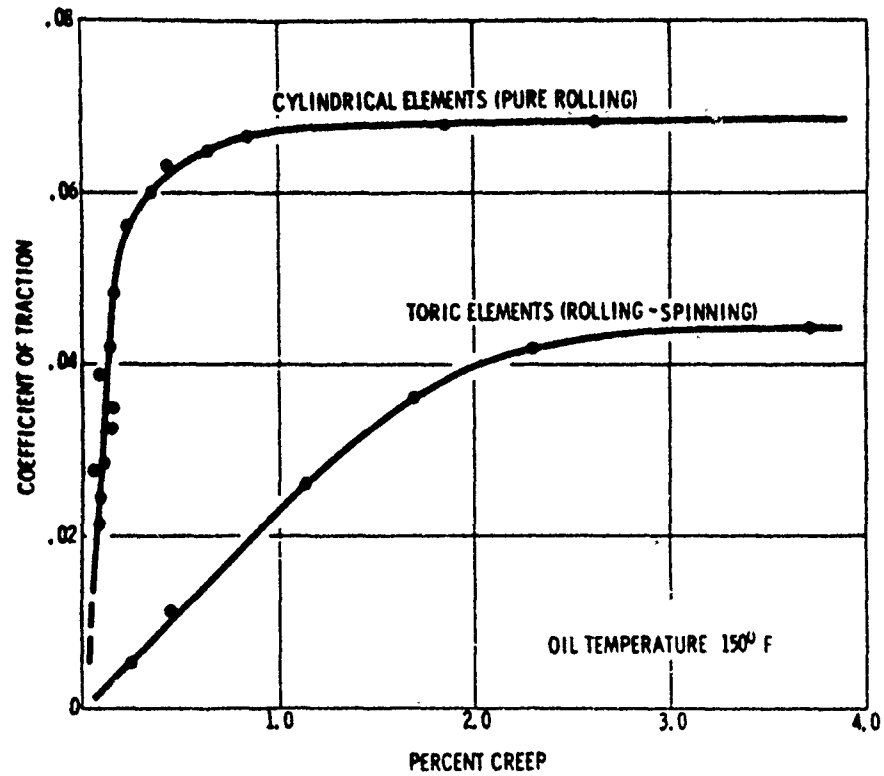

Figure 60. Size and shape of the traction coefficient as a function of pure rolling versus rolling-spinning in a ball bearing, form (86).

banding). The surface distress (wear) and the continued traction behavior of such balls would significantly differ from an idealized multi-track ball.

It appears then that the traction coefficient should be measured in a contact configuration closely approximating the real contact that exists in an actual bearing. This would preclude the substitution of erroneous traction coefficients into six-degrees-of-freedom computer models (such as SEPDYN or any other fully dynamic bearing diagnostics program) and eliminate the resultant, erroneous prediction in bearing behavior.

Based on these caveats, MTI designed and constructed, using internal funds, the parallel-shaft, rolling contact traction and wear simulator depicted in Figure 54b (83). This apparatus accommodates a uniaxially spinning ball or crowned roller (depending on the size of the real ball, a crowned roller can be substituted due to the limitation of size), pressed against a real inner race of a bearing. This provides the most realistic depiction of contact geometries. An added feature enables the angle of the two parallel shafts to be slightly displaced. The traction coefficient at various contact angles and the formation of single and double transfer films under such conditions can also be determined. This design concept accommodates most of the prescribed requirements except that it does not enable the ball to spin. However, this kinematic constraint is judged to be acceptable since ball spin is normally small, and in a solid lubricated bearing would likely be even less significant as the larger traction forces enhance ball tracking. Moreover, it is known that spin can be introduced by tilting one disc or the ball (91, 92, 93).

We at Hughes contributed to the MTI designs by funding a mechanical/thermal computer analysis on the pin-to-disc and ball-on-disc MTI tribometer configurations to show that mechanical responses attributed to undesirable stiffness-frequency characteristics will not unduly influence the validity of the traction and wear data generated.

We also procured specimens for both testers, fabricated from a variety of ceramics and ceramic composites. MTI's work with the traction tester (APPENDIX O) also included the measurement of traction coefficients of powder-lubricated ceramic interfaces to temperatures as high as 1000°C, using potential high temperature lubricants such as pulverized rutile, h-BN and MoS_2.

3.0 TRIBOLOGICAL PROPERTIES OF SELECTED CERAMICS, HARDCOATS AND SOLID LUBRICANTS IN EXTREME ENVIRONMENTS

Currently available ceramics used in tribological applications are far too impure to serve as fully controlled model compounds. At the same time, specially prepared, ultra-high purity ceramic samples or single crystals do not represent reality, because such purity and structure are not achieved during commercial production. This is especially true where the repeatability of the preparation process is poor. The present program was, therefore, designed both to develop surface stabilization methods that will render available (impure) triboceramics acceptable for immediate use and to fully elucidate the physical-chemical interactions of the baseline (yet unstabilized), polycrystalline ceramics themselves. Therefore, both commercially available and specially prepared ceramics and ceramic composites were selected as baseline and advanced "model" compounds. In addition, single crystals of selected materials were examined where appropriate.

The crystal structure of the ideal surfaces for most practical ceramics is generally one of two major types: cubic or hexagonal. All engineering surfaces deviate from these ideal structures. Most real surfaces have grain boundaries which develop during the solidification of crystalline solids. These grain boundaries may be thought of as defects in the bulk solids, extending to the surface, bridging the crystal structure of the two adjacent grains. They are highly active and are energetic. There are also lesser defects, such as dislocations, twins, interstitials and vacancies.

Real engineering ceramics also contain impurities, which are inadvertently or unavoidably included (e.g., iron or tungsten contamination of Si_3N_4 powders originating from ball milling with iron on Co-WC balls), or purposely added (e.g., MgO, Y_2O_3, BeO or CeO_2 sintering aids in preparing hot-pressed or hot-isostatically-pressed Si_3N_4), or surface doping of ceramic materials by ion-implantation to change their microstructures and tribological properties.

The application of elevated temperatures to ceramics sets several mechanisms in motion. Contaminants migrate to and diffuse within grain boundaries, and accumulate at the boundaries and/or on the surface. Meanwhile, the inherent crystal structure of the grains containing crystallographic defects (dislocations, twins) undergoes an ordering process, making these grains larger and more perfect than before (the annealing process). In other words, both the bulk and the surface of ceramics change, if heated at sufficiently high temperatures, for long enough periods.

In elevated temperature air, the grain boundaries are equally convenient channels for the in-diffusion of oxygen. This leads to reactions with contaminants out-diffusing to the surface and reactions with the chemical composition of the grain itself. These reactions often result in low melting, glassy grain boundaries. While these glasses aid in the consolidation of certain ceramics, they invariably increase the oxidation kinetics of the grains and their migration to the surface profoundly influences the friction and

wear mechanisms. The surface shear strength changes significantly due to shearing a viscous layer. Thermal cycling leads to sintering of the contacting surfaces joined by a glassy layer into a monolithic structure. Rupture of the vitrifying bonds on cool-down may result in serious rolling/sliding surface damage.

The purity of the base ceramics' chemistry and the chemical composition of the dopants and sintering aids affect the friction and wear of the mating surfaces, even in the absence of any external lubrication. These factors will also influence the initial and continued adhesion, smear transport, and wear of any pre-applied or replenished solid lubricant layer. Oxidation products of the base ceramic, cermet or hard metal coating (e.g., $TiC + 2O_2 \rightarrow TiO_2 + CO_2$) may occasionally be considered as high temperature solid lubricants, in the form of lubricious oxides. Oxidation products of certain high temperature lubricants can also act as friction-increasing glassy layers ($4BN + 3O_2 \rightarrow 2B_2O_3 + 2N_2$). Prior to determining whether or not these second phases are harmful, neutral, or perhaps even beneficial in some cases, we first needed some means of predicting their formation.

Therefore, a literature review was conducted (APPENDIX P) to survey the reported surface chemical interactions of silicon carbide (SiC) and silicon nitride (Si_3N_4) ceramic sliding interfaces with molybdenum sulfide (MoS_2), boron nitride (BN) and titanium nitride (TiN) solid lubricants from room temperature to 850°C (1500°F), in an oxidizing (air) environment. The SiC was considered both in its pure state and in its boron and aluminum oxide-sintered forms. Phase equilibrium diagrams were utilized to give the general relationship within each system. Relevant chemical studies were reviewed in the literature with the results being of interest to the subsequent design of tribological experiments.

An important consideration was the phase equilibrium diagrams for the appropriate systems. While equilibrium would not likely be achieved under tribological conditions, a knowledge of eutectic melting temperatures and phase relations would certainly be helpful in predicting or interpreting the results of model experiments.

In order to better understand the basic ceramic/solid lubricant interactions, the variables investigated must be carefully controlled. Therefore, a review of first the binary system phase equilibrium diagrams, then pertinent ternary systems (where available) provided basic information on eutectics, intermediate compounds and solid solutions which may form.

The following conclusions can be made based on the review of the phase equilibria literature cited in APPENDIX P:

- Minimizing experimental variables with single crystals and solid surfaces of extreme purity and perfections would facilitate determination of tribological fundamentals of these materials. However, commercial materials and real surfaces are of interest as well.
- The use of sintering aids, required to densify covalently bonded SiC and Si_3N_4, as well as the presence of impurities introduced in processing, makes the prediction of chemical interactions more difficult.

- The review of phase equilibria relations between the ceramics and solid lubricants has provided basic information concerning the condition under which liquid phase and crystal phase transformations may occur.
- The presence of liquid phases, above the eutectic points, will affect the surface shear strength as well as greatly accelerate chemical reaction rates at elevated temperatures.
- Diffusion controlled surface oxidation would be expected to occur at elevated temperatures in air on both the ceramic solid lubricant surfaces, to form layers of oxides (SiO_2, B_2O_3, TiO_2, MoO_3), as well as oxides of the impurity and sintering aid compounds.
- The presence of alkali or alkaline earth oxides can be expected to markedly suppress the silica liquidus and solidus temperatures, to form eutectic points and to yield numerous intermediate compounds.
- The complex phase relations of the SiO_2-MgO system (applicable to the MgO-containing Si_3N_4) included reference to pressure-temperature studies. Higher pressures were reported to shift the eutectic points toward the higher SiO_2 composition regions while simultaneously increasing the eutectic, liquidus, and subsolidus temperatures.
- The effect of MoO_3, Y_2O_3, and WO_3 on the phase relations of the ceramic/solid lubricant systems is much less well known. While a phase diagram for the MoO_3-SiO_2 is not yet available in the literature, a eutectic below the 795°C melting point of MoO_3-SiO_2 liquid will form at least at the melting point of 795°C, which would corrosively attack the ceramic substrates. MoS_2 (ergo MoO_3) is not recommended as a solid lubricant for SiC or Si_3N_4 at the higher temperature regime of 795° to 850°C in an oxidizing environment.
- There is rapid oxidation of MoS_2 through the bulk at 350°C according to TGA studies in air. The oxidation reactions have been reported in the literature to occur as follows:

$$MoS_2 \longrightarrow MoO_2 \text{ @ } 307\text{-}342°C$$

$$MoS_2 \longrightarrow MoO_3 \text{ @ } 372\text{-}427°C$$

- The review of phase equilibria relations are of critical importance to the design of tribological experiments. However, the attainment of equilibrium conditions requires lengthy periods at temperature with highly silica rich melts due to the high glass viscosities and low atomic mobilities of SiO_2.
- The careful determination of experimental temperatures and pressures is extremely important in understanding and interpreting tribological fundamentals. Although experimental constraints make the measurement of temperature especially difficult, both accuracy and rapid scan speed are critical requirements.
- The growth of large, high purity, bulk single crystals of SiC, Si_3N_4 and AlN is extremely difficult, making chemical vapor deposited (CVD) films an attractive alternative.
- It is apparent that much more information is needed to even begin to understand the surface chemical interactions of the ceramic substrates and solid lubricant systems of interest.

3.1 BARE AND MODIFIED α-SiC AND Si_3N_4

3.1.1 The Effect of Preparation Method and Sintering Aid on the Friction and Wear of Polycrystalline α-SiC

3.1.1.1 Summary of Crystal Structure Fundamentals. SiC crystallizes in a variety of modifications. At room temperature the cubic ß-SiC represents a stable modification. At temperatures exceeding 2000°C, ß-SiC is enantiotropically converted into a hexagonal or rhombohedral α-SiC modification.

The structures are based on tetrahedrally coordinated polyhedron units which form basic layer planes that are successively stacked in different sequences to yield the different polytypes. Several notations have been applied to describe the numerous SiC polytypes, but the notation shown in Table 6 is normally used.

The polytypes consist of mixture of the cubic and the hexagonal stacking layer sequences. In the cubic stacking layer sequence, C, the third layer does not lie directly above the first, an order which directly corresponds to the usual ABCABC cubic stacking layer sequence with different displacements above and below each plane. When alternate layers are directly positioned above one another the structure is that of the hexagonal stacking sequence, H, corresponding to the familiar ABAB stacking.

A useful way to consider the SiC polytypes is that each polytypic structure consists of the close-packed stacking of double layers of Si and C atoms (94). One can think of each double layer as consisting of two layers of spheres in the lower layer (Figure 61a). This figure is a cross-sectional view of one of the SiC polytypes. The atoms in each of the two layers are all of the same element and are arranged in a close-packed manner (the "A" spheres in Figure 61b). The stacking of the double layers follows that of the close-packed stacking of spheres, i.e. there are only three possible relative positions of the double layers. As previously mentioned, these positions can arbitrarily be labeled A, B, and C (Figure 61b). The stacking direction is called the C-axis in the hexagonal frame of reference. Table 6 is a listing of stacking sequences of some selected SiC polytypes. For example, the cubic (ß) polytype has the stacking sequence ABCABC... A common method of designating the polytypes in Table 6 consists of a number followed by a letter. The number designates the number of double layers in a stacking repeat sequence and the letter designates the structure.

As a result of the low stacking fault energy of SiC, this material can be grown in these various polytypes having different stacking sequences along the directions perpendicular to the closest-packed planes. A nearly infinite number of combinations of these C and H stacking layers sequences exists, including one cubic structure (the 3C), and more than 140 hexagonal and rhombohedral structures, such as the (2H), (4H), and (6H) and the (15R), (21R), and (33R), also see (95, 96). Remember that the (3C) cubic form is known as ß-SiC, while the various hexagonal and rhombohedral forms are collectively

Table 6. Notation, stacking sequence and hexagonal fraction of SiC polytypes (94).

	Notation	Stacking Sequence	Hexagonal Fraction (h)
(cubic or beta)	3C	ABCABC...	0
(alpha)	6H	ABCACBABCACB...	.33
	15R	ABCBACABACBCACBAB...	.40
	4H	ABACABAC...	.50
	2H	ABAB...	1

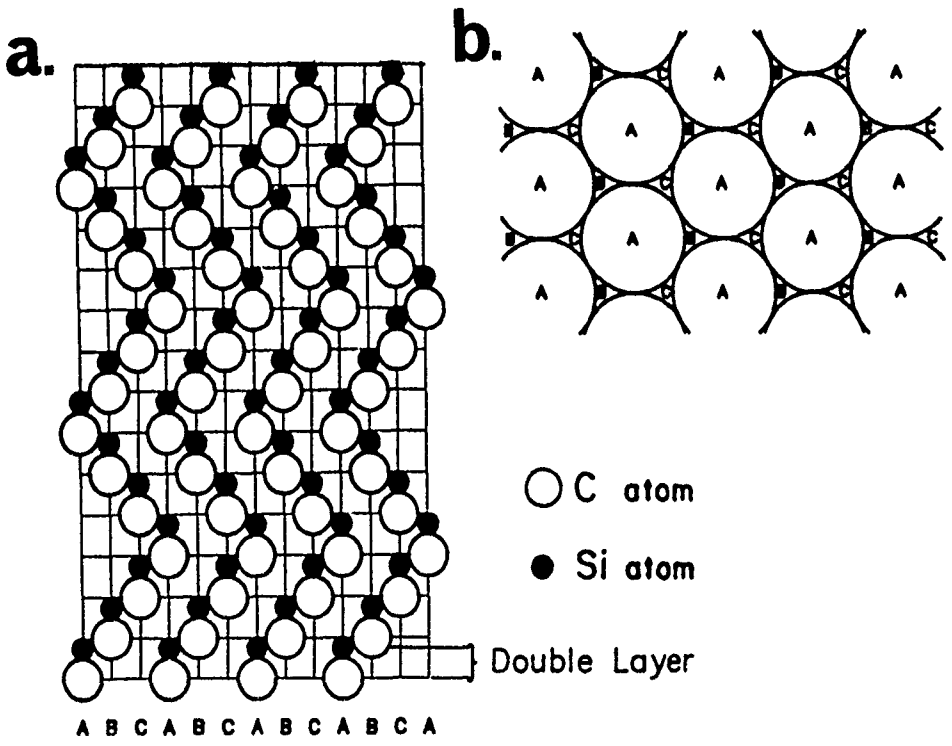

Figure 61. Stacking sequence of 6H polytype of α-SiC; (a) side view: (b) top view (94).

referred to as α-SiC. Impurities, either inadvertently or purposely introduced by doping, or the careful control of the growth method can stabilize SiC to a particular crystal structure.

The arrangements of the atoms in the (111) plane of 3C-SiC and the (0001) plane of 6H-SiC are essentially identical. Therefore, if 3C-SiC grows on 6H-SiC in the manner as $(111)_{3C} \| (0001)_{6H}$, the lattice mismatch between them is extremely small (less than ~0.3%) at any temperature.

Most of the SiC polytypes are extremely stable, with the 6H polytype being the most stable. However, the 2H polytype is unstable and can transform to other polytypes at temperatures as low as 400°C (94). ß-SiC can transform above 2000°C to α-SiC, as pointed out before.

Since only the α-SiC has technological significance with respect to tribology (i.e., all monolithic bearing ceramics fabricated from SiC are currently of the α–SiC polytype), only the hexagonal form is addressed in this section.

3.1.1.2 Summary of the Crystal Preparatory Method of α-SiC by the Acheson Process. The α-SiC crystals are produced in an electric resistance furnace from the purest quartz sand (99.9% SiO_2 content) and low ash (~0.2%) oil coke, mixed in almost stoichiometric proportions. The overall reaction is as follows (97):

$$SiO_2 + 3C = SiC + 2\,CO\uparrow \quad (-618.5kJ = -147.8\ kcal)$$

The reaction is highly endothermic; about 7 kg of raw materials and 4.3 kWH electrical energy is required for 1 kg SiC. The quartz/coke mixture, with additions of NaCl to volatilize the metallic impurities by metal chloride formation, is heated to ~2500°C in the furnace (the Acheson process). The furnace itself is a trough-like container, the narrow (4 m) ends of which are equipped with carbon electrodes attached to refractory plates. The electrodes are connected with a graphite core running along the ~20 m length (and middle) of the furnace. Resistance heating of this core to ~2400° to 2500°C causes SiO_2, SiO and Si to evaporate and to be absorbed by the coke, resulting in the formation of SiC. The evaporation process also plays an important part in the purification process.

The SiC forms a "tube" around the graphite core. The layers near the core are the purest (light silver-green in color) and have the largest crystal size. The outer layer consists of finer crystallites dark blue-to-black in color. The different coloring is attributed mainly to minor impurities, inherent in the crystal lattice of SiC.

With respect to the impurities and morphology of the reaction aggregates, these crystal agglomerates begin to grow columnar normal to the core. As growth continues, the size of the crystals in the columns and the number of the well-ordered single crystals both increase. Examples of these aggregates are shown in Figure 62.

Well-developed, blue-black hexagonal/rhombic α-SiC single crystals are depicted in Figure 62, comprising pieces of Acheson process-produced core aggregate from Electroschmelzwerk Kempten

a.

b.

Figure 62. Pieces of α-SiC reactor core aggregate formed by the Acheson process: (a) from ESK, W. Germany, and (b) from Carborundum, in the U.S.

(ESK) GmbH, Munich, West Germany and from the Carborundum Co., Niagara Falls, NY. Since the temperature of the developing aggregate's surface is becoming closer to the high, actual reaction temperature as it is growing closer to the reactor core, larger single crystals grow on the hotter inner zone due to the annealing effect. Spectrochemical analysis confirmed Fe and Al and Ni as the main impurities (98, 99) in the US version and boron in the W. German-equivalent, see Table 7.

Single crystals may be removed from the aggregates by cutting with a diamond saw, as depicted in Figure 63. X-ray diffraction of one large piece indicated good quality 6H fragments, stacked with the parallel basal Si (0001) and C (000$\bar{1}$) planes rotated with respect to each other, with no azimuthal order. The cut interface here also shows the columnar nature of the growth, characteristic to all CVD-type processes.

The graded inner-outer core material is broken into pieces and subsequently pulverized. Iron dust in the pulverizer is removed with a magnetic separator. The remaining impurities (e.g., free Si, SiO_2, metallic contaminants) are acid and lye solution-leached, followed by rinsing, drying and sifting for particular particle sizes.

The sequence of the α-SiC preparation process by the Acheson method is described in Figure 64.

The following sections deal with the microscopic-macroscopic and continuum mechanical tribometry of single-crystal and polycrystalline α-SiC, in vacuum, in partial and full atmospheric pressure of air, under a variety of PV conditions and temperatures ranging from R.T. to 850°C. The tribochemical changes are correlated with the crystal (grain) structure, the type of sintering aid, and the resultant differences in surface oxidation and wear.

3.1.1.3 Micro/Macroscopic-Analytical Tribometry of α-SiC. The Ecole-Centrale de Lyon/ SORETRIB surface analytical tribometer (Fig. 11) was employed to determine the tribological behavior of a Carborundum Hexoloy SA-80T pin vs. Carborundum α-SiC crystallite basal plane (removed from a reactor core aggregate in Figure 62b by the method depicted in Figure 63). This behavior was determined at room temperature, in ultrahigh vacuum (~$1x10^{-8}$ Pa = $1.33x10^{-10}$ torr) and in partial pressures of air (P_{air} = 50 Pa = 0.38 torr).

The details of the experiments are included in APPENDIX Q. The original version of the paper resulting from this work was presented previously in APPENDIX E.

Essentially, SORETRIB determined the tribochemistry of the interacting surfaces in the unheated condition. Alpha-SiC surfaces were shown to graphitize on heating in vacuum beyond 600° to 700°C (100, 101, 102), reducing F_k beyond 800°C. More recent information indicated that due to the

Table 7. Semi-quantitative emission spectroscopy of various α-SiC single crystal samples (percent elemental contents indicated).

Element	ESK Reactor Aggregate	Carborundum Reactor Aggregate
Si	69.1	69.0
B	0.41	ND
Mg	0.0013	0.0023
Fe	0.0089	0.048
Al	0.0088	0.055
V	ND	ND
Cu	0.0034	0.040
Ti	ND	0.031
Zr	ND	ND
Ni	0.0053	0.037
Ca	0.0012	0.0045
Cr	ND	ND

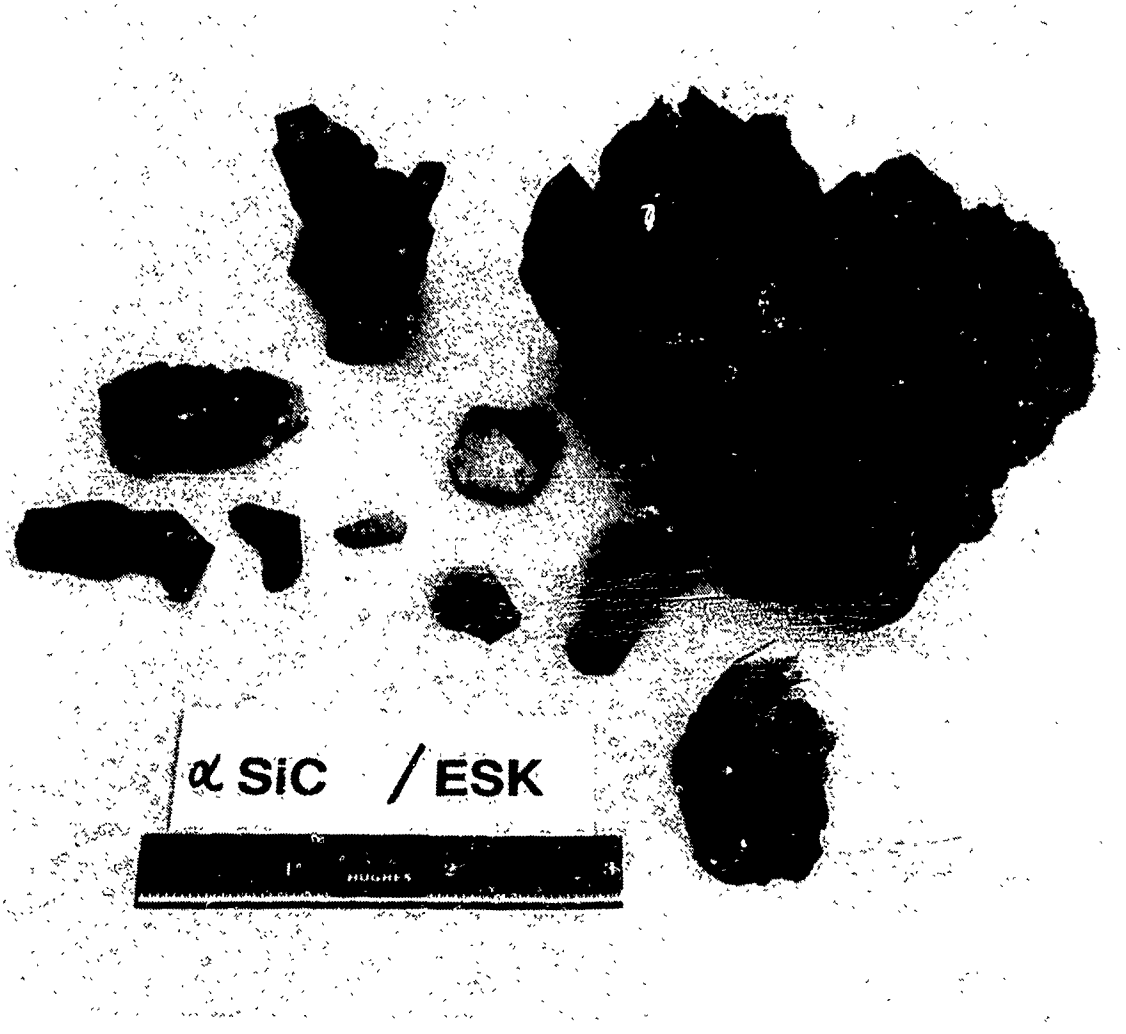

Figure 63. Single crystal α-SiC pieces removed from the ESK reactor core aggregate shown in Figure 62a, by diamond saw cutting.

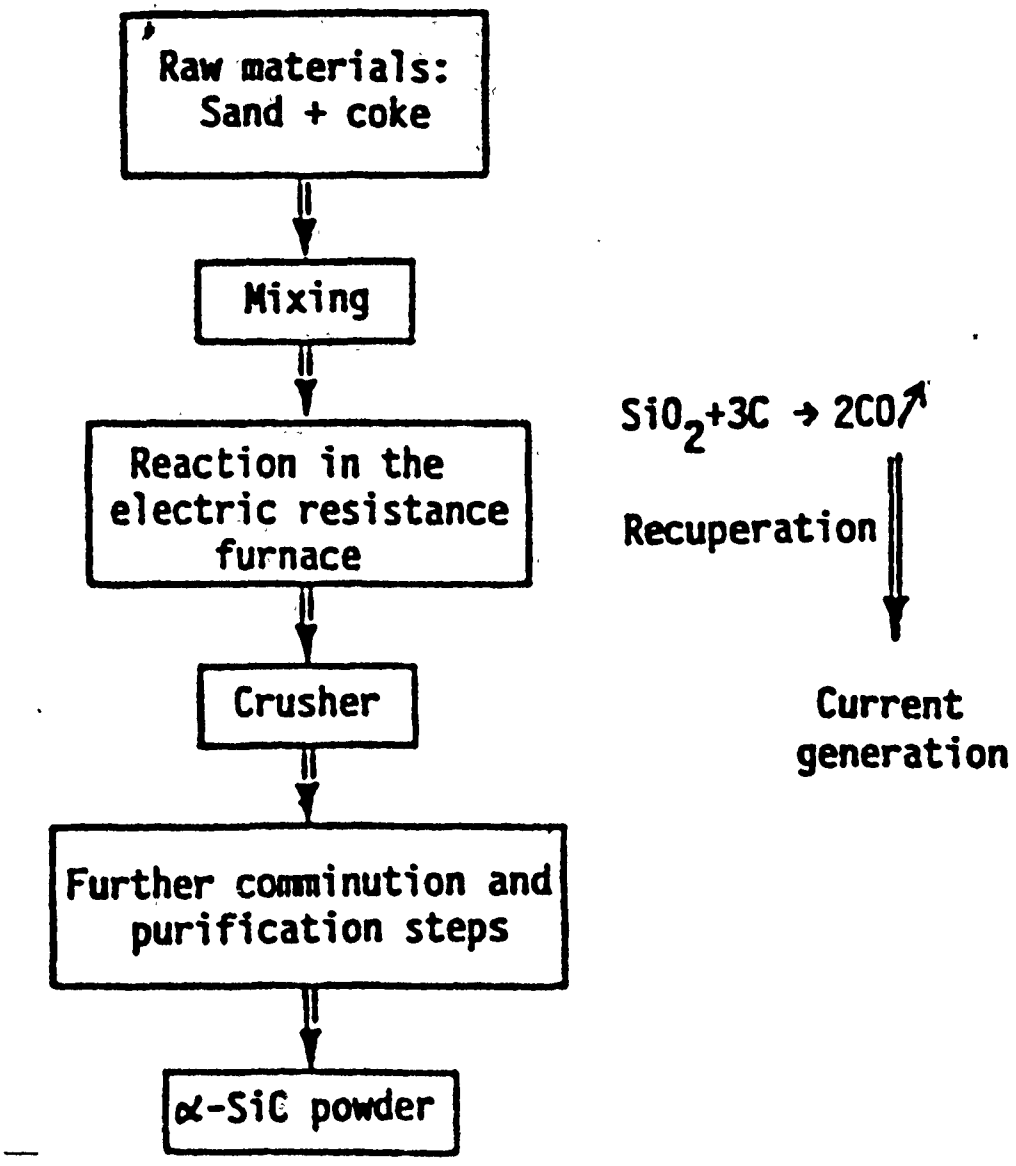

Figure 64. SiC processing by the Acheson process, from (97).

characteristic segregation of C-atoms on the $(000\bar{1})$ side and Si-atoms on the (0001) side of the α-SiC basal plane (Figure 65), the high temperature behavior of these sides is different (103):

1. There are three distinct temperature regions with different carbon surface segregation kinetics on the $(000\bar{1})$. On the (0001) only one temperature region for C-segregation is observed.
2. Below 630°C, no spectroscopic differences between the two surfaces are observed.
3. Between ~630°C and ~1030°C, both faces are terminated by a surface graphite layer, and the C-rich $(000\bar{1})$ face shows an additional C-surface-segregation process.
4. Above ~1030°C, the C-terminated face graphitizes at a higher rate than the Si-terminated face, due to sublimation of the Si(g) from the SiC.

Inasmuch as our studies concentrated on not only the tribological effects of graphitization, but also on the influence of tribooxidation in the presence of high temperature air, it was of interest to utilize test tools at our disposal to elucidate the effects of the combined phenomena.

The SORETRIB tribometer flat was a Carborundum α-SiC single crystal (XTL) polished to a 0.1 μm surface finish, to remove most of the surface oxide layers. Note that the Carborundum XTL was selected over the ESK equivalents shown in Figure 63, because neither polishing, nor subsequent ion-etching could remove the oxide layer from the ESK XTL. As it was, the Carborundum sample itself had to be etched to a depth of 1200 nm before the surface SiO_2 disappeared (APPENDIX Q). The oxide layer thus remaining on the XTL basal plane used in the experiments was estimated to be only 5 nm, before sliding.

The test conditions were:

- normal loads: 2N;
- Hertzian stress (max.), starting: 1 GPa;
- oscillatory sliding speed: 2×10^{-4} m • s^{-1};
- length of stroke = 3×10^{-4} m;
- no. of passes = 160
- temperature = 20°C.

The first experiment was carried out under UHV (10^{-8} Pa); the second in air atmosphere of P_{O_2} = 50 Pa. The same specimens were reused for the second test by slightly turning the pin and displacing the flat to introduce fresh surfaces to the interface.

The results of the investigation were first condensed in the EUROTRIB '89 paper in APPENDIX E and in an updated paper for the 1990 International Tribology Conference, Nagoya, Japan, attached here as APPENDIX Q. The experimental details not necessarily given in these papers are presented in the

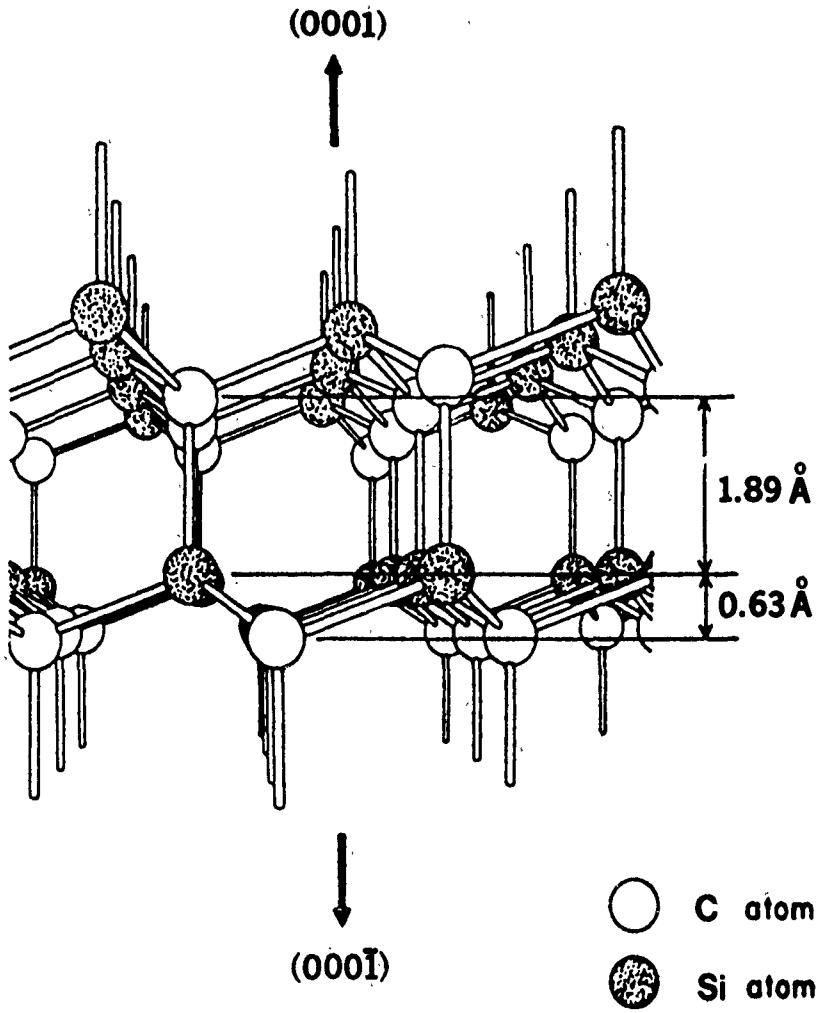

Figure 65. A ball-spoke model of the (hexagonal) α-SiC basal planes depicting dangling bonds on the Si (0001) and C (000$\bar{1}$) sides.

collection of monthly reports by SORETRIB (APPENDIX R). The friction, wear and surface analytical results may be summarized from all sources, as follows:

1. The friction of α-SiC in vacuum is dominated by fracture, compaction and attrition of spheroidal grains in the interface region. No preferential shear planes appear to form, but there is amorphization of the grain edges. High friction ($f_k \cong 0.8$) is the result (Figure 66a).

2. In 50 Pa partial pressure of oxygen, α-SiC quickly oxidizes at the interface, producing silicon oxide and some graphitization of residual carbon from the carbide. The viscosity of this oxide-pregraphitic carbon mixture was apparently just right for the formation of "rolling pins" between the tribopin and the triboflat, similar to the ones generated by an eraser being rubbed against paper. The major axis of the "rolling pins" appeared to be normal to the direction of sliding. The pre-graphitic components in the presence of the oxide, having low energy shear planes (and possibly assisted by the unique "rolling pin" morphology) are believed to be responsible for the low coefficient of friction ($f_k \cong 0.1$, see Figure 66b).

3. With respect to the surface chemistry of the interface associated with the low friction conditions, silicon is preferentially bound to oxygen inside the wear track (Figure 67a). Furthermore, the carbon Auger signal disappeared there. Outside the track (Figure 67b), the argon peak is still visible and oxidation is slight. It appears that oxidation in the track was tribocatalyzed. It is interesting to note that the pin wear scar exhibited only a very small oxygen peak, the oxide being most depleted (removed) there. Overall, it is the silicon oxide's presence that can be linked directly to the low friction, with some contribution from the pregraphitic carbon.

4. The wear scars on the pin and on the flat (Figure 68) reflect the differences between the physical wear mode in vacuum and chemical wear in 50 Pa P_{O_2}. The wear scars are rough (vacuum) and smooth (P_{O_2}). However, total pin wear is less in vacuum, but total pin/flat combined wear is less in P_{O_2}, because some of the semi-viscous oxide from the pin became transferred to the flat.

In order to double-check SORETRIB's results, we performed several Hughes SEM tribometer experiments with a sinter-HIP, polycrystalline α-SiC pin sliding against a flat fabricated from the same ceramic. The load was the customary 0.49 N (50 g), with the accompanying, standard oscillatory velocity of 2.33 mm • s^{-1}. The first two experiments were conducted in 1.33×10^{-3} Pa (1×10^{-5} torr) vacuum, and the last two (using the same specimens) in 13.3 Pa (1×10^{-1} torr) P_{air}. The optical photograph of the wear scars in Figure 69 is associated with the respective friction data in Figures 70 and 71 in the following way:

1. Test track No. 1 = Figure 70a (Vacuum);

2. Test track No. 2 = Figure 70b (Vacuum);

3. Test track No. 3 = Test terminated after 150 cycles due to equipment malfunction (P_{air});

4. Test track No. 4 = Figure 71 (P_{air}).

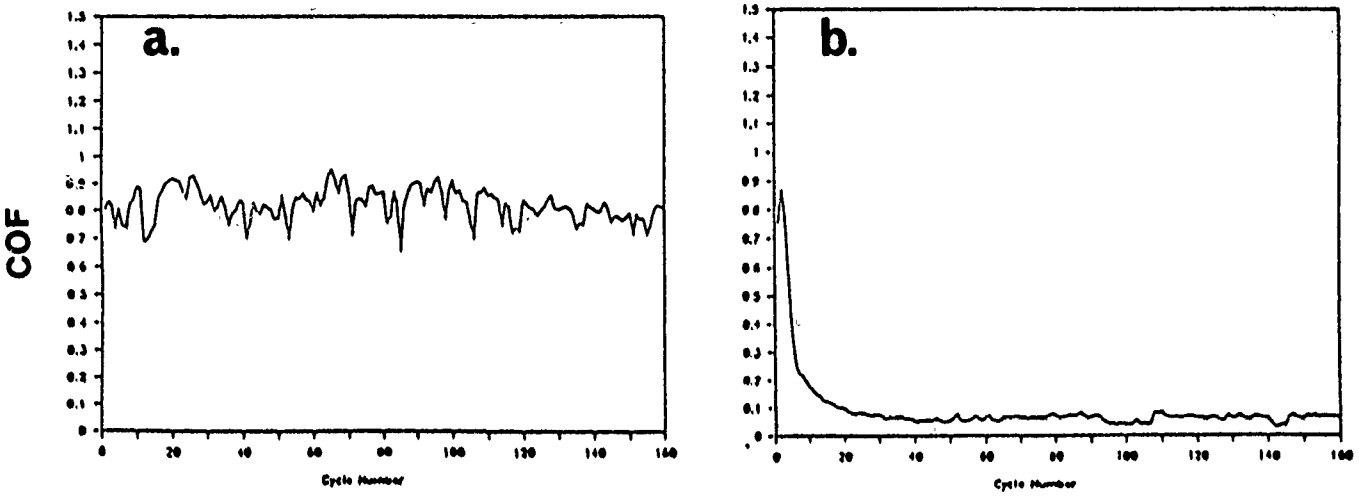

Figure 66. SORETRIB Auger (AES)/XPS tribometer friction traces of α-SiC versus itself in (a) vacuum, and (b) 50 Pa P_{O_2}.

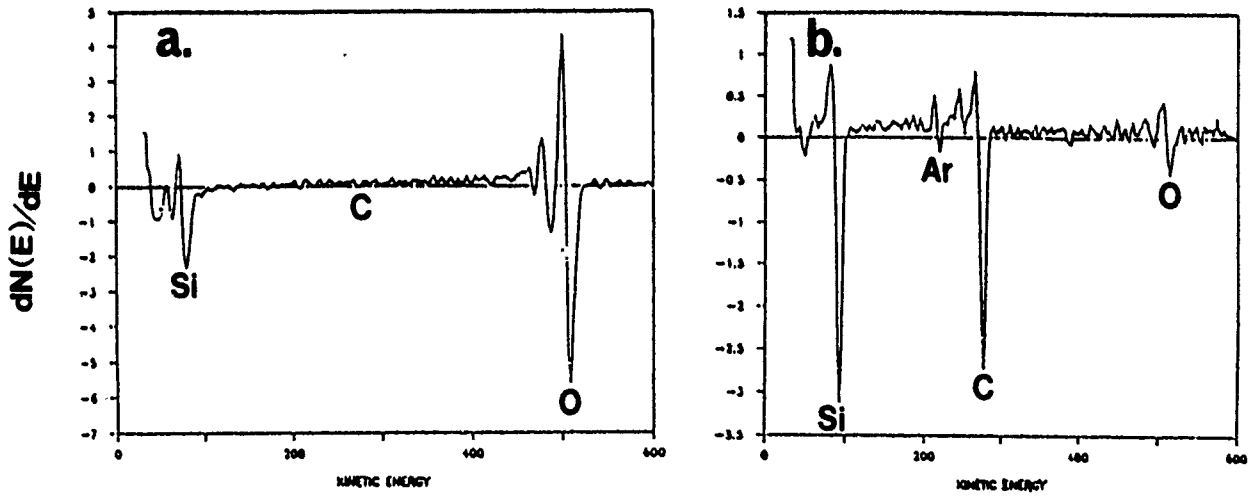

Figure 67. AES spectra of the α-SiC at the end of the P_{O_2} test, from (a) inside the wear scar, and (b) outside the wear scar (also see Figure 66).

WEAR ON PIN

WEAR ON FLAT

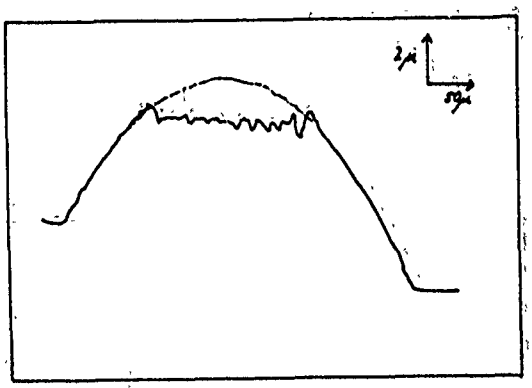

VACUUM

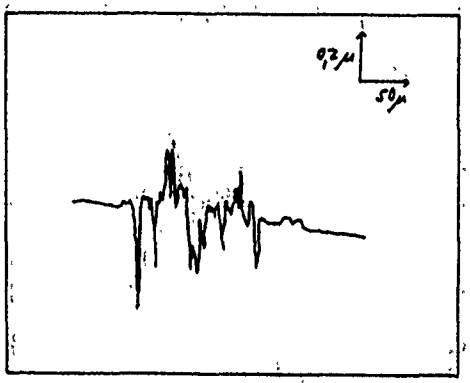

VACUUM

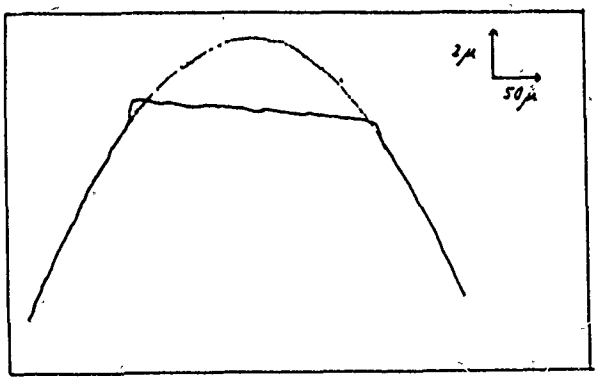

50 Pa Oxygen

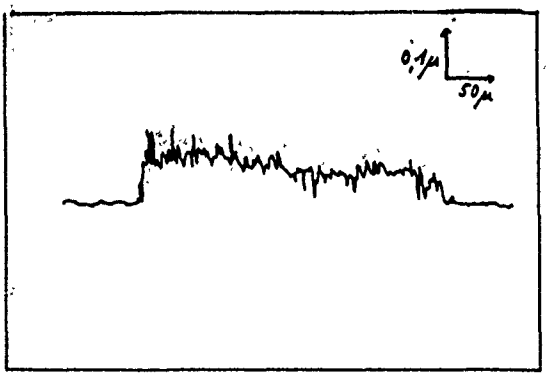

50 Pa Oxygen

Figure 68. Pin and flat wear scars associated with the data in Figures 66 and 67.

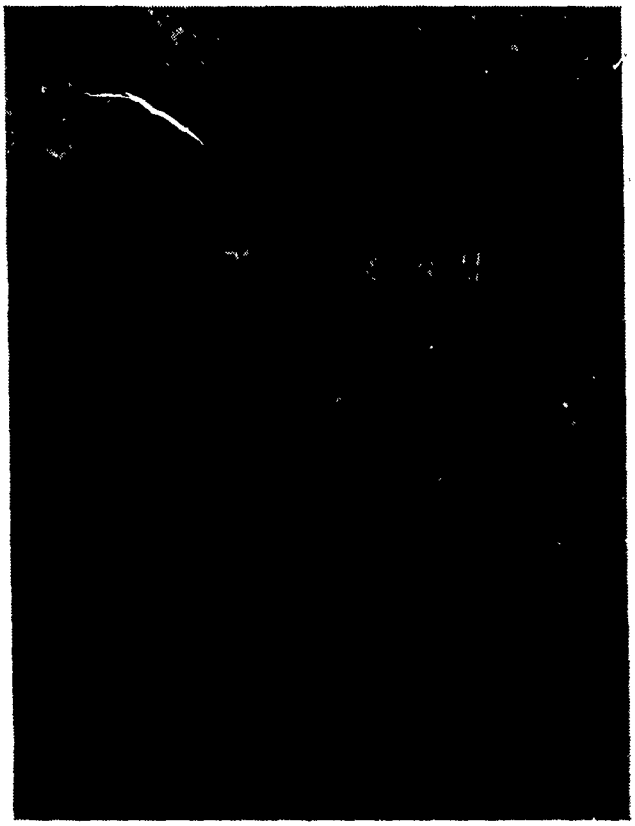

Figure 69. Test tracks of 2 ea. vacuum tests and 2 ea. P_{air} tests with the Hughes SEM Tribometer; for the associated test data, see Figures 70 and 71.

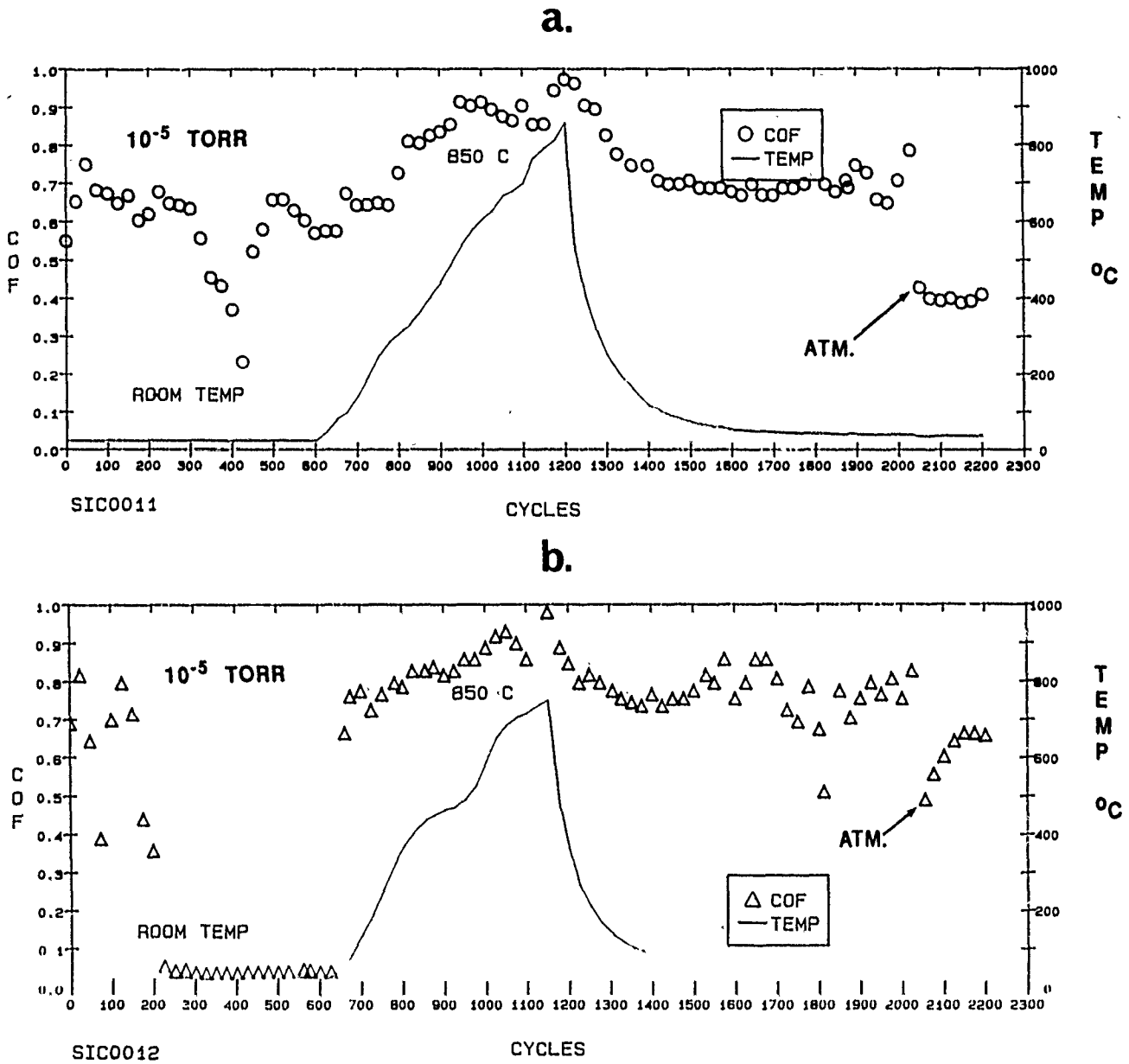

Figure 70. SEM tribometer coefficient of friction (COF) data with α-SiC vs. itself as a function of temperature in a vacuum (1.33×10^{-3} Pa = 1×10^{-5} torr) environment: (a) Test track No. 1 (Figure 69), (b) Test track No. 2 (Figure 69).

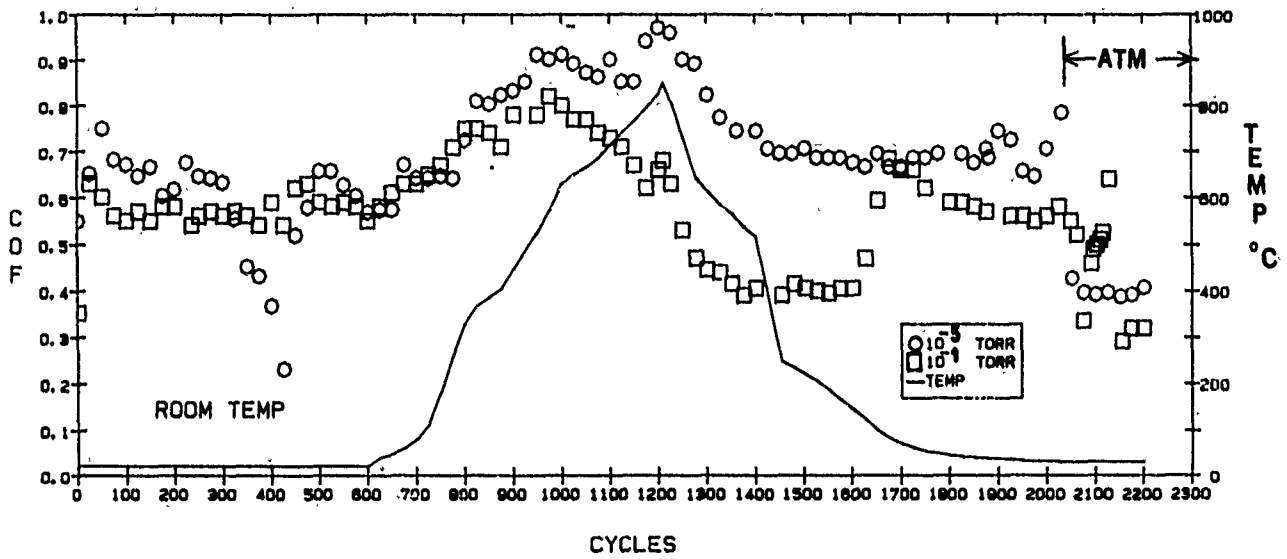

Figure 71. SEM tribometer coefficient of friction (COF) data with α-SiC vs. itself, as a function of temperature, in a P_{air} (13.3 Pa = 0.1 torr) environment. Test track No. 4 (Figure 69), compared with the vacuum data in Figure 70a.

Our data in Figure 70a and 70b generally agree with those of SORETRIB's in Figure 66a in that the friction of α-SiC is high in vacuum. The initial drop in friction in both Hughes vacuum tests can only be attributed to the effects of an oxide (or other residual contaminant) layer formed on the rubbing surfaces *before* the respective tests. The desorption of hydrogen-bonded moisture may have also contributed to the friction drop. In the first test, this layer was extremely thin (say 4-5 nm) on the as-polished and solvent-rinsed samples, and it wears off quickly. At the higher temperature, the friction becomes and stays high, but drops as atmospheric oxygen is bled into the chamber (Figure 70a).

Bleeding oxygen back into the chamber during the last 200 cycles of operation of the first vacuum test had to have created a thicker oxide layer on and next to a well-developed wear scar, both on the heat-activated flat and the pin tip. As the next (second) vacuum test began (Figure 70b), the friction dropped even more precipitously than in the previous test and remained unusually low (f_k = COF ≅ 0.03) for hundreds of cycles, at room temperature. Apparently, the reduced unit load (due to the increased wear scar on the previously used pin), combined with a thicker oxide layer, helped maintain the low friction. The friction remained low, at least until the onset of heating. Here, during the second "vacuum" test, the data closely matched those of SORETRIB's performed in 50 Pa P_{O_2} (compare the data in Figure 70b with those in Figure 66b).

Simply stated, whatever oxide/contaminant product(s) were on the surface at the beginning of the first test were rubbed off rapidly in vacuum. It did not become regenerated on the pin tip and, to a much lesser degree, become replenished statically on the yet-unrubbed portions of the flat until air was bled back into the chamber. When the used pin was moved over to that yet-unused portion of the flat, the combined pin tip/flat oxide content became just high enough to provide low friction for a longer period of time, as helped by a lower unit load stemming from a larger pin wear scar.

Unfortunately, the initial results of the 13.3 Pa P_{air} test (Figure 71) are confusing, because there the friction remained high until more substantial amounts of the oxide began to form around 500°C (the onset of friction drop). Based on the previous results, a significant and rapid oxide-induced reduction in starting friction was anticipated. This reduction, although not as precipitous as the starting friction drop in Figure 70b did, however, begin at ~500°C during heating and persisted until ~150°C of the cool-down cycle. At that time, the removal rate of the oxide on cooling must have exceeded its formation rate, because the f_k (COF) began to rise again to ~0.6. On backbleed of atmospheric air, the f_k dropped again, this time to 0.3.

SORETRIB's AES/XPS analysis of the SEM triboflat's wear scars and the adjacent, unused areas (APPENDIX S) revealed only carbide- and oxycarbide-like carbon—no pregraphitized carbon was found anywhere. Oxygen was present everywhere as oxycarbide, not as silicon oxide. Wear track No. 4 (P_{O_2} test) had more oxycarbide in the track (~3 nm thick) than outside of it.

The Hughes data generally agreed with those of SORETRIB's on the role of thin surface layers of oxide and/or oxycarbide, with respect to some reduction in friction of the mating, pure α-SiC surfaces. It will be shown next, by presenting tribodata in the continuum regime, that more massive amounts of glassy oxide-oxycarbide layers indeed significantly reduce the surface shear strength of polycrystalline (i.e., bearing grade) α-SiC, at elevated temperatures, in air. Unfortunately, this reduction in shear strength is commensurate with substantially increased tribooxidative wear of the rubbing surfaces.

3.1.1.4 Tribometry of α-SiC in the Continuum Regime. This section deals with the microstructural and chemical aspects of α-SiC friction and wear, as further influenced by the preparation process of the monolithic specimens. The test machines used here were operated in the PVT range and contact configurations closer to those normally found in the engineering regime than those of the more tribological fundamentals-oriented tribometers previously described. By utilizing the low-to-medium PV, high T Tester 2A (see para. 2.2.3), complemented by the high PVT friction/traction tester(s) of MTI (see para. 2.2.4), the widest possible friction and wear test regime of α-SiC was thus traversed, from the microscopic scale of the AES/XPS/SEM tribometers to the continuum region of the larger bench testers.

With both continuum-mechanical testers, the specimens were fabricated from three different kinds of α-SiC. Two exhibited the same chemistry but somewhat different fabrication techniques (from Elektroschmeltzerk-Kempten GmbH, W. Germany); the third was prepared by an entirely different fabrication methodology and sintering aid chemistry by Carborundum in the U.S. (Table 8). The differences in the associated α-SiC microstructures are depicted in Figures 72 and 73.

The ESK HIP α-SiC microstructure (Figure 72) is comprised mostly of equiaxed, fine grains. The much larger and higher aspect ratio grains of the sinter-HIP process are the direct result of the material having been heated twice (as explained later in this report), which always leads to annealing and additional grain growth. The second significant difference between the HIP and the sinter-HIP material is the small grain-equiaxed grain size (HIP) vs. larger grain-bimodal grain size (sinter-HIP) distribution. The respective fracture surfaces indicate that the HIP material tends to fracture in a more intergranular manner, while the sinter-HIP equivalent fractures more transgranularly.

The microstructure of the pressureless-sintered material, in terms of grain size and distribution, appears to lie somewhere in between those of the HIP and the sinter-HIP analogs (Figure 73). The appearance of the fracture surface in this figure is closer to that of the sinter-HIP material than the HIP equivalent. The porosity of the pressureless-sintered α-SiC is far greater (estimated to be in the range of 2 to 4%) than either of the other two high-pressure-consolidated versions.

A large number of room temperature (R.T.) and ~850°C (H.T.) Tester 2A experiments were completed with the α-SiC materials. The typical repeatability of the tribodata was shown previously in Table 5. Typical friction traces of R.T. and H.T. tests were also previously given in Figures 42 and 43, respectively. In addition, the modulus, (E), hardness (H_k) and fracture toughness (K_{Ic}) of the as-machined and H.T.-exposed rubshoes were measured by the Knoop hardness indentation (H_k) technique, on unrubbed areas.

Table 8. Tester 2A and MTI's tribometer specimen materials fabricated from α-SiC.

MATERIAL	PROCESSING	SINTERING AGENT	CHARACTERISTIC
ESK Ekasic α-SiC	HIP (Fully canned)	Al/GRAPHITE (≈ 0.03% Al)	SMALL GRAINS
HEXOLOY 80T-SA	PRESSURELESS SINTERED	B_4C/GRAPHITE (≈ 0.42 % B)	INTERMEDIATE GRAINS
ESK Ekasic α-SiC	SINTER + HIP	Al/GRAPHITE (≈ 0.3 % Al)	LARGER GRAINS (2 heats)

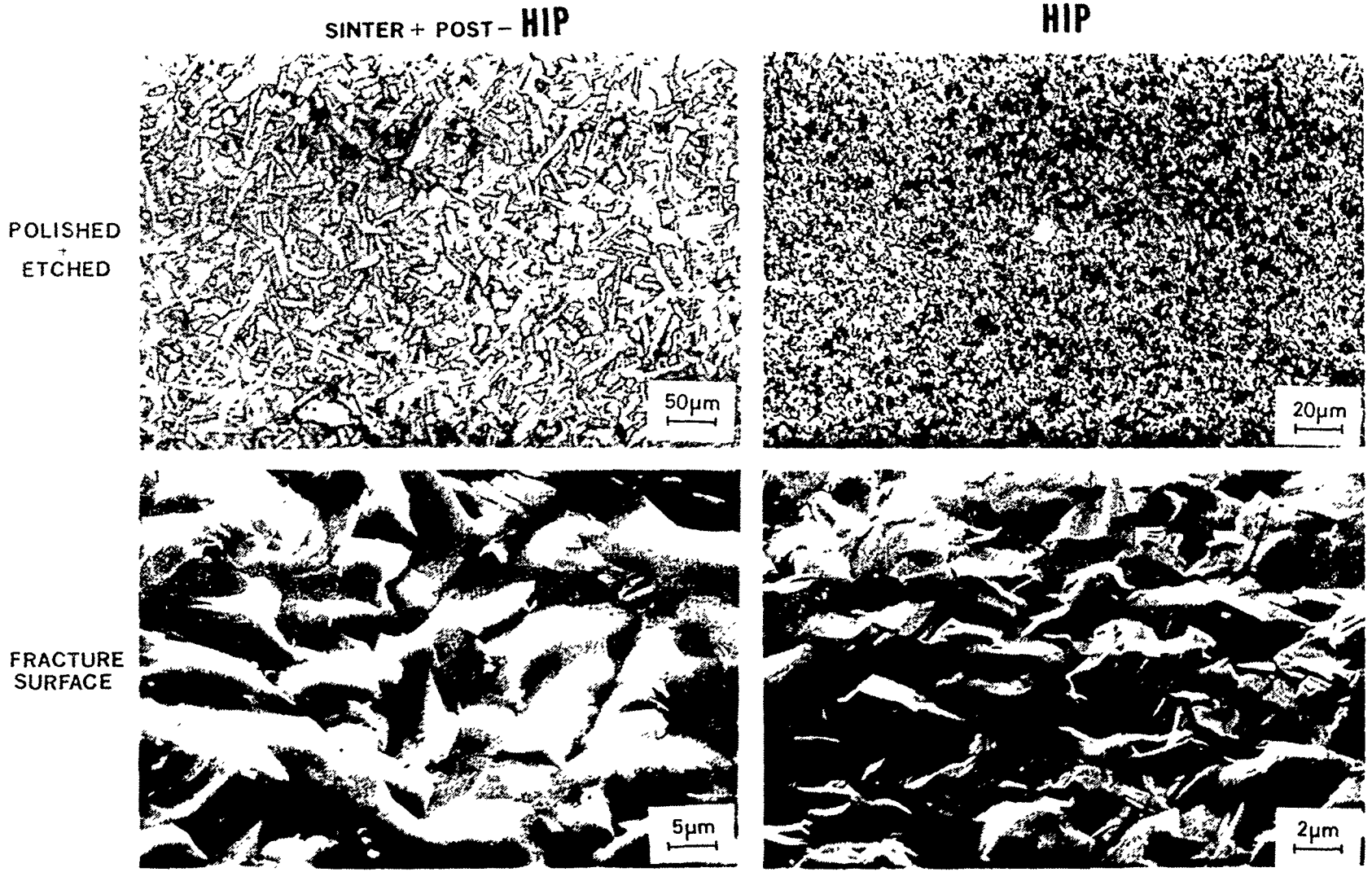

Figure 72. Microstructure of sinter-HIP and fully can-HIP Ekasic® α-SiC by ESK.

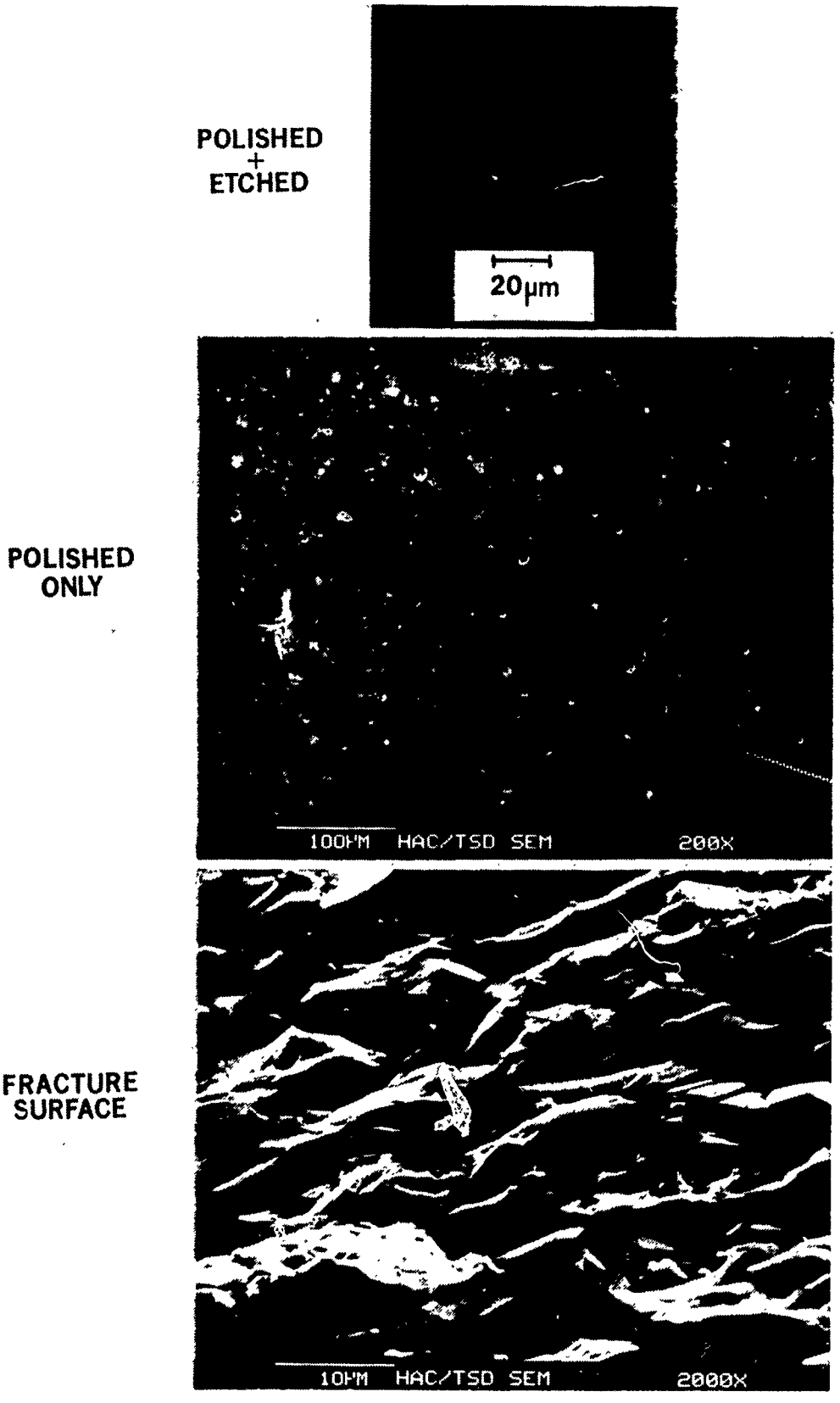

Figure 73. Microstructure of pressureless-sintered Hexoloy® SA-80T α-SiC by Carborundum (formerly SOHIO Engineered Materials).

The $E/H_k/K_{IC}$ values are shown in Table 9; the f_k (COF) with the converted apparent surface shear strength ($\tau_s = F_k/A_{app.}$) data are in Table 10; the associated mean values of wear are in Figure 74.

The results indicated high f_k (COF) and frictional variations ("hash") at any temperature, with slightly higher f_k values and much higher wear in the high temperature region. The wear *volume* of the rubshoes was the quantitative measure of α-SiC stock removal, as a function of microstructure, sintering aid chemistry and temperature. The respective rubshoe wear scars (e.g., see Figures 75 and 76) were used to calculate the volume wear rates as well as the apparent areas of contact ($A_{app.}$).

The wear data indicated a three-order-of-magnitude increase of wear from room temperature to the high temperature regime. The Al (actually Al_2O_3) sintering-aid-containing ESK sinter-HIP material wore slightly, but consistently less than the much less (also Al_2O_3) sintering aid-containing, fully-can-HIPed version, at any temperature. The pressureless-sintered α-SiC, which has higher porosity and contains a different (B_4C) sintering aid, exhibited the highest wear at room temperature, but comparably low wear at high temperatures. As a consequence, the τ_s values (Table 10) were significantly lower at H.T. because of the presence of the same friction forces (F_k) but different $A_{app.}$, (i.e., $\tau_s = F_k/A_{app.}$) among the three types of materials.

The high PVT MTI tests with the friction/traction tester in the sliding pin-on-disc (friction) mode (see Figure 54a) led to the data attached here in Table 11 (wear), Table 12a (friction) and Table 12b (τ_s), resulting from the F_k and $A_{app.}$ values taken from APPENDIX O.

Comparing the Tester 2A wear data in Figure 74 with the identically normalized wear factors in Table 11, due to the increase of surface speed from 0.35 $m \cdot s^{-1}$ (Tester 2A) to 30 $m \cdot s^{-1}$ (MTI pin-on-disc tester), the ESK HIP/sinter-HIP wear rates increased by an order of magnitude at H.T., but reduced the τ_s (compare Tables 10 and 12b) by a factor of five-to-six. It is important to note again that the f_k (COF) is a systems parameter; τ_s is a better measure of surface shear behavior, because this value is normalized at least to each apparent (if not real) contact area.

The following discussion is aimed to shed some light on the microstructural and chemical influences which help explain the wear data. It also points to essential physical property and surface analytical measurements which had to be additionally performed for a more complete elucidation of the wear mechanism.

3.1.1.4.1 Inconsistencies with Respect to Grain Size and Sintering Aid Dependence on α–SiC Wear. As explained by Wu et al (104), a large variety of polycrystalline, single-phase ceramics (Al_2O_3, MgO, $MgAl_2O_4$ and ZrO_2) exhibit Hall-Petch type behavior, in that the inverse of the wear rate (W^{-1}) is a positive slope, linear function with $G^{-1/2}$, where G is the grain size. However, the y-intercept is not zero. Intercept values, being equal or less than single crystal values (i.e., signifying higher wear), were attributed to thermal expansion and elastic anisotropy of the grains (104, 105). Wu et al (106) found the Hall-Petch relationship to hold for several SiC ceramics, sintered α-SiC included. These arguments generally agreed with previous work on similar dependence of the strength of brittle, polycrystalline

Table 9. Modulus, hardness and fracture toughness data on α-SiC at R.T. (as-received) and H.T.-tested (HTT).

GRAIN SIZE ↓

	E (GPa)		H_k (GPa)		K_{IC} (MPa·$m^{1/2}$)	
MATERIAL	AS REC'D	HTT	AS REC'D	HTT	AS REC'D	HTT
ESK HIP	260±73 (400-450)	190±62	26.1±0.6 (25.5)	21.4±1.2	3.31±0.16 (4.8-5.5)	2.40±0.13
HEXOLOY SINTERED	269±103 (410)	216±72	26.8±0.8 (27.4)	25.7±1.5	2.72±0.18 (4.60)	2.40±0.11
ESK SINTER +HIP	288±86 (400-500)	204±51	26±0.8 (25.5)	24.0±1.1	3.34±0.12 (4.8-5.5)	2.29±0.18

Table 10. Coefficient of friction (COF) and apparent surface shear strength (τ_S) data on α-SiC at R.T. and H.T.

	Room Temp.		High Temp.	
MATERIAL	**COF (Variation)**	**τ_s (MPa)**	**COF (Variation)**	**τ_s (MPa)**
ESK HIP	**0.6** (0.2-0.8)	**1.80**	**0.8** (0.3-1.3)	**0.55**
HEXOLOY SINTERED	**0.65** (0.3-0.8)	**1.67**	**0.8** (0.2-1.3)	**0.67**
ESK SINTER +HIP	**0.5** (0.2-0.8)	**2.57**	**0.8** (.2-1.3)	**0.56**

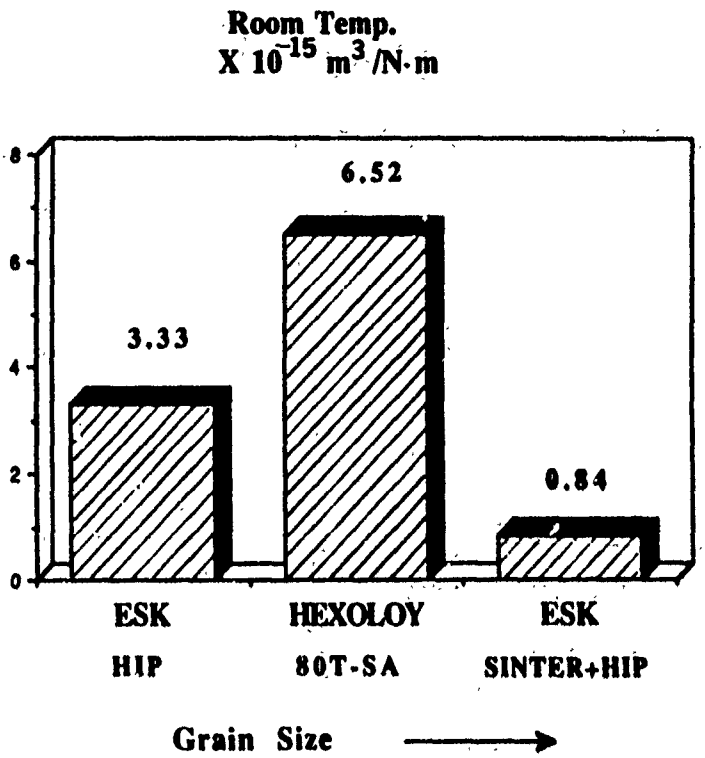

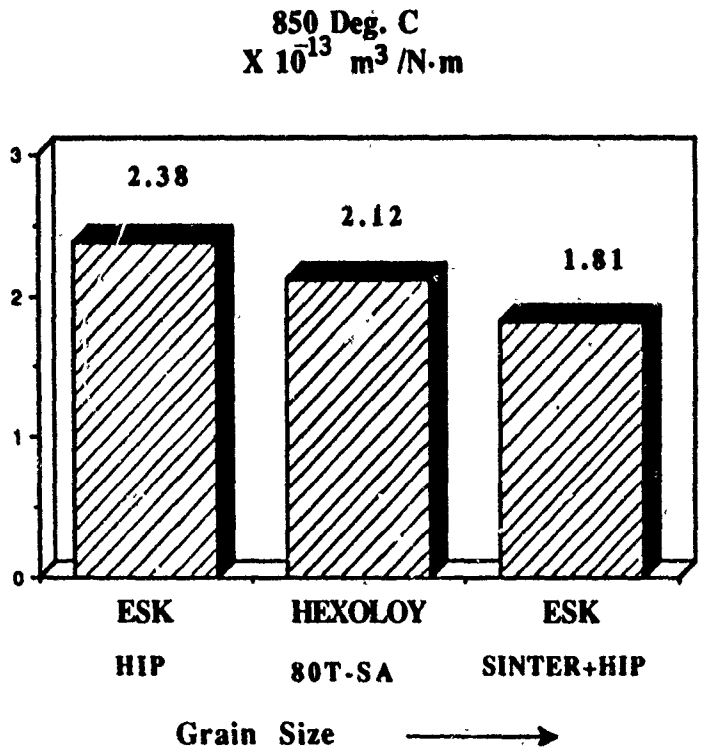

Figure 74. Normalized mean wear rates of the α-SiC materials at R.T. and H.T.; Tester 2A.

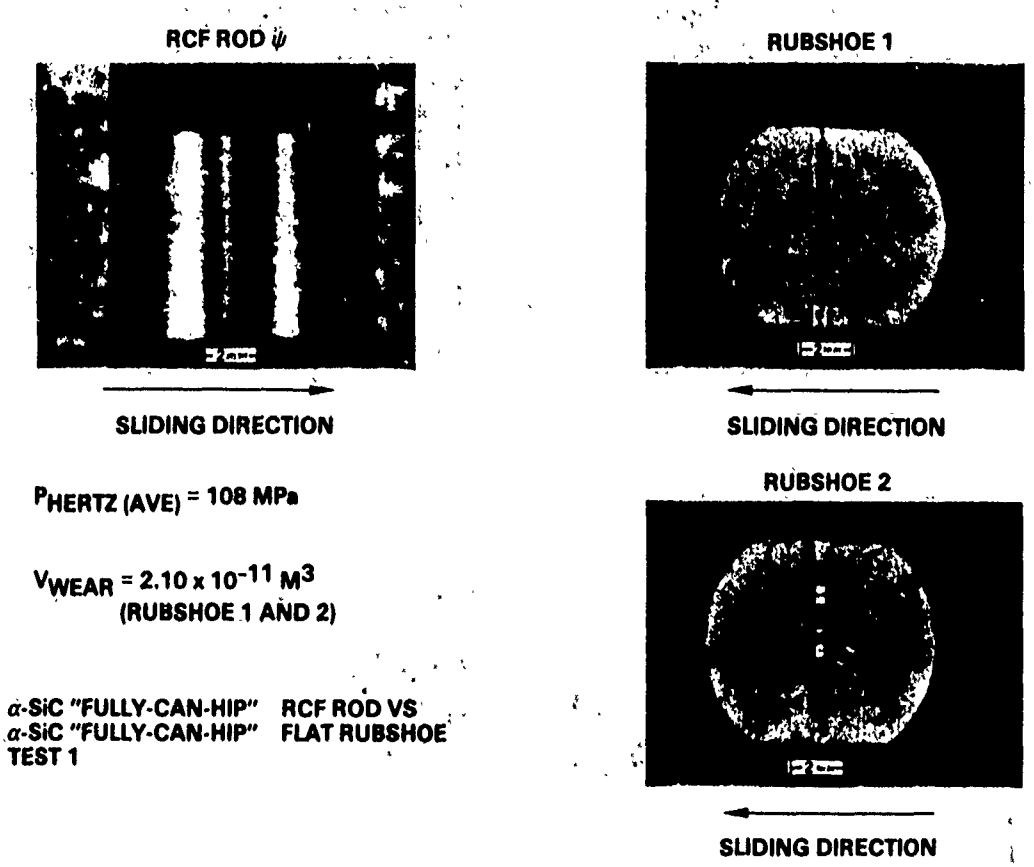

Figure 75. Rod/rubshoe wear scars, starting average Hertz stress and volume wear of an ESK α-SiC (fully can-HIP) R.T. test, Tester 2A.

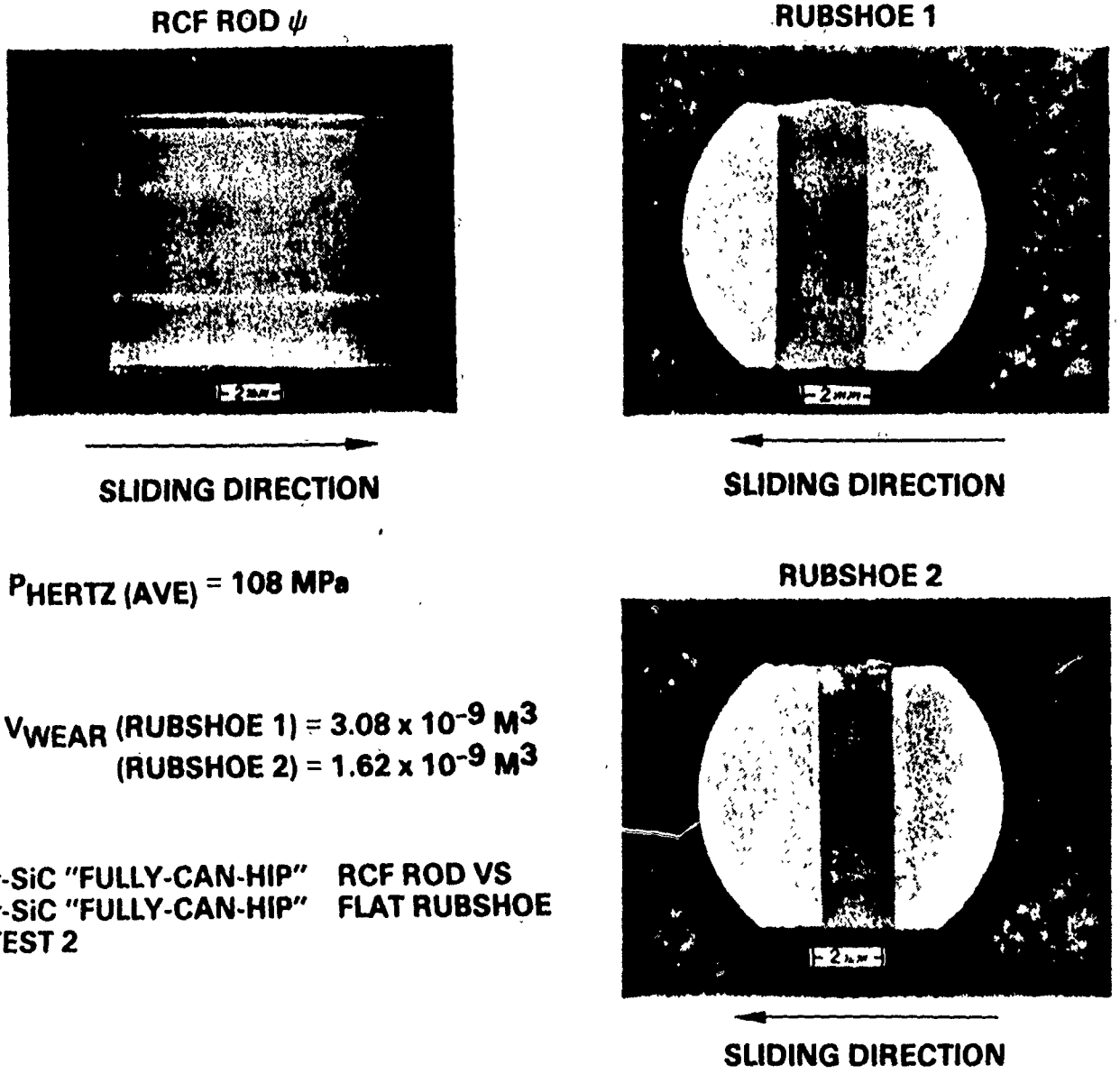

Figure 76. Rod/rubshoe wear scars, starting average Hertz stress and volume wear of an ESK α-SiC (fully can-HIP) H.T. test; Tester 2A.

Table 11. Normalized mean wear rates of a variety of ceramic couples, ESK α-SiC included, at H.T. and high V; MTI pin-on-disc tester.

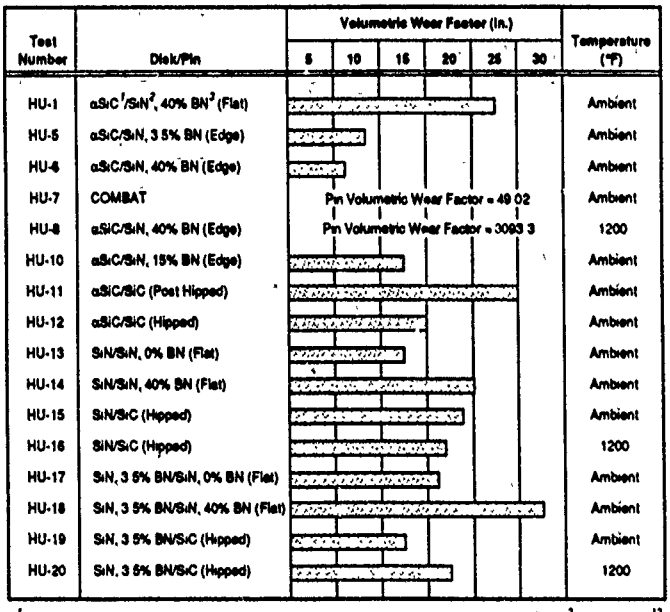

[1]Silicon Carbide
[2]Silicon Nitride
[3]Boron Nitride

All values expressed in $([M^3]/[Nt \cdot M]) \times 10^{13}$
where M = Meters and Nt = Newtons

Table 12. Speed-controlled friction (a) and mean τ_S values (b) with selected ceramic couples from Table 11.

a.

Test Number	Disk/Pin	Speed (rpm) 3000	5000	7000	9000	Average	Average Standard Deviation
HU-1	αSiC[1]/SiN[2], 40% BN[3] (Flat)	0.266	0.112	0.073	N/A	0.150	0.096
HU-5	αSiC/SiN, 3.5% BN (Edge)	0.240	0.145	0.172	0.256	0.203	0.091
HU-6	αSiC/SiN, 40% BN (Edge)	0.134	0.099	0.088	0.117	0.110	0.096
HU-10	αSiC/SiN, 15% BN (Edge)	0.227	0.180	0.132	0.100	0.159	0.084
HU-11	αSiC/SiC (Post Hipped)	0.507	0.321	0.261	N/A	0.363	0.091
HU-12	αSiC/SiC (Hipped)	0.481	0.310	0.238	N/A	0.343	0.085
HU-13	SiN/SiN, 0% BN (Flat)	0.070	0.057	0.036	0.023	0.046	0.079
HU-14	SiN/SiN, 40% BN (Flat)	0.091	0.081	0.039	0.015	0.052	0.079
HU-15	SiN/SiC (Hipped)	0.378	0.297	0.161	N/A	0.249	0.096
HU-16	SiN/SiC (Hipped)	0.477	0.394	0.416	0.418	0.426	0.092
HU-17	SiN, 3.5% BN/SiN, 0% BN (Flat)	0.078	0.060	0.060	0.073	0.082	0.081
HU-18	SiN, 3.5% BN/SiN, 40% BN (Flat)	0.115	0.049	N/A	N/A	0.082	0.075
HU-19	SiN, 3.5% BN/SiC (Hipped)	0.360	0.209	0.138	0.101	0.202	0.093
HU-20	SiN, 3.5% BN/SiC (Hipped)	0.537	0.477	0.486	0.507	0.504	0.088

[1]Silicon Carbide
[2]Silicon Nitride
[3]Boron Nitride

b.

	Pin Material	Disk Material SiC	SiN	SiN, 3.5% BN
Ambient Conditions	SiN, 40% BN (Flat)	13.1	13.9	23.4
	SiN, 3.5% BN (Edge)	36.5		
	SiN, 40% BN (Edge)	35.1		
	SiN, 15% BN	26.2		
	SiC (Hipped)	116.1		16.5
	SiC (Post Hipped)	102.0	54.5	
	SiN, 0% BN		17.9	13.1
1300°F	SiN, 40% BN (Edge)			
	SiC (Hipped)		93.1	
	SiC (Hipped)			144.1

[1]τ = Frictional force ÷ contact area of wear scar. Expressed in Newtons per square meter.

ceramics (α-SiC not included in that study) on grain size (107). It is most important to recognize that the Hall-Petch relationship does not necessarily hold where a second phase (e.g., in glassy grain boundaries) is present in the ceramic.

Disagreeing with the findings in (104), Cranmer et al (108) found the Hall-Petch mechanism inoperative in dense, hot-pressed (HP) α-SiC. They demonstrated that the strength failure of the material is caused by machining-induced flaws, whose size and severity interact with the grain size to produce a *combined* effect. The severity of the flaws decreased with small grain size for a given machining grit size, and the size of the flaws decreases with increasing grit size. Smoak and Kraft's work (109) essentially agrees with these findings by showing that the strength of sintered α-SiC does not follow Hall-Petch type behavior. As depicted in Figure 77 taken from (109), the large grain structure, ~98% dense, pressureless-sintered α-SiC (obtained by post-sintering heat-treatment of the commercially prepared, fine grain structure material originally exhibiting 7 to 10 μm size, equiaxed grains) actually exhibited a slightly higher strength than the fine grain structure material. The problem with Smoak and Kraft's conclusion was the obfuscating (deleterious) effect of pores, just as deleterious as the machining flaws, which influenced the results in (108). Degradation was especially noticeable, where small-grain samples failed flexurally at lower loads.

One important observation was similar to what we found in the present study: the fracture of the large grain α-SiC appeared to be transgranular, while in the small-grain homolog it was intergranular (but heavily influenced by the porosity). Another key observation from a different source (110) was the similar type of intergranular failure the small-crystalline and pressureless-sintered α-SiC material [also used in (109)] suffered during unlubricated, room-temperature tribotests. In other friction and wear tests, again with the same α-SiC, both intra- and transgranular failures occurred at room temperature (111).

These data appear to be somewhat inconsistent. There could be other variables, which had not been accounted for in fully explaining the mechanism of wear. One such variable may be the chemistry of the sintering aid.

It is known that pressureless-sintered α-SiC does not have glassy grain boundaries (110). Yet, pure α-SiC powder cannot be conventionally sintered into a fully dense state without the addition of sintering aids. The most prevalent additives are elemental C, as well as B and Al-containing phases (Table 8). Although the role of the graphite additive (and that of the carbon in B_4C) has been pretty well established (i.e., C reduces the thin SiO_2 layer covering each grain of finely ground α-SiC to permit fusion of the pure α-SiC particle facets), the solubility, lattice position and the detailed role of the B and Al remain unclear (112). On the one hand, researchers in (110) and (113) claim that B and Al segregate to the grain boundaries. In (110) it was suggested that the segregated impurity atoms embrittle the grain boundaries, causing the intergranular failure during unlubricated wear. On the other hand, More et al (112) and

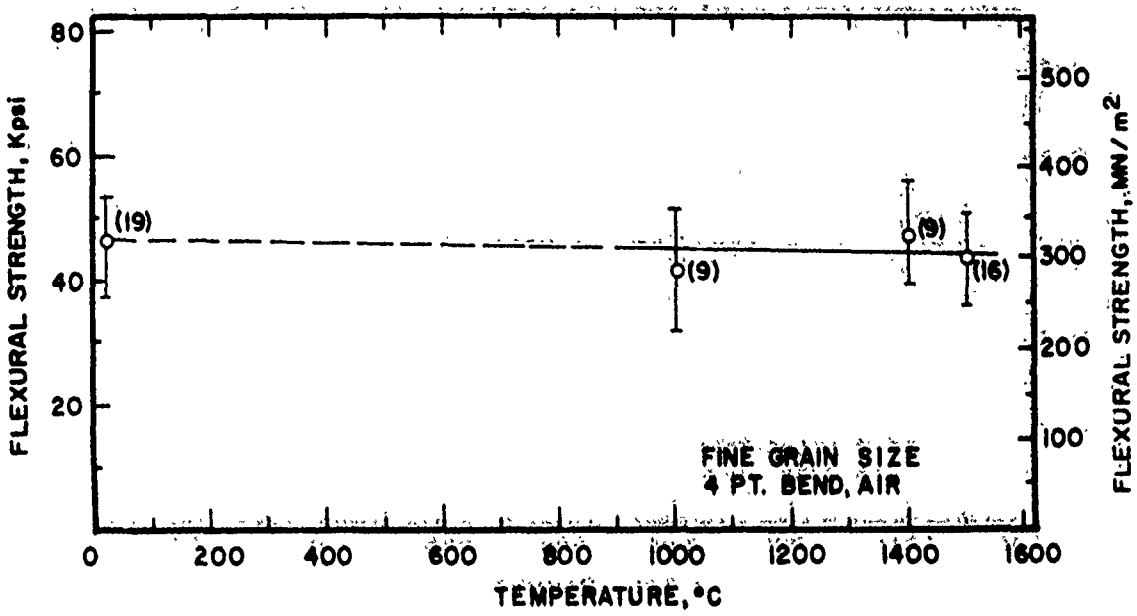

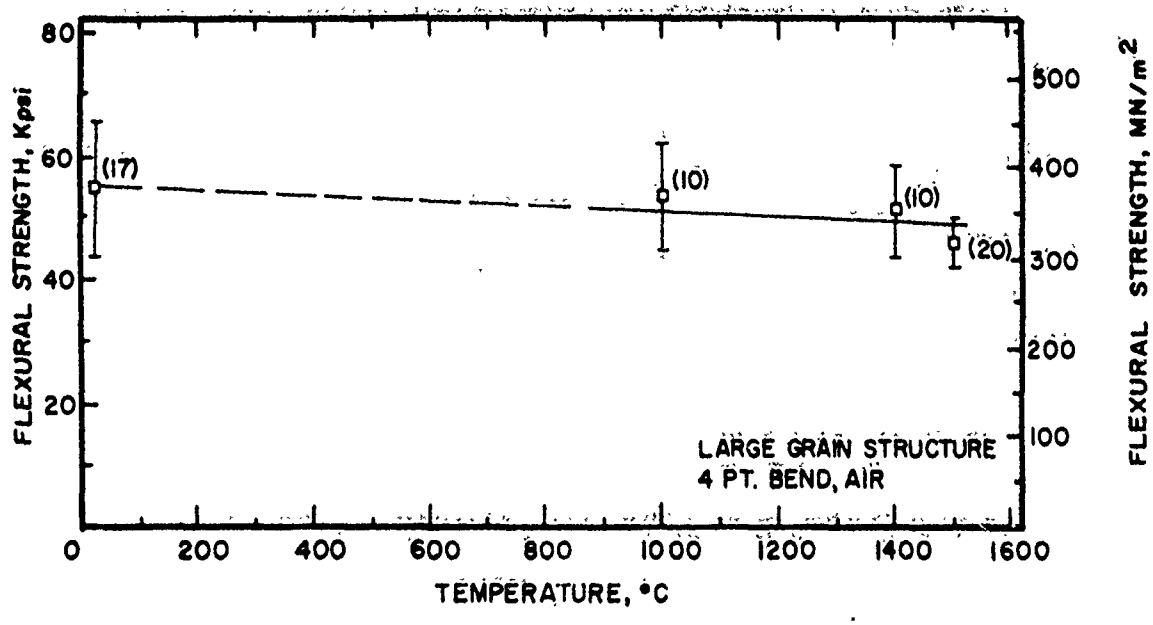

Figure 77. Mean flexural strength of fine and coarse grain α-SiC as a function of test temperature (109).

Browning et al (114) report grain boundaries which were free of any intergranular enrichment of B and Al. Instead, sintered α-SiC contain fine, second phase particles of C, silicon oxide, B_4C and BN (presumed to form by the reaction of B_4C with the N_2 sintering atmosphere). Our own, in-house EDX of polished and worn ESK α-SiC surfaces failed to show any preferential Al segregation anywhere.

According to current belief, the sintering aids enhance grain growth by lowering the grain boundary energy. The controlling mechanism is the increase in the rate at which atomic jumps occur at the grain boundaries (115, 116). Mutual interdiffusion is thus aided by enhanced dislocation motion. The same mechanism also acts within the grains themselves, making them not only larger, but also more perfect. For example, a recent surface analytical examination of the Al/SiC interface indicated that their interaction is sufficiently strong to weaken or break Si-C bonds (117). Aluminum may then be considered as a catalyst for breaking and remaking Si-C bonds, especially at the grain boundaries. The effectiveness of the catalysts depends on the degree of interaction between the host and impurity atoms. Since there is aluminum carbide formation on the carbon-rich sides of the SiC habit planes [e.g., the (111) in the β-SiC and the $(000\bar{1})$ in α-SiC, also see (117)], that particular reaction may influence the degree of catalytic action.

As Dr. Irwin L. Singer (NRL) described it in his presentation at the Nov. 1989 Final Program Review in Dayton, OH, one must not lose sight of the formation of various binary, ternary and quarternary phases (e.g., mullite, silica glass) when SiC and Al_2O_3 interact in the presence of oxygen (Figure 78). The highly adherent, SiAlON-like grain boundary phase (if any) appears to be an efficient adhesive for the grains, even though the more refractory nature of these phase(s) always require HP or HIP processes for pore-free consolidation.

Additionally, between B and Al, B tends to cause more pronounced grain growth during pressureless sintering and any post-sintering densification (e.g., HIP) than Al (118). *Excessive* grain growth due to the presence of B and/or high post-sintering densification temperatures had a negative effect on the flexural strength of the α-SiC (118).

So far it is reasonably apparent that the proper balance of temperature/sintering aid/post-sinter-densification must be struck to impart the best structural integrity to a polycrystalline, α-SiC monolith. Nevertheless, the fundamental understanding of a microstructure-to-wear (or strength) relationship is still not sufficiently elucidated to provide unambiguous explanation of α-SiC consolidation practice vs. wear resistance (see continued discussion).

3.1.1.4.2 Consolidation Process vs. Wear in the Continuum Regime. The three densification techniques combined with the two different sintering aid packages described in Table 8 represent the most often used α-SiC preparation techniques

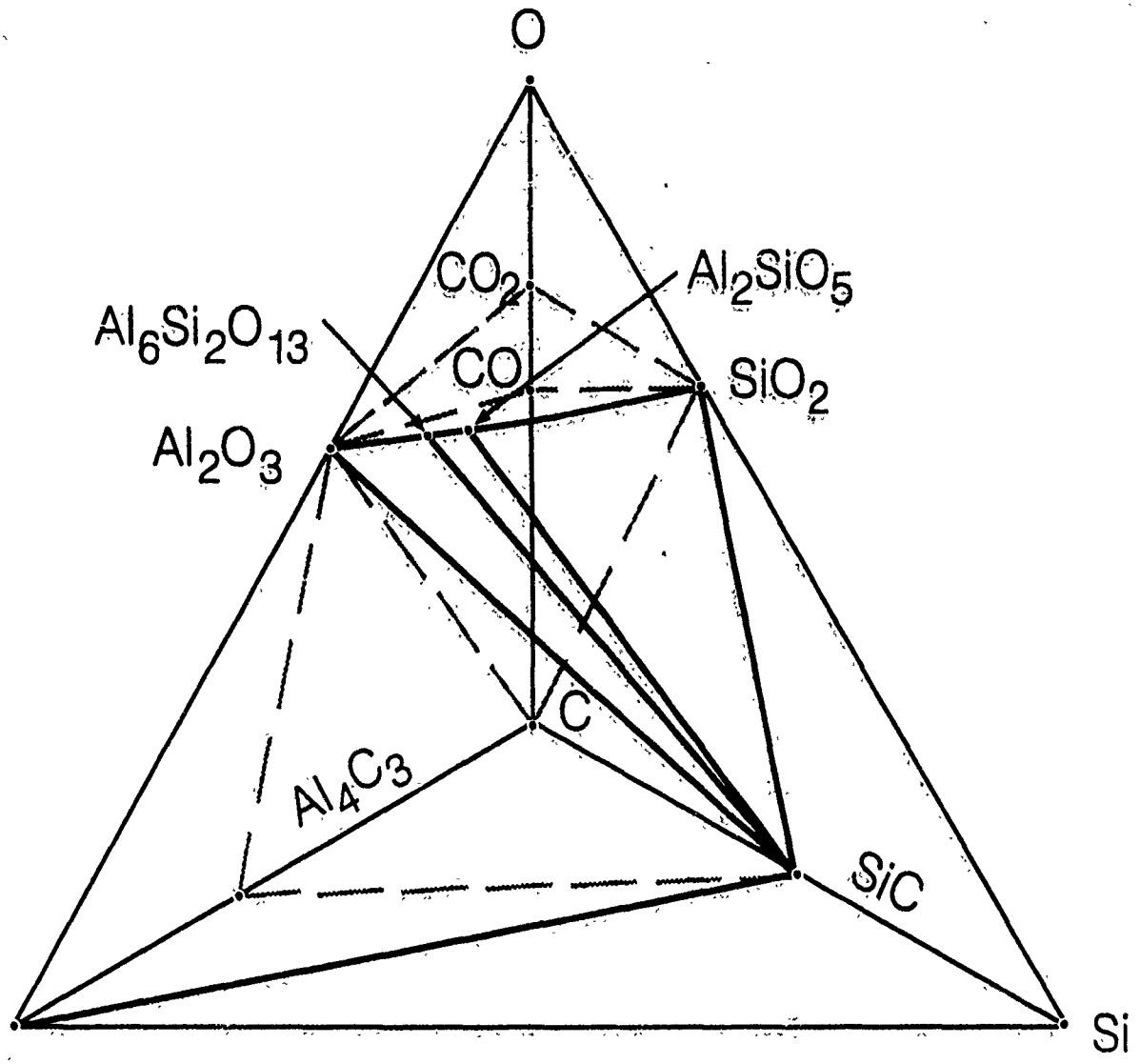

Figure 78. Oxidation of the ternary system Al-Si-C: a schematic quarternary phase diagram (courtesy of Dr. Irwin L. Singer, NRL).

Pressureless sintering is the oldest and most widely employed fabrication method. Full can-HIPing and sinter-HIPing, in two separate steps or in one all-encompassing process, comprise the most advanced consolidation techniques [see Figure 79, taken from (119)].

As shown in Figure 79, during pressureless sintering and HIPing, the powder mass under consolidation is heated only once. When an α-SiC mold is compacted by HIP after sintering, the material is heated twice; these are two separate processes, with a cool-down in between. This up-down temperature cycling is considered deleterious, because of the previously explained thermal expansion and elastic anisotropy-caused residual stresses developing between the grains. After considerable research (118, 120, 121), ESK has developed their modern HIP (single process) and sinter-HIP (also in a single process) methods. The data in Figures 80 and 81 show the outstanding strength vs. temperature and thermal conductivity characteristics of the HIP-processed α-SiC, in contrast with those provided by the older pressureless sintering and hot-pressing (HP) methods. These data also reveal (a) the poorer intergranular vs. transgranular strength of HP α-SiC, (b) the relative insensitivity of α-SiC strength as a function of temperature (typical of a ceramic missing the glassy grain boundary phase; also see (121) for similar strength data on α-SiC), and (c) the greater electron and phonon thermal conductivities of both the HIP grains and grain boundaries. The latter property is attributed to more perfectly fused grains and grain boundaries and the much lower porosity of the HIP ceramic. Efficient high pressure and temperature enhanced diffusion in the HIP α-SiC was demonstrated, when a fractured α-SiC cylinder was rebonded by the HIP process with no help from any interfacial, sintering aid "adhesive" purposely applied. The original structure integrity was fully recovered at the bondline (121). Indeed, consolidation by HIP allows the use of much less sintering aid (Table 8).

Inasmuch as the strength of the pressureless sintered α-SiC is less than that of the other two, more advanced (HIP) versions, one would expect higher relative wear of the former at any temperature. Such higher relative wear did occur at room temperature, but not at high temperature. It appears that at room temperature, the bimodal grain size distribution controls both the strength and the fracture toughness (as measured by the critical stress intensity factor K_{Ic}). According to Faber and Evans (123), K_{Ic} generally increases with increasing grain aspect ratio, as confirmed by experiments on Si_3N_4 ceramics. The high fracture toughness of HP-Si_3N_4 is itself attributed to the high aspect ratio of the rod-like β–Si_3N_4 grains intertwined to form an interlocked structure. A crack propagation path through a fine, equiaxed grain material (where fracture is more intergranular) should be less tortuous than in a coarser, more interlocked grain structure counterpart. Yet, the wear of the smallest grain size ESK HIP α-SiC here is lower at room temperature than the higher grain size, more porous, pressureless-sintered version. In contrast, the wear of the HIP α-SiC is also the highest at high temperature among all of the candidates.

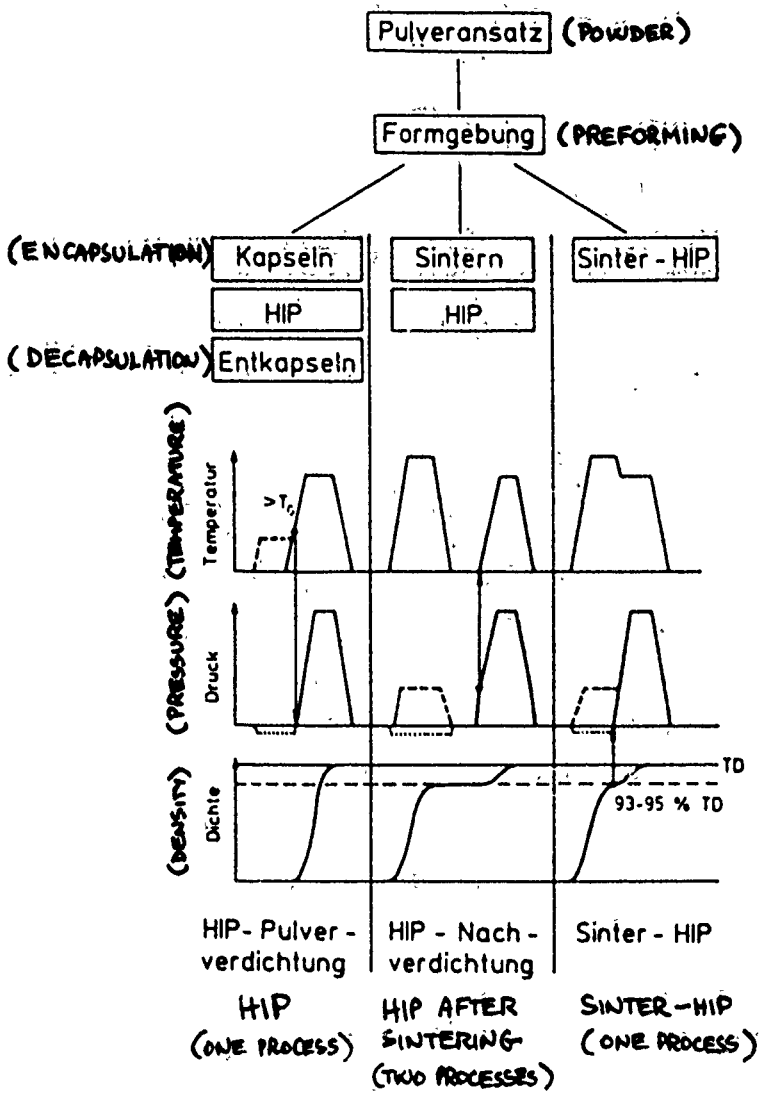

Figure 79. Various ceramic powder consolidation processes (also used for α-SiC), involving hot-isostatic pressing (HIP); (119).

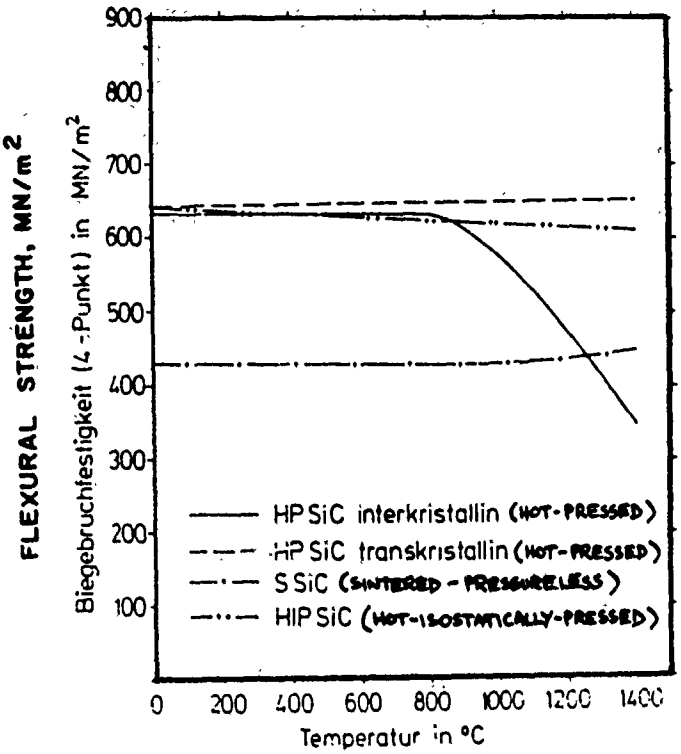

Figure 80. The effect of temperature on the flexural strength of variously prepared, α-SiC, 4-point bending strength specimens (120).

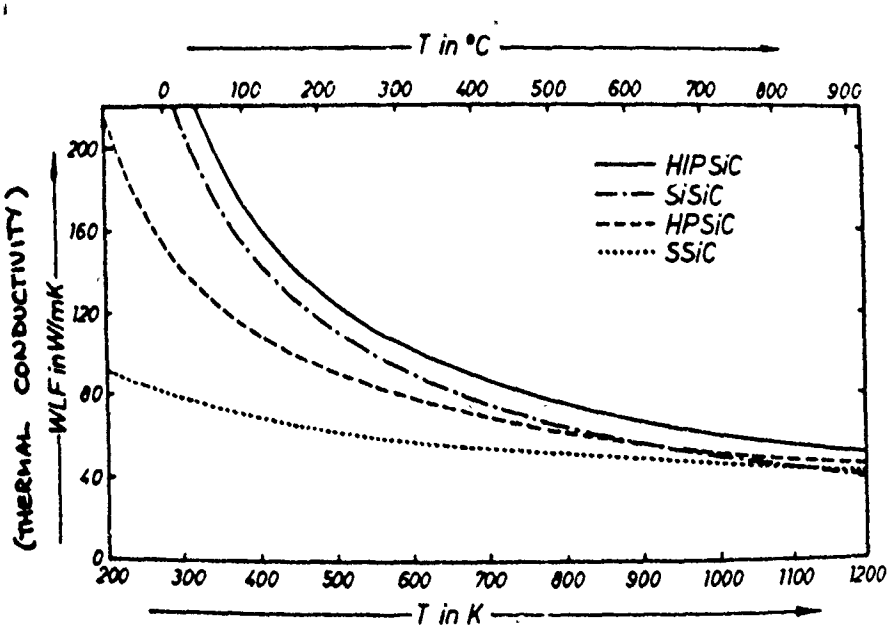

Figure 81. The effect of consolidation methods on the thermal conductivity of α-SiC (120).

Generally, the rate of diffusion-controlled plastic deformation has an inverse proportionality to the square or cube of the grain size (depending on the actual deformation mechanism), see (124). In fact, certain ceramic-type materials [e.g., TiO_2 and CaF_2, see (125)] exhibit unusually high ductility at low temperatures, where their polycrystalline versions were consolidated with a crystalline size of only a few nanometers. However, in most ceramic materials, diffusional creep is significant only at temperatures greater than 1000°C (125, 126). Therefore, it is unlikely that higher *apparent* wear with α-SiC can be caused by diffusional creep. Therefore, the highest wear of the fine-grain HIP-SiC at ~850°C cannot be explained by this mechanism. It is a lot more likely that the application of the high HIP pressure alone, in the absence of a sintering aid, could not quite achieve optimum grain boundary fusion. As a consequence, the small-grain-size structure, exhibiting slightly weaker grain boundaries more conducive to crack propagation, may have caused the HIP version to wear more than the sinter-HIP α-SiC.

This argument, however, does not explain why such low wear was exhibited by the more porous (albeit larger and more bimodally distributed grain size), pressureless-sintered material at elevated temperatures, see Figure 74.

It is suspected that high temperature wear of polycrystalline α-SiC is influenced not only by the differences in grain size and grain boundary action at elevated temperatures, but also by the possible formation of glassy surface layers on the respective materials' rubbing surface. The relatively low-temperature-melting, glassy layers may alter the interfacial shear stress state and consequently, change the degree of surface/subsurface cracking and wear.

3.1.1.4.3 Glassy Surface Layer Formation. Although B-containing grain boundary phases do not exist in B_4C-sintered α-SiC, there is the probability of B diffusion to the ceramic's surface at ~850°C and oxidation to B_2O_3. B_2O_3 then reacts with the oxidation produce of SiC (i.e., SiO_2) and forms a thin, glassy layer. To a certain extent, this low shear strength film may act as a high temperature "lubricant." It is well-known that the B_2O_3-SiO_2 liquidus occurs at less than 400°C, at 1 atmosphere.

Progressively higher B concentrations and an oxygen atmosphere both increase the diffusion coefficient of B in Si (127, 128). B also tends to segregate at the Si/SiO_2 and Si/Si_3N_4 interfaces at 850°C. It follows that the oxidation of B to B_2O_3 at the polycrystalline α-SiC sliding surface, combined with the oxidation of α-SiC to SiO_2+ CO/CO_2 can form the precursors for low-melting, borosilicate-type, glassy surface layers. Such layers were observed on Carborundum's pressureless-sintered α-SiC; this type of a layer began to increase the break-away friction force at temperatures as low as 900°C in air, at *very low* sliding *speeds* (129). On the other hand, at *higher speeds*, the glassy B_2O_3-phase generated from the oxidation of TiB_2-containing ceramic composites reduced the f_k to as low as 0.1 to 0.2 at 700° to 800°C (130). It is also known that in the absence of an oxidizing environment, B does diffuse to the surface of vacuum-heated (to 800°C), nitrogen-strengthened austenitic stainless steel and becomes converted to BN there; BN was similarly generated on the surface of laboratory-melted 304 stainless steel doped with N and B, and that doped with N, B and Ce (131). The high oxidation resistance of h-BN

(132) notwithstanding, some finite oxidation to B_2O_3 does occur. Boria can react with a borosilicate glass to further reduce its melting point and increase friction (133), at least at low sliding speeds and especially during break-away, as also in (129). B_4C itself oxidizes into B_2O_3 (134), yielding a high friction, glassy surface (135).

Although SiC exhibits oxidation resistance much higher than Si_3N_4 (136, 137), the type of sintering aid in SiC does influence (i.e., increase) the oxidation kinetics of the ceramics. This difference can be substantial in our temperature range of interest (~850°C), see Figure 82. It stems from the differences in the chemistry of the respective silica glasses that form on oxidation of SiC and Si_3N_4.

In the case of the residual B/B_4C in the pressureless sintered Hexoloy SA-80T α-SiC, the SiO_2 content formed (statically) on an oxidized surface increases gradually with time, then it saturates. This is caused by the difference in the formation rates of SiO_2 and B_2O_3 from the respective carbides (138, 139). This difference is depicted in Figure 83. Inasmuch as it is well-known that (a) the oxidation of the respective substrates is dependent on the diffusion of oxygen through the glassy layers generated, (b) the diffusion of oxygen through B_2O_3 is greater than through SiO_2, (c) the excellent diffusion barrier properties of SiO_2 became degraded by the presence of dopants/contaminants, and (d) the degree of degradation depends on the chemistry of the dopant (140, 141), it is essential that an SiO_2 protective layer of sufficient thickness, containing the least O_2-diffusion-accelerating specie(s) be present on a tribooxidated ceramic surface. Indeed, the presence of SiO_2 formed from the oxidation of SiC protects graphite and B_4C from oxidation (i.e., from weight loss) better than the B_2O_3, which is formed from the oxidation of B_4C alone (Figure 84), see (142). As another example, the temperature of BN oxidation shifts to lower temperatures with increased B_2O_3 content; at the same time, the oxidation kinetics increase (143).

Although the diffusivity of O_2 through borosilicate glasses is greater than through mullite ($3Al_2O_3 \cdot 2SiO_2$), increased amounts of Al_2O_3 sintering aid in dense HP α-SiC themselves increase the oxidation kinetics of the ceramics (144). The relative ability of the cation to promote oxidation probably stems from the cation's ability to split molecular oxygen and transfer it to SiC (145).

The above argument about the undesirability of the glassy layers is confirmed by our friction and wear data in Tables 5, 10, 11 and 12, as well Figures 74 through 76: the glassy layers do reduce the shear strength of α-SiC at high temperatures, but at the cost of substantially increased wear rates. The comparison of the data in Table 10 and Figure 74 is especially revealing: the α-SiC which exhibits the highest wear rate at R.T. (Hexoloy) and, as such, has the largest wear scar, also shows the lowest apparent τ_s; the lowest wear rate/smallest scar (ESK sinter-HIP) has the highest τ_s; the ESY HIP is in the middle in both cases. At H.T., where glass formation is copious in all cases, the τ_s values are equalized (more-or-less) by the high wear rate. It is, therefore, important to understand not only how thick the oxide layer becomes and what causes the thickness differences in terms of sintering aid chemistry, but what enables

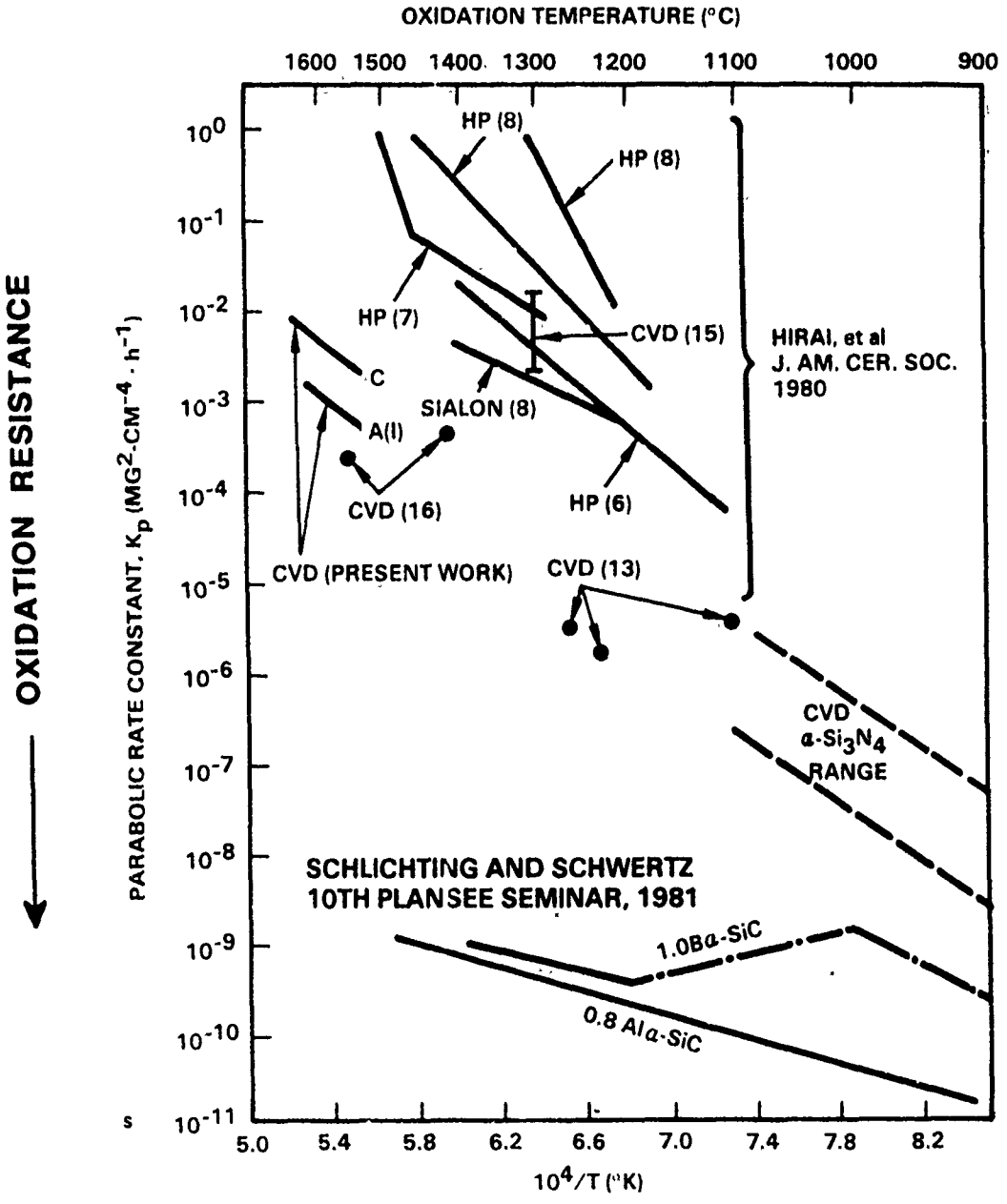

Figure 82. The oxidation kinetics of SiC and Si_3N_4 (136,137).

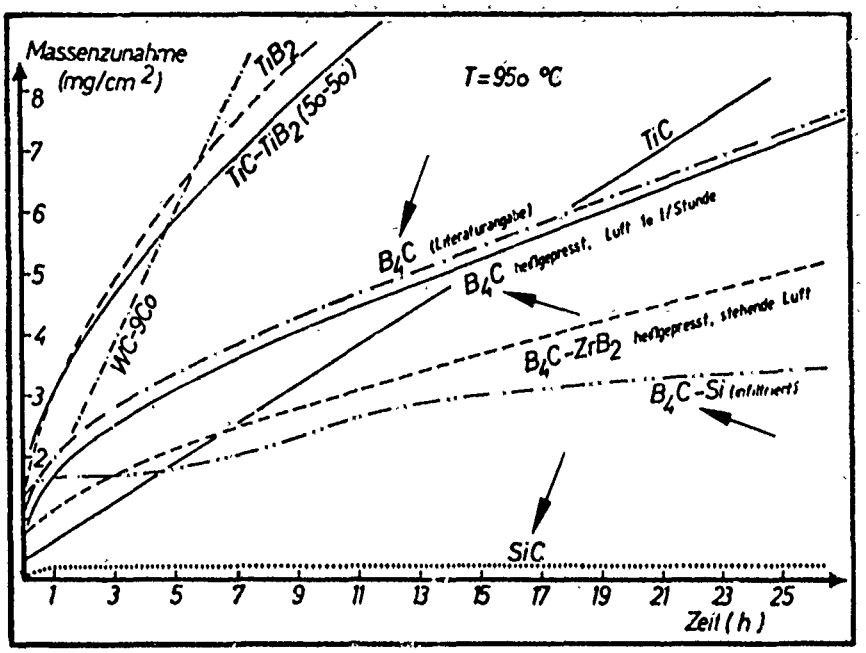

Figure 83. Oxidative weight gain vs, time functions of various ceramic materials (139).

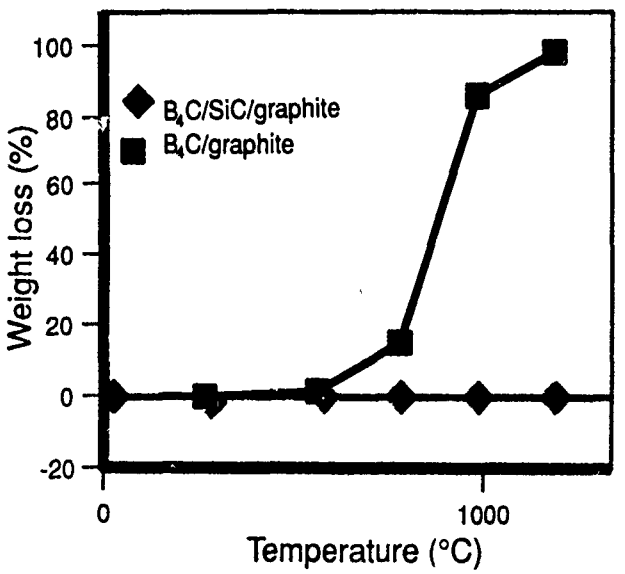

Figure 84. Weight loss of B4C/graphite and B4C/SiC/graphite (3 hours exposure, flowing steam-saturated argon); from (139).

(or prevents) the glassy layer to display the kind of load-carrying capacity (associated with the low shear strength) normally attributed to oil-based elastohydrodynamic (EHD) films.

As shown in Figures 85 through 88 depicting new and R.T.-tested α-SiC rubshoes, surface glass forms even when the specimen combination is not externally heated, i.e., formed by frictional heating alone. Most of the glass, however, is being displaced out of the wear scar. The act of sliding under load sweeps the layer into the exit region. AES/XPS analysis of both the middle and exit regions (the ~1 μm thick, cracked glassy layers) indicated that (a) there was no substantial glassy layer in the middle of the scar (only a < 1 nm layer was left behind), and (b) the exit glass did not contain measurable amounts of B or Al. Note that the 5000X magnification photos here also depict the grain structure differences previously shown in Figures 72 and 73.

The poor load-carrying capacity of the SiO_2-based glasses is not surprising in view of their well-known, anomalous compressive behavior.

In crystalline solids, the hydrostatic pressure derivatives of the bulk and shear moduli are positive: the higher the pressure, the more difficult it is to compress or shear the solid. In parallel, the temperature derivatives of these moduli are negative: the higher the temperature, the easier compression and shear becomes. In complete contrast to this is fused silica, BeF_2, Pyrex glass and selected other glasses, because their bulk modulus decreases with increasing pressure to about 2.5 to 3.0 GPa (the more the glass is compressed, the easier it is to compress it further). These materials have negative pressure and positive temperature dependencies of both the shear and bulk elastic moduli and negative thermal expansion at low temperatures (146 through 149), see Figure 89.

As explained by Hazen and Finger (150), the basic building blocks of the quartz structure are silicon-centered tetrahedra. Each tetrahedron shares four corners with four other tetrahedra to form a three-dimensional network. The small tetrahedra are rigid, changing less than 1% (by vol.), even at pressures as high as 10^4 atmospheres. Yet, quartz is ten times more compressible than its constituent tetrahedra, because the angles between the shared corners are free to bend. The bending of the bond angles between the silicon and oxygen ions requires much less energy than shortening the bonds between them. As a consequence, polyhedron-tilt becomes a more efficient mechanism of compression.

These data indicate an explanation for the marginal load-carrying capacity of glassy oxide layers generated on tribooxidatively degraded SiC and Si_3N_4 surfaces.

To further exacerbate matters, the layers that vitrify on or near the sliding surfaces tend to crack even if no load were applied (e.g., see Figures 86 and 88). Cracking occurs because of the molar volume reduction-induced tensile stresses that exist there. When load is applied, its amplitude to initiate a fatigue crack was used in (151) to calculate the applied stress intensity factor amplitude shown in Figure 90. For the range of thickness shown, there is an 18% decrease in the load necessary to initiate a crack in the silica glass scale formed on a Al_2O_3-SiC ceramic composite. The presence of this vitrified surface glaze

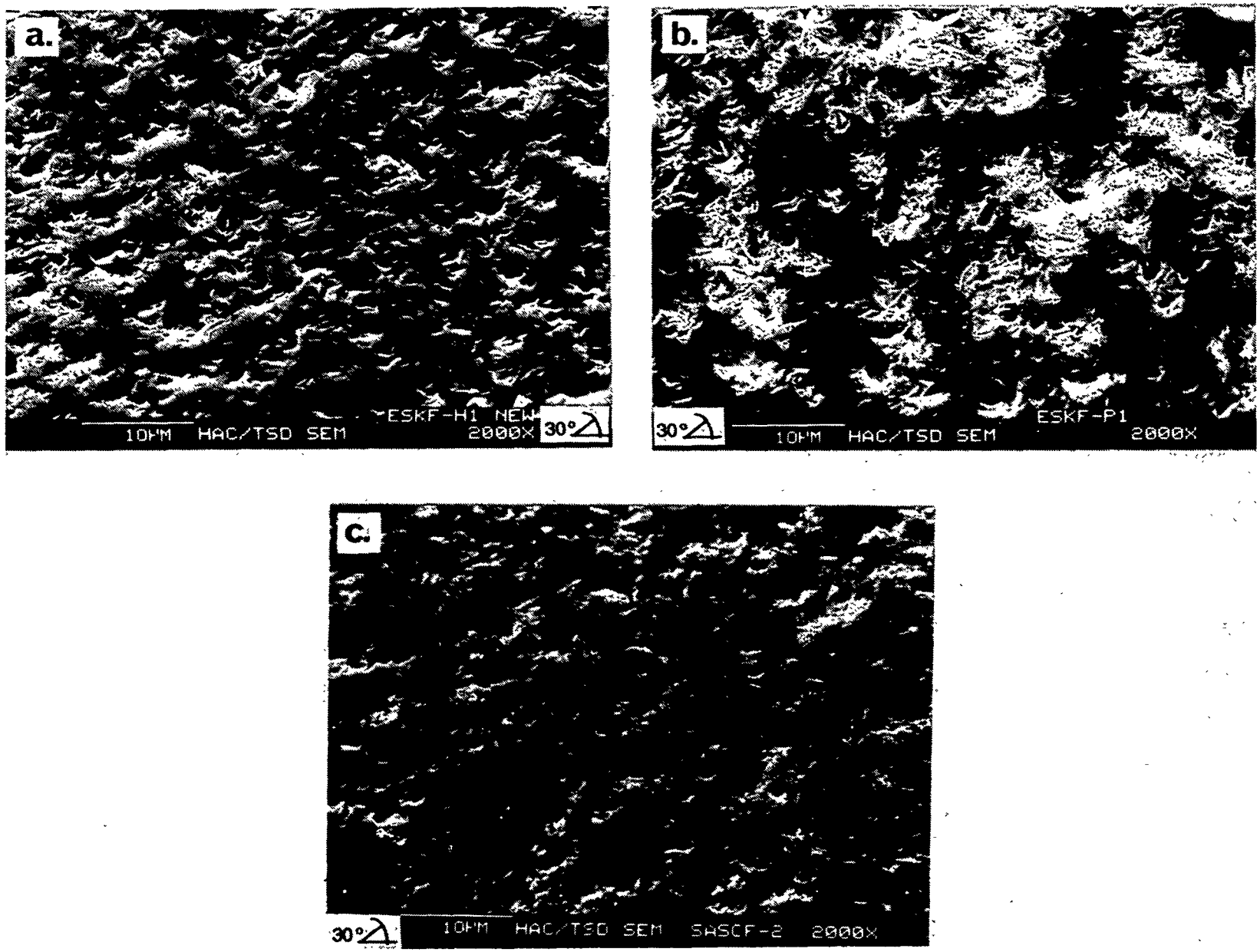

Figure 85. SEM photomicrographs of as-polished, α-SiC Tester 2A rubshoe surfaces: (a) ESK fully can-HIP (rubshoe No. ESKF-H1), (b) ESK sinter-HIP (rubshoe No. ESKF-P1), and (c) Hexoloy SA-80T (rubshoe No. SASCF-2).

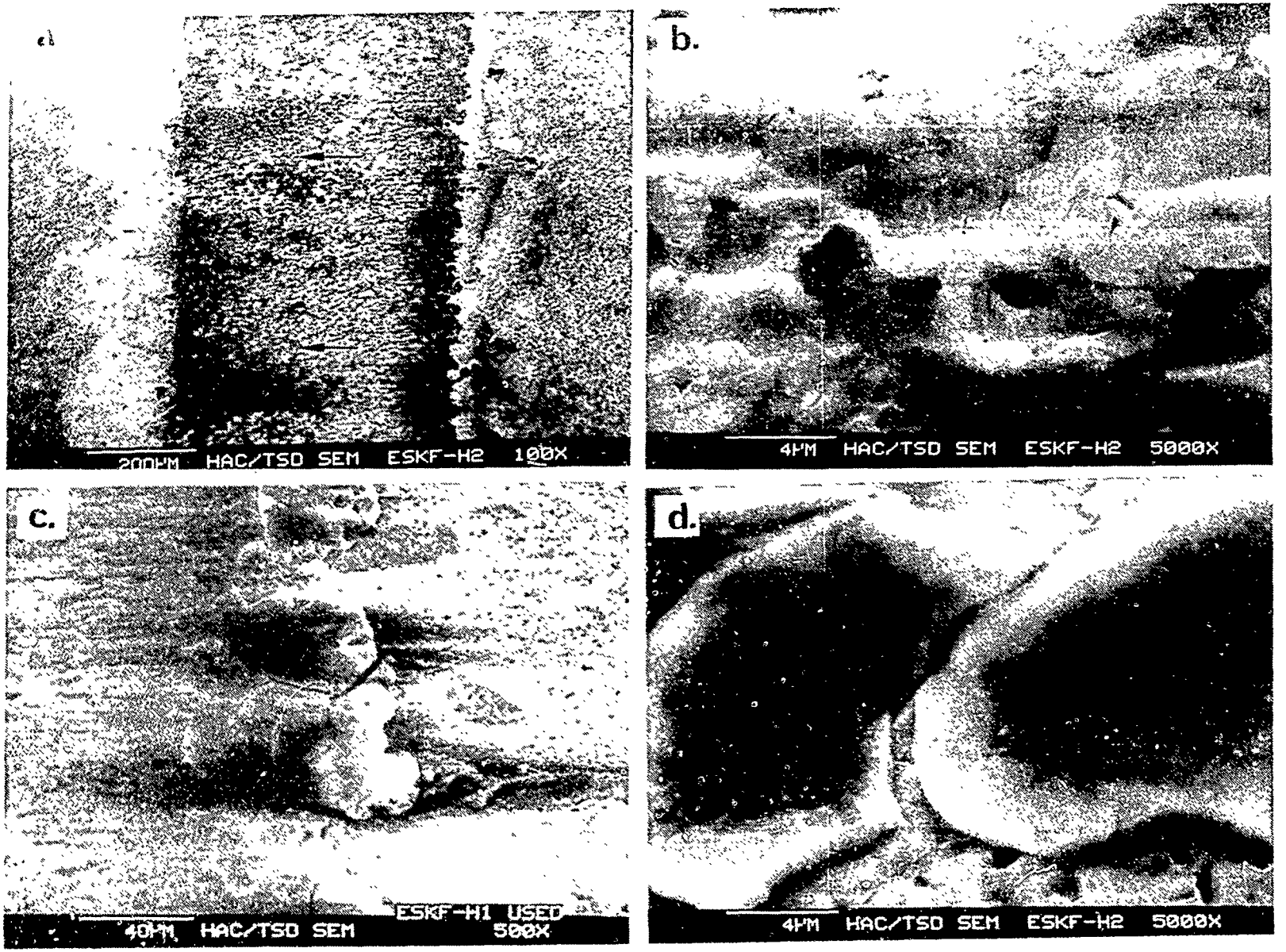

Figure 86. SEM photomicrographs of the used (R.T.) Figure 85a (ESK-HIP) rubshoe wear scar: (a) the wear scar, with arrows indicating the direction of sliding, (b) middle of wear scar, (c) and (d) edge of wear scar at the outlet region, depicting cracked glassy layer

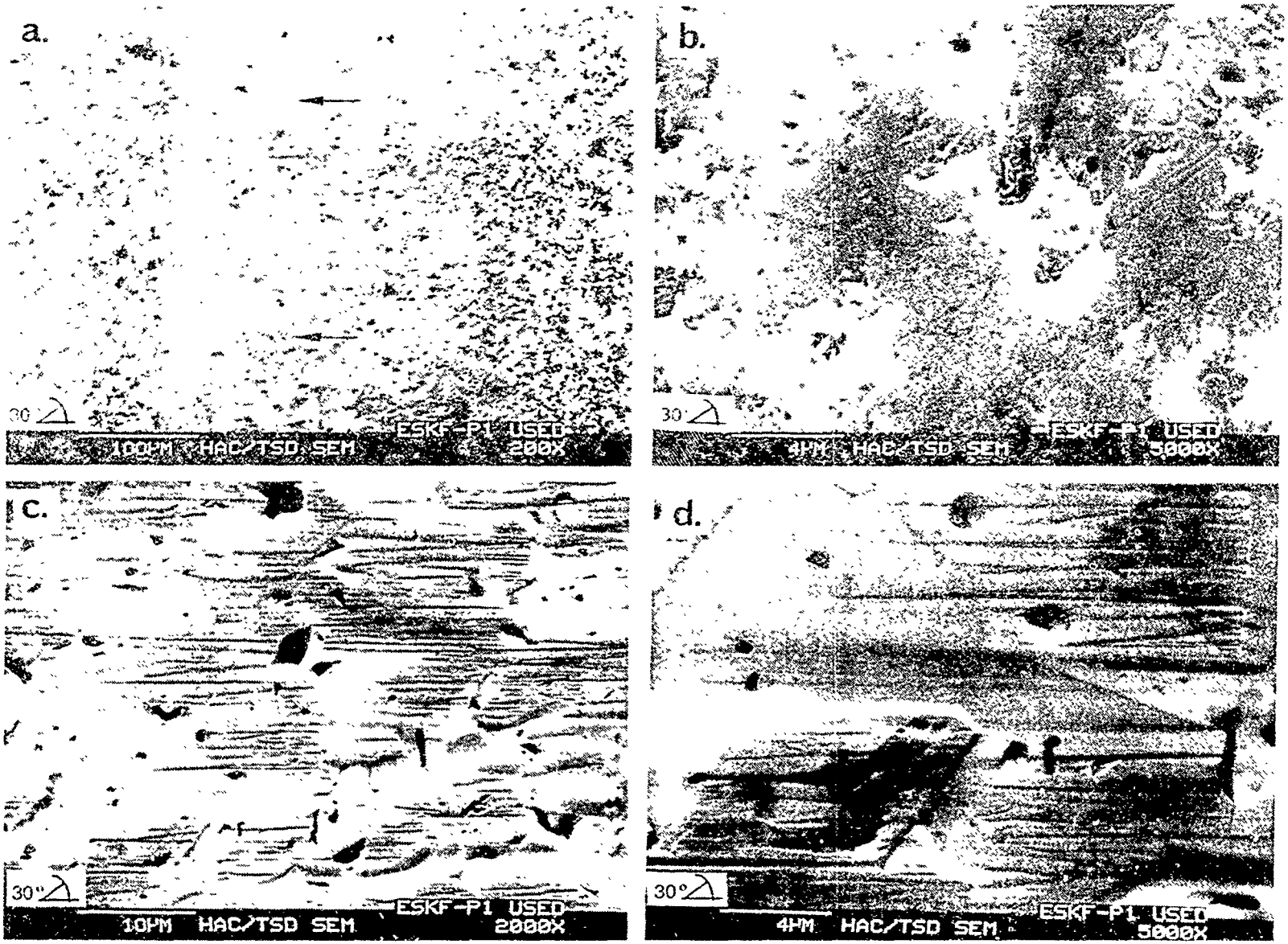

Figure 87. SEM photomicrographs of the used (R.T.) Figure 85b (ESK-HIP) rubshoe wear scar. (a) the wear scar, with arrows indicating the direction of sliding, (b) unused portion adjacent to wear scar with little evidence of accumulated glassy layer, (c) and (d) middle of wear scar.

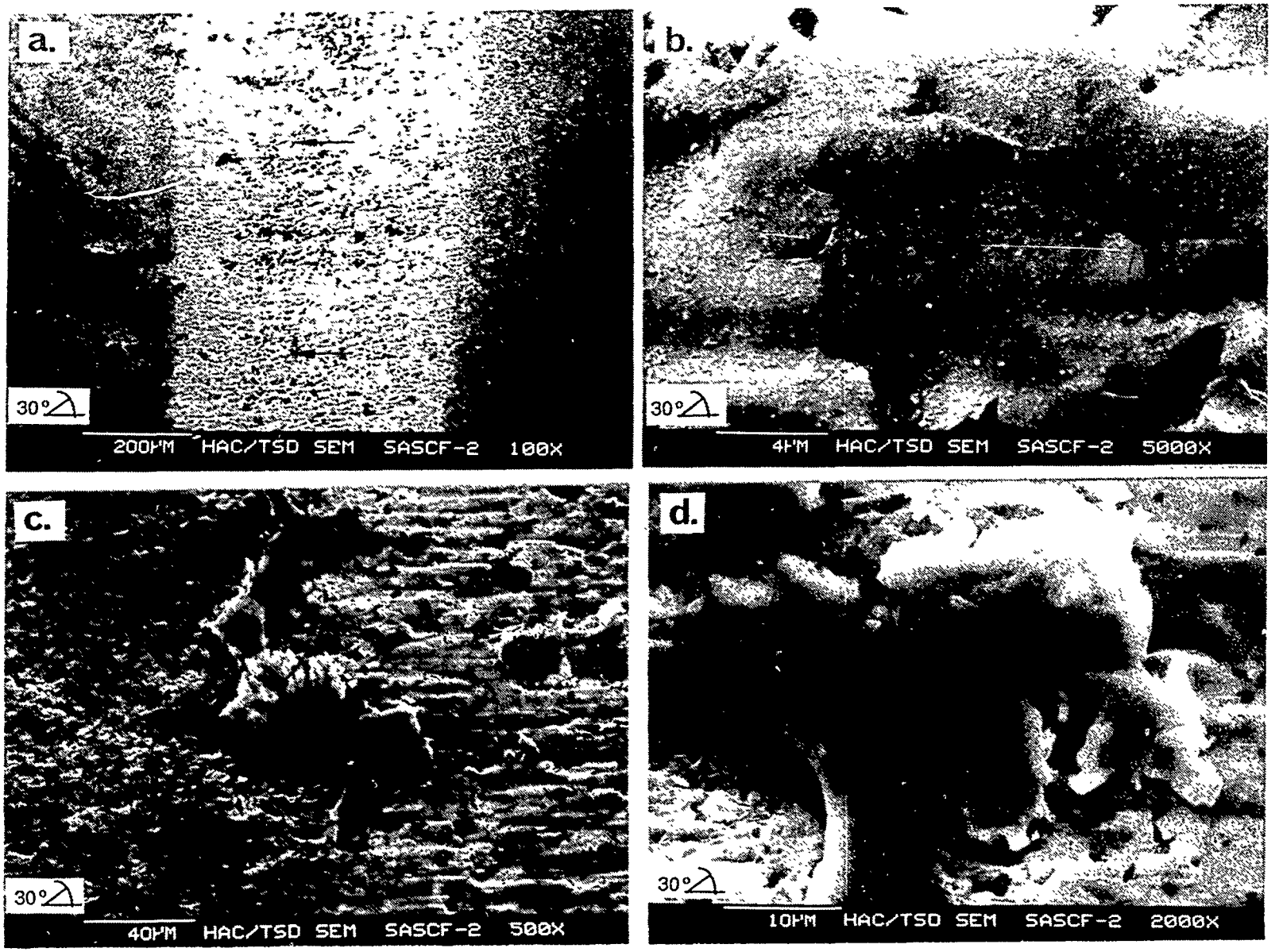

Figure 88. SEM photomicrographs of the used (R.T.) Figure 85c (Hexoloy) rubshoe wear scar: (a) the wear scar, with arrows indicating the direction of sliding, (b) middle of wear scar, (c) and (d) edge of wear scar at the outlet region, depicting cracked glassy layer.

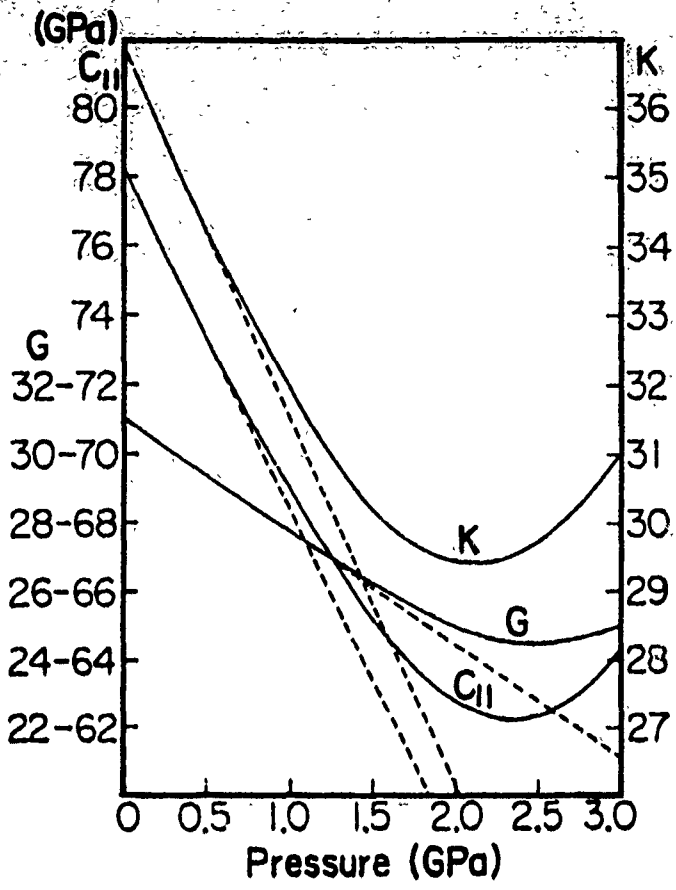

Figure 89. The elastic moduli of fused quartz as a function of hydrostatic pressure; C_{11} = longitudinal, G = transverse (shear) and K = bulk moduli (147).

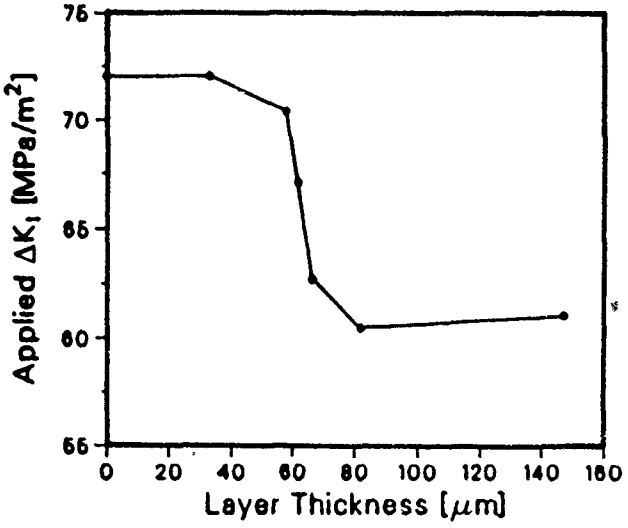

Figure 90. Decrease in the magnitude of the applied load needed for surface crack initiation as a function of silica glass scale thickness on Al_2O_3-SiC composite (151).

increases the susceptibility of the material to crack initiation. Once the crack starts, it tends to grow larger and wider, penetrating the unreacted substrate. It will be shown later in 3.1.3 herein that Hughes Vickers hardness (H_v)-indentation-induced critical stress intensity factor (K_{Ic}) measurements also showed a distinct reduction in fracture toughness of oxide-glaze-containing α-SiC and Si_3N_4 surfaces.

Such cracking is made worse by the thermo-mechanical action of a high-speed friction load (152, 153). Superimposed is the role of interfacial grain-bridging sliding friction on the crack and grain pull-out resistance of the substrate (154) and some steady-state creep of Al and B-containing α-SiC at high temperatures, under load (155).

3.1.1.5 The Tribological Behavior of α-SiC Ceramics (Conclusions) and Potential Applications for α-SiC.

Based on the above information, the following main conclusions may be drawn:

1. At R.T. the controlling factor for wear is the grain structure-related fracture toughness and hardness of α-SiC.
2. At H.T. a less oxidation-resistant α-SiC forms more glassy oxide layers, which do provide a lower τ_s; the surface glass is removed rapidly, however, and thus the wear rate is increased substantially.
3. Under thermal cycling, the glassy layer-induced reduction in fracture toughness at R.T. will result in increased wear, at or near R.T.
4. In terms of overall wear resistance, the bimodal grain size/shape distribution of the ESK sinter-HIP α-SiC (Al-based sintering aid) was judged best, at any temperature.
5. Alpha SiC is a useful bearing material for high temperature air applications, in spite of its reported lower strength and fracture toughness compared to Si_3N_4. In fact, based on the data examined so far, the high temperature, tribooxidative wear rate of Si_3N_4 should be greater than that of α-SiC, the highest values of R.T. K_{Ic} associated with HP/HIP-Si_3N_4 notwithstanding. It is indeed the case, as will be shown in the following paragraphs.

3.1.2 The Effect of Preparation Method, Sintering Aid and Lubricant Additives on the Friction and Wear of Polycrystalline Si_3N_4

If our hypothesis is correct concerning the effects of tribochemically generated, glassy layers on reducing the friction but disproportionately increasing the wear of silicon-ceramics, then α-SiC should behave better (i.e., wear less) than Si_3N_4 as a bearing ceramic at low-to-moderate loads. However, the stress-altering nature of the soft, low shear strength surface layers should beneficially influence (i.e., lower) crack initiation and propagation in the subsurface, on the surface and at the layer/substrate interface with each material, in a complex manner. Any purposely added inclusions in the ceramics will further alter the cracking (therefore, wear) mechanism.

Consequently, during this portion of the work, we first investigated the theory and practice of predicting the wear of ceramics at room temperature by a continuum mechanical method found pleasing to a theorist and useful to an engineer. This was followed by tribotesting to 850°C in the same continuum regime to investigate the influencing parameters in high temperature air.

3.1.2.1 Wear Equations for Si_3N_4 Ceramics

3.1.2.1.1 Preliminary Theoretical Efforts at Hughes. From the atomistic point of view, crack initiation in ceramic substrates within the hierarchy of microscopic and macroscopic space-time domain models depends on the atomic structure and the nature of the cohesive bonds, the defects within the ceramic as well as the mechanical, chemical and thermal history of the material. Real tribocontacts of varying geometry must also be addressed from a more global, continuum mechanical point of view. There, the sites of crack initiation heavily depend on the geometric configuration, the contact loads and the mode of motion, i.e., rolling, sliding or a combination of both.

Regardless of the mode of motion, the nature of asperity contacts between triboceramics lies anywhere between the extremes of ideally elastic and ideally plastic deformation. The Hertzian (blunt) indentation is characterized by a perfectly elastic contact such that crack initiation is controlled by pre-existing surface flaws (e.g., cracks) whereas Vickers (sharp) indentation is characterized by elastic-plastic contact, such that the subsurface flaws (cracks) are produced by the contact process itself.

Due to the extreme inhomogeneity of the Hertzian elastic field and the overwhelming influence of the surface condition of the ceramic prior to indentation with a ball (i.e., characteristic surface damage in the form of microcracking, as induced by a particular machining process), there is no exact analytical solution to correlate the critical load which causes the ring and cone crack with the initial surface flaw size and fracture toughness. One can only apply expressions for the limiting cases of small and large flaws.

On the other hand, measurements of the radial cracks produced by Vickers indentation can lead to quantitative determination of a ceramic's fracture toughness, as shown by the fundamental considerations described in APPENDIX T. After reviewing the most recent publications on indentation fractography of the normally-loaded Vickers indentor and sphere-on-plane ceramic goemetries (e.g., see 156 through 162), the theory of ball-vs-diamond-pyramid fracture mechanics used to determine the critical stress intensity factor (K_{Ic}) was assessed. Other parametric means describing an as-polished or a tribooxidatively stressed, bare or solid lubricated ceramic surface's tendance for cracking were also examined.

Based on this assessment in APPENDIX T, it was recommended that as a first step towards characterizing the usefulness of as-machined ceramic surfaces for tribological applications, Hertzian ring/cone cracking of these surfaces should be calibrated by Vickers indentation, then investigated for the cracking effects of the Hertzian indentor (ball) diameter (i.e., to determine whether we are in Griffith's or Auerbach's range in terms of surface flaw size, large or small).

It follows, therefore, that the Hertzian cone cracking tests on various ceramic flats must always be accompanied by Vickers fracture toughness tests, at least for this line of reasoning.

Glassy layers which are inevitably generated on the ceramic flats through chemical reactions at high contact temperatures constitute a surface phase distinctly different from the bulk. On cooling, the vitrified surface phase may craze or not, depending on physical properties that control the stresses at the interface. The structural integrity of the altered ceramic surface influences both the Vickers analysis (i.e., the fracture toughness) and even more so, the Hertzian ring and cone cracking results. A similar argument may be made for the presence of not glassy and hard but low shear strength, solid lubricant layers on a ceramic. In the latter case, changes stem much less from coating vs. substrate interfacial stresses than from the stress-altering (-ducing) effects of the softcoat within the ceramic subsurface, under the contact (see second part of APPENDIX T).

A Hughes-developed ceramic wear model, valid under rolling conditions only (APPENDIX U) was subsequently developed, indicating that in addition to thermomechanical stresses, terms describing subcritical crack growth characteristics, the fracture toughness, the initial surface flaw size and surface residual stresses are all important and necessary for accurate modeling of ceramic tribocontacts. Since all of these parameters can be measured, the wear equation in APPENDIX U may be useful for practical applications. A preliminary correlation of NC-132 HPSN RCF data with the predictions of this equation was attempted:

$$t_f = \left[\left(\frac{2}{2-n}\right) Y^{-n} \cdot A^{-1}\left(\sum_{J=1}\sigma_j\right)^{-n}\right] \exp\left(\frac{Q}{RT}\right)\left[\left(\frac{K_{Ic}}{Y \cdot \sum_{J=1}\sigma_j}\right)^{2-n}\right] - \tilde{C}_i^{(2-n)/2}$$

where

t_f = the time-to-failure;

σ_j = the total stress = $\sigma_R + \sigma_T + \sigma_A$, where

σ_R = calculable from H_v;

σ_T, σ_A = determined by thermomechanical stress analysis;

$\tilde{C}_i$ = the initial surface crack (flaw) depth;

K_{Ic} = fracture toughness;

R = gas constant

T = absolute temperature (K) at maximum $\sum\sigma_j$

Y = geometrical factor;

A, n and Q = empirical terms obtained from subcritical crack growth studies.

The agreement with the data in Figure 91 is satisfactory, but only with some caveats. The HPSN bearing fatigue data used there were developed under oil-lubricated conditions. For the predictions in APPENDIX U to coincide with the 0.10 μm crack eventually propagating into a fatigue spall, a 617°C asperity temperature had to be assumed for an oil-lubricated, rolling element bearing tribosurface. While Ward Winer's past work at Georgia Tech indicated that the asperity temperatures ("hot spots") of even oil-lubricated ceramic (sapphire) surfaces could occasionally reach values perhaps as high as that, we do not know if the Parker/Zaretsky study's surface temperatures (see APPENDIX U) could have reached 617°C, because those temperatures were not measured.

Also, this wear equation does not yet take into account any abrasive wear, which occurs under tangential sliding (165 through 169). However, as small as it may be under close-to-rolling conditions (depending on the degree of ball skid and the traction coefficient), an abrasive wear parameter must still be added to an all-encompassing wear equation to superimpose the effects of both wear mechanisms. For this reason, this line of wear prediction was discontinued, and the validity of a simpler wear relationship was pursued, based on indentation-type hardness and fracture toughness experiments (see following sections).

3.1.2.1.2 Vickers Indention and Hertzian Cone Cracking Experiments at Hughes. Four each, 1 cm x 1 cm x 0.3 cm NC-132 hot-pressed silicon nitride (HPSN) coupons, polished on one 1 cm x 1 cm face to less than 2.54×10^{-8} μm (1 μin) CLA, were exposed to high temperature air for 4, 8 and 24 hours in a muffle furnace. Four coupons were retained in the as-polished, original condition. This material represented a good, bearing quality batch used in the previous DARPA/Hughes program (38).

The coupons were exposed for the indicated durations while resting (polished side up) on the center of a Ceralloy 147Y-1 (Y_2O_3-pressed) HPSN plate (Ceradyne, Inc., Santa Ana, CA) acting as a chemically inert, support platform. The temperature of this base plate was monitored continuously with a Type K (chromel/alumel) thermocouple in contact with the top center of the plate. It was assumed that the temperature of the plate was equivalent to the temperature of the coupons. At the end of each time duration, the furnace was turned off and allowed to cool to room temperature with the oven door closed. This procedure was designed to induce no thermal shock to any glassy layer which formed on the polished surface and thus minimize surface cracking/crazing. Excessive crazing would have excessively disturbed the Vickers/Hertzian indentation correlation. It is reasonable to presume that most ceramic moving mechanical assemblies operating at high temperatures would not be thermal-shock-cooled on periodic deactivation.

One as-polished coupon and one ea. of the 4/8/24-hours-exposed coupons were subjected to Vickers indentation tests at 29N (6.5 lbs) to establish test reliability and to calculate the K_{Ic} value and the elastic modulus from the crack size. The data indicated $K_{Ic} = 4.08$ MPa•$m^{1/2}$ for unoxidized NC-132; the literature values for NC-132 range from 4 to 6 MPA•$m^{1/2}$ depending on the method (i.e., indentation or notched/chevroned 3 or 4-point bending tests), with the indentation method-developed value clustering around 4. Note that a higher K_{Ic} value indicate a higher fracture toughness. The crack-length-based

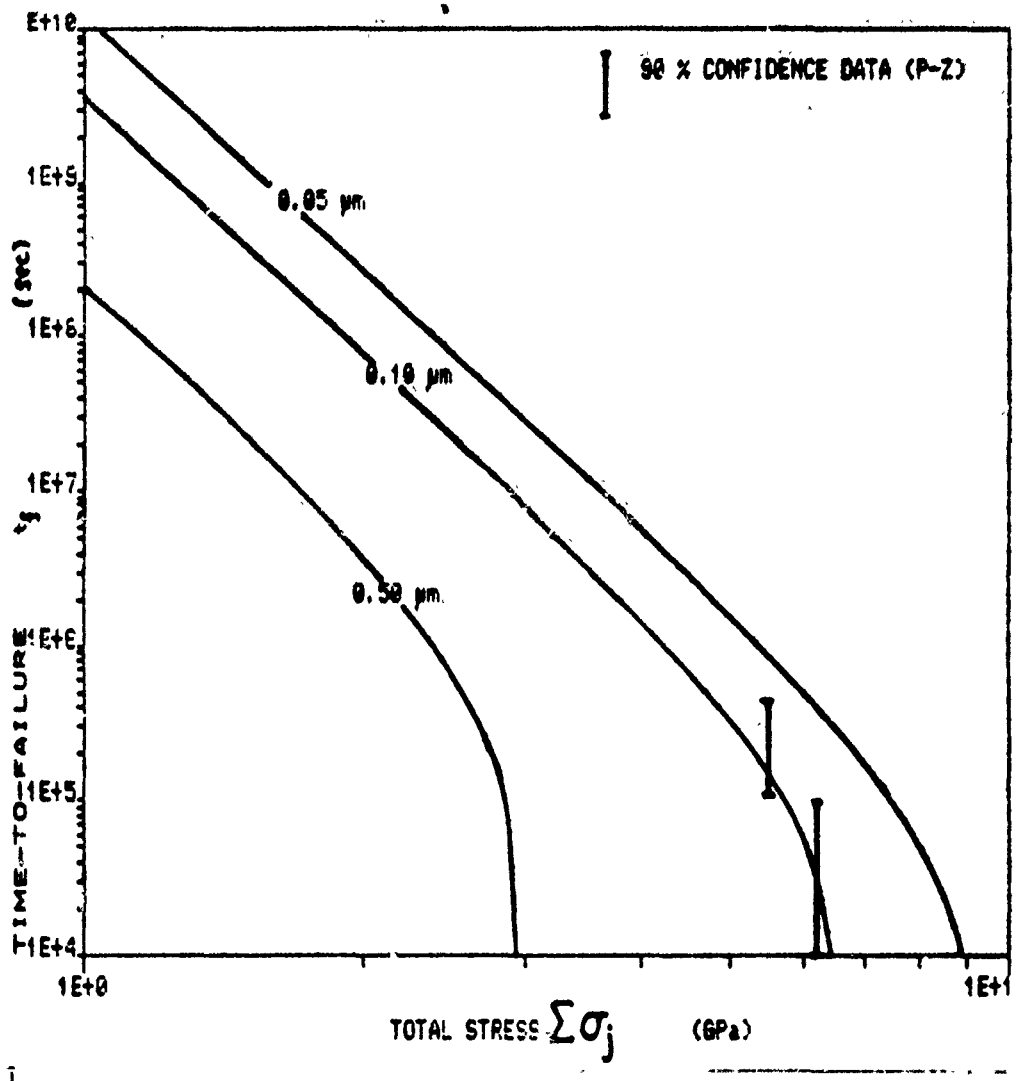

Figure 91. Time-to-failure predictions of NC-132 HPSN tribocontacts containing various initial surface cracks, under high speed motion; assumed operating temperature = 617°C.

Young's modulus was calculated to be 321 GPa = 46.6 x 10^6 psi; Norton's data for NC-132 is 279 GPa = 40 x 10^6 psi.

Since (a) the particular NC-132 HPSN batch tested here was thoroughly examined during the previous DARPA program by scanning laser acoustic microscopy and found to be flaw-free, (b) Saphirwerk (Switzerland) was able to polish Grade 3 (very high precision) balls from this batch for tests with the Williams F-107 cruise missile engine's No. 3 bearing indicating high homogeneity, and (c) not one of these ceramic balls fractured during the severe, high temperature (316°C = 600°F) test using hybrid ceramic balls/steel races -- containing solid-lubricated bearings, the good fracture toughness and modulus values measured here were not unexpected.

The data in Table 13 indicate that at least in the case of the 4-hour-exposed coupon, the very thin, vitrified glassy layer on the surface is detrimental to the fracture toughness of the ceramic substrate bulk, at room temperature. The experimental results were born out by theory (161), in that the stresses developed between a complete glassified layer and the ceramic substrate are in the tensile mode. At 816°C, the thermodynamics of NC-132 oxidation indicate only the generation of α-crystobalite (SiO_2), because the kinetics of magnesium silicate formation [$MgO{\bullet}SiO_2$(enstatite) or $2MgO{\bullet}SiO_2$(forsterite)] from SiO_2 and the MgO sintering aid are extremely slow at the relatively low temperature. Since the molar volume of a complete SiO_2 film is less than that of Si_3N_4, the stresses become tensile at the interface, on vitrification.

The Vickers indentation experiments were done on a conventional microhardness tester (Leitz Miniload), which characteristically generated somewhat lower K_{Ic} data than equivalent values on the same materials obtained elsewhere. At the same time, an existing cone cracking apparatus constructed during the previous Hughes/DARPA program (38) was redesigned to permit semiautomatic measurement of ring/cone cracking of ceramics under load with a spherical indentor. The method utilized was originally described by Grzybowski and Ruoff (162).

Essentially, as-fabricated and high-temperature-oxidized ceramic flats were indented by new, high modulus Co-WC cermet and TiN-coated, Ni-Mo-TiC cermet balls of various diameters at room temperature, to determine the microstructural effects of static load-carrying capacity attributed to inherent crystal structure and second-phase surface layer formation, in concentrated contacts. The rupture of a thin, electrically conductive, RF-sputtered layer of approximately 500-1000Å of chrome-gold on the ceramic flat, on cone-cracking, interrupts a circuit between the metal layer and an electrically conductive ball indenter. In this way, the load can be automatically increased in a controlled manner until, at a critical load, cone-cracking is indicated by a marked increase in contact resistance. This load is sensed by a force transducer installed in-line with the dead-weighted loading rod. Progressively increased loads are applied by mechanical or hydraulic means. One simple means of applying dead weight loads is by pouring fine lead shot into a weighing pan through a funnel equipped with orifices of controlled size. Changing the ball indenter diameter and the lead-shot orifice size of the loading funnel permits

Table 13. Selected mechanical properties of Norton Noralide NC-132 HIPSN, as measured by the Vickers indentation method at Hughes Aircraft Company.

PROPERTY / TECHNIQUE	E (GPA)	H (GPA)	K_{IC} (MPA $m^{1/2}$)
CONVENTIONAL (LITERATURE)	310	17.64 - 19.60	4 - 6
INDENTATION* (THIS STUDY)	321 ± 44	18.02 ± 0.92	4.14 ± 0.11

* INDENTATION LOAD USED RANGED FROM 29N TO 45N

measurements of the critical normal-load-to-fracture of the ceramic flat as a function of indenter radius (i.e., stressed subsurface volume), and as a function on loading rate.

Inasmuch as Lucek (162) demonstrated that new and oxidized NC-132 HPSN flats are cracked by small Co-WC balls at around 9 GPa, the range of experimental variables seemed tractable.

The preliminary Hughes report more thoroughly describing the development of this apparatus is enclosed here as APPENDIX V.

The first few tests at loads up to 7 kg with a 2.38 x 10^{-3} m (3/32 in.) diameter Co-WC cermet ball loaded against an unpolished NC-132 HPSN coupon could not reveal the minute increase in contact resistance necessary to resolve the formation of cone (ring) cracks through tearing the chrome/gold topcoat. First, we thought that the somewhat too thick (approximately 200 nm) and relatively low modulus conductive metal film applied to the first test coupon acted as a subsurface-stress-reducing topcoat (164).

Then, a detailed review of Grzybowski and Ruoff's article (161) revealed that their equation describing the Hertzian stresses between a ball and a flat was wrong. They inverted exponential loading factor of 3/4 into 4/3 (see the second part of APPENDIX V). Inasmuch as during our initial work their equation was used in the first part of APPENDIX V, the resulting load ranges leading to stresses at or above 9 GPa were too low: they were around only 44.5 N (10 lbs.)

The correct loads reached 122.3 N (27.5 lbs) with a 2.381 x 10^{-3}m (3/32 in) diameter, 339.2 N (76.2 lbs) with a 3.968 x 10^{-3} m (5/32 in.) diameter, and 663.3 N (149.8 lbs) with a 5.56 x 10^{-3} m (7/32 in) diameter Co-WC cermet ball loaded against an NC-132 HPSN flat, to reach the approximately 9 GPa unit stresses required to crack the surface of the flat. Inasmuch as the use of the Hertzian cone-cracking technique to determine the size and effects of the surface flaws was abandoned in favor of the H_V-measured K_{Ic} and the toughness/hardness parameters' influence on ceramic wear, further work on rebuilding the Hertzian cone-cracking apparatus and conducting tests therewith was abandoned.

3.1.2.1.3 The H_V and K_{Ic} Dependence of the Polishing Wear of Ceramics

3.1.2.1.3.1 Theoretical Basis. The best-established, independent mechanical strength factors which have been proposed as those determining the wear rate of ceramics are penetration hardness (H_V) and fracture toughness K_{Ic}, (see 170 through 173). Most of the proposed wear relationships were relevant to contact conditions resembling particle impingement or grinding; i.e., where abrasive particles indent, crack and remove stock by abrasive wear from the ceramic substrates, under various degrees of impingement and sliding/rolling mode combinations.

Current technical disclosures as to the applicability of K_{Ic} and H_V-based wear equations center around the following arguments:

1. Mechanical hardness is not a fundamental property, but rather depends on both the elastic and plastic response of the material.

2. K_{Ic}, as measured either by indentation or by bend strength testing, highly depends on the residual stresses and inherent surface flaws left behind by the grinding/polishing process used to prepare a ceramic specimen (174, 175). The machining technique similarly influences the strength (176) and rolling contact fatigue resistance (177, 178) of ceramics.

3. It is suspected but not yet proven whether or not there is any interdependency between H_v and K_{Ic} and if there is, is it the same regardless of the material. Also, the few data which appear to confirm $K_{I_c}^{\alpha} \bullet H_v^{\beta}$-dependent wear equations to some degree may only be fortuitous (172) and, on the whole, may not be as valid as some might hope (179).

According to Rabinowicz (180), when the stressing at the interface is predominated by shear (e.g., during adhesive and abrasive wear debris generation), hardness is generally the most important factor. When the contact stresses are largely normal (e.g., erosion), fracture toughness is more important. Suh and Sin (181) state that, at least in the case of metals, raising the hardness reduces the subsurface deformation, hence the crack nucleation rate; raising the ductility (i.e., the fracture toughness) decreases the crack growth rates. Since most engineering materials cannot be made both ductile and hard, the microstructure must represent the careful optimization of these two different properties. Ludema in (179) agrees that hardness is a fairly reliable parameter of wear, where abrasion is the major cause of it, provided hardening does not occur by cold working.

In the present case, as encouraged by Baldoni, et al's previous work (172), Evans and Wilshaw's wear relationship (171) was utilized to fit the wear of precision ground/polished HP/HIP Si_3N_4 bearing balls during the stock-removal process to the K_{Ic} and H_v values determined for the near-net-shape balls:

$$V \propto \frac{1}{K_{Ic}^{3/4} \bullet H^{1/2}} \sum_{i=1}^{i=n} P^{5/4} \bullet d$$

where

V = wear volume;
K_{Ic} = fracture toughness;
H = hardness;
P = normal load;
N = number of abrasive particles;
d = sliding distance.

We presumed that if the polishing load and the diamond polishing compound were standardized, then the stock-removal rate would only be the function of the inherent wear rate of a given Si_3N_4 material. Also, the steady-state sphericity of the balls would be the function of the isotropic nature of the base stocks.

3.1.2.1.3.2 Grinding and Polishing Precision Bearing Balls. To combine theory with practice, i.e., to provide actual ceramic hardware while gaining some quantitative understanding of the ceramic

candidates' wear resistance, Spheric, Inc. and its home factory in England (Spheric Engineering Ltd. and its subsidiary, Spheric Special Products) was asked to grind and polish precision (requested Grade 10 or better), 1.27 cm = 0.5 in. ceramic bearing balls from rods of the Al_2O_3/Y_2O_3 sintering aid-containing Si_3N_4 materials listed below:

- Cercomp® 3.5% h-BN HIPSN: In an effort to reduce the dielectric constant and increase the thermal shock resistance of Si_3N_4, AFWAL/WRDC researchers hot-pressed Si_3N_4 with 5% to 50% (by wt.) hexagonal (h)-BN, using 6% (by wt), alkoxy-derived CeO_2 as a sintering aid (182). The thermal diffusivity of these composites exhibited considerable anisotropy with respect to the direction of hot-pressing, owing to the preferred orientation of the platelet-like, pyrolitic h-BN particle inclusions,with the basal planes normal to the direction of hot-pressing (183). The high diffusivity of the composite normal to the hot-pressing direction (= 0.27 $cm^2 s^{-1}$ at a 30 w/o h-BN content) has prompted the Babcock & Wilcox Lynchburg Research Center's R&D Division (Lynchburg, VA) to begin commercially preparing various grades by hot-pressing for ceramic heat exchanger use, but now employing an Al_2O_3/Y_2O_3 sintering aid package (184). Selected physical properties of these materials are presented in Figures 92 and 93. The composition of interest in the present case was a HIP version of the 3.5% h-BN-containing material, which exhibited a measurable maximum in K_{IC} at this BN content (Figure 92). Note that the single-notched and chevroned 3-point bending tests in Figure 92 yielded higher fracture toughness values, because these tests (especially the "Chevron NB") measure dynamic fracture toughness associated with crack propagation. The indentation fracture toughness technique determines subcritical (static) crack growth, i.e., it deals with crack initiation. The HIP processing was presumed to render the material sufficiently isotropic for the fabrication of precision bearing balls, prepared from a ceramic which may be considered "self-lubricating" due to the h-BN content.
- Cercom PAD-1 HP/HIPSN: Cercom, Inc. (Vista, CA) is one of the few firms in the US that prepares a bearing-grade Si_3N_4 by nitriding silicon power, along with the utilization of an Al_2O_3/Y_2O_3 additive package. The result is a high hardness, specific strength and oxidatively resistive material, where the excellent properties are at least partially attributed to the unique method of engineering the grain boundaries (Table 14). These boundaries are at least partially devitrified, a procedure shown favorable for strengthening and toughening Si_3N_4 materials (185 through 188). This ceramic is normally hot-pressed. Due to the acicular nature of the hexagonally structured α- and ß-Si_3N_4 (α transforms to ß between 1500 °and 1600°C), the C-axis of the hexagonal crystallites tends to form in line with the direction of hot-pressing. The resulting anisotropy in strength is depicted in Figure 94. Although it was demonstrated that Grade 3 (spherical within 3 µin ≅ 75 nm), 0.56 cm = 7/32 in. dia. NC-132 HPSN balls could be polished from hot-pressed plates of NC-132 (38), polishing larger e.g., 1.27 cm = 0.5 in. dia. from HPSN to Grade 3 or Grade 5 was considered risky. Therefore, Cercom was asked to attempt, for the first time, HIP-ing their PAD-1 composition, processed at Battelle Columbus Laboratories, Columbus, OH. It will be shown later in this report that our initial concern was justified: the HIPSN did, but the HPSN did not constitute an acceptably isotropic base-stock for 1.27 cm = 0.5 in. dia., Grade 5 balls. Unfortunately, due to some problems with properly engineering the second phase in the grain boundaries, the wear rate of the HIP material was too high, the isotropic nature of the stock nonwithstanding.

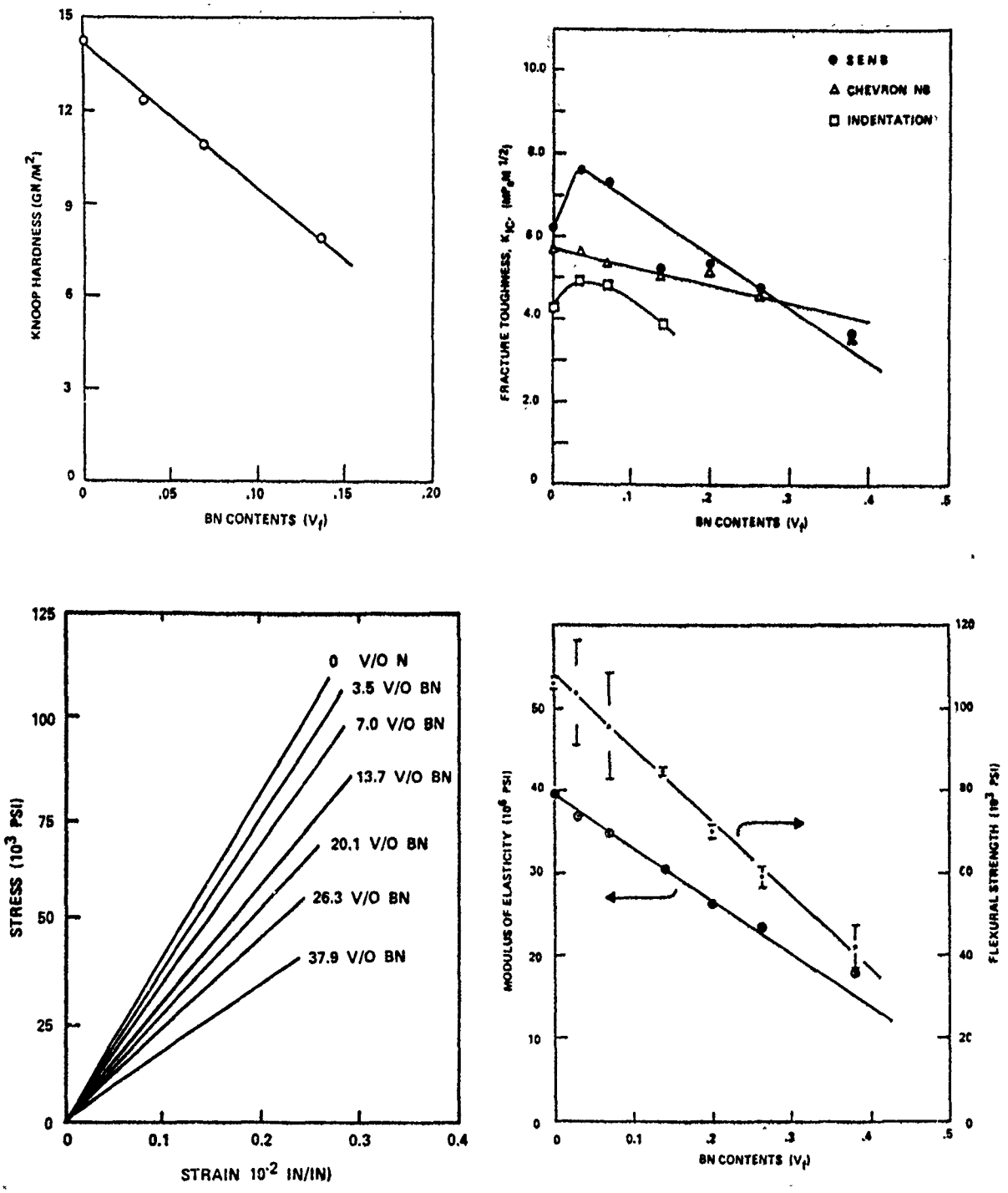

Figure 92. Selected physical properties of the Cercomp® h-BN/Si_3N_4 composites as a function of h-BN content (184).

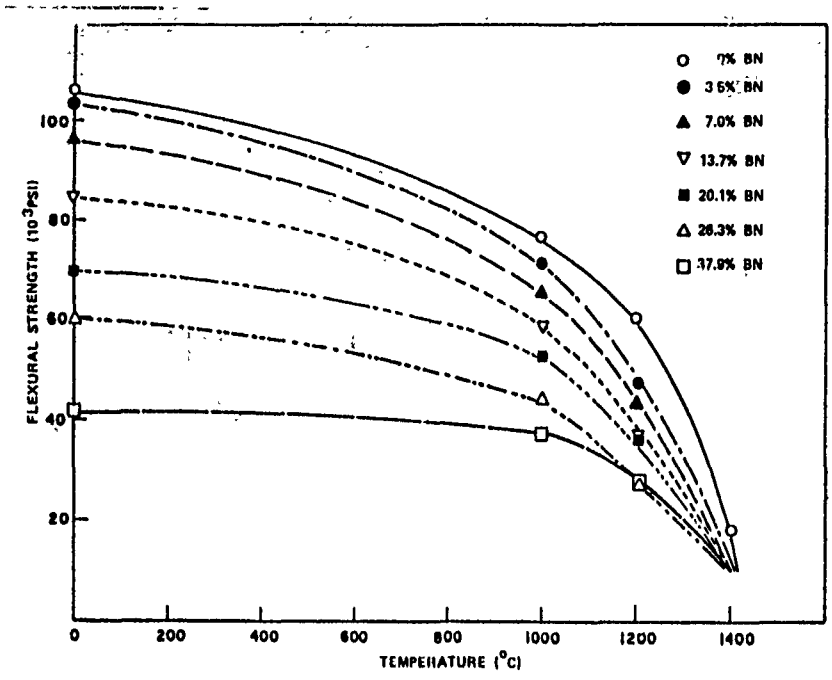

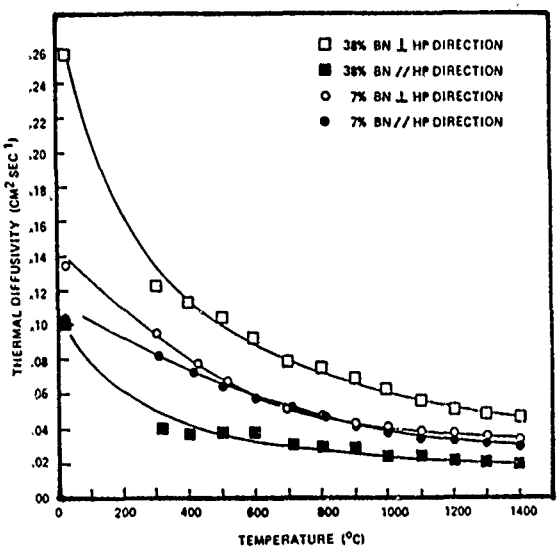

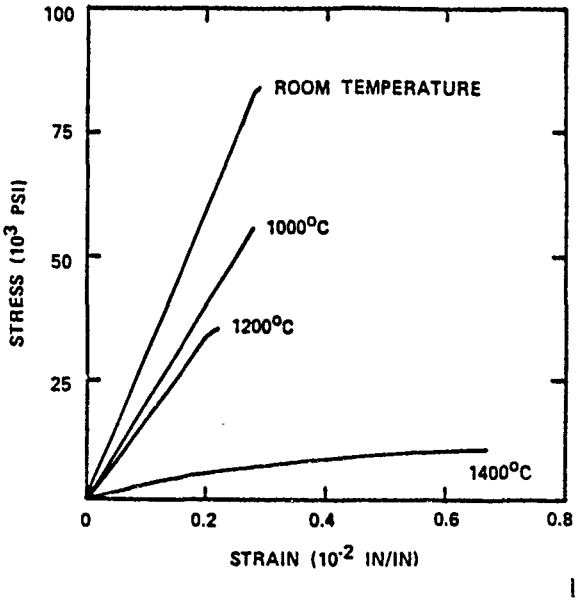

Figure 93. Selected physical properties of the Cercomp® h-BN/Si_3N_4 composites as a function of temperature (184).

Table 14. Selected physical properties of the Cercom PAD-1 HPSN.

Properties	
Type	β-Si_3N_4
Bulk Density (gm/cc)	3.31
Porosity	0.001 – 0.008
Hardness 45 N Scale	90
Fracture Toughness ($K_{I\varepsilon}$ MNm-3/2)	6.0 – 6.3
Grain Size μm (average)	0.35 – 0.50
Flexural Strength (RT) (4 point, average)	
MPa	906
ksi	132
Flexural Strength (1000°C)	
MPa	868
ksi	126
MOE (10^6 psi)	45
Poisson's Ratio	0.27
ΔT_ε (°C)	600 – 700

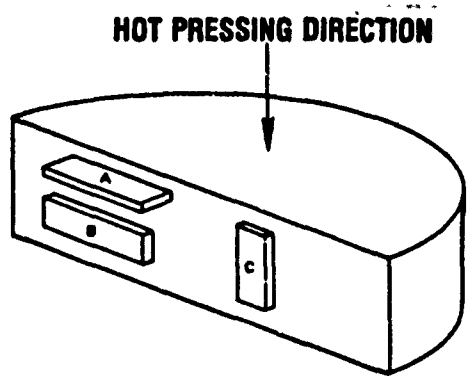

STRENGTH DATA MEASURED BY NORTON COMPANY

	A	B	C
AVERAGE STRENGTH, $\bar{x}$ 4-PT. FLEXURE	876 MN/m² (127,100 psi)	762 MN/m² (110,500 psi)	713 MN/m² (103,400 psi)
STANDARD DEVIATION, σ	105 MN/m² (15,300 psi)	142 MN/m² (20,600 psi)	92 MN/m² (13,300 psi)

Figure 94. Strength vs. orientation of hot-pressing direction, with HPSN (data from the Norton Co.).

- Toshiba/UBE HIPSN: Spheric's experience with a variety of rod-stock and, later, with spherical-near-net-shape ball blanks resulted in identifying only one source which was capable of repeatably delivering high quality ball blanks resulting in Grade 3 or 5, high surface finish balls. This source was the Toshiba Corporation in Japan, and the material designation is TSN-03H (see Table 15). Spheric also reported that the Toshiba base-balls did not suffer from a "skin effect", i.e., were not disturbed by the presence of a surface layer, which had a different hardness and grinding/polishing rate than the bulk. This "skin" normally originates from a glass-based on other types of "jackets" often used for HIP-ing ball blanks. It appeared that Toshiba rough-ground the skin off prior to selling the base-balls to polishing vendors. Subsequently, UBE was also selected by Spheric as an alternate ball-blank source from Japan (also see Table 15), even though UBE normally concentrates on selling Si_3N_4 powder and not monolithic shapes or parts. Note, however, that during this initial round of ball grinding and polishing, the Toshiba/UBE stocks consisted of ~12 cm long, ~1.4 cm dia HIP rods, because near-net-shape base-balls were not available on a commercial basis at that time.

- Norton NBD-100: This is the only material which was made available in spherical, near-net-shape form, during the final phases of the project. Note that NBD-100 is the upgraded, HIP version of the MgO-pressed NC-132 HPSN, the current U.S. standard of bearing-grade Si_3N_4. Inasmuch as rapid degradation in microhardness was observed to occur at ~750°C for MgO-pressed, and ~900°C for Y_2O_3-pressed materials due to the softening of the glassy grain boundaries [see (189); also see APPENDIX P], NBD-100 was a standard of interest for the reasons of determining its room temperature polishing rates and, eventually, determining its high temperature wear rate, as a function of grain boundary behavior and tribooxidative resistance, resulting from the difference in the sintering aid (i.e., MgO versus Y_2O_3/Al_2O_3).

First, the rods were ground cylindrically to 1.37 cm (0.54 in.) dia. by using the same set of metal-plated diamond grinding wheels for all the materials listed in Table 10. Flood lubrication with a special machining coolant was utilized. Observations were made as to the grinding characteristics of the materials, as compared to other, conventional ceramics similarly ground in the past. A die-penetrant NDE technique was employed after grinding to examine the machined surfaces for flaws (exposed pores, inclusions, cracks, etc.).

Rough-ground balls were then produced from the finished rods by centerless form grinding with specially shaped wheels at the SKF Engineering Research Center, Utrecht (The Netherlands) under flood lubrication, as previously described. A stack of five (5 ea.), metal-plated diamond wheels were set aside and used for all the materials described above, except for the NBD-100, which was supplied in the near-net shape (spherical) form. Five (5 ea.) balls per each bar were produced, with some rod ends remaining. The rod ends were polished and Vickers hardness (H_V) tested at a 5 kg load. The diagonal crack extensions were then used to calculate the critical stress intensity factor K_{Ic} (a measure of fracture toughness) of each ceramic in accordance with the well-accepted method of Evans and Charles (170) To establish a baseline for H_V and K_{Ic}, these values were also determined for Norton Noralide NC-132, a

Table 15. Selected physical properties of (a) Toshiba TSN-03H, and (b) UBE HIPSN materials subjected to ball polishing at Spheric.

a.

DENSITY	3.22 - 3.24 g/cm^3
POROSITY	LESS THAN 0.6%
HARDNESS	Hv 1400 - 1500 (LOAD 20kg)
FLEXURAL/RUPTURE STRENGTH (ROOM TEMPERATURE)	3-POINT FLEXURAL STRENGTH MEAN VALUE 980MPa
WEIBULL MODULUS (FOR ABOVE)	12 (TYPICAL)
TOUGHNESS (ROOM TEMPERATURE)	INDENTATION K_{Ic} = 6 - 6.5 MPa$\sqrt{m}$
ELASTIC (YOUNG'S) MODULUS	3.0 - 3.1 x 10^4 kgf/mm^2 (TYPICAL)
POISSON'S RATIO	0.26 - 0.28 (TYPICAL)
THERMAL EXPANSION COEFFICIENT	2.9 - 3.2 x 10^{-6}/ °C (R.T. - 800°C)
SPECIFIC HEAT	0.65 - 0.70 J/gK (TYPICAL)
THERMAL CONDUCTIVITY	24 - 31 W/mK (ROOM TEMP.)

b.

	UBE SILICON NITRIDE BALL BLANKS				UBE SILICON NITRIDE ROD
LOT NO.	NS-2001	NS-2002	NS-2003	NS-2004	NS-2005
PROCEDURE	NS+HIP	NS+HIP	NS+HIP	NS+HIP	NS+HIP
QUANTITY	200	100	100	100	8
SIZE (mm)	x=12.37 (13.12~13.39)	x=18.00 (17.87~18.11)	x=24.33 (24.23~24.41)	x=24.36 (24.22~24.45)	0.53"x 6"
DENSITY (g/cm3)	3.35	3.35	3.35	3.35	3.35
FLEXURAL STRENGTH (kg/mm2)	125	131	137	123	125
VICKERS HARDNESS (kg/mm2)	1,700	1,700	1,700	1,700	1,700
SILICON NITRIDE POWDER	UBE SN E-10	UBE SN E-10	UBE SN E-10	UBE SN E-10	UBE SN E-10

HP- Si_3N_4 acting as a long-time industry standard of bearing ceramics in the U.S. The K_{Ic}/H_v values for the NBD-100 balls were determined on base-balls cut in half.

Ball finishing was carried out using single row production techniques, in three steps:

- Step 1: "rounding", in which the ground, spherical blanks were brought to the same size and approximately spherical. The grinding load was 0.625kg/ball and cast iron plates with a 0.45 μm diamond paste were used.
- Step 2: "grinding", during which the size of each ball was reduced to approximately 7.62×10^{-6} m (0.0003 in.) above the final target size of 1.27×10^{-2} m (0.50000) in. Both "rounding" and "grinding" used the same plate/polishing compound combination, but the per-ball starting load was 2.5 kg/ball, reduced eventually to 1 kg/ball.
- Step 3: "polishing", was the final process step, using brass plates, 1μm diamond paste and a 1.5 kg/ball load.

Each finished ball was subjected to thorough metrology. The details of the above steps may be found in the series of Spheric reports previously included in (189), and their Final Summary Report attached here in APPENDIX W.

The various stock removal rates were quantified and recorded during Step 2 ("ball-grinding") of the operation, through statistical sampling and metrology of balls from each batch. The diametral reduction as a function of grinding time was used as the measure of wear resistance of the particular ceramic. Since the process was standardized in terms of grinding compound type and grinding/polishing procedure and loads, the only parameter which was different was the processing time: each Step 2 process duration depended on a particular material's wear resistance.

The summary of the data is presented in Table 16, and the ceramic volumetric wear rates (y) are plotted as a function of $1/K_{Ic}^{3/4} \cdot H_v^{1/2}$ (x) in Figure 95. The empirically curve-fitted equation describes the wear rate as:

$$y = 3.28\, e^{-9}\, x - 5.55\, e^{-12}$$

with a 0.99 correlation coefficient, see Figure 95.

Representing the essence of the theoretical part of our work, the data in Table 16, the linear plot in Figure 95 and the associated wear equation describe the wear of marginally lubricated ceramics under severe boundary conditions. The ball grinding process used a standard set of diamond polishing compounds consisting of diamond particles suspended in a hydrocarbon carrier. As such, the polishing process resembled the operation of a single-groove, hybrid ball thrust bearing (i. e., ceramic balls, cast iron or bronze "races"), operated in an abrasive-slurry-like, semi-lubricated condition. The results, therefore, resemble realistic ceramic ball wear in the boundary mode.

Table 16. Ball/grinding/polishing data for precision bearing balls fabricated from selected HP/HIP-Si_3N_4 materials.

MATERIAL		CERCOM HIP	B&W	CERCOM HP	NORTON	TOSHIBA	UBE
SPHERIC DATA							
BALL GRADE		5	5	25	10	5	5
START DIA	in.	0.510500	0.519500	0.508350	0.512260	0.522047	0.517717
END DIA	in.	0.500900	0.501530	0.500450	0.500900	0.499409	0.500236
TIME	hours	6	11	9	12	60	63
HARDNESS Hv (5kgf)	Kg/mm^2	1655	1390	1570	1820	1545	1610
TOUGHNESS	MPa m^1/2	4.70	5.60	5.82	5.00	6.93	6.97
DIA REDUC. RATE	in./hr	0.001600	0.001633	0.000877	0.000946	0.000377	0.000277
HV x TOUGHNESS		7778.5	7784.0	9137.4	91000.0	10706.9	11221.7
VOL CHANGE RATE	in.^3/hr	0.000642	0.000668	0.000350	0.000381	0.000154	0.000112
1/Hv ^1/2		0.002581	0.026822	0.025237	0.023440	0.025441	0.024922
1/TOUGHNESS^3/4		0.313275	0.274700	0.266874	0.299069	0.234126	0.233117
1/(TOUGH^3/4)(Hv^1/2)		0.007700	0.007368	0.006735	0.007010	0.005956	0.005809
CONVERTED TO SI UNITS							
START DIA	m	0.012967	0.013195	0.012912	0.013011	0.013260	0.013150
END DIA	m	0.012723	0.012739	0.012711	0.012723	0.012685	0.012706
TIME	sec	21600	39600	32400	43200	216000	226800
VOL CHANGE RATE	m^3/sec	2.92E-12	3.04E-12	1.60E-12	1.74E-12	7.03E-13	5.14E-13
HARDNESS Hv	MPa	16230.59	13631.73	15396.99	17848.74	15151.82	15789.27
TOUGHNESS	MPa m^1/2	4.70	5.60	5.82	5.00	6.93	6.97
1/(TOUGH^3/4)(Hv^1/2)		.002459	.002353	.002151	.002239	.001902	.001855

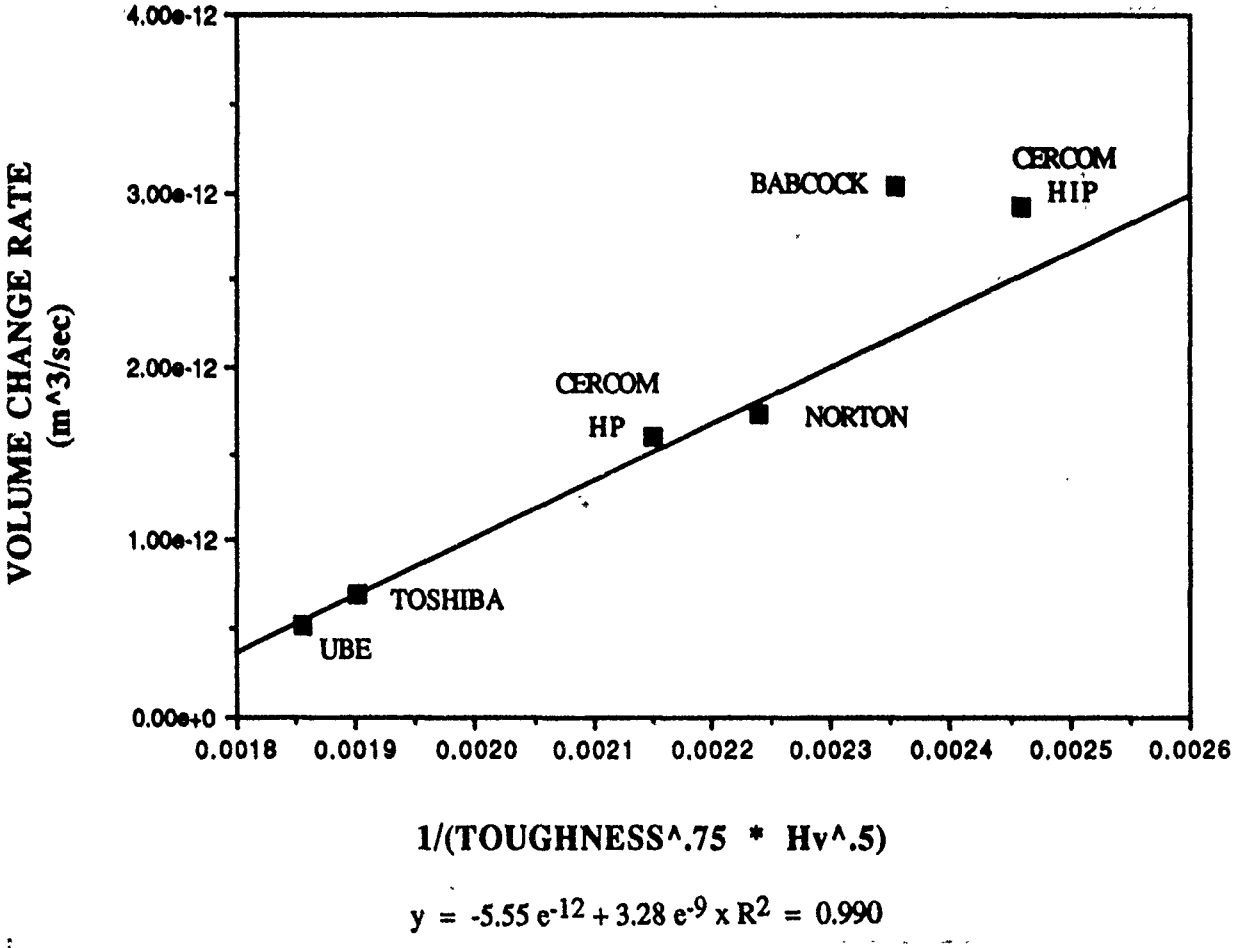

Figure 95. The validity of the Evans-Wilshaw wear relationship with a variety of HP/HIP Si_3N_4 ceramics.

The data in Table 16 show that the Cercomp®, the Cercom-HIP, the Toshiba and the UBE balls were all Grade 5. This was an outstanding achievement for Spheric--polishing large-size balls to such high precision, from a variety of isotropic base-stocks.

The high wear rate of the Cercom-HIP material indicated that better grain boundary engineering is needed before this ceramic can be used reliably in low-wear ceramic bearings. Improvements along these lines are now being instituted under the auspices of the ongoing Part II portion of this program.

The apparent softness of the B&W Cercomp® 3.5% h-BN may or may not preclude this ceramic composite from future use in bearings. If the h-BN preferentially accumulates on the ball surfaces during the initial stages of rolling as it has been demonstrated in previous room temperature and elevated temperature sliding tests, the Cercomp® balls may turn out to be self-lubricating, perhaps even in liquid cryogens and perhaps even under the condition of poor transfer film lubrication from a composite ball bearing retainer. The use of such a self-lubricating ceramic in rolling element bearings would be a first in the science of tribology and first in the bearing industry.

The poorer surface finish of the UBE balls, in spite of their lowest measured grinding rates, places these balls behind the quality of those fabricated from the Toshiba ceramic. The surface skin problem of the UBE HIP Si_3N_4 [for details, see (189)] further reinforces the Toshiba material's place on the top of the quality list.

The directional (anisotropic) nature of the HP Cercom PAD-1 clearly prevented its fabrication into precision balls [for the details on all the polishing problems, again see (189)], its acceptable K_{Ic} and good H_V properties notwithstanding.

The Norton NBD-100, in spite of the fact that it is also prepared by HIP, could not be polished to better than a Grade 10 condition. Since a Grade 10 ball is still quite acceptable for a ball of this size for precision bearing applications, our finding should be construed only as an indication of the relative differences that exist between the best Japanese and U.S.-made materials. Note that since this work has been completed, several batches of near-net-shape Toshiba TSN-03H ball blanks of this size were polished by Spheric to Grade 5 or better.

Our research demonstrated that the abrasive wear of silicon nitride ceramics at room ambient temperature may be predicted by knowing the ceramics' fracture toughness (K_{Ic}) and hardness (H_V). Even though these parameters do not represent fundamental properties, the usefulness of H_V and K_{Ic} is both intellectually and practically appealing. Simple Vickers hardness indentations and the attendant crack-tip-extension-indicated K_{Ic} measurements could offer convenient means of quality control for ceramic ball or bearing race blanks. It is especially important to take this simple step prior to subjecting inferior base stocks blindly to the time-consuming and expensive grinding and polishing processes.

The balls resulting from the present work (i.e., the 1.27 cm = 0.5000 in dia. size) were prepared with practical applications in mind:

1. The ball size of the Rocketdyne cone/3-ball cryogenic tribotester and one of the Space Shuttle engine's LOX turbopump bearings is 1.27 cm = 0.5 inch. Some of the balls polished here have already been forwarded to Rocketdyne and to the NASA-Marshall SFC Materials Laboratory for testing under the auspices of Part II of the program.
2. The ball size of the NTN-Bower RCF tester (used to determine the rolling contact fatigue of bearing steels and ceramics, see Figure 31a) is of the same dimension.

3.1.2.2 Tribometry of Monolithic h-BN and Cercomp® Si_3N_4 + h-BN Composites

3.1.2.2.1 Hexagonal BN as a Solid Lubricant - A Brief Review of the Fundamentals. Hexagonal boron nitride (h-BN) is a layered compound which is isoelectronic to graphite. Both crystals consist of a stacking of two-dimensional arrays with honeycomb structure, and are characterized by strong intralayer bonds and weak interlayer interaction. The electronic states are similar and, in a simple linear combination of atomic orbitals (LCAO) picture, the sequence of their energy bands with increasing energy is σ and π bonding, π and σ anti-bonding, with the Fermi energy E_F located in the middle of the π bands. The major difference between the two materials is that the π-bonding and π-antibonding bands overlap weakly at the Brillouin-zone boundary in graphite, which is thus a semimetal, whereas these bands are separated by an energy gap of several eV in BN, which is therefore an insulator.

As discussed in (191), the ESCA core level binding energies indicated some charge transfer from boron to nitrogen but the evidence is that BN is less ionic than B_2O_3, as would be expected on the basis of electronegativities. The observation of hybridization between the s and p orbitals of each atom and overlap between the electron densities of different atoms gives strong support for covalent bonding in BN.

This can be understood by considering the crystal structure of boron nitride which is composed of planar layers of fused-hexagonal rings similar to graphite. The atoms of all adjacent planes are aligned vertically, thus B-N-B, etc. This structure is very similar to graphite except that in graphite the carbon atoms of alternate layers are aligned.

The crystal structure of BN is consistent with simple sp^2 hybridization of the boron and nitrogen orbitals within planes, resulting in trigonal σ bonding. This would require all the boron valence electrons (except those donated ionically to nitrogen) to be involved in σ bonding. Similarly, three of the nitrogen electrons are used in the planar covalent bonds while the remaining two p electrons in p_x orbitals. Overlap between these nitrogen p_z electrons and empty p_x orbitals of adjacent borons in the same ring will form π bonds or, more accurately, a π density somewhat delocalized around the ring. Since these "π bonds" contain no boron electrons, they may be described as (p $\longrightarrow$ p) π interactions.

Although there is also alignment of filled N $2p_x$ and unfilled B $2p_x$ orbitals in adjacent layers, there is unlikely to be significant bonding normal to the layers because of the large, 3.33Å interplanar distance. It was speculated that bonding between the BN layers is of an electrostatic nature, since oppositely charged boron and nitrogen atoms in adjacent layers are aligned. Similarly, in graphite interplanar bonding is considered weak due to van der Waals interaction only (191).

The similarity of the graphite and h-BN lattice structure led to the supposition by many that both are good solid lubricants. Many forget that atomic-molecular-level calculations on graphite and h-BN indicated some interlayer attraction in terms of π -band interaction (191, 192). More recent work also found unoccupied interlayer states in the lower portion of the h-BN conduction bands, just as they were found in graphite (193). This implies that the interlayer adhesion and shear strength may not be as low a it could be, if these states did not exist.

For example, the π -band interaction in graphite can be reduced only by donor or acceptor intercalants. In the case of donors (e.g., alkali metals), there is charge transfer to the graphite layers. With acceptor-type intercalants (e.g., metal chlorides, Br_2), electrons are transferred from the graphite to e.g., a metal chloride layer. In either case, the conductivity is improved and the interlayer shear strength is reduced. It is well-known, that graphite is a good solid lubricant only when it is intercalated by moisture or by other species (see forthcoming discussion in Section 3.2.2). Although some attempts were successful to intercalate h-BN with potassium (194), charge transfer between the K and BN bands was small.

In view of the above discussion, it may not be surprising that h-BN as a solid lubricant for metallic and ceramic substrates has been a subject of continued controversy. Rowe (195) reported unspectacular f_k values of outgassed h-BN versus itself of 0.4 to 0.7, in vacuum, at temperatures to 1000°C. The room temperature friction was reduced from 0.5 to ~0.2 on admitting organic vapors, but was unresponsive to dry oxygen, nitrogen or air. Buckley (196) reported a high $f_k \cong 1.0$ of h-BN sliding against itself in vacuum and a linearly decreasing f_k function from 1.0 to 0.5 with d-metals, where an increased d-bond character (i.e., reduced reactivity) was commensurate with a reduced f_k value. It was reported that Cr, Ni, Ag and Au vapor deposits in e-beam evaporators will not adhere to h-BN coatings (197), although Ni does react with h-BN at 1200 °C, under a purified hydrogen atmosphere (198). Rabinowitz and Imai (199) reported $f_k = 0.2$ for h-BN sliding versus steel in 50% R.H., room temperature air, but $f_k = 0.4$ to 0.6 at 200°C to 1000°C.

Most of the most recent adhesion, friction and wear work has been done on ion-beam-deposited, hard and brittle BN films on metallic (200) and nonmetallic (201, 202) substrates, or on both simultaneously (203). The adhesion to Si, SiO_2 and certain steels was good, while to GaAs, InP and some other steels poor. On the whole, the friction coefficients were around 0.1 to 0.2, a relatively low value, at room temperature, both against steel and ceramic-type materials. These coatings did not, however, exhibit h-BN characteristics. Interestingly and importantly, it was reported in (201) that friction tended to increase

with increasing B/N ratios. Nitrogen vacancies can enhance the interaction of BN with a counterface willing to participate in charge transfer, as screening by the nitrogen atoms is reduced.

Where Cercomp®-precursor, 90% Si_3N_4 + 10% h-BN composite blocks were sliding against NC-132 HSPN rings, in ~500°C air, under ~100N load and at moderate speeds, the f_k fell into the 0.6 to 0.90 range, and the HPSN/h-BN composite's wear rate was between 1×10^{-11} to 1×10^{-12} $m^3/N \bullet m$. These results did not indicate good high temperature, tribological performance (190).

One objective of the present program was, therefore, the investigation of the tribological properties of h-BN and h-BN containing Cercomp®, Si_3N_4-based composites sliding against α–SiC and Si_3N_4 ceramics, at various temperatures and in various atmospheric environments. The test machines employed traversed the microscopic tribometry region (see Figure 11) to the continuum-tribometric regime (Figures 31 and 54a).

3.1.2.2.2 Test Specimen Materials and Preparation. The Babcock & Wilcox Cercomp® series can be extended to 100% h-BN content by considering 1 to 2 mm thick, flat molds of the Atomergic CVD h-BN [see Figures 96 as well as 97 and 98 depicting a layered, "onionskin"-like structure; also see (204)], or by considering Sohio Engineered Materials (Carborundum) Company's Combat® BN (205). Among the four (4) commercially available grades (A, HP, M, and M-26) of Combat® BN, Grade A seemed best as a model compound, as shown by the data in Table 17. This conclusion may be drawn by comparing thermal conductivity, chemical analysis and oxidation rate of Grade A with those of the Atomergic Chemetals' pure CVD h-BN, where the hexagonal platelets are reportedly aligned, to some degree, parallel with the mold surface (see Figure 96). The CVD fabrication method of h-BN is described, in greater technical detail, in (206).

The fact that the thermal conductivity of the Grade A Combat® BN is significantly greater in-plane (perpendicular to the direction of hot-pressing) means that the hexagonal crystallites are aligned more-or-less perpendicular to that direction, just as in the Cercomp® materials. This alignment during hot-pressing is helped by the molten (6%) B_2O_3, which acts as a sintering aid in consolidating the crystalline particles of BN. The alignment of plate-like particles in the shear field of a viscous, flowing medium is a well-known phenomenon. However, the presence of B_2O_3 also increases the oxidation rate. It is known that the temperature of onset of BN oxidation shifts to lower temperatures with increased B_2O_3 content; at the same time, the oxidation kinetics also increase (207). As before with α-SiC and Si_3N_4, the greater diffusivity of oxygen through a glassy intergranular and surface layer phase within this h-BN/B_2O_3 material is responsible for increased oxidation. It is also suspected that above the melting point of glassy B_2O_3[ca. 450°C, see (208)], the stress relaxation through creep will cause dimensional changes at a concentrated tribocontact, which might be interpreted as apparent wear. The well-known affinity of B_2O_3 to combine with SiO_2 (the tribo-oxidation product of SiC and Si_3N_4) to form a borosilicate glass does not bode well for these ceramic substrates in contact with the boric oxide during high temperature sliding, in air. The fluxing effect would be extremely harmful.

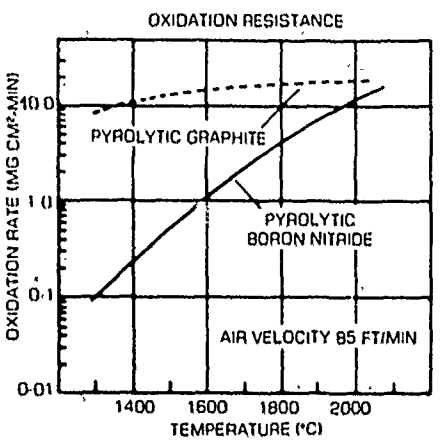

Density:
~ 2.1 gm cm^{-3}

Impurities:
< 30 ppm total metallic impurities

Thermal shock resistance:
Excellent; can withstand repeated quenching in water from 1300°C.

Oxidation resistance:
Very good; no appreciable weight loss up to 1300°C; see graph for weight loss above this temperature

Porosity:
Helium admittance 2 x 10^{-11} cm sec^{-1}

Thermal conductivity:
Parallel to surface ("a" direction) 0.628 watts cm^{-1} $°C^{-1}$ at 100°C (Similar to conductivity of iron)

Perpendicular to surface ("c" direction) 0.0166 watts cm^{-1} $°C^{-1}$ at 100°C (similar to pyrex glass)

Electrical conductivity:
Parallel to surface ("a" direction) 10^{7} ohm cm at 1000°C

Perpendicular to surface ("c" direction) ~ 10^{9} ohm cm at 1000°C

Dielectric constant:
Parallel to surface ("a" direction) - 5 at 20°C (4 x 10^{9} cps)

Perpendicular to surface ("c" direction) ~ 3 at 20°C (4 x 10^{9} cps)

Figure 96. Selected properties of CVD h-BN by Atomergic Chemetals Corp., Plainview, N.Y., from (204).

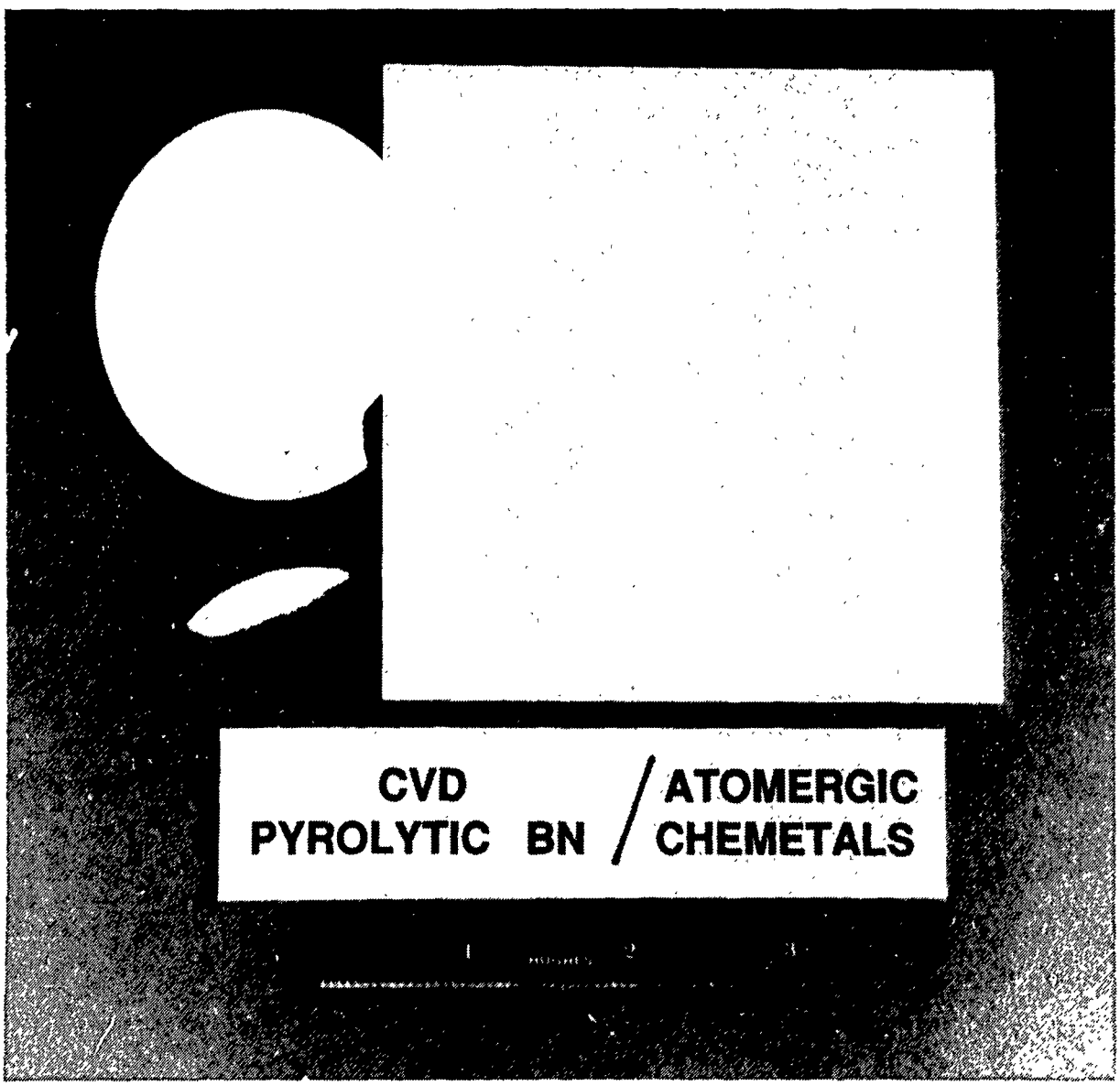

Figure 97. Shapes of CVD h-BN molds obtained from Atomergic Chemetals Corp.

Figure 98. Close-up of a fractured CVD h-BN disc, indicating layered, onionskin-like structure.

Table 17. Properties of Combat® BN solids; from (203).

Typical Physical Properties	Grade A		Grade M		Grade HP	
	Parallel*	Perpendicular*	Parallel*	Perpendicular*	Parallel*	Perpendicular*
Compressive strength 25°C (ACMA-1) lb/in²	45 x 10³	34 x 10³	46 x 10³	42 x 10³	16 x 10³	15 x 10³
Modulus of elasticity 25°C (sonic)	9.4 x 10⁶	6 x 10⁶	13.6 x 10⁶	15.4 x 10⁶	6.2 x 10⁶	11.4 x 10⁶
Modulus of rupture lb/in²						
@ 25°C	11,705	13,940	14,200	15,400	7,665	6,350
@1000°C	9,095	9,730	—	—	6,305	6,760
@1350°C	5,235	5,250	11,200	11,300	4,070	3,495
Density (ASTM C20), g/cm³	2.08	2.08	2.12	2.12	1.90	1.90
Hardness	385 (K100)	385 (K100)	89.5 (15T)	89.5 (15T)	205 (K100)	205 (K100)
Water absorption, % weight gain†	1.1	1.1	0.04	0.04	0.16	0.16
†% weight gain in 168 hours @25°C and 80%-100% relative humidity.						
Typical Thermal Properties						
Thermal expansion °C⁻¹ x 10⁻⁶						
75°C to 500°C	2.3	1.1	1.8	0.20	0.0	0.0
75°C to 1000°C	2.8	0.9	2.5	0.40	0.0	0.0
75°C to 1500°C	6.7	1.8	—	—	1.2	0.09
75°C to 2000°C	6.2	2.0	—	—	0.7	1.30
Thermal conductivity, W/m°C						
@100°C	23.1	44.0	9.1	25.2	60.6	39.7
@350°C	18.1	36.3	7.2	19.8	52.5	31.2
@700°C	16.3	31.6	6.8	15.9	44.0	28.8
Maximum use temperature:						
Inert or reducing atmosphere	>2775°C	>2775°C	1400°C	1400°C	>2775°C	>2775°C
Oxidizing atmosphere	985°C	985°C	1400°C	1400°C	1200°C	1200°C
Typical Chemical Analysis						
Oxidation rate in air (wt loss — mg/cm²·h):						
@ 1200°C	0.16	0.16	0.059	0.059	0.08	0.08
@1000°C	6.2	6.2	0.110	0.110	0.1	0.1
Total Boron (B)	40%	40%	18%	18%	41%	41%
Total Nitride (N)	50	50	22	22	51	51
Boric Oxide (B_2O_3)	6	6	0.2	0.2	0.3	0.3
Calcium (Ca)	0.2	0.2	0.03	0.03	3	3
Silica (SiO_2)	0.2	0.2	59	59	0.1	0.1
Other	3.6	3.6	0.77	0.77	4.6	4.6

* These values depend upon orientation to pressing direction.

In order to investigate the wide-environmental-regime, tribological properties of h-BN, XPS/AES tribometer discs and flats (Figure 12) were prepared from the CVD h-BN plates in Figures 97 and 98, along with flats fabricated from Combat® BN and Cercomp® h-BN/Si_3N_4 composites, with the hexagonal platelets arranged parallel ["flat" configuration (=)] or perpendicular ["edge" configuration (⊥)] to the direction of hot-pressing, see Figure 99. Tester 2A rubshoes (Figure 37) and MTI tribopins (Figure 55a) were also similarly machined in the (=)/ (⊥) orientations from the same materials. The respective counterfaces were fabricated from α-SiC and Si_3N_4 materials, as described in the following sections.

3.1.2.2.3 XPS/AES Tribometry of h-BN with Debris Analyses by EELS/EXELFS/STEM/SAD. Using hot-pressed h-BN sliding against variously cleaned but otherwise untreated ceramic and h-BN flats, and employing the AES/XPS surface analytical tribometer described in Section 2.2.1, SORETRIB investigated the adhesive transfer and the resultant chemical, physical and tribological property changes of h-BN pins and flats machined in two BN particle alignment: (a) particle basal planes parallel with the direction of sliding (=); and (b) particle basal plane edges in line with the direction of sliding (⊥), see Figure 99. They performed experiments in dry and moist air, in partial pressures of oxygen, nitrogen, carbon monoxide and in high vacuum, at room temperature. Ceramic counterfaces consisted of HP-Si_3N_4 (NC-132) and sintered/post-HIPα-SiC from ESK.

Employing the pin/flat materials configuration, they determined the friction and wear of the respective specimens, the chemistry and physics of these specimens, as well as the chemistry and physics of the respective interfaces by in-situ, AES/XPS surface analytical instrumentation combined with tribometry and debris analyses. The tribotests were followed by electron energy loss spectroscopy (EELS) and extended electron loss fine structure (EXELFS) spectroscopy of the wear debris, using a scanning transmission microscope (STEM) in the analytical mode. The use of EELS complemented EXELFS on the thin, plate-like, boron-nitride-containing wear debris.

EELS involves measuring the energy lost by an incident beam of electrons as a result of interaction with the specimen. In particular, the energy losses caused by excitation of core electrons are characteristic of the atom with which the interaction occurred, enabling analytical work. EELS is more sensitive to light elements, e.g., B, C, O and N than energy dispersive X-ray spectrometry (EDX) and is capable of differentiating between the amorphous-hexagonal-cubic allotropic forms of BN. EELS is also capable of determining the orientation of the hexagonal BN layers by interrogating the near-edge structure of h-BN. Since the π^* orbitals are normal to the planar-hexagonal lattice and the σ^* orbitals are in-plane, molecular orbital mapping as a function of electron beam incidence and diffraction angles is possible. As a consequence, crystalline orientation on a fully microscopic-scale (2 nm dia. electron beam probe attainable!!!) can be determined. In addition, the peak shifts (electronic transitions) in the near-edge structure of EELS can provide information on interface chemistry, such as the extent of adhesion of h-BN to its ceramic substrate, the extent of tribooxidation of h-BN in high temperature air, or the reaction of h-BN (or h-BN oxidized to B_2O_3) with a ceramic countersurface.

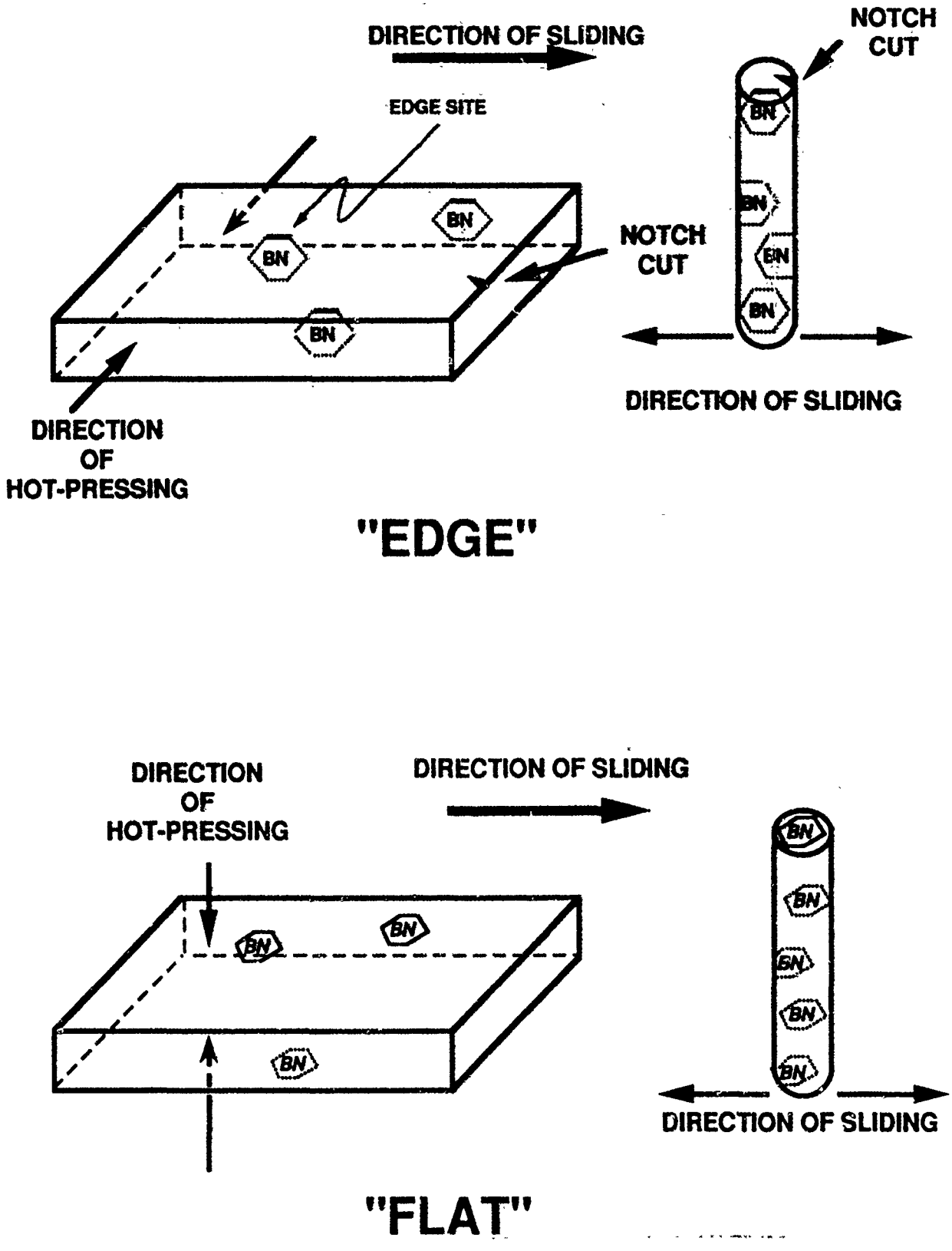

Figure 99. Directionally machined pins and flats from the anisotropic Combat® BN and Cercomp® h-BN/Si_3N_4 compositions.

EXELFS lends itself best to determining the nearest-neighbor environment of boron by the extraction of the boron K-edge modulation. Through the appropriate Fourier transform of this modulation, the determination of the radial distribution function of the probed element (and thus the local crystallography of BN) can be realized. As EELS is better than EDX for light elements, EXELFS is better then the determination of extended x-ray absorption fine structures (EXAFS) for low Z (low atomic number) materials. In fact, for high temperature EXAFS of molten materials, pure pyrolytic h-BN wafers are often used as test cells, because they do not interfere with the EXAFS measurements.

3.1.2.2.3.1 Baseline Analytical Instrumentation Data for h-BN Specimens. The calibration of the various surface analytical instrumentation with standard h-BN samples and the comparison of the data with the corresponding literature values are presented in APPENDIX X. This addendum also contains the initial analyses of the 1 mm-thick, CVD h-BN mold and the Combat® h-BN, performed to (a) establish a baseline and (b) to determine which version lends itself best as the specimen material for friction and wear testing. The summary of findings is as follows:

1. Although the CVD material appeared stoichiometric, it contained a high quantity of oxygen and carbon, even after ion-etching. Peeling the surface layer of the flat (which was in contact with the graphite mold) did not improve purity. It was presumed that ≅ 10 to 20 at.% carbon was included in the structure, probably as a carbonitride (209, 210). Carbon contamination can occur during the deposition process [see (206)]. EELS indicated that carbon is present in the amorphous form, with sp^2 hybridization. SIMS confirmed the presence of carbon, and the ratio of C^-/C_2^- showed that carbon was indeed, graphitic. In addition to oxygen (O^-), hydrogen (H^+) and a weak OH^- peak were observed. The analytical data concluded that the ≅ 10 at.% oxygen was not present as water, boric oxide, carbon oxide or nitrogen oxide. SORETRIB suggested that it may be intercalated in the graphite structure as a gas.

2. The Combat® BN also contained ≅ 20 at.% carbon segregated in the microstructure. The material itself exhibited (a 1 cm^2 surface was probed with XPS) a (BN) B/N ratio ranging from 0.96 to 1.27. The XPS showed the carbon as free atoms. Nitrogen is present as two Gaussian peaks, one with the energy of B-N, the other representing NH_3 or N_2O_2. The oxygen in the samples appeared to be a function of surface fabrication methodology (e.g., the diamond-ground/polished samples from Saphirwerk (Switzerland) contained far less surface oxygen than the samples prepared at Ceramic Form Grinding, Santa Ana, CA). EELS of individual flakes did not indicate the presence of carbon, but showed stoichiometric BN. According to SIMS, carbon and oxygen was present (confirming the XPS data), with Mg and Si impurities in more significant quantities than in the CVD h-BN sample.

3. The lattice fringes imaged within a small flake sampled from inside the 1 mm thick CVD h-BN plate (Figures 97 and 98) indicated that contrary to the manufacturer's claims, the BN crystallites are not oriented with their C-axis perpendicular to the flat mold's surface. The orientation is more random. The diffraction fringes are shown in Figures 100 and 101. The fine resolution of the 3.3Å lattice spacings is especially noteworthy, as shown in Figure 101.

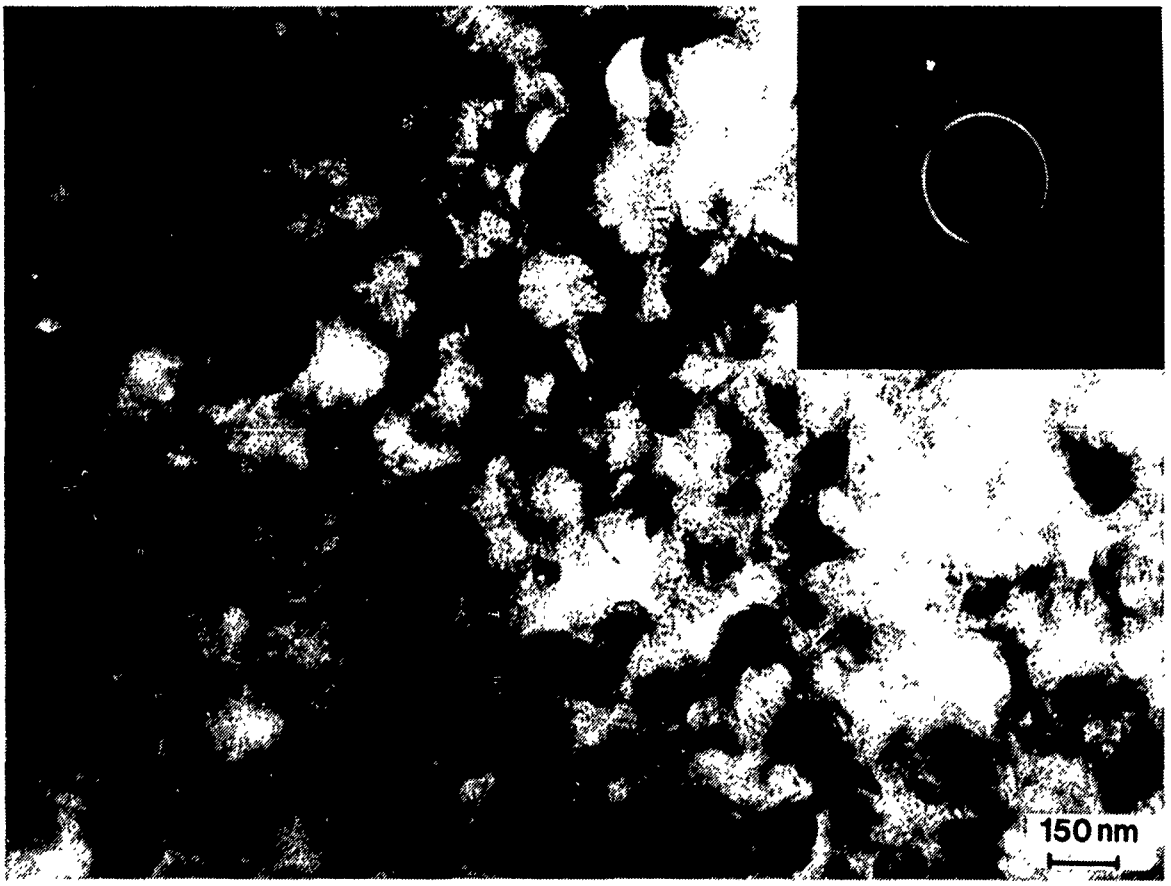

Figure 100. Selected area (electron) diffraction (SAD) pattern of the CVD h-BN plate with the electron beam normal to the mold surface, with the corresponding bright field image, indicating random crystallite orientation.

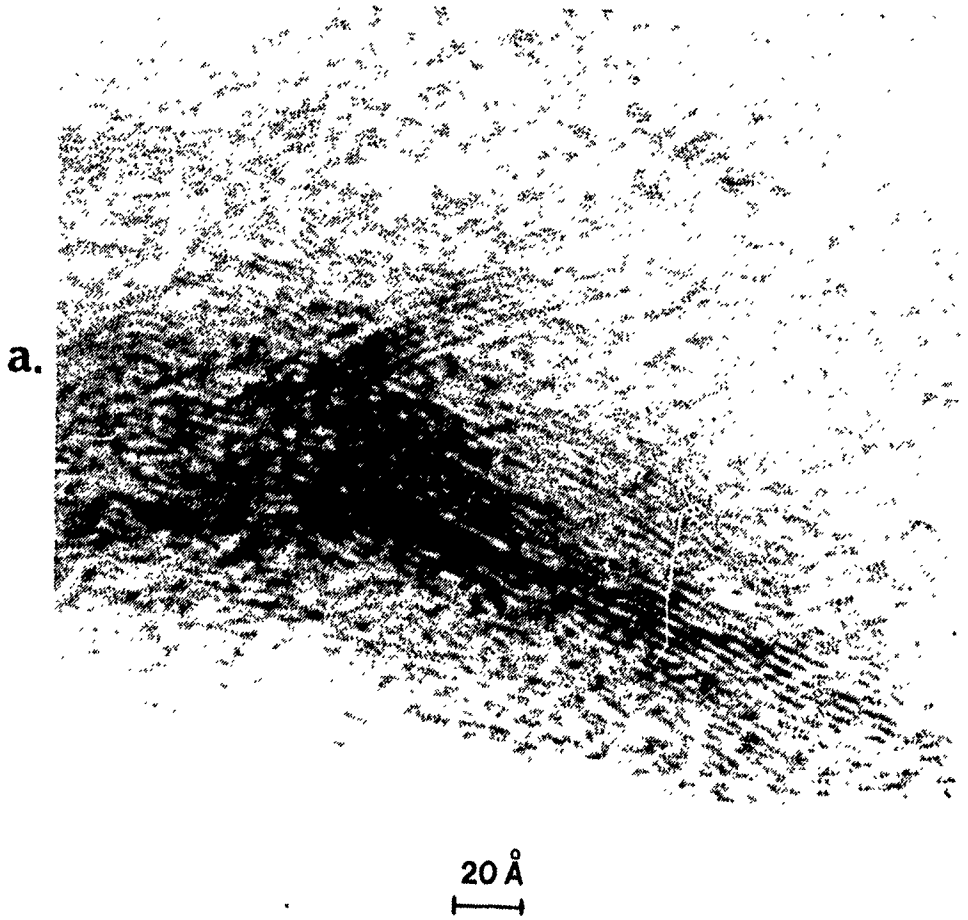

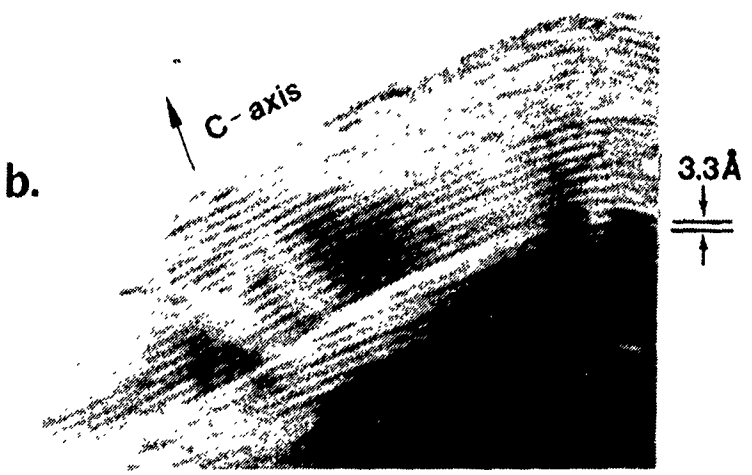

Figure 101. Electron diffraction patterns from the CVD h-BN plate's sample flake: (a) large volume sample showing more-less random orientation, and (b) lattice fringes of flake portion with the flake crystallite's c-axis parallel with the surface, (i.e., the basal planes are normal to the mold surface); notice excellent resolution of the 3.3Å lattice spacings of the h-BN layers.

4. In the hot-pressed Combat® h-BN (=) sample the basal planes were, on the other hand, found well-oriented with the C-axis perpendicular to the external face, i.e., in line with the direction of hot-pressing.

The above data led to the decision to select the (=) and (⊥) Combat® h-BN samples for further XPS/AES and continuum-mechanical tribometry and to abandon all further efforts with the somewhat disappointing CVD h-BN sample.

Using the XPS baseline data in Table 18, (see APPENDICES X and D), samples of (=) and (⊥) Combat® BN flats were subjected to various cleaning procedures first to determine which pretreatment process would provide the cleanest and most stoichiometric surface for further tribometry. The procedures consisted of: (a) a propanol-2 rinse, (b) a propanol-2 rinse + argon ion etching at a 3 keV energy, for 15 minutes, and (c) a propanol-2 rinse with a subsequent 450°C vacuum bake (12 cycles of one minute per cycle).

The data in Tables 19 through 21, as compared with the standards in Table 18 (taken from APPENDIX D), indicate the following:

- Propanol-2 rinse alone (Table 19): the surface is composed mainly of h-BN, boron oxide and the carbon contaminant. The boron oxide is superstoichiometric, the O/B ratio being 4.8, compared to 1.6 in B_2O_3.
- Rinse + ion-etch (Table 20): etching renders the surface nitrogen-deficient (B/N = 1.5) and gray-to-black in color due to the presence of free electrons left behind on the surface. Surprisingly, selective sputtering of nitrogen either did not shift the B 2s binding energy, or the apparatus was not sensitive enough to detect the shift. There is ≅ 13.5 at.% residual carbon appearing different from hydrocarbons, but similar to graphitic and/or carbidic bonding. The presence of carbonitride cannot be excluded.
- Rinse + bake (Table 21): The C-H contribution completely disappeared from the surface. Only a residual amount of ~2 at.% graphitic carbon is left on the surface after annealing. The BN stoichiometry is preserved, but the boron oxide remained superstoichiometric.

In low-Z element such as BN, the thickness probed by XPS is ≅ 1.0 nm. It was, therefore, difficult to know if hydrocarbons remained adsorbed on the surface only or absorbed (percolated) into the material. It seemed unlikely that hydrocarbons could remain in the bulk after the hot-pressing process.

With respect to the superstoichiometry of the boron oxide, there may be three possible explanations:

- the presence of BO_4;
- O_2 or H_2O intercalated in the material;
- the presence of other oxides.

Table 18. **XPS analysis of h-BN and h-BN-related standards at SORETRIB (all energies in eV).**

	B1s	C1s	N1s	O1s	δ( )	Atomic % ratio
h-BN	190.3	/	397.9	/	δ(B-N) = 207.6	B/N = 0.9
B_2O_3	193.4	/	/	533	δ(B-O) = 339.6	O/B = 1.7
B_4C	186.3	283	/	/	δ(B-C) = 96.7	/
B_{el}	187.7	/	/	/	/	/
Cg	/	284.2	/	/	/	/

Table 19. XPS analysis of propanol-cleaned Combat® BN (=)/(⊥) specimens (all energies in eV).

	E(eV)	atomic %	δ(eV)
B1s B_{-N}	190.3	35.3	δ(B-N) = 207.6
B1s B_{-O}	192.5	1.6	δ(B-O) = 339.6
N1s	397.9	39.2	/
C1s	284.5	16.2	/
O1s	532.2	7.7	/

$\frac{B_{-N}}{N_{-B}}$	0.9
$\frac{O_{OX}}{B_{-O}}$	4.8

Table 20. XPS analysis of propanol-cleaned and argon-ion-etched Combat® BN (=)/(⊥) specimens (all energies in eV).

	E(eV)	atomic %	δ(eV)
B1s B-N	190.3	29.1	δ = 207.5
B1s B-O	192.7	6.3	δ = 339.8
N1s	397.8	19.5	/
C1s	283.7	13.5	/
O1s	532.5	25	/

B/N	1.5
O/B	4

Table 21. XPS analysis of propanol-cleaned and 450°C-heat-treated Combat® BN (=)/(⊥) specimens (all energies in eV).

	E(eV)	atomic %	δ(eV)
B1s B-N	190.3	41.4	δ = 207.6
B1s B-O	192.8	3.0	δ = 339.8
N1s	397.9	44.5	/
C1s	284.2	2	/
O1s	532.6	10.1	/

B/N	0.93
O/B	3

The complete XPS/SIMS data indicated that the best explanation lies by considering the existence of mixed-oxide glasses (e.g., borosilicate, boroaluminate etc.) which may have formed in the presence of B_2O_3 (6%) and impurities (SiO_2, Al_2O_3, CaO, etc.) shown by SIMS. Under such conditions, there would be only a small increase in the O 1s peak in the XPS spectrum.

For all practical purposes, water was not detected on the h-BN surface under vacuum, due probably to its weak sorption.

Overall, annealing at 450°C in vacuum yields clean h-BN, free of contaminants. The stoichiometry of boron oxide remains unaffected by heating. As a consequence, only propanol-rinsed and 450°C-annealed samples were subjected to tribotesting.

3.1.2.2.3.2 XPS/AES Tribometry of (=)/(⊥) Combat® BN Samples. The following test parameters were identical for all samples:

- normal load = 2N;
- average oscillatory velocity = 6×10^{-4} m•s^{-1};
- length of stroke (wear scar) = 3×10^{-3} m ;
- number of cycles = 75 ;
- test temperature = room ambient ≅ 300K.

The only variables were the crystallite alignment, cleaning technique and atmospheric environment of the pins and flats. The effects of these variables on the friction of Combat® BN are presented in Figures 102a through 102g.

The data may be summarized as follows:

1. Repeated experiments showed that "flat" (=) vs. "flat (=) and "edge" (⊥) vs. "edge" (⊥) both exhibited lower friction in the rinsed condition (0.3 - 0.4 steady-state) than in the annealed condition (0.6 - 0.7 steady-state), in UHV (Figure 102a). The same trend was shown for the "edge" (⊥) vs. "edge" (⊥), although the general level of friction was higher (Figure 102b). The f_k difference with both cleaning procedures clearly shows higher friction in the case of the "edge" (⊥) crystallite alignment (Figure 102c).
2. The friction becomes drastically reduced to ($f_k \cong 0.1$ to 0.2) in atmospheric air, regardless of the crystallite alignment of the sliding surfaces (Figure 102d).
3. Various gases at various partial pressures affect the lowest overall friction combination of "flat" (=) vs. "flat" (=) the following way:
   (a) The "as-received" (propanol-rinsed) specimen exhibited about the same friction in UHV as in 1×10^{-5} torr = 1.33×10^{-3} Pa partial pressure of water ($f_k = 0.4$). The same, low P_{H_2O} had virtually no effect on the high ($f_k = 0.65$) friction of the annealed specimens (Figure 102e).

a.

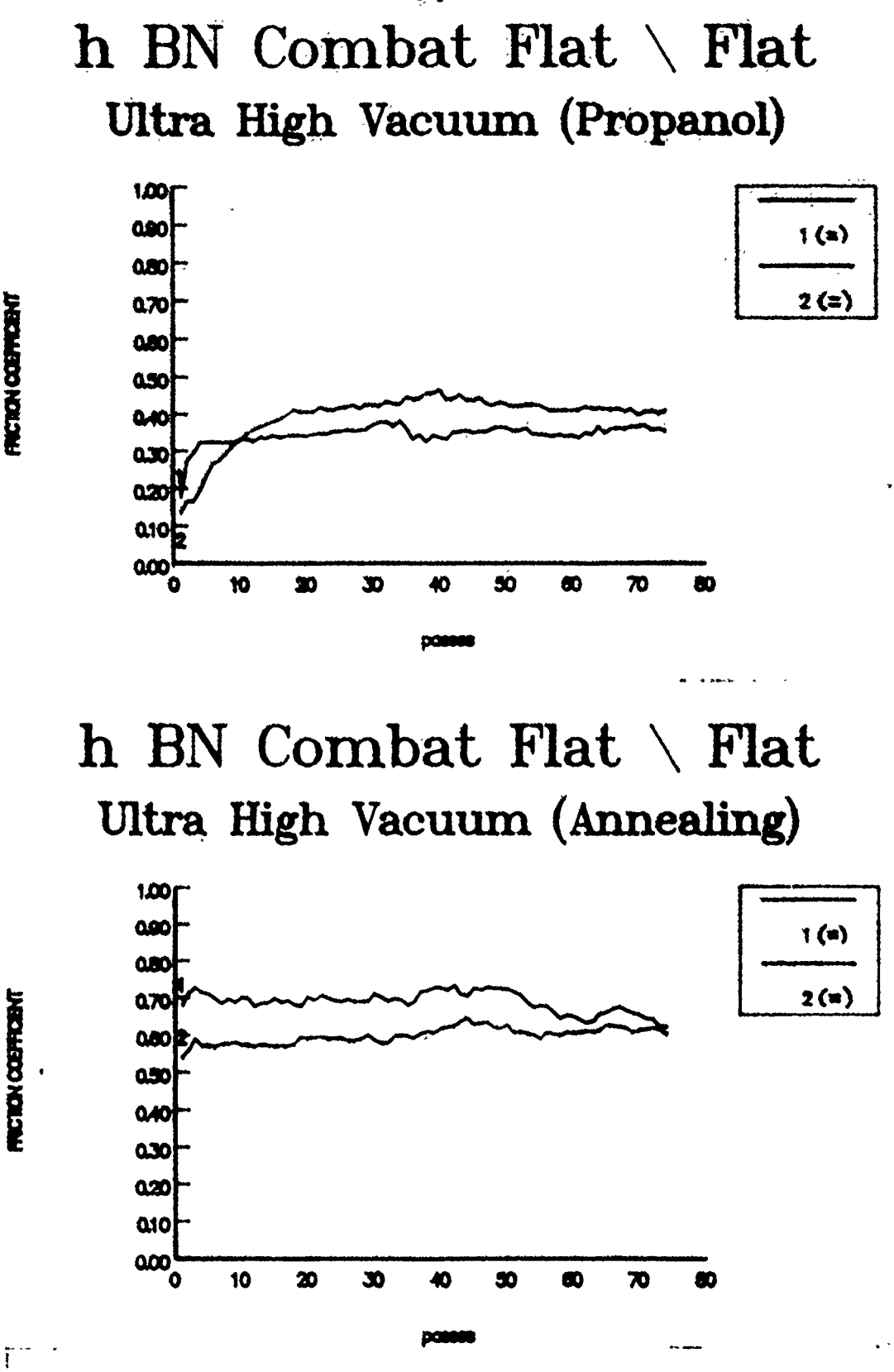

Figure 102. The friction behavior of variously treated, Combat® "flat" (=) and "edge" (⊥) samples in various atmospheric environments, at room temperature (XPS/AES tribometry, computer-averaging f_k data as a function of the number of oscillatory passes):

(a). Rinsed versus annealed (=) specimens in 10^{-8} Pa UHV.

b.

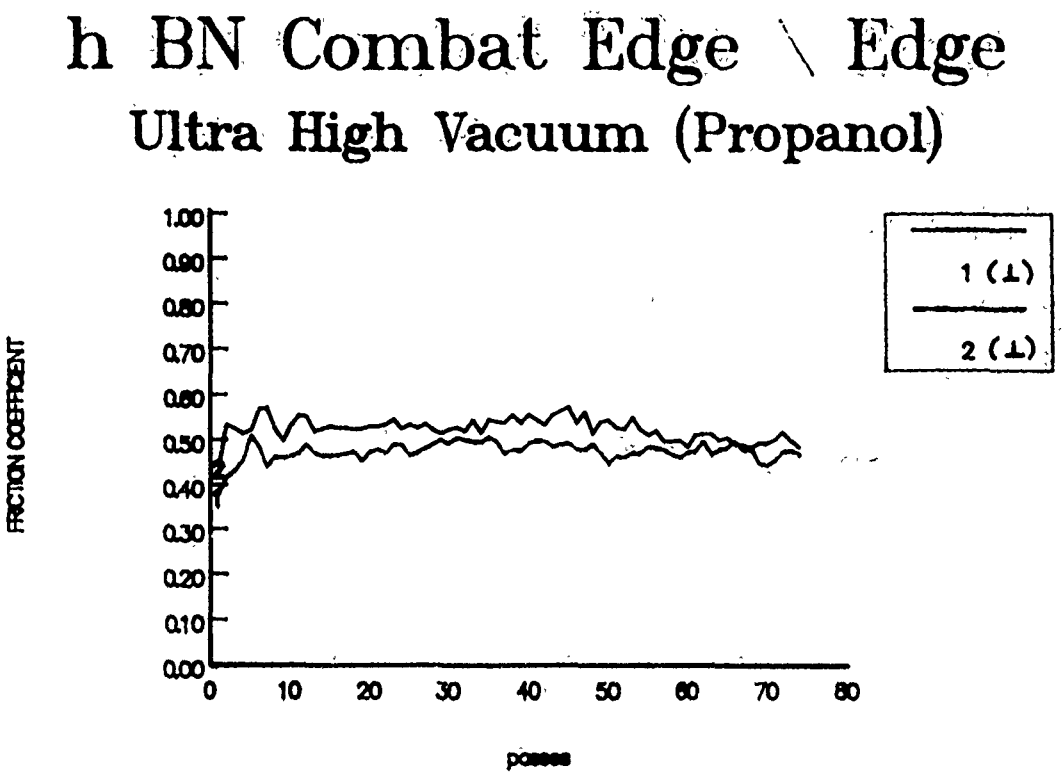

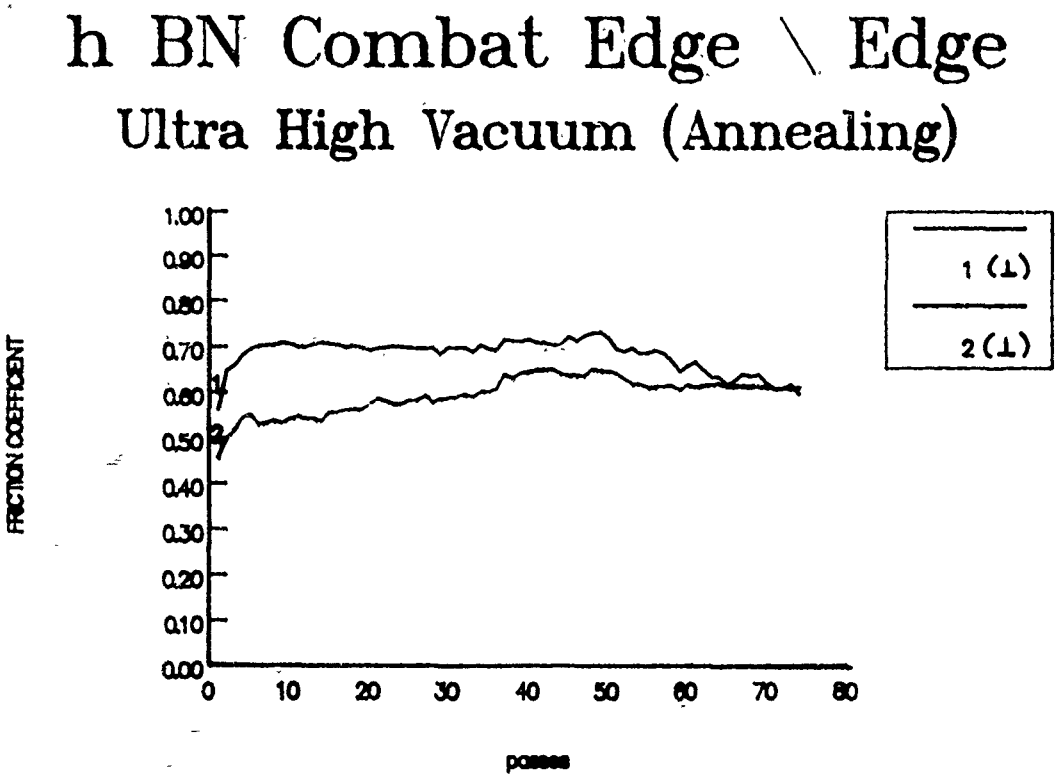

Figure 102 (b). Rinsed versus annealed (⊥) specimens in 10^{-8} Pa UHV.

c.

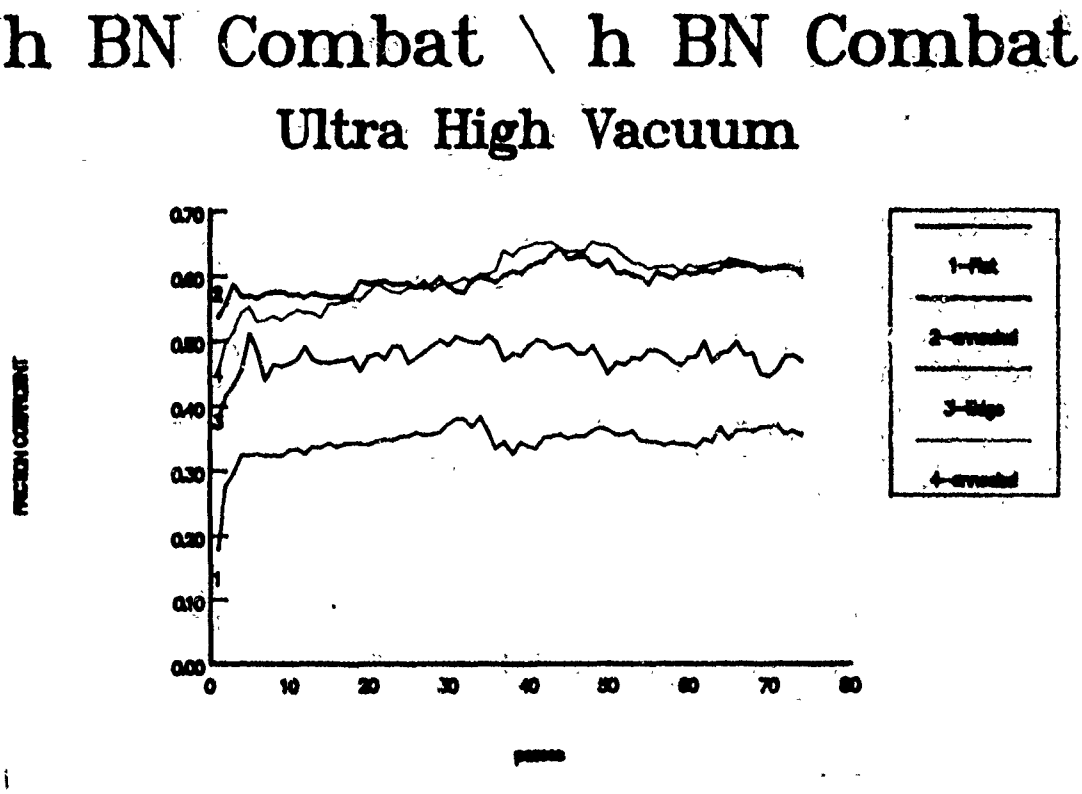

Figure 102 (c). "Flat" (=) versus "edge" (⊥) specimens in 10^{-8} Pa UHV.

d.

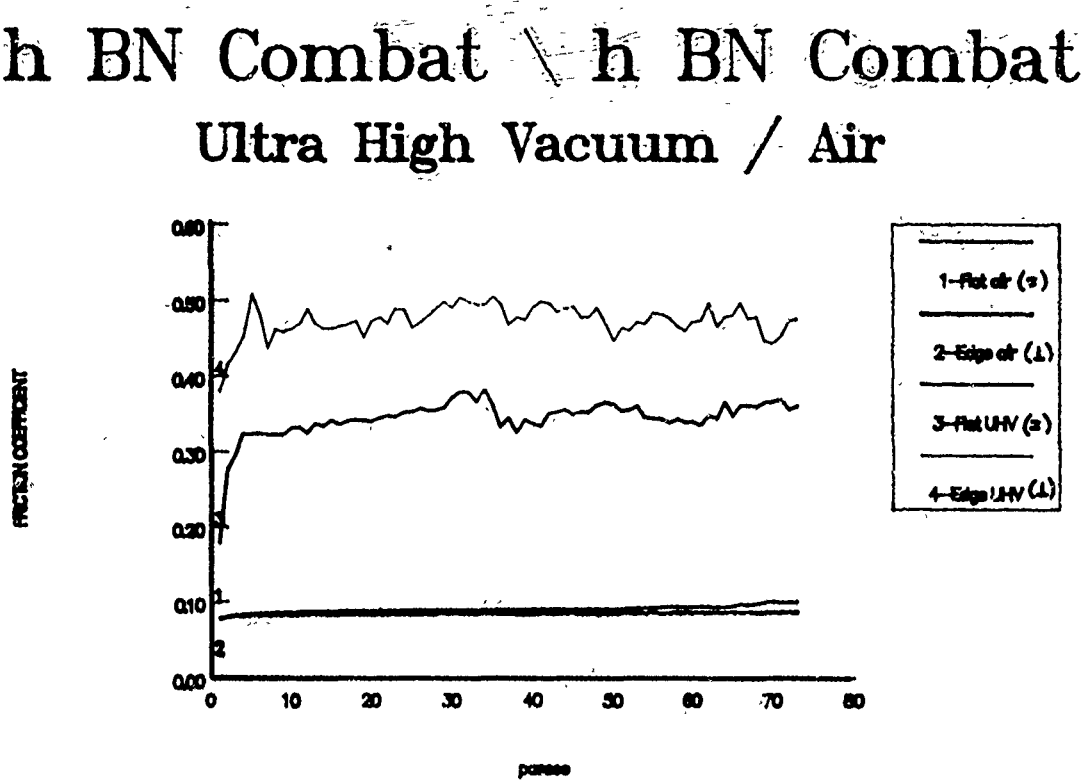

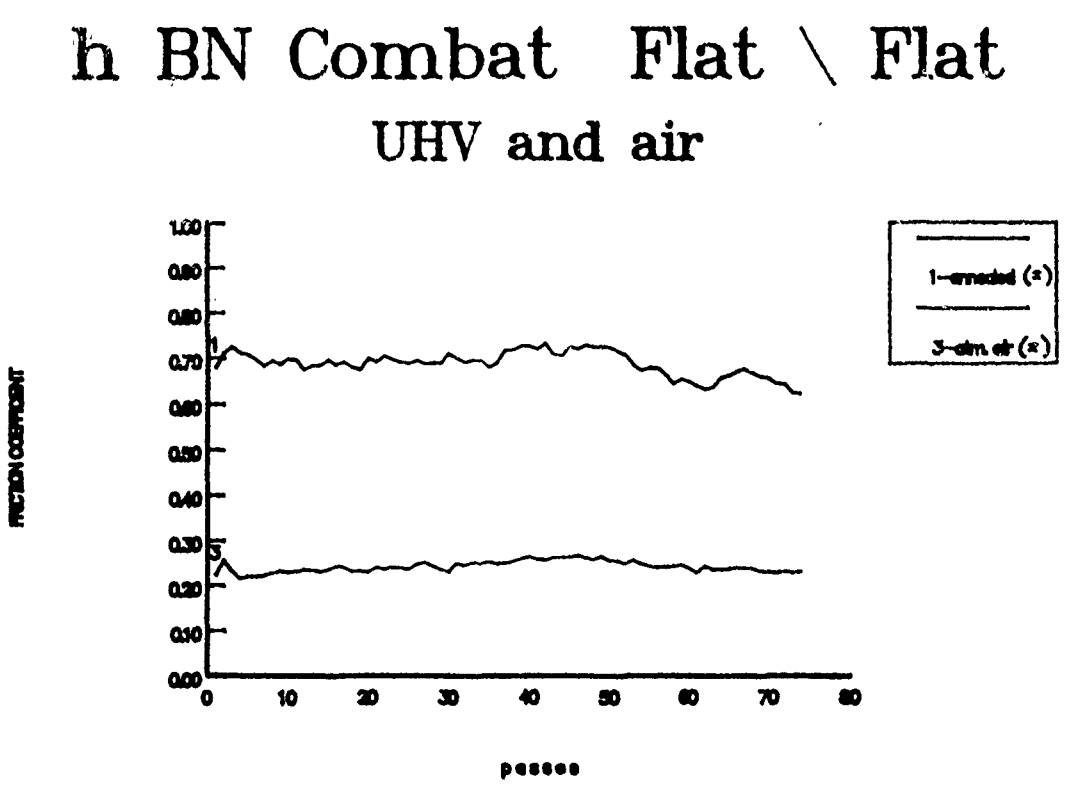

Figure 102 (d). "Flat" (=) versus "edge" (⊥) and "flat" (=) versus "flat" (=) combinations in 10^{-8} Pa UHV and atmospheric air.

e.

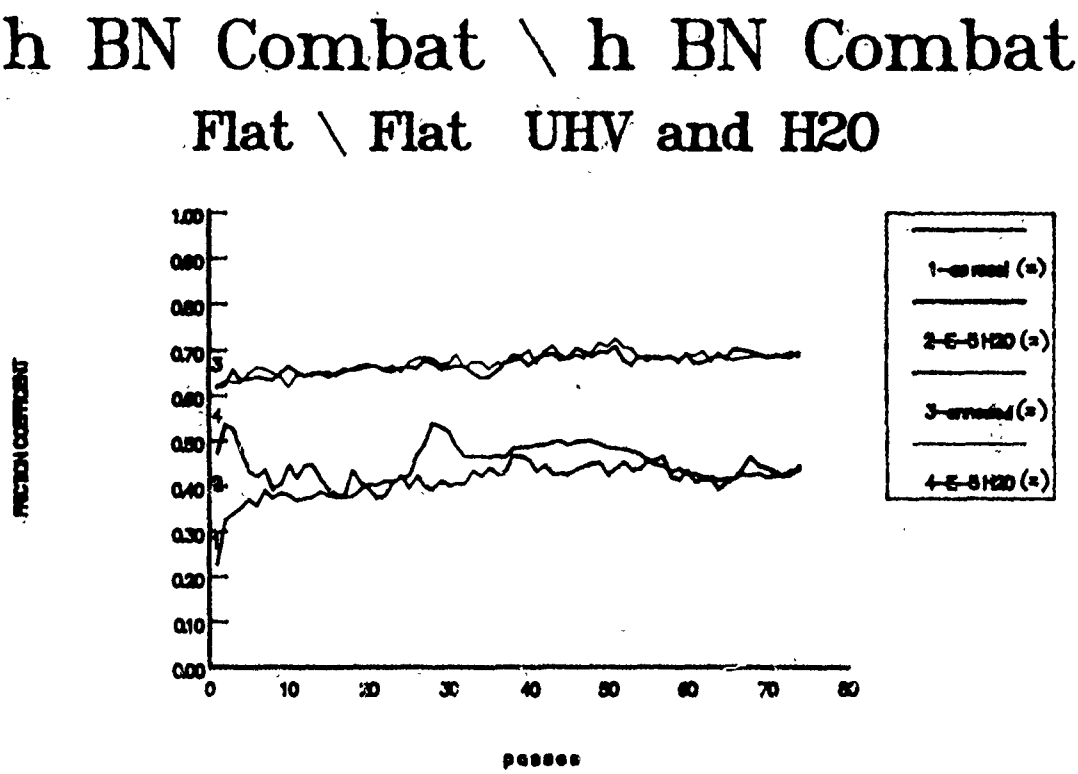

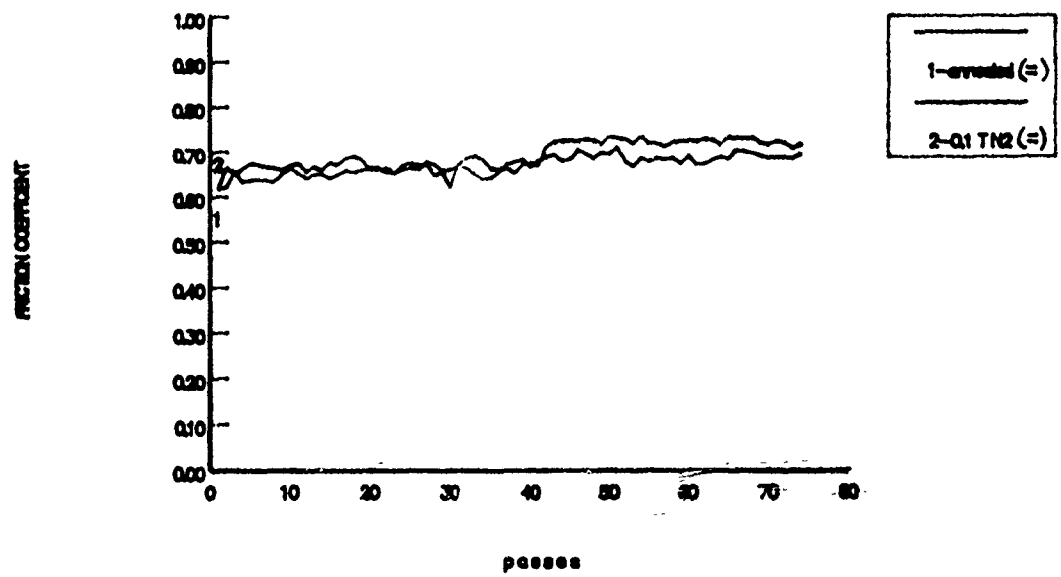

Figure 102 (e). "Flat" (=) versus "flat" (=) in 10^{-8} Pa UHV, 1.33 x 10^{-3} Pa H_2O and 13.3 Pa N_2.

f.

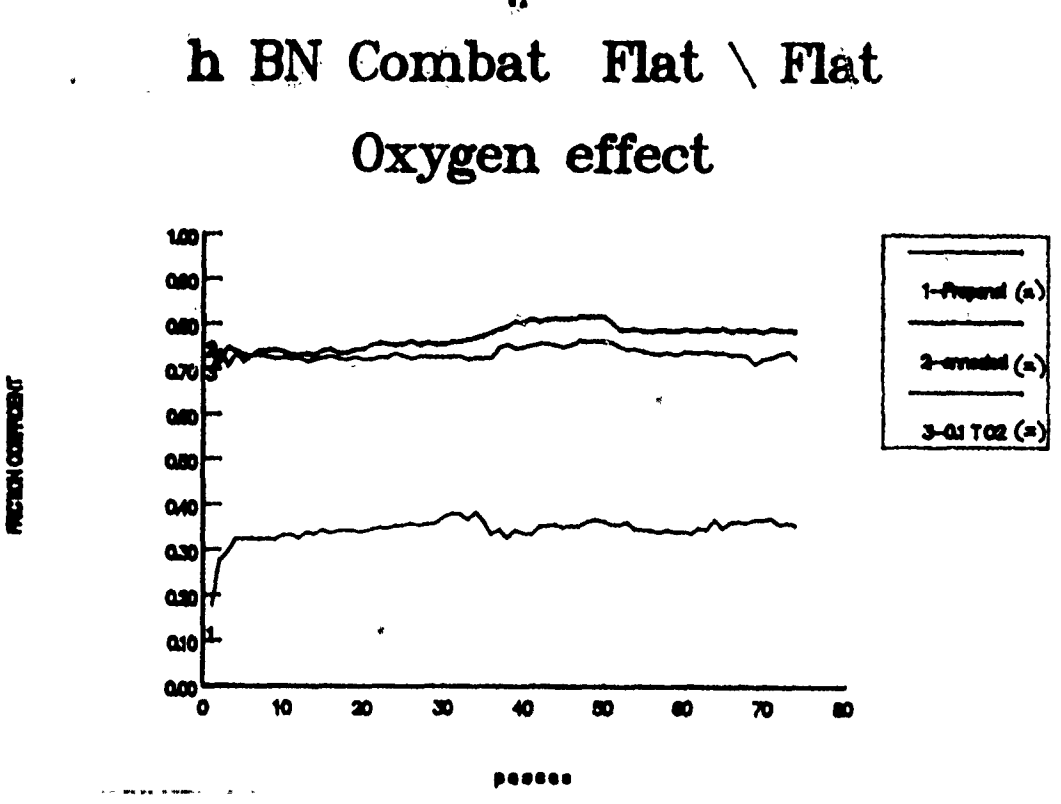

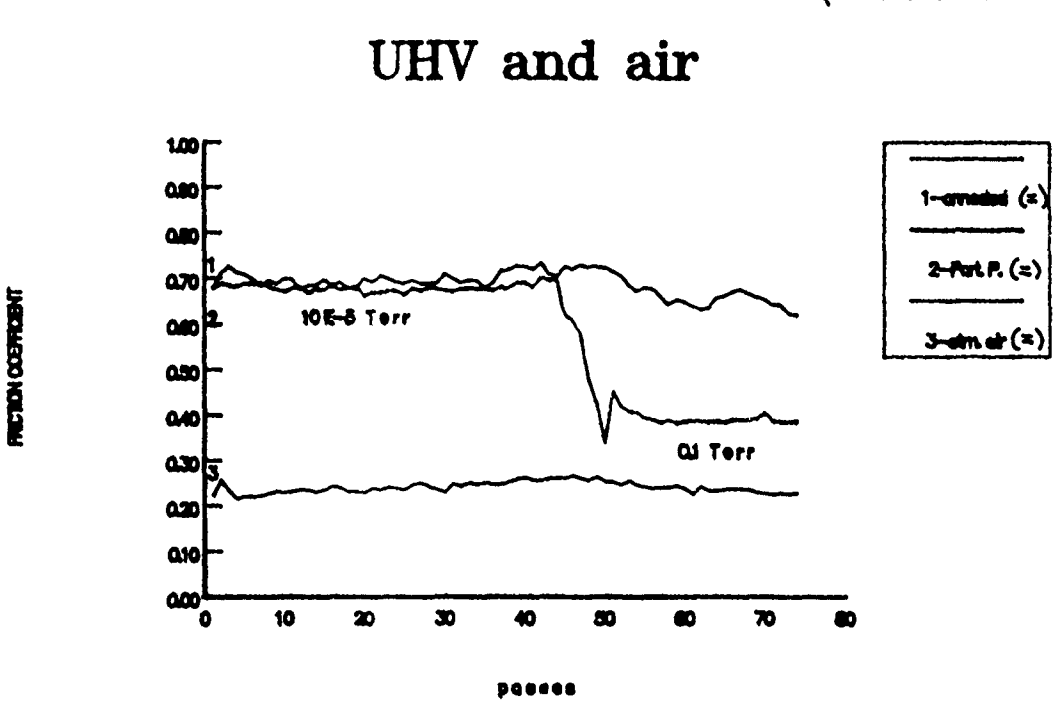

Figure 102 (f). "Flat" (=) versus "flat" (=) in 10^{-8} Pa UHV, 13.3 Pa O_2 as well as 1.33×10^{-3} Pa and atmospheric air.

g.

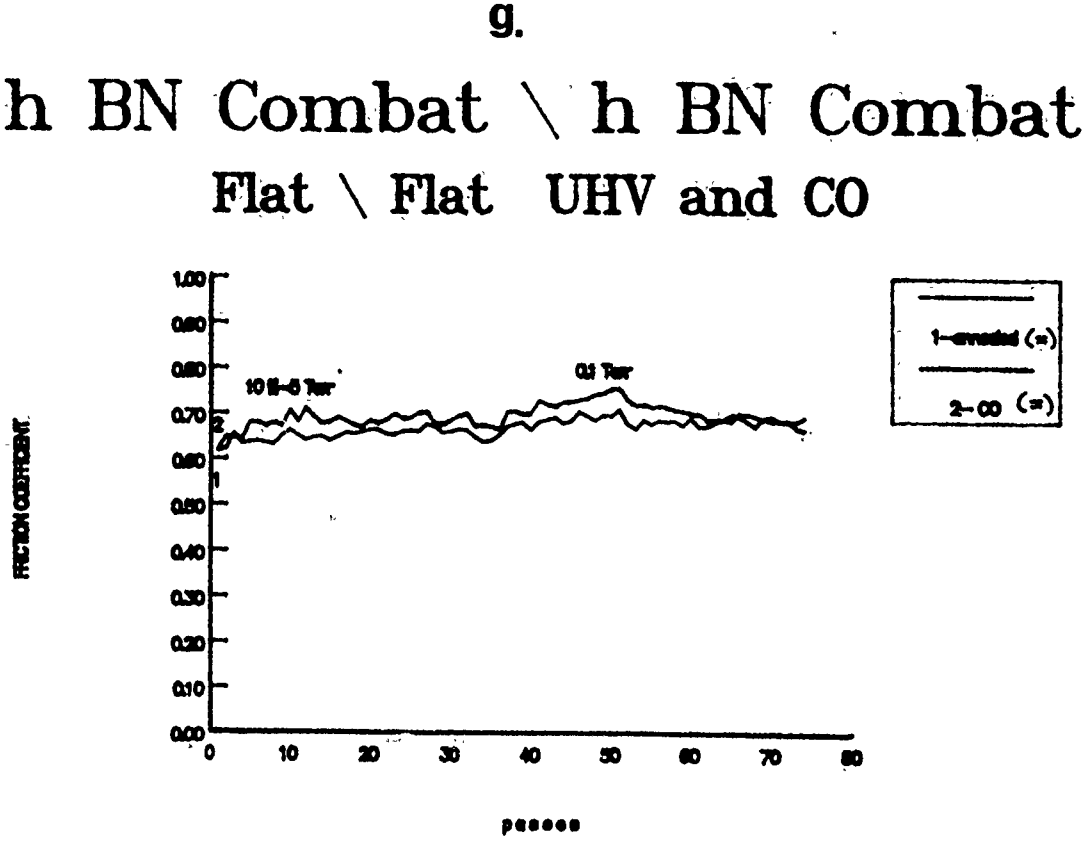

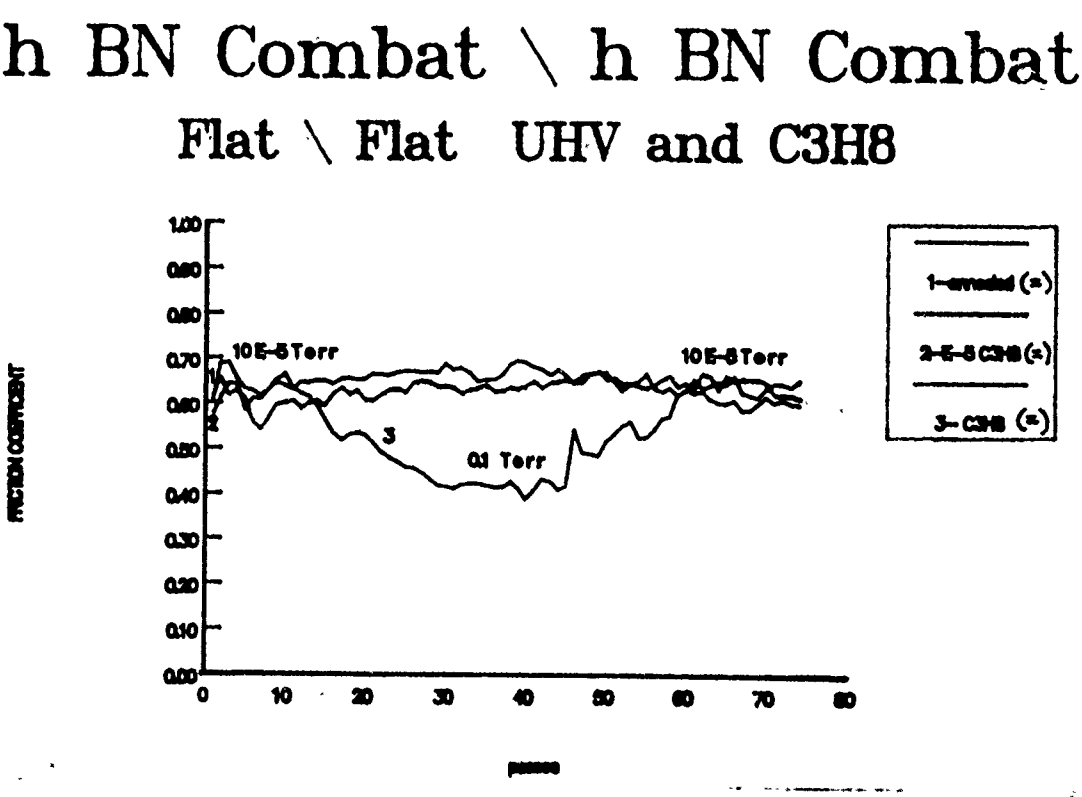

Figure 102 (g). "Flat" (=) versus "flat" (=) in 10^{-8} Pa UHV, 1.33 x 10^{-3} Pa and 13.3 Pa CO and 1.33 x 10^{-3} Pa and 13.3 Pa C_3H_8.

(b) The low (0.1 torr = 13.3 Pa) or 1 x 10^{-5} torr = 1.33 x 10^{-3} Pa air partial pressures themselves had virtually no effect on the high ($f_k \equiv 0.7$) friction of the annealed specimens, in UHV. The propanol-rinsed sample continued exhibiting about one half of this f_k value. Admitting full atmospheric pressure of air again reduced the friction to 0.2 (Figure 102f), just as previously observed in Figure 102d.

(c) Carbon monoxide could not affect the high, annealed-f_k value (~0.7) in the 1.33 x 10 -3 Pa to 13.3 Pa range. Propane is slightly more effective, but only in the higher partial pressure range (Figure 102g).

The summary of the friction and wear data is enclosed in Tables 22 and 23. Clearly, h-BN can be considered as a solid lubricant in air only, which contained at least ≅50% relative humidity. The similarity with graphite is striking. Under such conditions the effect of crystalline alignment, so clearly observed in the propanol-rinsed state in UHV, disappeared. In the same way, no effect of the alignment was seen in the annealed state, in UHV. Low partial pressures of air, H_2O, O_2, N_2 and CO were ineffective in reducing the annealed condition's friction. Propane and air were slightly more effective, but only at the higher (13.3Pa) partial pressure. It is suspected that it was really the moisture content in air that exhibited the greatest effect on reducing friction.

The analytical electron microscopy of the wear debris indicated five different types of wear debris, designated as Types a through e in Table 23:

- Type a: basal-plane-slip flakes;
- Type b: small, bent flakes;
- Type c: crumpled flakes;
- Type d: rolled-up flakes ("rolling pins");
- Type e: amorphized, spheroidal grains.

Generally these types of wear fragments were present in all situations, but the proportion of each type depended on the particular type of test (see Table 23). Surprisingly, in air, only Type a particles were observed, regardless of the crystallite alignment. Undoubtedly, the role of moisture and hydrocarbon contaminants is of prime importance in determining the total amount of wear and the debris morphology.

More thorough discussions of all aspects of the XPS/AES tribometry and surface analytical work with h-BN may be found in APPENDIX D.

3.1.2.2.4 Tester 2A Experiments with Combat® BN and Cercomp® 40% h-BN/Si_3N_4 Composite in the Medium PV/High T Regime. The Tester 2A experiments were completed to determine the usefulness of nearly 100% h-BN and 40% h-BN/Si_3N_4 as solid lubricant materials for single and double transfer applications, at room temperature and at ~850°C, in air.

Table 22. The friction of Combat® BN as the function of test atmosphere.

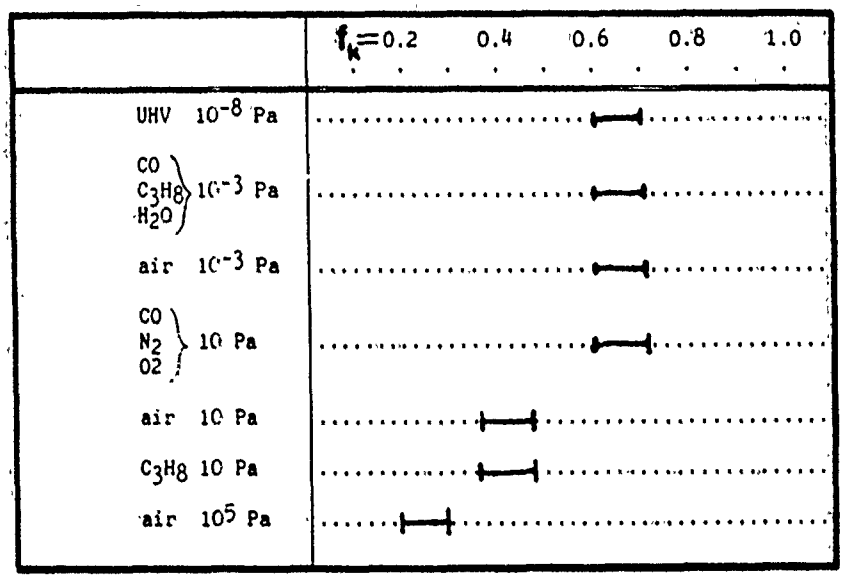

Table 23. The most significant friction and wear findings with Combat® BN, using XPS/AES tribometry.

Preparation Environment	Crystal Configuration	f_k Average	Pin Wear Scar Value	Flat Wear Scar Diameter	Wear Particle Types				
					a	b	c	d	e
Propanol air	*flat/flat*	0.09	Not visible	Not visible	+++	+	+		
Propanaol air	*edge/edge*	0.08	Not visible	Not visible	+++	+	+		
Propanol UHV	*flat/flat*	0.40	≈ 1 mm	++	+	+++	+++	+++	+++
Propanol UHV	*edge/edge*	0.50	≈ 1.3 mm	Not visible		+++	+++	+++	+++
Heat treated UHV	*flat/flat*	0.65	≈ 0.8 mm	++++	+	+++	+++	+++	+++
Heat treated UHV	*edge/edge*	0.65	1.4 mm	+		+++	+++	+++	+++

Single transfer constituted two flat, h-BN-containing rubshoes sliding against a Hexoloy SA-80T α-SiC RCF rod. In a double-transfer contact one rubshoe was h-BN-containing, the other was α-SiC, both mated against the α-SiC rod (see Figure 31b; the drawings of the rod and rubshoes used here are shown in Figures 35(-1) and 37). In the former case, the shear strength and absolute wear rate of the h-BN against α-SiC was measured. In the latter case, the ability of h-BN to transfer to the α-SiC rod and the capacity of this supposedly low-shear-strength transfer film to reduce the wear of the bare α-SiC rubshoe were measured.

The standard normal load for all tests was 13.34 N (1.36 kg = 3.0 lbs), the unidirectional sliding speed 0.35 $m \cdot s^{-1}$ (700 rpm), and the test duration ≅ 20 minutes. In some cases, especially at high temperatures, the wear rate of the Combat® h-BN (6% B_2O_3+94% h-BN) was so high that the normal spring load was relieved (reduced) considerably. In such cases, the test was terminated at the time when a 4.45 N (0.45 kg = 1.0 lb) normal load was reached. For that test, the average normal load was then taken as 8.9 N (0.9 kg = 2.0 lbs) in calculating the average wear rate in $m^3/N \cdot m$.

The test matrix and the data are included in Figure 103. Basically, both the 40% h-BN/Si_3N_4 and the ~100% h-BN materials were tested at room and at high (~850°C) temperatures, in the single-transfer and double-transfer modes, mostly with the h-BN blocks machined in the "plane" (=) configuration. Due to the possible variability of surface emissivities from material-to-material and condition-to-condition, the Vanzetti pyrometer's emissivity was set at ε=1.0. Therefore, the exact (high) test temperature is not precisely known. A few single/double transfer tests were also completed in the "edge" (⊥) alignment. Mainly, we wanted to see a presence or absence of any correlation with SORETRIB's work, with respect to the higher friction/lower wear nature of the (⊥) crystallite alignment.

The data in Figure 103 indicate the following:

1. Room temperature, single transfer, (=) only: The 40% material wore, surprisingly, nearly as much as the 100% (~1 x 10^{-12} $N^3/N \cdot m$), also see Figure 104. This wear rate is very high. The shear strength of the 100% was, however, one-third of the 40%. In general, the shear strength is very low. It is important to note that the coefficient of friction (f_k/COF, see Figure 105 for the respective tests' friction charts) is a systems parameter and its magnitude needs to be normalized to the apparent contact area. The normalized value is $\tau_{app.}$ (the apparent contact area = the projected area of the rubshoe wear scar). For example, the COF values in Figure 104 are not necessarily as low as the $\tau_{app.}$ values would indicate. $\tau_{app.}$ is low, because F_k is distributed over a large $A_{app.}$, due to the high wear rate of the materials.

2. High Temperature, Single Transfer, (=) vs. (⊥): The high temperature wear rate of both (=) materials is 3-to-4 times higher than the equivalent room temperature value. In comparing the (=) vs. (⊥) high temperature data the (⊥) wear rate is, in turn, 3-to-4-times lower than the (=). The wear-reducing ability of the (⊥) is surprisingly commensurate with no real change in surface shear strength. Note that the $\tau_{app.} \cong 0.05$ MPa is an extremely low value in view of τ_s = 8-10 MPa for MoS_2 films in vacuum. The low $\tau_{app.}$ is most probably caused by the fact that the real area of contact (A_r) is hundreds of times less than the wear-scar-area - estimated $A_{app.}$

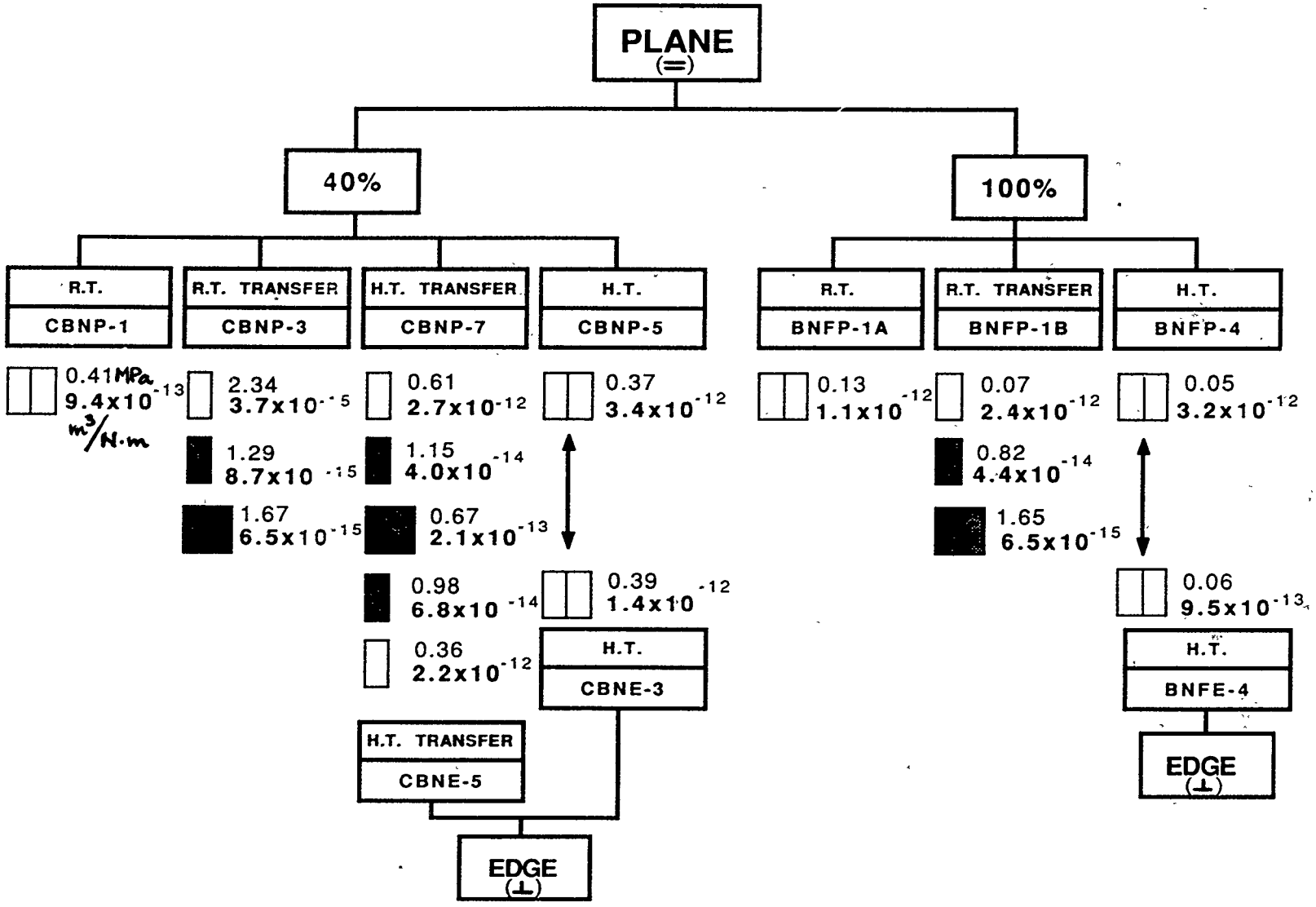

Figure 103. Tester 2A text matrix and data of the 40% h-BN containing Cercomp® and 100% h-BN Combat® BN; two white blocks (h-BN versus h-BN) signify single transfer h-BN wear; one white/one black (h-BN versus α-SiC versus α-SiC); bold-face number on the bottom of each set is the wear rate in $m^3/N \cdot m$; the plain-face number on top is the apparent shear strength in MPa, calculated on the basis of the projected wear scar area on each rubshoe block.

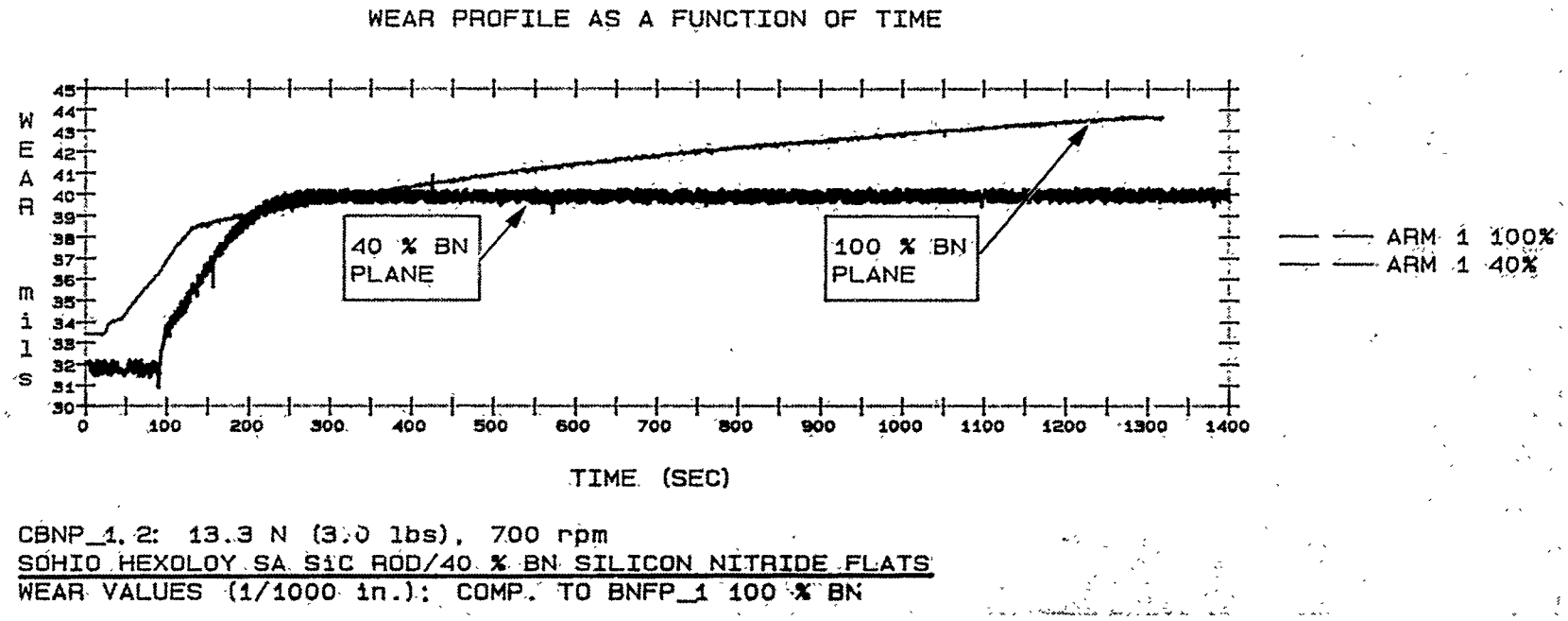

Figure 104. Wear rate differences between single transfer, 40% vs. ~100% h-BN rubshoe wear; R.T. (=) tests.

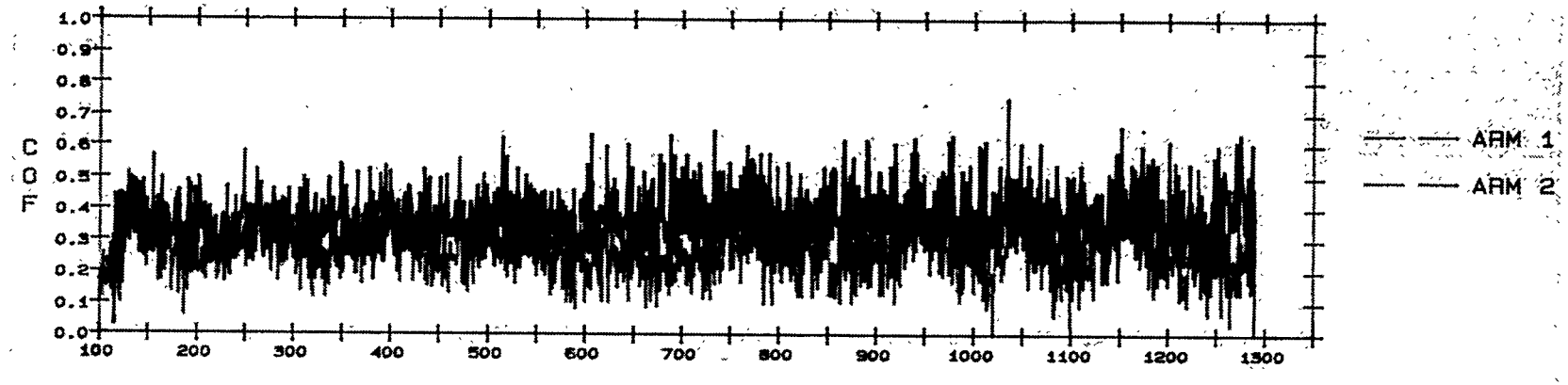

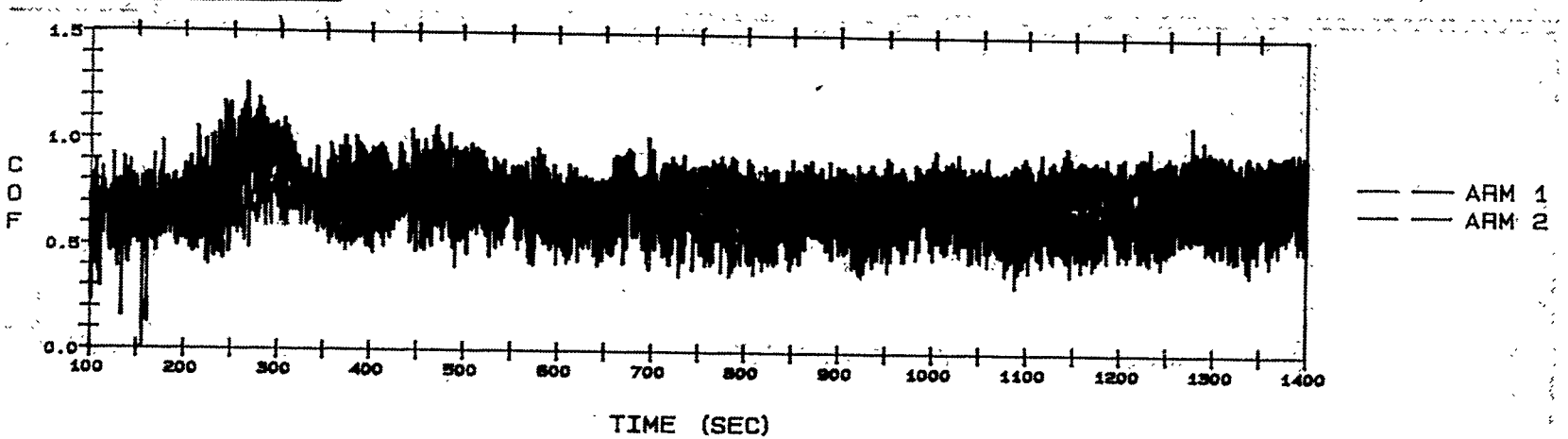

Figure 105. Coefficient of friction (COF) charts for the R.T. single-transfer tests in Figure 103 (Test Nos. CBNP-1/BNFB-1).

Note that due to the high wear rate, the effective normal load in these tests was the low average of 8.9N (0.9 kg = 2.0 lbs).

3. Room Temperature, Double Transfer, (=) only: The 40% h-BN/Si_3N_4 does not act like a self-lubricating composite. It did not reduce the wear of the companion α-SiC block (Test CBNP-3) by the formation of an effective transfer film: the wear rate was nearly the same as with an all-SiC vs. SiC rubbing combination, although some slight reduction in $\tau_{app.}$ was observed from 1.67 MPa (all SiC) to 1.29 MPa [(=) vs. α-SiC) rubshoes]. Interestingly, the wear of the h-BN-containing block was significantly less than its single-transfer (CBNP-1) counterpart. The ~100% h-BN was a lot more effective as a solid lubricant. The transfer film reduced the $\tau_{app.}$ of the α-SiC rubshoe by about a factor of two, and the wear rate of the α-SiC rubshoe by an order of magnitude. As shown in Figure 106, small particles of the h-BN do transfer to the mating α-SiC rod and get trapped in the α-SiC rubshoe's wear scar (thereby lie the large reduction in α-SiC rubshoe wear and the reduction in surface shear strength). The adhesion of the rod's transfer film is poor: a gentle wipe with a clean rag essentially removed all of the h-BN layer. Due to the high wear rate of the h-BN block itself (2.4×10^{-12} $m^3/N \cdot m$), the wear scar was wide and deep and, as such, the final load reached the lower limit = 4.45 N (0.454 kg = 1.0 lb) level. The average calculated load here, therefore, was also 8.9 N (0.9 kg = 2.0 lbs). Interestingly, as shown in Figure 107, the friction of ~100% h-BN was not much different from that of the single-transfer mode in Figure 105 and the friction of the transfer-film-coated α-SiC block (from Figure 106) was almost exactly the same as that of the bare α-SiC at R.T. (see Figures 42 and 43). Yet, the associated unlubricated/lubricated τ_s of the α-SiC blocks differed by a factor of two, due to the identical friction force (F_k) but a factor-of-two difference in $A_{app.}$, as shown in Figure 103. This is another good example of f_k(COF) acting as a systems parameter and not as an intrinsic material property. Although the average wear rate of the single-transfer ~100% h-BN is about one-half of its double-transfer rate (compare Test No. BNFP-1A with 1B), the real (time-dependent) wear rates shown in Figure 108 are different. The double-transfer rate is more gradual, but does not reach a higher plateau. The wear rate differences between the h-BN and α-SiC blocks are striking (i.e., the α-SiC wears much less).

4. High Temperature, Double-Transfer, 40% h-BN/Si_3N_4, (=) vs. (⊥); (CBNP vs. CBNE): The h-BN-containing and α-SiC block wear rates are virtually identical with each other. Both (=) and (⊥) crystallite configurations appear to reduce the wear of unlubricated α-SiC by about a factor of five, but at the cost of being accompanied by a ~50% increase in τ_s. The wear rates of the h-BN containing block are high (Figures 109 and 110). The ability of the double-transferred h-BN to be retained not only on the α-SiC rod, but on the α-SiC rubshoe wear scar (double-transferred from the rod) appears to be greater at high temperature. The accompanying (=) vs. (⊥) friction traces in Figure 111 indicate that the transferred h-BN particles act more like a vibration-damping medium in reducing the frictional variations ("hash") than an absolute shear strength-level-reducing entity. Due to the similarity of wear scar sizes and friction force magnitudes, this is one of the few cases when the f_k (COF) and τ_s values have a one-to-one

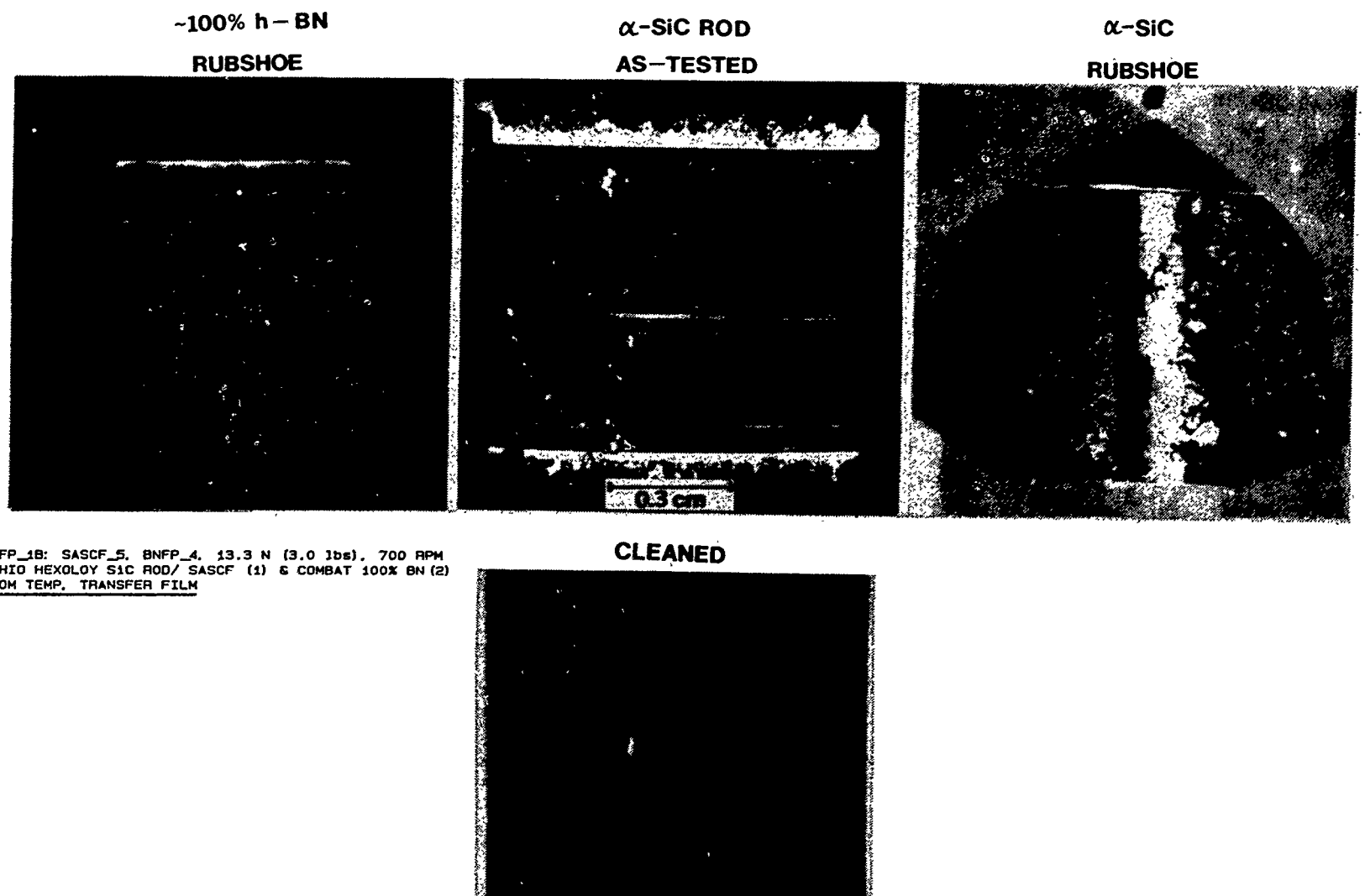

BNFP_1B: SASCF_5, BNFP_4, 13.3 N (3.0 lbs), 700 RPM
SOHIO HEXOLOY SiC ROD/ SASCF (1) & COMBAT 100% BN (2)
ROOM TEMP, TRANSFER FILM

Figure 106. Room temperature (R.T.) double-transfer of ~100% h-BN (Combat® BN) to α-SiC.

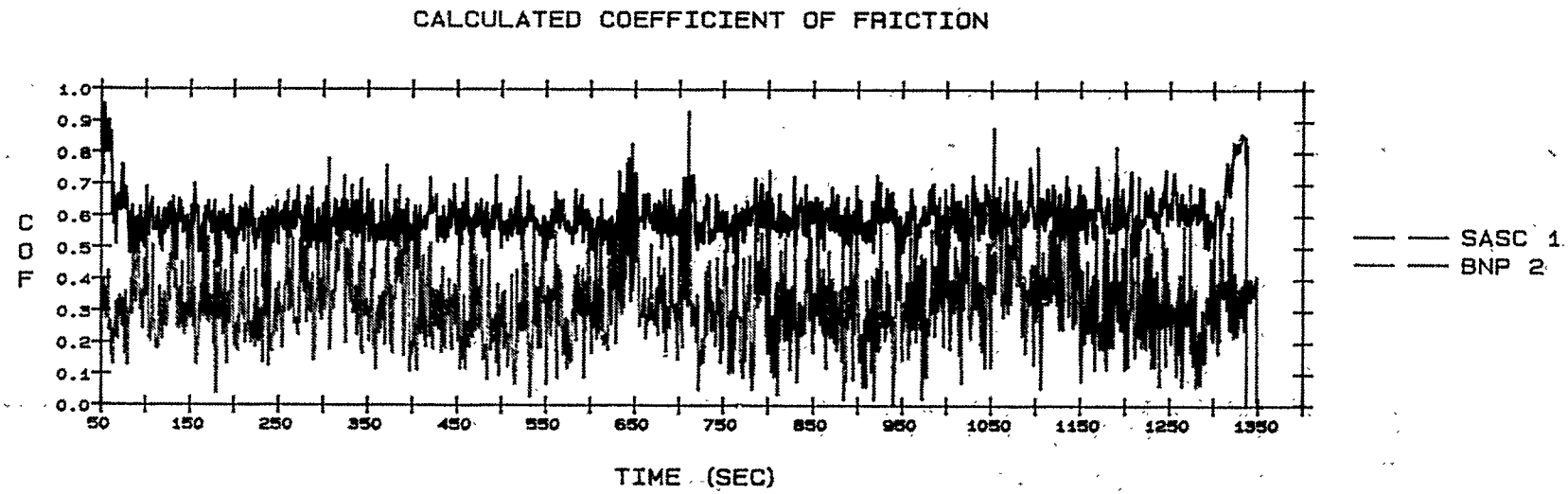

Figure 107. Room temperature (=) double transfer friction traces for ~100% h-BN and α-SiC.

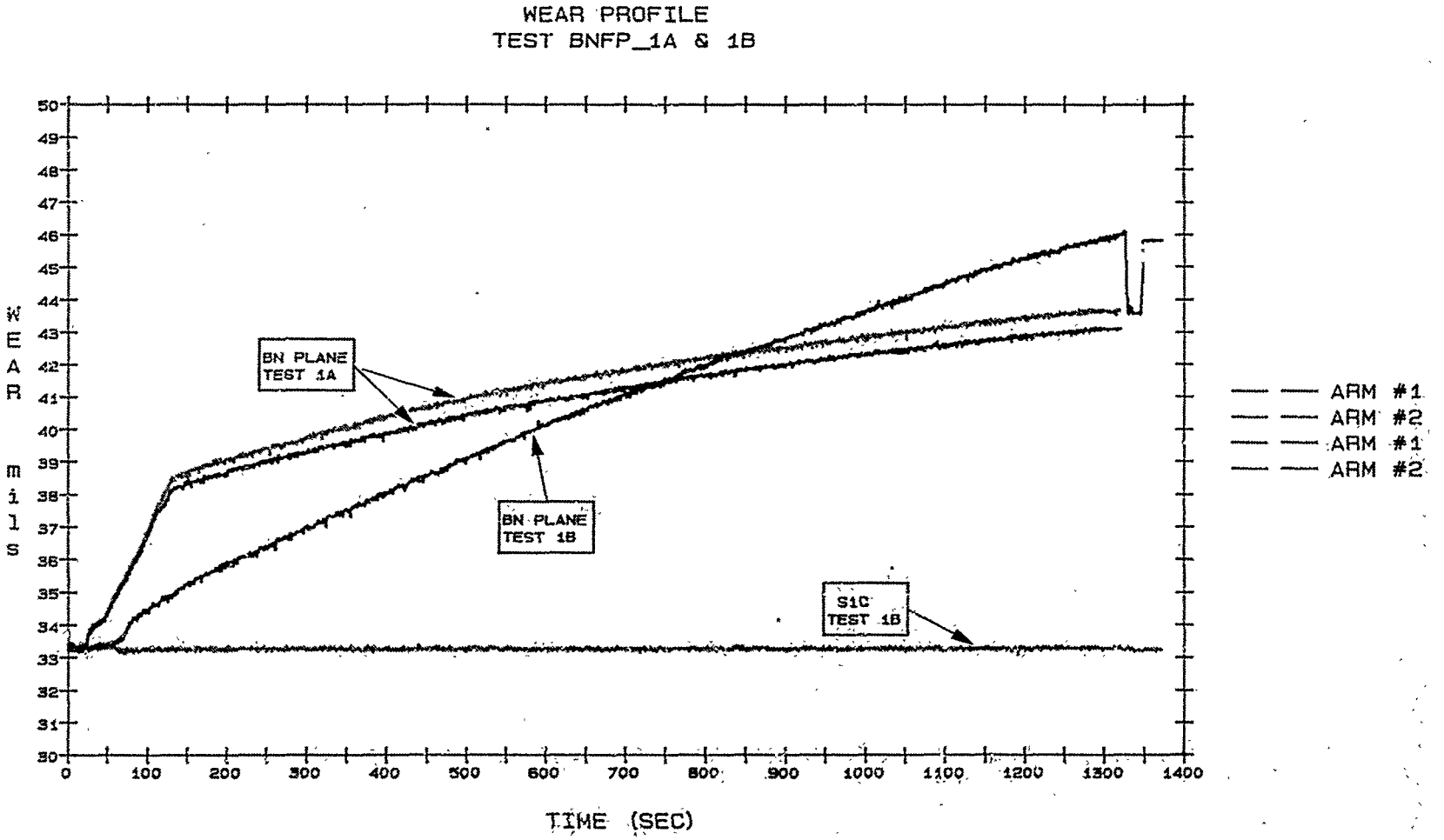

Figure 108. Room temperature, time-dependent wear rates of the (=) single and double-transfer ~100% h-BN blocks.

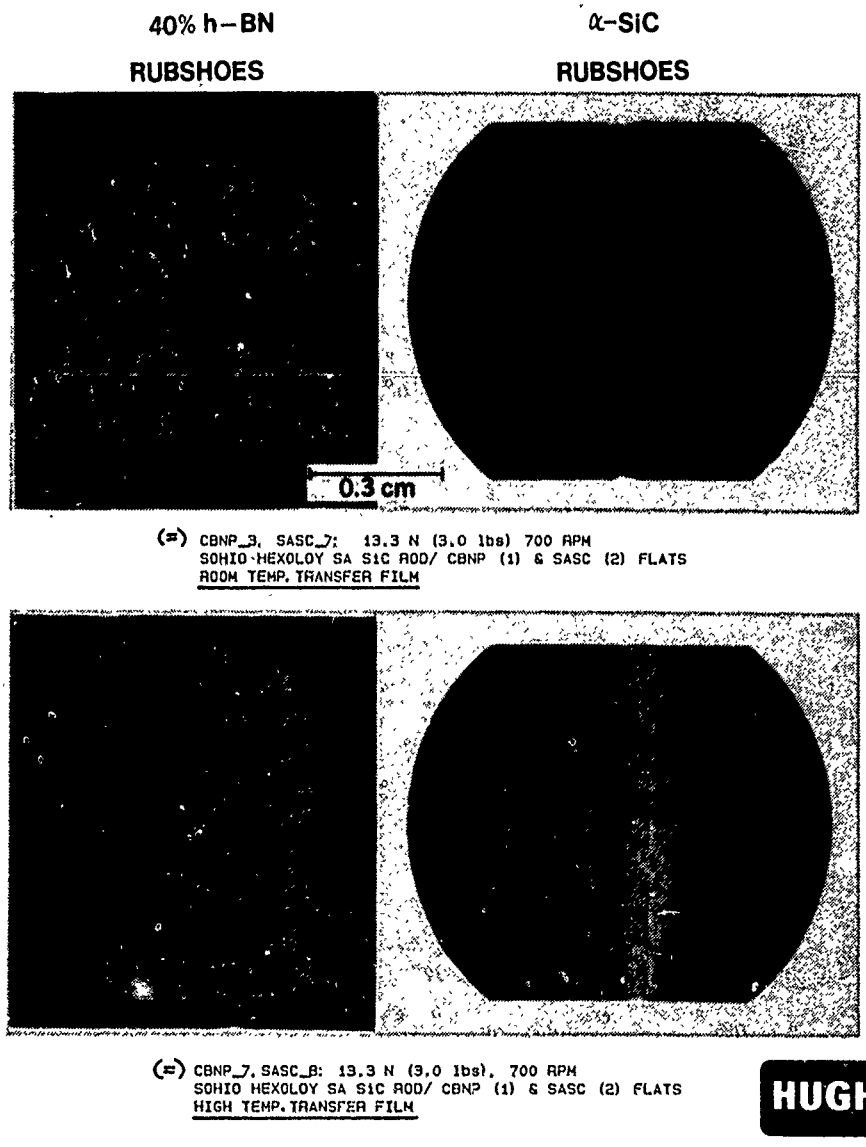

Figure 109. Appearance of (=) h-BN-containing Si_3N_4 and mating α-SiC rubshoes after R.T. and high temperature double-transfer tests.

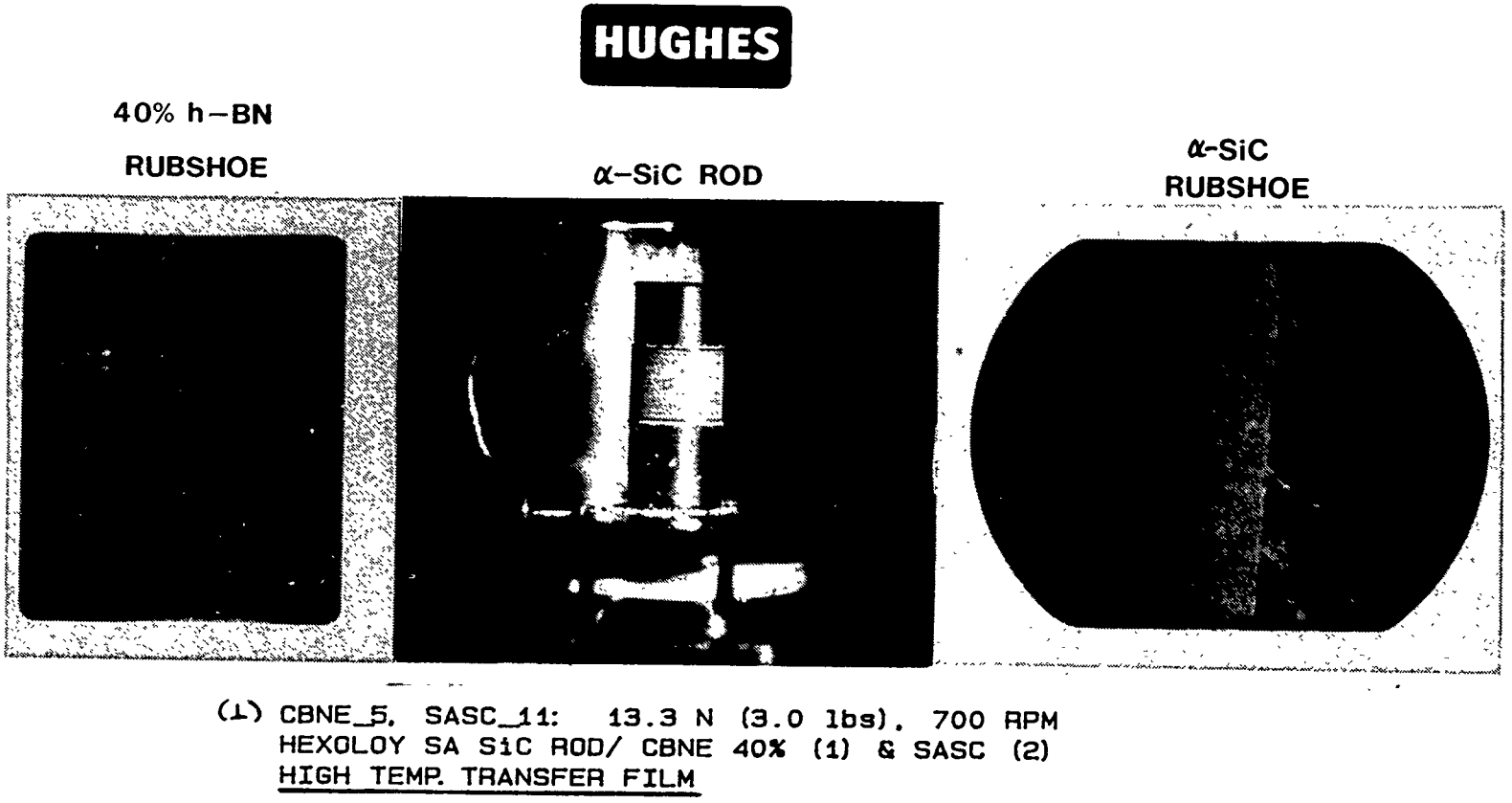

Figure 110. Appearance of (⊥) h-BN-containing Si_3N_4 and mating α-SiC rubshoes after high temperature double-transfer test.

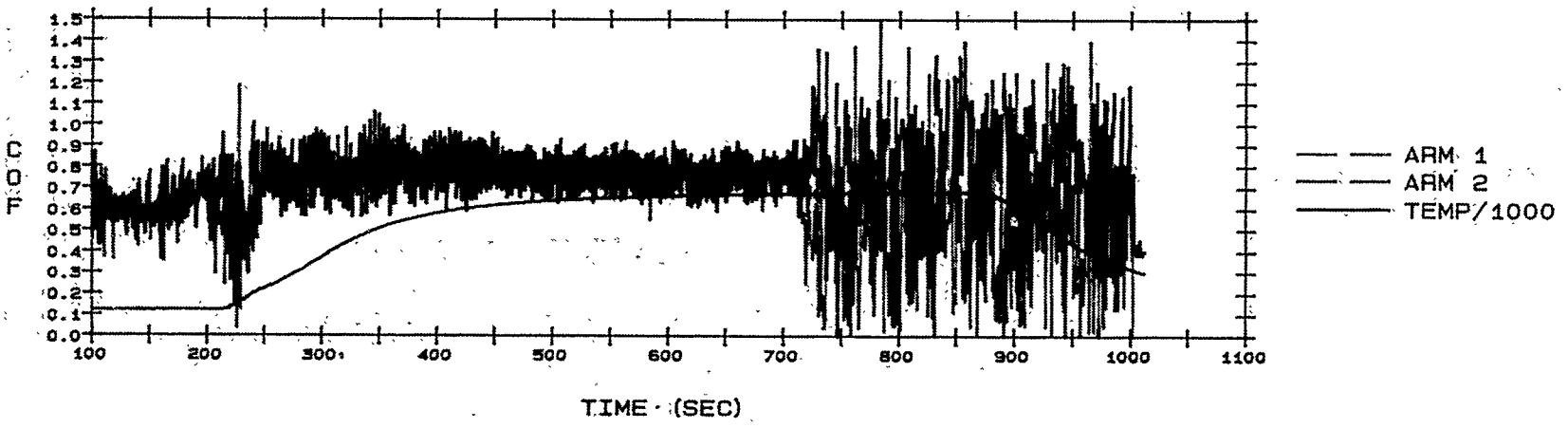

CBNP_7, SASC_8: 13.3 N (3.0 lbs), 700 RPM
SOHIO HEXOLOY SA SiC ROD/ CBNP(=)(1) & SASC (2) FLATS
HIGH TEMP. TRANSFER FILM

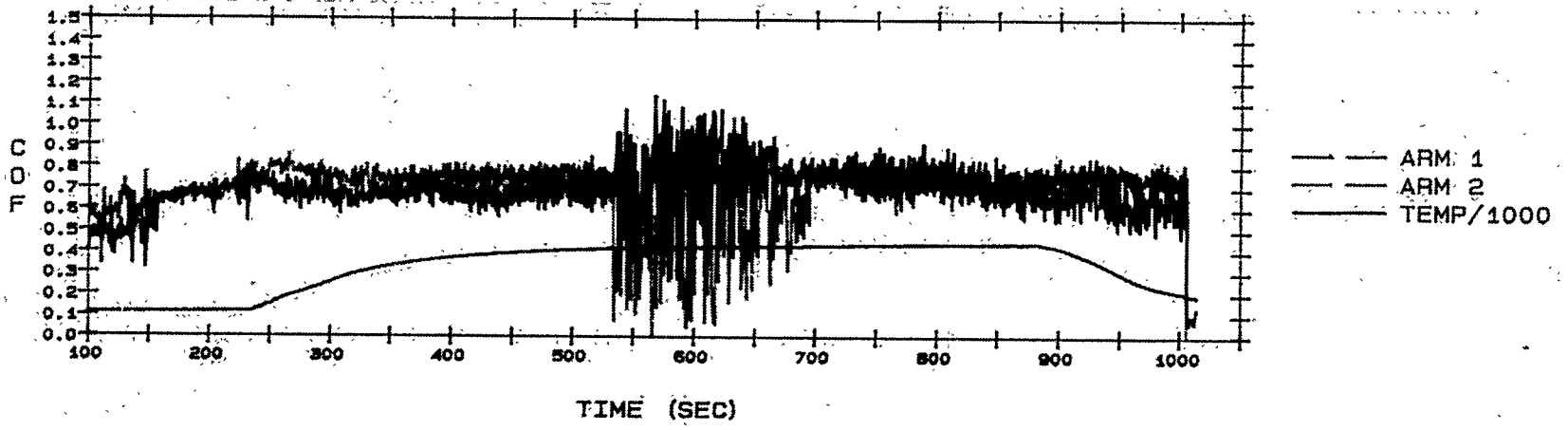

CBNE_5, SASC_11: 13.3 N (3.0 lbs), 700 RPM
HEXOLOY SA SiC ROD/ CBNE 40(⊥)(1) & SASC (2)
HIGH TEMP. TRANSFER FILM

Figure 111. Coefficients of friction (COF) charts for the high temperature (=) vs. (⊥) double-transfer film tests.

correlation. It is noteworthy that due to some yet unexplainable cause, the vibration damping ability of the transfer film can be temporarily (or permanently?) disturbed during a given test. This disturbance is manifested by a sudden appearance and disappearance of high "hash". However, as shown in Figure 112, the high-temperature transfer film is more efficient in such "damping" than the room temperature version. Note that no equivalent high temperature tests were run with the ~100% h-BN due to its extremely high wear rate.

The overall results may be summarized, as follows:

1. In air, pure or Si_3N_4-bonded h-BN is a poor lubricant at room temperature.
2. In air, only the Si_3N_4-bonded h-BN is a viable "self-lubricating" composite, but only at high temperatures. The wear rate of ~100% h-BN is far too high at any temperature.
3. Any shear strength- or frictional-variation-reducing ability of h-BN transfer films appears to be attributed more to the vibration-damping capability of the debris films than to the low shear strength of the films themselves.
4. The h-BN materials with exposed basal plane edge sites have the same shear properties, but measurably lower wear than those with the exposed basal plane sites.
5. The hot-pressed, 40% h-BN/Si_3N_4 Cercomp® compact is recommended only as a base-stock for reasonably wear-resistant, self-lubricated composite parts. The resultant friction/traction would be, however, high. All composite parts should be fabricated in the "edge" ($\perp$) configuration for maximum wear resistance, with no significant increase in surface shear strength of the sliding combination.

3.1.2.2.5 *High PVT Pin-on-Disc (Sliding) and Disc-on-Disc (Rolling) Experiments at MTI.* The materials tested during pin-on-disc wear tests were supplied by Hughes and consisted of:

- Three a-SiC discs;
- One Si_3N_4 disc containing 0.0% BN;
- One Si_3N_4 disc containing 3.5% BN;
- Si_3N_4 pins containing 0.0% BN;
- Si_3N_4 pins containing 3.5% BN;
- Si_3N_4 pins containing 15.0% BN;
- Si_3N_4 pins containing 40.0% BN;
- α-SiC pins (HIP);
- α-SiC pins (post-HIP).

A total of 20 tests were completed on the 5 discs by designating four separate test paths (wear scar sites) on each disc. Table 24 contains the test matrix developed, maximizing the number of variations of material combinations that could be tested within the constraints of the program. These tests were intended as PV extensions of the Tester 2A experiments to higher loads and speeds.

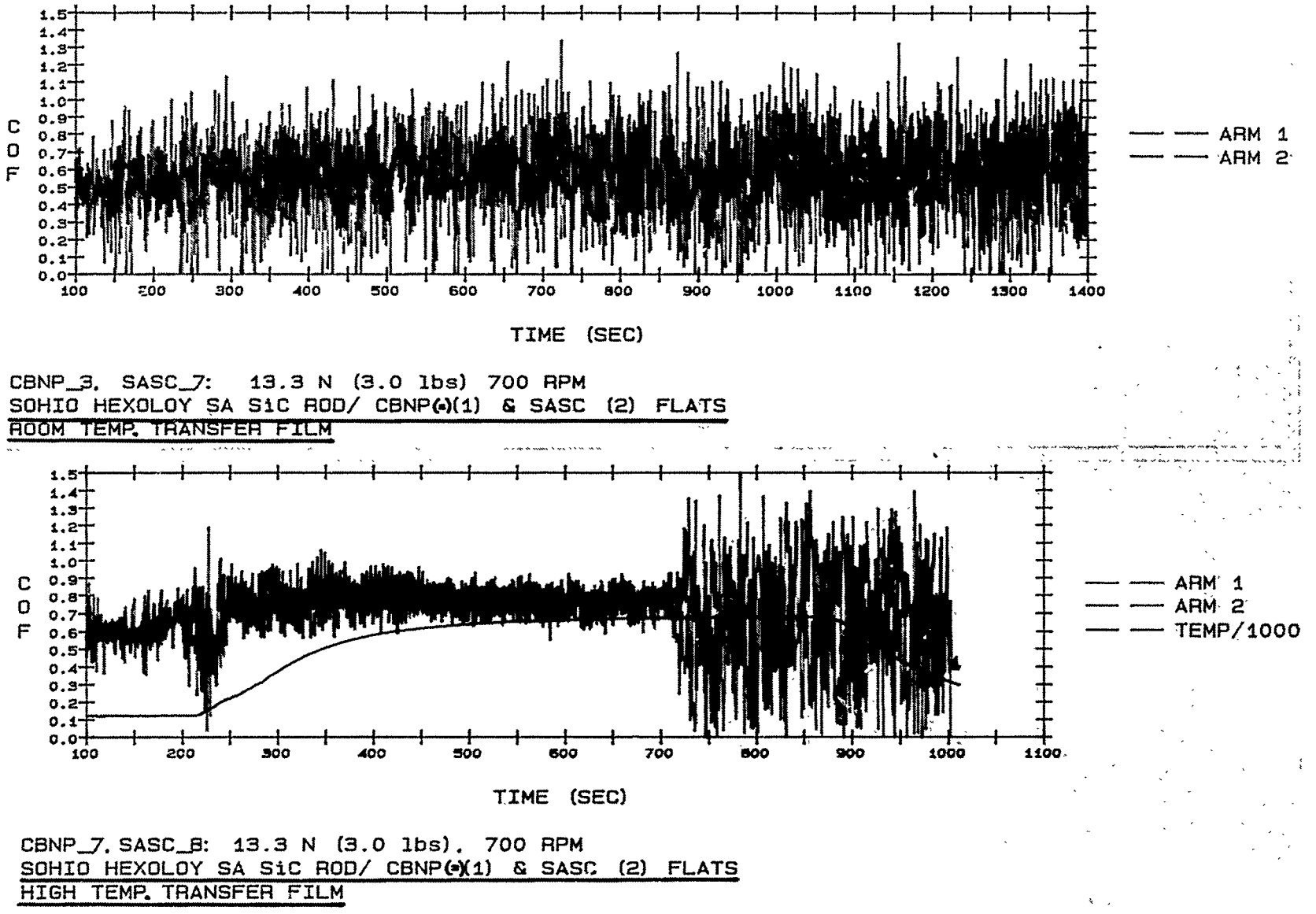

Figure 112. Coefficients of friction (COF) charts for R.T. vs. high temperature (=) double-transfer film tests.

Table 24. MTI pin-on-disc test matrix and summary of the results.

		Test No.	Track	Material	Process	Temperature	Comments
SiC[1] Disks	Disk 1 αSiC (Hipped)	HU-1	1	40% BN[3]	Flat	Ambient	7000 rpm Maximum Speed
		HU-2	2	40% BN	Flat	1200°F	Destroyed
		HU-3	3	40% BN	Edge	Ambient	Destroyed
		HU-4	4	40% BN	Edge	1200°F	Destroyed
	Disk 2 αSiC (Hipped)	HU-5	1	3.5% BN	Edge	Ambient	Completed
		HU-6	2	40% BN	Edge	Ambient	Completed
		HU-7	3	COMBAT	Edge	Ambient	Completed
		HU-8	4	40% BN	Edge	1200°F	1000 rpm Maximum Speed; Pin Wore Out
	Disk 3 αSiC (Hipped)	HU-9	1	SiC	Hipped	Ambient	Inconclusive
		HU-10	2	15% BN	Edge	Ambient	Completed
		HU-11	3	SiC	Post Hipped	Ambient	5000 rpm Maximum Speed
		HU-12	4	SiC	Hipped	Ambient	7000 rpm Maximum Speed
SiN[2] Disks	Disk 4 0% BN in Disk	HU-13	1	0% BN	Flat	Ambient	Completed
		HU-14	2	40% BN	Flat	Ambient	Completed
		HU-15	3	αSiC	Hipped	Ambient	7000 rpm Maximum Speed
		HU-16	4	αSiC	Hipped	1200°F	Completed
	Disk 5 3.5% BN in Disk	HU-17	1	0% BN	Flat	Ambient	7000 rpm Maximum Speed
		HU-18	2	40% BN	Flat	Ambient	Completed
		HU-19	3	αSiC	Hipped	Ambient	Completed
		HU-20	4	αSiC	Hipped	1200°F	Completed

[1]Silicon Carbide
[2]Silicon Nitride
[3]Boron Nitride

There were five distinct speeds used for this testing:

- 3.990 $m \cdot s^{-1}$ (1000 rpm, 157.08 $in \cdot s^{-1}$)
- 11.969 $m \cdot s^{-1}$ (3000 rpm, 471.24 $in \cdot s^{-1}$)
- 19.949 $m \cdot s^{-1}$ (5000 rpm, 785.40 $in \cdot s^{-1}$)
- 27.929 $m \cdot s^{-1}$ (7000 rpm, 1099.56 $in \cdot s^{-1}$)
- 35.908 $m \cdot s^{-1}$ (9000 rpm, 1413.72 $in \cdot s^{-1}$)

The contact stresses were varied between 0.89 GPa and 1.11 GPa, depending on the anticipated wear rate of the materials. The temperature was either room ambient (i.e., no heat added, except the naturally developed frictional heating) or ~650°C = 1200°F, raised by a resistance-heated oven. For the overall view of the apparatus see Figure 54; the test specimen drawings are included in Figure 55.

The test results were previously presented in Tables 11 and 12. To preface data interpretation, the Si_3N_4 pins - with or without the h-BN additive - had a significantly lower frictional force when running against either Si_3N_4 or SiC disc, than α-SiC pins. On the other hand, the wear of these Si_3N_4 pins was greater than that of the α-SiC pins, especially at elevated temperatures. In fact, in ~650°C air, the volumetric wear of the Si_3N_4 pins was almost 200 times greater than the equivalent SiC pins.

All test procedures and data analysis techniques are described more thoroughly in APPENDICES O and Y.

As shown in Table 11, the 40% h-BN/Si_3N_4 Cercomp® demonstrated remarkably low wear at room temperature, but extraordinarily high wear (1000x more) at ~650°C. The "edge" (⊥) orientation wore less than the "flat" (=) version, compare Test No. HV-1 and HV-6. The relatively high wear of the ~100% h-BN is obvious (see Test No. HV-7). These results confirm similar ones obtained with the Tester 2A.

Based on the friction data from Table 12 and the pin/disc wear scar dimensions, the equivalent $\tau_{app.} = F_k/A_{app.}$ surface shear strength data are included in Table 25. The data at R.T. indicated that:

1. The τ_s of the 40% h-BN/Si_3N_4 (⊥) is significantly (~2-to-3 times) higher than the (=). Lowering the h-BN content to ~3.5% did not significantly change that high value. In any sliding couple, as long as the one specimen contained some h-BN, τ_s ($\tau_{app.}$) was always less than 0.002 MPa.

2. The highest apparent shear strength ($\tau_{app.}$) was observed with α-SiC vs. α-SiC unlubricated (~0.01 MPa). The presence of any Si_3N_4 in a sliding combination reduced this value by 50-to-100 times, depending on the absence or presence of h-BN in the Si_3N_4 sample, respectively.

At high temperatures and at high PV, only a few combinations survived well enough to allow $\tau_s = \tau_{app.}$ calculations based on wear scar sizes. The results indicated that τ_s of α-SiC vs. Si_3N_4 combinations at ~650°C is about 2-to-10-times higher than at R.T.

The overall results appear to confirm the hypothesis that under severe tribooxidative conditions the tribooxidative wear resistance, in terms of glassy surface layer formation, is the controlling factor in determining the wear rate of silicon ceramics. The lower oxidation resistance of Si_3N_4 (see Figure 82),

Table 25. Normalized surface shear strength (τ_S) values of the MTI pin-on-disc test matrix, in units of $N \cdot m^{-2}$ (Pa).

	Pin Material	Disk Material		
		SiC	SiN	SiN, 3.5% BN
Ambient Conditions	SiN, 40% BN (Flat)	13.1	13.8	23.4
	SiN, 3.5% BN (Edge)	36.5		
	SiN, 40% BN (Edge)	35.1		
	SiN, 15% BN	26.2		
	SiC (Hipped)	115.1		16.5
	SiC (Post Hipped)	102.0	54.5	
	SiN, 0% BN		17.9	13.1
600°C ~ 1200°F	SiN, 40% BN (Edge)			
	SiC (Hipped)		93.1	
	SiC (Hipped)			144.1

[1] τ = Frictional force ÷ contact area of wear scar. Expressed in Newtons per square meter.

combined with the higher thermal conductivity of α-SiC to dissipate frictional heat away from the interface outweigh the effects of the slightly higher hardness (Figure 113) and fracture toughness of Si_3N_4 materials in controlling the wear rate. At the same time, the larger amounts of glass formed and sheared at the interface reduce the shear stress $\tau_s = \tau_{app.}$ to the lowest values (and the highest wear) measured in high temperature air.

As also shown in APPENDIX O, the powder lubrication phase of the MTI program was conducted with Kyocera HPSN and ESK α-SiC (post-HIP) tribospecimens. The powder lubricants used were titanium dioxide (TiO_2) in the rutile polymorph, h-BN and molybdenum disulfide, (MoS_2). The investigation was carried out using the disc-on-disc machine (Figure 54b) and measurements were made for a range of loads and ambient temperatures up to 650°C. A matrix of the test conditions is provided in Table 26.

The traction data at room temperature, using h-BN, gave surface yield shear stresses ($\tau_{app.}$) that were much lower than those for the unlubricated tests. At ~650°C, the yield shear stresses were more comparable to the unlubricated data. At room temperature, damage to the surface of the plain disc was not excessive. At high temperatures, the wear track showed significant damage with particles of the h-BN powder embedded in the track. The crowned disc suffered similar damage. Contrary to its high temperature utility in the sliding mode to some extent, h-BN powder is a poor high temperature lubricant in the rolling mode.

3.2 LAYERED HEXAGONAL SOLID LUBRICANTS

3.2.1 Single Crystals and Sputtered Films of MoS_2

3.2.1.1 Oxidation of Single Crystals of MoS_2 by Environmental SEM Video and Photomicrography. The well-known anisotropic, layered-hexagonal crystal structure and the strong intralayer and weak interlayer forces resulting therefrom render MoS_2 the best solid lubricant for vacuum applications (211). As discussed by Jones and Hoover (212) and Gardos (213), the two major shortcomings are the abrasiveness of the hard and chemically active edge sites (Figure 114) and the ready oxidation and hydration of these crystallite edges. As further discussed in (213), oxidation of MoS_2 results in a substantial increase in friction. Although higher in friction than MoS_2, the stable oxide generated from it is the soft, relatively non-abrasive MoO_3. The higher friction, yet still lubricating properties of MoO_3 have been attributed to the low τ_s of the (010) planes, where no bonds are broken during cleavage or shear. Nevertheless, the friction and wear mechanism changes during the $MoS_2 \rightarrow MoO_3$ transformation remained unclear beyond Gänsheimer simple model in (214), see Figure 115. Since MoO_3 will preferentially form at the active sites [e.g., the ratio for the rate of MoS_2 oxidation along the c-axis to the parallel with the basal planes was found to be 10^{-1} at emergent screw dislocations, 10^{-2} at the non-basal edge dislocations and 10^{-11} at ideal, perfect sites on the basal surface, see (213)], the picture in Figure 115 appears somewhat simplistic.

CERAMIC	THERMAL CONDUCTIVITY (W/mK)
HSPN	10-40
α-SiC	90

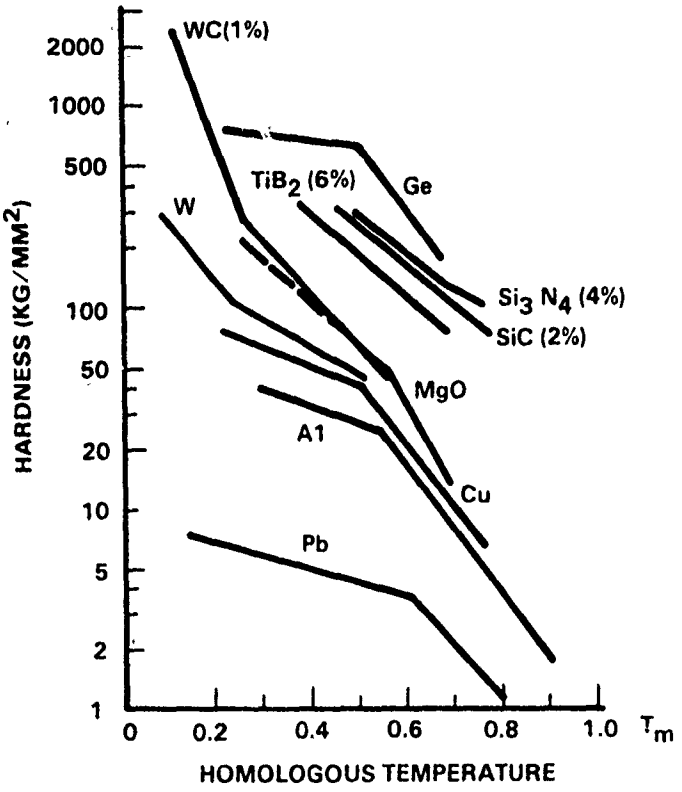

Figure 113. Hardness and thermal conductivity comparison of α-SiC and Si_3N_4.

Table 26. Disc-on-disc traction test conditions at MTI.

Lubricant	Room Temperature					≈ 800°F					≈ 1200°F				
	Load (lb)														
	4	10	15	20	25	5	10	15	20	25	5	10	15	20	25
None	4*	4	3								4	2			
TiO_2**	3	2									4	3			
BN	6	3	4								8	5			
MoS_2	6	1	2	1	1	1	1	4	1	4	2	1	4	2	2

*Number of repeated tests.
**TiO_2 - Rutile form, < 2 μm

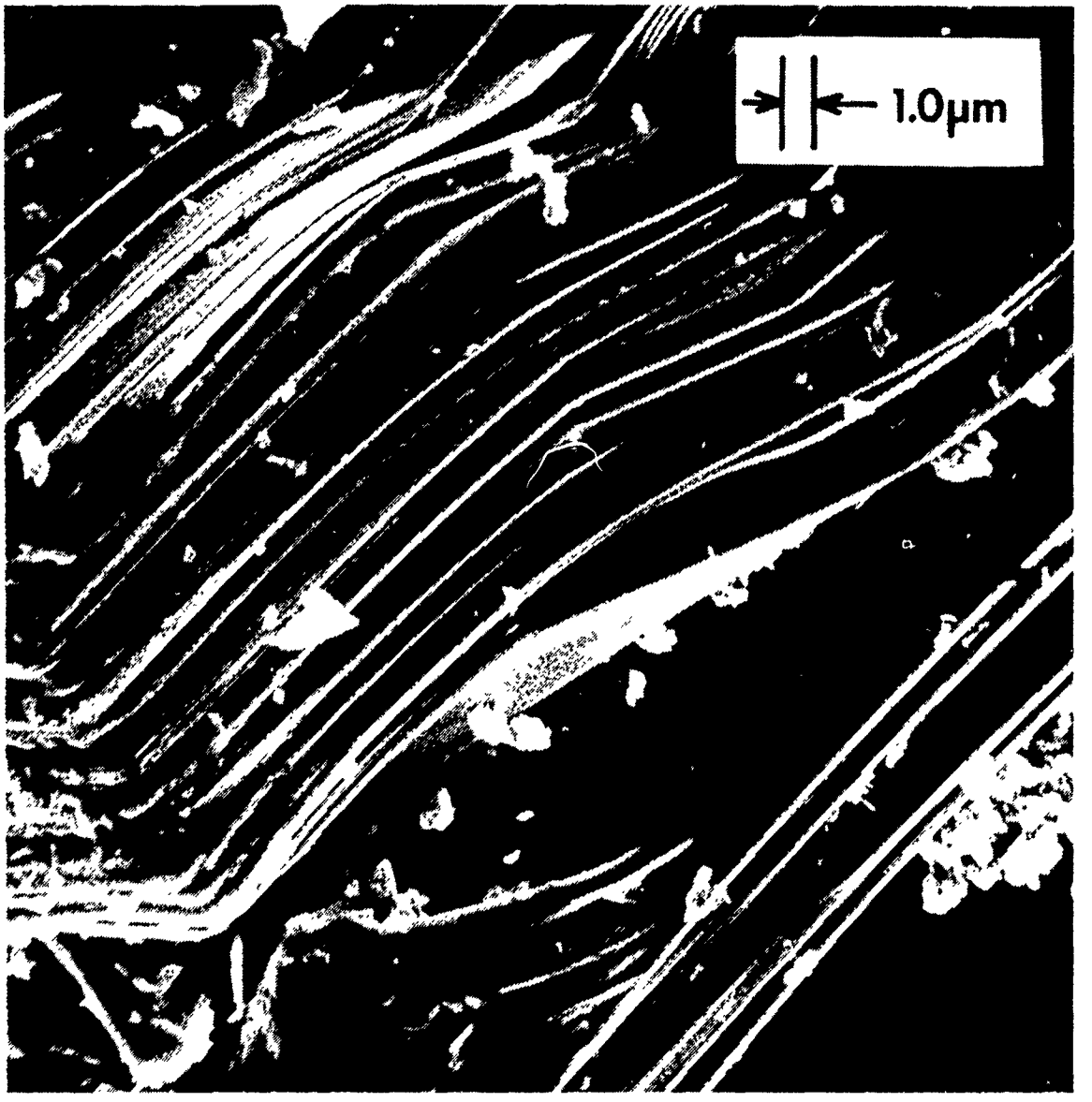

Figure 114. SEM photomicrograph of natural molybdenite crystal edge sites (211).

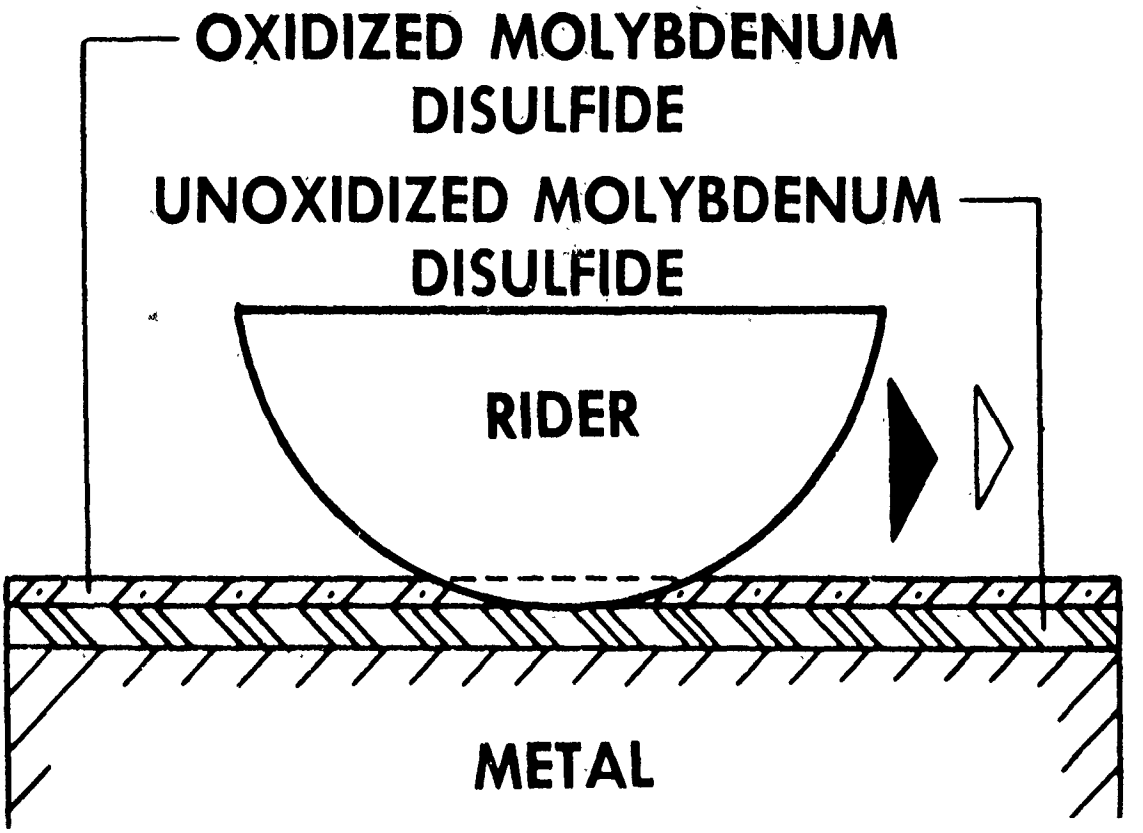

Figure 115. Gänsheimer's schematic on the lubrication properties of partially oxidized MoS_2 film (214).

To gain a more realistic picture of MoS_2 topography changes during the oxidation of MoS_2 crystallites, environmental SEM photomicrography was performed with MRL Inc.,'s SEM hot-stage depicted in Figure 13. A small flake was cleaved (under LN_2, using an X-acto knife) from a large, freshly cleaved molybenite crystal (Figure 116). The flake was placed on the hot stage and exposed to a sequential test protocol, in the following order:

- 650°C/1.33 x 10^{-3} Pa = 1 x 10^{-5} torr vac./5 min.
- 650°C/133 Pa = 1.0 torr P_{O_2}/5 min.
- 650°C/1.33 x 10^{-3} Pa = 1 x 10^{-5} torr vac./~30 sec.
- 850°C/1.33 x 10^{-3} Pa = 1 x 10^{-5} torr vac./5 min.
- 850°C/133 Pa = 1.0 torr P_{O_2}/5 min.
- 850°C/1.33 x 10^{-3} Pa = 1 x 10^{-5} torr vac./~30 sec.

The appearance of the MoS_2 flake's surface was continuously monitored by video. After each heating cycle which induced visible changes on the sample, high resolution SEM photomicrography was performed to reveal topographic and crystal morphology changes at various SEM magnifications.

SEM video and photomicrography revealed no observable changes at 650°C, not even in P_{O_2}. Only at 850°C/133 Pa P_{O_2} and vacuum heating afterwards induced visible alterations on the surface:

1. As shown in Figure 117, oxidation of MoS_2 does initiate and propagate at the basal plane edge sites. Note that during the 5-minute heating cycle, the small MoS_2 islands (indicated by arrows) became wholly converted into the oxides. Due to the differences in charging between the oxides and the sulfide, the degradation was clearly identified by video. Owing to the well-known volatility of molybdenum oxides (215), some of the oxide(s) converted from the sulfide sublimed at 850°C (see the reduction in the size of the sulfide and oxide flakes indicated by the arrows).

2. The layer-by-layer oxidation of the arrow-indicated flakes in Figure 117 is depicted with even more clarity in Figure 118a. The more exposed, top oxide layer became evaporatively depleted more than the somewhat more protected sulfide/oxide sheet underneath. As the edge sites progressively volatilize, the needle-like, blocky oxide crystallites remain behind on their highly inert, basal plane support. Although most of the basal plane surfaces appeared extremely oxidation resistant, others did contain scratches, ledges, steps and point defects, where oxidation initiated and propagated preferentially (Figure 118b).

3. The morphology of the oxides forming at the basal plane edges at 850°C/1.0 torr P_{O_2} is depicted with special clarity in the Figure 119a SEM photomicrographs. The needle-like oxide whiskers grow with their c-axis parallel with the (0001) basal plane of MoS_2. Based on literature information (216 through 220), these crystallites are most likely to be a mixture of MoO_3 and its suboxides. The amount of oxides left on the yet-unreacted MoS_2 basal planes depend on the balance of oxide formation and sublimation kinetics. The oxide volumes depicted in Figure 119a largely volatilized on subsequent heating, at 850°C, in vacuum. This treatment left rounded and blocky oxide crystallites behind at the reacted edge sites.

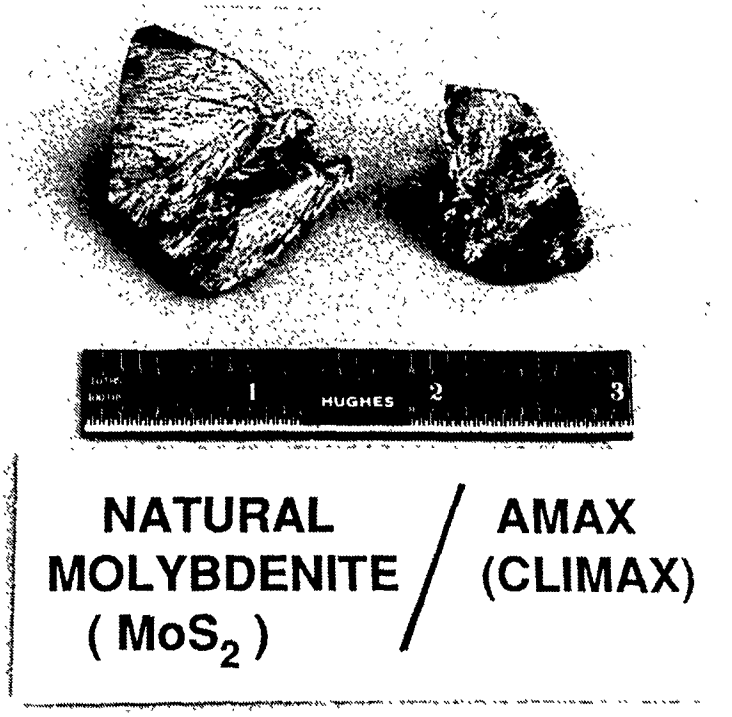

Figure 116. Large, natural molybdenite crystal (provided by Mr. Thomas J. Risdon of AMAX/Climax, Ann Arbor, MI), cleaved in liquid nitrogen at Hughes.

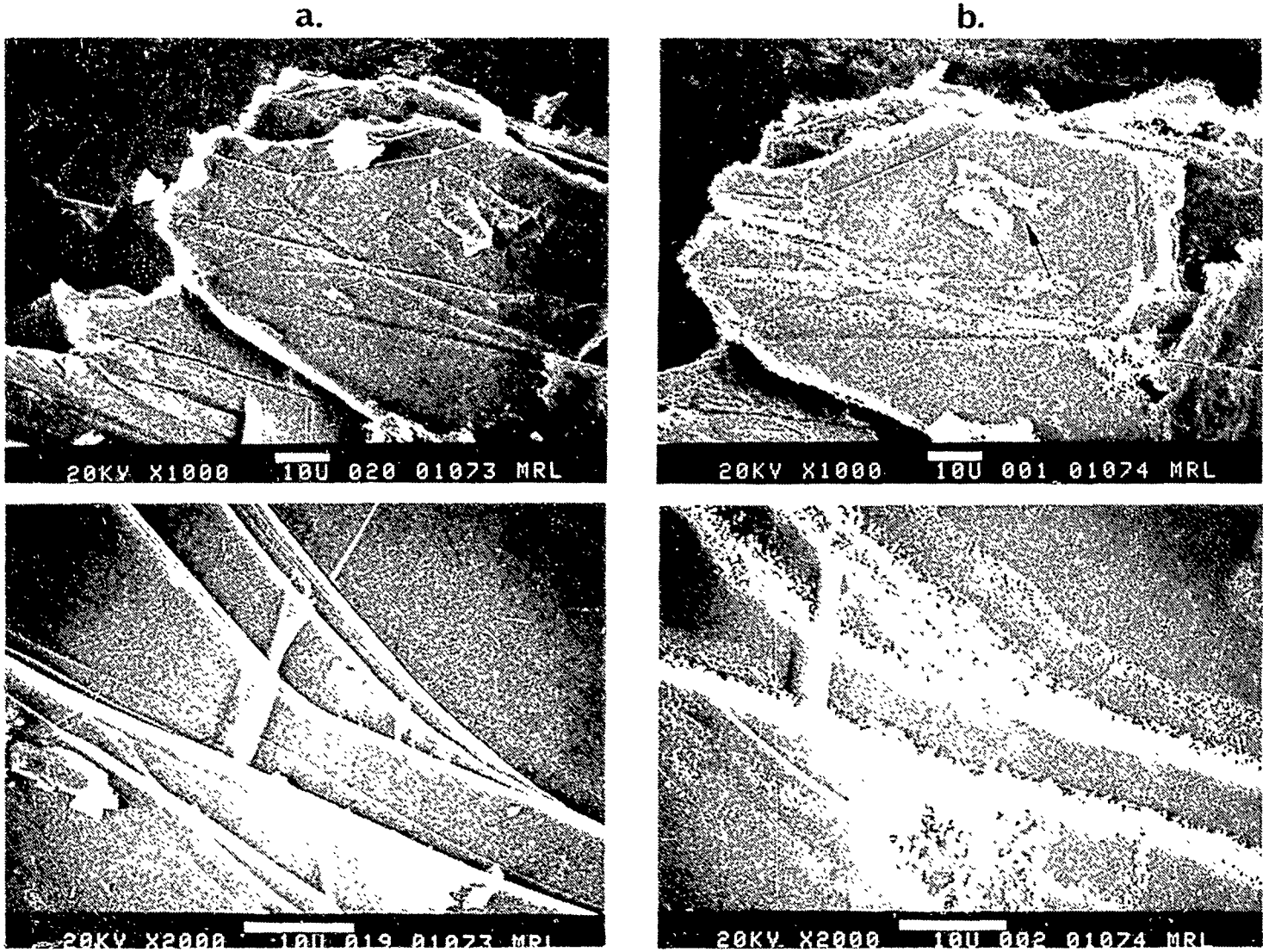

Figure 117. SEM photomicrographs of natural molybdenite flake (a) before and (b) after oxidation for 5 minutes, in 133 Pa = 1.0 torr O_2 at 850°C, on the hot-stage of the MRL, Inc. environmental-SEM Knudsen-cell (see Figure 13).

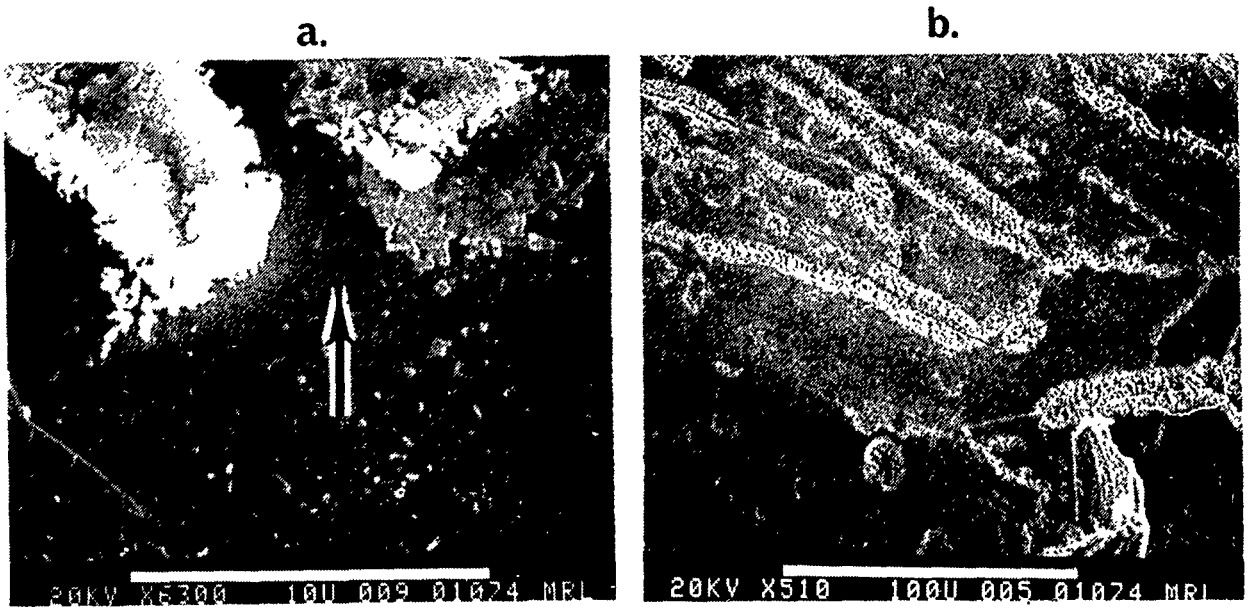

Figure 118. Salient features of the oxidized flake in Figure 117 by SEM photomicrography: (a) close-up of MoS_2 flake (see arrow) entirely converted to molybdenum oxides, in layers; (b) preferential oxidation at basal plane scratches, step-sites and point defects.

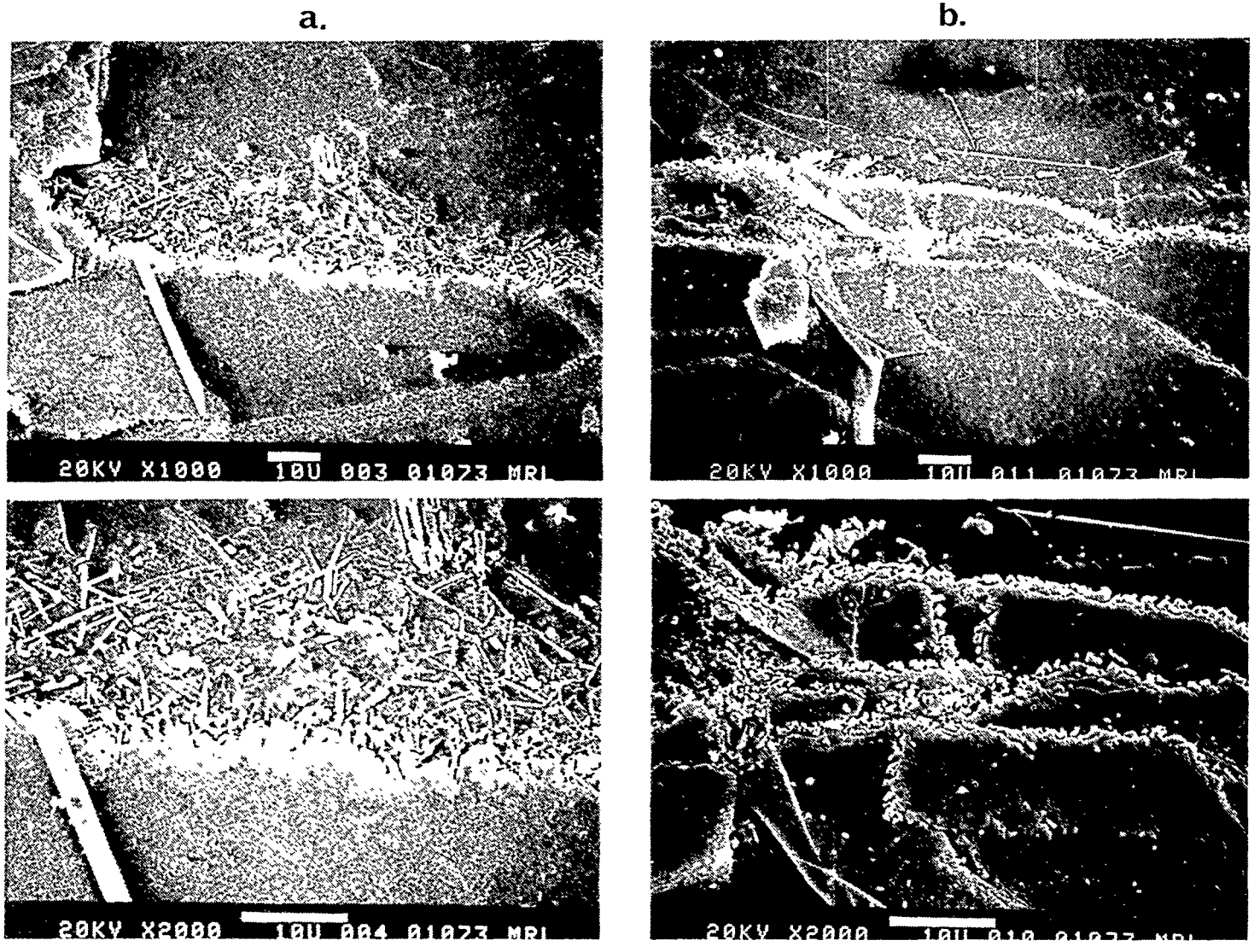

Figure 119 High magnification SEM photomicrographs of oxidized basal plane edge sites from Figure 117 (a) before and (b) after exposure to 1.33×10^{-3} Pa = 1×10^{-5} torr/850°C, for 10 seconds.

The data indicate that Gänsheimer's simple scheme in Figure 115 is quite accurate. As the edge sites of MoS_2 oxidize, the converted material remains behind, supported by the underlying basal planes.

The rubbing counterface will preferentially slide against the oxides now partially or fully covering the basal planes aligned in the plane of sliding.

3.2.1.2 SEM Tribometry of Sputtered MoS_2 Films. A great deal of effort has been expended by the SDI-funded Tribology Insertion Working Group (TIWG), a group of U.S. Government (DoD) scientists, whose charter currently includes sputtering MoS_2 films with progressively improved friction and wear properties. Most noteworthy of these workers are Dr. Paul D. Fleischauer and his staff at the Aerospace corporation (El Segundo, CA) and Dr. Irvin L. Singer and his staff at NRL, whose fundamental work in the field have also been partially funded by DARPA and subsequently transitioned into the SDI effort.

Dr. Paul D. Fleischauer's in-house activities have dealt with the enhancement of adhesion between sputtered MoS_2 films and ceramic substrates (5). The greatest significance of his and his staff's research lies in showing that active sites on the surface of carbon-contaminated or thin oxide-hydroxide covered ceramics cause orientation of the MoS_2 lamellae/crystallites perpendicular to the substrate. The removal of such sites (by e.g., chemical etching of the surface layer with an HF/HNO_3 solution) results in the deposition of the MoS_2 basal planes parallel with the substrate. A perpendicular alignment would lead to higher adhesion than a parallel alignment due to greater anchoring of the reactive MoS_2 edge sites at the active sites on the ceramic substrate. Precursor work by Bertrand (6), using methanol-rinsed and HF-etched Si(111) surfaces as substrates for RF-sputtered MoS_2, has confirmed this hypothesis first, leading to similar work with MoS_2 on polycrystalline α-SiC.

Our program interacted with the Aerospace Corporation by utilizing the SEM tribometer to measure the adhesion, friction and wear of ambient substrate temperature-deposited (AT) and high substrate temperature-deposited (HT), 200 nm thick RF-MoS_2 layers sputtered onto methanol-rinsed and HF-etched α-SiC, as well as on solvent-rinsed, steel triboflats (7), see Table 27.

The operating vacuum of the system was in the 10^{-3} Pa (10^{-5} torr) regime. The pin in the present case was a 90° single crystal (XTL) of Al_2O_3, which was checked for wear after each set of tests on a sample (Figure 17). The normal load applied to the pin was 60-65 g, which corresponded to an $\cong$ 1.8 GPa maximum Hertzian stress on the α-SiC flat. The samples were oscillated at 1 mm • s^{-1} for 15 cycles, and then at 4 mm • s^{-1} for the remainder of the test. The pin track length was approximately 3.5 mm. Two tests were run on each sample at room temperature (R.T.). Where delamination and/or film wear-out could not be achieved at room temperature, two-to-three additional tests were run on the same triboflat by cycling first at R.T. for 65 cycles, then 50 cycles each at the successively higher temperatures of 50°, 100°, 150° and 200°C. If the coating still did not delaminate after 50 cycles at 200°C, an additional 50 cycles were added there, followed by 50 cycles each at 150° and 100°C as the temperature was ramped downward.

Table 27. Substrates and preparation techniques for the Aerospace Corporation's 200 nm thick AT/HT sputtered MoS_2 films.

SUBSTRATE	PREP.	DEPOSITION
α-SiC Sinter + HIP	Etch	AT HT
	MeOH	AT HT
	Mo Underlayer	AT HT
17-4 PH Steel	Polished	HT
	Ground	AT

The friction force, applied load, and triboflat temperature were measured continuously with the computerized data logging and analytical interface, as described previously herein. The average coefficient of friction per cycle (COF) was calculated from real-time data. The films were judged to have failed when the COF became greater than 0.1 in the higher speed mode. While the wear tests were in progress, real-time images of the developing wear scars were recorded on videotape, using the SEM electron optics. Typical friction traces are shown in Figures 120, 121 and 122, depicting COF vs. the number of oscillatory cycles, with or without temperature ramping.

Typically, the low-speed initial break-away COF for all films was higher than the high-speed, steady-state friction (also see Table 28). In general, failure was easy to determine as the film delaminated: since MoS_2 is more electrically conductive than α-SiC, the denuded wear path charged more (became considerably and suddenly brighter) than the still-adhering MoS_2 film. This delamination was clearly evident in the SEM video. At the same time, COF increased catastrophically, as indicated by the traces in Figures 120 through 122.

Table 29 contains the cycles-to-failure of the various films on the different (and differently pre-treated) substrates.

The average room temperature (R.T.) wear lives indicate that all films deposited on α-SiC had significantly shorter wear lives than films deposited on steel. The latter did not fail before the tests were terminated at 1000 cycles; they had to be thermally stressed by ramping to induce failure. AT films deposited on the methanol-rinsed and Mo interlayer samples exhibited longer wear lives than HT films deposited on similarly prepared substrates. Finally, the different sample preparations had a significant effect on wear lives for both AT and HT films. Films deposited on substrates rinsed in methanol exhibited wear lives about (or more than) a factor of 2 greater than films deposited on the acid-etched α-SiC. The Mo interlayer films exhibited average wear lives somewhere between those of the other two films, although then individual tests varied widely for the Mo/SiC samples.

The COF results in Table 28 are less clear cut than those of the wear data. The initial COF for all films was greater than the steady-state value, indicating that a run-in period is required for optimum film performance. The films deposited on steel seemed to have, in general, both lower initial friction values and lower steady-state friction values than similar films deposited on the harder α-SiC. In comparing the various MoS_2/α-SiC films, the most significant finding was the lower initial friction measurements on the acid-etched substrates. Both the AT and HT films had a lower initial COF than similar films on the methanol-rinsed substrates. The HT/acid-etched film had the lowest initial COF: 0.06. The minimum steady-state friction exhibited no clear trend with film type or sample treatments and ranged from 0.02 to 0.05. It is noteworthy that Swiss REVETEST® scratch test experiments with RF-MoS_2 on various substrates showed the same mode (appearance) of adhesive delamination as the one observed here on the SEM flats.

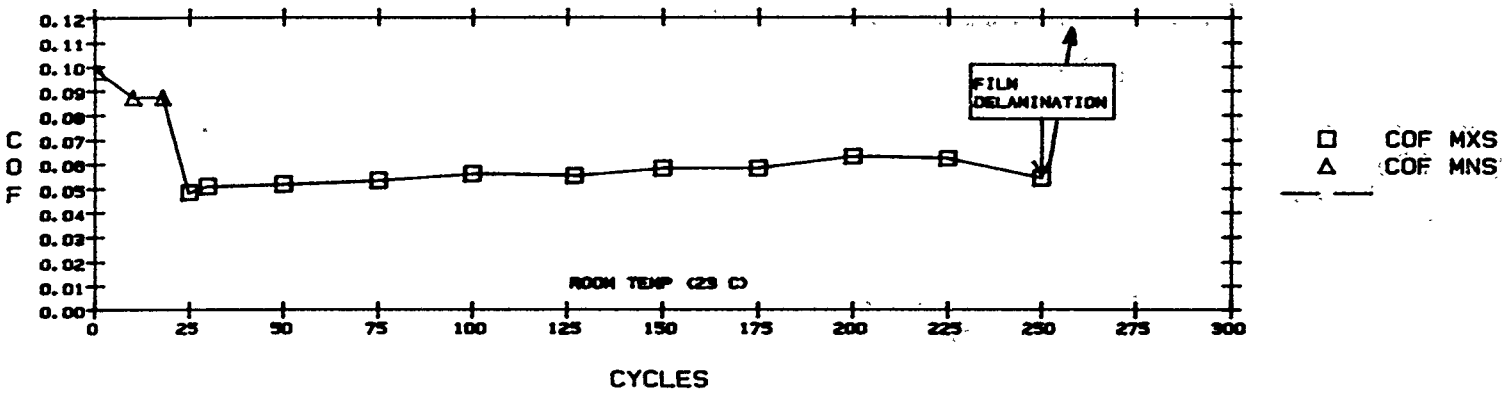

MOS0021: ROOM TEMPERATURE

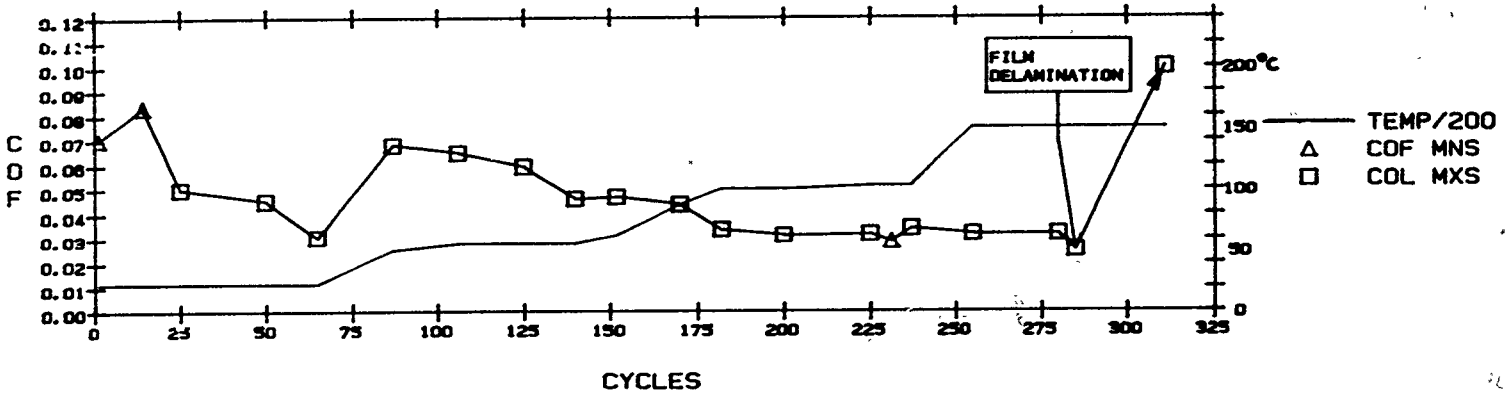

MOS0023:
MNS - MIN. SLIDING SPEED
MXS - MAX. SLIDING SPEED

Figure 120. Room temperature and elevated-temperature-ramped friction traces for The Aerospace Corporation's 200 nm thick AT/MoS_2 film on α-SiC sliding against a XTL sapphire pin.

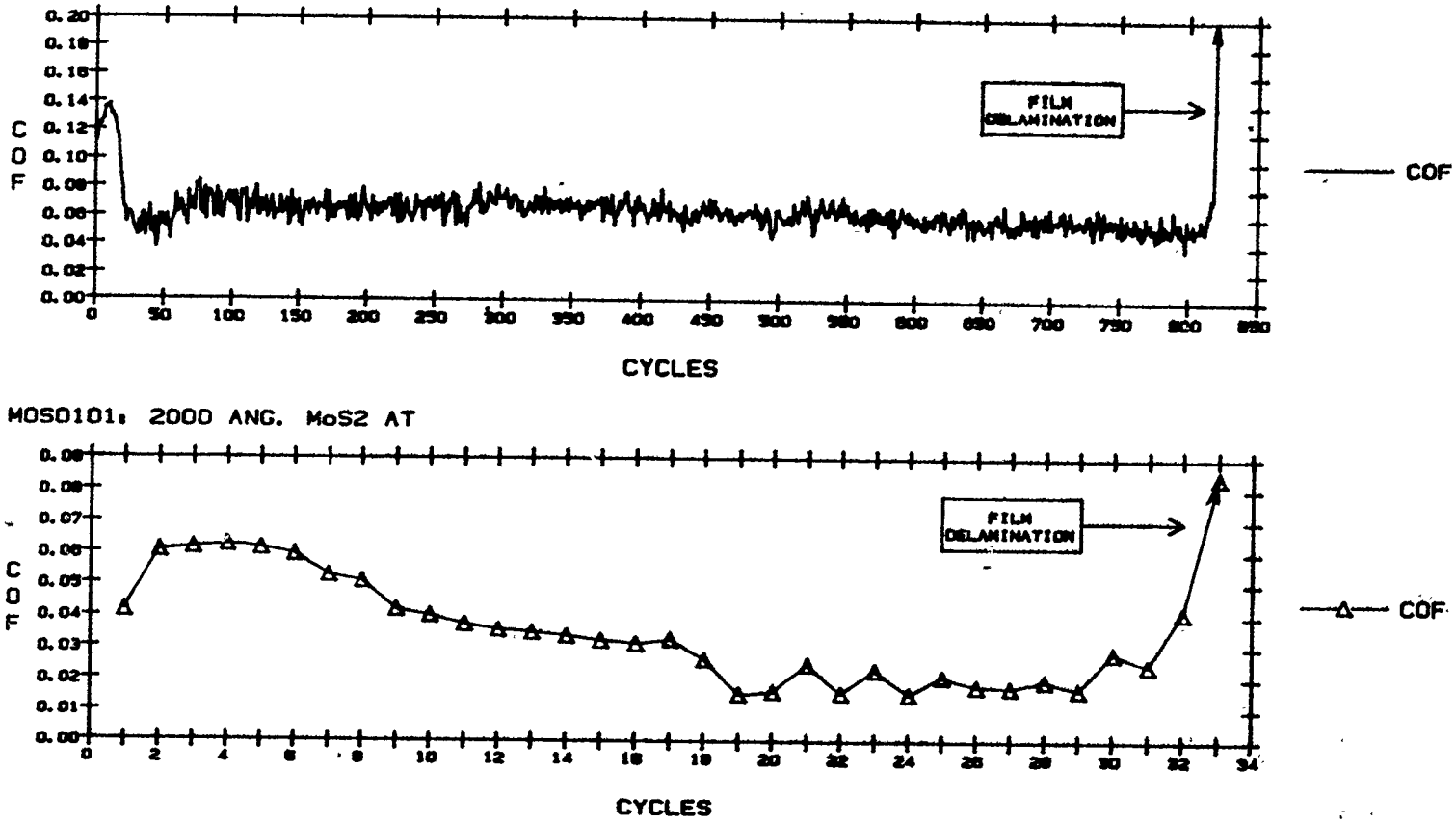

Figure 121. Room temperature friction traces for The Aerospace Corporation's 200 nm thick AT/MoS_2 film on α-SiC with and without a Mo underlayer, sliding against an XTL sapphire pin.

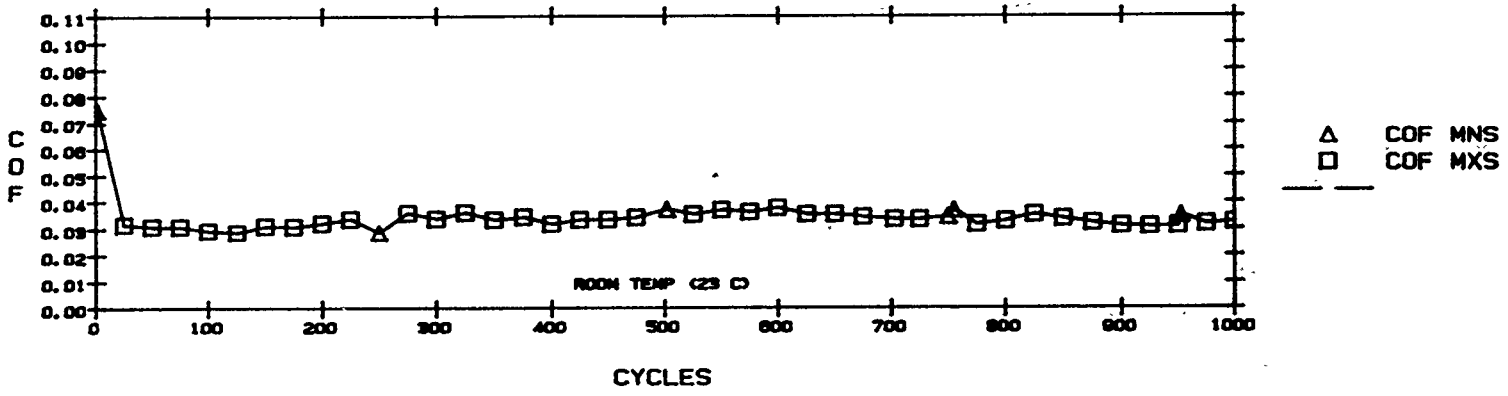

MOS0071: ROOM TEMPERATURE

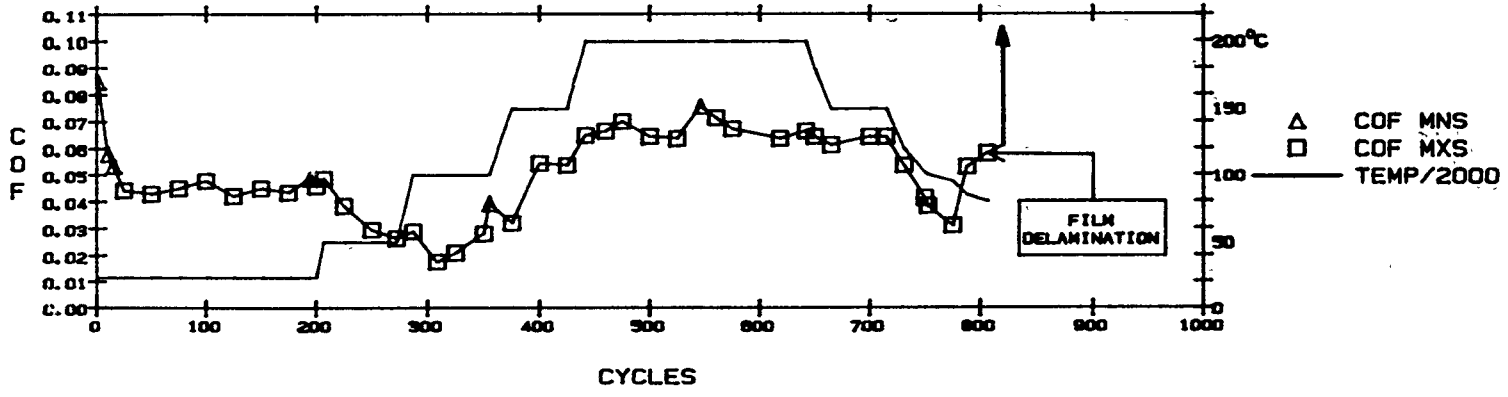

MOS0073:
MNS - MIN. SLIDING SPEED
MXS - MAX. SLIDING SPEED

Figure 122. Room temperature and elevated-temperature-ramped friction traces for The Aerospace Corporation's 200 nm thick AT/MoS_2 film on 17-4 PH(H900) steel (R_C40), sliding against a XTL sapphire pin.

Table 28. Room temperature, SEM tribometer friction data for The Aerospace Corporation's 200 nm thick AT/HT sputtered MoS_2 films.

			COF	
SUBSTRATE	PREP.	FILM	START	MINIMUM
α-SiC Sinter + HIP	Etch	AT	0.08	0.04
		HT	0.06	0.05
	MeOH	AT	0.10	0.05
		HT	0.10	0.03
	Mo Underlayer	AT	0.12	0.02
		HT	0.11	0.05
17-4 PH Steel	Polished	HT	0.08	0.03
	Ground	AT	0.08	0.02

Table 29. SEM tribometer wear life data for The Aerospace Corporation's 200 nm thick AT/HT sputtered MoS_2 films.

SUBSTRATE	PREP.	FILM	CYCLES TO FAILURE R.T.	H.T.
α-SiC Sinter + HIP	Etch	AT	166	93
		HT	147	135
	MeOH	AT	456	278
		HT	318	80
	Mo Underlayer	AT	318	- -
		HT	227	- -
17-4 PH Steel	Polished	HT	1000*	473
	Ground	AT	1000*	689

* NO FAILURE

A somewhat surprising result of the present work is the relatively poor performance of the MoS_2 films deposited on the Mo interlayer surfaces. In comparison to the steel substrates, the Mo interlayer films had much shorter wear lives (Table 29), indicating that simply having metal atoms at the interface is not sufficient to improve wear life.

The friction and wear tests are consistent with the active site model brought forth by our Aerospace Corporation colleagues. The most important comparison should be drawn between the methanol-rinsed and acid-etched α-SiC. Acid-etched α-SiC has significantly less surface carbon contamination, and hence fewer active sites, for the edge-bonded MoS_2. This weaker adhesion produced shorter wear lives for AT and HT films deposited on the acid-etched α-SiC. In addition, HT films generally have shorter wear lives than AT films deposited on similarly prepared substrates (with the exception of the acid-etched α-SiC, where there is essentially no difference in wear lives). This generally shorter wear life of HT films could relate to the removal of the active sites at the 220°C deposition temperature. Finally, a comparison of the HT films on the methanol-rinsed and acid-etched α-SiC reveals a much lower initial COF for the acid-etched surface. Only HT films were observed to have parallel orientation and this orientation has been shown to depend on surface pretreatment. The low initial COF for the HT film on etched SiC, therefore, supports the notion that films with greater parallel orientation of crystallites should have lower initial friction.

It is interesting to speculate on why the COF tended to increase on raising the temperature (see Figures 120 and 122). Since (a) MoS_2 basal planes are aligned more-less-parallel with the plane of sliding, (b) active sites are exposed on the sliding surfaces, and (c) thermal desorption of gases from some of the active sites at temperatures as low as 200°C could generate dangling bonds on the sliding surface, a larger number of exposed active sites would be commensurate with higher COF.

Natural molybdenite may indeed depend on some special substance to render the active sites inert (221, 222). The data in Figure 122 appears to support but, on the other hand, the data in Figure 120 refute this hypothesis. Other researchers, in previous work (223), tried to thermooxidatively stabilize MoS_2 with Ag and Ni. The thermograms in Figure 123 appear to prove the existance of some stabilizing effect. Inasmuch as metals tend to decorate active sites on MoS_2 (213), the protective mechanism by the oxidatively stable Ag preferentially accumulated at these sites is plausible. It should be noted, however, that recent thermal desorption spectroscopy indicated that SO_2 vaporization from sputtered MoS_2 is not measurable until 292°C in vacuum (224).

Inasmuch as the SEM tribometer was shown eminently capable of measuring the adhesion-related wear life of MoS_2 films (as indicated by friction and real-time video data), we were encouraged to further determine the wear life of sputtered MoS_2 films coated onto the same type of unetched α-SiC substrate by ion-beam-assisted-deposition (IBAD), see (8). This new process was performed in the laboratories of Dr. Irvin L. Singer (NRL) by Robert N. Bolster. This coating is in fact the replication of a Japanese method (9), whereby the IBAD-MoS_2 is sputtered onto thin (~40 nm) BN interlayer-coated ceramics,

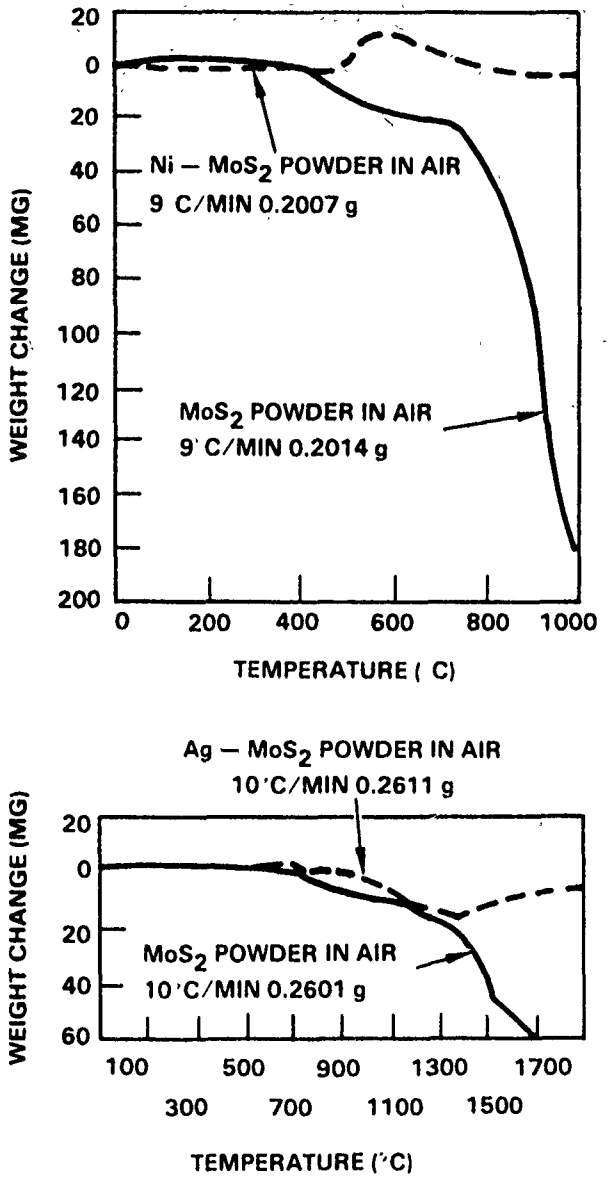

Figure 123. Thermograms of MoS_2 powder/Ni and MoS_2 powder/Ag composites in high temperature air (223).

yielding extraordinarily long wear lives. Ultra-low friction and frictional insensitivity to atmospheric moisture (a ubiquitous problem with other types of sputtered MoS_2 films) were added benefits with this new coating system.

A 240 nm film of MoS_2 was deposited on α-SiC triboflats by cosputtering MoS_2 and sulfur with a 1000 V ion-assist beam (ion/atom = 0.16), then vacuum-annealed for 2 hours at 300°C. The final stoichiometry of the film was not determined. Again, the mating pin was 90° XTL sapphire.

As shown by the typical friction traces in Figure 124, our SEM tribotests found the IBAD-MoS_2 on α-SiC far superior to those of the RF-MoS_2 versions, equivalent to the long wear life of RF-MoS_2 on steel. However, with both the RF/IBAD films, thermal cycling the triboflats during sliding to 200°C (max., or lower) and back to room temperature significantly decreased wear life. Since 200°C is too low for chemical degradation, it is believed that the nature of the stress is strictly physical (thermal).

When the relatively featureless RF-sputtered AT/HT films, which exhibited classical interfacial delamination (see Figure 125) are compared with the rubbed IBAD-MoS_2 (Figures 126 and 127), the IBAD film has a mottled appearance. The surface is covered with closed and opened blisters. In spite of the presence of these blisters, film delamination was patchy (not as complete as that shown with the RF film in Figure 125). The unused IBAD-MoS_2 film itself already exhibited blisters; note that EDX of the film indicated considerable Ar content, possibly causing their formation. The silver globules in Figure 128 probably originated from nearby fixturing, an unfortunate contamination of the triboflat.

3.2.2 Metal-Chloride Intercalated Graphites

It is a well-know fact that the inability of graphite to act as a solid lubricant in high vacuum or at elevated temperatures stems from the desorption of the intercalated moisture from the van der Waals gaps. The main method of mitigating this shortcoming is the chemical insertion of molecules or elemental species more stable than water between the carbon layer planes of the graphite. Composition is designated mainly by stage, e.g., the number of graphite layer planes between adjacent, inserted intercalant layer planes.

Until recently, graphite (a semi-metal) has been converted to a true metal by intercalation mostly for use in the electronic industry [e.g., see (225)]. It was Conti's award-winning ASLE (now STLE) paper in 1983 (226) which demonstrated that $CoCl_2$ - intercalated graphite was found to exhibit over a fivefold increase in enduance life in resin-bonded solid lubricant films, while the $NiCl_2$-intercalated version provided greater than a twofold increase in load-carrying capacity relative to pristine, highly ordered pyrolytic graphite (HOPG). By such intercalation, graphite was made equivalent to the inherently better solid lubrication properties of MoS_2. Unfortunately, TGA experiments by Prof. F. Lincoln Vogel of Intercal Co. (Port Huron, MI) indicated that the thermal stability of his commercially prepared $CoCl_2$ (275°C = 525°F) and $NiCl_2$ (325°C = 620°F) limits their use at high temperature; at cryogenic temperatures they may show promise.

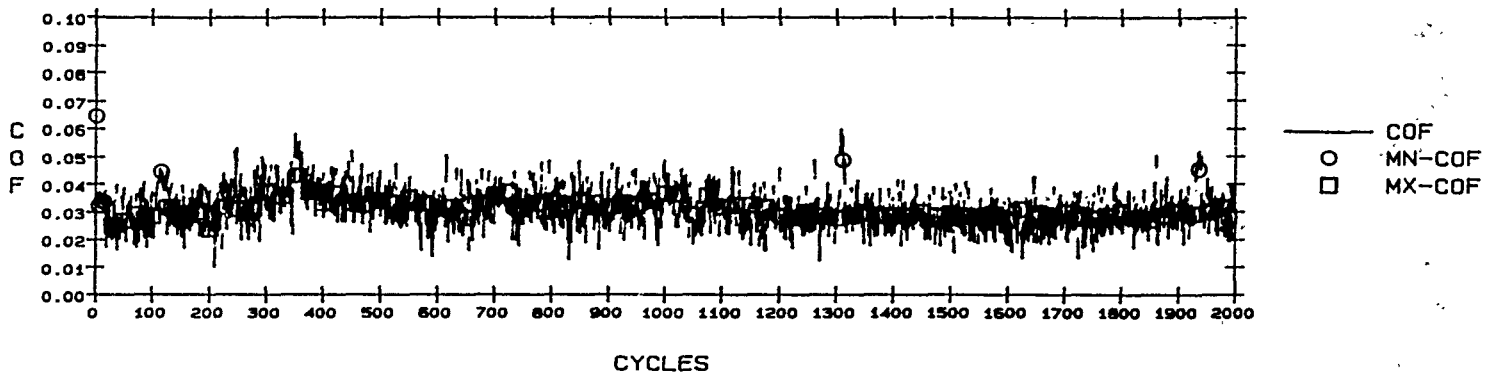

MOS0081: NRL MoS2 ON SiC

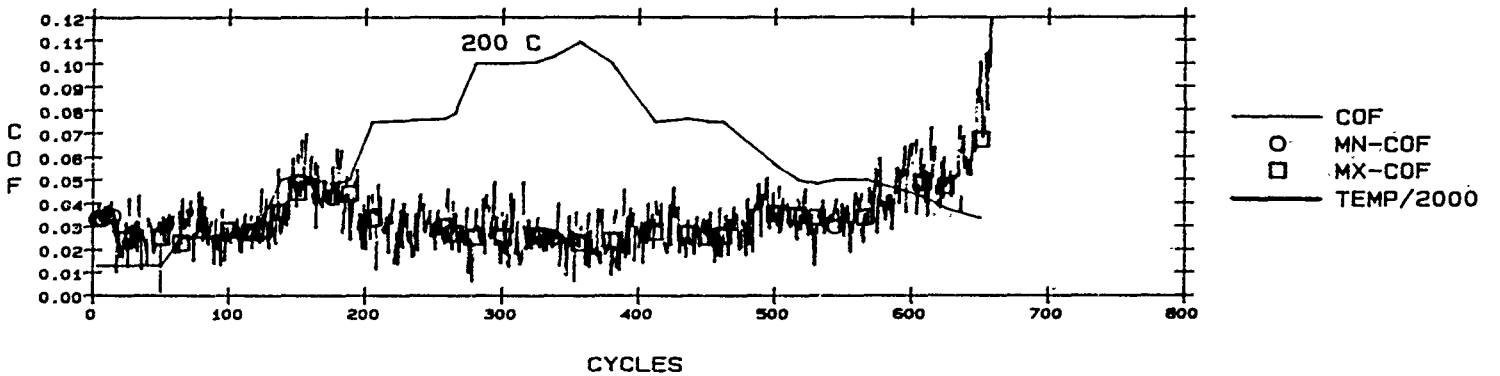

MOS0084: NRL MoS2 ON SiC
64 gms NORMAL LOAD, HIGH TEMP
MN-COF=COF AT MIN. SLIDING SPEED
MX-COF=COF AT MAX. SLIDING SPEED

Figure 124. Room temperature and elevated-temperature-ramped friction traces for the NRL 240 nm thick IBAD-MoS_2 film on α-SiC, sliding against a XTL sapphire pin.

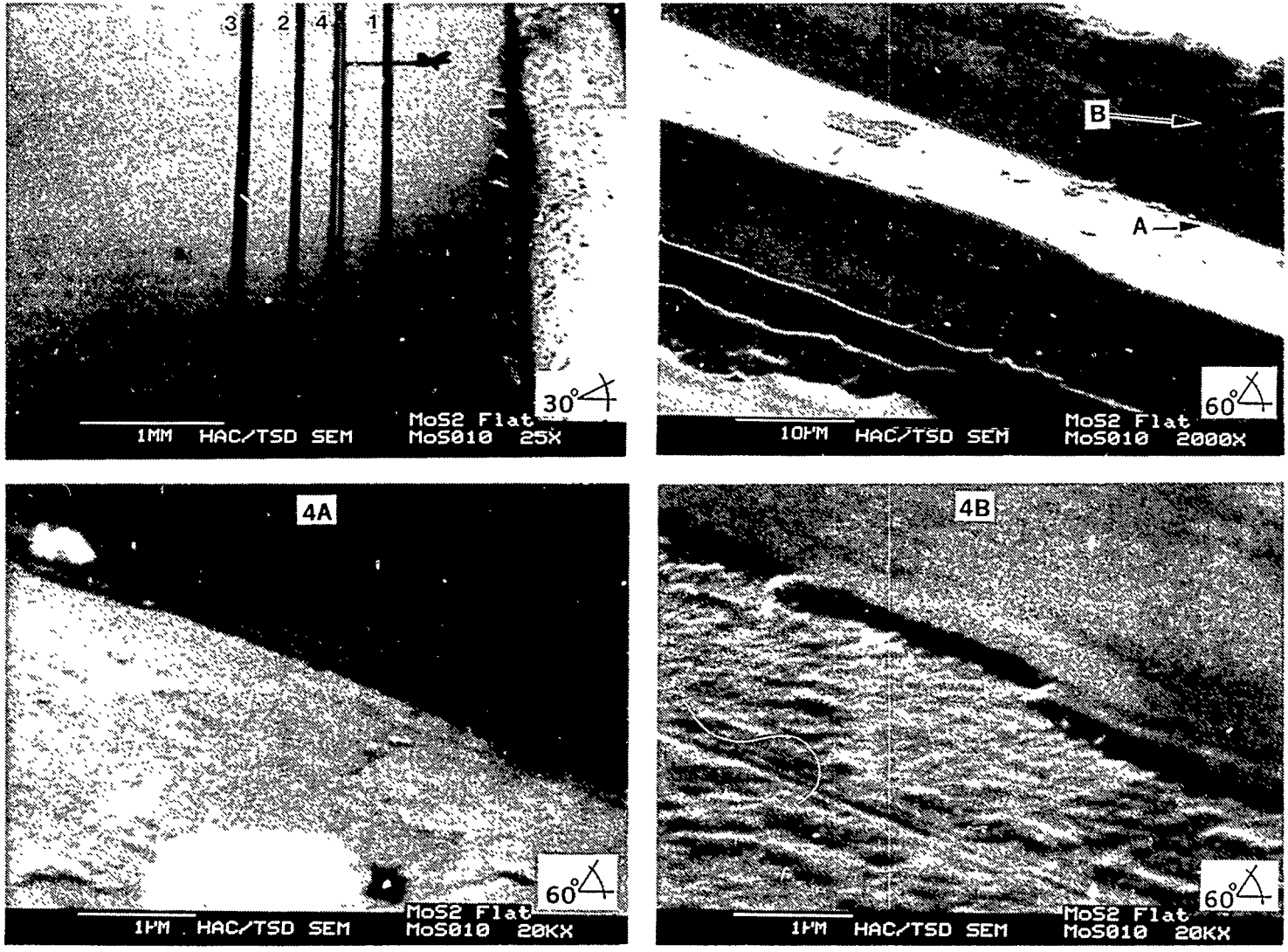

Figure 125. SEM photomicrographs of the Aerospace Corporation's 200 nm RF-AT MoS_2 film with Mo underlayer (higher mag. photos of Wear Track No. 4, R.T. test).

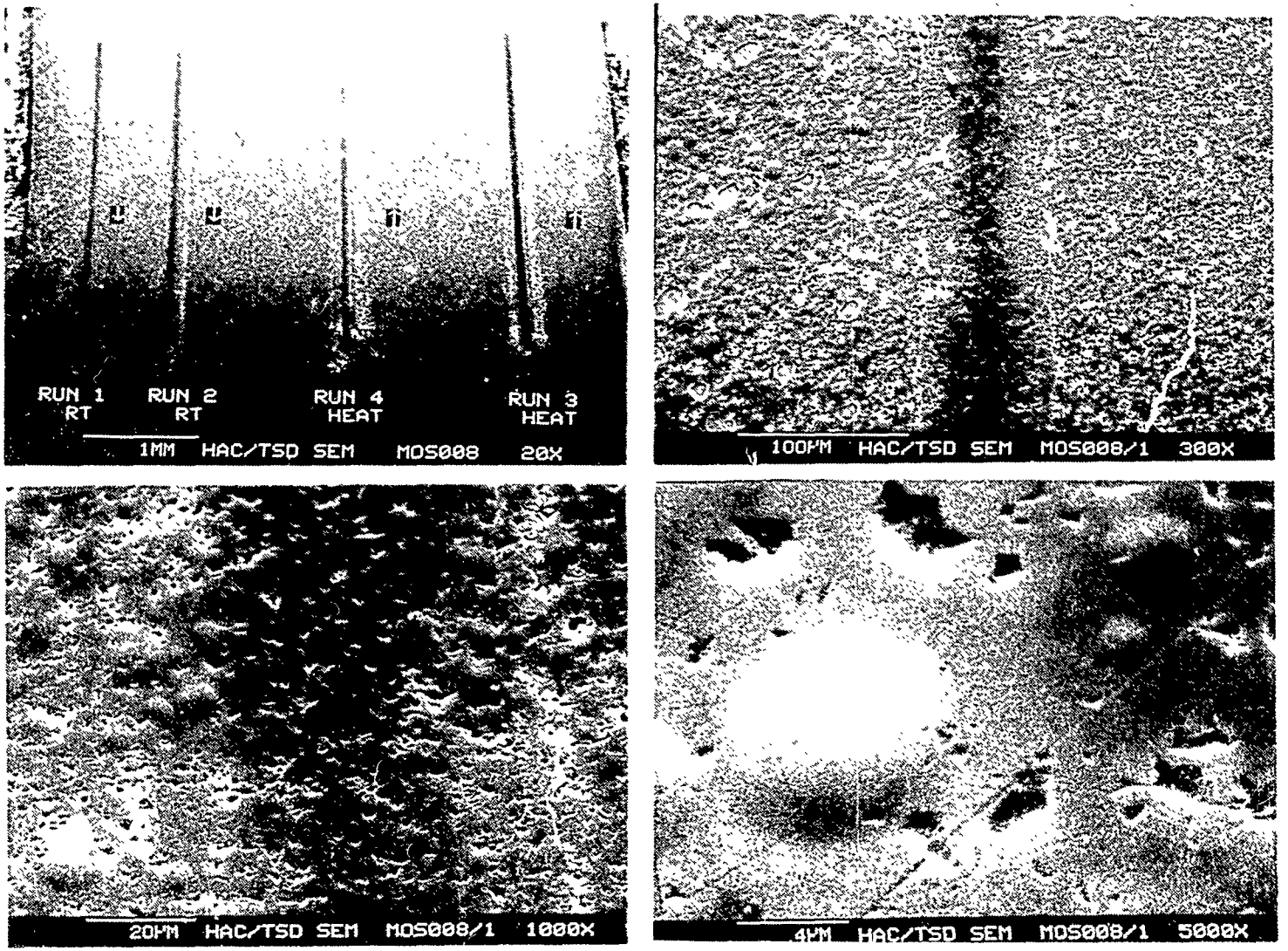

Figure 126. SEM photomicrographs of the used, NRL 240 nm IBAD-MoS_2 film with BN underlayer (higher mag. photo of Wear Track No 1, R T test, also see Figure 124).

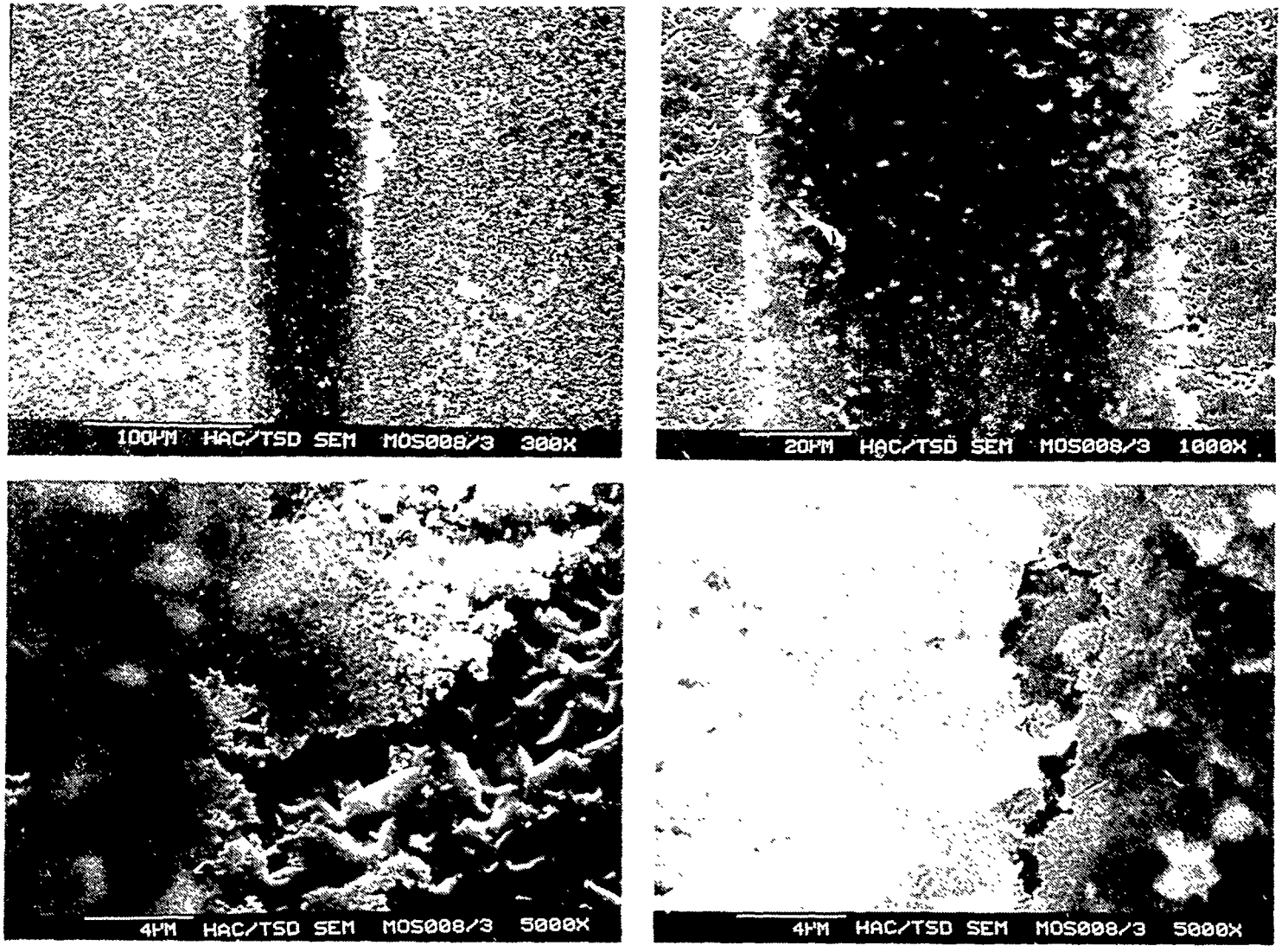

Figure 127. SEM photomicrographs of the used, NRL 240 nm IBAD-MoS_2 film with BN underlayer (higher mag. photos of Wear Track No. 4, H.T. test, also see Figure 124).

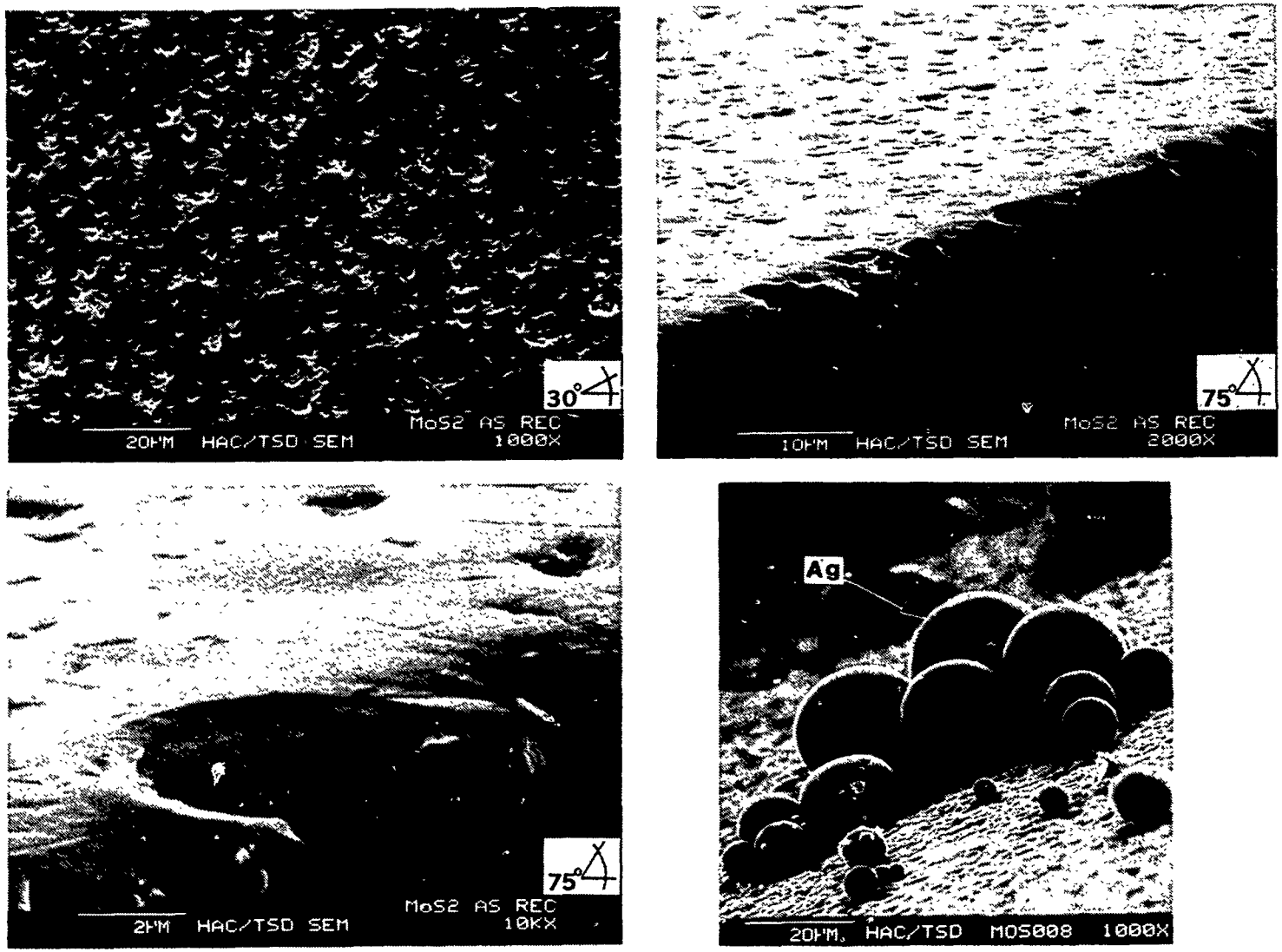

Figure 128. SEM photomicrographs of the new, NRL 240 nm IBAD-MoS_2 film with BN underlayer, depicting blistering and silver globules on the triboflat edges.

Lipp and Stern's previous work (227) suggested, however, that $CrCl_3$-intercalated HOPG may be an excellent high temperature lubricant from 38°C to 816°C (100°F to 1500°F), providing a coefficient of sliding friction (f_k) less than 0.10 within this temperature range. The $CrCl_3$-intercalated HOPG was included as a developmental product (DP) among the host of other metal-chloride-intercalated HOPG Intercal Company was manufacturing commercially (see Table 30). Under the auspices of the present program, Intercal was funded for warm-isostatic-pressing, in inert gas/vacuum atmospheres, solid blocks (molds) of selected, intercalated HOPG. From these molds, SEM triboflats were fabricated. The main object of immediate interest was to correlate intercalant desorption temperatures (measured on powders by TGA/DSC, in air and in argon) with SEM tribotests at progressively higher temperatures and increased partial pressures of oxygen; we aimed to show the effects of de-intercalation on f_k and on wear rate changes.

3.2.2.1 Thermal Analyses of Intercalated Graphite Powders. As the first step, seven samples of powders obtained from Intercal (see Table 31) were analyzed by TGA/DSC in both argon and in air (reconstituted by mixing 20% oxygen and 80% nitrogen). The gas flow and heating rates during both types of analysis were 0.2 $l \cdot min^{-1}$ and 20°C$\cdot min^{-1}$, respectively. The TGA sample weights were close to 30 mg, and the DSC samples size was ~13.2 mg. The DSC sensitivity was set at 1.0 $mcal \cdot s^{-1} \cdot in^{-1}$.

All the wide temperature range (to 1000°C) TGA data are enclosed in Figures 129, 130 and 131. In order to more closely differentiate the effects of atmosphere on degradation, all of the expanded, low weight loss regime plots (extending down to 88 weight percent weight loss) are combined in Figure 132. The sample numbers in these figures may be further correlated with the master list of all specimen powders (see Table 31).

The TGA data indicate the following:

1. Both the low and high attenuation plots reveal greater sample stability (i.e., lower rate of weight loss) in argon, as expected. The weight loss rate is greater in the region of graphite oxidation, above ~600°C. Some of the metallic chlorides (or their residues) apparently influence the high temperature oxidation rate of the graphite host more than others.

2. The large particle size powders tend to exhibit greater (TGA) stability. If one assumes that the degradation (deintercalation and the resulting weight loss) in argon is as diffusion limited as it is in air [except that in air the species diffusing from the van der Waals gap also react with oxygen at (or near) the surface of the particle (228)], the above finding is reasonable. The large vs. small particle size stability difference is especially noticeable with the $NiCl_2$ intercalant. Furthermore, it has been demonstrated that the surface of metal-chloride-intercalated graphite may be more depleted of the intercalant than the bulk (229). As a consequence, small particle size compounds with large surface-to-volume ratios should show lesser degree of effective intercalation than the large particle size equivalents. This is indeed the case with the $NiCl_2/CrCl_3$ counterparts.

Table 30. Intercalcated graphite formerly available from the Intercal Co., Port Huron, MI.

Intercalant	Temperature Limit (°F/°C)	Formula[1]	Staging and Percent Intercalation[2]	Particle Size, Average (μM)	Intercal Product No.	Price ($/lb)
$CuCl_2$	(300/500)	$C_{13.4}CuCl_2$	III; >95%	200	SP 3,001	75
		$C_{19.2}CuCl_{2.1}$	III; >95%	100	SP 26,001	75
		$C_{14.1}CuCl_2$	III; >90%	45	SP 36,001	75
		$C_{17.7}CuCl_{2.2}$	III; >90%	44	SP 12,001	75
		$C_{12.7}CuCl_2$	III; >85%	20	DP 52,001	75
		$C_{18.1}CuCl_{2.2}$	II/III; >75%	5	SP 13,001	75
$CdCl_2$	(525/275)	$C_{12.8}CdCl_2$	II; >80%	88	DP 26,121	85
$CoCl_2$	(525/275)	$C_{9.3}CoCl_2$	II; >85%	88	DP 26,141	82
$NiCl_2$	(620/325)	$C_{9.0}NiCl_2$	II; >80%	100	SP 50,011	78
		$C_{68.0}NiCl_{3.7}$	II/III; >75%	100	SP 26,011	78
		$C_{16.6}NiCl_2$	II; >85%	50	SP 12,011	78
		$C_{9.1}NiCl_2$	II; >80%	50	SP 49,011	78
		$C_{9.2}NiCl_2$	II; >65%	10	SP 54,011	78
		$C_{16.7}NiCl_{2.2}$	II/III; >70%	5	SP 13,011	78
$CrCl_3$	(930/500)	$C_{23.8}CrCl_{3.5}$	II/III; >80%	100	DP 26,030	95
		$C_{18.7}CrCl_{3.1}$	II/III; >63%	15	SP 13,030	95

[1]Typical data; not normally obtained for every batch.
[2]Obtained by Debye-Scherrer X-ray diffraction on every batch.

Table 31. Intercalcated graphite powder samples (from Intercal) for TGA/DSC analyses.

Sample No.(1)	Intercalant	Formula(2)	Staging and Percent Intercalated	Particle Size (μM)	Intercal Product No.
1	$NiCl_2$	$C_{8.9}NiCl_2$	2; ~65%	10	DP 54,011
2	$NiCl_2$	$C_{68.0}NiCl_{3.7}$	2/3; ~75%	100	SP 26,011
3	$CrCl_3$	$C_{15.8}CrCl_3$	2/3; ~80%	100	SP 26,030
4	$CrCl_3$	$C_{18.7}CrCl_{3.1}$	2/3; ~63%	15	DP 13,030
5	$CdCl_2$	$C_{12.8}CdCl_2$	2; ~80%	88	SP 26,121
6	$CuCl_2$	$C_{19.2}CuCl_2$	3; ~95%	100	SP 26,001
7	$CdCl_2$ + $CuCl_2$ + Cu (16%)	$C_{12.8}CdCl_2$ + $C_{10.9}CuCl_2$ + Cu	2; ~80% + 1/2/3; ~35% + N/A	88 + 10 + ?	SP 26,121 + SP 8,001 + N/A

(1)These numbers appear in Figures 129 through 132 also.
(2)Typical data reported by the manufacturer; not normally determined for each batch.

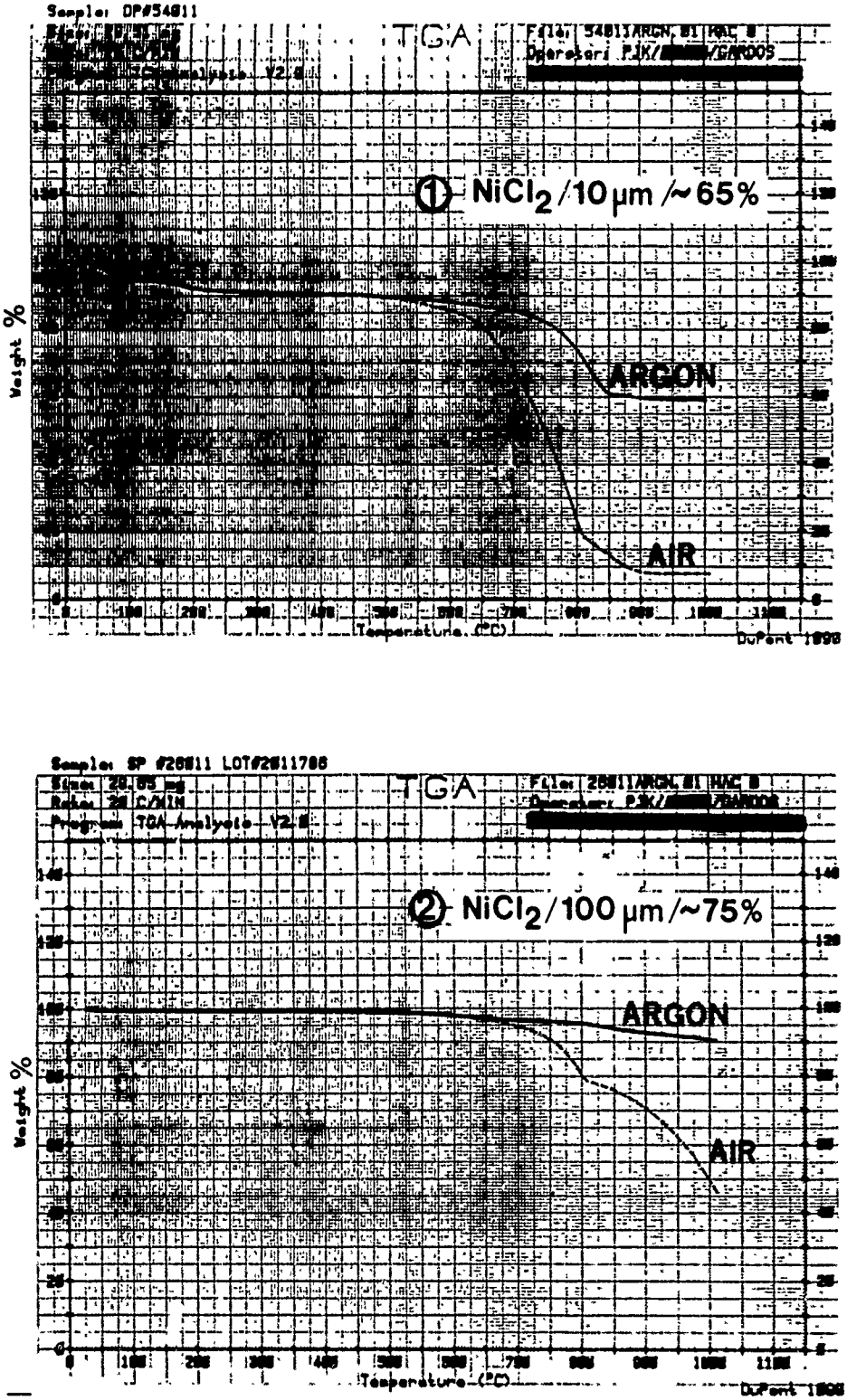

Figure 129. TGA of $NiCl_2$-intercalated graphite powders (also see Table 31).

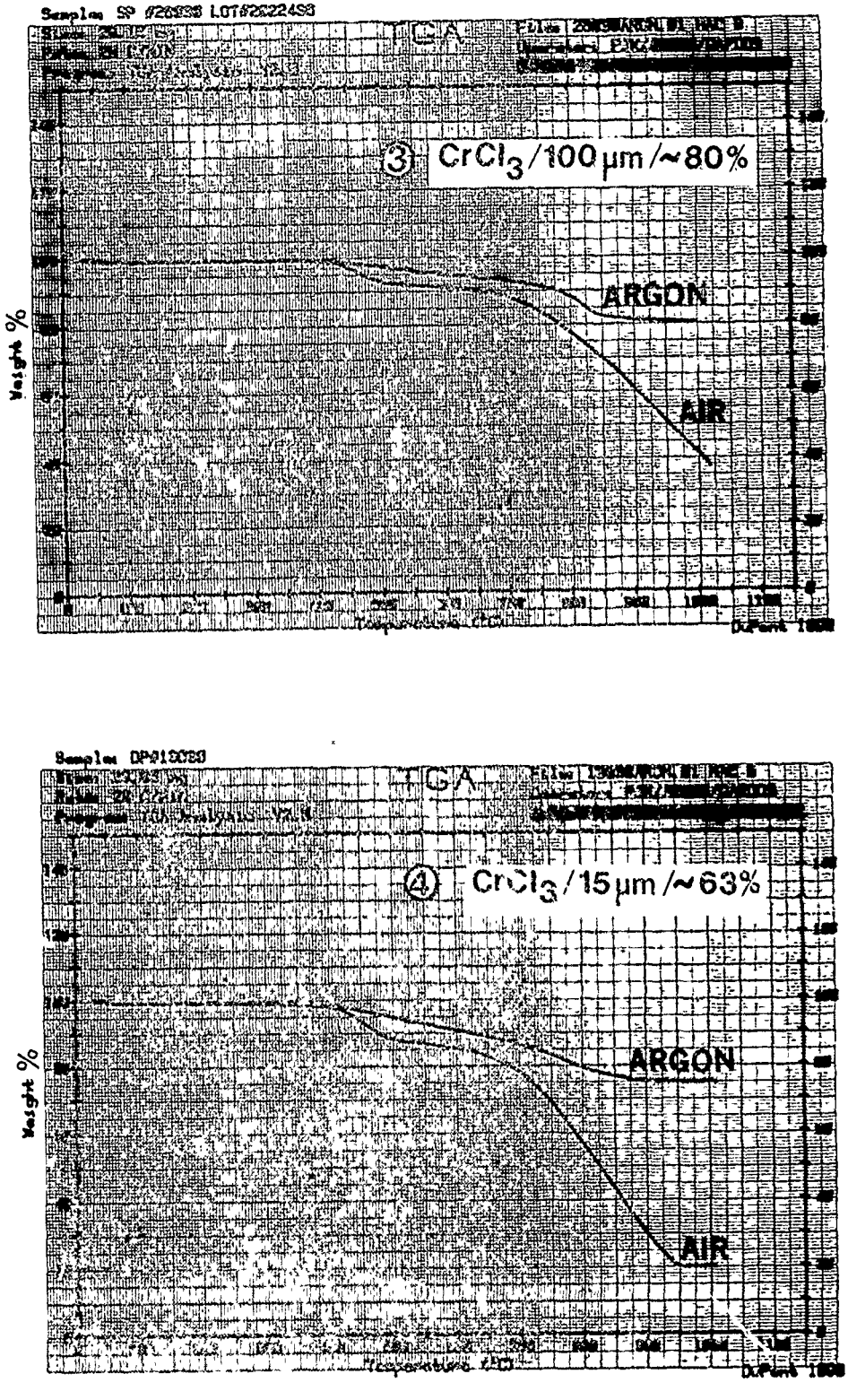

Figure 130. TGA of $CrCl_3$-intercalated graphite powders (also see Table 31).

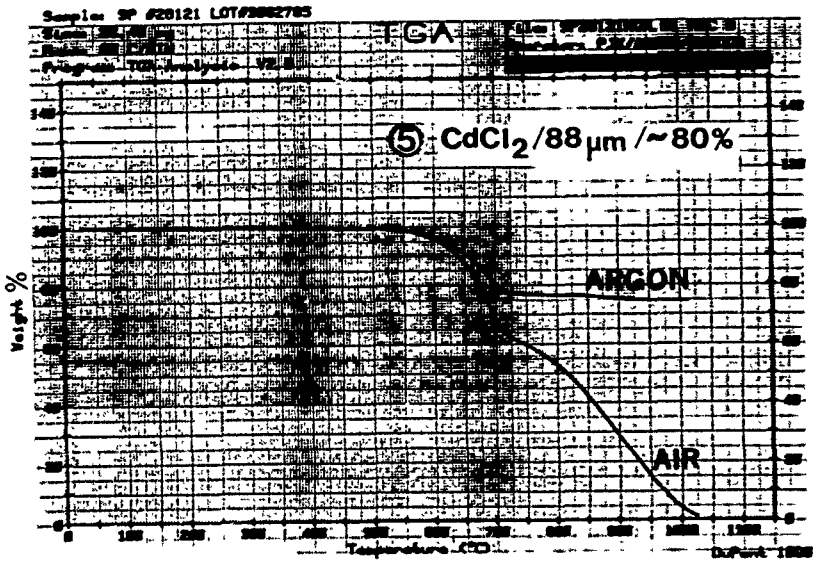

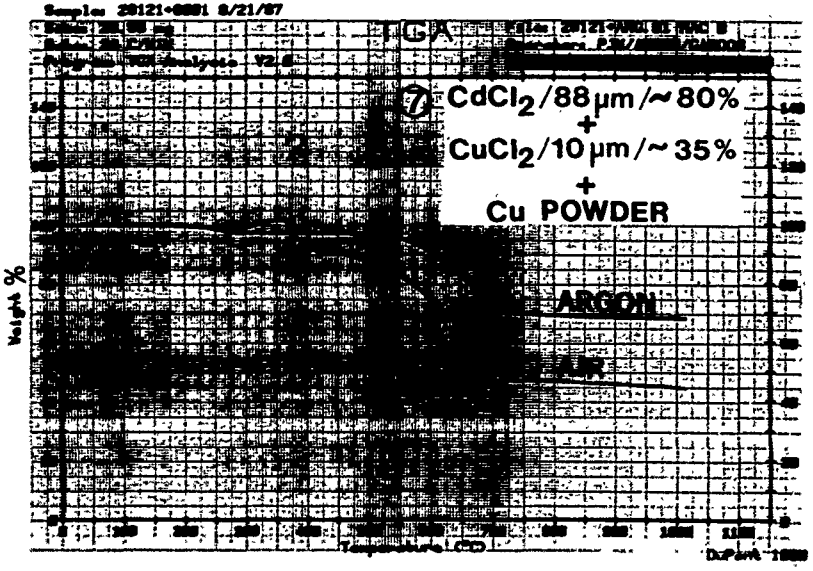

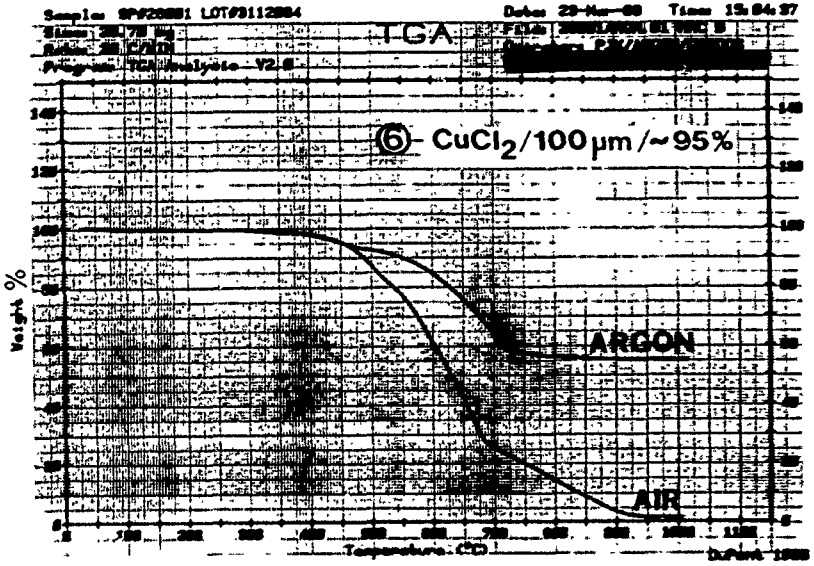

Figure 131. TGA of $CdCl_2$ and $CuCl_2$ intercalated graphite powders and TGA of such powders mixed with Cu powder (also see Table 31).

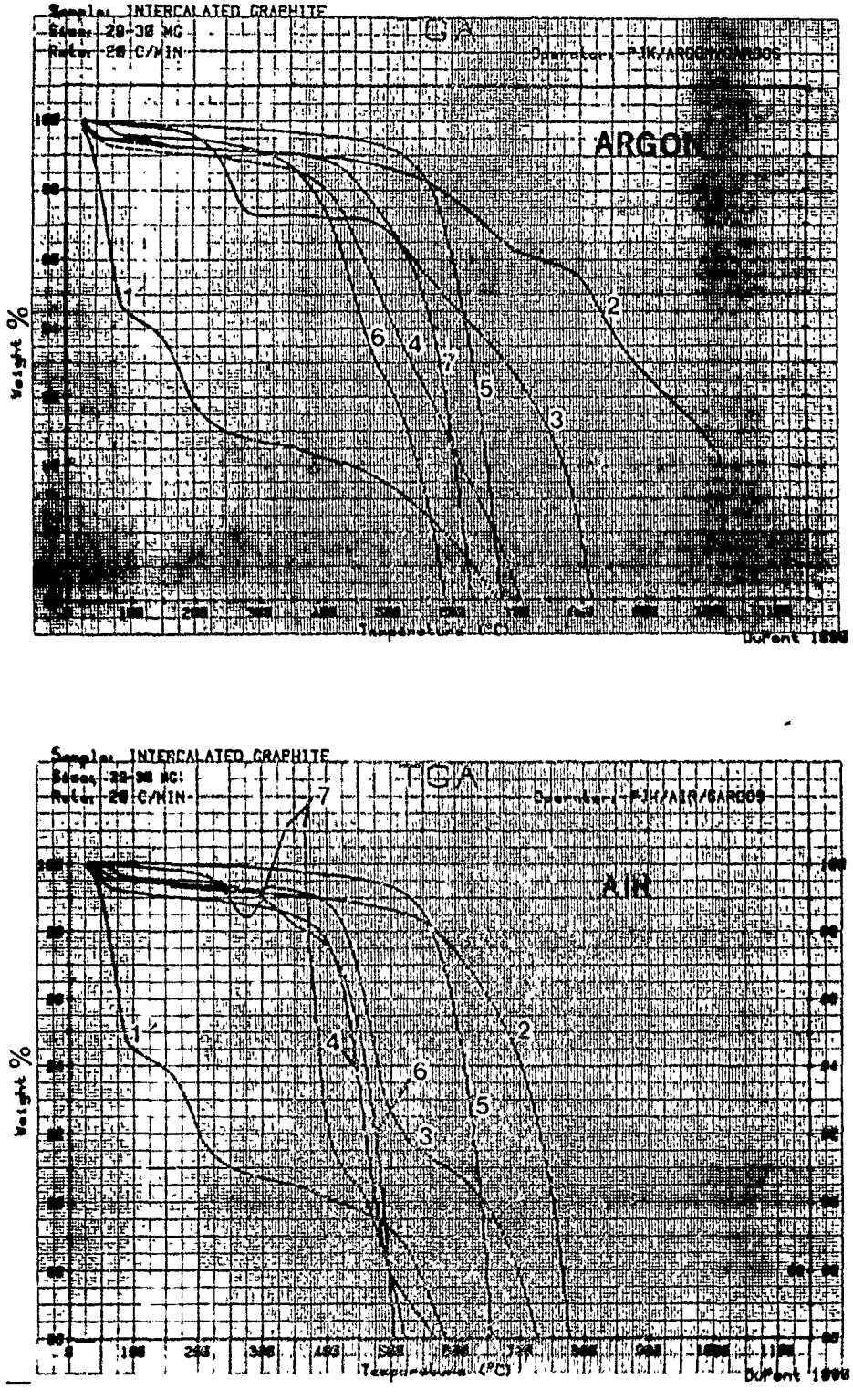

Figure 132. Expanded TGA of selected, metal chloride intercalated graphite powders in the low weight loss regime (also see Table 31).

3. The $CdCl_2$-intercalated product exhibits the best and the $CuCl_2$-containing products exhibit the worst overall stability, both in argon and in air. By far, the largest rate of weight loss of the small particle size $NiCl_2$ compound renders this material the single, most unstable intercalated graphite powder among all the ones tested, in both atmospheres.

4. The combination powder (Sample #7) behaves anomalously in air between 275° and 375°C by repeatedly showing a weight gain instead of a weight loss. This can only be attributed to the oxidation of the copper powder. The presence of pulverized copper also appears to catalyze (speed up) the degradation rate of both the $CdCl_2$ and $CuCl_2$ intercalated graphite constituents dramatically. Note that Intercal was able to consolidate this particular powder mixture best into molds of reasonable structural integrity and high electrical conductivity. The actual values of these properties are not yet available.

The DSC plots in Figure 133, 134 and 135 complement the TGA data for better understanding of the degradation transitions:

1. The 55°, 110° and 215°C major endotherms for the small particle size $NiCl_2$ material (Sample #1) in Figure 133 agree well with the major weight loss rate TGA change on the equivalent samples in Figure 132. For the intercalated layers (see Figure 136 for the schematics of staging), intraplanar structural transitions, order-disorder transformations and interplanar stacking order transitions occur as the temperature is increased. Generally, each type of transition is characterized by its own transition temperature. It is clear from Figures 133 and 134 that thermal induced moisture desorption and/or de-intercalation of Sample #1 occurs at the major endotherms. During tribotesting a flat consolidated from this powder, one might anticipate friction and wear transition at these temperatures. Interestingly, the endotherms for the large particle size $NiCl_2$-containing powder are located at the same temperatures as those for the small particle size equivalents, but their magnitudes are much smaller. Consequently, one would expect less dramatic tribological changes with the monolithic version pressed with the large particle size powder. Indeed, some initial dip in the TGA curve of Sample #2 around 50 to 70°C in Figure 132 is not followed by another major one until 600°C is reached, beyond the relatively invariant DSC plot's scale in Figure 133.

2. The above phenomenon occurs with the more stable $CrCl_3$ material (Samples #3 and #4) in Figure 134, but to a much lesser extent. Shallower endotherms are presumed to be commensurate with a lower rate of deintercalation and weight loss (Figure 132).

3. The DSC endotherms and exotherms in Figure 135 confirm the high TGA stability of the $CdCl_2$-intercalated graphite (Sample #5). The much lower stability of even the large particle size, $CuCl_2$-intercalated powder (Sample #6) and the copper-powder-catalyzed degradation of the mixed product (Sample #7) are equally confirmed. The correlation between the respective TGA/DSC plots to identify transitions is excellent.

A tribologist's thought-experiment might intuitively predict friction and wear transitions of intercalated graphites in a qualitative manner, as a function of staging.

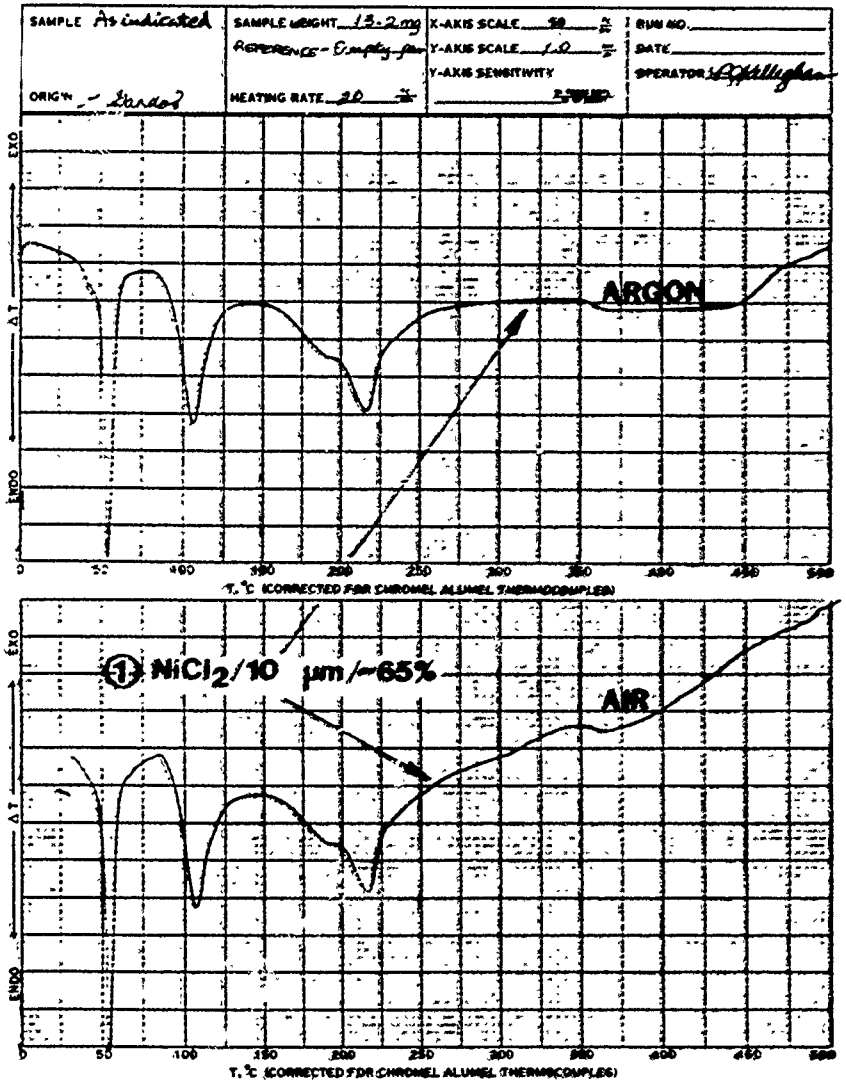

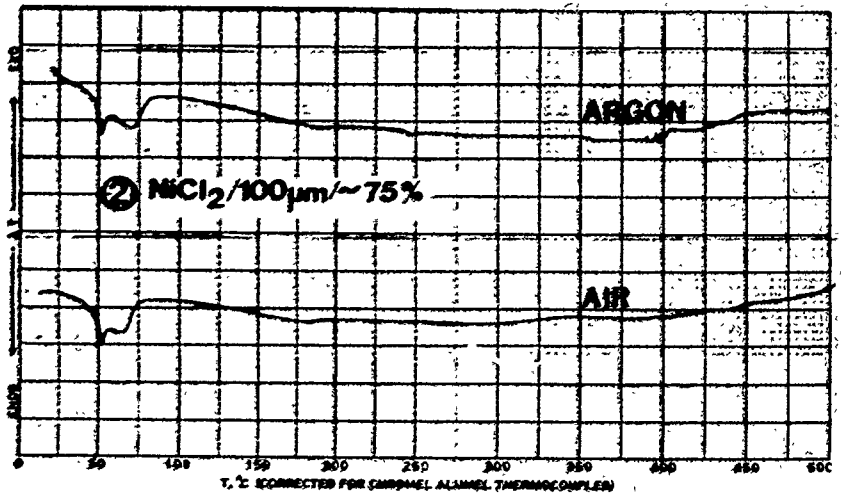

Figure 133. DSC of $NiCl_2$-intercalated graphite powders (also see Table 31).

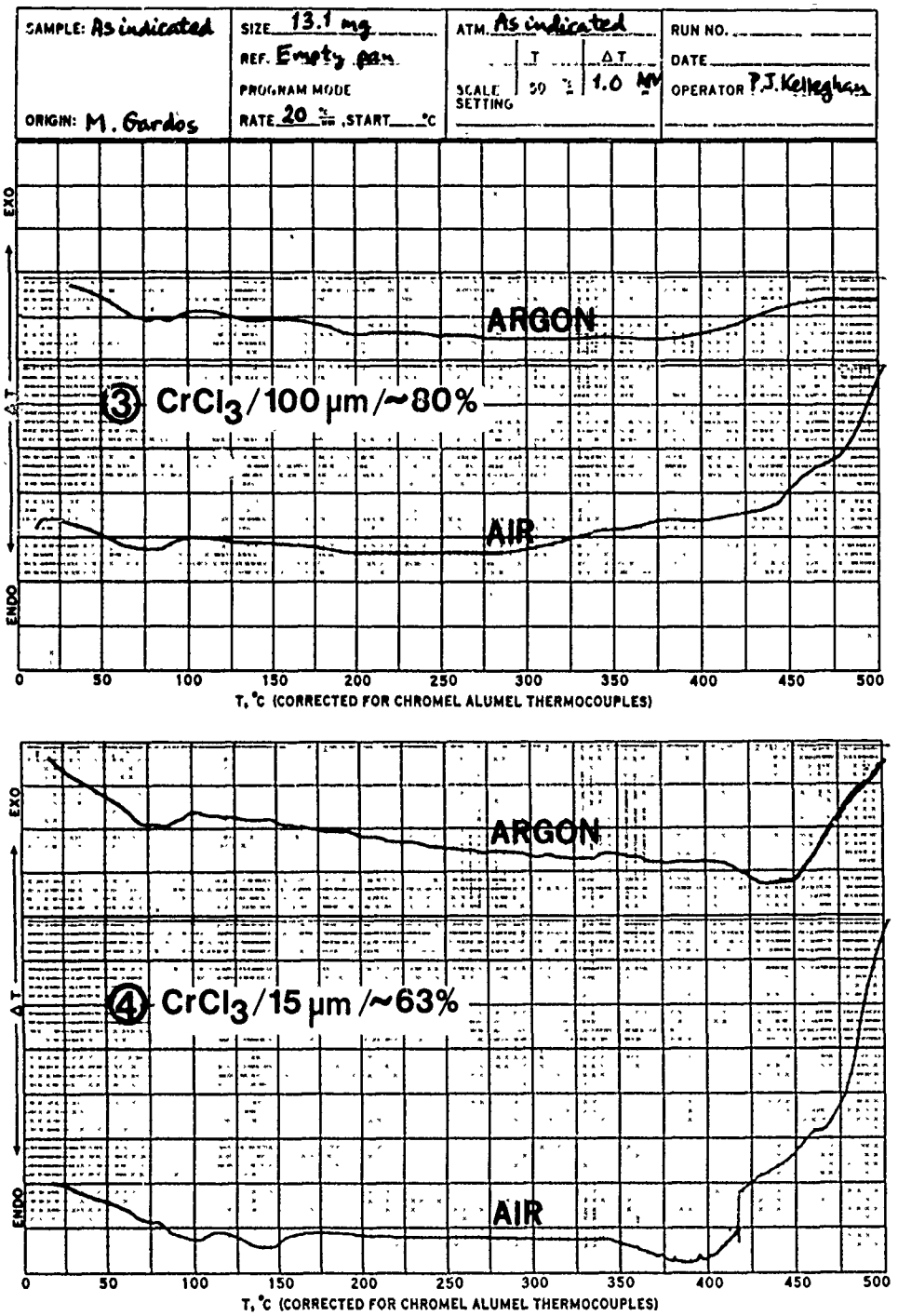

Figure 134. DSC of CrCl3-intercalated graphite powders (also see Table 31).

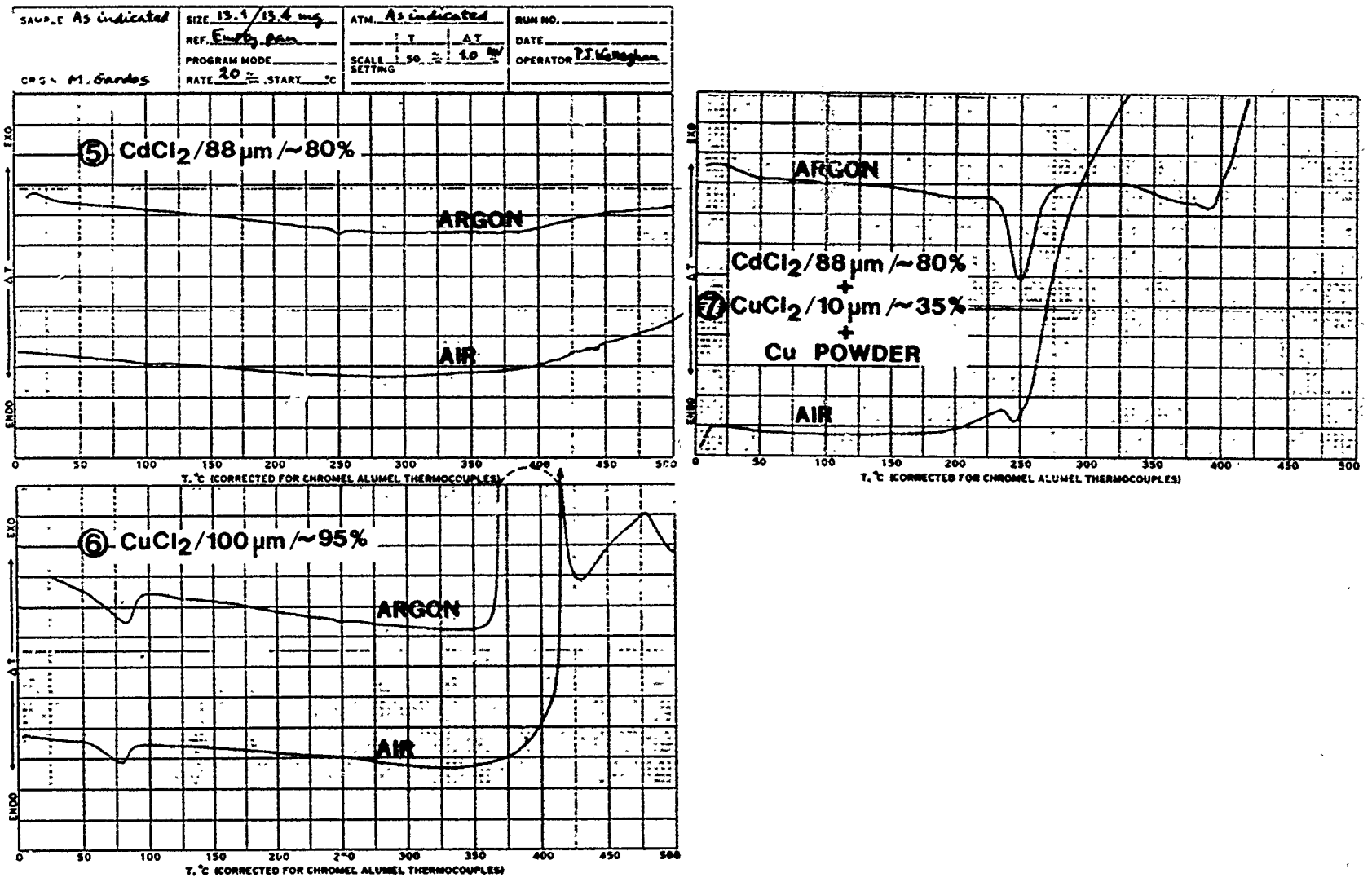

Figure 135. DSC of $CdCl_2$ and $CuCl_2$ intercalated graphite powders and DTA of such powders mixed with Cu powder (also see Table 31).

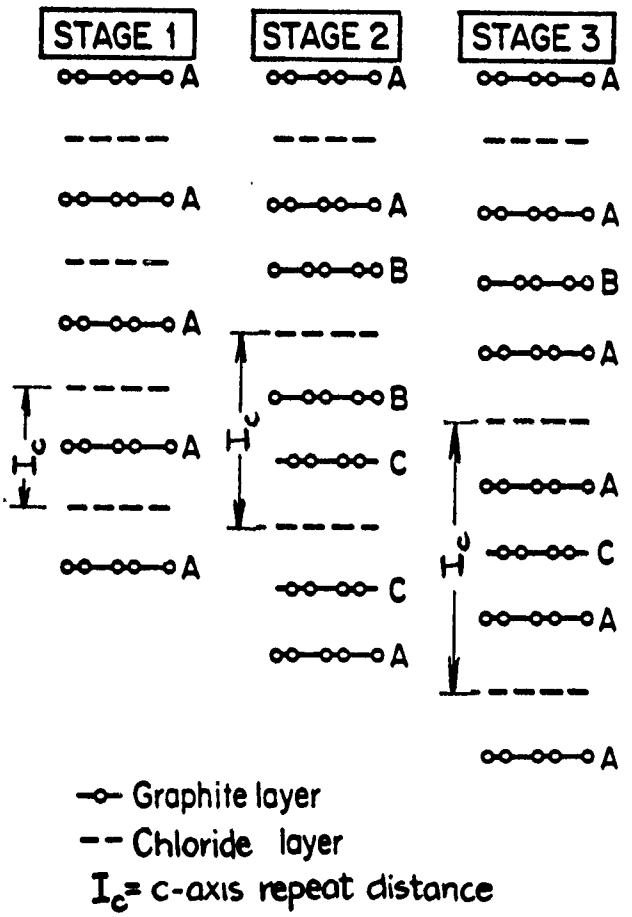

Figure 136. Schematic of staging in intercalated graphites; interlayer stacking of adjacent graphite planes remains AB AB as in pure graphite, although the stacking order can change across the intercalated layers, as indicated.

Since tangential shear occurs easiest within an intercalated layer, the shear strength of a compound of any stage (see Figure 136) should be the same, provided the crystallinity of the starting (initial) graphite powder (i.e., the degree of kinking, and turbostratic or better-aligned distribution of the crystallite domains) is the same in each case. Wear is another matter, yet removal rate from a monolithic piece should also be the function of staging. A Stage 3 material should wear in larger particle sizes than a Stage 2 equivalent and a Stage 1 compound should, in turn, produce smaller wear particles from its rubbed surface than from a Stage 2 state. Furthermore, preferential accumulation of a low shear strength layer on the rubbed surface, comprised of displaced but not removed micro-crystallites, should occur most readily with a lower-staged material.

Kamimura (230) explained that transitions between stages are abrupt, because these transactions are simply the result of (a) the intercalant's lateral motion within the kinks (see Figure 137), and (b) the propagation of these kinks, and the assocoated energetics of these transitions are manifested in quantum jumps. Since energy is required in quanta to produce these transitions, energy is equally required to cause stepwide deintercalation on heating.

It must be stressed again, however, that the exact identification of a given transition is important to the tribologists only in terms of serious friction and wear degradation in the environment of interest. The set of TGA/DSC plots presented here are intended to be helpful in anticipating such transitions. They helped in designing SEM tribometer tests with pressed molds of selected, intercalated graphites, as shown later in this report.

3.2.2.2 Intercalant Distribution within, and Stability of, the Pressed Molds. Table 32 describes the selected powders which were consolidated into molds and the pressing conditions. Basically, the powders were uniaxially pressed to ~50% density at R.T. in air, followed by (a) green-pressing, then (b) warm-isostatic pressing (at 200°C) in appropriate containers. These molds are listed in an order of increasing thermal and oxidative stability of the starting powders. It has been previously determined (see 3.2.2.1) that the small particle size, $NiCl_2$-intercalated DP 54,011 (Table 30) was the single, most thermally and thermooxidatively unstable material. The larger particle size $CrCl_3$ was better and the large particle size, $CdCl_2$-intercalated DP 26,121 (Table 30) exhibited the highest stability by far, both in argon and in air.

Since the surface of the metal chloride intercalated graphite tends to be more intercalant-poor than the bulk (229), we suspected that during the "warm" (200°C)-pressing of monolithic pieces, the mold surfaces would be equally intercalant-depleted. As such, the surface of a mold should be removed to produce a useful lubricant compact. A good analogy is the well-known "skin-effect" of polymer-based, molded self-lubricating composites: their as-molded surface is polymer-rich and lubricant-pigment-starved. The polymer-enriched surface "skin" also needs to be removed before fabricating the composite into a bearing part capable of forming a good transfer film and exhibiting low wear rate (231). Furthermore, it was also suspected that molds "warm-pressed" from an inherently unstable powder would metamorphose into something even more unstable, i.e., degraded to an even greater degree.

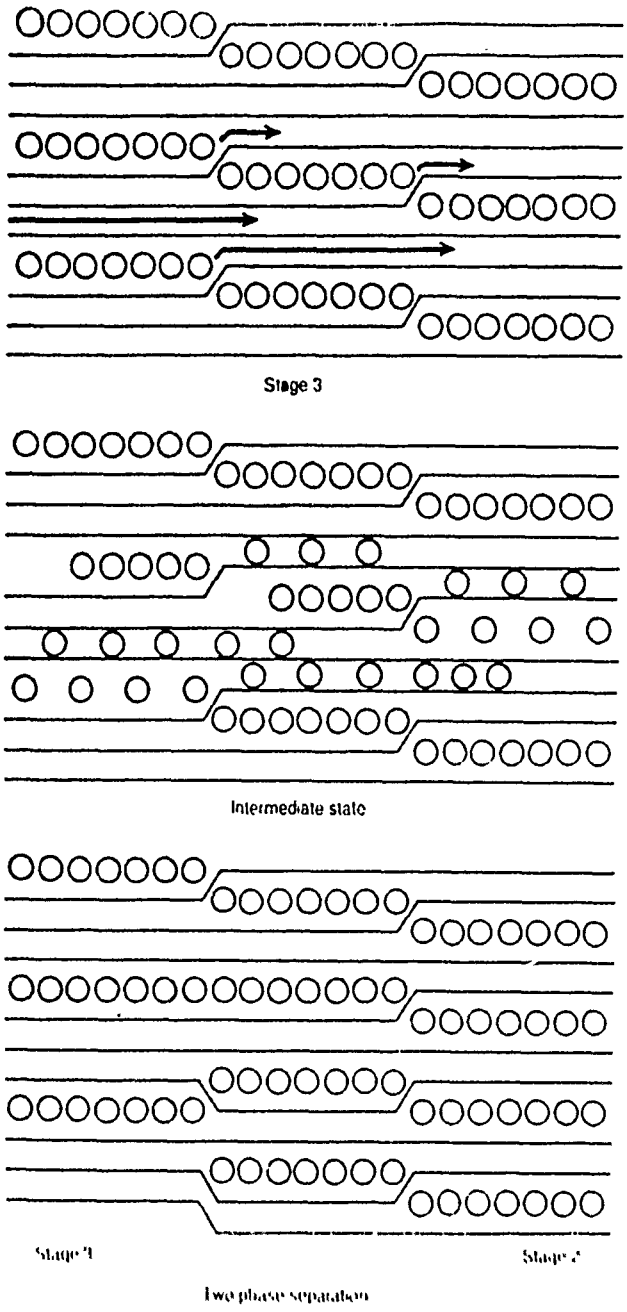

Figure 137. Mechanism for transition between stages according to the Daumas-Herold domain model (230).

Table 32. Pressed flat molds (~10 mm x 5 mm x 3 mm) of selected, intercalated graphite powders (from Intercal).

Intercalant	Base Powder Particle Size (μm)	Intercal Product Number	Pressing Parameters		Specific Gravity ($g \cdot cm^{-3}$)	Number of Flats
			Load (lbs)	Temperature (°C)		
$NiCl_2$	10	DP 54,011	23,000	(1)	2.67	8
$CrCl_3$	100	DP 26,030	23,000	200	2.43	8
$CdCl_2$	88	DP 26,121	23,000	200	2.72	8

(1)Not reported.

As one method of investigating these important issues, argon and air atmosphere TGA and DSC were performed (as before) on (a) the same lots of powders used to press the molds (Table 32), (b) on powders scraped off the mold surfaces, as well as (c) on powders sampled from inside of the molds. With respect to the sampling technique, the average, as-received thickness of the molds was ~3 mm. Scraping the surfaces with a clean X-acto knife removed a thin surface skin, on both sides of each molded flat. Then, the remaining surfaces were gently sandpapered with bonded α-SiC grit -type, fine particle size (Grade 600) sheets, until the mold thicknesses were eventually reduced to ~0.8 mm. At that time, additional powder samples were scraped from the thinned flats.

One molded flat per each intercalated graphite formulation was used throughout this last series of tests. In some cases, the tests were run in duplicate to establish some repeatability.

The TGA data in Figures 138, 139 and 140 indicated that our initial concerns were justified. In the case of the less stable $NiCl_2/CrCl_3$ compounds the starting powders exhibited greater resistance to thermal and thermooxidative degradation than any samples taken from the molds. In fact, at least with the least-stable $NiCl_2$-based material, the mold center (designated as "mc" in the figures) indeed appeared to be more stable than the mold surface (designated as "ms"). On the other hand, the $CdCl_2$-intercalated molding powder and the "ms" and "mc" samples have all shown stable and equivalent behavior. The high thermooxidative stability of this latter material was, therefore, confirmed, both for the pulverized and molded forms. It is noteworthy that TGA stability of all the samples examined here is generally greater in argon than in air, as found before.

The DSC plots in Figures 141, 142 and 143 (starting powder data omitted for greater clarity of the presentation) simply indicate flatter, more featureless functions with the progressively more stable products. Again, the three endothermic DSC transitions of $NiCl_2$ (between 50° and 225°C, see Figure 141) closely correlate with the triple TGA transition within the same temperature range (see Figure 138). On the whole, TGA appears to be a more sensitive method of determining thermal and thermooxidative stability of these metal chloride intercalated graphites than DSC.

By and large, the TGA thermograms of the original powder samples in Figures 129 and 132 agree with those of the latter powder batches used to press the molds (Figures 138 through 140). The exception seemed to be the $CrCl_3$-containing material (DP 26030). The general shapes of these thermograms for the original powder samples, the starting mold powders, and the "ms" samples are similar for each gas atmosphere. However, weight loss transitions are greater for the molding powder and mold samples; also, less residue remains from them in argon than from the early powders described in Figures 129 through 132.

There are similar variations in the corresponding DSC data. The original, $CrCl_3$-intercalated powder yielded thermograms with no sharp peaks (see Figure 134). The more recent molding powder exhibited sharp endotherms in air (not shown in any of the figures) while the "ms" mold samples had sharp endotherms in argon (Figure 142). These data indicate some batch-to-batch variation of the $CrCl_3$-type powder lots and/or variation in the stability of certain parts of the molds, even within the same scraped region.

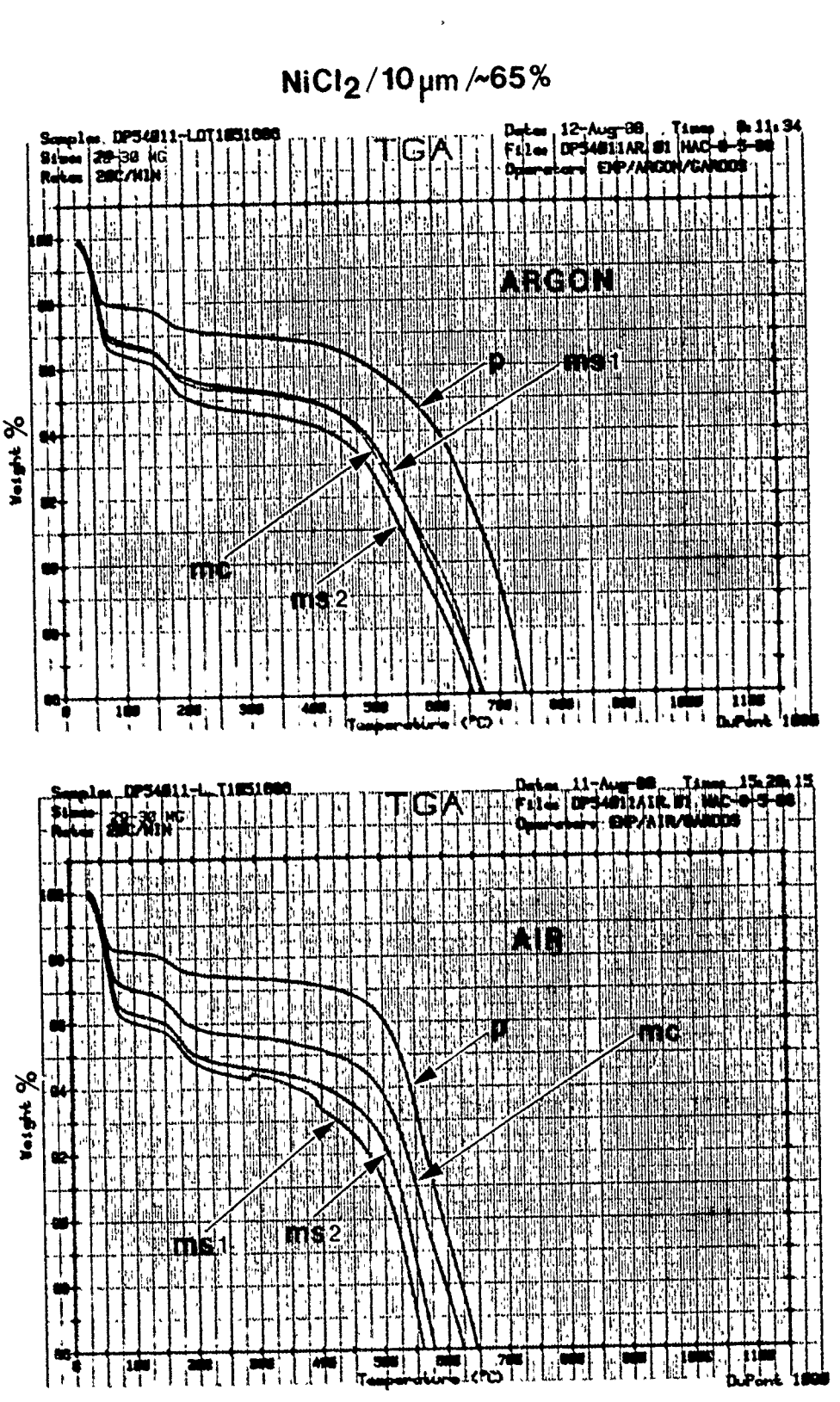

Figure 138. TGA of $NiCl_2$-intercalated graphite mold sites and starting powder (p = powder; ms = mold surface; mc = mold center).

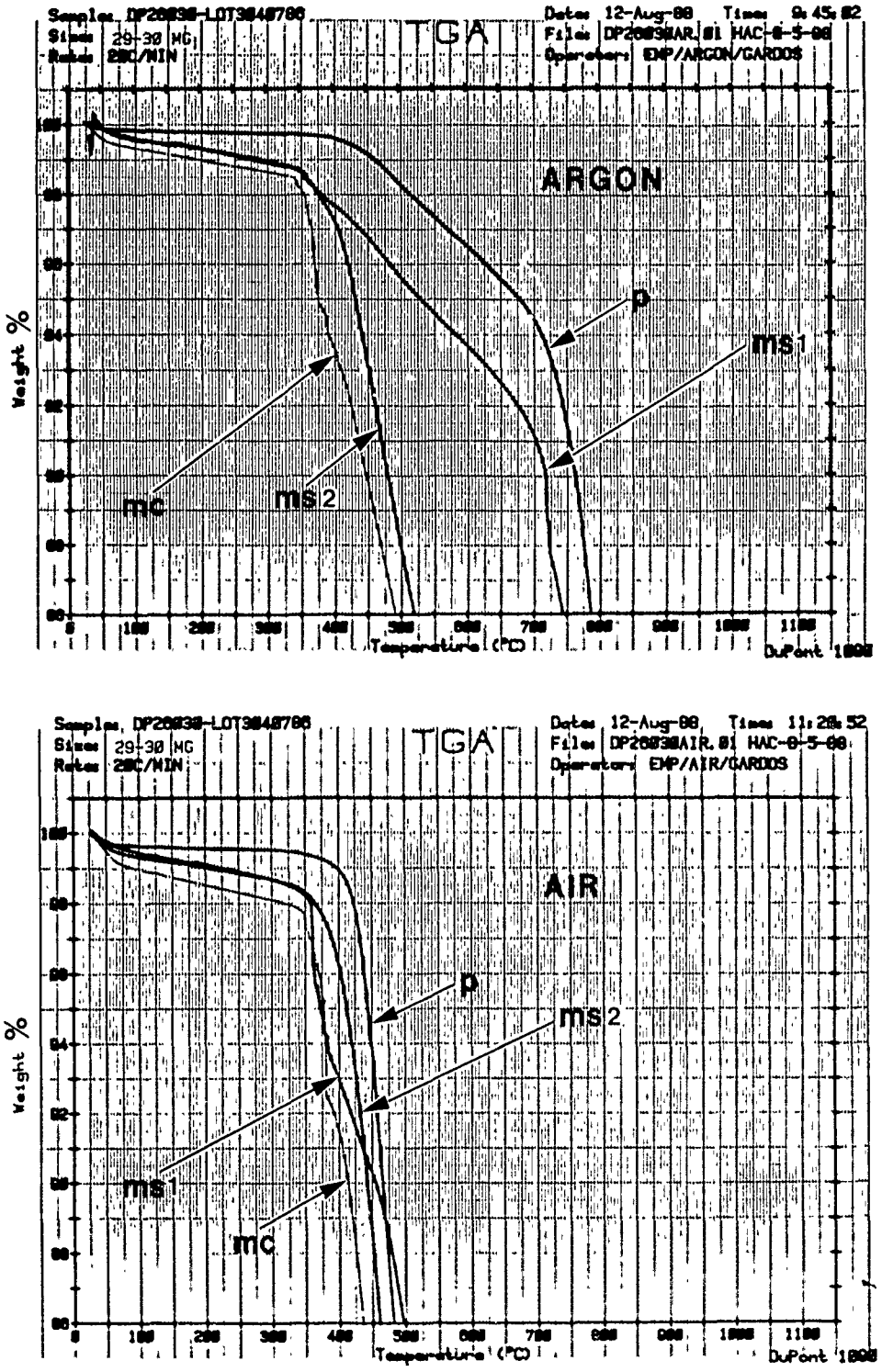

Figure 139. TGA of $CrCl_3$-intercalated graphite mold sites and starting powder (p = powder; ms = mold surface; mc = mold center).

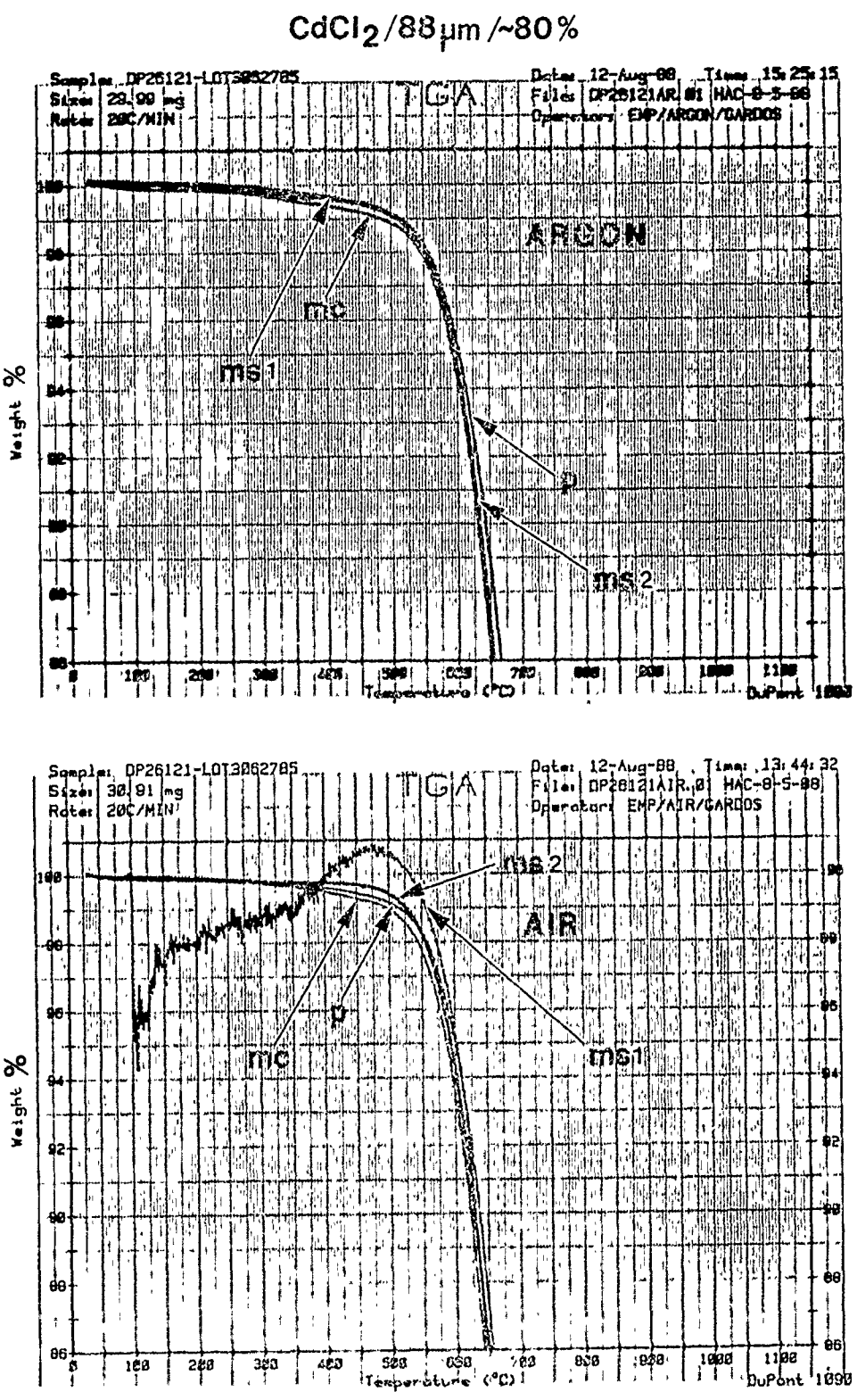

Figure 140. TGA of $CdCl_2$-intercalated graphite mold sites and starting powder (p = powder; ms = mold surface; mc = mold center).

$NiCl_2$ / 10 µm /~65%

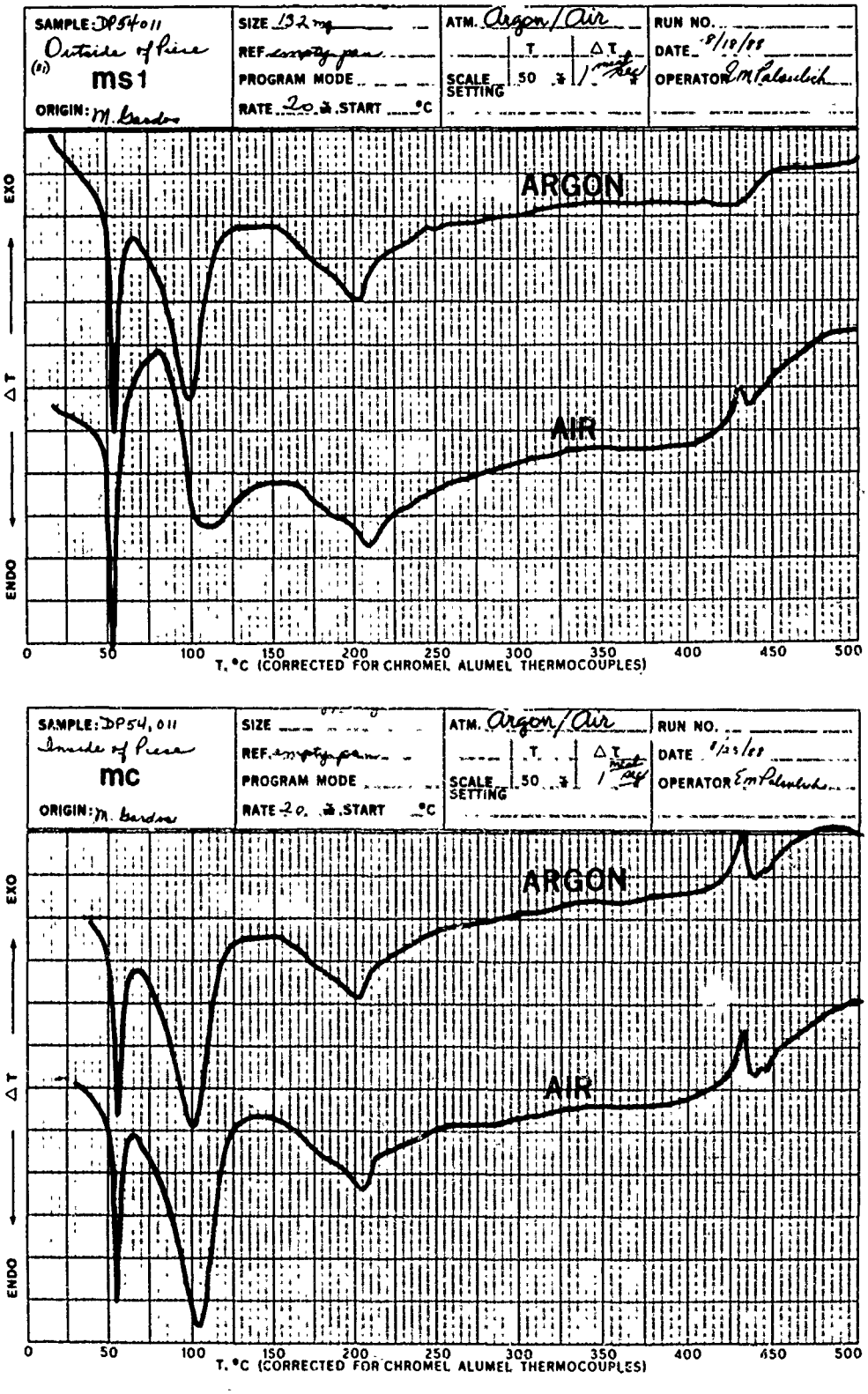

Figure 141. DSC of $NiCl_2$-intercalated graphite mold sites and starting powder (p = powder; ms = mold surface; mc = mold center).

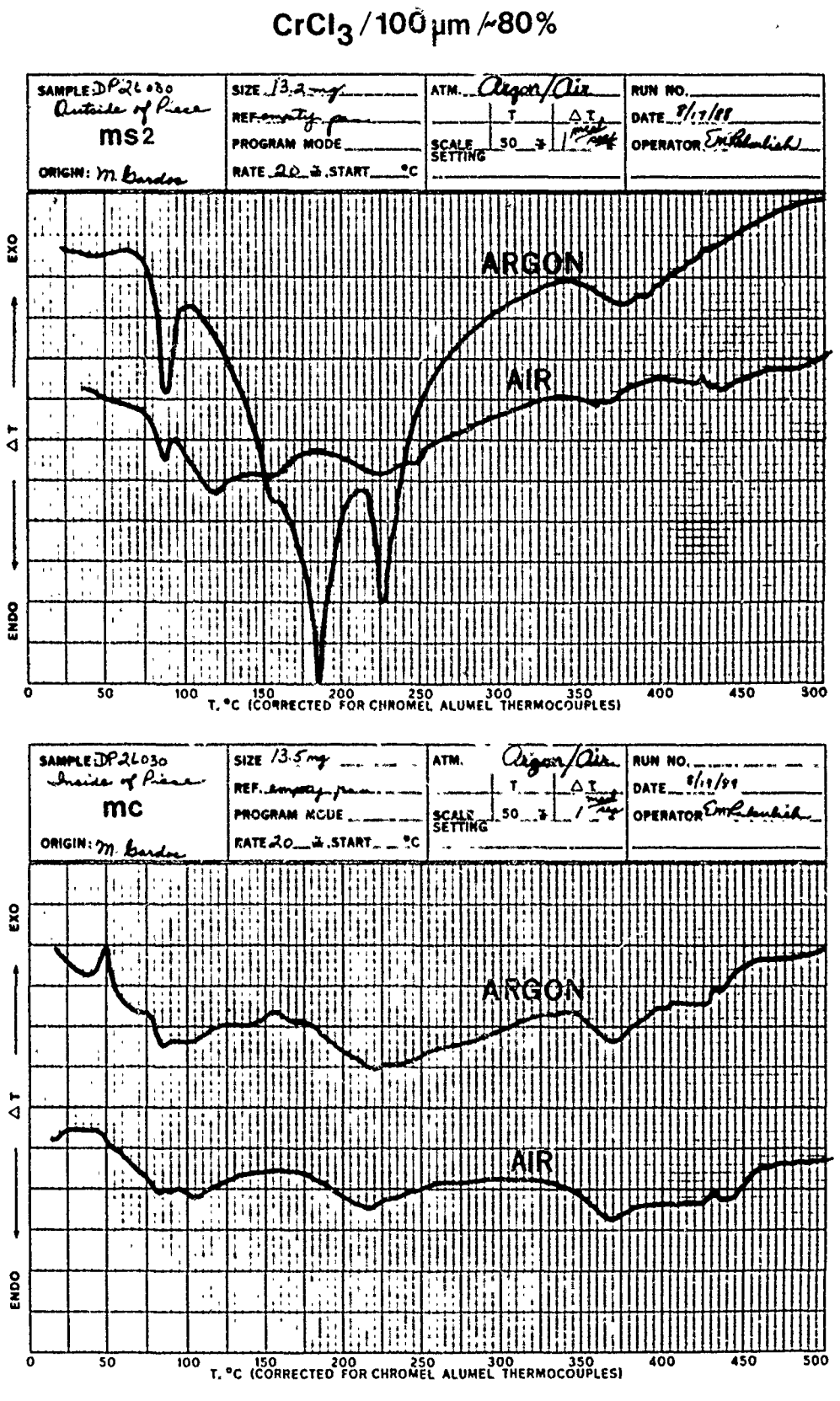

Figure 142. DSC of $CrCl_3$-intercalated graphite mold sites and starting powder (p = powder; ms = mold surface; mc = mold center).

$CdCl_2$ / 88 µm / ~80%

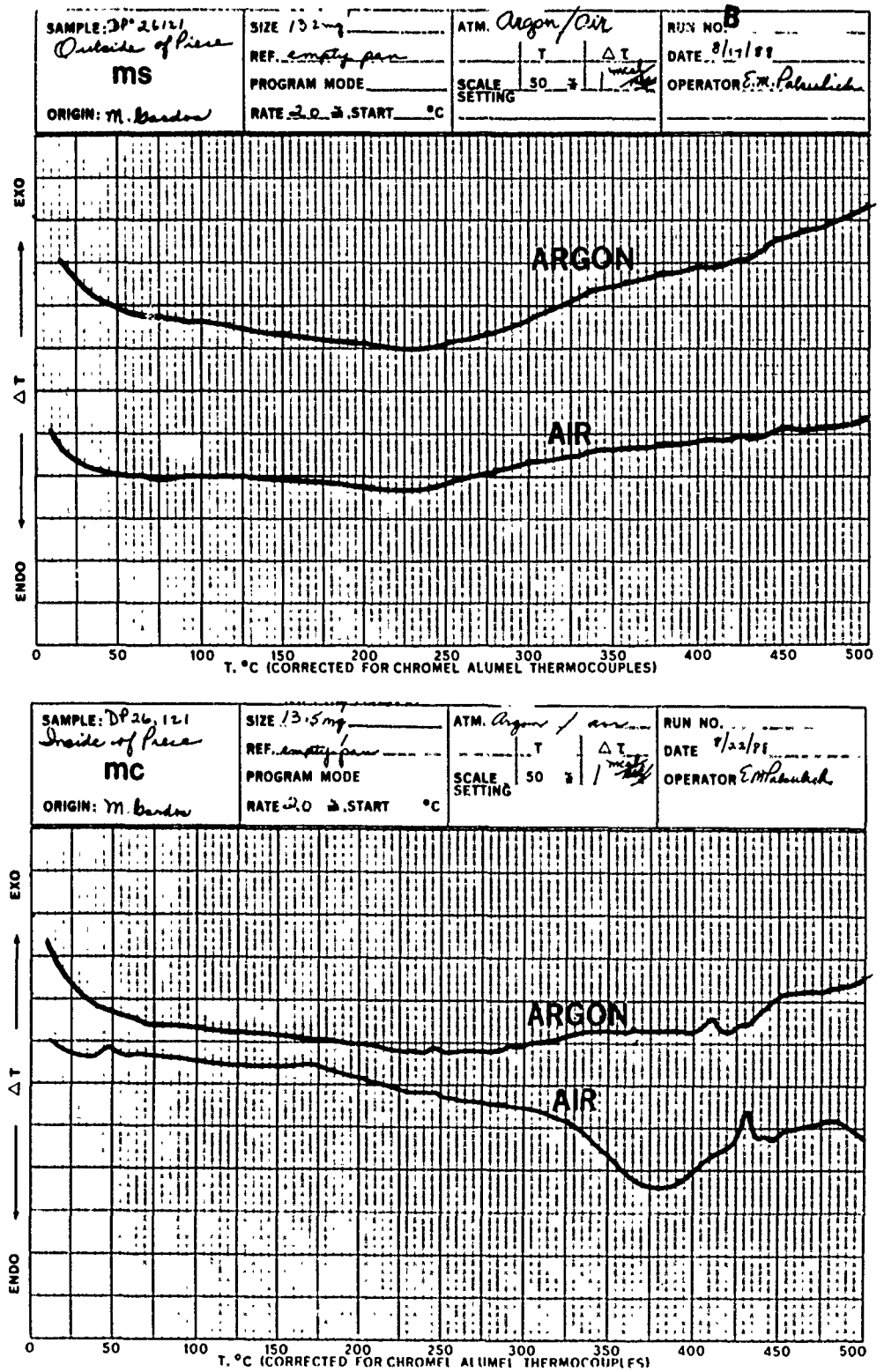

Figure 143. TGA of $CrCl_3$-intercalated graphite mold sites and starting powder (p = powder; ms = mold surface; mc = mold center).

3.2.2.3 SEM Tribometry of Intercalated Graphite Molds. Triboflats hand-cut, α-SiC paper-sanded and fine diamond paper-polished from $NiCl_2$/HOPG and $CdCl_2$/HOPG (to remove the outer 0.5 mm "skin" for the best surface purity) were subjected to SEM tribotests at progressively higher temperatures in vacuum (1.33×10^{-3} Pa = 1×10^{-5} torr). The aim was to correlate their friction and wear behavior with any deintercalation.

With respect to formulating the model SEM tribotester experiments, the SEM triboflats fabricated from the least thermally stable ($NiCl_2$) and most thermally stable ($CdCl_2$) molds were made to slide against ceramic (90° XTL sapphire) tribopins. The normal loads employed were low (0.147N = 15g) to mitigate the formation of excessively large wear scars. Running these tests in vacuum and in a partial pressure of air, while ramping the flat's temperature to and from the ~700°C maximum, was supposed to determine tribothermal stability. We intended to (a) correlate TGA/DSC transitions with any friction/wear changes and thus (b) indicate the intercalated HOPG's usefulness for vacuum and air applications. The significance of being able to use intercalated graphites for lubricating ceramic bearings in high vacuum was one main driving force behind these experiments.

As depicted in Figure 144, each triboflat received three tests with the same XTL sapphire pin. In developing each of the three wear tracks, sliding proceeded per the following protocol:

- Track No. 1: Atmospheric air (~100 cyc.) + vacuum (~900 cyc.) + Atmospheric air (~100 cyc.), all at R.T.
- Track No. 2: Atmospheric air (~100 cyc.) at R.T. + vacuum (~1000 cyc.) at temperature ranging from R.T. to ~700°C and back to R.T. + atmospheric air (~100 cyc.) at R.T.
- Track No. 3: Atmospheric air (~100 cyc.) at R.T. + vacuum (~100 cyc.) + atmospheric air (~100 cyc.), all at R.T.

Any tribological behavior differences between the tests on Track Nos. 1 and 3 were to be attributed to heating the flat on Track No. 2, where the test thermally stressed the materials. Therefore, the final tests associated with Track No. 3 were designed to reveal the effects of any previous tribothermal degradation on friction and wear. Since sliding in partial or full atmospheric pressures of air was always at or near R.T., tribooxidative degradation and its influence were presumed minimal compared to tribothermal degradation in vacuum.

In all tracks, the normal load on the pin was only 0.147N = 15 g, except during the first test (Track No. 1 of $CdCl_2$), where the load was 0.245N = 25 g. Owing to the unexpectedly large wear scar resulting therefrom (see Figure 144), the load was reduced to 15 g in all subsequent tests.

Employing the time-dependent development of the wear scar widths (shown in Figure 144) by measurements from the video-log (for an example, see Figure 145) and the coefficients of friction (COF) measured during the tests (for example, see Figure 146), the development of the COF and $\tau_s = F_k/A_{app}$. was computer-calculated for the respective materials and tests in Figure 147 (Test Tracks No. 1), Figure 148 (Test Tracks No. 2), and Figure 149 (Test Tracks no. 3). The data indicate the following:

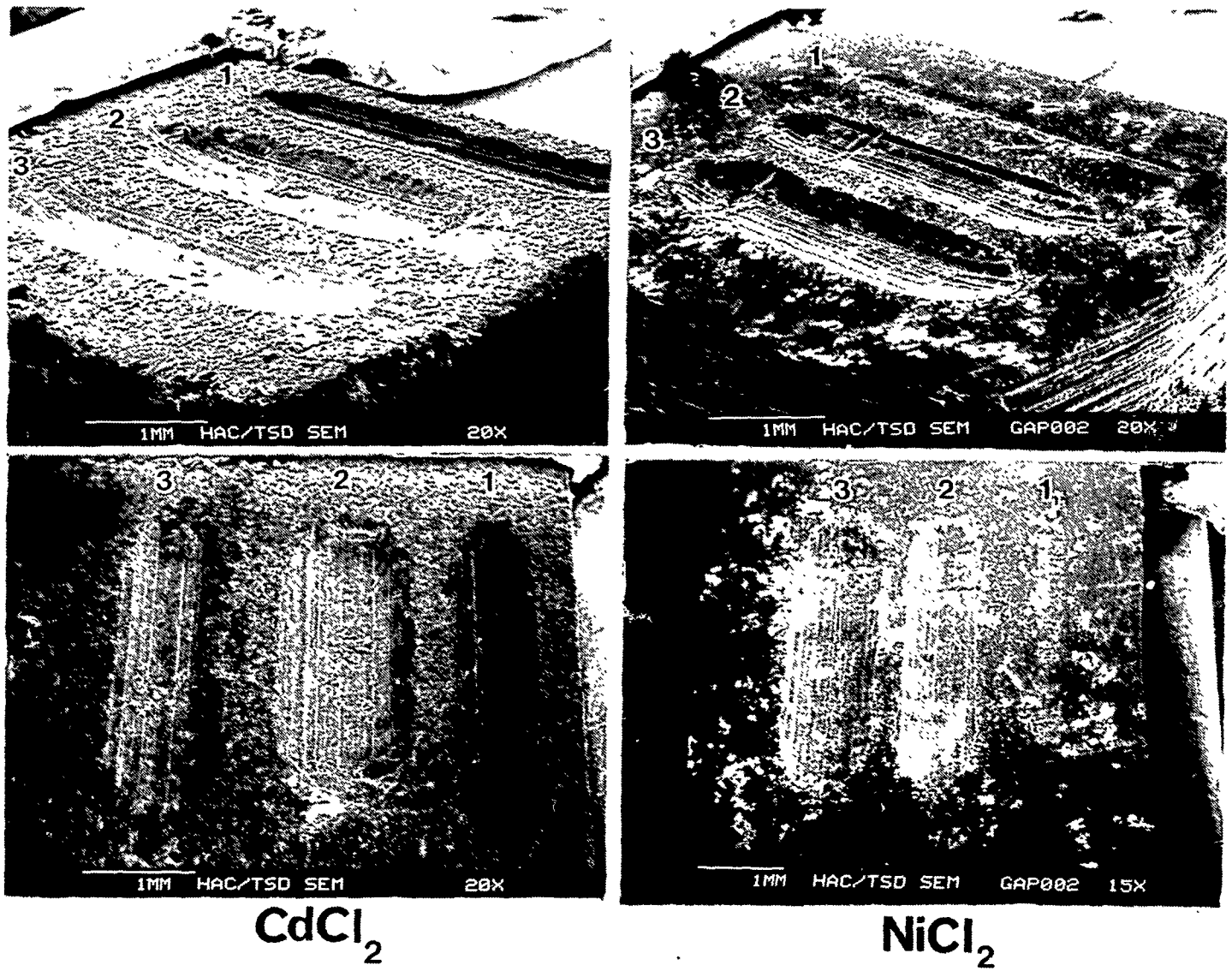

Figure 144. SEM photomicrographs of the used $CdCl_2$/$NiCl_2$-intercalated HOPG triboflats; numbers refer to Test and/or Test Track (Wear Scar) number.

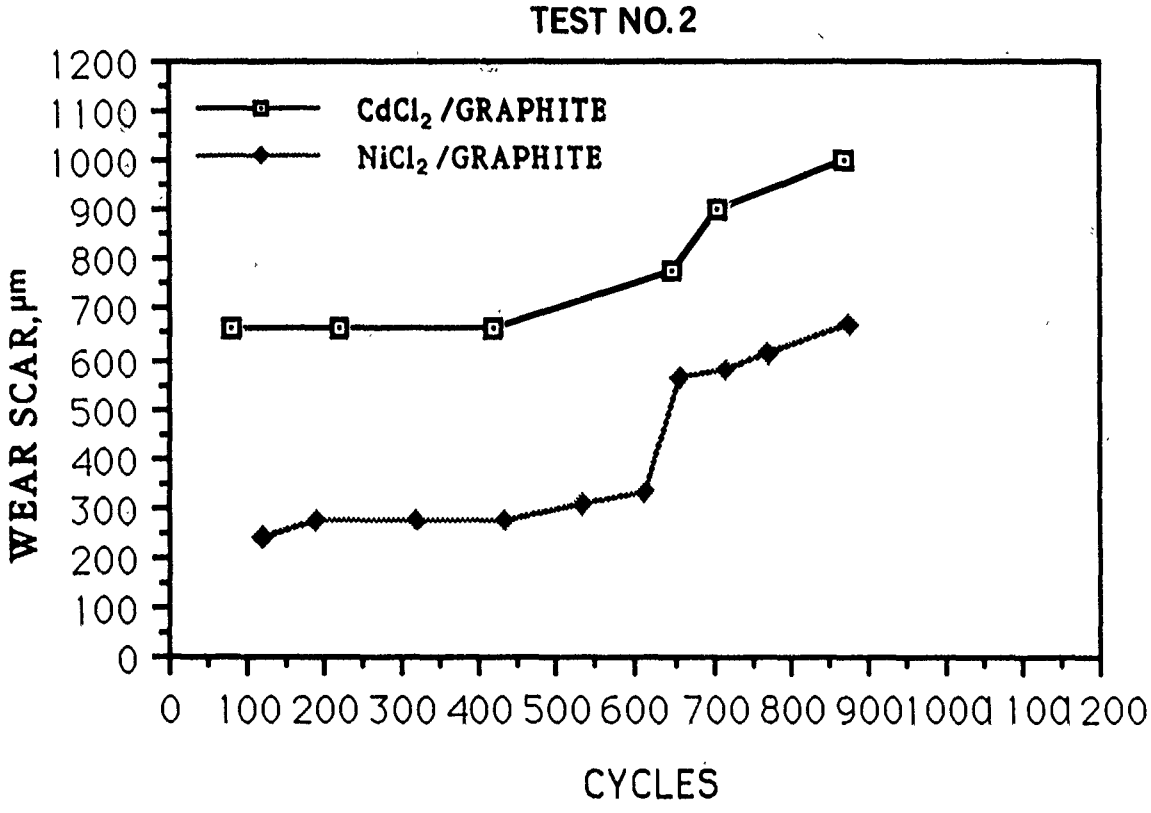

Figure 145. Wear scar width development on $CdCl_2/NiCl_2$-intercalated HOPG triboflats during the respective second tests (see Track No. 2's in Figure 144).

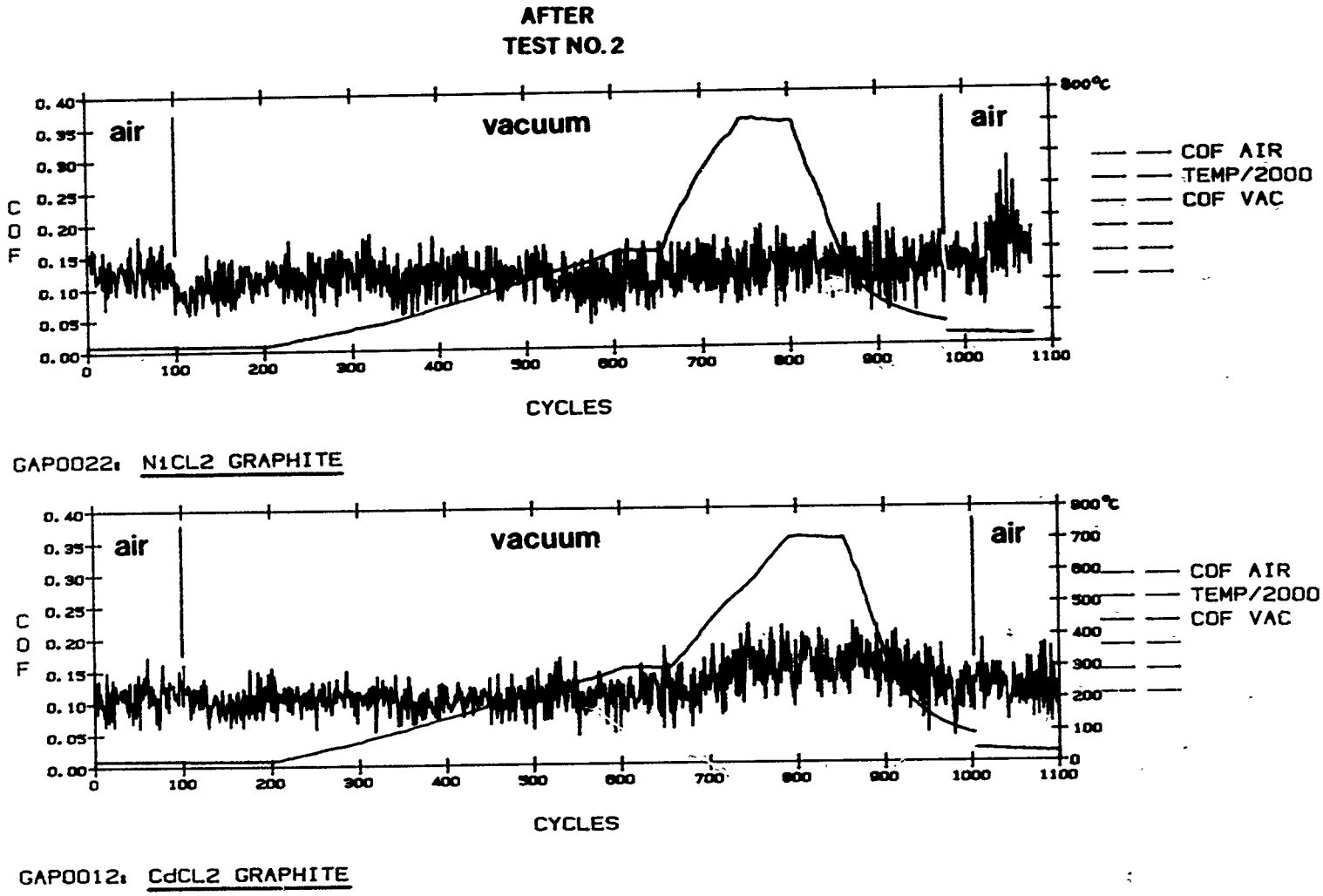

Figure 146. Average coefficients of friction (COF) of $CdCl_2/NiCl_2$-intercalated HOPG triboflats during the respective second tests (see Track No. 2's in Figures 144 and 145).

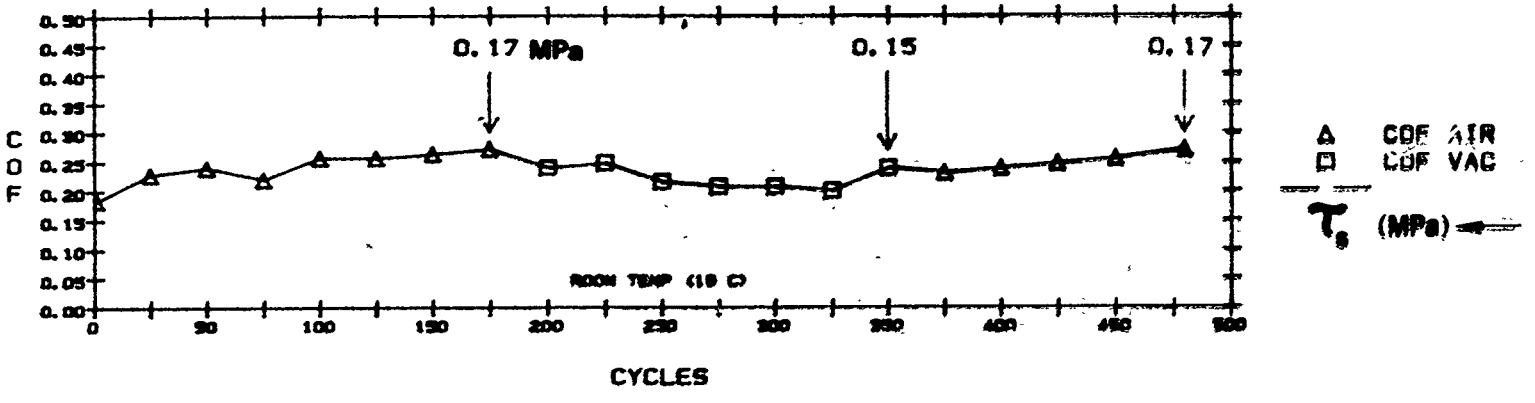

GAP0011: ROOM TEMPERATURE; $CdCl_2$; TEST No. 1 (25 CMS.)

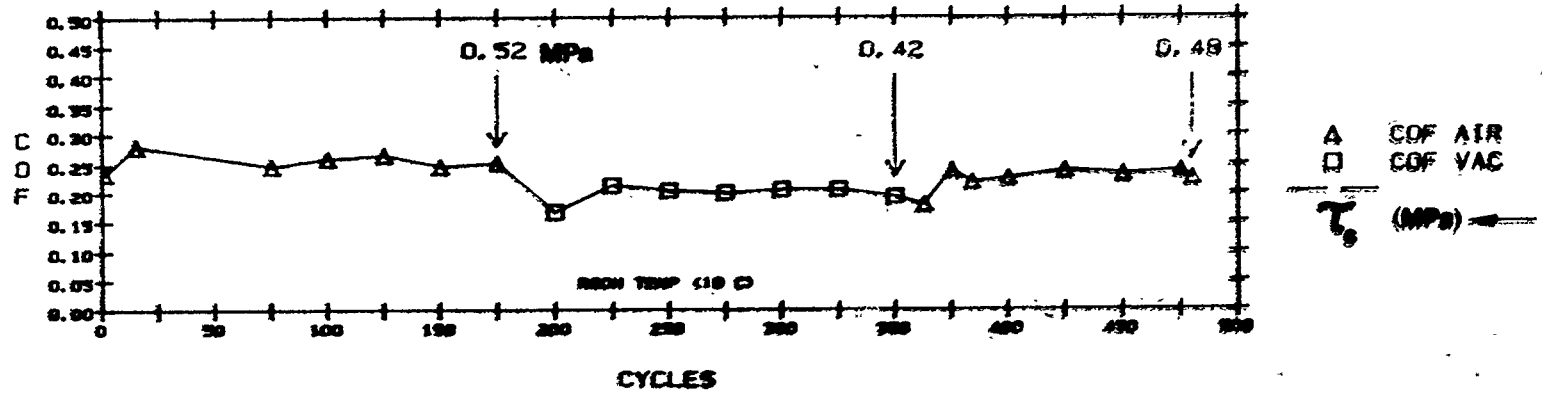

GAP0021: ROOM TEMPERATURE; $NiCl_2$; TEST No. 1 (15 CMS.)

Figure 147. Average coefficients of friction (COF) and apparent surface shear strength (τ_s) of $CdCl_2/NiCl_2$ intercalated HOPG triboflats during the respective (R.T.) first tests (see Track No. 1's in Figure 144).

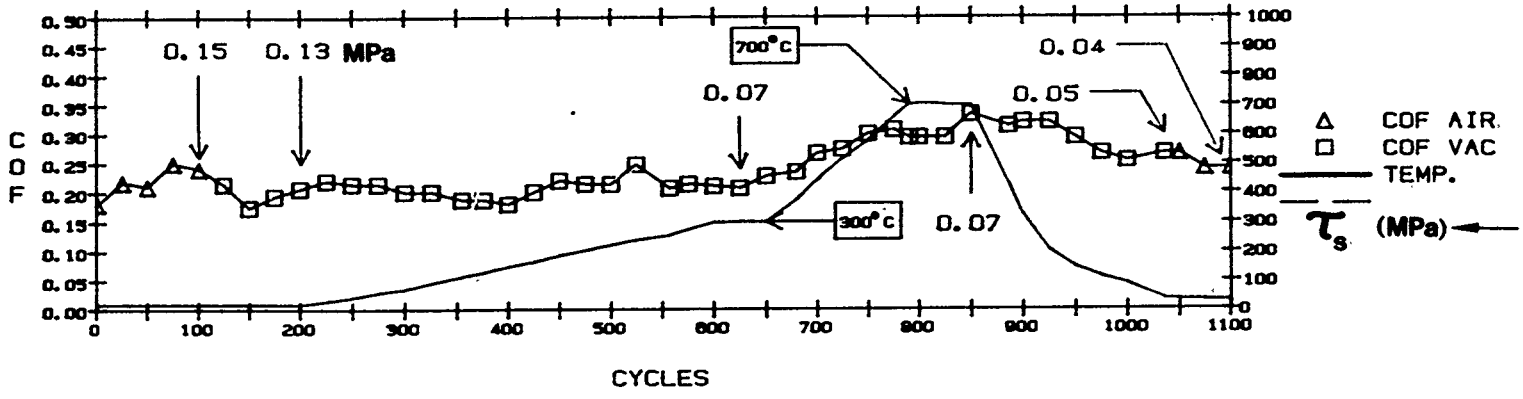

GAP0012: CdCl2: TEST No. 2 (15 GMS.)

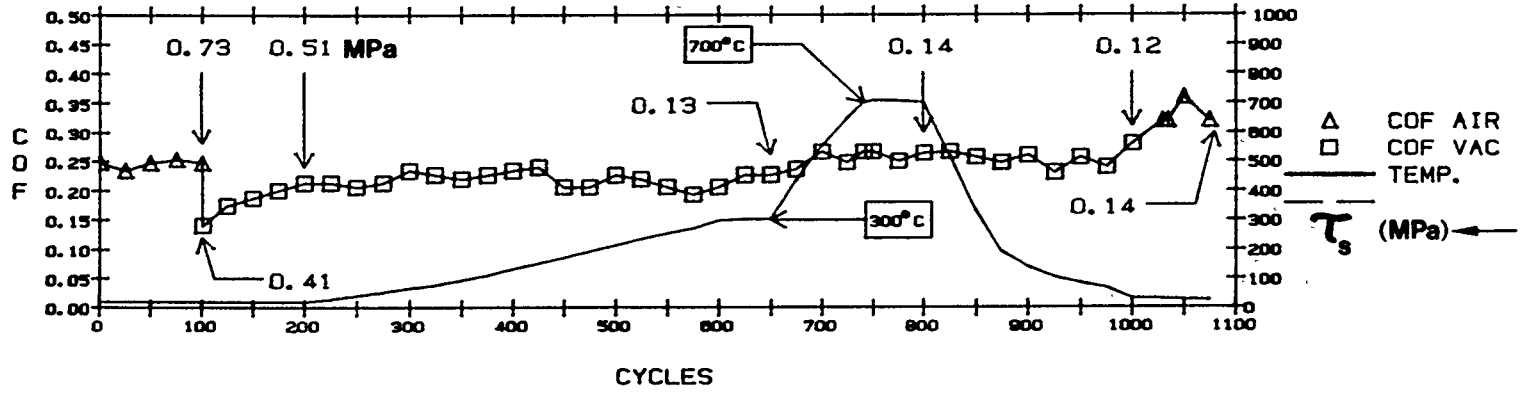

GAP0022: NiCl2: TEST No. 2 (15 GMS.)

Figure 148. Average coefficients of friction (COF) and apparent surface shear strength (τ_S) of $CdCl_2/NiCl_2$-intercalated HOPG triboflats during the respective heated second tests (see Track No. 2's in Figure 144).

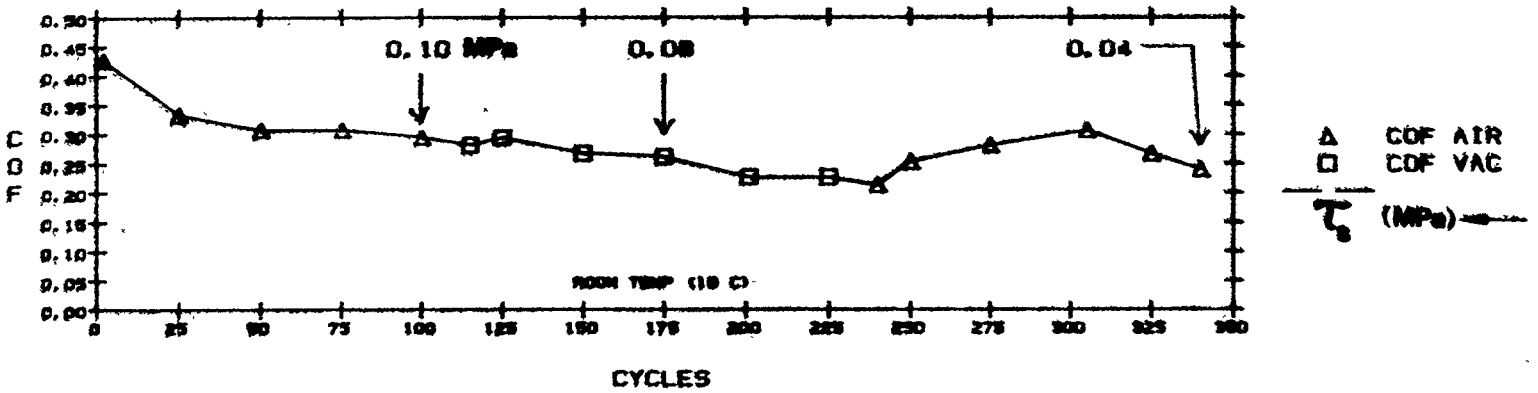

GAP0013: ROOM TEMPERATURE: CdCl2: TEST No. 3 (15 CMS.)

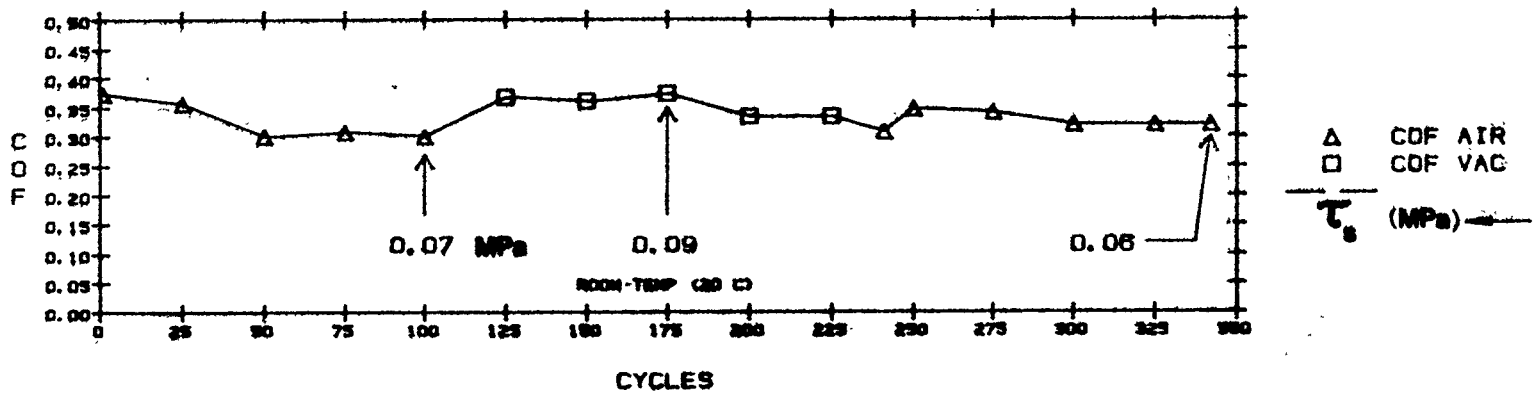

GAP0023: ROOM TEMPERATURE: NiCl2: TEST No. 3 (15 CMS.)

Figure 149. Average coefficients of friction (COF) and apparent surface shear strength (τ_S) of $CdCl_2/NiCl_2$-intercalated HOPG triboflats during the respective (R.T.) first tests (see Track No. 3's in Figure 144).

1. The $CdCl_2$/HOPG exhibits higher wear rate than the $NiCl_2$/HOPG. Heating to ~700°C rapidly increased the wear of both materials, where the rate of increase was considerably greater for the $NiCl_2$/HOPG.

2. The COF/τ_S results in Figure 147 show little difference in the air/vacuum τ_S. These data also demonstrate, again, the systems-dependent nature of COF values. The friction of both materials is about the same, yet the wider wear scar on the $CdCl_2$ flat resulted in a lower τ_S, with little wear-in effect. Since the τ_S of MoS_2 films in vacuum, on hard substrates (in concentrated contacts where $A_{app.}$ is very close to A_{real}) is in the 8-15 MPa range, it is suspected that in the present case the apparent area of contact ($A_{app.}$) calculated from the wear scar is about 50 to 100 times larger than the real area of contact (A_{real}) between the pin and the flat. As shown in Figure 150, the $CdCl_2$/HOPG did transfer heavily and unevenly to the tip of the XTL sapphire pin. The transfer of the $NiCl_2$/HOPG was similar. The resultant wear tracks in Figures 151 through 155 reveal considerable grooving of the scars by the transferred, highly adherent and compacted mother material. Chatter marks also developed, becoming aligned more-or-less perpendicular to the direction of sliding. The high τ_S $NiCl_2$/HOPG exhibited more distinct chatter marks than $CdCl_2$/HOPG (compare Figures 152 and 155). Alignment of the flat, platelet like crystallites in the plane of sliding is obvious (Figure 153). The SEM photomicrographs corroborate the uneven nature of the contact surfaces on the microscopic scale, lending credence to the reasonable supposition that $A_{app.} >> A_{real}$.

3. The respective second tests' "start-up" COF/τ_S values in air and in vacuum, at room temperature, agree well with those of the first tests, see Figure 148. Heating to ~700°C induces considerable malleability to the respective surfaces: the progressively reduced τ_S values indicate a clearly observable run-in phenomenon. Run-in is just as distinct with the lower τ_S $CdCl_2$/HOPG (from 0.13 MPa to as low as 0.04 MPa at the end of the test) as it is with the higher τ_S $NiCl_2$/HOPG (0.51 MPa 5 to ~0.12/0.13 MPa). The steady-state air-vacuum-air τ_S values are remarkably close, indicating no major variations on changing the atmospheric environment. The smooth COF/τ_S curves do not reflect any of the well-defined transitions previously observed by DSC (Figure 144) or TGA (Figure 138) on $NiCl_2$/HOPG. Visual examination of the used pin/flat specimens after the respective second tests showed a white, film-like residue covering the XTL sapphire pin and pin holder. Chemical analysis of the residue found the material to be pure $CdCl_2$, sublimed from the heated triboflat and condensed on the colder superstructure. Fortunately, the $CdCl_2$/HOPG tests were done after the $NiCl_2$-equivalents, where no visible condensate was observed and sampling the condensing surfaces did not show the presence of any $NiCl_2$. This information, combined with the TGA data, leads to the conclusion that $CdCl_2$ sublimes without decomposition, while the $NiCl_2$ is probably decomposes to Cl_2 (g) and a Ni-Cl residue compound, which remains non-volatile at ~700°C.

4. The third (R.T.) test on each flat actually shows significant τ_S improvements with both materials, especially with the $NiCl_2$/HOPG. The commensurate and very large degradation in wear resistance is, however, clearly observable in Figure 144: Test Track No. 1 of the $NiCl_2$/HOPG developed after ~460 cycles, both under a 15 g load. A similar trend can be

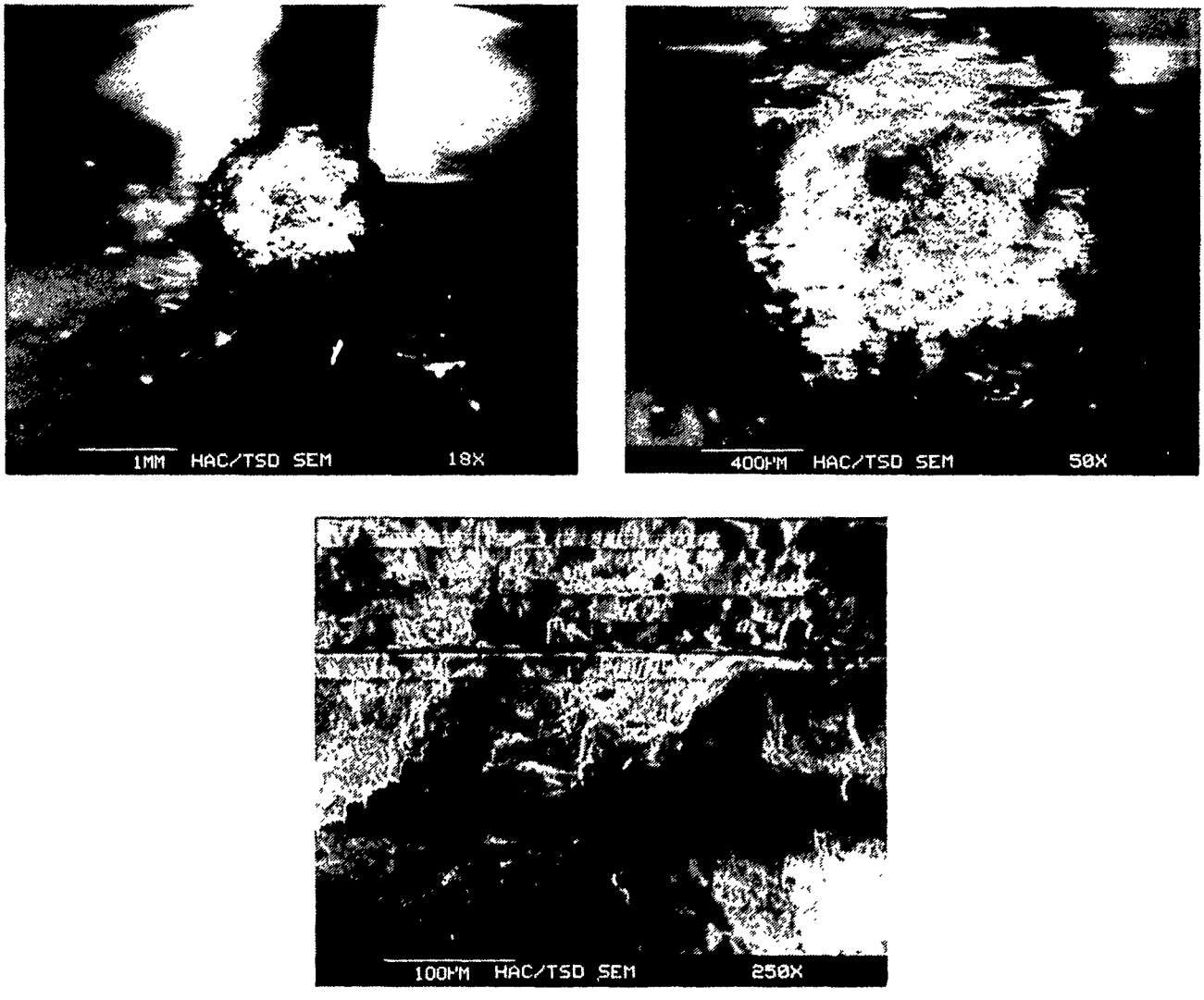

Figure 150. SEM photomicrographs of $CdCl_2$/HOPG transferred to the tip of the XTL sapphire pin, after all three tests.

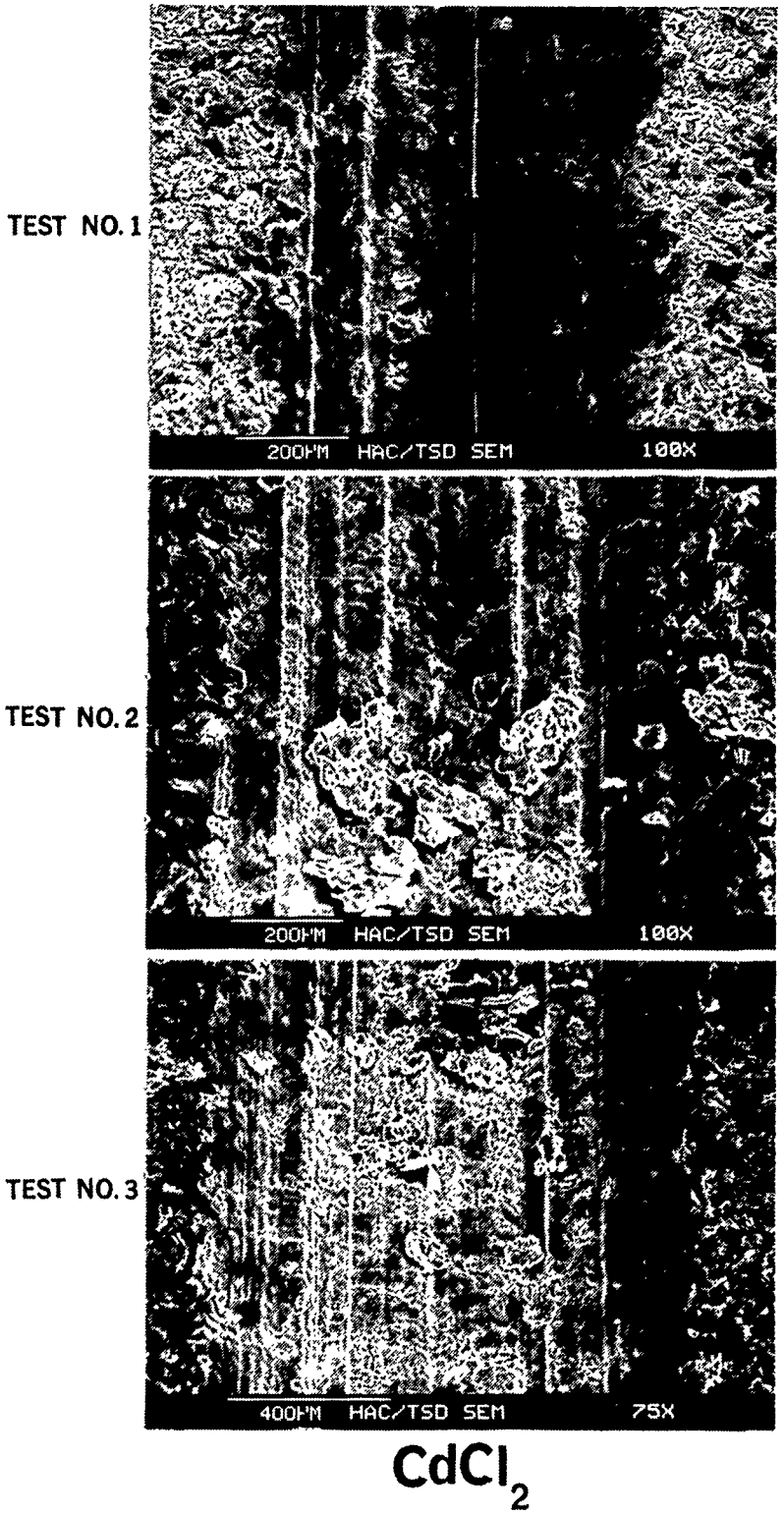

Figure 151. SEM photomicrographs of the Test No. 1/2/3 $CdCl_2$/HOPG wear tracks (from Figure 144), at 75x to 100x magnifications.

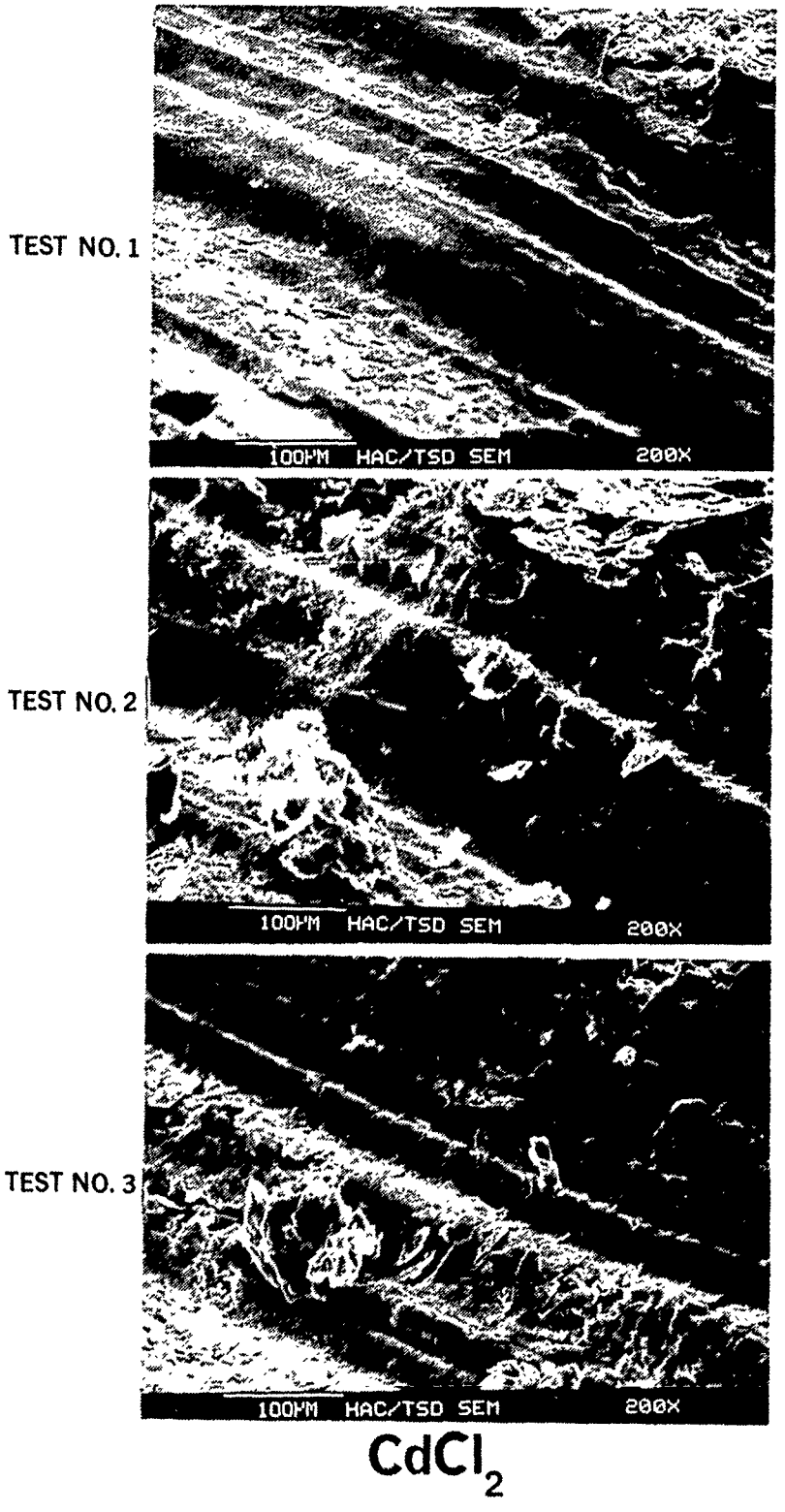

Figure 152. SEM photomicrographs of the Test No. 1/2/3 $CdCl_2$/HOPG wear tracks (from Figures 144 and 151), at 200x magnification.

TEST NO. 3

$CdCl_2$

Figure 153. SEM photomicrographs of the $CdCl_2$/HOPG Test Track No. 3 at 1000x magnification, showing run-in alignment of the flat crystallites.

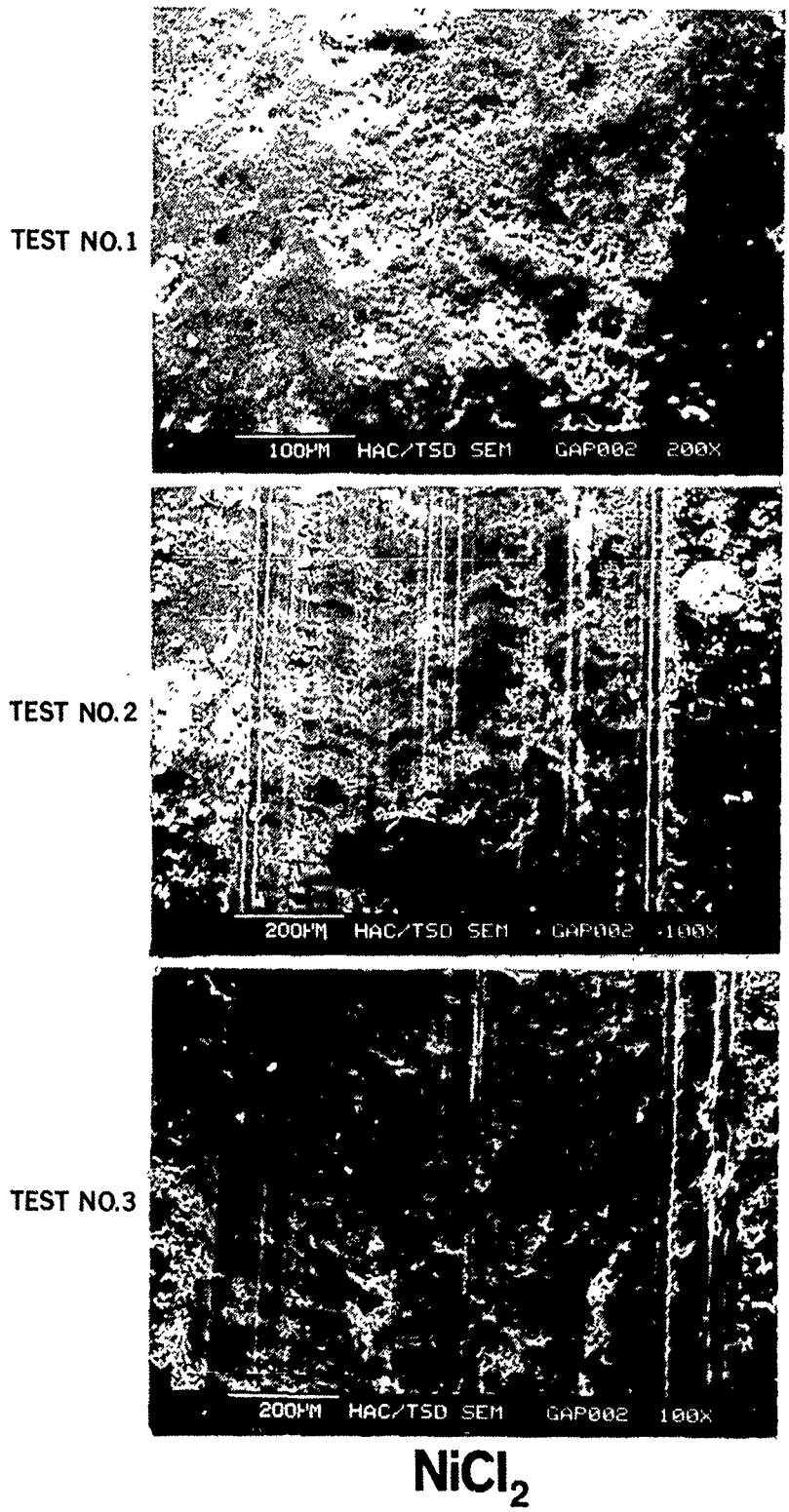

Figure 154. SEM photomicrographs of the Test No. 1/2/3 $NiCl_2$/HOPG wear tracks (from Figure 144), at 100x to 200x magnifications.

TEST NO. 3

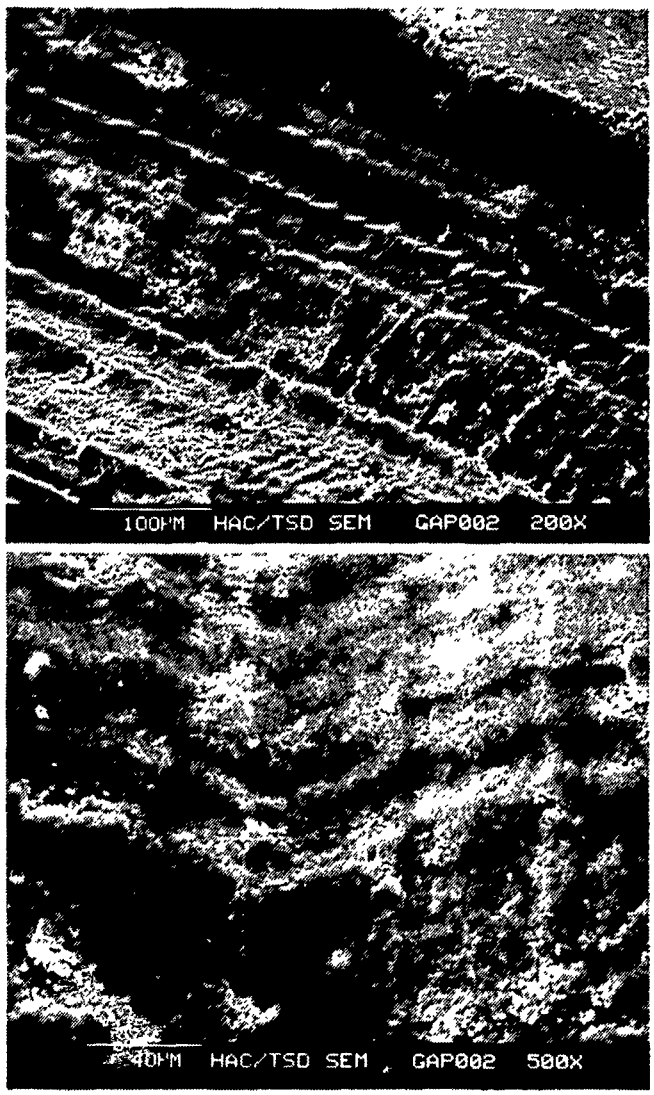

$NiCl_2$

Figure 155. SEM photomicrographs of the $NiCl_2$/ HOPG Test Track No. 3 at 200x to 500x magnifications.

observed with the $CdCl_2$/HOPG, although an equivalent comparison is not as clear-cut. There, Test Track No. 1 formed after ~460 cycles under a 25 g load (again, see Figure 147), while the wider and deeper Test Track No. 3 was generated after ~330 cycles, at only a 15 g load.

EDX analog spectra of the new and used flats did not reveal anything out of the ordinary. For example, EDX of the scarred and unrubbed portions of the used $CdCl_2$/HOPG flat after Test No. 3 (Figure 156) agreed with that of the material transferred to the pin. Equivalent EDX of the new and used $NiCl_2$/HOPG (see Figures 157 and 158) indicated that the molds were contaminated with $CrCl_3$. It is not known whether contamination originated from an inadvertently blended starting powder, or from contamination during pressing.

The SEM tribometer results may be summarized as follows:

1. Both the $CdCl_2$/$NiCl_2$-intercalated HOPG retain low shear strength properties in air and in vacuum, even after heating to ~700°C. These materials may comprise a new class of solid lubricants for space applications. They may also be equally useful for service in low humidity air.
2. The $CdCl_2$/HOPG is a lower shear strength, higher wear rate lubricant than the $NiCl_2$/HOPG.
3. The low shear strength properties of these materials are retained despite:
   (a) mass sublimation of $CdCl_2$ out of the triboflat at elevated temperatures; and
   (b) possible decomposition of $NiCl_2$ at elevated temperatures.
4. The strength of molded bodies prepared by warm isostatic pressing of the intercalated graphite powders is not considered high enough to fabricate monolithic bearing parts from them. These powders may, however, be utilized as lubricant pigment additives blended into suitable matrices to form self-lubricating composites. Such composite parts should be operated in low-moisture environments. At high humidities, the intercalated chloride salts decompose even at moderate temperatures and tend to become corrosive.

3.2.3 CVD-deposited h-BN

Similar to the elevated temperature environmental SEM examination of a flake of natural molybdenite described in 3.2.1.1, a small CVD h-BN flake was delaminated from the broken disc-mold in Figure 98 (also see Figure 97), and examined in the Knudsen-cell apparatus (Figure 13), using the same 650°C/850°C/0.1 torr test protocol described previously in 3.2.1.1.

The videolog and the SEM photomicrographs in Figures 159 and 160 do not show any visible signs of thermooxidative degradation after exposure in the high temperature Knudsen cell. The findings are in line with previous results presented on the oxidation-resistant nature of h-BN. At full atmospheric pressure, and at temperatures near 850°C however, one must be aware of the fluxing nature of any B_2O_3 formed above its softening point of 450°C, when interacting with such triboceramic of interest as surface-oxidized Si_3N_4 (232).

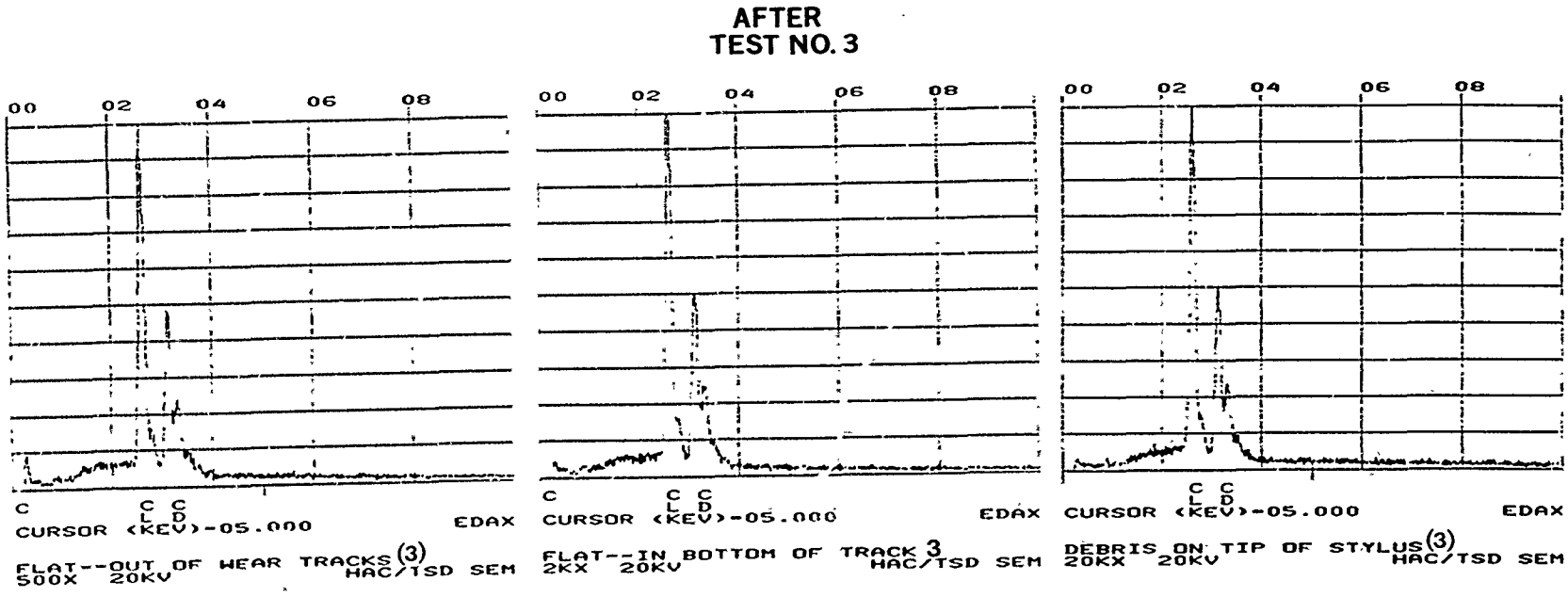

Figure 156. EDX spectra of used $CdCl_2$/HOPG triboflat sites on Test Track No. 3.

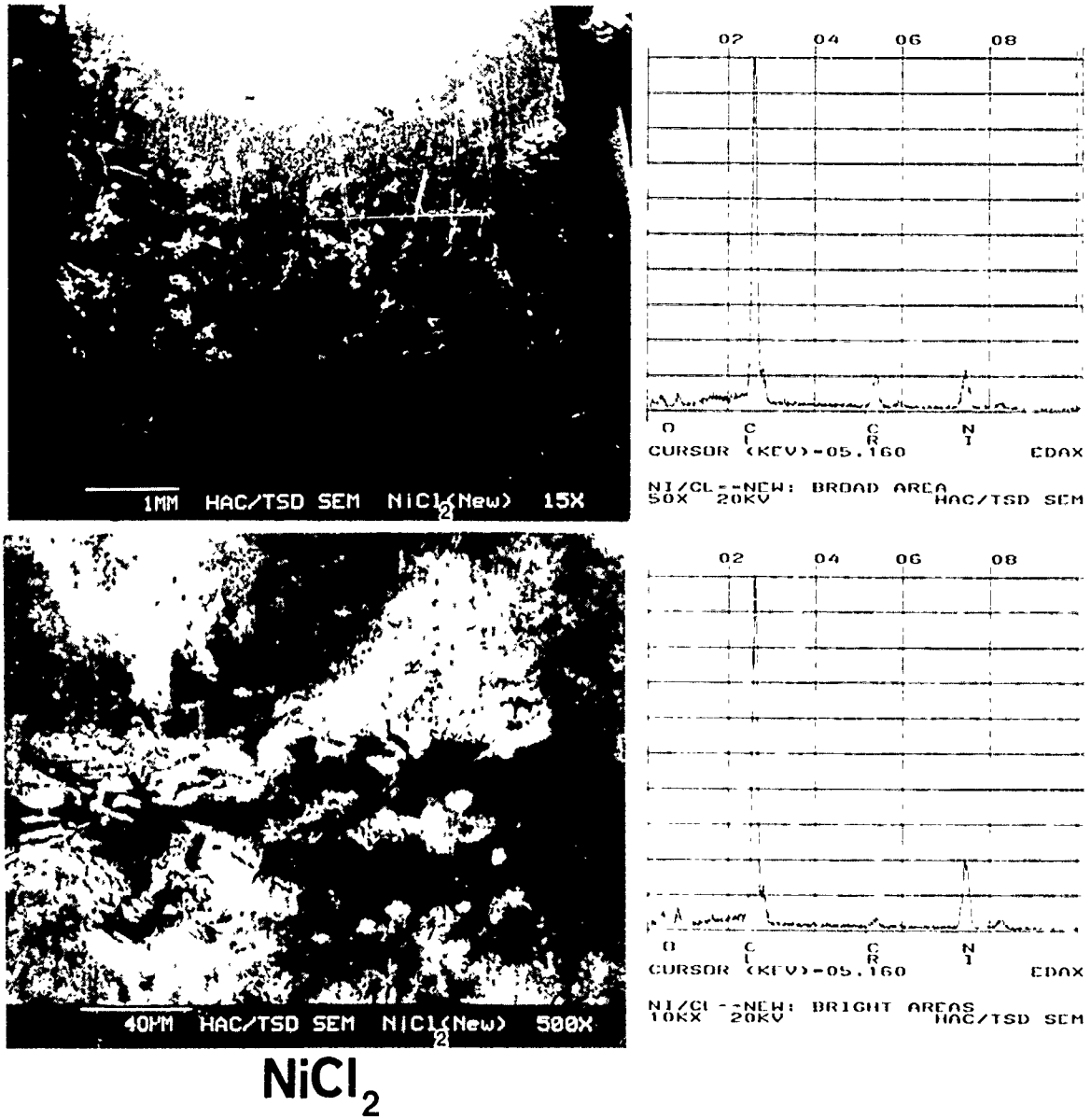

Figure 157. SEM photomicrographs and EDX spectra of new $NiCl_2$/HOPG triboflat showing contamination with $CrCl_3$.

AFTER TEST NO. 3

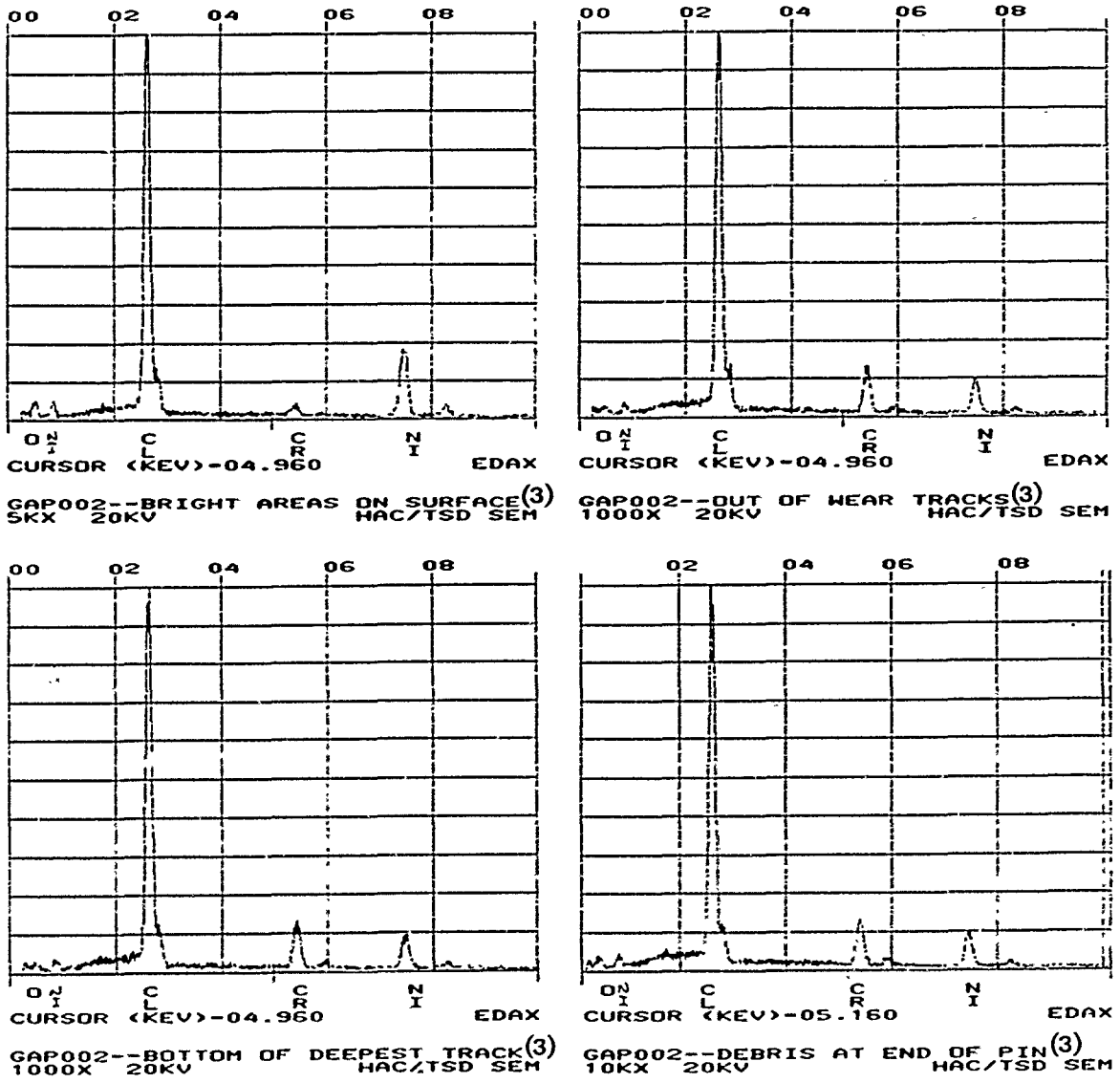

Figure 158. EDX spectra of used $NiCl_2$/HOPG triboflat sites on Test Track No. 3, showing contamination with $CrCl_3$.

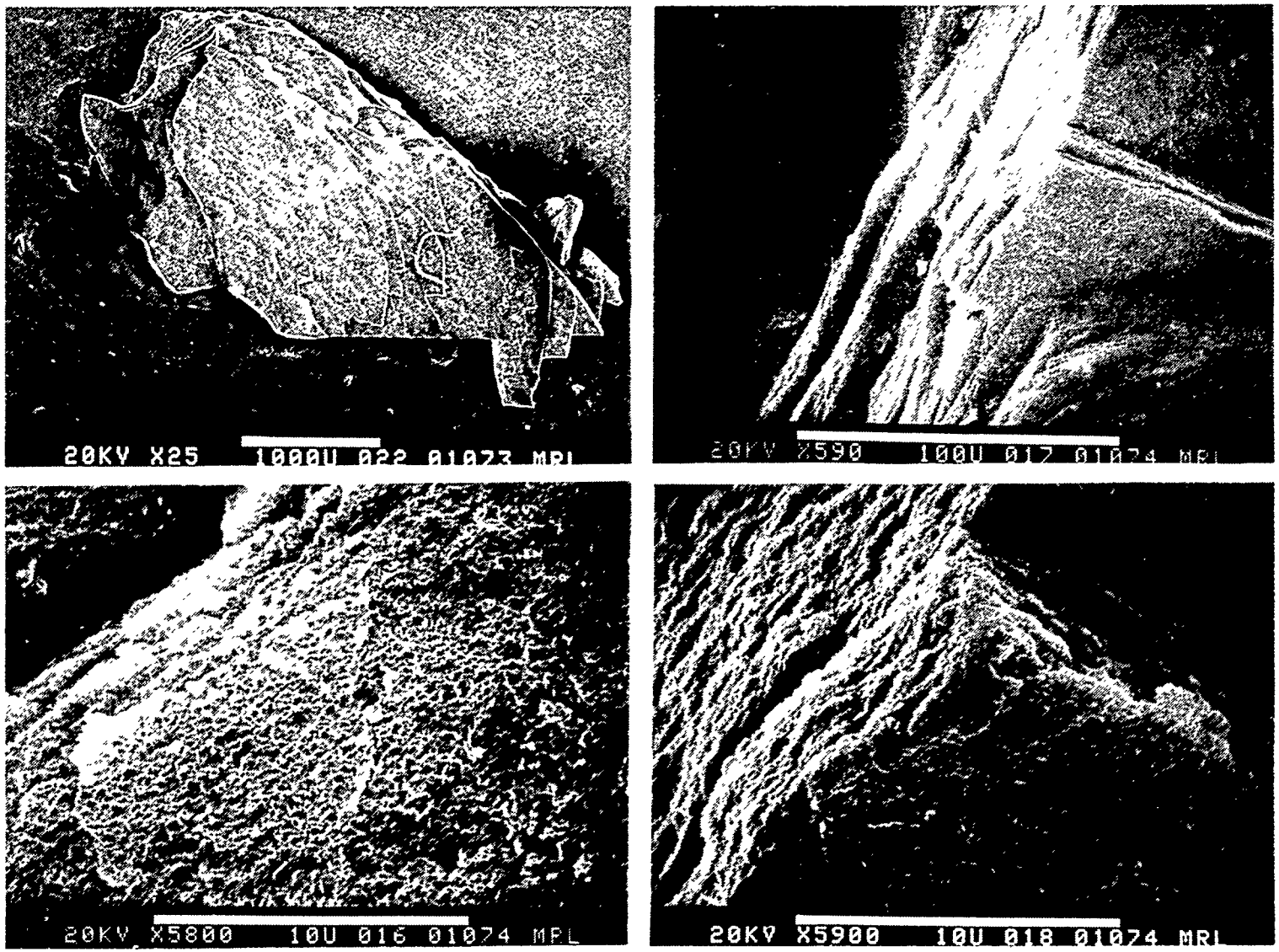

Figure 159 SEM photomicrographs depicting the topography of a small flake of h-BN cleaved from the broken mold shown in Figure 98.

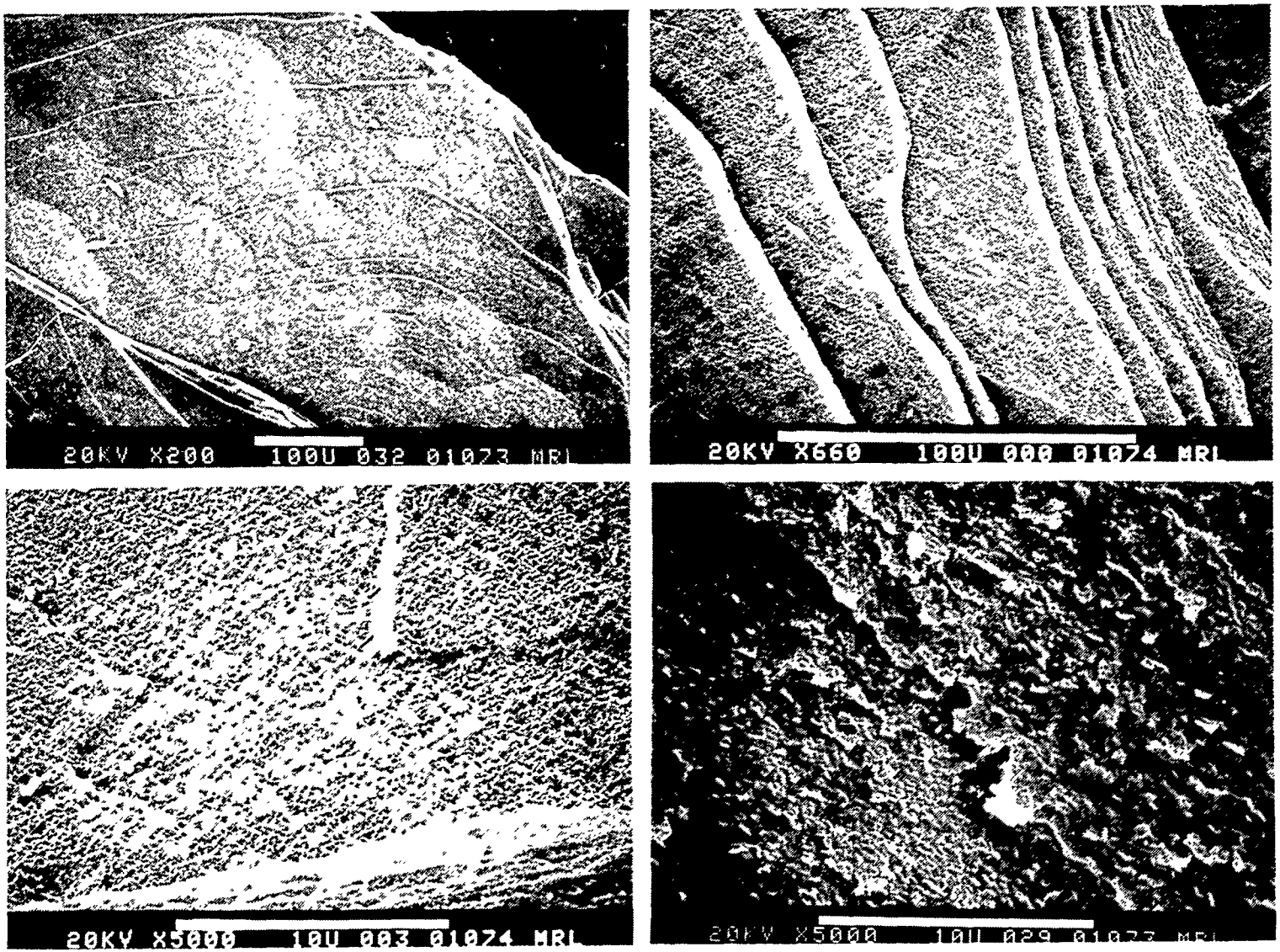

Figure 160. SEM photomicrographs of the flake shown in Figure 159, exposed to 650°/850°C/0.1 torr environments in the MRL Inc. environmental SEM cell previously shown in Figure 13.

In view of our decision not to use the CVD h-BN as a model compound (see previous text), all further work with this material was discontinued. It is noteworthy to see the microscopically rough nature of what was supposed to be the smooth, basal-planar-surface of the h-BN flakes. The electron diffraction data in Figures 100 and 101 showing no preferential alignment of the crystallites should not be surprising.

3.3 RUTILE (TiO_{2-x}) AS A LUBRICIOUS OXIDE

Stable oxides would be ideal (and in certain cases, the only feasible) high temperature lubricants for critical high temperature applications in air (e.g., for Integrated High Performance Turbine Engine Technology (IHPTET) MMA's), except for the highly abrasive (high friction) nature of these oxides. Note that the IHPTET initiative's goal is to double propulsion performance. This will be achieved through innovative designs attaining higher cycle temperatures through the use of advanced materials. Parallel to this initiative, the Advanced Turbine Technology Applications Project (ATTAP) is intended to advance the technological readiness for commercialization of an automotive ceramic gas turbine engine, the feasibility of which was established and demonstrated during the recently-concluded Automotive Gas Turbine (AGT) Project. Superimposed is an urgent need for cryogenic tribomaterials capable of operation in the liquid oxygen (LOX) turbopumps of the Space Shuttle and the SDI Advanced Launch System (ALS) rocket engines, during repeated flights, under extremely severe environmental conditions.

The apparently ubiquitous problem of thermooxidatively stable albeit high friction oxides has been overcome by a major breakthrough in the Part I portion of this program. Using the rutile polymorph of titanium dioxide as a model compound, it was demonstrated that the defect plane structures (widely known as the Ti_nO_{2n-1} Magnèli phases composed of a family of crystallographic shear (CS) planes) that form on progressive reduction of rutile (TiO_{2-x}) exhibit distinctly different shear strengths (τ_s). If the CS planes' oxygen stoichiometry is not altered, these phases remain thermally stable at temperatures in excess of 1000°C.

3.3.1 Anion Vacancy Effects on Shear Strength (Single Crystal Rutile)

As discussed in (12, 13 and 14), anything that is done to an oxide's surface can, and often will, change its composition. In almost all cases, the surface becomes oxygen-deficient.

Rutile is equally vulnerable to this ubiquitous phenomenon. It was shown that the mechanical (strength and shear) properties of a TiO_{2-x} rutile single crystal surface and bulk are controlled by the stoichiometry-related changes in Magnèli phases at the respective regions (Figure 161a). The nature of the altered states ultimately depends on the related changes in interatomic bonding between the CS planes, as driven by an increasingly larger number of oxygen vacancies. In a remarkable parallel (13, 233, 234), these changes also manifest themselves in the predictable electronic behavior of the TiO_{2-x} (see Figure 161b). Its bulk and surface conductivities become convenient yardsticks in measuring the magnitude and the location of those metastable, anion-vacancy-generated crystal structures which eventually end up controlling the tribological properties of rutile in extreme environments.

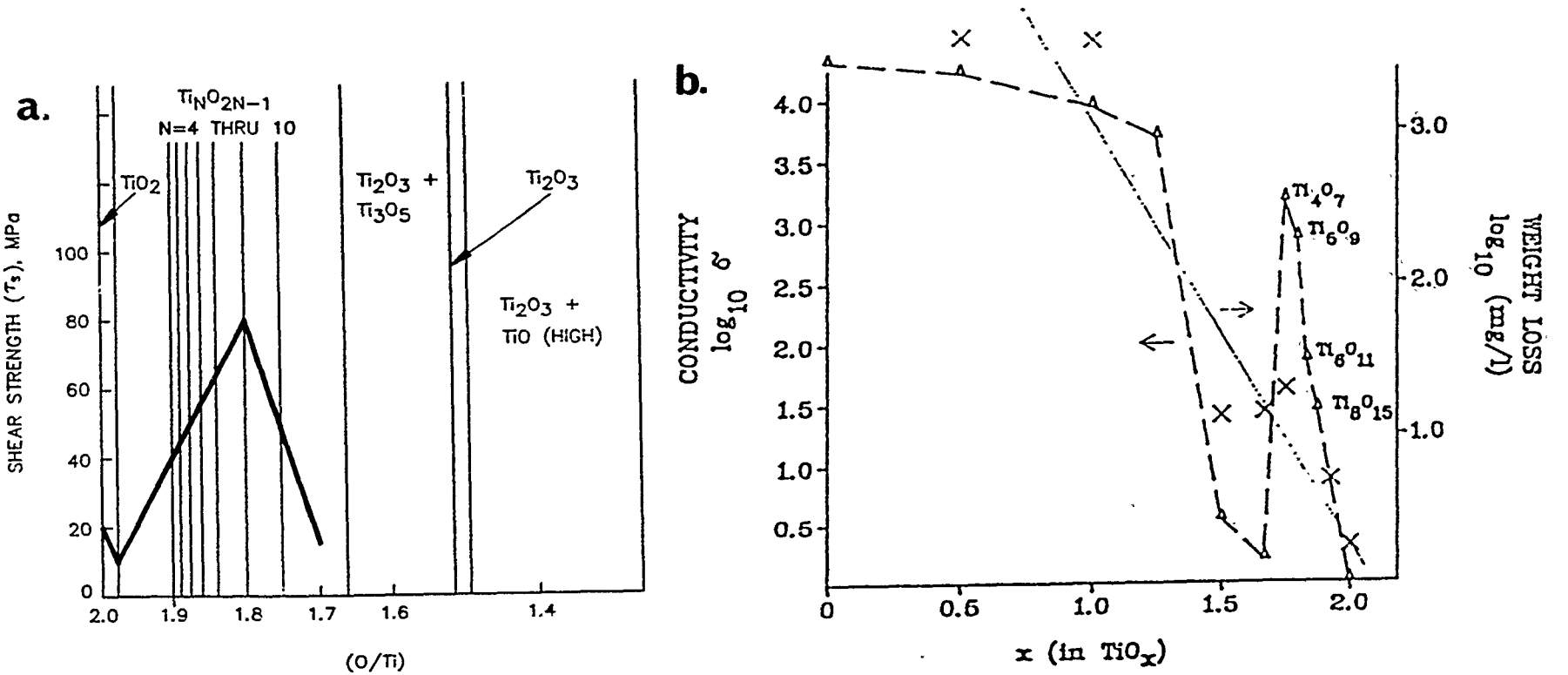

Figure 161. The effects of oxygen vacancies on the shear strength, electrical conductivity and weight loss of rutile (TiO_{2-x}): (a) shear strength (τ_S) of rutile, changing with oxygen stoichiometry and the consequent formation of Magnèli phases (13); and (b) electrical conductivity and weight loss, changing with oxygen stoichiometry and the consequent formation of Magnèli phases (233, 234).

The O/Ti ratio as a function of various surface treatments (e.g., heating in air or in vacuum, argon ion bombardment or reduction by hydrogen, among others) indicates that oxygen is removed preferentially even from the most thermodynamically stable rutile cleavage planes. When oxygen is lost from the surface, two electrons are left in the oxygen vacancy to maintain electrical neutrality. Initially, the electrons may occupy the vacancies formed. As the reduction proceeds, a neighboring Ti^{4+} may change its charge state to Ti^{3+}; the other electron is essentially free. The color changes from the ivory-white (and somewhat semitransparent), stoichiometric rutile to the progressively darker, blue-gray-black coloration of a more anion-deficient sample.

The color change is caused by the absorption of red light by the conduction electrons, signaling a transformation from a large band gap insulator to an n-type semiconductor. Therefore, there will be vacancy point defects even on the most stable (110) plane. These can act as chemisorption sites for a variety of gases. The dissociation of chemisorbed oxygen at these active sites is possible even at low temperatures and the oxygen anneals the surface and bulk defects. The conduction electrons become depleted and the color changes back to an ivory-yellow-white. Beyond the maximum temperature of thermal desorption, oxygen reacts directly from the gas phase to annihilate the anion vacancies at the surface. Diffusion in the direction of electrochemical potential gradient rapidly anneals the vacancies in the subsurface regions also. For example, heating stoichiometric rutile to several hundred degrees centigrade in vacuum or in a reducing atmosphere results in a small number of oxygen vacancies in the bulk (up to about $10^{19}/cm^3$ at around 600°C). These can be annealed out by heating in air or oxygen.

Surface anion vacancies can also be annealed by oxygen migration from the bulk of the crystal. Therefore, at any temperature, at the various oxygen partial pressures above the TiO_{2-x} surface, the surface concentration of oxygen vacancies is determined by two competing processes: absorption and diffusion in reversible directions (the escape or capture of oxygen at the surface, as well as the diffusion of oxygen from the bulk to the surface, or from the surface to the bulk).

The generation of oxygen vacancies on the rutile surface will not necessarily lead to the formation of Magnèli phases. Some of the anion removal processes are not sufficiently energetic to induce the diffusion of the vacancies into the bulk oxide. This diffusion is important, because the self-arrangement of the vacancies into ordered, planar arrays is the dominant mechanism for creating the various CS planes. For example, irradiating rutile with an electron beam will cause removal of the oxygen only from the surface. Bombardment with energetic ions, heating to high temperatures in air, (or, more efficiently, in inert gases or vacuum and most efficiently, in hydrogen), shock loading or tribological action will not only remove oxygen from the surface, but also induce diffusion of the anion vacancies into the subsurface. A combination of these factors must be especially active in transforming the phases to progressively lower oxygen stoichiometries.

If rutile is only very slightly reduced ($TiO_{2.0}$ to $TiO_{1.98}$), some planar faults are created by oxygen vacancy formation. These starting faults were interpreted as fully stoichiometric {011}1/2[011] antiphase boundaries (antiphase boundaries (APBs) are regions containing nearest neighbors of similar atoms rather than dissimilar atoms), across which the oxygen lattice is continuous, but the titanium lattices are in

antiphase (see Figure 162a). Note that by the nature of arranging identical (ions) atoms against themselves, the electrostatic repulsion between them weakens the APB and provides a "defect" plane with reduced shear strength. Further work showed that these APB's can develop into a homologous series of {132}1/2[011] shear planes on removing oxygen from the lattice (Figure 162b and Figure 163). These new slip structures were given the term crystallographic shear (CS) planes, because across them the filled and empty rows of octahedral interstices are relatively displaced ("sheared") towards each other by the displacement vector of 1/2[011]. It was mentioned here previously that the more closely spaced titanium ions at these ABP's and newly formed CS planes experience some inter-ionic repulsion (see the lowest τ_S region at ~$TiO_{1.98}$ in Figure 161a). An infinitely wide lamella would be expected to correspond to an ordered {132} CS structure of $TiO_{1.98}$. As rutile is further reduced to the $TiO_{1.98}$ to $TiO_{1.93}$ region, the {132} CS plane arrays become fully developed. These planes tend to initiate at the surface.

In the intermediate composition range of $TiO_{1.93}$ to $TiO_{1.89}$, the CS planes have an index between (132) and (121) (the "swinging" CS plane region, see Figure 164b). As more oxygen vacancies form, the Ti-Ti distances at the CS planes boundaries are further reduced. During the gradual transition from $TiO_{1.90}$ down to the $TiO_{1.66}$ stoichiometry, the {121} CS planes (again originating from the surface) progressively predominate the system. This gradual change and the resultant foreshortening of the Ti-Ti distances have great significance in terms of increasing lattice strength, because τ_S increases radically as shown in Figure 161a.

The even more foreshortened Ti-Ti distances in the {121} system no longer yield ionic repulsion at the CS plane boundaries. A zone of increased bonding is entered and the strength of a crystal increases, resulting in low wear but very high friction at $TiO_{1.80}$.

Although the bulk conductivity of the various CS planes is an excellent indirect measure of lubricity (note from Figure 161a and 161b that all the low-shear/low friction Magnèli phases are electrical insulators and the high-shear/high-friction phases tend to be good conductors), no theoretical explanation can as yet be given to explain the low τ_S values as the stoichiometry changes from $TiO_{1.80}$ to $TiO_{1.70}$. It is presently believed that this final reduction in shear strength has a great deal to do with the long-range forces that combine in creating an overall effect within a large number of closely-spaced CS planes. It is further hypothesized that the τ_S trough (dip) at $TiO_{1.70}$ occurs because at this stoichiometry there is the onset crystal structure change from the tetragonal TiO_{2-x} to the cubic TiO.

3.3.2 Anion Vacancy Effects on Shear Strength (Polycrystalline Rutile)

All initial data confirming the hypothesis on lubricious rutile were generated on single crystal (XTL), friction and wear test specimens. Since the engineering world is polycrystalline, steps were taken to investigate polycrystalline (poly-XTL) rutile for lubricious behavior in the substoichiometric regimes of interest.

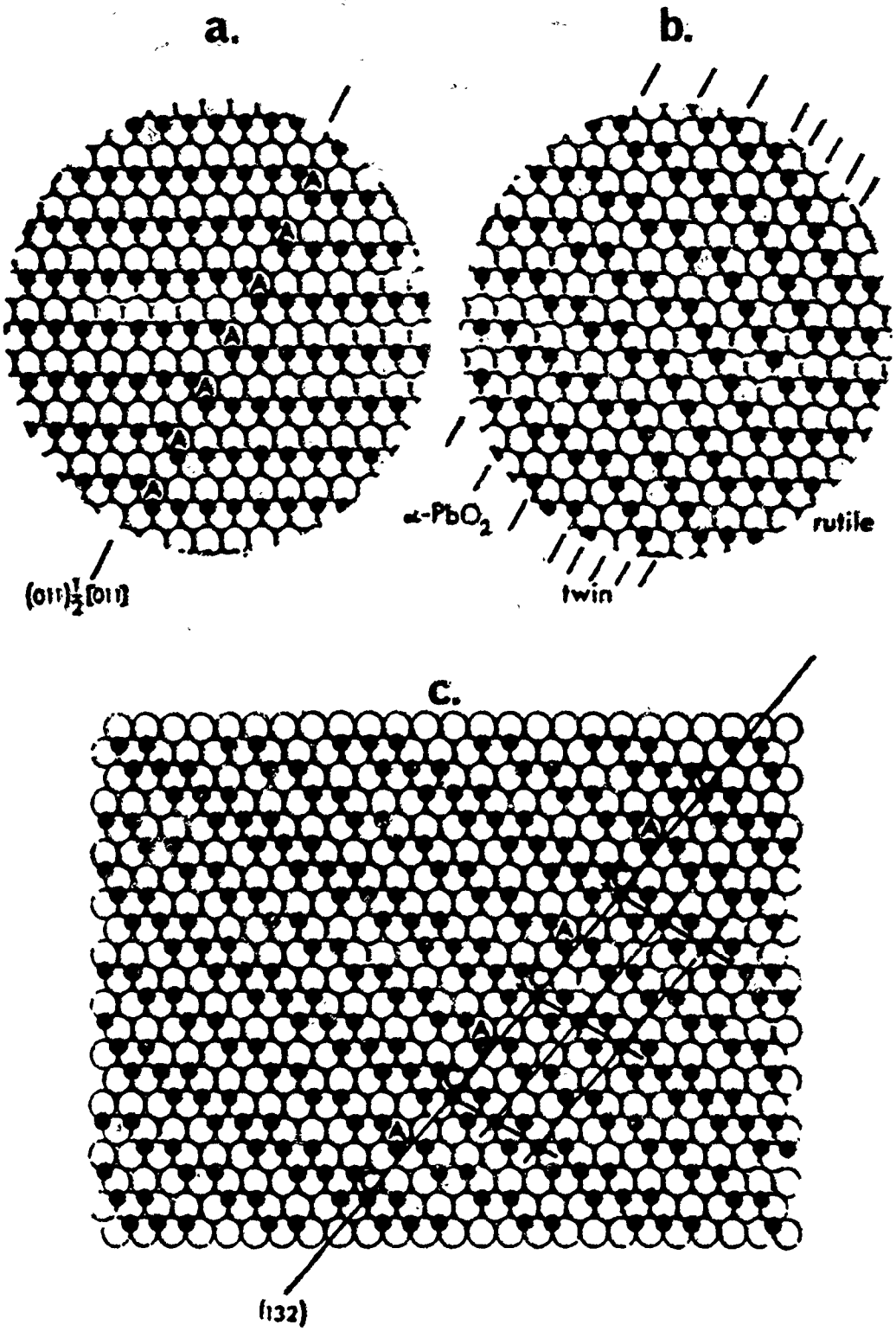

Figure 162. Close-packed billiard-ball model of the (100) plane of rutile: (a) the (011) 1/2[011], stoichiometric antiphase boundary (APB); (b) lamellae of α-PbO_2-type and rutile microtwin produced by repeating the APB operation on every second or every (011) oxygen plane; and (c) a family of Ti_nO_{2n-1} crystallographic shear (CS) planes aka. Magnèli phases (n=5), derived by the operation (132)1/2[011]; from (235).

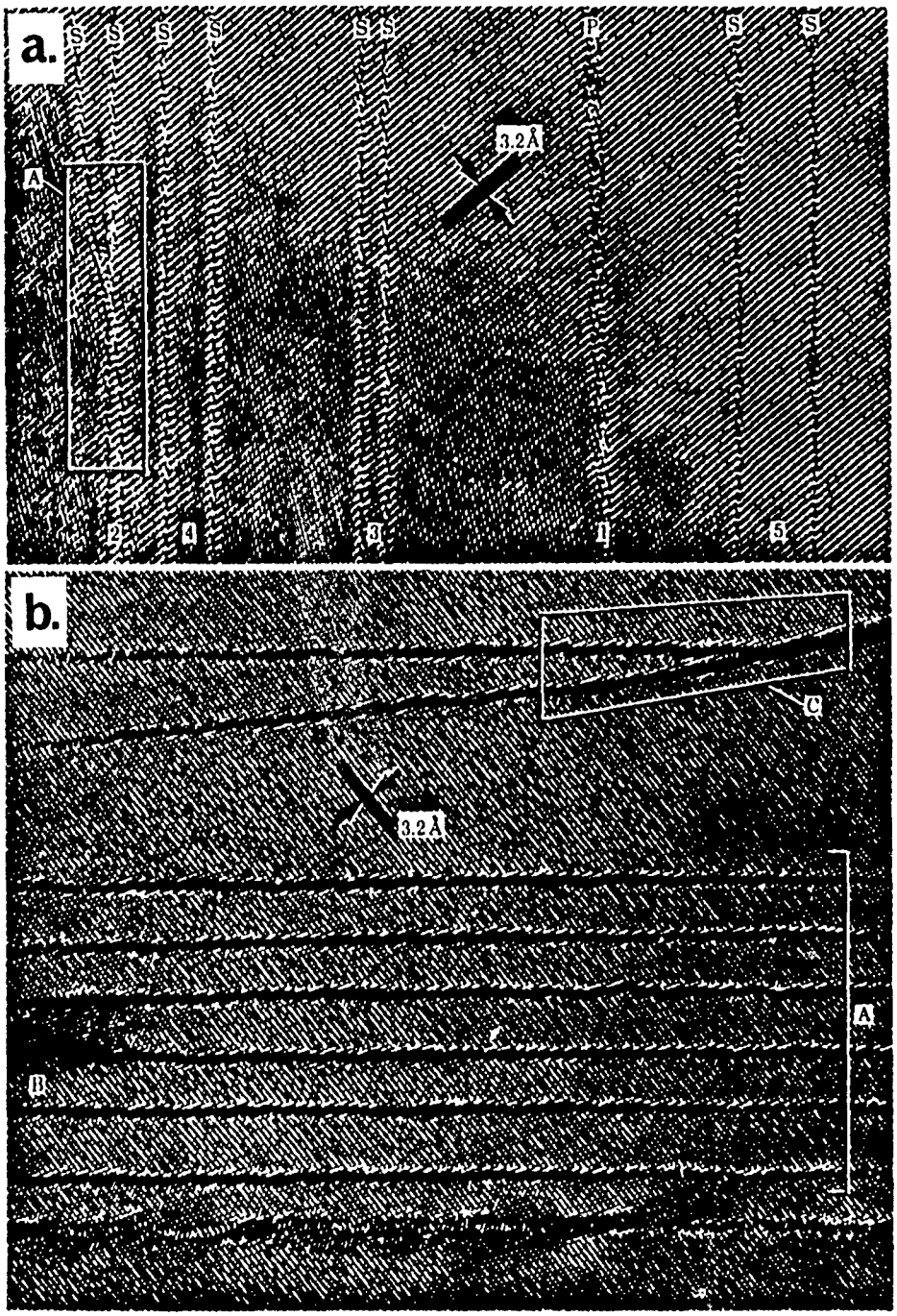

Figure 163. High resolution electron microscopy (HREM) of TiO_{2-x}: (a) a 500 kV [111] HREM image of (132) CS plane in $TiO_{1.9965}$; note single (S) and pairs (P) of CS planes; associated pairs are labeled 1 through 5, in order of increasing separation, and (b) 500 kV image of $TiO_{1.9965}$ showing lamellar (132) CS planes (A); also note hairpin defects (B and C); from (236).

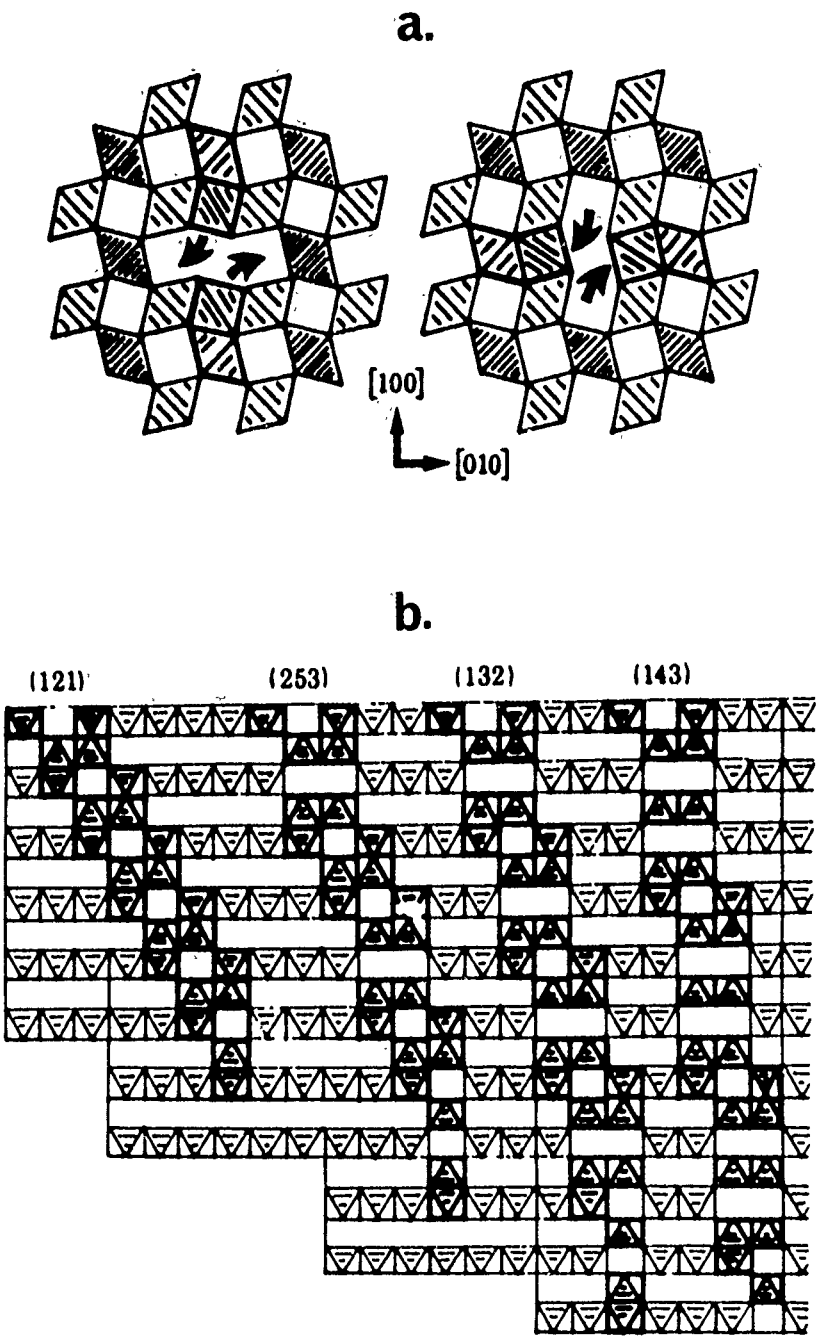

Figure 164. Schematic representations of CS plane structures: (a) interconversion of [100] and (132) [010]-type CS-plane-pair linear defects, and (b) bounded projection along [010] for the rutile structure containing a pair of (121), and pairs of (253), (132) and (143) CS planes; from (236).

3.3.2.1 SEM Tribometry of Polycrystalline Rutile. Since EBONEX, Inc. (Emeryville, CA) commercially prepares and sells substoichiometric rutile as an electrode material [see (233, 234) and Figure 161b], we took advantage of their ability to demonstrate some control over the stoichiometry of oxygen-deficient rutile. We ordered triboflats and tribopins from the following stoichiometries: $TiO_{2.00}$; $TiO_{1.95\text{-}2.00}$; $TiO_{1.90\text{-}1.95}$; $TiO_{1.80\text{-}1.85}$; $TiO_{1.70\text{-}1.75}$. Note that oxygen content control by the weight loss method cannot be made more precise than the stoichiometric ranges reported for these samples. Out of these samples, only the fully stoichiometric ($TiO_{2.00}$) triboflat was subjected to exactly the same SEM tribometry used to examine the (001)[110] rutile XTL in (14). That work basically consisted of sliding the $TiO_{2.00}$ XTL against a nonreactive, α–SiC tribopin interface in vacuum and in 13.3 Pa = 0.1 torr air, at progressively increasing, then decreasing temperatures. The main objective was to (a) vary the environment of the rutile XTL systematically in a way that would alter the oxygen vacancy concentration and CS plane (Magnèli phase) development, and (b) determine τ_s by friction measurements to see if its values also followed the predictions brought forth in Figure 161a. It was previously demonstrated in (14) that XTL rutile sliding against an α–SiC tribopin did exhibit the friction trend predicted in (13), exactly as shown in Figure 165 [taken from (14)]. In fact, the numerical estimation of τ_s presented in Figure 161a originated from (a) converting the f_k values in test No. 3 in Figure 165 into F_k [the adhesive friction force, see (14)] at the f_k minima and maxima and (b) employing the apparent area of contact ($A_{app.}$) estimated from the wear scar as close approximation of the real area of contact (A_r), and using the simple relationship $\tau_s = F_k/(A_{app.} \cong A_r)$. This estimation method and its results for XTL rutile are shown in Figure 166.

The friction (f_k or COF) charts for the three tests on poly-XTL rutile are included in Figure 167. Although the trends are less pronounced than the equivalent tests on XTL rutile in Figure 165, the close similarity between the respective vacuum and P_{air} tests is readily observable.

The detailed test procedure for both XTL and poly-XTL rutile was adequately described in (14). Briefly, the highly polished flats were final finished prior to test by gentle "sandpapering" on a 3 μm diamond polishing film under mild finger pressure, normal to the direction of sliding (3 strokes).

This final preparation step established across-the lay, rough ridges close to 3 μm in maximum height. The ridges were needed for the exact alignment of each wear track under the cell lid orifice, in the path of the electron beam, during the respective P_{air} tests. Sliding on the highly polished surface did not provide a visible wear scar which could be clearly discerned under an optical alignment microscope.

The small flats were oscillated against a 0.1 μm CLA surface finish α–SiC pin under a 0.49 N normal load. With a 3.5 mm wear path length and at a 40 cpm cycling speed, the average oscillatory sliding velocity was 4.66×10^{-3} m•sec^{-1}.

The used rutile flats and the α–SiC pins were examined in the SEM and under an optical microscope. The chart recorded data were reduced by digitizing and logging into files the coefficients of friction (COF or f_k) versus the number of cycles, atmosphere and temperature of a given XTL test, because at first, direct digitizing into a computer was not yet available. The data were then analyzed by data logging and

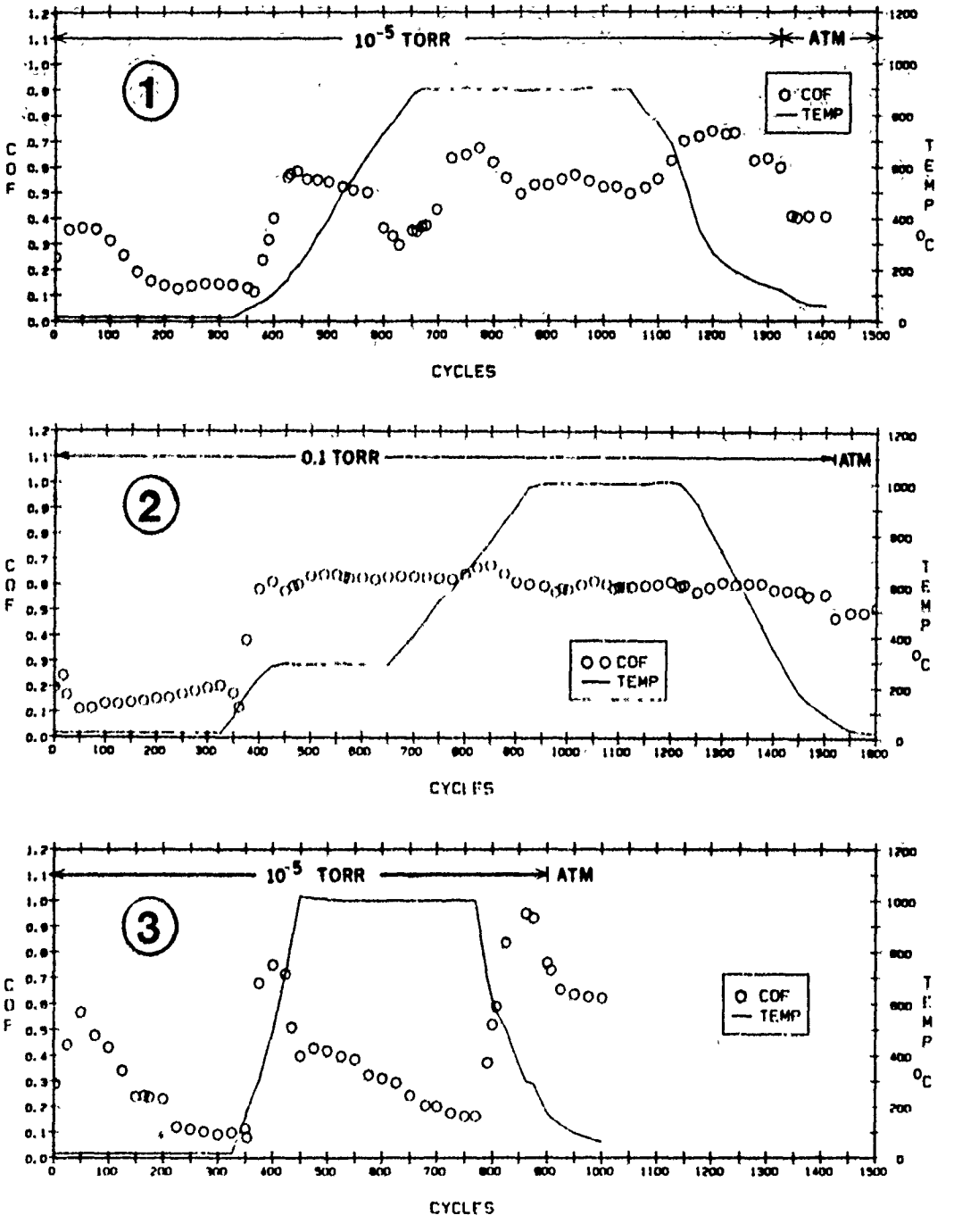

Figure 165. Average coefficients of kinetic friction (COF) of (001) [110] rutile as a function of SEM tribometer test cycles, temperature and atmosphere during the three tests reported in (14).

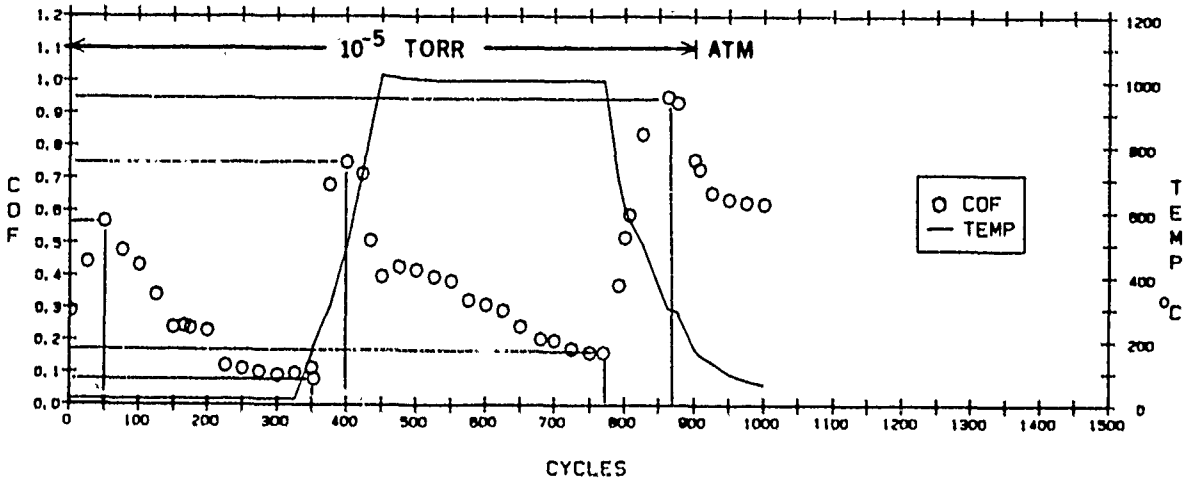

NO. OF CYCLES	f_k	SCAR WIDTH (mm)	F_k' (kg)	A (mm^2)	τ (MPa)	OXYGEN STOICHIOMETRY
2	0.29	$90x10^{-3}$	$15x10^{-3}$	$6x10^{-3}$	25	2.00
350	0.08	$90x10^{-3}$	$4x10^{-3}$	$6x10^{-3}$	7	~1.98
400	0.75	$90x10^{-3}$	$38x10^{-3}$	$6x10^{-3}$	62	1.80
870	0.95	$90x10^{-3}$	$48x10^{-3}$	$6x10^{-3}$	78	1.80
770	0.17	$90x10^{-3}$	$9x10^{-3}$	$6x10^{-3}$	15	1.70

Figure 166. Estimation method for τ_s as a function of single crystal (XTL) rutile stoichiometry, using the F_k values of Test No. 3 in Figure 165 and $A_{app.} \equiv A_r$ as reported in (14), also see Figure 168.

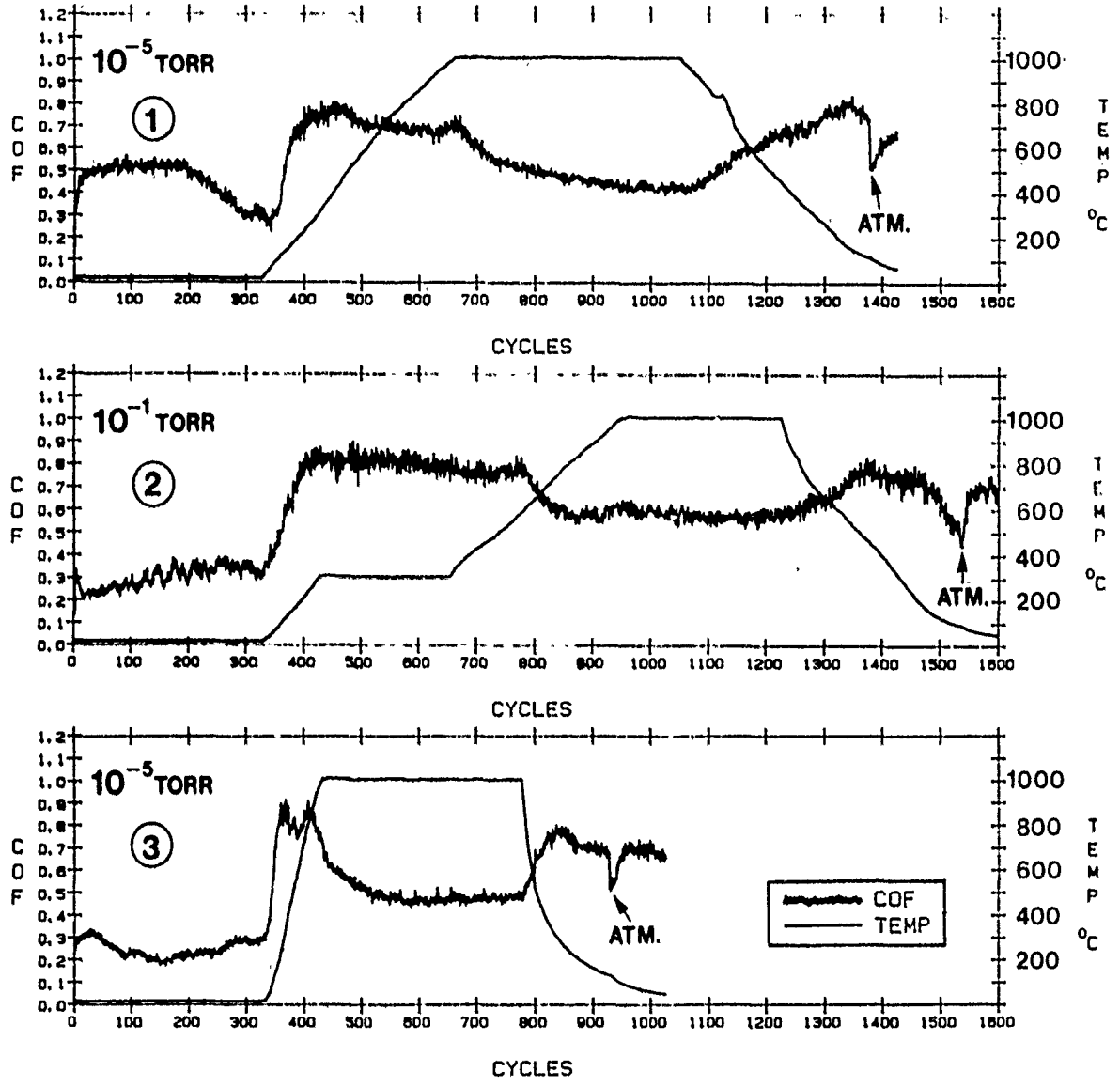

Figure 167. Average coefficients of kinetic friction (COF) of polycrystalline (poly-XTL) rutile as a function of SEM tribometer test cycles, temperature and atmosphere during three test runs identical to the ones described in Figure 165, per the methodology reported in (14).

analysis software running on a high-capacity, desk-top computer connected to a plotter, in the form depicted in Figure 165. In the case of the poly-XTL rutile tested later, the data logging and analysis system was fully integrated with the SEM tribometer for automatic logging and analysis, in real time.

The SEM photomicrographs of the used flats, taken at a medium angle of incidence (see Figure 168), depict the XTL and poly-XTL rutile flats with two major test tracks on each flat. The Test No. 1's were run in vacuum, Test No. 2's in 13.3 Pa = 0.1 torr P_{air} and Test No. 3's in vacuum again. The respective Test No. 3's were completed by continued sliding of the used α–SiC pins in the same tracks generated previously by the Test No. 2's. Note that to the right of the XTL rutile Test No. 1 (Figure 168) there are a few, faintly visible wear scars. There is one on the right of Test No. 1 of the respective, poly-XTL rutile flat also. These scars are representative of preliminary alignment checks routinely done to assure high quality videotape imaging of the pin/flat interface through the cell lid orifice, during the respective P_{air} tests. Precise positioning of the entire scar width within the video-frames was thus achieved. One temperature-ramped test on the XTL flat was aborted due to misalignment.

The wear scars in Figure 168 also indicate that the poly-XTL rutile flat wore significantly more than the XTL equivalent. In view of the larger $A_{app.} \cong A_r$ contact areas with the former, the friction trends in Figure 167 were similar, but not nearly as pronounced as in Figure 165. Nevertheless, the qualitative similarities between Figure 161a, and the shape of the heated-and-rubbed rutile specimens' friction curves are best observed with the respective vacuum tests and maintained only partially in the respective P_{air} tests.

Due to the unique dependence of (a) the friction force on the real area of contact (A_r) and on the changing τ_s of the rutile XTL's and poly-XTL's surfaces as a function of the environment, coupled with (b) the A_r of the sphere-on-plane contact as a function of the normal load (F_n), and (c) the changing yield pressure (P_y) of the XTL substrate as a function of the same environmental factors, the relationship between f_k , τ_s and stoichiometry in Figures 165 and 167 must be clarified.

As previously discussed in (14), the total microscopic friction forces (F_k) arising from the α–SiC pin tip vs. rutile flat contact geometry may be expressed as:

$$F_k = \Sigma F_1 + \Sigma F_2 + \Sigma F_3 + \Sigma F_4$$

where

F_1 = elastic asperity deformation events;
F_2 = plastic asperity deformation events;
F_3 = shearing of adhesive junctions;
F_4 = resistance to ploughing.

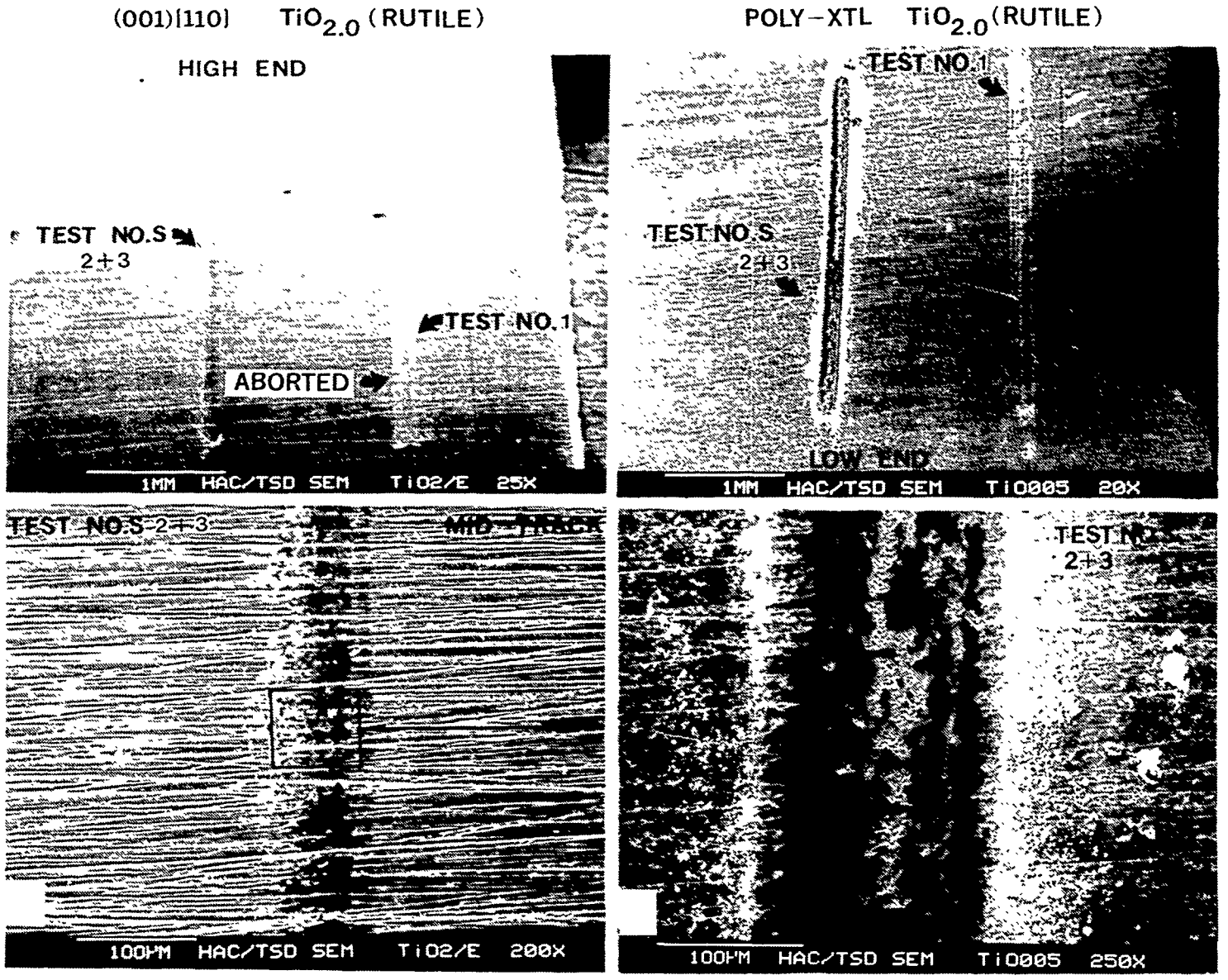

Figure 168. SEM photomicrographs of identically SEM-tribotested portions of the single crystal (XTL) and polycrystalline (poly-XTL) rutile flats, at various magnifications.

Since the calculated Hertzian stresses in an ideally smooth α–SiC sphere/rutile plane contact exceed 1.0 GPa and the actual micro-stresses at the asperity tips should be even higher, the contribution from F_1 is considered small compared to that from F_2. Also, gross ploughing did not occur, because ploughing associated with breaking the asperity peaks is small compared to the sum of the F_2 events.

It is reasonable, therefore, to neglect F_4 and approximate F_k as F'_k which is comprised of the remaining F_2 and F_3. This revised sum now represents the effective adhesive components of the total friction force.

It is known (51) that:

$$F'_k = \tau_s A_r \left(\text{or } \tau_s = \frac{F'_k}{A_r}\right)$$

and

$$A_r = \frac{F_n}{P_y}$$

It follows that:

$$f_k = \frac{F'_k}{F_n} = \frac{\tau_s}{P_y}$$

where all the parameters are as described before.

The last equation is perhaps the most significant relationship for interpreting the friction behavior of a tribological contact. It defines the most desirable combination: a thin, adherent, low shear strength layer on top of a hard and strong, high load-carrying capacity substrate. This yields the smallest real area of contact. Where there is contact, the shear strength must be as low as possible without excessive lubricant film removal.

The calculation of P_y is, however, not possible without complex and exacting measurement of the brittle or ductile nature of a material at a given temperature. Although the assumption that the Magnèli phases begin to form on the surface and do not exceed deep into the bulk during a short SEM tribotest is reasonable, it helps only in establishing a simple, direct proportionality of f_k with τ_s. The $f_k \propto \tau_s$ relationship is good only to reveal a qualitative comparison of the shape of the SEM tribometer friction charts with the shape of the predicted τ_s function in Figure 161a.

Even though the measurement of A_r is equally difficult (74,76), in the present case it offers the only possibility for numerical estimation of τ_s by using $\tau_s = F_k/(A_{app.} \equiv A_r)$ The measurement of $A_{app.} \equiv A_r$ from the high magnification videolog of each SEM tribotest (e.g., Figure 169), after-test SEM photomicrography (Figure 168) and from the consideration of the sphere-on-plane geometry led to reasonable estimates of the pin-on-triboflat contact as quantified in Figures 166 and 170. The actual $A_{app.} \equiv A_r$'s were estimated by the size and distribution of the burnished plateaus of the worn-down asperity tips, i.e., those representing the summed microareas of the real contact. These plateaus always appear differently on SEM photomicrographs, owing to their smooth topography and significant differences in secondary electron emission (i.e., charging). Since F'_k is measured throughout the test and changing wear scar width is also monitored in real time, τ_s can indeed be approximated from the $F'_k/(A_r \equiv A_{app.})$ ratio with some confidence.

The data in Figures 166 and 170, representative of the tests purposely intended to change to the stoichiometry of the rubbed surface layer the most rapidly by employing the fastest heating rate possible, indicate that the τ_s estimates as a function of rutile stoichiometry apply both to XTL and poly-XTL rutile in all stoichiometry ranges, except at ~$TiO_{1.80}$. There, $\tau_{s\ (poly\text{-}XTL)} \cong 40$ MPa while $\tau_{s(XTL)} \cong 80$ MPa. It is hypothesized that this large difference stems from the much higher wear rate of the poly-XTL rutile and certain rutile particle alignment features stemming therefrom:

Clearly, the amount of wear debris generated on poly-XTL rutile is greater (see Figure 168). Actually, it was these debris mounds bordering the poly-XTL wear track that falsely indicated a wider scar width via the videolog (i.e., the video falsely included the debris borders in the total track width, as measured directly off the TV screen in real time; these borders are much clearer in Figure 169). Only by after-test SEM photomicrography (Figure 168) were we able to clarify that the final wear scar was, by fact, narrower. Consequently, the corrected (fully linear) wear scar increase curve in Figure 169 was used for the best (corrected) estimate of $A_{app.} \equiv A_r$ and the τ_s values related to poly-XTL rutile.

It is hypothesized that not all poly-XTL rutile debris was expelled to the sides of the wear track. Some bound to remain burnished into the track, especially in view of the fact that the low-shear, easily-cleaved (132) CS planes should act exactly like the basal (0001) planes in MoS_2 or graphite crystallites (see Figures 114 and 117). These malleable, lamellar debris particles tend to become preferentially aligned within the plane of shear, similar to what happens to the plate-like particles of sputtered MoS_2 films or to similar particles on the worn surfaces of intercalated graphite molds (see Figure 153). The fact that poly-XTL rutile grains can be made to contain Magnèli phases is confirmed by the photomicrograph in Figure 171, showing CS planes emerging on the surface of suitably oriented grains (237). The same phenomenon manifests itself also, but not nearly as much, with the harder and more wear-resistant XTL sample. The desirably weak (132) CS planes developing around the stoichiometry of $TiO_{1.98}$ emerge on the (001) surface of XTL rutile at a step angle, generating a terraced surface. Due to the lack of grain boundary diffusion of oxygen in vacuum (i.e., there is a thinner active debris layer of changing CS planes

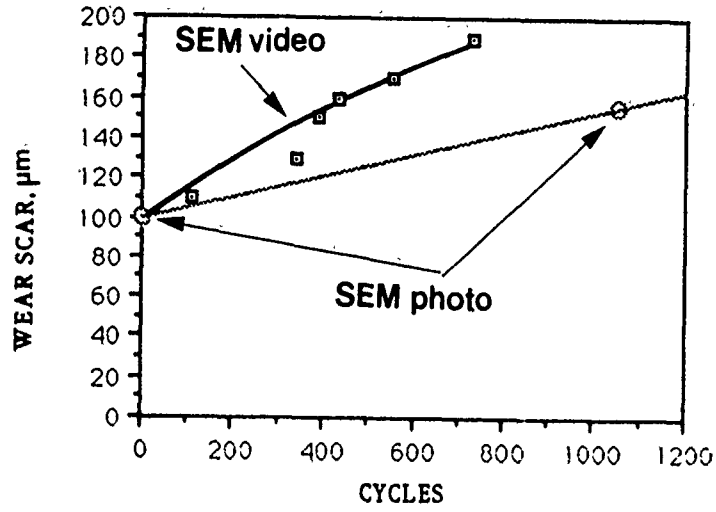

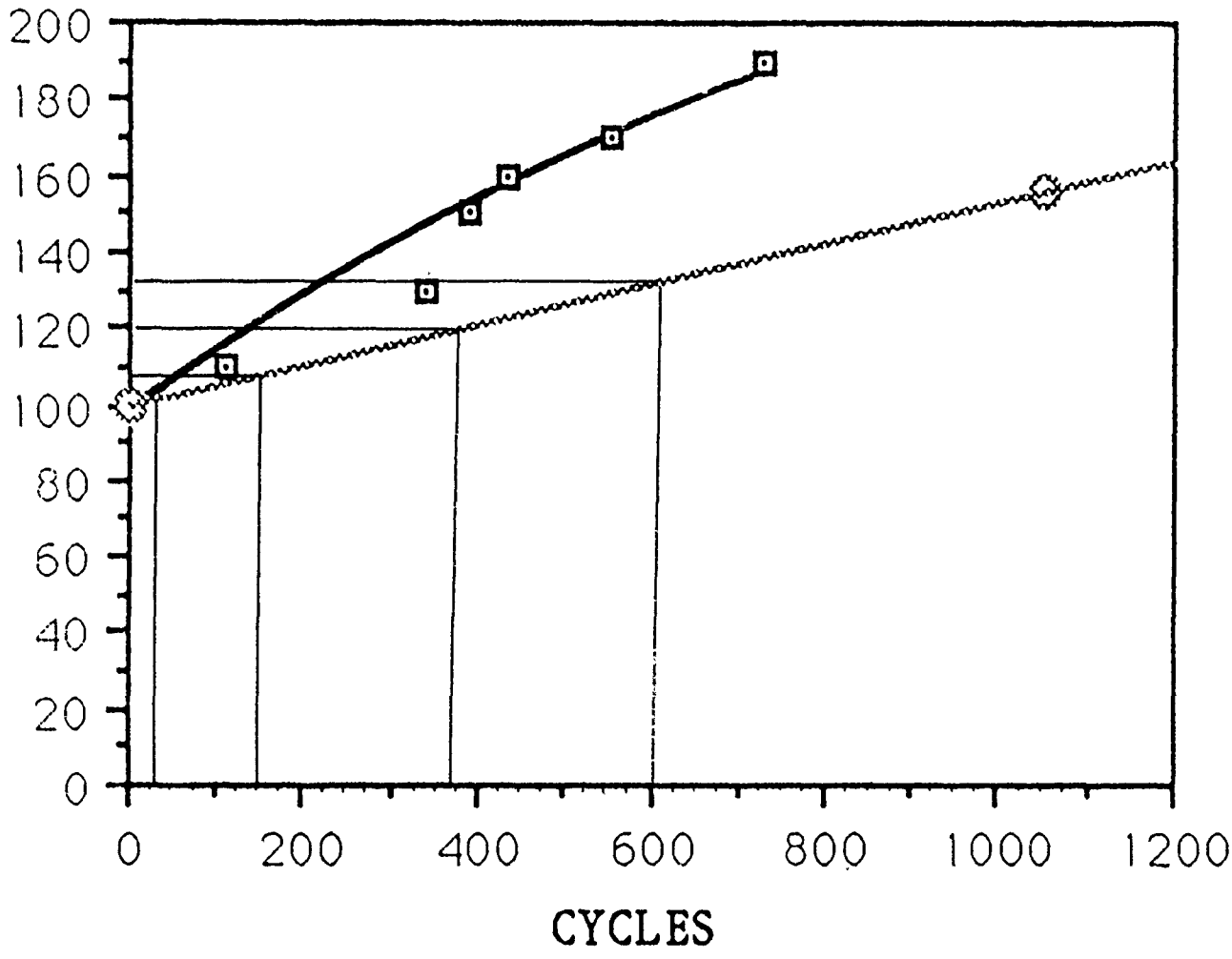

Figure 169. Linear wear scar width increase of the polycrystalline (poly-XTL) rutile flat during Test No. 3 (measured by video), with corrections incorporated by post-test SEM photomicrography, also see Figure 168.

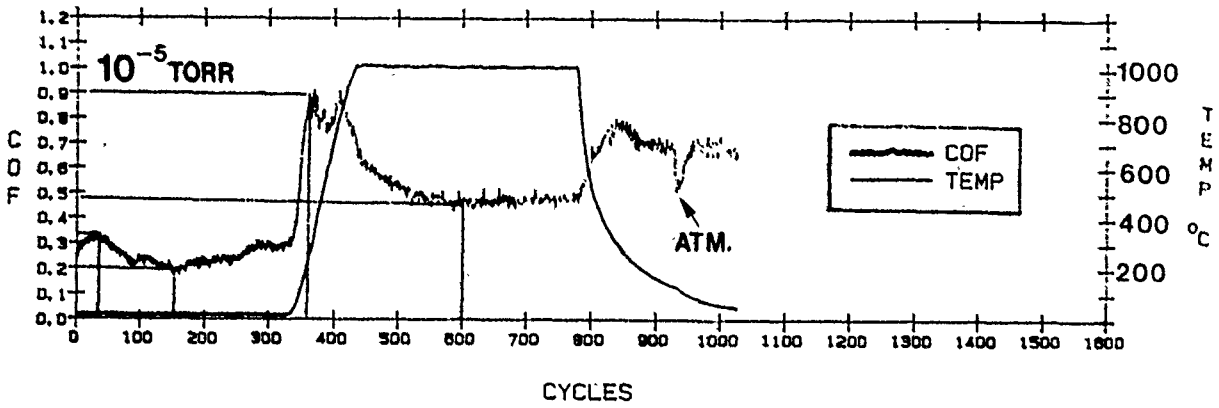

NO. OF CYCLES	f_k	SCAR WIDTH (mm)	F_k' (kg)	A (mm²)	τ (MPa)	OXYGEN STOICHIOMETRY
2	0.25	102×10^{-3}	17×10^{-3}	8×10^{-3}	21	2.00
150	0.20	108×10^{-3}	10×10^{-3}	9×10^{-3}	11	~1.98
370	0.90	120×10^{-3}	45×10^{-3}	11×10^{-3}	40	1.80
600	0.48	132×10^{-3}	24×10^{-3}	14×10^{-3}	17	1.70

Figure 170. Estimation method for τ_s as a function of polycrystalline (poly-XTL) rutile stoichiometry, using the Fk values of Test No. 3 in Figure 167 and the wear scar widths from Figure 169.

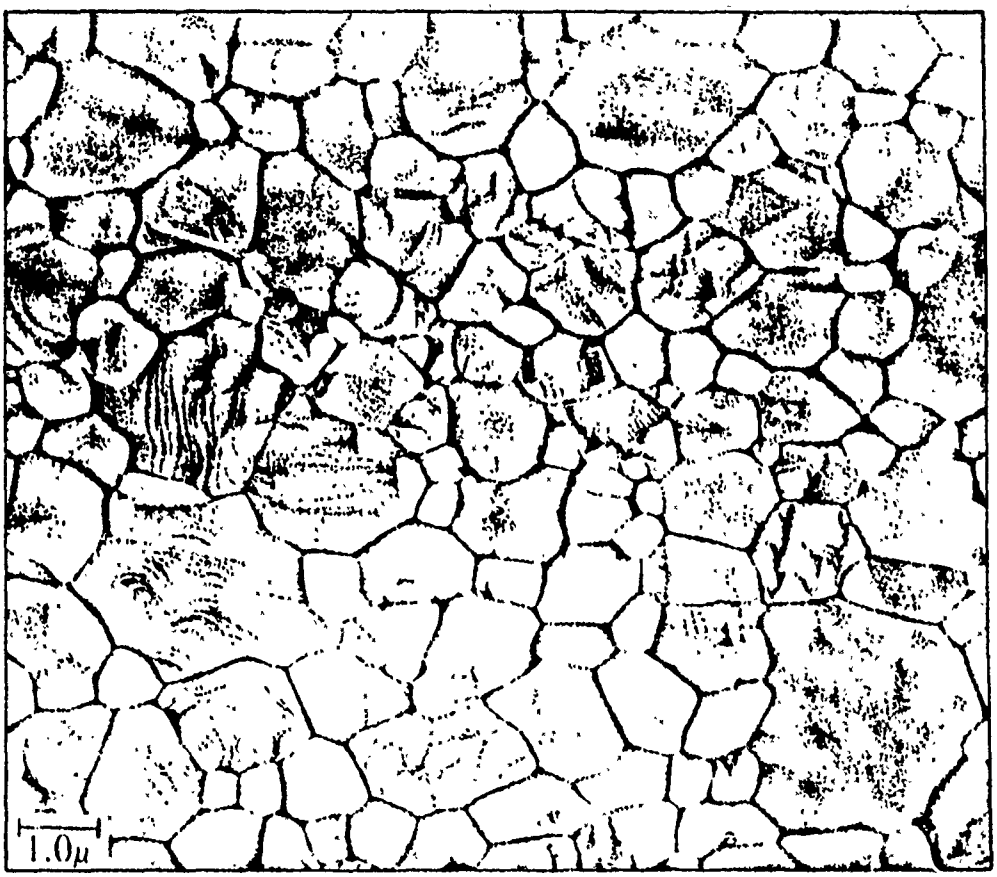

Figure 171. Theoretically dense, centrifugal rutile compact produced after approximately 4 hrs at 1000°C. The grain size is about 1.9 μm or ≥5 times the original particle size; from (237).

on the rubbed surface of XTL rutile), as compared to poly-XTL rutile combined with a much smaller $A_{app.} \equiv A_r$ there, the τ_s changes were more pronounced with the XTL than with the poly-XTL sample. For the same reason, the τ_s of poly-XTL rutile was significantly reduced in the "abrasive" ($TiO_{1.80}$) stoichiometric regime, because of this type of preferential prealignment.

All of the data generated to date indicate that the stoichiometry-controlled lattice energy of these rutile phases influences the surface and bulk shear strength of rutile of any monolithic form. Shear strength (τ_s) values were calculated for the (001)[110] XTL and the essentially isotropic poly-XTL surfaces as a function of oxygen stoichiometry. The τ_s of (001)[110] and the polycrystalline rutile at an estimated stoichiometry of $TiO_{1.98}$ appears to be as low as 8 MPa, equivalent to the τ_s of run-in MoS_2 films in high vacuum. Evidence was also found that beyond the τ_s maxima at $TiO_{1.80}$, τ_s becomes lower once more, as predicted by Figure 161a. The trend is continuing downward to a value as low as 15 to 17 MPa near $TiO_{1.70}$, as measured during the respective Test No. 3's.

3.3.2.2 Tester 2A Experiments With Polycrystalline Rutile. Since EBONEX, Inc., was able to deliver only thin ($\lesssim$ 4 mm) plates of stoichiometric or substoichiometric versions of poly-XTL rutile due to processing limitations, other vendors were surveyed for the availability of poly-XTL rutile in thicker cross-sections. Kyocera and Cercom Inc. were the only firms capable of delivering such materials. Cercom Inc. was subsequently funded to fabricate additional SEM triboflats and tribopins, as well as Tester 2A RCF rods and flat rubshoes from Kyocera T-792 TiO_2 and monolithic TiO_2 hot-pressed from pure titania powder in their own factory.

Small pieces were chipped off the respective molds and subjected to XRD, SEM and EDX to determine their crystal structure, microstructure and elemental purity. Note that the as-hot-pressed Cercom material was dark blue-gray (i.e., oxygen-deficient) and exhibited considerably greater fracture toughness (qualitatively) than its fully fired (at 1000°C), white-yellow version. Judging after its grayish-white-yellow color, the Kyocera material must have also been fully fired.

The X-ray diffractograms in Figure 172 indicate that both materials, in the as-pressed (substoichiometric) or fired (very close to stoichiometric) state have been fully converted to rutile by the high processing temperatures. The Kyocera rutile appears to be denser, exhibiting larger grains with more completely fused grain boundaries and mainly transgranular fractures. The Cercom material's fracture surface revealed a far greater degree of intergranular fracture and a finer grain structure (Figure 173). The fusion of the Kyocera crystallites was probably enhanced by a small amount of Al- and Si-containing sintering aids (most likely Al_2O_3 and SiO_2); the Cercom material was hot-pressed without any additives (Figure 174). Note that the Kyocera material has a reported 1.25×10^7 kg/m^2 (18,000 psi) flexural strength and a Vickers hardness (H_V at a 500 g load) of 850. The strength and hardness of the Cercom material was not characterized, because the machining behavior of both materials indicated that they would both be able to withstand continuum-mechanical tribometry. Nevertheless, only the better-characterized Kyocera material was subjected to Tester 2A experiments. In these tests, pairs of Kyocera

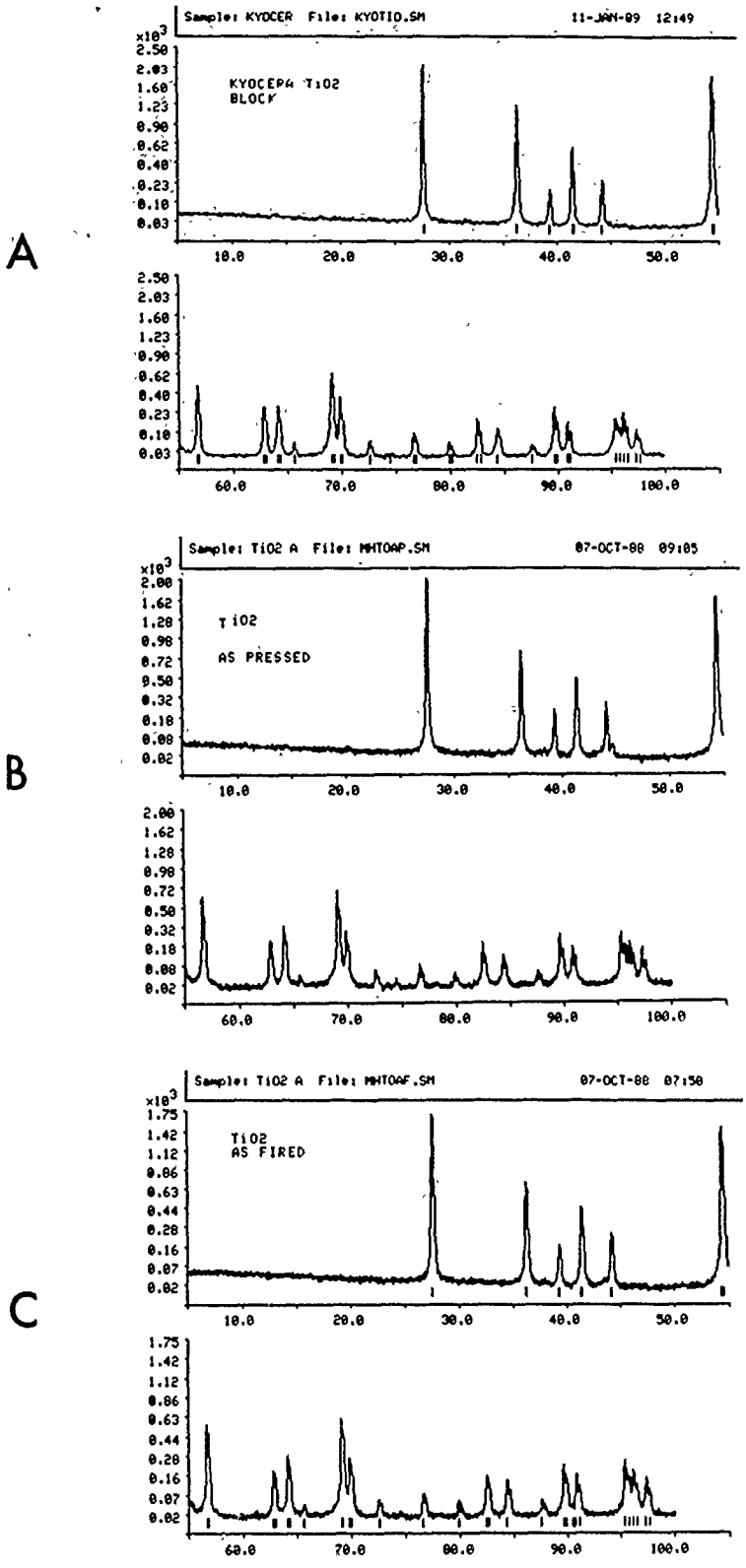

Figure 172. X-ray diffractograms of (a) Kyocera's TiO_2, (fired), (b) Cercom's TiO_2 (as-pressed), and (c) Cercom's TiO_2 (fired), indicating that all three samples consist of rutile.

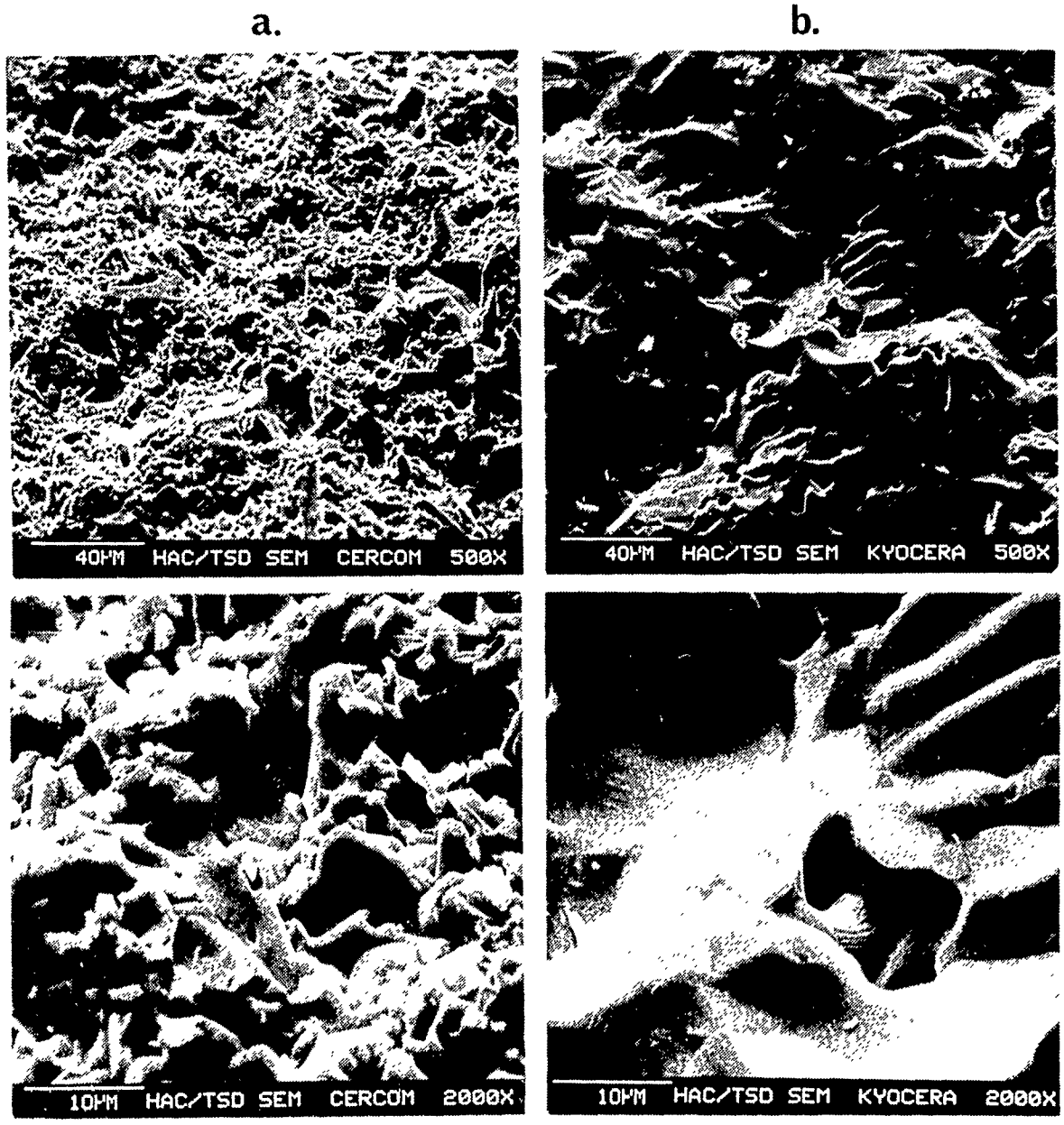

Figure 173. SEM photomicrographs of the fired (a) Cercom rutile and (b) Kyocera rutile fracture surfaces at 200x and 500x magnifications.

a.

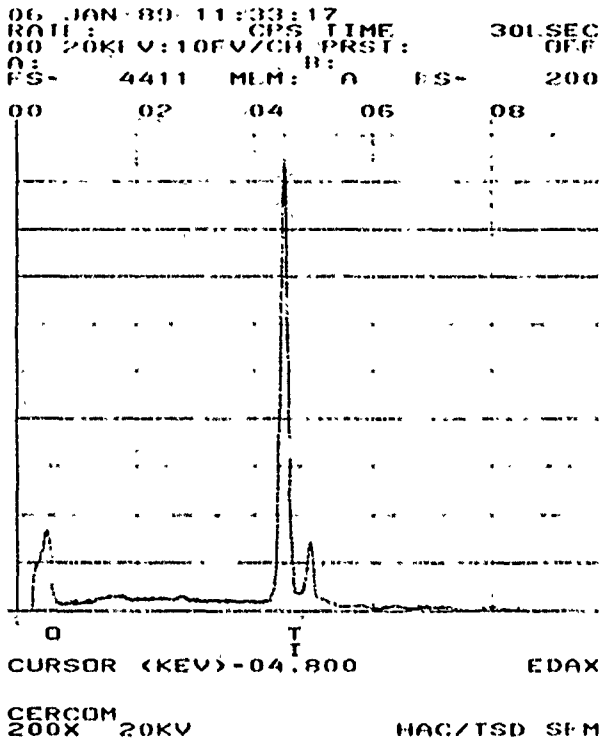

b.

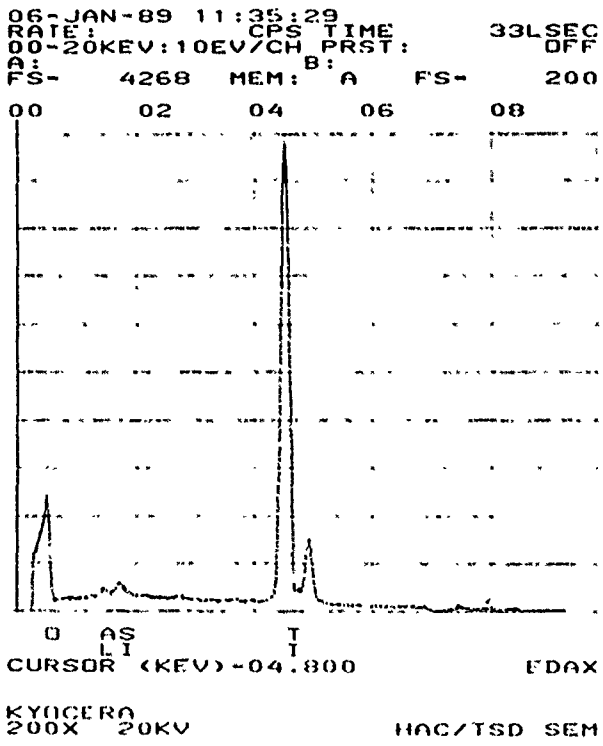

Figure 174. EDX spectra of the fired (a) Cercom rutile and (b) Kyocera rutile, indicating no sintering aid in the former and Al_2O_3/SiO_2 sintering aids in he latter.

rutile rubshoes were sliding against a Hexoloy-SA80T α-SiC RCF rod (Figures 175 through 179), and two Hexoloy-SA80T rubshoes were sliding against a Kyocera rutile RCF rod (Figures 180 and 181).

These tests were performed mainly to:

1. Observe any τ_s changes on heating and/or switching from an air-to-argon atmosphere.
2. Determine rutile/α-SiC wear rate differences as the test specimen (rubshoe/RCF rod) materials were interchanged.

The data on rutile rubshoes vs. α-SiC RCF rod in Figures 175 through 179 indicate the following:

1. The f_k (COF) and the frictional variations ("hash") are higher at lower specimen temperatures and lower at higher specimen temperatures (Figures 175 and 177). On heating, the COF does tend toward a minimum, in spite of the fact that the $A_{app.}$ is growing, due to increasing wear scars. It appears that some lubricious form of the rutile is being generated at elevated temperatures. Note that at the pyrometer setting of $\varepsilon = 1.0$ the true sliding interface temperature would be ~850°C, on the basis of considering the published combined emissivities of α-SiC ($\varepsilon = 0.86$, see Figure 46) and TiO_2 [$\varepsilon = 0.85$, see (238)].
2. Switching from air to argon to air and back to argon seemed to have no visible influence on COF at high temperatures.
3. The shape of the wear scars in Figures 176 and 178 indicate generally good rubshoe alignment and thus good repeatability of the tests (also see Table 5). The low rutile wear rates measured (5 to 6 x 10^{-14} $m^3/N \cdot m$) at the relatively low Tester 2A loads and sliding speed agree with the wear rate measured by Japanese researchers under higher loads and rolling conditions [~1 x 10^{14} $m^3/N \cdot m$, see (239) and Figure 179]. The low τ_s of ~0.6 to 0.7 MPa may be attributed to (a) the large (at least an order of magnitude) difference between $A_{app.}$ and A_r, as indicated by some transferred α-SiC at the real areas of contact in Figure 176 and the burnished high points in Figure 178, and/or (b) the inherently low shear strength of the glassy SiO_2, which may have formed on the surface of α-SiC (τ_s = 0.5 to 0.7 MPa, see Table 5a and Figure 103).

Where the test specimen materials were reversed (i.e., where α-SiC rubshoes vs. rutile RCF rod were run), the following observations may be made:

1. At the same heater lamp input, the temperature measured on the rutile RCF rod's exit region was only ~500°C, at $\varepsilon = 1$. At $\varepsilon = 0.85$, the estimated sliding surface temperature would still be only around 590°C. This significantly lower (estimated) surface temperature may have stemmed from the higher thermal conductivity of the α-SiC rubshoes (i.e., higher than those of the rutile rubshoes). Note that heat is preferentially partitioned into the rubshoes and thus their thermal conductivity becomes a controlling factor in determining the wear scars' temperature. At these lower scar temperatures, the COF and "hash" from R.T. (i.e., no-heat-added) to H.T. sliding exhibit virtually no change, although some reduction in COF at the higher temperature can be observed (Figure 180).

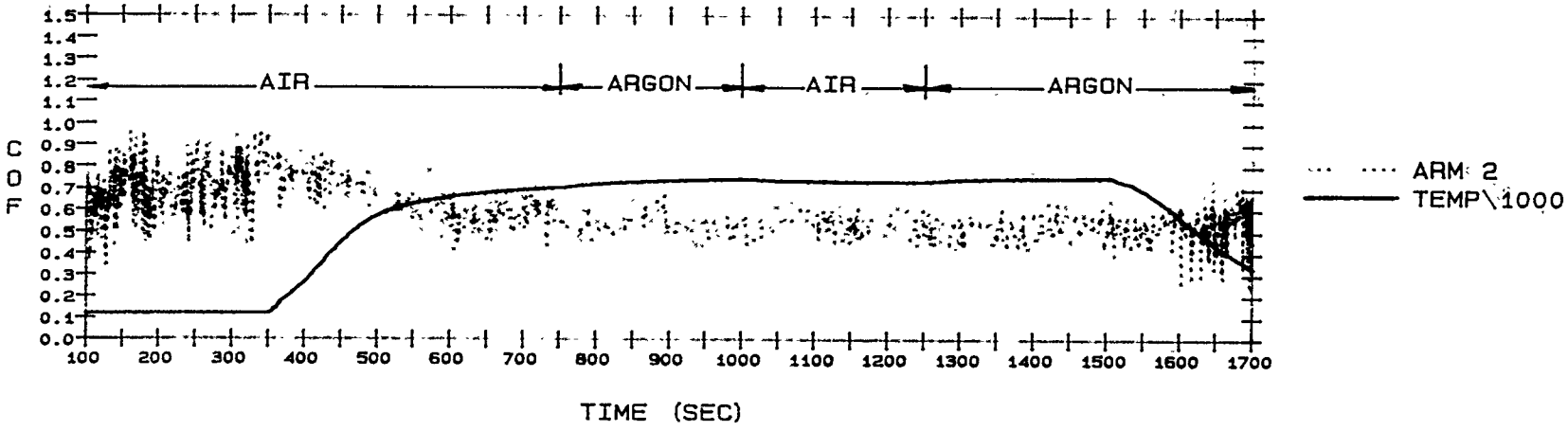

Figure 175. Tester 2A friction traces of a rutile rubshoe tested against an α-SiC RCF rod, under standard load/speed conditions, in various atmospheres (Test No. RUTF-1/2, Rubshoe No. 2), also see Figure 176.

ARM NO. 1

ARM NO. 2

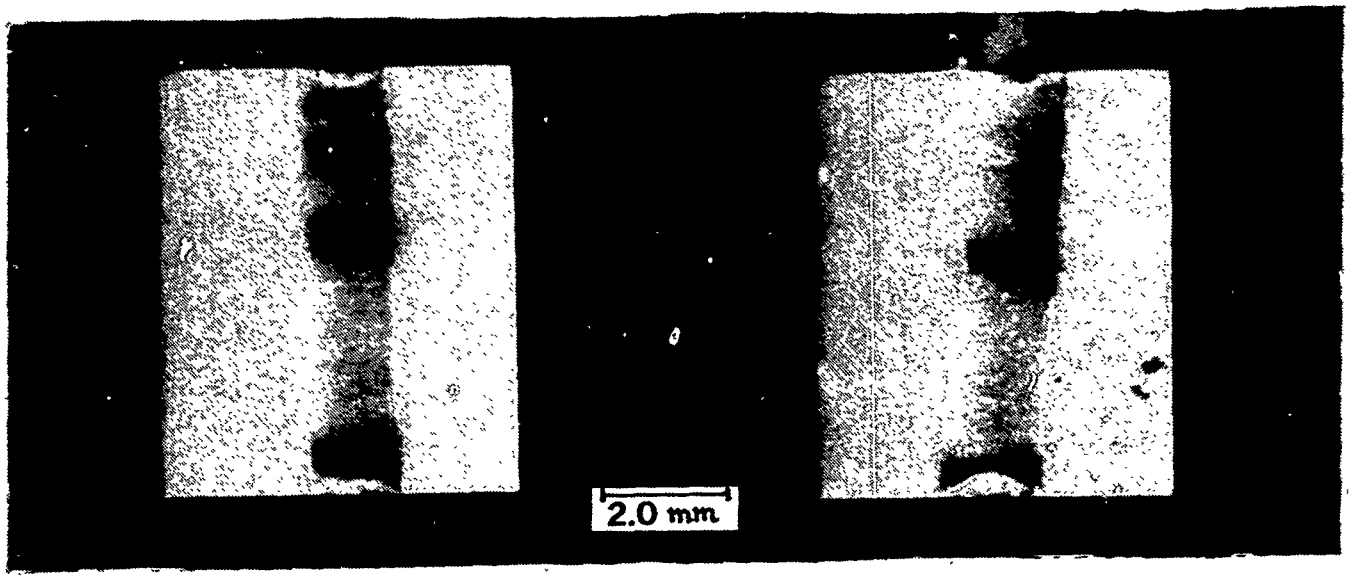

$A_{apparent}$ = 1.4 mm x 7.5 mm

NO FRICTION DATA AVAILABLE
(ELECTRONIC MALFUNCTION)

$\dot{V} = 4.87 \times 10^{-14}$ m^3/ N. m

$A_{apparent}$ = 1.3 mm x 7.5 mm

$$\tau = \frac{(0.49)(1.36\ kg)}{9.8\ mm^2} = 0.07\ kg/mm^2$$

τ = 0.7 MPa ; $\dot{V} = 6.16 \times 10^{-14}$ m^3/ N. m

RUTF_1, 2 13.3 N (3 lbs), 700 RPM
SOHIO HEXOLOY SA SiC ROD/KYOCERA FLAT
AIR/ARGON

Figure 176. Appearance of used Tester 2A rutile rubshoes tested against an α-SiC RCF rod, under standard load/speed conditions, in various atmospheres (Test No. RUTF-1/2), also see Figure 175 for the friction traces associated with the Rubshoe No. 2. contact.

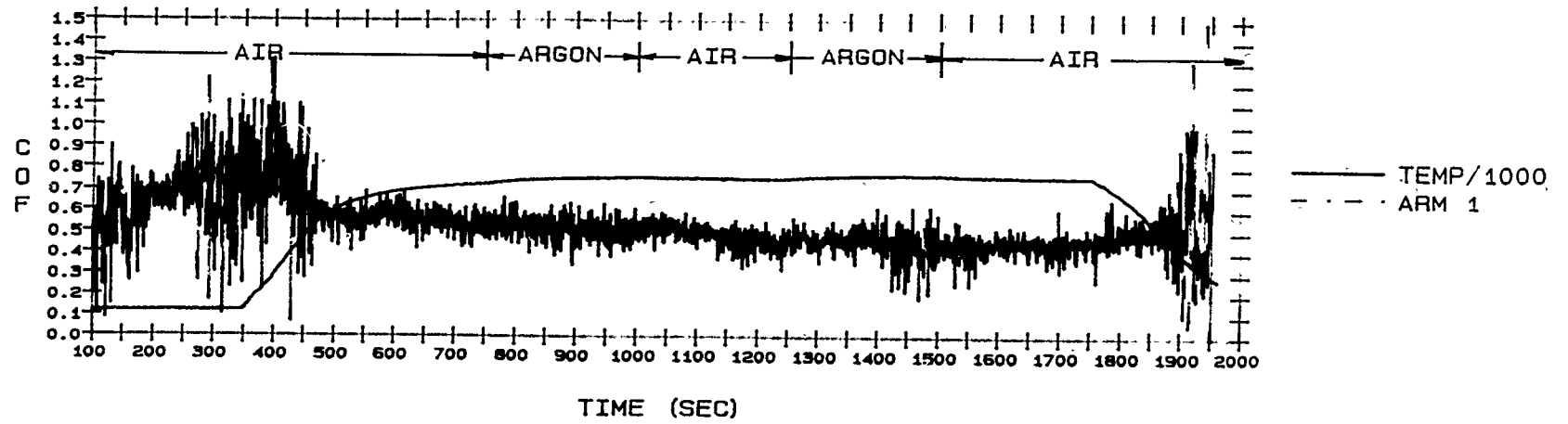

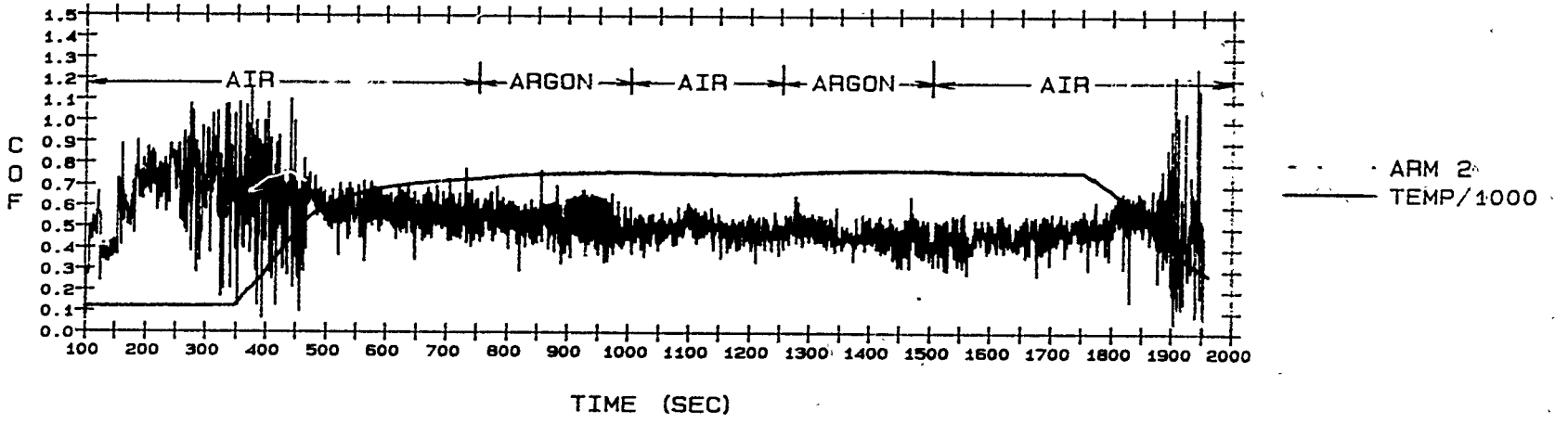

Figure 177. Tester 2A friction traces of rutile rubshoes tested against an α-SiC RCF rod, under standard load/speed conditions, in various atmospheres (Test No. RUTF-3/4, duplicates of Test No. RUTF-1/2, see Figure 175).

ARM NO.1

ARM NO.2

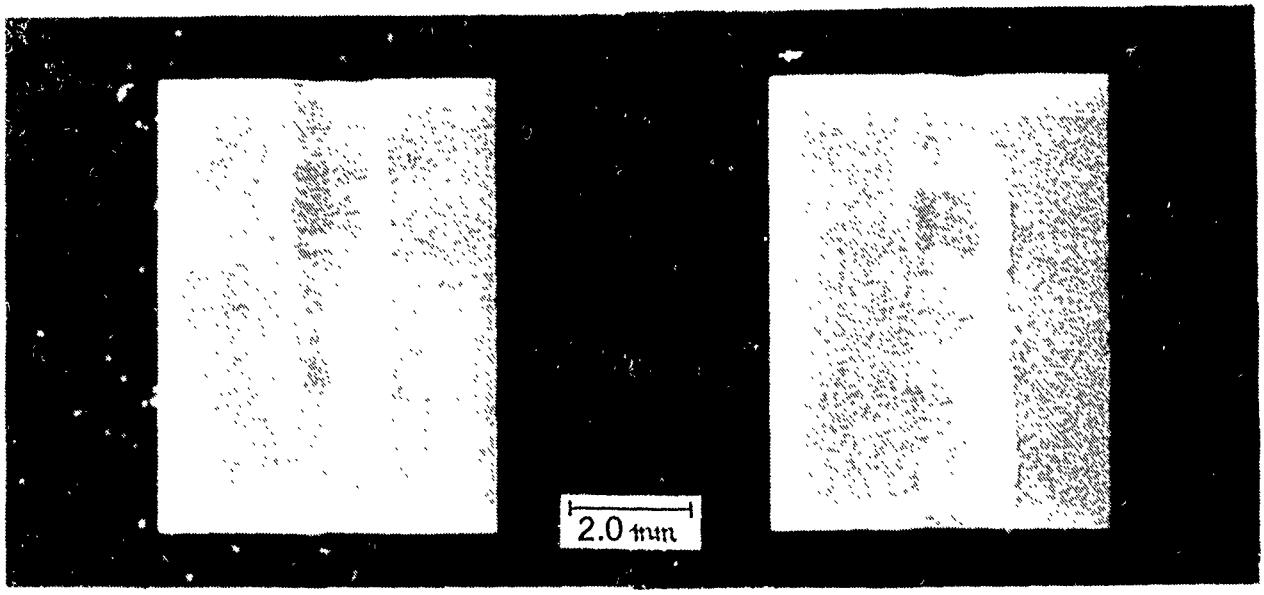

$A_{apparent}$ = 1.5 mm x 7.4 mm

$\tau = \frac{(0.48)(1.36\ kg)}{11.1\ mm^2} = 0.06\ kg/mm^2$

τ = 0.6 MPa ; $\dot{V} = 6 \times 10^{-14}\ m^3/N.m$

$A_{apparent}$ = 1.0 mm x 7.5 mm

$\tau = \frac{(0.48)(1.36\ kg)}{7.5\ mm^2} = 0.09\ kg/mm^2$

τ = 0.9 MPa ; $\dot{V} = 5.57 \times 10^{-14}\ m^3/N.m$

RUTF_3, 4: 13.3 N (3 lbs), 700 rpm
SOHIO HEXOLOY SA SiC ROD/KYOCERA FLAT
AIR/ARGON

Figure 178. Appearance of used Tester 2A rutile rubshoes tested against an α-SiC RCF rod, under standard load/speed conditions, in various atmospheres (Test No. RUTF-3/4, duplicates of Test No. RUTF-1/2, see Figure 176)

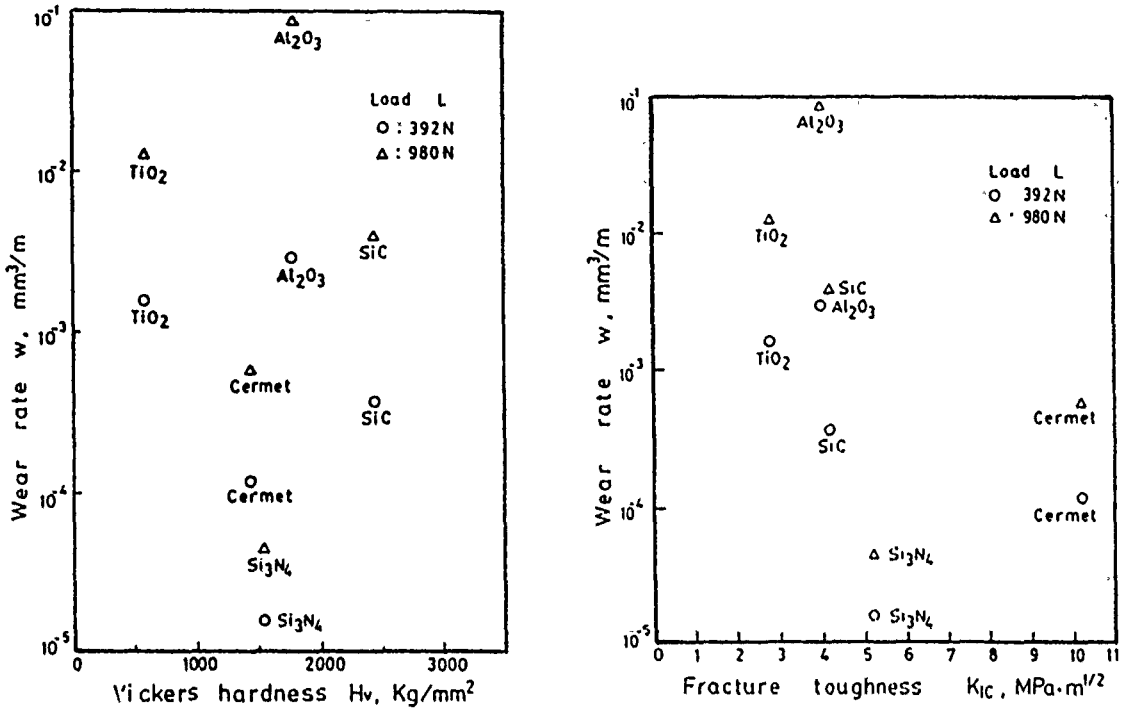

Figure 179. Correlation of volume wear rate of various ceramics (TiO_2 included), as functions of hardness and fracture toughness; from (239).

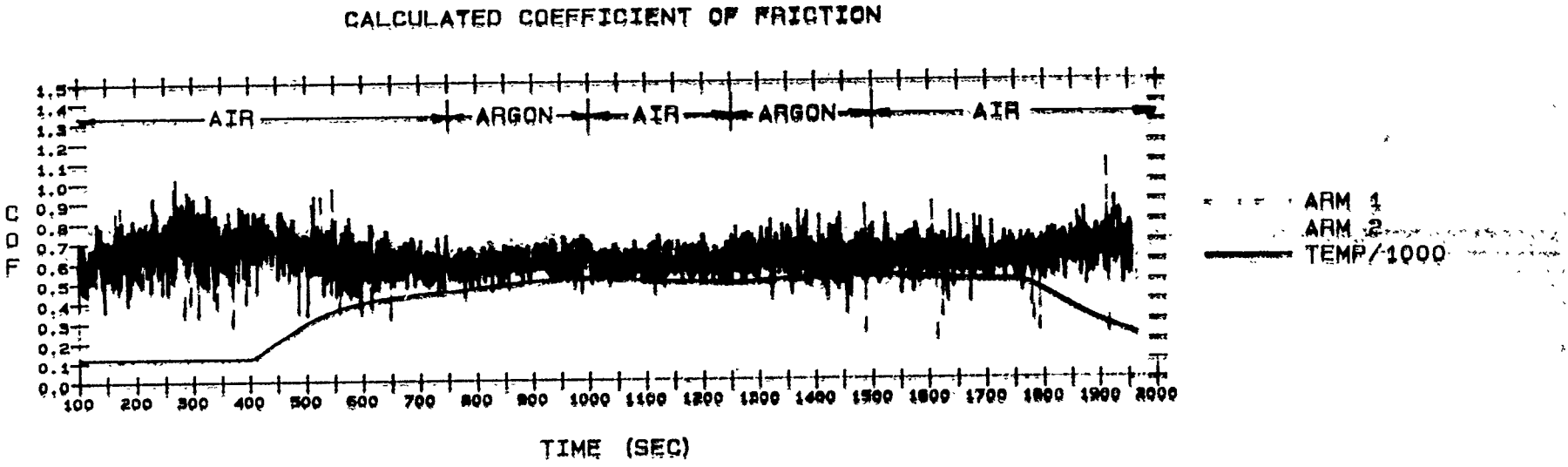

RUTR_1: 13.3 N (3.0 lbs), 700 RPM
KYOCERA RUTILE ROD/HEXOLOY SiC SASC_9, 10 FLATS
AIR/ARGON, HIGH TEMP.

Figure 180. Tester 2A friction traces of Hexoloy-SA80T α-SiC rubshoes tested against a Kyocera rutile RCF rod, under standard load/speed conditions, in various atmospheres, also see Figure 181.

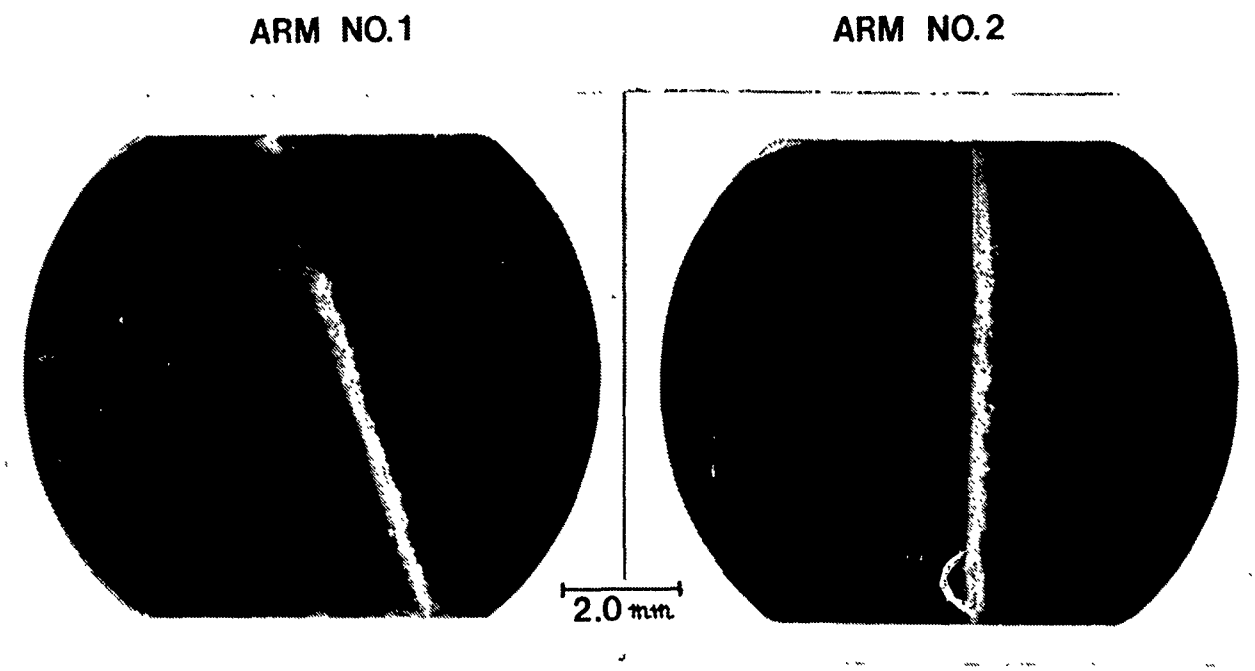

$A_{apparent} = 0.9\ mm \times 6.2\ mm$

$$\tau = \frac{(0.6)(1.36\ kg)}{5.6\ mm^2} = 0.15\ kg/mm^2$$

$\tau = 1.4\ MPa$; $\dot{V} = 1.35 \times 10^{-15}\ m^3/N.m$

$A_{apparent} = 0.5\ mm \times 7.9\ mm$

$$\tau = \frac{(0.6)(1.36\ kg)}{4.0\ mm^2} = 0.20\ kg/mm^2$$

$\tau = 2.0\ MPa$; $\dot{V} = 1.55 \times 10^{-15}\ m^3/N.m$

RUTR_1: 13.3 N (3.0 lbs), 700 RPM
KYOCERA RUTILE ROD/HEXOLOY SiC SASC_9, 10 FLATS
AIR/ARGON, HIGH TEMP.

Figure 181. Appearance of used Tester 2A α-SiC rubshoes tested against a rutile RCF rod, under standard load/speed conditions, in various atmospheres, also see Figure 180.

2. The average wear rate of the α-SiC rubshoes sliding against the rutile RCF rod [~1 x 10^{-15} m^3/N•m at elevated temperatures, (Figure 181)] is much less than that of α-SiC rubshoes sliding against an α-SiC RCF rod under the same conditions (~2 x 10^{-13} m^3/N•m, see Table 5 and Figure 103). The surface shear strength τ_s is, however, two-to-three times higher (1.4 to 2.0 MPa) with the mixed combination than with the all-SiC sliding system (0.5 to 0.7 MPa). Again, the lower α-SiC shoe vs. rutile rod interface temperatures are suspected to be responsible for the non-lubricious behavior of the cooler rutile RCF rod.

3.3.3 Oxidation of Rutile-Forming TiC and TiN Substrates

It was shown in a thorough literature survey and assessment of TiC and TiN oxidation (12) that both hardcoats are quantitatively converted to rutile on their surfaces.

Although the oxidation reaction of the less stable TiC results in thicker oxide layers than on TiN, the most prevalent film morphology and oxide structure on both TiC and TiN are the same as those generated on the much softer Ti and its alloys. In most cases of static oxidation and tribooxidation at high temperatures, the oxide layers grow in extremely thin (1 to 5 μm) sheets, which periodically delaminate from the substrate. These sheets form an array of loosely cohering (under static conditions) or tightly cohering (under triboconditions) scales, similar to the morphology of multilayered pastry dough. The most thermodynamically stable [(110)], natural habit plane of fully stoichiometric rutile crystallites tends to align preferentially in the plane of the peeling flakes, but without any azimuthal order. It was suggested in (12) that rutile may be rendered lubricious (a) by this unique structure, (b) by keeping its shear strength minimal by instrinsic (i.e., environment-independent) control of the number of oxygen vacancies within the oxide layers, and (c) by tailoring the load-carrying substrate used to form the rutile films in-situ. Accordingly, the removal rate of rutile and the friction coefficient provided by the oxide/substrate tribosystem may be further controlled by taking advantage of (a) the high, but still significantly different hardnesses and ideal, mostly (111) habit plane orientation of the TiC and TiN mother matrix underlays, and (b) the differences in the reaction kinetics of layered oxide growth on these highly oriented, hard metal coating matrices being reacted at elevated temperatures, in air.

It was of interest, therefore, to investigate experimentally the possibility of forming lubricious rutile in-situ by tribooxidating TiC and TiN underlays.

3.3.3.1 Rutile on TiC. As the first step towards experimental evaluation of rutile generated on a suitable hardcoat substrate, CSEM (Switzerland) produced and characterized three (3 ea) different types of TiO_{2-x} coatings deposited by CVD related techniques (APPENDIX Z):

- Type I: Water vaporation oxidation of CVD TiC at 850°C to form a thick native (rutile) oxide on the TiC surface;
- Type II: Conventional CVD of TiO_{2-x}, resulting mostly in anatase layers; and

- Type III: Conventional CVD of TiO_{2-x}, with further oxidation of the anatase layer into rutile in isopropanol vapor, at 800°C.

In all cases, the substrate consisted of CVD-TiC-coated AISI 440C stainless steel discs (Lot 4, 5, 6), preceded by some preliminary experiments on bare steel (Lot 1, 2,3), see APPENDIX Z. The schematic of final specimen preparation and the number of samples produced by each preparation type is given in Figure 182.

The coatings were physically and chemically characterized by the following techniques:

- crystal structure, texture and internal stresses (σ) by XRD;
- morphology and microstructure by SEM;
- chemical composition by microprobe;
- microhardness by Vickers indentation;
- coating adhesion by scratch testing;
- thickness by metallographic cross-section; and
- tribological characteristic by pin-on-disc tests performed in both dry and humid air and argon environments, at room temperature (AISI 52100 pin; 5N load; 0.2 $m \cdot s^{-1}$ speed), and in 600°C air.

The details of the various procedures may be found in APPENDIX Z. Essentially, CSEM was successful in producing TiO_{2-x} in the rutile form using the Type I and Type III methods; Type II yielded a mix of rutile and anatase (Table 33). The first two types also yielded oxide layers with compressive stresses ($+\sigma$ values); Type II stresses were tensile ($-\sigma$ value). The Type I oxide exhibited the lowest hardness, but high adhesion. SEM photomicrography of the Revetest® scratch test's critical load site (i.e., where the oxide began to delaminate at a characteristic load) indicated that (a) the failure was both adhesive and cohesive, and (b) the oxide layer exhibited the layered morphology previously described in (12), (see Figure 183).

One interesting observation CSEM researchers made was the presence of Ti_2O_3 XRD peaks and graying of the oxide scale after oxidation. Carbon diffusion from the TiC into the oxide coating and subsequent reduction of the oxide to the substiochiometric Magnèli phases was suspected, as also discussed in (12). The friction and wear data in Table 34 point to the high friction, low wear nature of suboxides close to the $TiO_{1.80}$ stoichiometry. The hard, abrasive nature of those TiO_{2-x} species was indicated by heavy transfer of the iron oxides from the 52100 steel ball to the TiO_{2-x} layers during sliding.

The overall tribological and other results may be summarized, as follows:

1. By selecting the appropriate duration time for static oxidation, all or only part of the TiC coating can be converted to rutile.
2. The rutile topcoat exhibits high (up to 20%) porosity, but it adheres well to the TiC substrate.

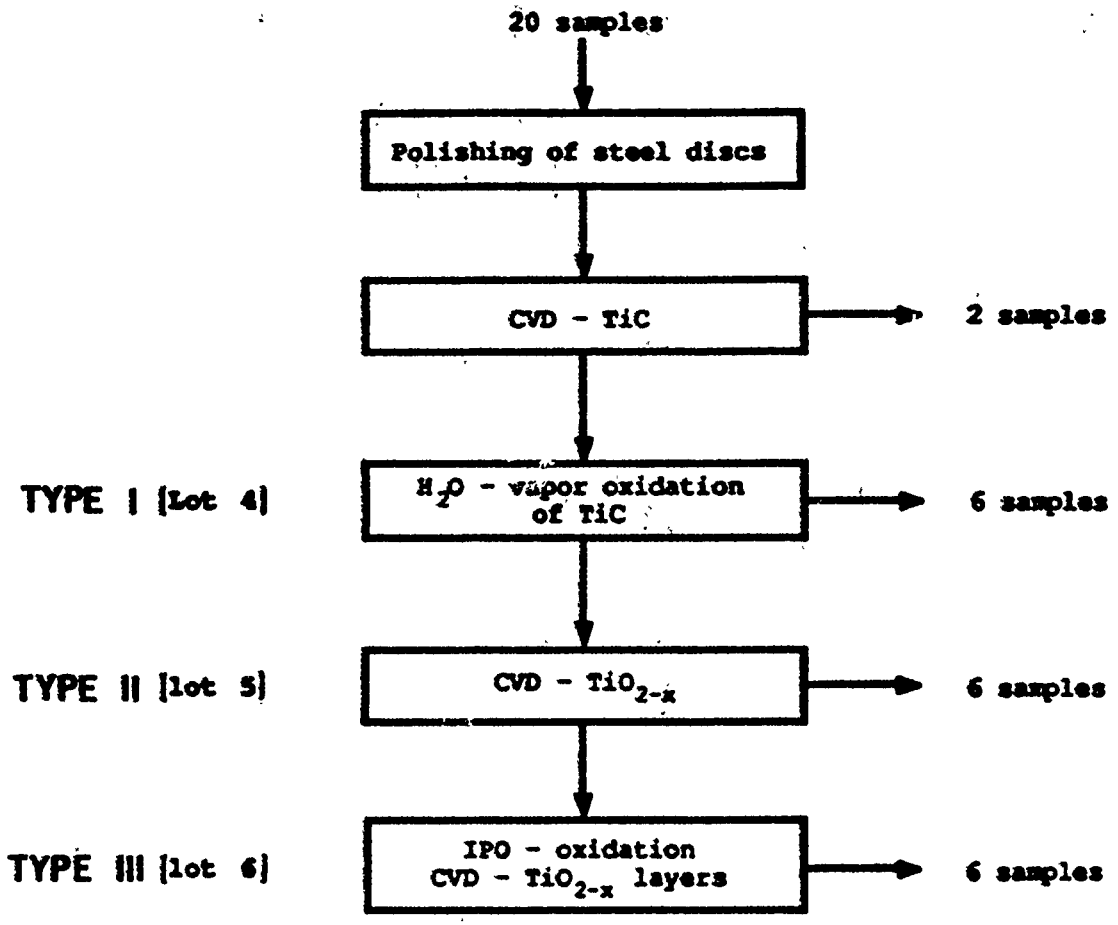

Figure 112. Schematic of rutile film preparation on CVD-TiC-coated AISI 440C steel specimens.

Table 33. Physical-chemical-mechanical characterization of rutile films grown by the processes described in Figure 182; σ = oxide film stress, (-) indicates compressive and (+) tensile stresses; L_C = scratch test critical load, indicating degree of oxide adhesion to TiC; and H_V = Vickers micro-hardness of oxide film under 1 g load.

	Crystal Structure	σ [MPa]	L_C [N]	H_V [MPa]
Lot 4 (Type I)	rutile (002) ±	–916	16	6300
Lot 5 (Type II)	rutile (002) anatase (220)+	+1786	9	7900
Lot 6 (Type III)	rutile + (002+(110)	–2889	16	20150

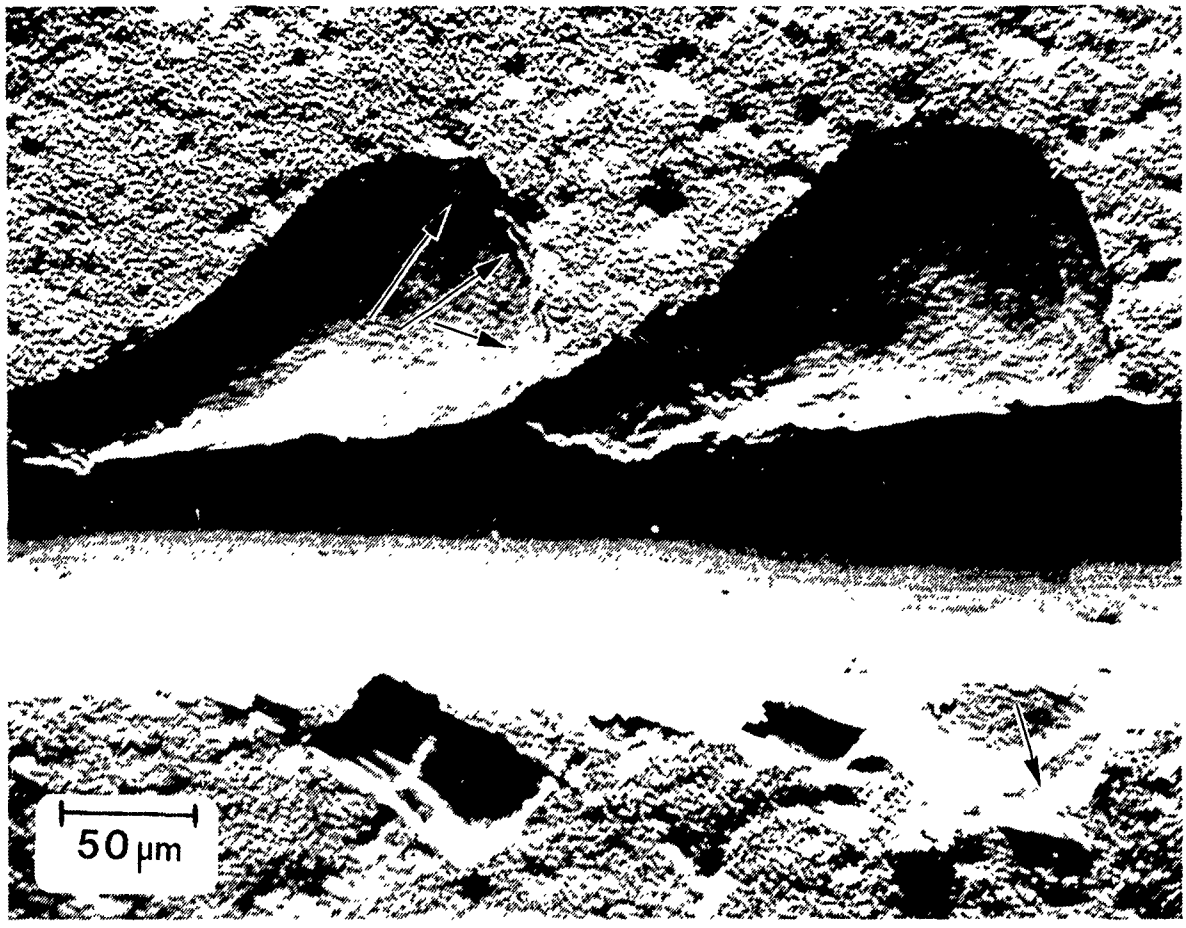

Figure 183. SEM photomicrograph (at 360x) of scratch test wear path of rutile formed on TiC by wet oxidation at 850°C (Type I), at the critical load (L_c in Table 33), where delamination of the oxide began; arrows indicate areas where the layered nature of the smeared and delaminating oxide is evident.

Table 34. Room temperature friction and wear of rutile films grown by the processes described in Figure 182, at high and low humidities.

RH %	Lot (Type)	Friction start	Coeff. (f_k) average	Revs. (f_k) <0.3	Disc wear rate 10^{-15} m^2/N	Ball wear rate 10^{-15} $m^3/N \cdot m$
99	4 (I)	0.35	0.42	250	dep.*	6.4
99	5 (II)	0.27	0.45	490	dep.*	6.1
99	6 (III)	0.27	0.43	700	dep.*	6.1
<1	4 (I)	0.27	0.50	18	162	63
<1	5 (II)	0.23	0.52	40	dep.*	60
<1	6 (III)	0.25	0.52	166	dep.*	55

*dep. = material transfer from the ball to the disc.

3. The tribological properties of the TiO_{2-x} coatings depends strongly on the surface roughness. When the TiO_2 samples are in the "as-coated" state, there is considerable transfer of steel from the frictional counterface to the TiO_2 surface. When the TiO_2 samples are polished prior to the friction testing, the transfer starts much later and when it takes place it is more reduced.

4. The friction coefficients between steel and the TiO_2 coatings were determined in two different environment conditions: 600°C/Air and RT/Argon. The presence of air lowers the friction to ~0.4. Under Ar the friction is high (0.8+) due to strong adhesive wear between the steel pin and the transferred material.

5. It was not possible to determine if there is a correlation between the stoichiometry of the TiO_2 and the tribological properties.

6. Although their friction was not extremely high, the tested TiO_2 coatings did not exhibit self-lubricating properties.

3.3.3.2 Reactive Evaporation of TiO_{2-x} Layers. CSEM's deposition of TiO_{2-x} by the conventional CVD method could not control the stoichiometry of the oxide layer to keep it in the lubricious regime and thus could not produce a low shear strength crystal structure. It would be advantageous to select a single deposition method which can control both of these parameters.

The U. of Arizona Optical Sciences Center has developed ion-beam-assisted deposition (IBAD) and reactive evaporation methodologies for selected oxides and fluorides to grow more abrasion resistant, anti-reflection (AR) coatings (240, 241, 242). The TiO_{2-x} was among the coatings candidates. Since other, similar work has indicated an ability to control at least the stoichiometry, purity and microstructure of TiO_{2-x} during the deposition (243, 244, 245), the U. of Arizona Center was asked to grow films of controlled stoichiometry TiO_{2-x} on SEM triboflats by the most advantageous method possible.

Single layers of TiO_{2-x} were deposited onto 7 mm x 5 mm x 2 mm fused silica (SiO_2) SEM triboflats by reactive evaporation. It has been shown that silica substrates does not interact with superconducting oxides (246). One must be careful that the ceramic substrate does not react with certain oxides (high T_c superconductors included), rendering them unacceptably and uncontrollably deficient in oxygen (247, 248, 249). Carbon diffusion from TiC into its own oxide constitutes a similar problem of oxygen depletion in rutile (12).

The main purpose of this project was to establish whether the oxygen-to-titanium ratio of thin titanium oxide films grown by reactive evaporation could be controlled by a proper choice of deposition parameters. Five sets of 1-μm thick (or less) films of five different oxygen-to-titanium ratios in the 1.6 to 2.0 range were deposited on the fused silica triboflats.

It was demonstrated that reactive evaporation can be employed to grow thin films of titanium oxides with various O/Ti ratios, see APPENDIX AA. The use of Rutherford backscattering spectrometry (RBS) allowed the determination of the appropriate deposition parameters. The films obtained by this technique were very pure and no other elements were detected. Hydrogen quantities remained the only unknown, since RBS is not sensitive to this element.

The mechanical properties appeared to be very critical at this early stage of the research, because cracking stopped U. of Arizona from delivering 1μm thick samples: the thickest TiO_{2-x} films that could be grown on SiO_2 without cracking could not exceed 50 nm.

The transformation of the amorphous films to crystalline rutile was not attempted in this project. The stability of the oxygen-to-titanium ratio at high temperatures and the mechanical integrity of the films would have been a concern if high temperatures were used during annealing. The possibility of purposely promoting rutile growth during deposition could be investigated in the future.

3.3.3.3 Tribooxidation of IBAD-TiN by Tester 2A Experiments. One avenue of cooperation with NRL scientists covered the area of in-situ lubricious oxide generation on ceramic surfaces. In particular, one of Dr. Irwin Singer's DARPA-funded tasks consisted of predicting likely methods to produce highly adherent TiN on HP/HIP Si_3N_4 bearing surfaces. By invoking the Si-N-Ti ternary phase diagram and the use of special deposition processes (10 and 11), he predicted that the best-adhering TiN films will form on nitrogen-deficient Si_3N_4. His hypothesis, combined with another by Gardos (12) on generating lubricious rutile by oxidizing TiN substrates, led to the idea of IBAD-deposition of TiN onto NBD-100 HIP-Si_3N_4 Tester 2A specimens (250). This deposition process was performed by Dr. Richard A. Kant of NRL. The coated specimens were then subjected to room temperature and ~850°C Tester 2A friction and wear experiments, in air, using bare NBD-100 specimens as the baseline.

Initially, the plan was to IBAD 200 nm of TiN on NBD-100 Tester 2A RCF rods, as well as NBD-100 rubshoes fabricated both in the conforming (Figure 38) and flat (Figure 36) configurations (see Figure 184), while bombarding the deposition sites with 40 keV Ti ions. The films were deposited in a

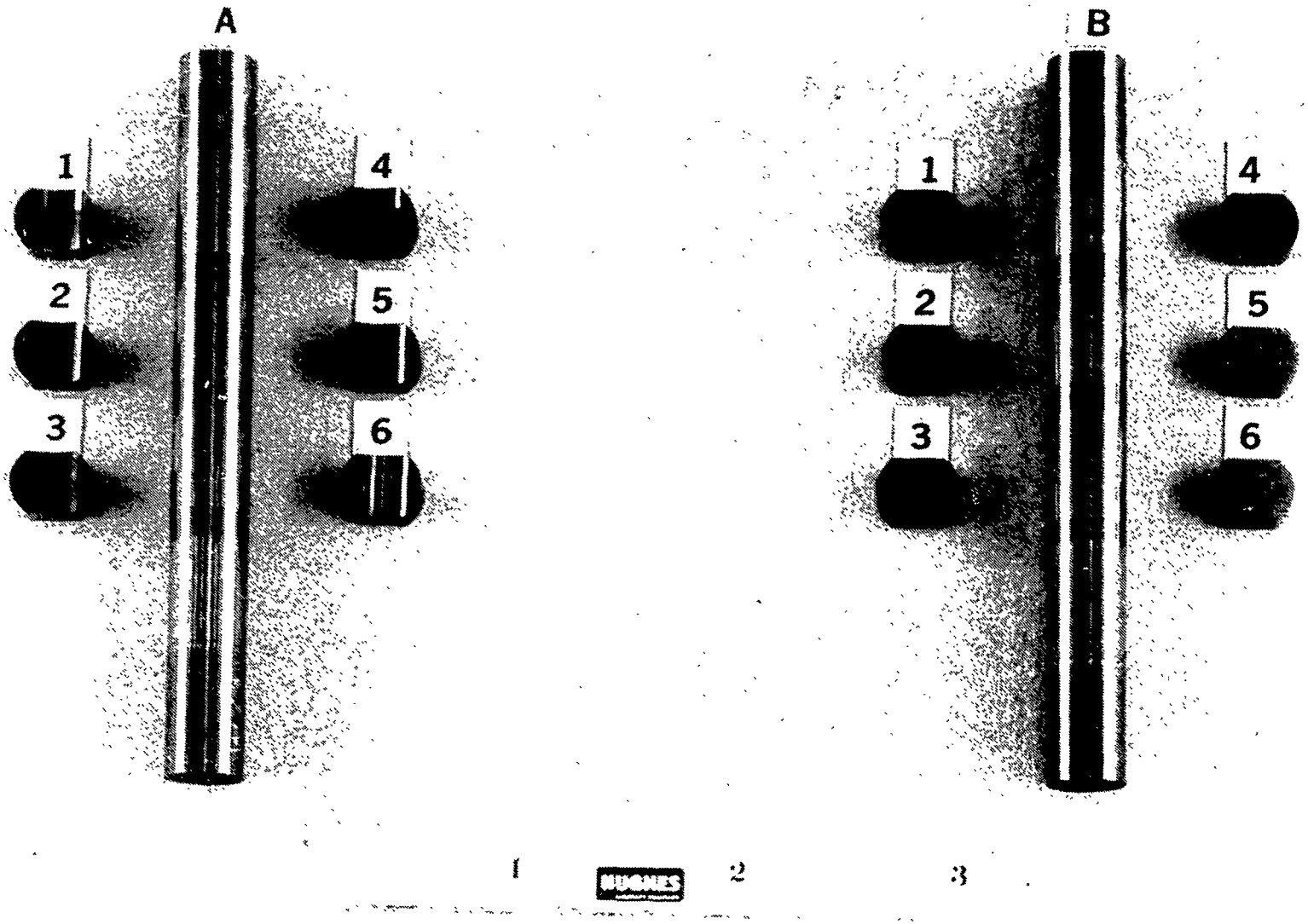

Figure 184. Photographs of IBAD TiN-coated NBD-100 HPSN Tester 2A specimens before tests: (a) stripe-coated RCF rod with coated (1 through 4) and bare (5,6) conforming rubshoes; (b) stripe-coated RCF rod with coated (1 through 4) and bare (5,6) flat rubshoes.

vacuum chamber (4×10^{-5} Pa = 3×10^{-7} torr base pressure), backfilled with N_2 gas to 1.33×10^{-3} Pa = 1×10^{-5} torr. Due to characteristic misalignment of the conforming rubshoes against their mating RCF rod, only the flat rubshoes could be characterized as to tribological performance.

The test matrix and the related τ_s data (in regular print) and average volume wear rate of the blocks (in bold print) are presented in Figure 185, in a manner similar to the data shown previously in Figure 103. The τ_s and wear rate data for α-SiC were transposed from Figure 74, for comparison.

The assessment of the data leads to the following conclusions:

1. Bare HPSN wears more and exhibits lower τ_s than bare α-SiC, at any of the two test temperatures. This finding is in line with the original hypothesis that the lower (tribo)oxidation resistance of Si_3N_4 leads to the generation of more glassy surface layers, which in turn induces greater wear but lower surface shear strengths. This inverse wear vs. τ_s trend manifests itself with both ceramics; it is also self-consistent with each ceramic.

2. The IBAD-TiN process seems to weaken the NBD-100 surface at R.T. sliding, but does provide some wear resistance at H.T., as compared to bare NBD-100. In the case of double transfer (i.e., one TiN-coated, one bare HIPSN rubshoe), the bare shoe's wear is also reduced at any temperature in the presence of oxidized TiN transferred from the other shoe. Even though the 200 nm (very thin) IBAD layer of TiN was removed fast at any temperature, its residual effects are quite noticeable at high temperature. Some contributing effect from the tribochemically generated, SiO_2-based glassy layer (i.e., forming a lower-temperature-melting, TiO_2-containing glass) cannot be discounted.

Interesting supporting data associated with the above conclusions are attached in Figures 186 through 189.

Figure 186 depicts the f_k (COF) curves of all-Si_3N_4 sliding combinations, at R.T. and H.T. Only in one case (Test No. NBDF-1/2, Rubshoe No. 1) was the room temperature friction low almost to the end of the test (~0.3), where both the general level and the "hash" suddenly increased. In all other cases, the COF was extremely variable and generally high (0.4 to 0.6). In Figure 187 it can be seen that the COF of NBD-100 is significantly and consistently higher at H.T. than at R.T. The effects of the oxidized IBAD-TiN are apparent in bringing the H.T. COF level of the NBD-100 HIPSN down considerably. Note that the thin TiN layer appears to be removed within the first 200 seconds of sliding, even before heating began. Nevertheless, the beneficial footprint of its presence is still clearly observable afterwards.

The rubshoe photomicrographs of the low and high wear of the bare NBD-100 rod at R.T. and H.T., respectively, are shown in Figure 188. The equivalent photos of worn bare and TiN-coated rubshoes are attached in Figure 189.

In the overall view, thin IBAD-TiN coatings, by themselves, cannot act as prolonged-capacity (i.e., sufficiently wear resistant) reservoirs for in-situ generated, lubricious rutile.

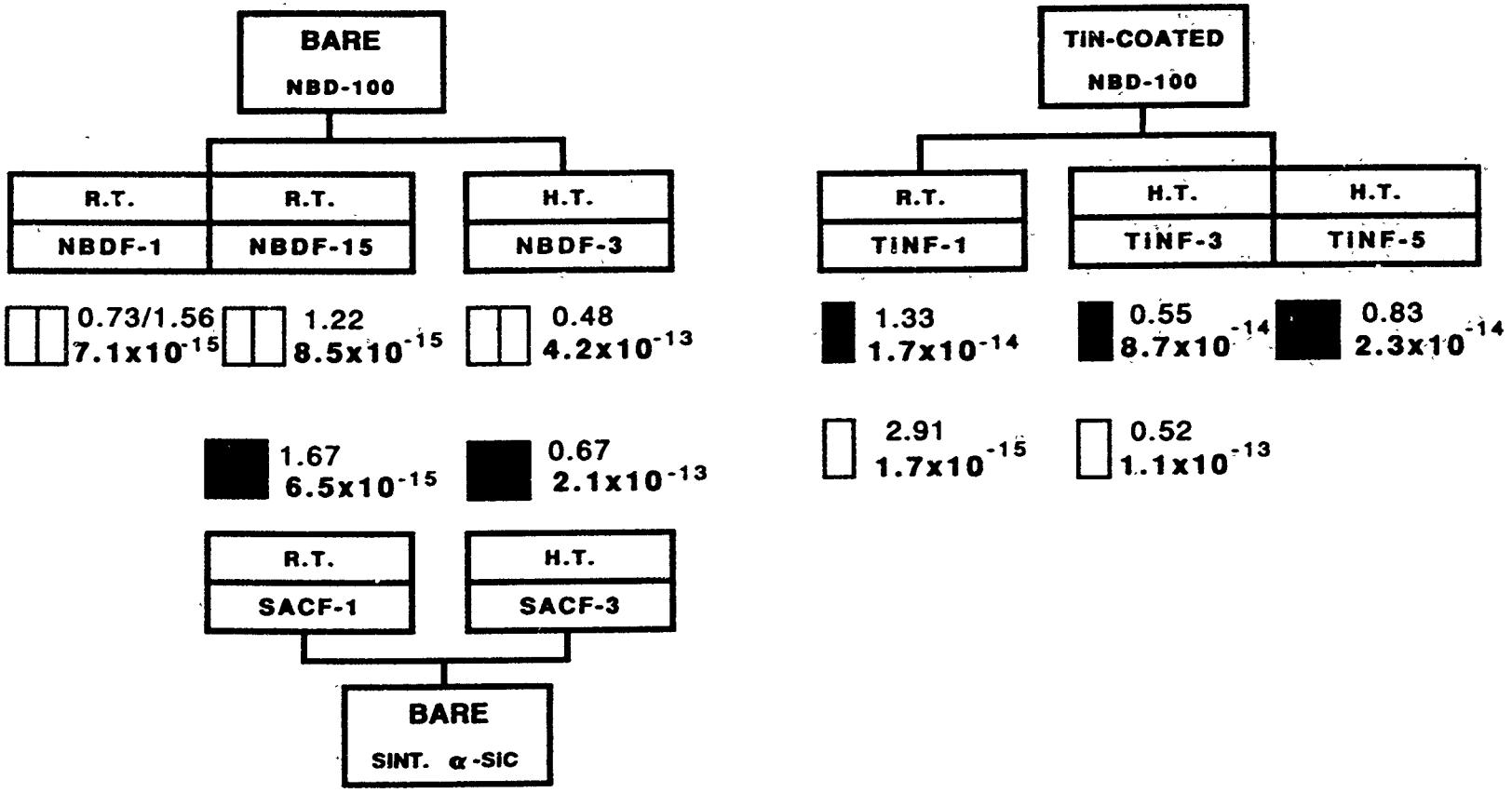

Figure 185. Tester 2A test matrix and data of bare and TiN-coated NBD-100 specimens, at R.T. and H.T., compared with the data associated with Hexoloy SA-80T α-SiC specimens; two white blocks under "bare NBD 100" signify all-Si_3N_4 rubbing combinations and two black blocks under "bare sint. α-SiC" mean all-SiC rubbing combinations; under "TiN-coated NBD-100", one white and one black blocks signify one uncoated and one TiN coated rubshoe sliding against a TiN-coated NBD-100 RCF rod, while two black blocks indicate an all-TiN-coated NBD-100 combination.

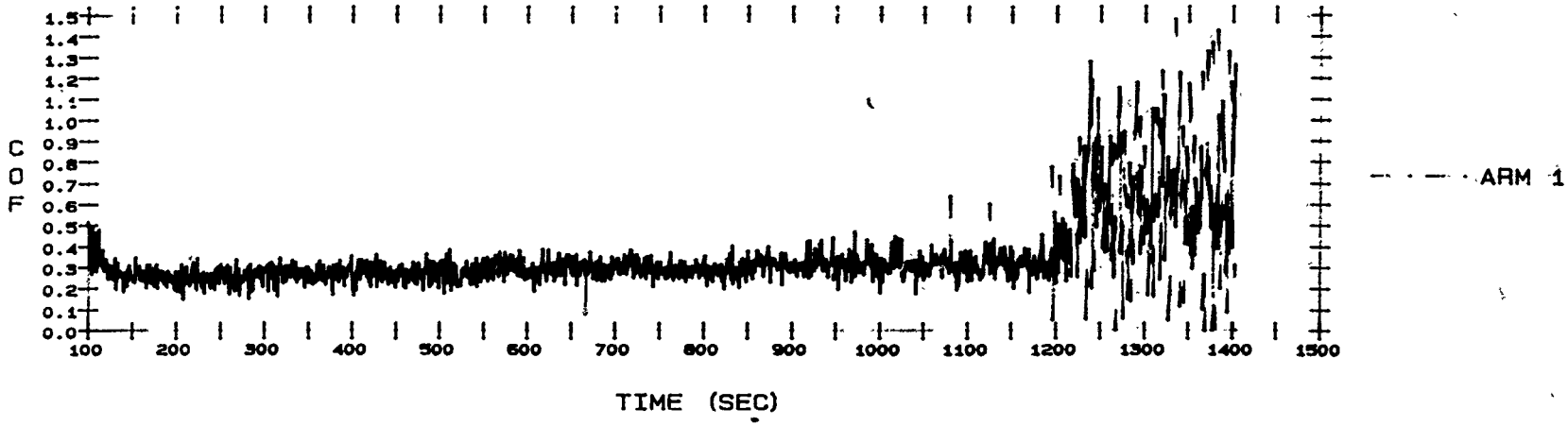

NBDF_1.2: 13.3 N (3 lbs), 700 RPM
NBD-100 SILICON NITRIDE ROD/FLAT
ROOM TEMP. BASELINE

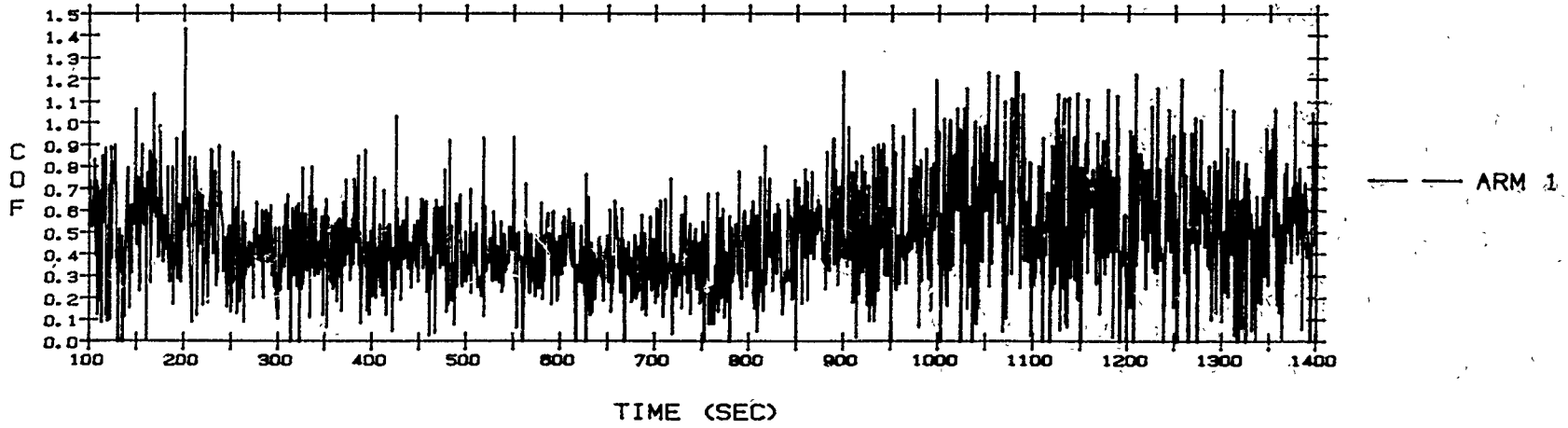

NBDF_15.16: 13.3 N (3.0 lbs), 700 RPM
NBD-100 ROD AND FLATS
ROOM TEMP. BASELINE

Figure 186. Tester 2A average coefficient of friction (COF) data with NBD-100 HPSN vs. itself as a function of temperature (baseline data).

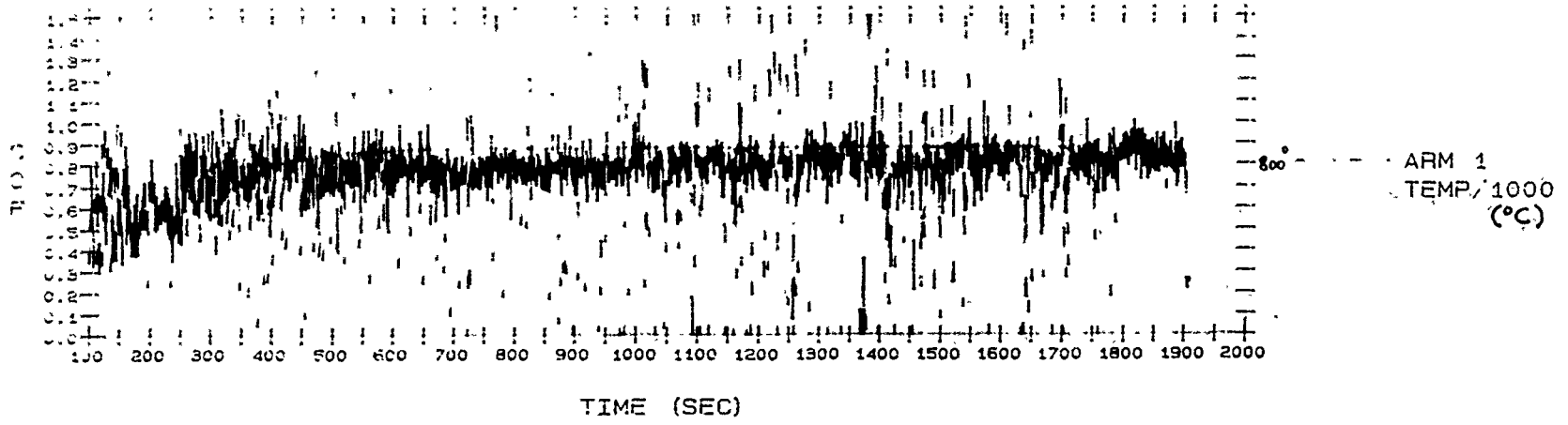

NBDF_3, 4: 13.3 N 93.0 lbs), 700 RPM
NBD-100 SILICON NITRIDE ROD/FLAT
HIGH TEMP. BASELINE

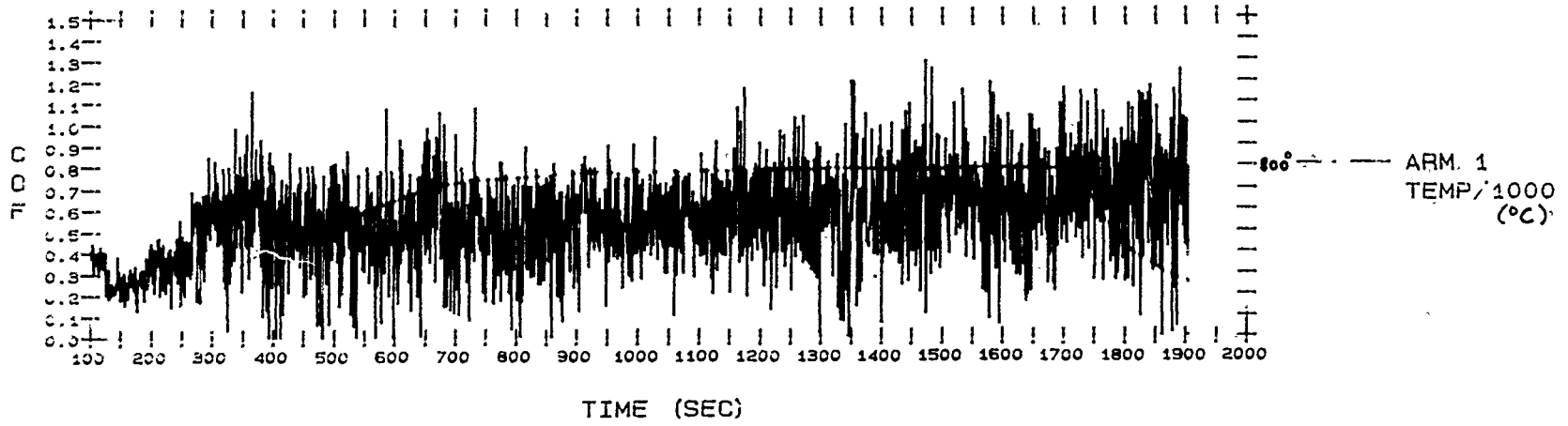

TINF_5, 6: 13.3 N (3.0 lbs), 700 RPM
NBD-100/TiN IMPLANT. ROD/FLAT
HIGH TEMP.

Figure 187. Tester 2A average coefficient of friction (COF) data at high temperature, with an all-bare-NBD-100 and an NBD-100 system IBAD-TiN coated.

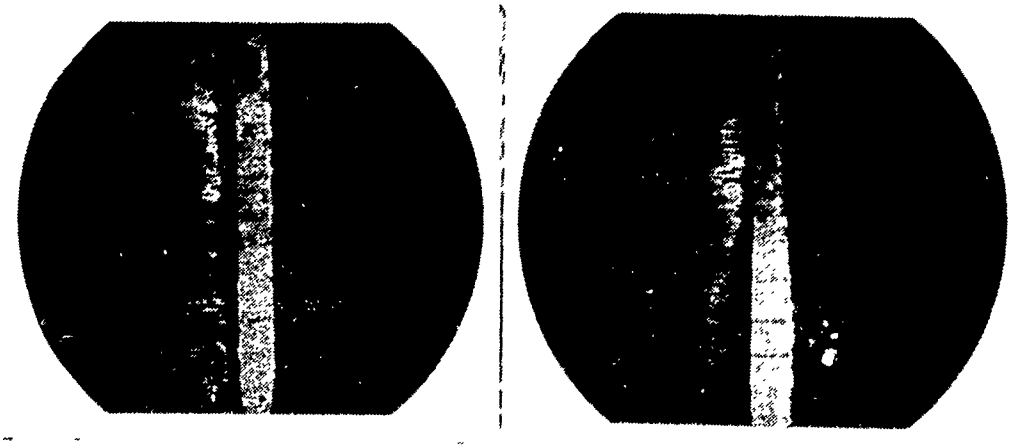

NBDF_1, 2: 13.3 N (3 lbs), 700 RPM
NBD-100 SILICON NITRIDE ROD/FLAT
ROOM TEMP BASELINE

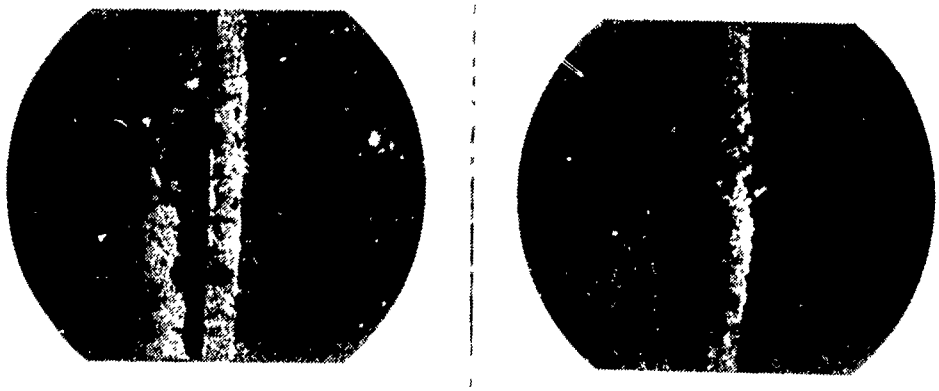

NBDF_15, 16; 13.3 N (3.0 lbs), 700 RPM
NBD-100 ROD AND FLATS
ROOM TEMP. BASELINE

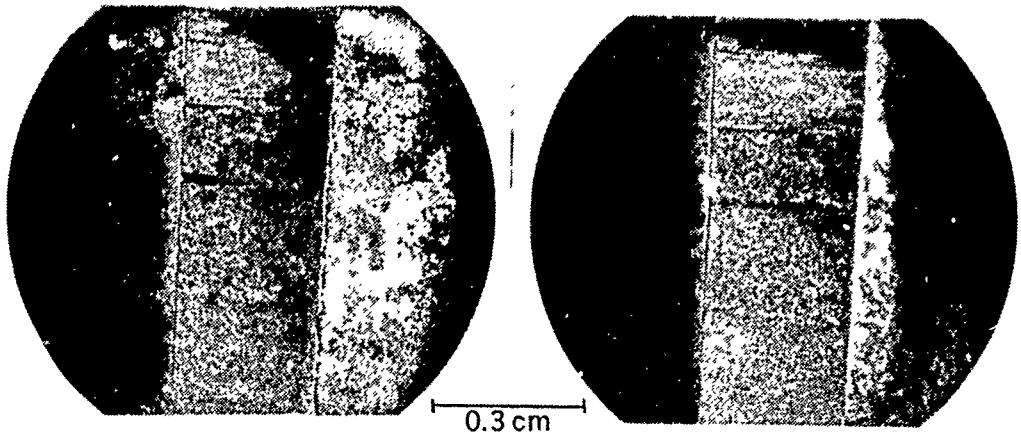

Figure 188. Optical photomicrographs of used NBD 100 HPSN Tester 2A rubshoes operated against a bare, NBD-100 HPSN RCF rod at various temperatures (baseline data).

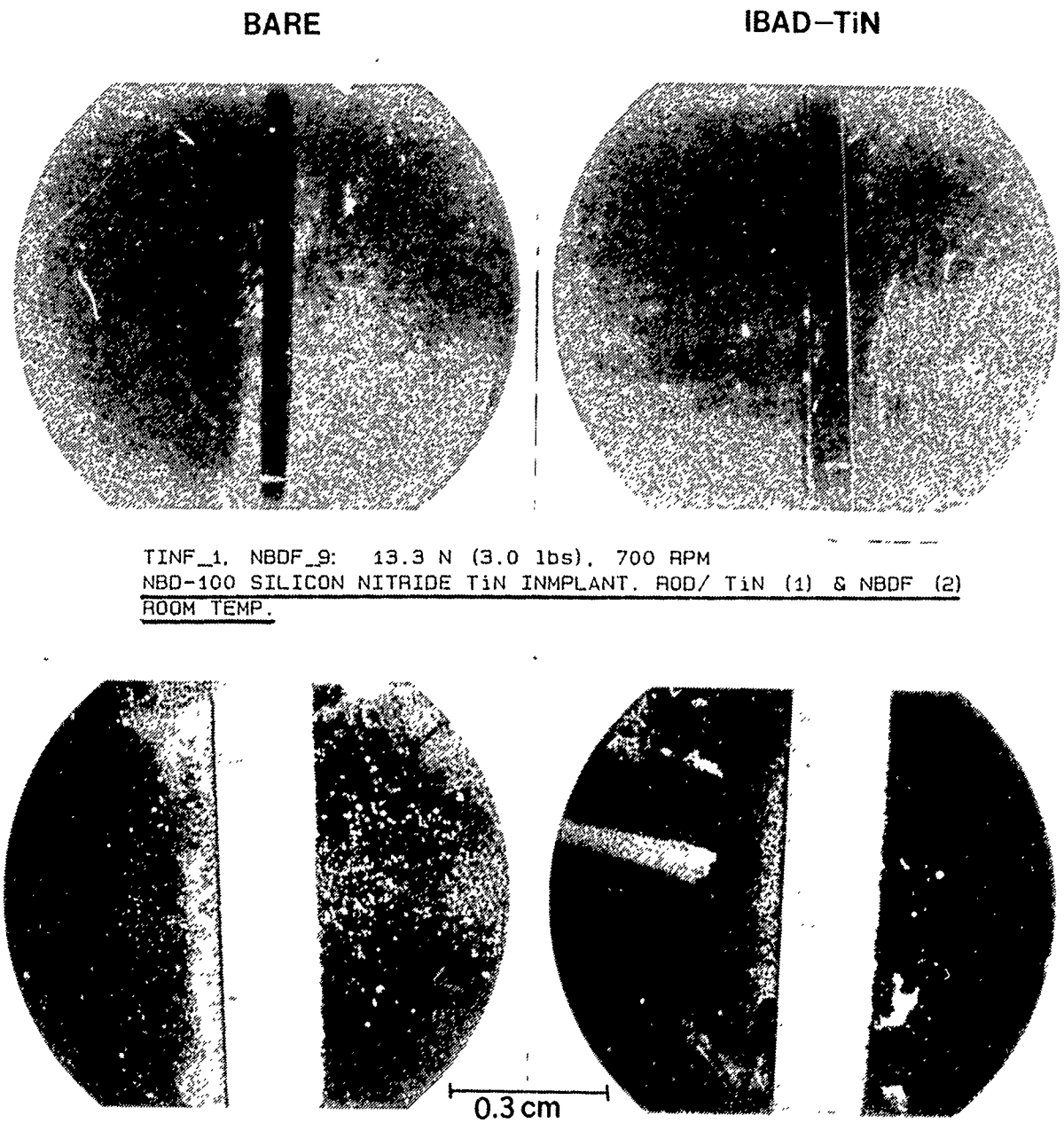

Figure 189. Optical photomicrographs of used, bare and IBAD-TiN-coated NBD-100 HPSN rubshoes operated against an IBAD-TiN-coated NBD-100 HPSN RCF rod, at various temperatures.

3.4 CaF_2 AND BaF_2 AS WIDE TEMPERATURE RANGE LUBRICANTS

3.4.1 Surface Shear Strength of Ultrapure CaF_2 AND BaF_2 (111)[$1\bar{1}0$] by SEM Tribometry

For the first time, the surface shear strength (τ_s) of CaF_2 vs. CaF_2, BaF_2 vs. BaF_2 and BaF_2 vs. CaF_2 single crystals (XTL's) was determined experimentally by scanning electron microscope (SEM) tribometry at room temperature, in vacuum. In each case, a spherical crystal tip was sliding against a mating crystal flat on the respective (111) contact planes, in the [$1\bar{1}0$] direction. The associated τ_s values were calculated by (a) multiplying the experimentally measured coefficients of friction (f_k) with the yield strength or yield pressure ($\sigma_y \cong P_y$) estimated from the best available literature values and calculation methodology, and (b) dividing the experimentally measured friction forces (F_k) by the real areas of contact (A_r), estimated either by the equations of the Hertzian (elastic) contact theory or measured from high magnification SEM photomicrographs depicting visible wear scars.

Inasmuch as (a) ultrapure (99.99%), oxide-hydroxide-free XTL's of CaF_2 and BaF_2 were available at Hughes (grown by the Bridgman method in a reactive atmosphere by Dr. Mort Robinson and his colleagues at the Hughes Malibu Research Laboratories, see (33 through 37), (b) CaF_2 and BaF_2 SEM triboflats and hemispherical pins of the scanning electron microscope (SEM) tribometer could be fabricated with well-controlled crystallographic planes and directions on the sliding surfaces, (c) CaF_2 and BaF_2 appeared to be ideal model compounds with respect to hardness, surface energy and size differences of the particles used in the MD calculations (see Table 2), and (d) their chemical inertness made specimen handling relatively easy and tribotesting in low-grade vacuum possible, Georgia Tech scientists embarked on predicting the τ_s of idealized CaF_2 vs. CaF_2, BaF_2 vs. BaF_2 and BaF_2 vs CaF_2 (111) [$1\bar{1}0$] surfaces by MD calculations. In parallel, SEM tribometer experiments were performed on these combinations to compare the predictions with the results of the controlled experiments. The interaction of the respective (111) planes should be minimal, due to the inert, fluorine-covered and nonpolar (111) surface of the fluorides as compared, for example, to the polar (100) planes (251). The $\tau_s \cong \tau_y$ data so developed would be more meaningful to a tribologist than the critical resolved shear stress (τ_{cr}) data provided by conventional, compressive τ_{cr}-determining techniques which use XTL boules, see Figures 190 and 191 taken from (252).

The basic objective of this work was to calculate the τ_s of (111)[$1\bar{1}0$] CaF_2 and BaF_2 XTL's by using the F_k and f_k values measured during SEM tribometry.

3.4.1.1 Specimen Preparation. Starting materials used for growth of the fluoride XTL's were prepared by reacting the high purity metal carbonate, (99.99% pure MCO_3 where M = Ba, Ca), with anhydrous HF (g). Typical impurities of the 99.99% BaF_2, as determined by emission spectrographic analysis, were 0.017% Si, 0.00042% Mg, 0.0011% Fe, 0.0014% A1, 0.00015% Cu, 0.079% Sr, and 0.028% Ca, with no other elements detectable. This HF treatment process yielded virtually oxide and OH^- free metal fluoride powders.

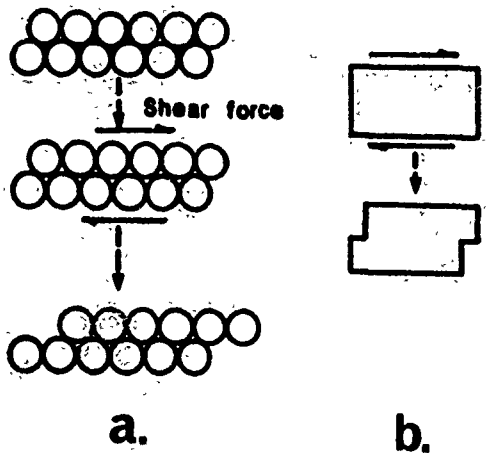

Figure 190. Schematic representation of the permanent deformation of a crystal by shear force-induced interplanar slip (252).

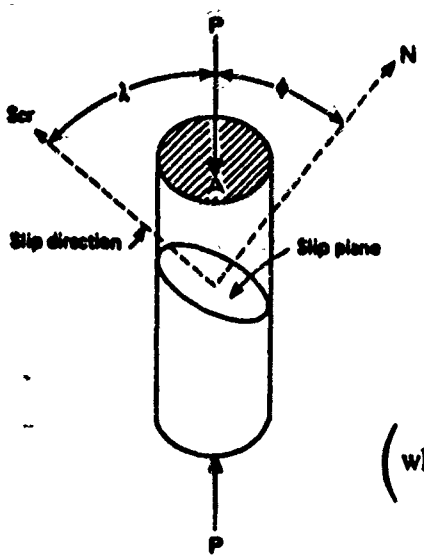

$$S_{cr} = \frac{P\cos\lambda}{A/\cos\phi} = \frac{P}{A}\cos\phi\cos\lambda$$

$$\left(\text{when } \phi = \lambda = 45° \longrightarrow S_{cr} = \frac{1}{2}\frac{P}{A}\right)$$

Figure 191. Conventional measurement of the critical resolved shear stress (S_{cr}, aka τ_{cr}), by compression of a XTL boule (252).

Single crystal boules of BaF_2 and CaF_2 were grown from these powders under a He/20% HF atmosphere by the Bridgeman technique (33 through 37). Growth rates were on the order of 2.0 $mm \cdot h^{-1}$. Transmission measurements in the near-infrared showed that the crystals had no absorption due to H_2O, OH^-, or oxide impurities.

These crystals were subsequently oriented and processed into the hemispherically-tipped tribopin vs. triboflat specimen combination of the SEM tribometer (Figure 192). Note that in the strictest sense of the reciprocating sliding directions, this direction is $[1\bar{1}0]$ during one of the 1/2 cycles, and in the $[\bar{1}10]$ during the second 1/2 cycle.

First, sections of the respective CaF_2 and BaF_2 XTL boules were oriented along the [111] direction using a back-reflection Laue x-ray diffraction technique with CuK_α radiation. Smaller sections were then cut and oriented normal to the [111] along the $[1\bar{1}0]$ direction, using the same technique. From these oriented sections, several 7 x 5 x 3 mm triboflat samples were prepared, with the largest (7 mm x 5 mm) face normal to the [111] direction and the smallest (5 mm x 3 mm) face perpendicular to the $[1\bar{1}0]$ direction, (see Figure 192). The precision of the Laue orientation is ± 0.5 degrees for the sample direction.

To more precisely align the samples along the [111] direction, a second orientation technique was incorporated before the final polishing of the sliding surfaces. The basic experimental set-up is schematically shown in Figure 193. This technique is based on the fixed angular diffraction of incident CuK_α radiation from the (111) crystallographic planes of the triboflat. The sample was wax-mounted to a goniometer, which was then slid along a fixed track until the surface of the sample became incident with the X-ray beam. A detector was positioned at the appropriate 2 Θ angle for reflection from the (111) planes of the fluoride crystal sample. Reflection intensity (and, therefore, alignment) was maximized by adjusting the sample positioning screws of the goniometer barrel holder. These screws are indicated as AS1 and AS2 in Figure 193. However, the set-up was modified to include a third positioning screw for increased precision. The barrel holder and mounted sample were then rotated by 90°, with the reflection intensity again maximized by readjusting the positioning screws. This iterative process was repeated until the intensity was at a maximum for all angles of rotation around the [111] direction. The precision of the alignment technique is approximately ± 25 arc seconds. The mosaic properties observed in the crystal samples did, however, reduce the accuracy of the alignment to within ± 1 arc minute.

To maintain this alignment throughout the polishing procedure, the barrel holder was designed so that it and the sample could be transferred to a polishing wheel without disturbing the previous positioning. Polishing was then performed normal to the mouth of the barrel holder, thereby creating a surface on the sample that was in the plane of the alignment. The opposite side of the sample was prepared by mounting the aligned face to a flat and polishing normal to the surface of the flat. All polishing was performed in ethylene glycol to avoid H_2O and related impurity contamination. The polishing compound used was 0.3 μm grit Al_2O_3. Final triboflat sizes were 7 x 5 x 2 mm.

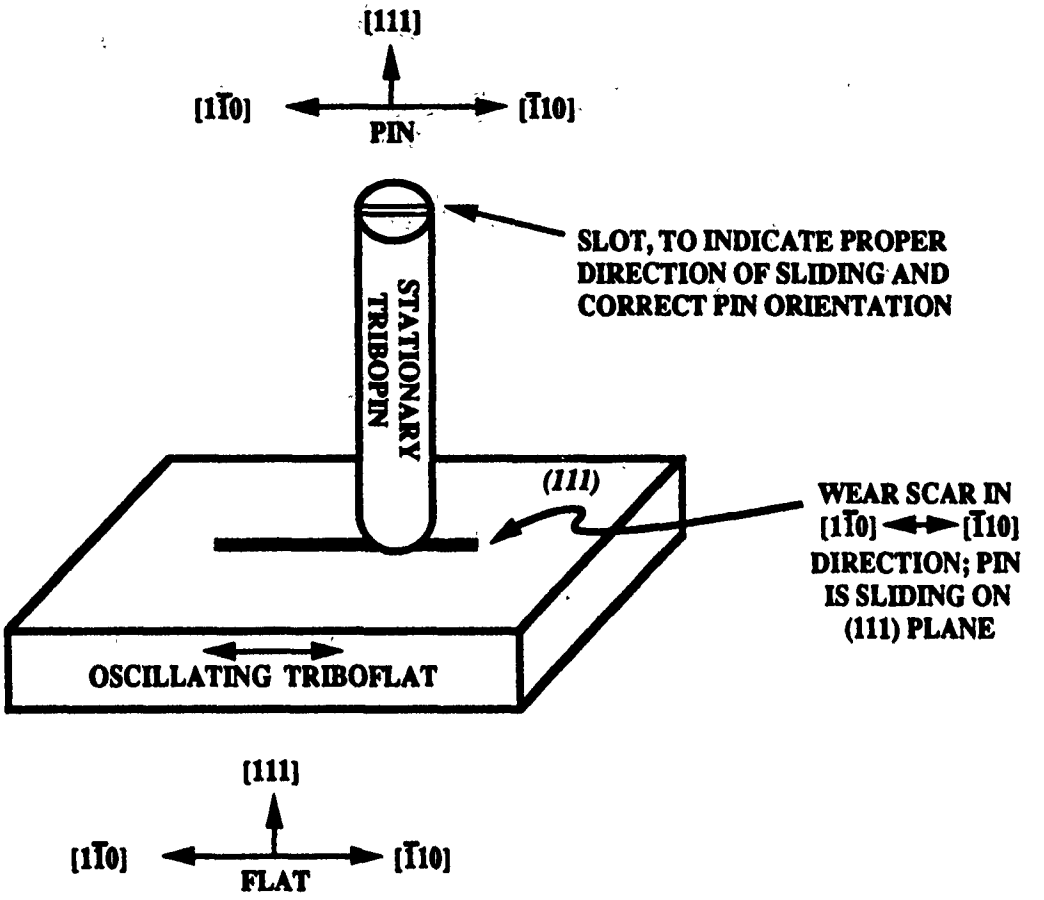

Figure 192. Orientation of the CaF_2 (111) tribopin sliding against the CaF_2 (111) triboflat in the [1$\bar{1}$0] direction.

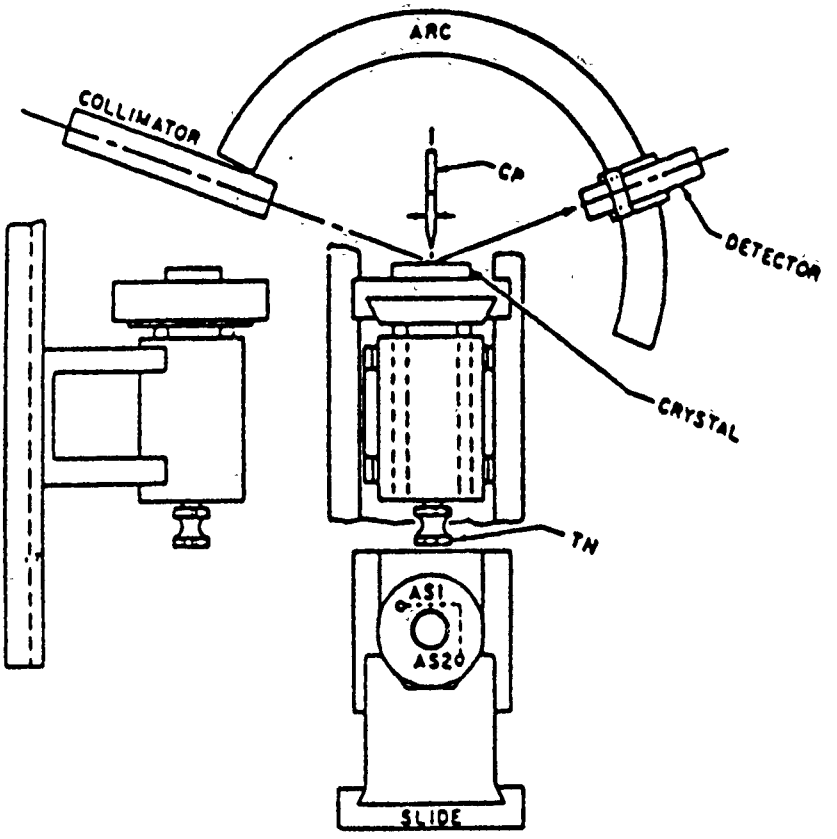

Figure 193. Crystal orientation goniometer used for aligning the tribopin and triboflat for Laue-reflection-aided cutting and polishing; the barrel holder is adjusted in the goniometer, then transferred to a polishing wheel.

The CaF_2 and BaF_2 tribopins were made from 3 x 3 x 11 mm sections, with the longest dimension oriented along the [111] direction by the back-reflection Laue technique. These square-cut, columnar pieces were then transferred to a brass shaping jig (Figure 194). The shaping jig consisted of two half pieces, with the bottom half containing a 3 x 3 x 50 mm V-shaped groove designed to accommodate the sample. The top half of the jig had an adjacent, 1 mm radial groove of the same length. By sliding the top half of the jig over the positioned sample in the presence of a 0.3 μm Al_2O_3 polishing slurry, a cylindrical shape was imparted to the top half of the sample. Rotation of the sample by 180° with subsequent sliding and polishing gave a cylindrical shape to the entire sample. Spherical-shaped tips were then hand polished onto one end of each pin 2.0 mm dia. x 10 mm length. The tribopins were also aligned normal to the [111] along the $[1\bar{1}0]$ direction using the back-reflection Laue technique: a line-notch representing this direction was scribed onto the top of the polished pin for future reference (see Figure 192).

X-ray photoelectron spectroscopy (XPS) and low energy electron diffraction (LEED) were used to characterize the chemical and physical state of the surfaces of the BaF_2 and CaF_2 triboflats during the various stages of the preparation process. XPS provides chemical identification of the species present in the outermost, one or two atomic layers of material, including absorbed foreign atoms and molecules. LEED indicates whether or not the regular crystalline order characteristic of the bulk crystal is maintained to the outermost atomic layers of the surface.

Initial LEED examination of polished CaF_2 and BaF_2 specimens failed to give any evidence of a diffraction pattern, indicating that the top atomic layers are left in a disordered condition after polishing. XPS showed a significant oxygen concentration in the surface region coupled with a fluorine deficiency, as well as contamination by adsorbed hydrocarbons originating from residual traces of the polishing compound.

In an attempt to correct the fluorine stoichiometry of the surface and to restore the surface crystalline order, the samples were annealed at 500°C in a dry He/20% HF atmosphere for 5 hours. After this treatment, the specimens were examined again using LEED and XPS. Well-defined electron diffraction patterns were observed after HF annealing, demonstrating the recovery of surface atomic order. The symmetry and spot locations in the diffraction pattern were indicative of a (111) surface crystallographic orientation, and were qualitatively identical to LEED patterns from a bulk sample of BaF_2 freshly-cleaved along the (111), used as a reference sample. Similarly, XPS showed that the surface composition after HF annealing was very close to that of the cleaved pieces.

From these measurements, it was concluded that large-area single crystal specimens of CaF_2 and BaF_2 having clean and ordered surfaces can be produced after the polishing operations with an appropriate annealing treatment in dry HF. This treatment successfully removes the surface damage and contamination left by the polishing step and replaces unwanted oxygen with fluorine. Both the composition and the atomic order of the surface were thus restored to those of an ideally terminated bulk

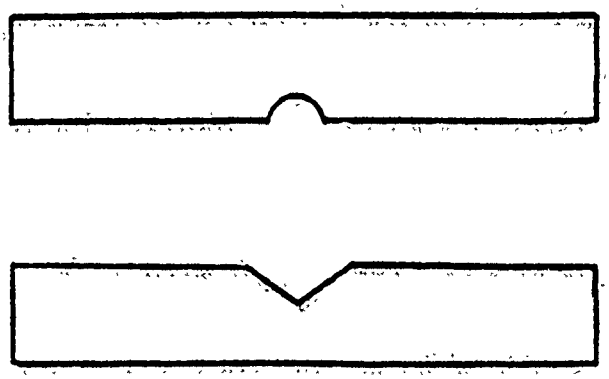

Figure 194. Side view of the brass polishing jig for the tribopin.

crystal. Note that the annealed surfaces could be exposed to room ambient humidity (50 ± 10% R.H.) for several hours without the loss of LEED pattern. Since the SEM triboexperiments were preformed within hours after removal from the HF annealing furnace, no degradation of the test surfaces was presumed during specimen transit and handling prior to the triboexperiments.

Note that the type of LEED measurements reported here are sensitive neither to atomic steps or ledges on the surface nor to the presence of small regions of disorder surrounded by an ordered matrix (i.e., mosaic patterning), such as those found during the X-ray alignment of the triboflats. It is clear, however, that the majority of the surface possesses the atomic order of the bulk crystal.

3.4.1.2 Test Procedures. The SEM tribometer (see Figure 14) housed and operated the pin/flat specimen combination described in Figure 192.

In the present case, the normal load on the pin (F_n) was the lowest reliably applied force (6g = 0.059N). The maximum Hertzian stresses associated with the particular contacts were: CaF_2/CaF_2 = 179 MPa; BaF_2/BaF_2 = 123 MPa; and BaF_2/CaF_2 = 143 MPa. The average oscillatory velocity over the ~3.5 mm wear track was also the slowest speed that could be reliably controlled to a steady-state value (1.1 $mm \cdot s^{-1}$). These low-stress parameters were selected to mitigate surface damage, ploughing, work hardening and adiabatic heating of the contact by excessive frictional heat generation. The tests were completed in the typical vacuum atmosphere of the SEM column, with the tribometer lid off. No heat was applied to the specimen flats.

Experiments were performed on three pin-on-flat combinations: CaF_2 vs. CaF_2, BaF_2 vs. BaF_2 and BaF_2 vs. CaF_2, respectively. Each combination received two different types of testing protocols, one following the other without breaking vacuum, using the same pin/flat combination in each case. The first type of test consisted of reusing the same pin tip to slide over 3 half-cycles each way on the triboflat, where each triple-traverse over the flat occurred on a fresh, unused portion of the flat (see Figure 195). This was achieved by repositioning the flat laterally by a second XY tribometer stage located underneath the oscillating stage housing the flat, after each undirectional, 3.5 mm movement, back or forth. The 3 half-cycle procedure was instituted to determine the F_k and f_k of contacting specimen surfaces, which remained as fresh and unused as possible (reusing the pin tip was inevitable). Also 3 half-cycles were the minimum number of oscillations required to establish a "floating" friction force zero for each wear path and determine the absolute magnitude between the maximum and minimum friction forces. By the use of a simple program, the computer automatically measured the average of the absolute values of the (+) and (-) friction forces and divided the average F_k with the specific normal loads to calculate f_k (Figure 196).

After the 3 half-cycle tests, each flat was repositioned under the slightly used pin to a final, unused area to complete a 100 cycle test over that last wear track, as indicated by the heavy wear track line shown in Figure 195. The rationale behind this multi-cycle test was to determine the steady-state f_k and compare it with the initial, 3-half-cycle values.

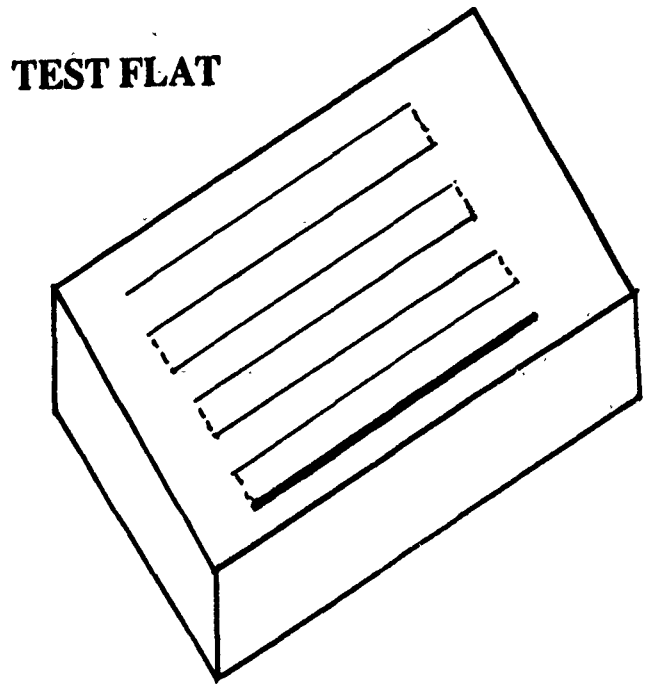

Figure 195. The 3-cycle, once-over test track pattern on the fluoride triboflats (thin lines) followed by 100 cycles in the same track (heavy line).

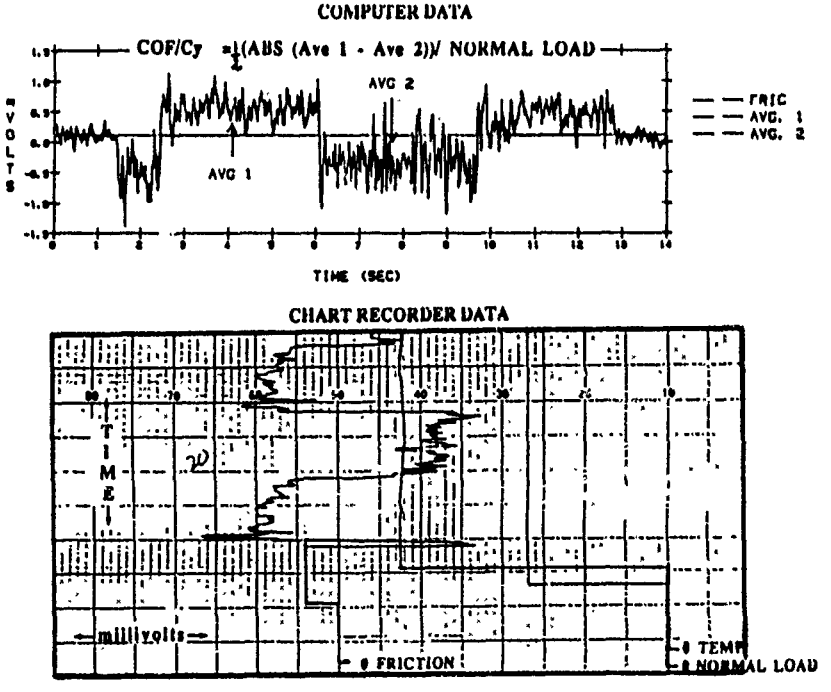

Figure 196. Computer friction traces and method of averaging the coefficients of friction during oscillatory sliding, shown with the corresponding chart recorder friction traces combined with temperature and normal load recording.

3.4.1.3 Test Results. The 3-cycle and 100-cycle f_k data of the CaF_2 vs. CaF_2, BaF_2 vs. BaF_2 and BaF_2 (pin) vs. CaF_2 (flat) combinations are attached in Figures 197, 198 and 199, respectively.

The results indicate that the hardest combination (CaF_2 vs. CaF_2, see Figure 197) exhibited the lowest friction values (0.04 - 0.05) during the 3-cycle tests. During the 100-cycle test, the starting f_k was the lowest measured anywhere ($\cong$ 0.01), increasing only slightly to the average value just below 0.06. SEM photomicrography of both the thrice-over and 100-cycle (most heavily worn) tracks after the experiments could not discern any visible wear scars or any sign of wear debris anywhere on the tracks or on the pin tip, even at magnifications as high as 5000X, except in the case of the BaF_2/CaF_2 sliding couple.

The soft vs. soft (BaF_2 vs. BaF_2) combination's f_k (Figure 198) was significantly higher and more variable than the hard vs. hard (CaF_2 vs. CaF_2) equivalent in Figure 197. During the very first, 3-cycle test movement of the flat against the new pin, the f_k dropped immediately and precipitously from 0.13 to 0.07, where it remained until the last 1/2-cycle traverse, further lowering its value to 0.05. The long-term test's f_k seemed to follow the same downward trend for the first 5 cycles, after which the average friction rose monotonically for a steady-state value of $\cong$ 0.12. Again, SEM photomicrographic examination could not find any evidence of visible wear scars on the pin or the flat.

The soft vs. hard (BaF_2 pin vs. CaF_2 flat, see Figure 199) combination exhibited the most steady, 3-cycle f_k, remaining at exactly 0.08. The long-term test f_k values rose near-linearly from an average starting value of $\cong$ 0.07 to a final value of $\cong$ 0.10. Here, the friction function did not seem to level off to a more-less steady-state value previously noted with the soft vs. soft (BaF_2 vs. BaF_2) pair's equivalent data shown in Figure 198. The debris transferred from the softer BaF_2 pin to the harder CaF_2 flat helped to identify the only wear scar discernible by SEM photomicroscopy, in Figure 200. The BaF_2 debris was identified by energy dispersive X-ray spectrometry.

The 3-cycle f_k values were averaged in each sliding combination's case and used in the τ_s calculations, as follows: f_k (CaF_2 vs. CaF_2) = 0.043, f_k (BaF_2 vs. BaF_2) = 0.077, and f_k (BaF_2 vs. CaF_2) = 0.080. Note that although f_k is being reported to the nearest 0.01 in Figures 197 through 199, in the following calculations the arithmetic means are substituted to the nearest 0.001.

3.4.1.4 Surface Shear Strength Calculations. According to (253), the components of the total microscopic friction force F_k are:

$$F_k = \Sigma F_1 + \Sigma F_2 + \Sigma F_3 + \Sigma F_4$$

where

F_1 = elastic asperity deformation events;

F_2 = plastic asperity deformation events;

F_3 = shearing of adhesive junctions;

F_4 = resistance to ploughing, as described before in Section 3.3.2.1, and in (14).

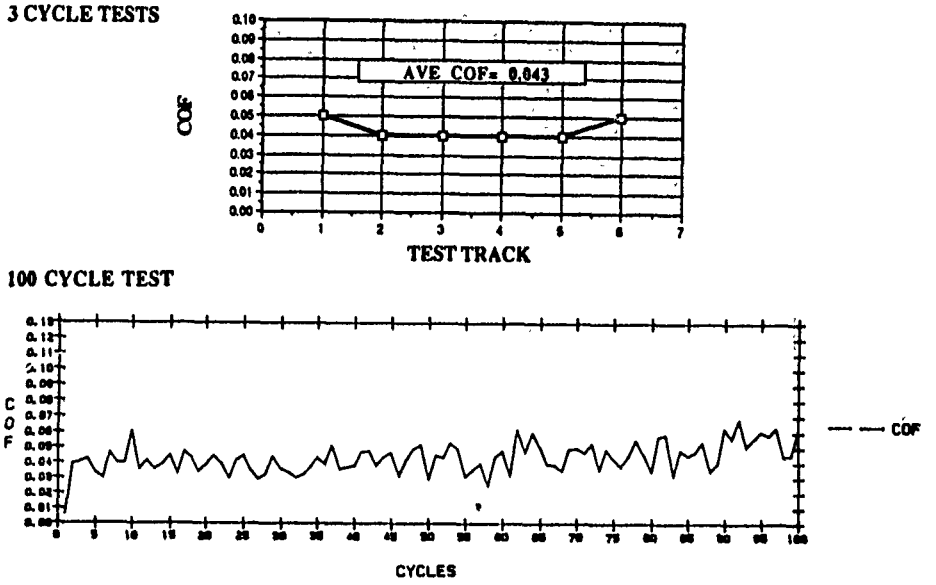

Figure 197. The coefficients of friction of the 3-cycle (once-over) and 100-cycle (repeated) test with a CaF_2 pin vs. a CaF_2 flat in the (111)[$\bar{1}10$] sliding combination.

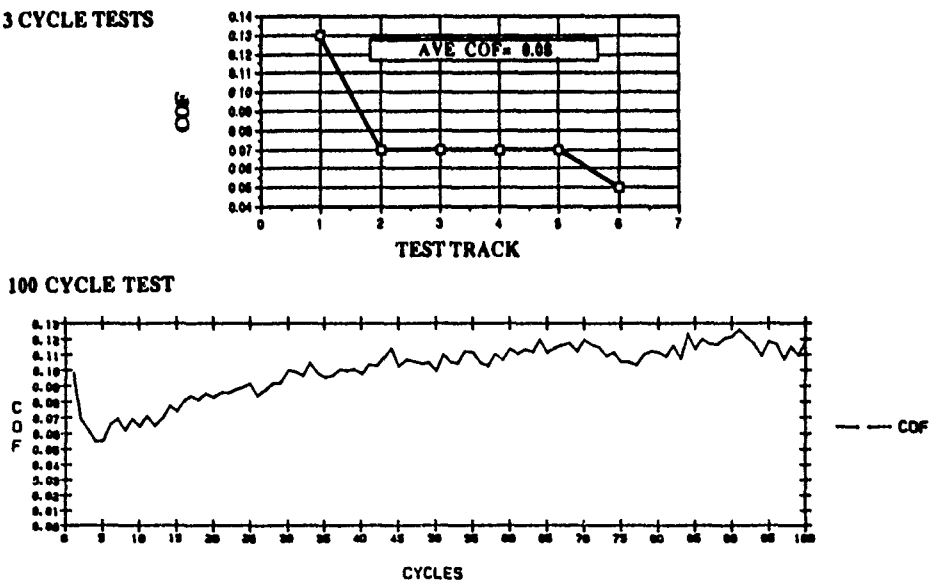

Figure 198. The coefficients of friction of the 3-cycle (once-over) and 100-cycle (repeated) test with a BaF_2 pin vs. a BaF_2 flat in the (111)[$\bar{1}10$] sliding combination.

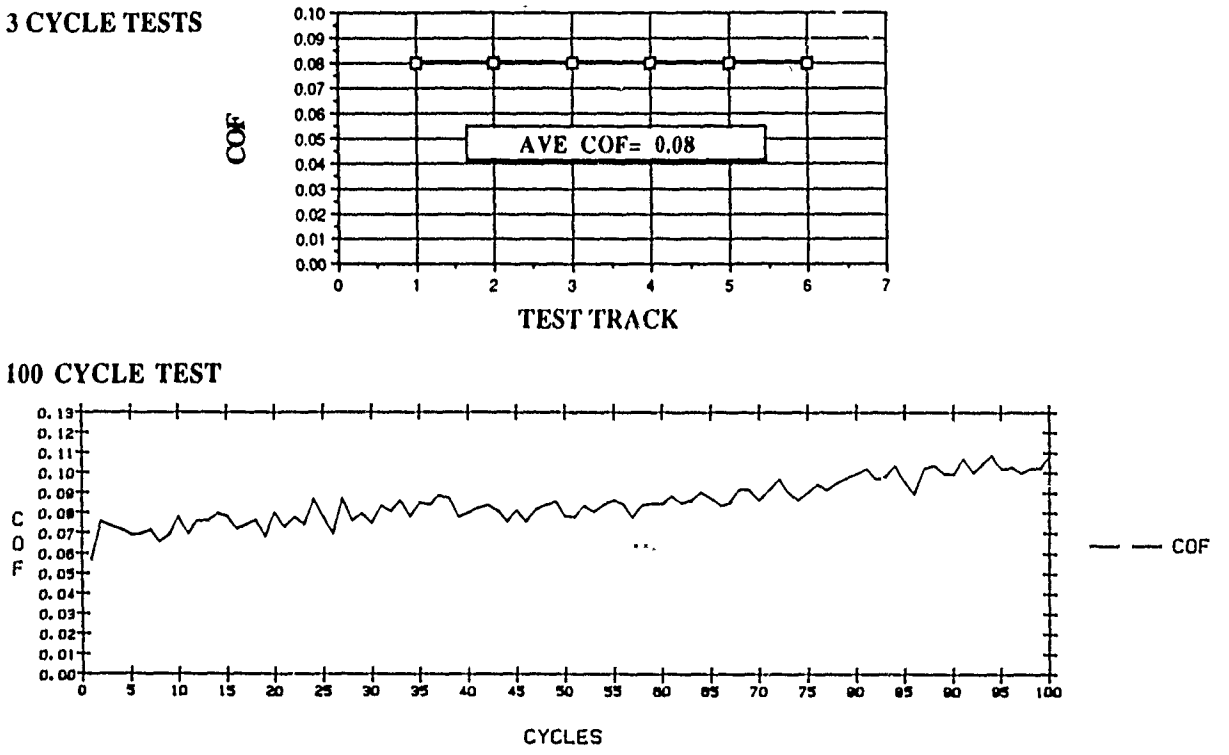

Figure 199. The coefficients of friction of the 3-cycle (once-over) and 100-cycle (repeated) test with a BaF_2 pin vs. a CaF_2 flat in the (111)[$1\bar{1}0$] sliding combination.

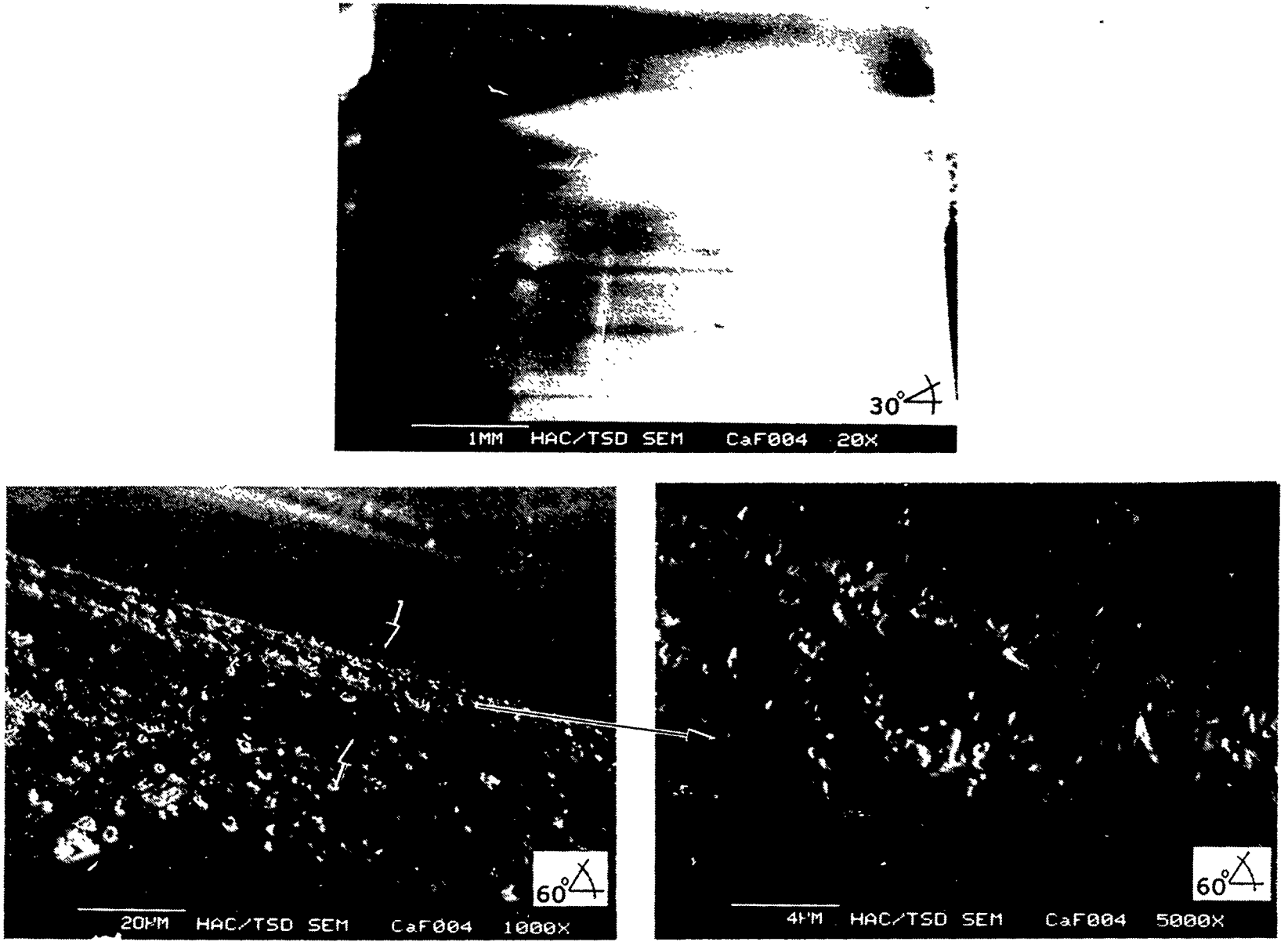

Figure 200. SEM photomicrographs of the 100-cycle wear track of the BaF_2 (pin) vs. CaF_2 (flat) combination, at various magnifications; arrows indicate the boundaries of the wear scar; debris was shown to be transferred BaF_2 particles.

At the light loads employed here, ploughing is presumed minimal inasmuch as permanent plastic deformation was not measurable (i.e., there was no visible wear scar on the flats) in two out of the three cases. Therefore, the dominant force in the tribocontact may be attributed to adhesive interaction, similar to what we presumed for rutile. Therefore, the $\tau_s = \tau_y$ of the material combinations here may be calculated by the following standard methods:

- Method 1 ——> $\tau_s = f_k \bullet P_y$
- Method 2 ——> $\tau_s = F_k/A_r$

With both methods, the f_k and F_k values were fist experimentally measured by SEM tribometry, and then the P_y and A_r parameters were estimated by the best available literature data and calculation techniques. It will be shown here that both methods have their own characteristic advantages and shortcomings. As such, both are employed here to eventually select the most reasonable τ_s values.

3.4.1.4.1 Shear Strength ($\tau_y \cong \tau_s$) as a Function of Yield Strength (σ_y); [Method 1]. To calculate σ_y by this method, its value must be determined for a given temperature (in our case, at room temperature). Since $P_y = \sigma_y$ were not measured here as a function of temperature, its value may be approximated by a number of different ways: (a) estimated from H_v measured at various temperatures (literature data), (b) extrapolated from high temperature τ_s (literature) data down to room temperature, or (c) calculated from known τ_y values using the Tresca Yield Criterion. All of these approaches are followed here to determine which involves the least error. Finally, the best P_y is selected for each material combination, multiplied by the average, (3-cycles) f_k data obtained by SEM tribometry, to yield the results by Method 1.

Using the H_v of various materials, P_y was estimated in (254) by the following approximations (see Figure 201):

- Brittle Materials ——> $P_y = H_v/35$
- Ductile Materials ——> $P_y = H_v/3$

The problem with approximating P_y with these simple formulae lies in the uncertainties of determining whether a material of interest is brittle or ductile at a given temperature. Along these lines, it was reported in (255) that both CaF_2 and BaF_2 undergo a brittle-to-ductile transition between 100° and 400°C, depending on the strain rate. In order to apply either approximation in Figure 201 it is indeed essential to know if a material is brittle or ductile at a specific temperature of interest. H_v data are available for both CaF_2 and BaF_2, from room temperature to 800°C (Figure 202). Temperature-dependent σ_y values could be found for CaF_2 only (Figure 203). The graph of the H_v vs. σ_y of CaF_2 in Figure 204 clearly shows that neither of the "rule-of-thumb" approximations is valid, because the true CaF_2 yield points fall between the linear brittle and the ductile functions. Surprisingly, at the elevated temperatures the behavior is more brittle than ductile and as the temperature is reduced, the behavior tends more toward ductile than brittle. Intuitively, one would expect an opposite trend. It is suspected

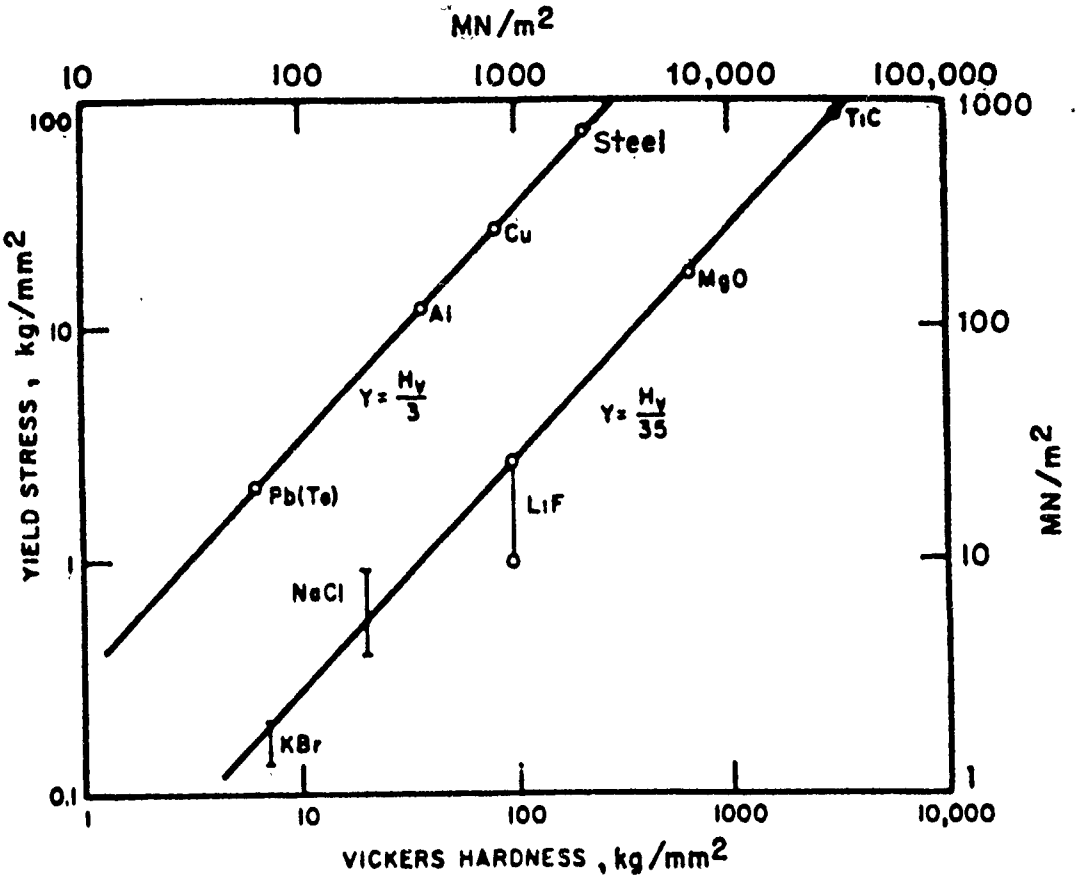

Figure 201. Correlation lines for metals and ionic crystals, relating hardness numbers and yield stresses (254).

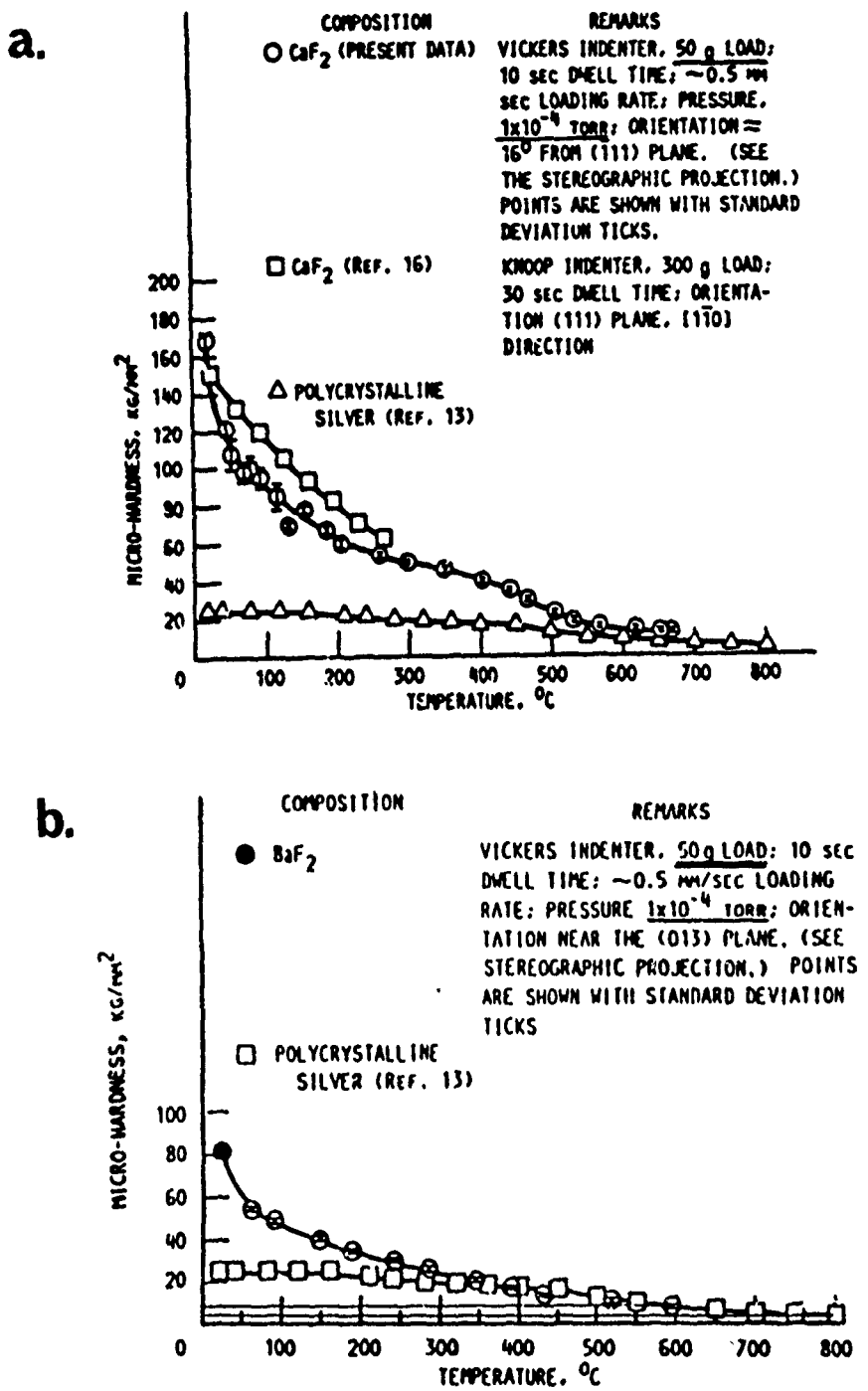

Figure 202. Micro-hardness of XTL (a) CaF_2 and (b) CaF_2, along with poly-XTL silver, as a function of temperature (255).

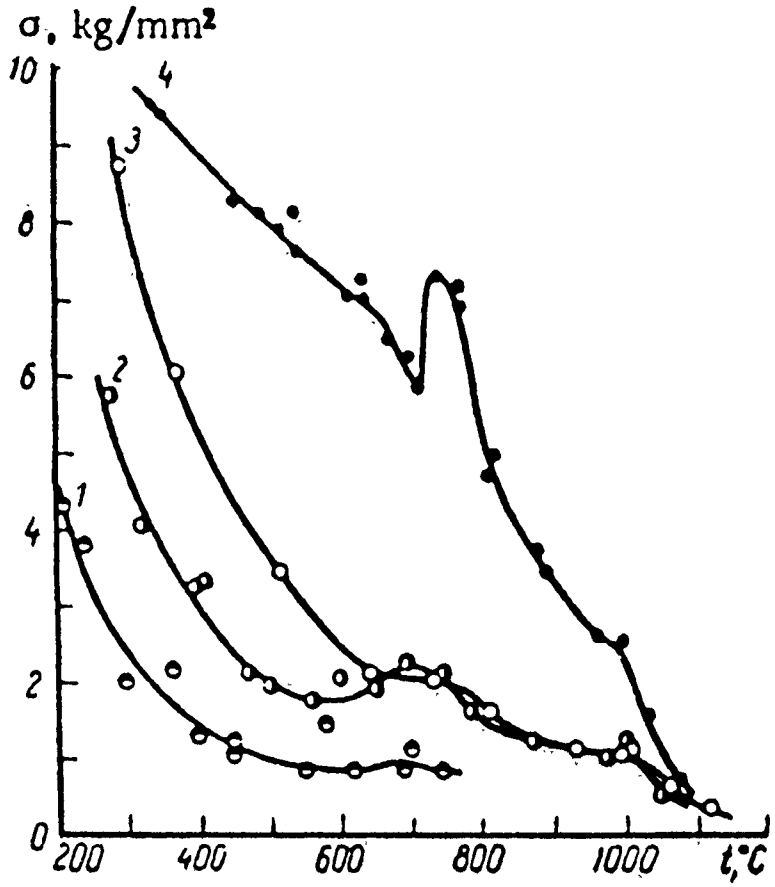

Figure 203. Temperature dependence of yield point of CaF_2 single crystals. 1) natural fluorite, 2,3,4) synthetic fluorite containing Sm^{3+}, Sm^{2+}, and Nd, respectively (256).

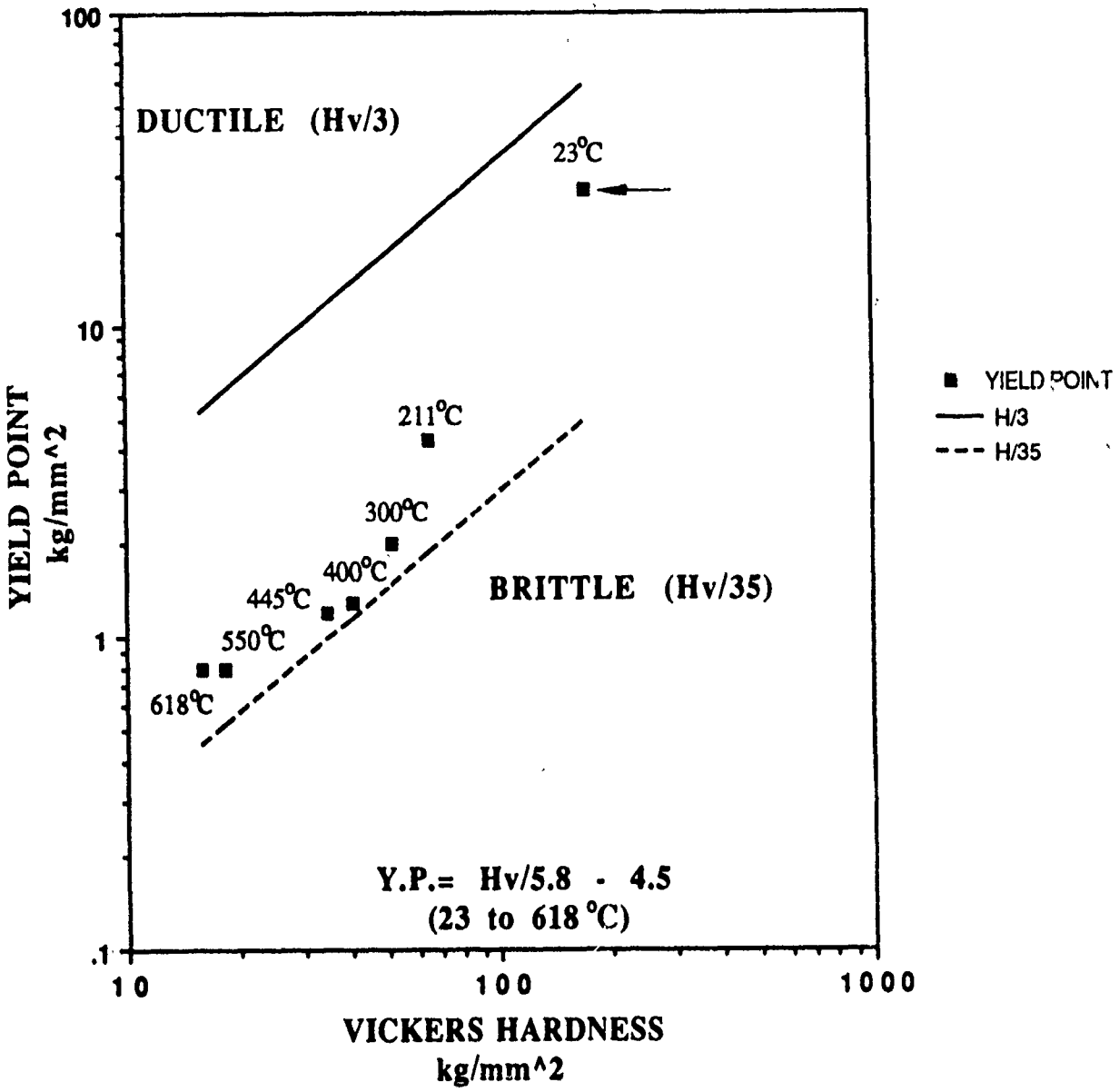

Figure 204. Yield point of single crystal CaF_2 as a function of hardness for various temperatures; after (255 and 256).

that the strain rates associated with the experimental determination of H_v (255) and σ_y (256) may have been different, resulting in this unexpected trend. The unusual nature of this function notwithstanding, it is nevertheless clear that neither $H_v/35$ or $H_v/3$ truly represent the yield strength behavior of CaF_2 in the range of 200° to 700°C (ignoring the 23°C data point marked with the arrow, for the moment). Fitting the data points ranging from 211° to 618°C to a straight line (excluding the 23°C point), the relationship can be best expressed as:

$$\sigma_y = P_y = \frac{H_v}{16} - 0.61$$

Since a room temperature value for σ_y (CaF_2) was not available in Figure 203, it had to be approximated in two successive steps. The description of these steps will follow here, explaining the rationale behind the room temperature value plotted in Figure 204 (see arrow). The "overall-best" yield point equation is also presented in Figure 204, now including that 23°C data point:

$$\sigma_y = P_y = \frac{H_v}{5.8} - 4.5$$

The above relationship is now fully representative of the H_v vs. σ_y function for the entire temperature range of 23° to 618°C. The two-step estimation method for the 23°C (R.T.) yield point (σ_y) is described below.

3.4.1.4.1.1 Step 1: R.T. Yield Point (σ_y) Based on the Tresca Yield Criterion. In addition to the data in Figure 203, τ_{cr} ($\equiv\tau_y$) values at R.T. were uncovered in the literature, for both CaF_2 (70 MPa) and BaF_2 (35 MPa), see (257) . Inasmuch as in this reference the R.T. CaF_2 value was extrapolated from Phillips' high temperature data in Figure 205, see (258), the accuracy of the extrapolation was checked, because it seemed too low.

Based on Phillips' paper (258) τ_y of CaF_2 {111} and CaF_2 {110} was best fitted by the equation:

$$\tau_y \ (\equiv \tau_{cr}) = \tau_0 \exp (k/T)$$

Taking τ_y of CaF_2 {111} @ 600°C (873K) = 875 psi and @ 800°C (1073K) = 600 psi from Figure 206, substituting the appropriate values twice into the $\sigma_y = P_y$ relationship and dividing that with the equation above, τ_0 falls out and one can calculate the magnitude of k:

$$\frac{875 \text{ psi}}{600 \text{ psi}} = \exp\left[k\left(\frac{1}{873\text{K}} - \frac{1}{1073\text{K}}\right)\right]$$

$$\underline{\underline{k = 1767.1\text{K}}}$$

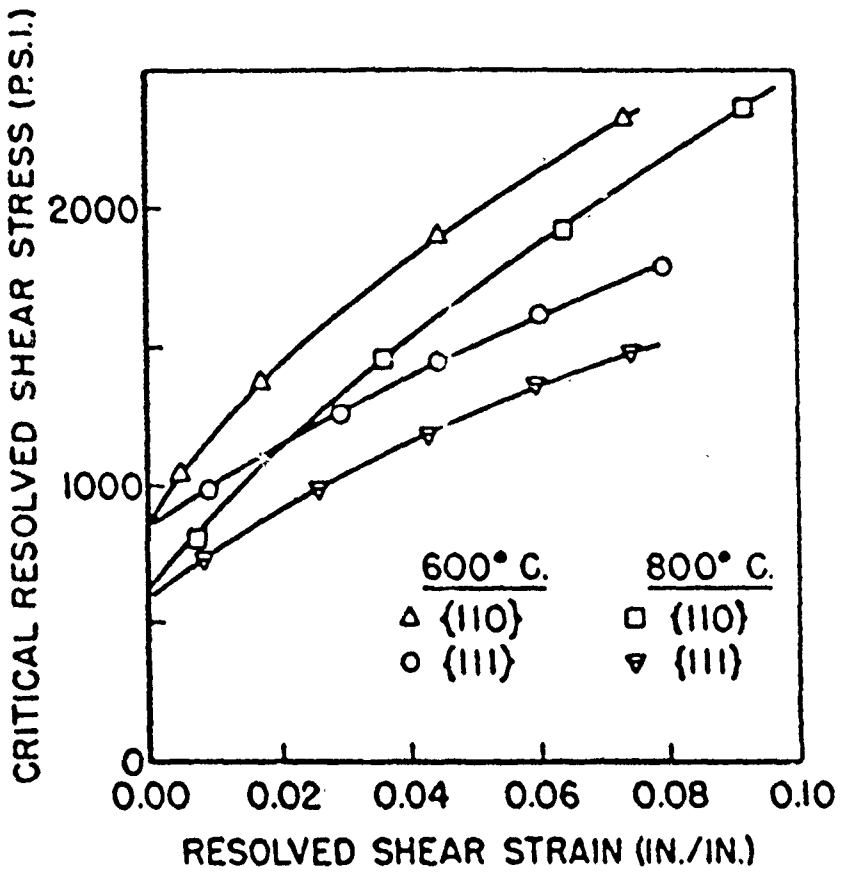

Figure 205. Stress-strain curves of as-cleaved CaF_2 XTL in which the (111) and the (110) planes were normal to the applied compressive stress (258).

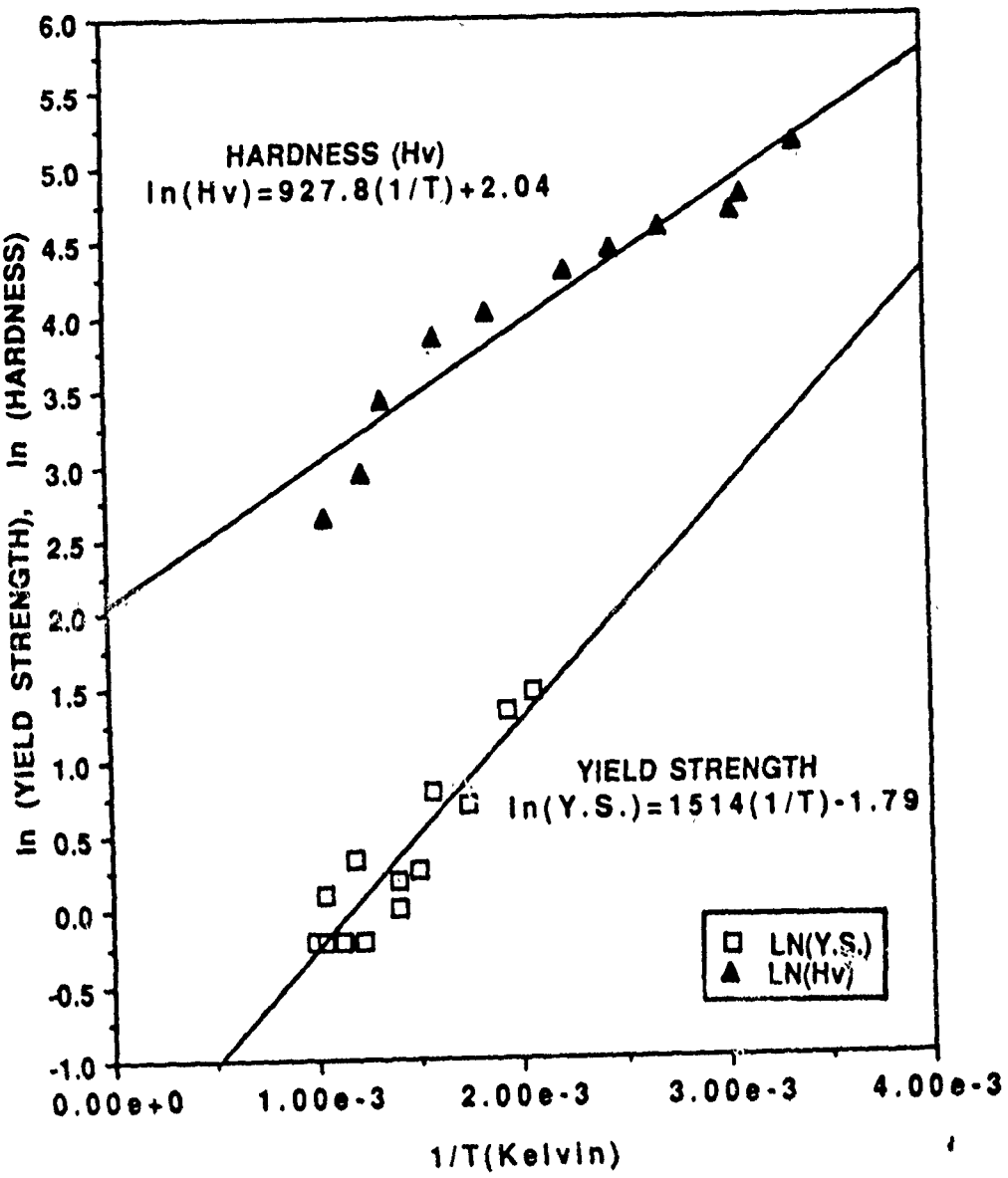

Figure 206. Yield strength and hardness as a function of temperature. The data are estimated to be in the form Y=B exp (k/T) and curve fit by the straight line ln y = ln b + k(1/T).

Substituting $\underline{k}$ into the $\sigma_y = P_y$ relationship again and entering the τ_y value of 875 psi @ 600°C, one can calculate the pre-exponential factor τ_o:

$$875 \text{ psi} = \tau_o \exp\left(\frac{1767.1}{873K}\right)$$

$$\tau_o = \underline{\underline{115.6 \text{ psi} = 0.081 \text{ kg/mm}^2 = 0.794 \text{ MPa}}}$$

Next, the R.T. τ_y of CaF_2 {111} can be calculated, because τ_o is not a function of temperature:

$$\tau_y \text{ [or } \tau_{cr} \{111\}] = 0.794 \exp\left(\frac{1767.1}{298K}\right) = \underline{\underline{300.27 \text{ MPa}}}$$

Clearly, the R.T. τ_y value of CaF_2 (111) obtained by Becher and Freiman (257) as 70 MPa, by extrapolating Phillips' elevated temperature data (258) to R.T., is radically wrong. This incongruity cannot be explained, given the available literature information.

Because the yield point at R.T. is sought, a method was needed next to correlate the state of stress to yielding. The Tresca Yield Criterion was applied here (259) to simply and conservatively calculate σ_y based on τ_y:

$$\tau_y = \frac{(\sigma_{max} - \sigma_{min})}{2}$$

where $\sigma_{max} = \sigma_y$, and $\sigma_{min} = 0$. Therefore,

$$\sigma_y = \underline{\underline{2\tau_y}}$$

The only other method, describing the Von Mises criterion, would be more difficult to apply, with no guarantee of a better approximation (259).

3.4.1.4.1.2 Step 2: Extrapolation of σ_y to R.T.: Based on the above assumption that σ_y is proportional to τ_y, the elevated temperature σ_y data were extrapolation to R.T. by further assuming that the yield point follows the same exponential increase as τ_y:

$$\sigma_y = \sigma_o \exp\left(\frac{k'}{T}\right)$$

This assumption is reasonable, given the shape of Curve No. 1 (for CaF_2) in Figure 203. After digitizing the data from there and fitting them to the σ_y exponential relationship, $\underline{k}' = 1514K$, and $\sigma_o = 0.167\ kg/mm^2 = 1.638$ MPa. Therefore, for CaF_2:

$$\sigma_y\ (R.T.) = 1.638\ MPa\ \exp\left(\frac{1514K}{298K}\right) = 26.86\ kg/mm^2$$

$$= \underline{\underline{263.53\ MPa}}$$

This result was assumed as the best R.T. σ_y data for CaF_2 and thus plotted in Figure 204 (see arrow).

The overall results of σ_y and H_V as a function of temperature can both be estimated in the exponential equation form of $A = B \exp(k/T)$, and curve fit by the straight line $\ln A = \ln B + k(1/T)$, as shown in Figure 206. The resulting linear equations are:

$$\ln H_V = \frac{927.9}{T} + 2.04$$

and

$$\ln \sigma_y = \frac{1514}{T} - 1.79$$

where both H_V and σ_y are in the units of kg/mm^2.

The equivalent values for BaF_2 (111) could not be developed due to the lack of the corresponding literature data. Therefore, the reported (257) $\tau_y = 3.57\ kg/mm^2 = 35$ MPa @ R.T. and the Tresca Yield Criterion were employed to estimate $\sigma_y\ (R.T.) = 7.14\ kg/mm^2 = 70$ MPa.

The corresponding τ_y values of CaF_2 (111), estimated by the fluorides' yield strengths [Method 1] are summarized in Table 35.

3.4.1.4.2 Shear Strength ($\tau_y \cong \tau_s$) as a Function of the Real Area of Contact (A_r); [Method 2]. In any tribological contact, A_r is very difficult to determine, as previously discussed in this report. Consequently, A_r can only be approximated by:

(a) the Hertzian area of contact between the sphere-on-plane combinations, and

(b) the apparent area of contact ($A_{app..}$), as estimated from the dimensions of a measurable wear scar.

Table 35. The shear strength (τ_s) of CaF_2 (111) and BaF_2 (111), as estimated by their yield strength (σ_y) and the equation $\tau_y = f_k \sigma y$.

Pin	Flat	f_k	σ_y kg/mm^2 (MPa)	$\tau_y \cong \tau_s$ kg/mm^2 (MPa)
CaF_2	CaF_2	0.042	26.86 (263.42)(1)	1.13 (11.06)
BaF_2	BaF_2	0.077	7.14 (70.02)(2)(3)	0.55 (5.39)
BaF_2	CaF_2	0.080	7.14 (70.02)(2)	0.57 (5.60)

(1)Extrapolated from (256).
(2)Tresca Yield Criterion applied to (257).
(3)The yield strength of the weakest (i.e., BaF_2) material was used in the calculations

In view of the fact that the only wear scar on a triboflat observable even under high (5000X) SEM magnifications was associated with the BaF_2 pins vs. CaF_2 flat combination (see Figure 200), that was the only case where $A_{app.}$ could be estimated as 8.73×10^{-4} mm^2.

The Hertzian contact areas for all three sliding combinations were calculated by the well-known relationships of the Hertz theory:

$$a = [(3/4)\pi \cdot P (K_1 + K_2) R]^{1/3}$$

where $K_1 = \frac{1 - \nu_1^2}{E_1}$ and $K_2 = \frac{1 - \nu_2^2}{E_2}$, and

$$q_o = \frac{3}{2} \cdot \frac{P}{\pi \cdot a^2} = \frac{3}{2} \cdot \frac{P}{A}$$

where $A = \pi \cdot a^2$ (the Hertzian area of contact).

Having found the Young's Modulus (E) values for both CaF_2 and BaF_2 normal to the (111) faces in (26), with $E(CaF_2) = 114 \times 10^9$ N/m^2 and $E(BaF_2) = 65.2 \times 10^9$ N/m^2, assuming ν as 0.3 for both materials, using the experimental normal load = 6g = 0.059 N and the measured friction forces (F_k), the corresponding τ_y data are presented in Table 36.

Comparing the results from Tables 35 and 36, the best agreement is found with the hard versus hard (CaF_2 vs CaF_2) combination. In all other cases the $A_{app.}$ - estimated τy values were about one to three-times higher than those estimated by the respective yield strengths. The average values of $\tau_y \cong 1($ MPa for all combinations indicate that the shear strengths of CaF_2 and BaF_2 are equivalent to that of sputtered MoS_2 films at room temperature, in vacuum (τ_s = 10 to 20 MPa). Inasmuch as the sulfur-terminated, inert basal (0001) plane of MoS_2 exhibits a calculated surface energy of only 260 ± 20 dynes/cm (261),

Table 36. The shear strength (τ_s) of CaF_2 (111) and BaF_2 (111), as estimated by their Hertzian/ apparent areas ($A_r/A_{app.}$) of contact and the equation $\tau_y = F_k/A_r$.

Pin	Flat	q_o (MPa)	F_k (kg)	A_r (m^2)	$\tau_y \equiv \tau_s$ Kg/mm^2 (MPa)
CaF_2	CaF_2	354.4	0.26×10^{-3}	2.50×10^{-10}	1.04 (10.21)
BaF_2	BaF_2	286.8	0.52×10^{-3}	3.62×10^{-10}	1.44 (14.07)
BaF_2	CaF_2	244.2	0.52×10^{-3}	3.09×10^{-10}	1.68 (16.52) 0.78 (7.67)*

*From measured wear scar width in Figure 200:

$$A_{app.} = 8.73 \times 10^{-4}\ mm^2$$

$$\tau_s\ (app.) = \frac{0.52 \times 10^{-3}\ kg}{8.73 \times 10^{-4}\ mm^2} = 0.60\ \frac{kg}{mm^2} = 5.84\ MPa$$

but the experimental/theoretical surface energy of CaF_2 (111) is is in the 450 to 550 dynes/cm range (34, 260), the SEM tribometer-generated $\tau_y \equiv \tau_s$ values of the fluorides are somewhat lower than expected. The fact that the shear modulus (C_{44}) of MoS_2 is only 18.9 GPa (262) compared to that of C_{44} (CaF_2) = 33.6 GPa (263) seems to corroborate this concern. It may be argued the amorphization of the reused pin tip or possible damage by the 5 keV SEM e-beam (264) may have influenced the results. The data in Figure 197, however, shows little change in f_k with the number of traverses in the 3-cycle tests. Moreover, the surface blistering on BaF_2 attributed to e-beam damage in (264) could not be seen on any portion of the SEM triboflat, rubbed or unused. It is more likely that the many assumptions taken during estimating the stress-strain parameters rendered the approximations somewhat less than accurate.

The possible discrepancy with the absolute magnitude of the fluoride τ_y values notwithstanding, it is of interest to compare these values with the respective shear moduli G ($\cong C_{44}$). Since C_{44} (CaF_2) = 33.6 GPa, see (263) and C_{44} (BaF_2) = 25.7 GPa, see (265), it can be observed that the mechanical behavior of these ionic crystals falls between that of metals and covalently bonded solids (e.g., diamond, Si or Ge). Inducing plastic deformation in covalent crystals, rather than fracture, is more difficult than in most ionic and all metallic solid matter. The pronounced directionality of the covalent bond leads to high Peierls stresses, which resist dislocation motion. This, in turn, leads to the typically low fracture toughness of covalently bonded ceramics, such as Si, Ge, SiC, Si_3N_4 or even diamond. The τ_{cr} of covalent single crystal cleavage planes are likely to be in the region of 10^{-2} G (where G is the bulk shear modulus), rather than in the 10^{-5} G characteristic to metals (266). In the case of the alkaline earth fluorides measured here, the τ_y/τ_{cr} (CaF_2 and BaF_2) appear to be in the 10^{-3} to 10^{-4} G range.

Finally, it should be reiterated that the best method(s) of estimation of the τ_y values presented here have taken the following assumptions into account:

- Ploughing of the pin into the flat was negligible; adhesive forces at the sliding interface were thus dominant.
- The yield strength (σ_y), shear strength (τ_s)and hardness (H_v) are isotropic. Because of this assumption, $\tau_y \cong \tau_s$. They can be expressed as a function of temperature by $A = B \exp(k/T)$, where T is the temperature in Kelvin.
- The Tresca Yield Criterion is valid, i.e., $\sigma_{min} = 0$ and $\sigma_{max} = \sigma_y$, due to its simple and conservative nature.
- The dynamic contact area is equal to the static contact area.
- The real area of contact (A_r) is best approximated by the Hertzian sphere-on-plane contact area, but might be measured from SEM photomicrographs, but only where a wear scar was visible under high magnifications.

The data indicated a $\tau_y \cong \tau_s$ value close to 10 MPa for all fluoride combinations, a value equivalent to the τ_s of sputtered MoS_2 films in vacuum. Although the 10 MPa value is somewhat lower than expected from surface energy considerations in the absolute sense, the relatively low value is attributed to the fluorine-terminated, nonpolar nature of the (111) fluoride cleavage planes and, possibly, to the degrees of error in the assumptions used during the calculations. The mechanical behavior of the fluorides appears to fall between that of covalent solids and metals.

The experiments described in this report represent the first attempt to compare microscopic tribometry data of $\tau_y \cong \tau_s$ with critical resolved shear stress (τ_{cr}) values generated by conventional, compressive strength-type tests and by MD calculations. Such τ_{cr} tests are normally performed with oriented XTL boules compressed or pulled apart in mechanical property testers, such as the well-known Instron apparatus. Comparing τ_y with τ_{cr} here is only an approximation, because no given shear plane's displacement is clearly "resolved" during macroscopic tangential sliding, between the specimens of a friction and wear tester. The degree of characteristic error associated with this measurement technique was minimized by employing the lowest reliable load and speed of the SEM tribometer, and by careful preparation of the (111)[1$\bar{1}$0] sliding surfaces.

3.4.2 Surface Shear Strength of Commercial Purity CaF_2 (111) and BaF_2 (111) Single Crystal Surfaces Against (0001) Sapphire in a Wide Environmental Regime, by SEM Tribometry.

For the past decades, Harold E. Sliney of NASA-LeRC has pioneered the use of both CaF_2 and BaF_2, as well as their eutectic composition as wide temperature range lubricants, which can be operated in a variety of atmospheres (255). It was, therefore, of interest to investigate the fundamentals of high temperature tribological behavior of commercial-purity CaF_2 and BaF_2 XTLs both in vacuum and in 13.3 Pa P_{air}, employing the SEM tribometer.

SEM triboflats cut and polished from commercially-grown XTL boules of the respective alkaline earth fluorides were procured from Atomergic Chemetals Corp., Plainview, NY. The sliding surface (the 5 mm x 7 mm plane) was specified to be the (111) plane. No particular crystallographic sliding direction was requested. At elevated temperatures, the anticipated heavy interaction of a large number of slip systems (leading to high ductility and malleability) did not warrant the time-of-preparation and costs involved in obtaining ultrapure and ultra-precisely aligned specimens similar to the ones used in the room temperature study described in 3.4.1.

Laue X-ray-diffraction of the CaF_2 and BaF_2 triboflats indicated that the CaF_2 sample's sliding surface was 15° off the (111) plane, with the sliding direction(s) in the $[10\bar{1}]/[11\bar{2}]$ while the BaF_2's alignment was a perfect (111) $[01\bar{1}]/[0\bar{1}1]$. The counterface in each case was a 90° XTL sapphire pin, i.e., the (0001) basal plane of sapphire was parallel with the plane of sliding (see Figure 17).

The SEM tribotests were performed under near-standard PV conditions (P = 50g = 0.49N; V = 20 cpm = 2.33 mm•s^{-1}) in 1.33 x 10^{-3} Pa (1 x 10^{-5} torr) or in 13.3 Pa = 0.1 torr P_{air}. The thermal cycles to which the various alkaline earth fluoride triboflats were exposed represented the usual up-and-down ramping of the temperature. The main goal was to reveal some manifestation of a brittle-to-ductile transition, as influenced by the possibility of CS plane formation. It was demonstrated by Hyde (267), see Figure 207, that Magnèli phases can be generated in CaF_2 also. Furthermore, we wanted to compare the τ_{cr} of {111} and {110} CaF_2 at 600° and 800° (Figure 205) with the τ_s estimated from the experimental friction forces and from the calculated $\sigma_y = P_y$ of our specimens, at the same temperatures.

The COF data on CaF_2 are given in Figures 208 and 209. The data indicate that:

1. The undulating COF on heating is very similar to those of XTL rutile in Figure 165. While the periodic variations in friction, by themselves, are no positive proof of CS planes-caused τ_s changes, this phenomenon bears future attention.

2. There appears to be little, if any, difference in friction behavior as a function of the presence or absence of the SEM beam rastering the sliding surfaces of CaF_2 in vacuum. The electron beam damage, therefore, appears to be negligible compared to the damage to the XTL by the rubbing action itself. However, the initial increase in COF, which did not manifest itself until ~200°C under no imaging, did occur faster and at a lower temperature during the imaging test. This would happen if the e-beam assisted in the removal of fluorine ions from the lattice and cooperated with mechanical action to soften the near-surface layer by Magnèli phase(s) generation, and to increase the real area of contact by the gradual penetration of the pin. The increase of A_r was indeed commensurate with the initial increase in COF. This phenomenon was even more pronounced with the (softer) BaF_2 specimen, as discussed later in this section.

3. There is hysteresis in the COF values at 600° and 800°C, on heat-up (↑) and cool-down (↓). This anomaly may be further proof of CS plane formation, alteration and regeneration.

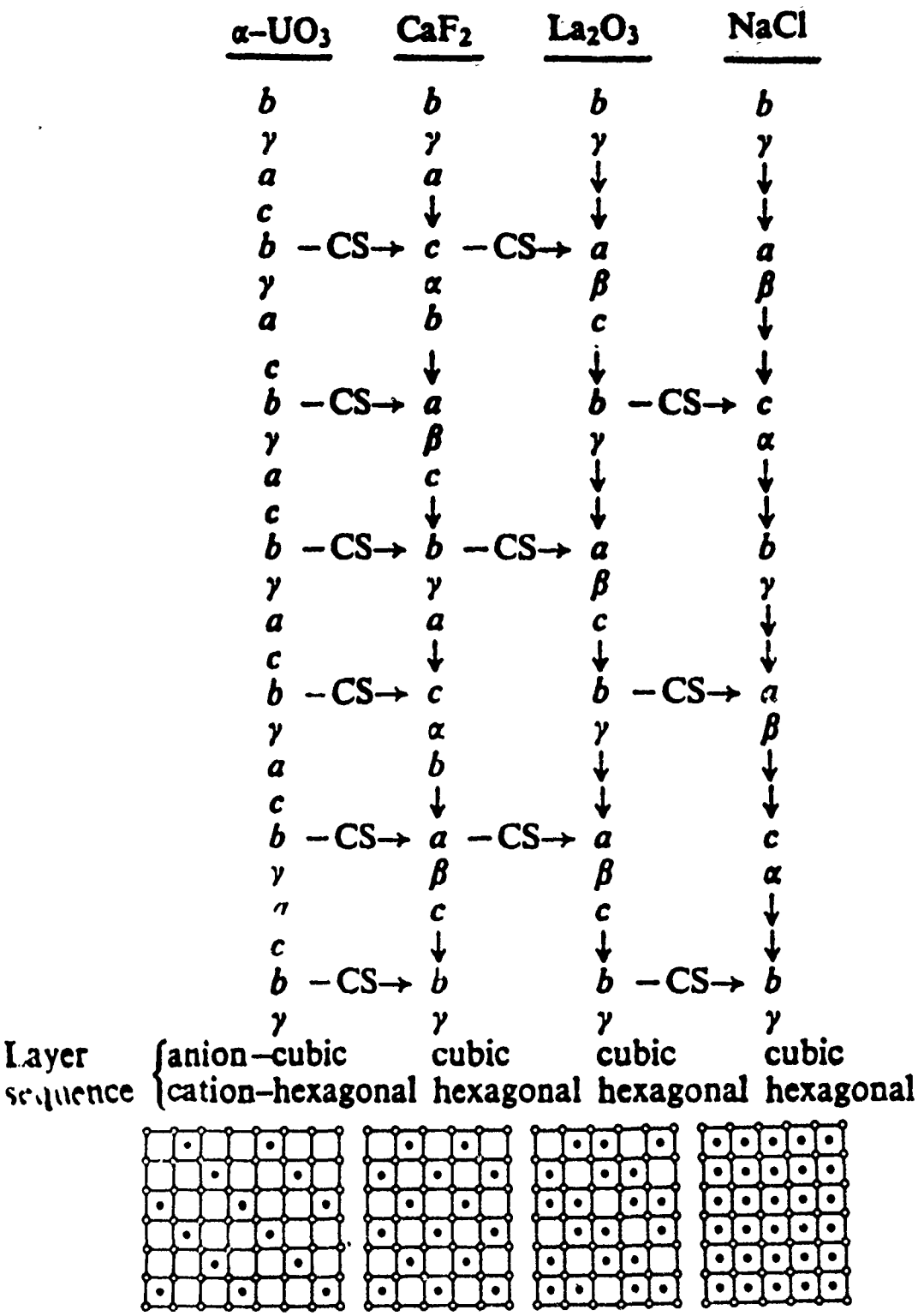
α-UO3
CaF2
La2O3
NaCl
b γ a c b γ a c b γ a c

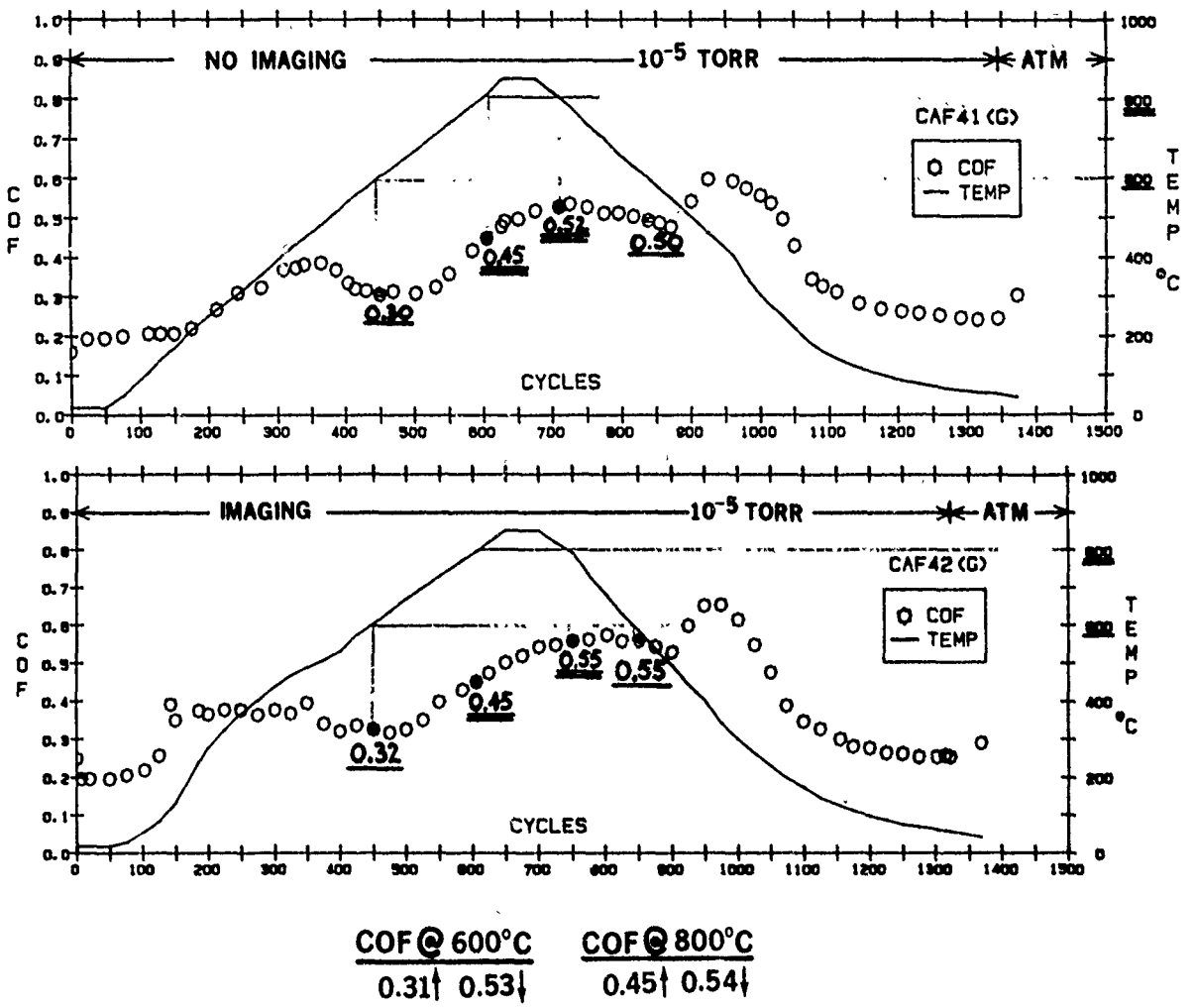

Figure 208. The coefficients of friction (COF) of CaF_2 (15° off 111) [10$\bar{1}$/11$\bar{2}$] in vacuum (1.33 x 10^{-3} Pa = 1 x 10^{-5} torr), with or without impingement of the imaging SEM beam, at various temperatures (90° XTL sapphire pin).

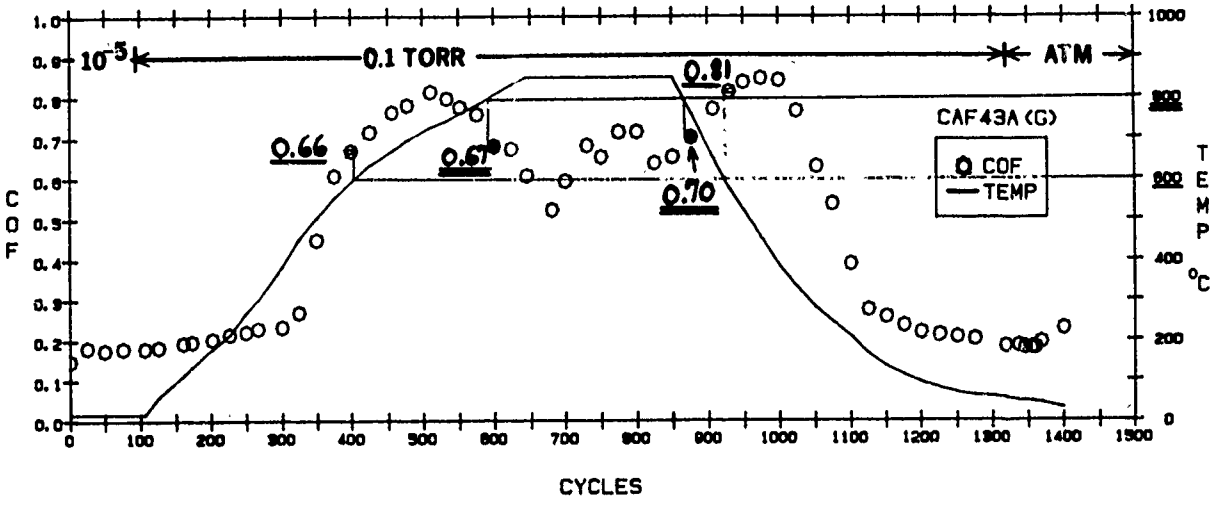

COF @ 600 °C = 0.66↑; 0.81↓

COF @ 800 °C = 0.67↑; 0.70↓

Figure 209. The coefficients of friction (COF) of CaF_2 (15° off 111) [10$\bar{1}$/11$\bar{2}$] in P_{air} (13.3 Pa = 0.1 torr) at various temperatures; SEM beam on (90 XTL sapphire pin).

4. The far higher COF of CaF_2 in P_{air} (as compared to those in vacuum) cannot be attributed to a simple increase in A_r. As shown in the photomicrographs in Figure 210, the final wear track of the P_{air} test was, in fact, narrower than those of the vacuum test run under otherwise identical conditions. It is well-known that CaF_2 and BaF_2 react with oxygen and/or moisture to form the repective harder and more abrasive oxides and fluorine gas. The oxides have much higher shear strength and hardness than the fluorides. In the present case (since $f_k = \tau_s/P_y$), the increase in f_k indicates that the rate of increase in τ_s of the surface layer was higher than the commensurate rate of subsurface hardening due to oxidation.

The equivalent COF charts for the BaF_2 tests are enclosed in Figures 211 and 212:

1. The friction undulations occurred here also.
2. Although there were some differences in the image/no-image vacuum COF charts, the general levels of friction remained approximately the same. Note that the sudden increase in the friction force immediately at the onset of R.T. sliding, both in vacuum and in P_{air}, was accompanied by a simultaneous and equally sudden increase in the widths of the wear track (See Figure 213). The equation $F_k = \tau_s \cdot A_r$ clearly explains this phenomenon. Due to the softer nature of BaF_2, this friction and A_r increase with BaF_2 was significantly more pronounced than with the CaF_2 specimen.
3. There is a COF hysteresis with BaF_2 also, both at 600° and 800°C, on up-and-down ramping of the temperature (Magnèli phase formation?).
4. No significant changes in the general level of COF from vacuum to P_{air} and no observable differences in the vacuum/P_{air} track widths in Figure 214 indicate greater tribo-oxidative stability on the part of BaF_2 than CaF_2. As shown by the free energy of oxidation of the respective reactions in Table 37 the more stable product (BaF_2) has a more positive ΔG°_f at the temperatures of interest (268).

The τ_s data, calculated from the experimental F_k and from the uncorrected, rough estimate of $P_y = H_v/3$ compared with the $P_y \cong \sigma_y$ corrected per Figure 206 (i.e., $P_y = P_{y0}e^{k/l}$), are listed in Table 38. The uncorrected (U) and corrected (C) data indicate the following:

1. Not using the corrected P_y equation for CaF_2 leads to a larger error in τ_s. Although an equivalent equation is not available for BaF_2, the trend there should also be the same.
2. The τ_s of CaF_2 is always higher on heat-up ($\uparrow$) than on cool-down ($\downarrow$), at both test temperatures and in both atmospheric environments. This phenomenon is also attributed to possible Magnèli phase formation. The BaF_2 material does not follow the same trend, and the ($\uparrow$)/($\downarrow$) values are much closer together than those of the CaF_2.
3. The τ_s increase on oxidation of CaF_2 is greater than on oxidation of BaF_2.
4. Since we do not have any data on the strain and strain rate of the sheared CaF_2/BaF_2 surfaces, one cannot reliably compare the τ_{cr} values for CaF_2 in Figure 205 with the τ_s values for CaF_2 in Table 38. The data are, however, within the same order-of-magnitude range.

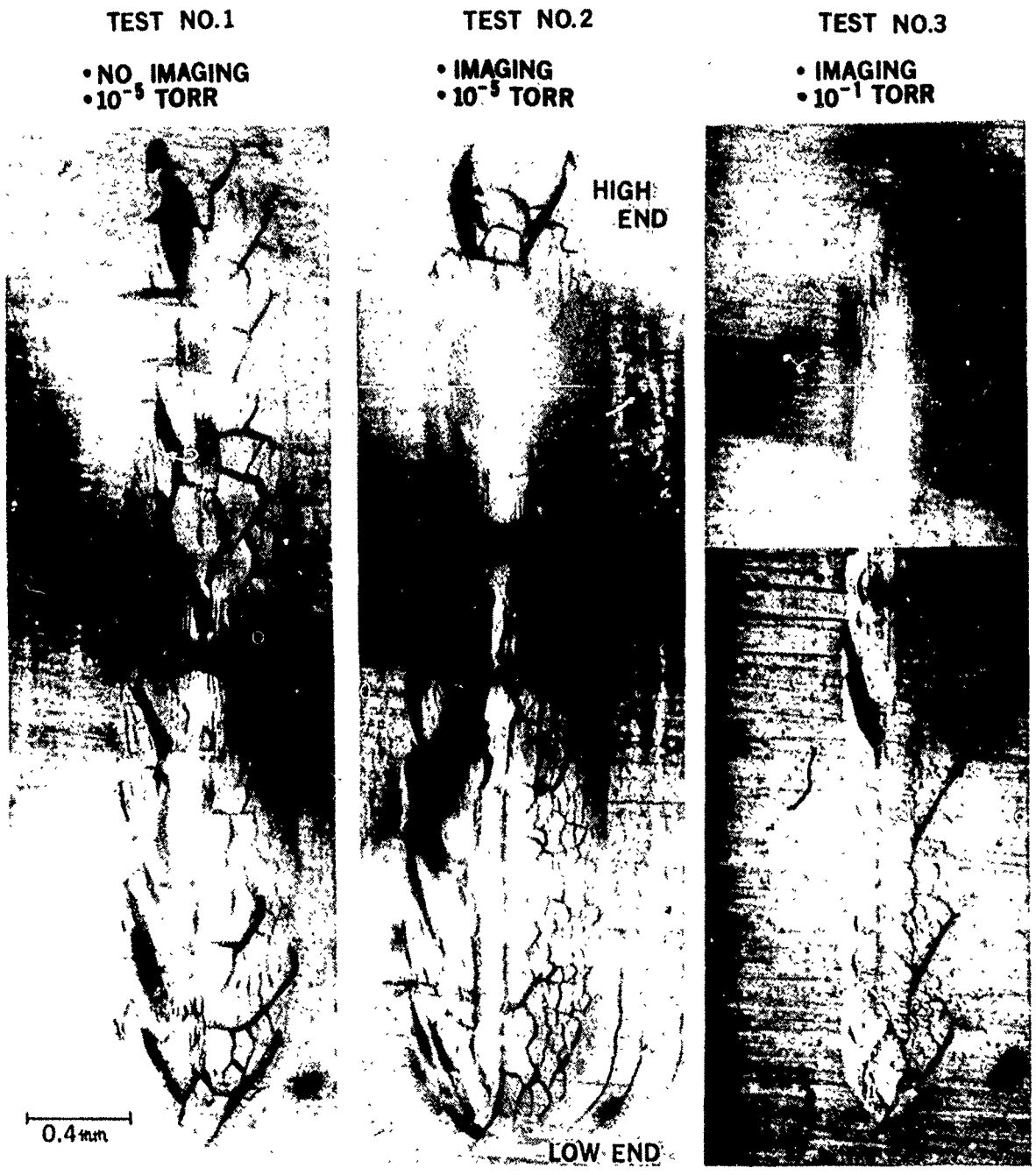

Figure 210. Optical photomicrographs of the CaF_2 wear tracks associated with the tests described in Figures 208 and 209.

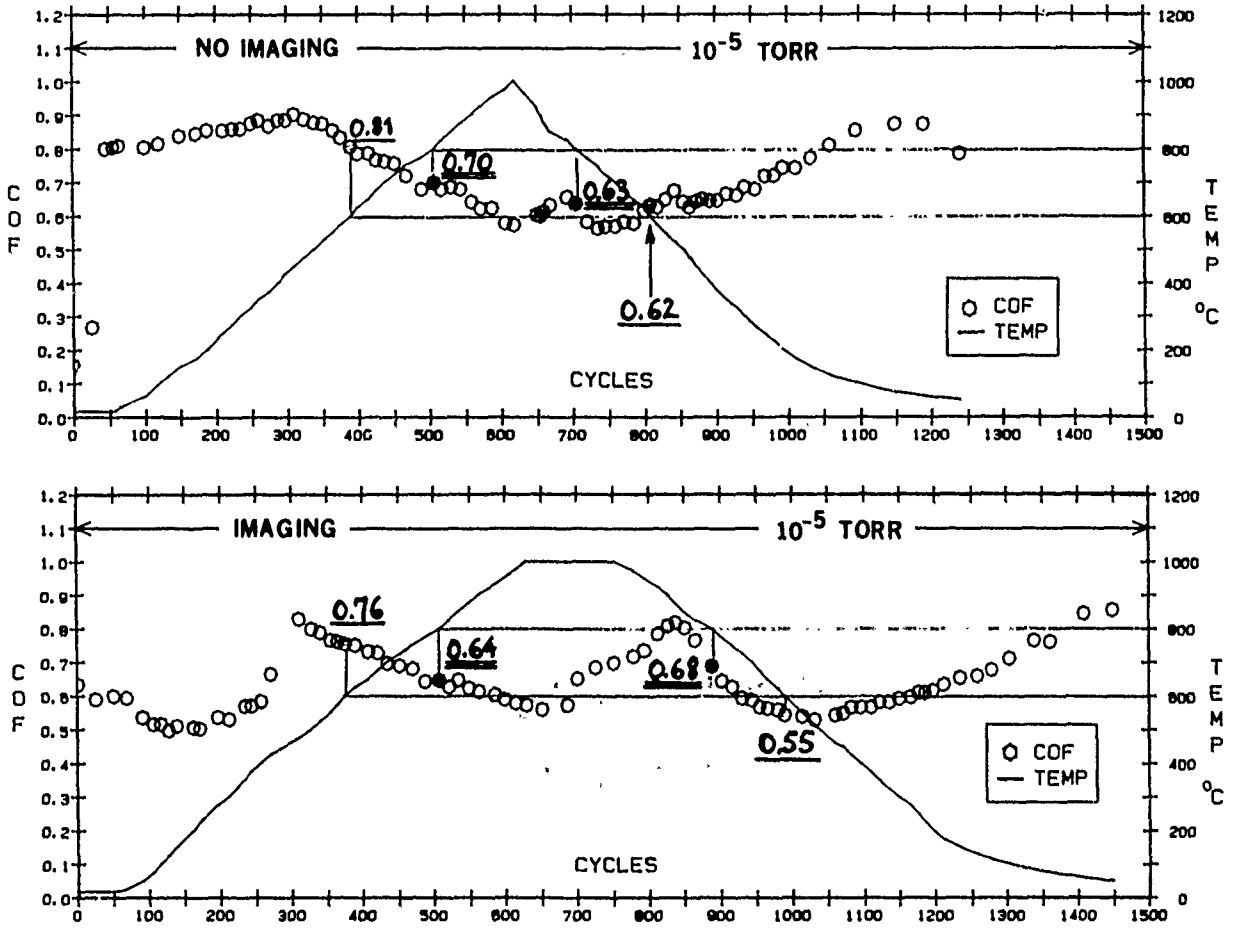

COF@ 600°C		COF@ 800°C	
0.79↑	0.59↓	0.67↑	0.66↓

Figure 211. The coefficients of friction (COF) of BaF_2 (111) [01$\bar{1}$/01$\bar{1}$] in vacuum (1.33 x 10^{-3} Pa = 1 x 10^{-5} torr), with or without impingement of the imaging SEM beam, at various temperatures (90° XTL sapphire pin).

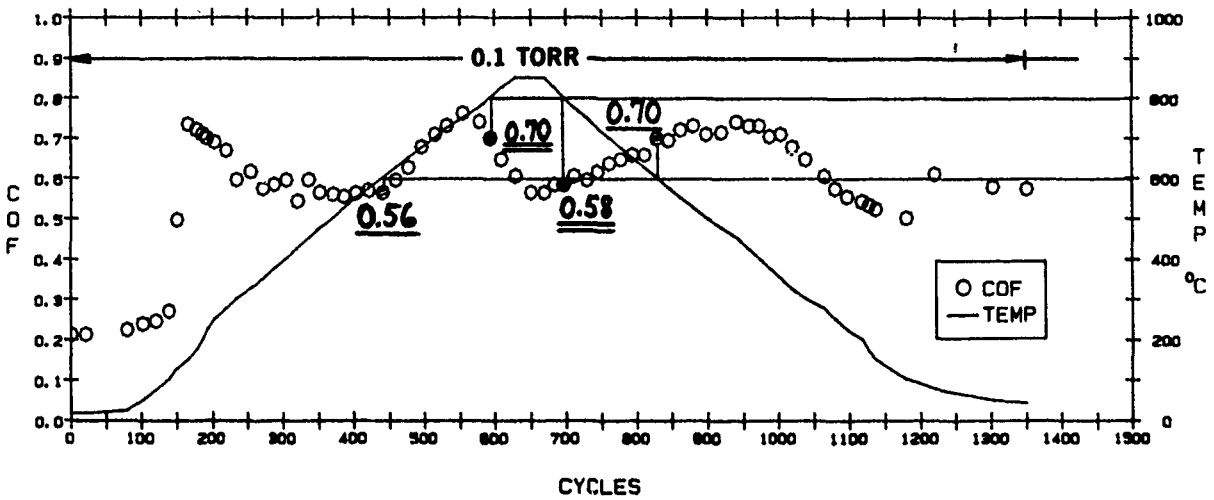

COF@ 600°C = 0.56↑; 0.70↓

COF@ 800°C = 0.70↑; 0.58↓

Figure 212. The coefficients of friction (COF) of BaF_2 (111) [01$\bar{1}$/01$\bar{1}$] in P_{air} (13.3 Pa = 0.1 torr) at various temperatures; SEM beam on (90° XTL sapphire pin).

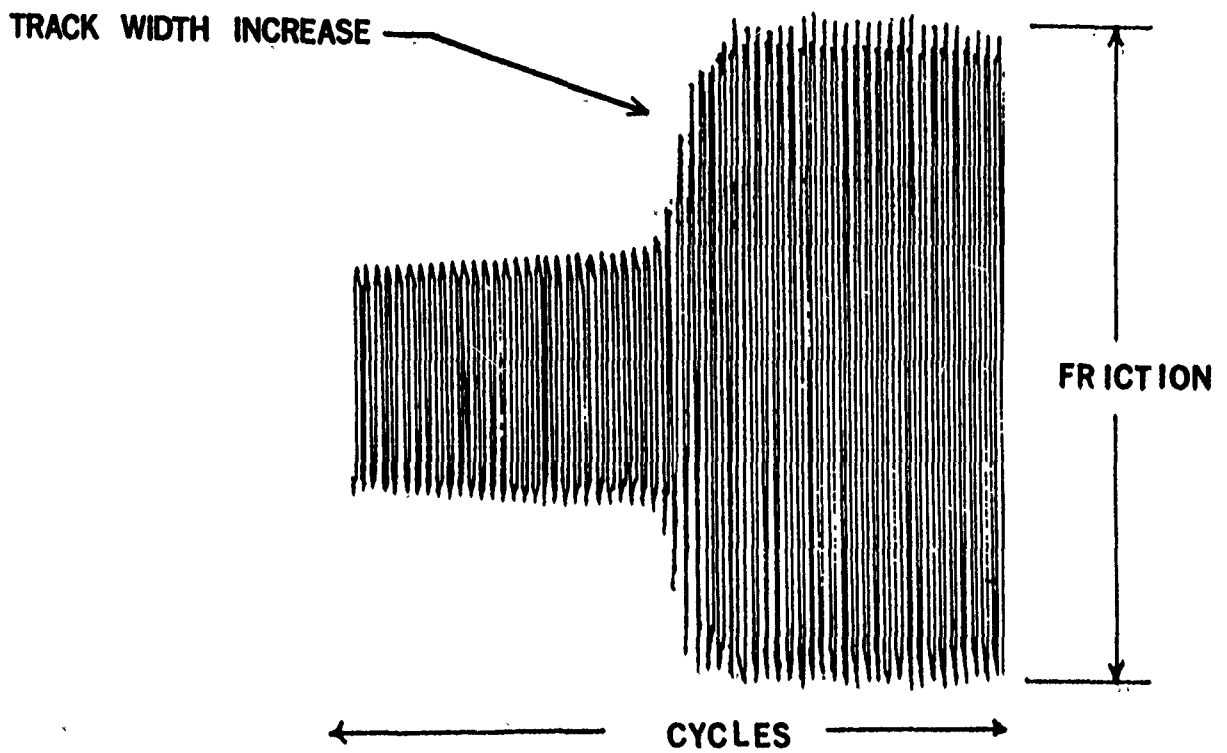

Figure 213. The effect of wear track width on the coefficients of friction (COF) of BaF_2, during the tests described in Figures 211 and 212.

Figure 214. Optical photomicrographs of the BaF_2 wear tracks formed during the imaged vacuum and P_{air} tests described in Figures 211 and 212.

Table 37. Selected thermodynamic data on the oxidation of CaF_2 and BaF_2, after (268).

	MELTING POINT (°C)	REACTION TEMPERATURE (K)	STANDARD FREE ENERGY OF REACTION, ΔG_f^o (kcal / mole)	EQUILIBRIUM CONSTANT, K_{eq}
CaF_2	1360	500 1000 5000	+131 +123 +114	10^{-57} 2×10^{-27} 3×10^{-17}
BaF_2	1280	500 1000 1500	+144 +135 +128	3×10^{-63} 5×10^{-30} 3×10^{-19}

Table 38. SEM tribometer-measured surface shear strength of CaF_2 and BaF_2 as a function of temperature and atmosphere, using uncorrected (U) and corrected (C) values of P_y in estimating $\tau_s = f_k \cdot P_y$.

XTL	TEMP. (°C)		τ_s (kg . mm^{-2}) IN VACUUM	τ_s (kg . mm^{-2}) IN P_{air}
CaF_2	600°	U	1.80 ↑ ; 3.10 ↓	3.92 ↑ ; 4.81 ↓
		C	0.35 ↑ 0.47 ↓	0.62 ↑ 0.77 ↓
	800°	U	1.50 ↑ ; 1.80 ↓	2.23 ↑ ; 2.33 ↓
		C	0.31 ↑ 0.35 ↓	0.45 ↑ 0.47 ↓
BaF_2	600°	U	2.50 ↑ ; 1.87 ↓	1.78 ↑ ; 2.22 ↓
		C	— —	— —
	800°	U	0.94 ↑ ; 0.92 ↓	0.98 ↑ ; 0.81 ↓
		C	— —	— —

5. The tribotest-indicated brittle-to-ductile transitions are way below the 500° to 600°C temperatures reported by Sliney (255).

Some of these data shed light to research results generated at Hughes over 15 years ago, evaluating a CaF_2/BaF_2 eutectic- containing porous nichrome composite for use at 850°C, in helium (269). There, a time-dependent compositional change (i.e., BaF_2 -enrichment) of the repeatedly rubbed eutectic occurred, tentatively attributed to a preferential fragmentation within the (softer) BaF_2 phase. The present results corroborate the postulate in (269), in view of preferred shear in the much lower τ_s BaF_2.

The higher oxidative stability and lower τ_s of BaF_2 indicate that this lubricant may be the material of choice for high temperature lubrication of assemblies, for air applications.

3.5 THE TRIBOLOGICAL BEHAVIOR OF POLYCRYSTALLINE, CVD DIAMOND FILMS

3.5.1 Environmental and Purity Effects

Under contract to Hughes as of June 1987, for the following two years Crystallume researchers (Menlo Park, CA) were depositing thin, polycrystalline diamond films on B-doped (electronic grade) silicon wafers and on α/β-SiC specimens. The initial efforts (see APPENDIX BB) dealt with films in the 100 to 500 nm thickness range switching to thicker films later, correlating CVD deposition parameters with film crystal structure, homogeneity, purity and adhesion. Crystallume's in-house characterization included scanning electron microscopy (SEM), Raman spectroscopy and microhardness measurements. Hughes evaluated the diamond films in the SEM tribometer using the general methodology described previously in this report and by other techniques [such as Fourier Transform Infrared (FTIR) spectroscopy for hydrocarbon contamination]. The details are presented below.

3.5.1.1 Diamond-on-Si(100). A total of nine deposition runs were completed with Si(100) wafers as a substrate. During the first five, the synthesis of ~100 nm thick films was attempted on p-type (B-doped), (100) silicon XTL, producing material which consisted of islands of nuclei, which did not coalesce into continuous diamond films. During the next four depositions 500 nm thick films were tried on the same type of substrate with greater success. On the whole, the films were more continuous. They resisted room temperature HNO_3/HF etch, a rapid and effective means of locating pinholes as little as 1 μm in diameter. Some areas, however, suffered delamination, as indicated by visual inspection and manual scratching.

Two of the 10 cm (4 in.) dia. silicon wafers of the last series of runs, designated as EASI-20-K and EASI-36-I, were diced into SEM-triboflat -sized samples (7 mm x 5 mm) and mapped as shown in Figure 215. Those areas which contained poorly adhering film portions were not forwarded to Hughes.

The detail of the deposition and a more thorough account of the analyses are attached in APPENDIX BB.

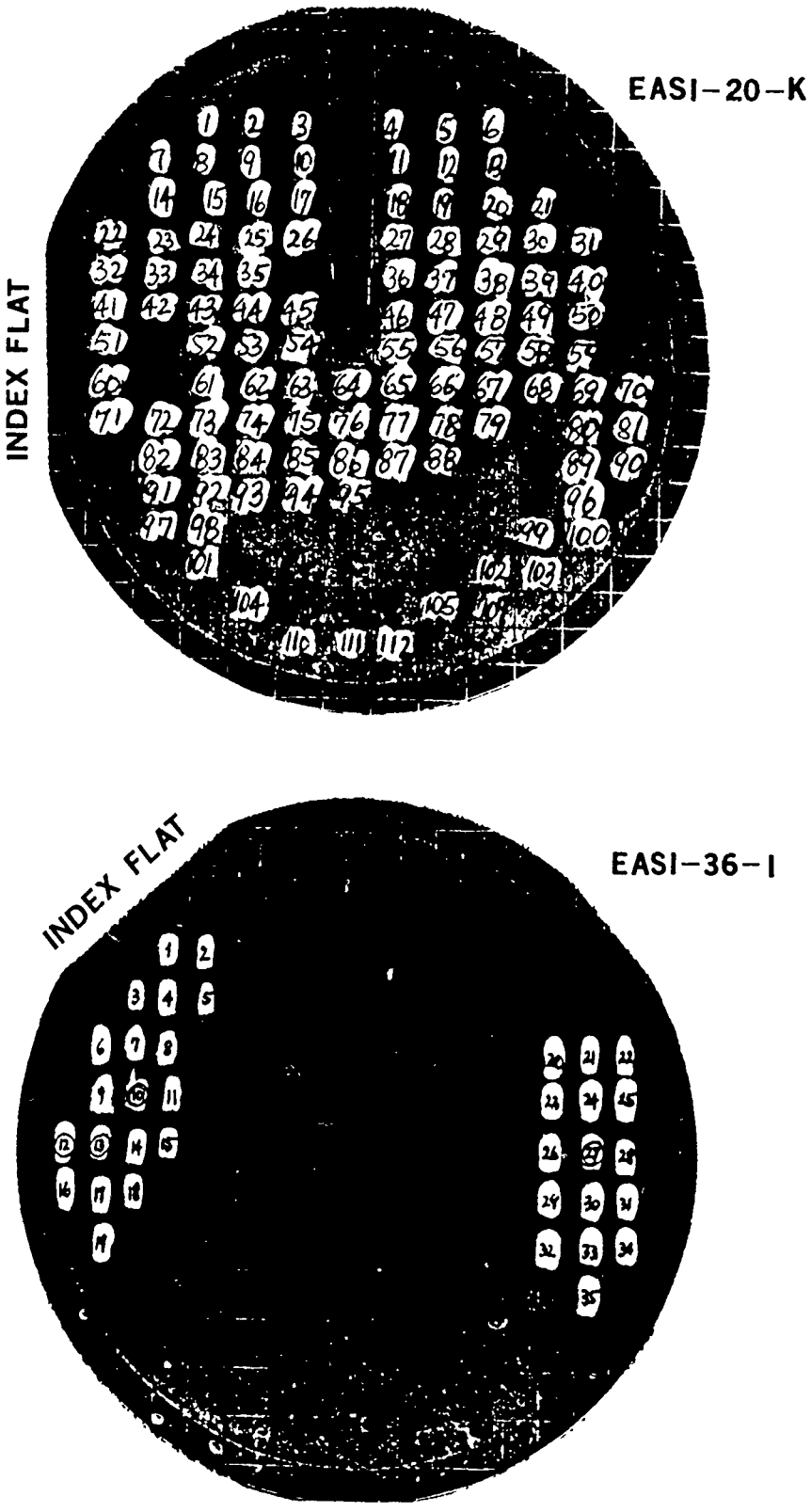

Figure 215. Sample maps of two diced, 4 in. dia. silicon wafers with CVD diamond films deposited by Crystallume.

Basically, the thinner films of EASI-20-K showed discontinuous areas under SEM (Figure 216), and faceted growth (Figure 217). As the film becomes thicker growth of inverted-cone-like columns with a "cauliflowered" surface appeared, typical of films which have been deposited under low adatom mobility.

On the EASI-36-I where the films are thicker, "cauliflowering" is even more pronounced (Figures 218 and 219). Sample No. 27, showing a relatively even but still faceted surface (Figures 220 and 221), appeared to be a good candidate for wide temperature range, SEM tribotests in vacuum and in P_{air}.

Typical Raman spectra of both runs in Figure 222 indicated impure, graphitic carbon-contaminated diamond films. For tribological purposes the presence of graphite may not necessarily be harmful (it may even be beneficial), as long as the film is stress- and pinhole-free. We already suspected at the time that under high load, temperature and tangential shear diamond films may undergo a phase transformation of $sp^3 \rightarrow sp^2$ (i.e., to a surface layer of graphite), providing some reduced wear and friction simultaneously.

SEM triboflats were selected from the 35K run (48 hr. deposition, 0.3% CH4, essentially pure "sp^3" diamond per the Raman spectra) and from the 51K run (45 hr. deposition, 0.5% CH4, sp^2 bonding contaminated, "sp^2 + sp^3" film per the Raman spectra). SEM tribotests were performed with these samples, as depicted in Figure 223. The results of this round of experiments were published in (17).

The theoretical basis for all of the experiments with CVD diamond films was established by Pepper (23) and Goddard (22) stating that desorption of gases (mainly hydrogen) upon heating single crystal diamond in vacuum creates dangling bonds on the surface. These unoccupied orbitals interact with those on the sliding counterface to create high friction forces. Resorption of selected adsorbate gases (mainly hydrogen) caps the dangling bonds and lowers the friction. Graphitization and oxidation of the surfaces at high temperatures further influence this basic mechanism by superposition.

The small, 5 mm x 7 mm triboflat specimens, diced from selected portions of the "sp^3" and "sp^2 + sp^3" -coated wafers, were oscillated against stationary, hemispherically tipped, 2 mm dia., polycrystalline α-SiC pins under a 0.49N load, at an average velocity of 4.7×10^{-3} m•s^{-1}, in 1.33×10^{-3} Pa (1×10^{-5} torr) vacuum and in various partial pressures of air. In one case the counterface α-SiC pin was coated with a thick (~40 μm) film of DC-PACVD diamond (see Figure 223).

As shown in Figures 224 and 225, both the "sp^3" and the "sp^2 + sp^3" films displayed essentially the same friction behavior against the bare, sintered and hot-isostatically pressed, α-SiC pins. The coefficients of kinetic friction (f_k or COF) always exhibited their lowest values (COF ≅ 0.10) after some sliding in vacuum, at or near room temperature. This reduction in friction from the ambient atmospheric value of 0.5+ to the low friction in vacuum is attributed to the desorption (or removal by sliding) of surface oxygen, moisture and other contaminants. Further heating in vacuum to 300°C and above (to 850°C max.) resulted in a substantial increase of COF to ≅ 0.7+ due to the desorption of hydrogen and the

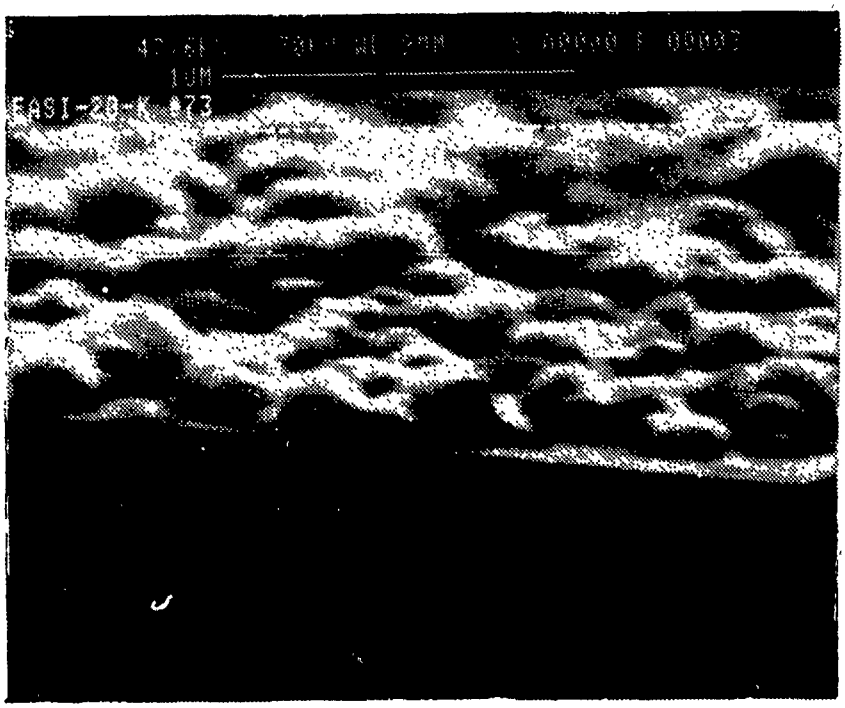

Figure 216. Discontinuous portion of CVD diamond film, showing island-like nucleation; EASI-20-K, Sample No. 73 (also see Figure 215).

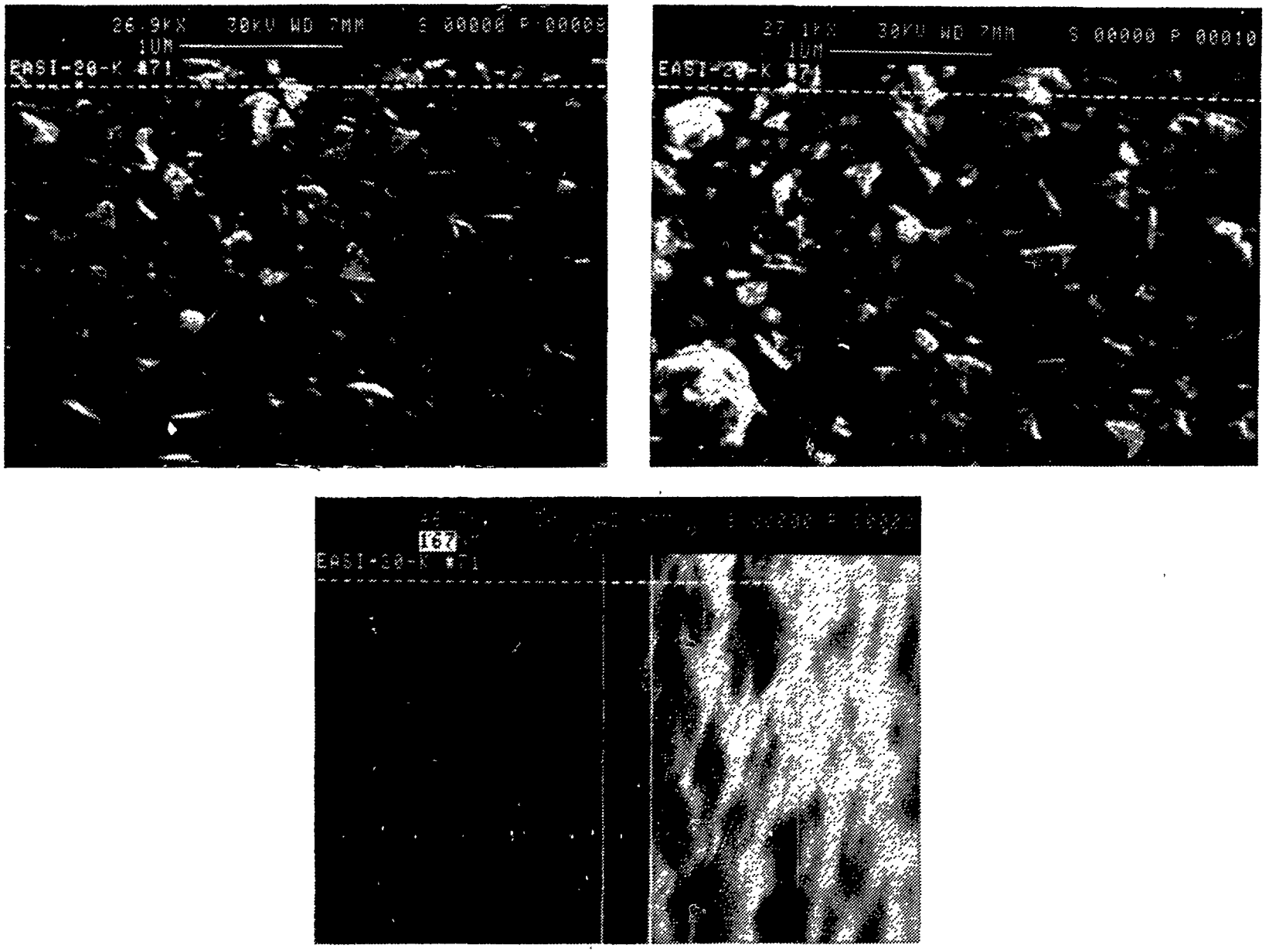

Figure 217. Faceted growth of a thin, but continuous CVD diamond film; EASI-20-K, Sample No. 71 (also see Figure 215); parallel white borders indicate film thickness.

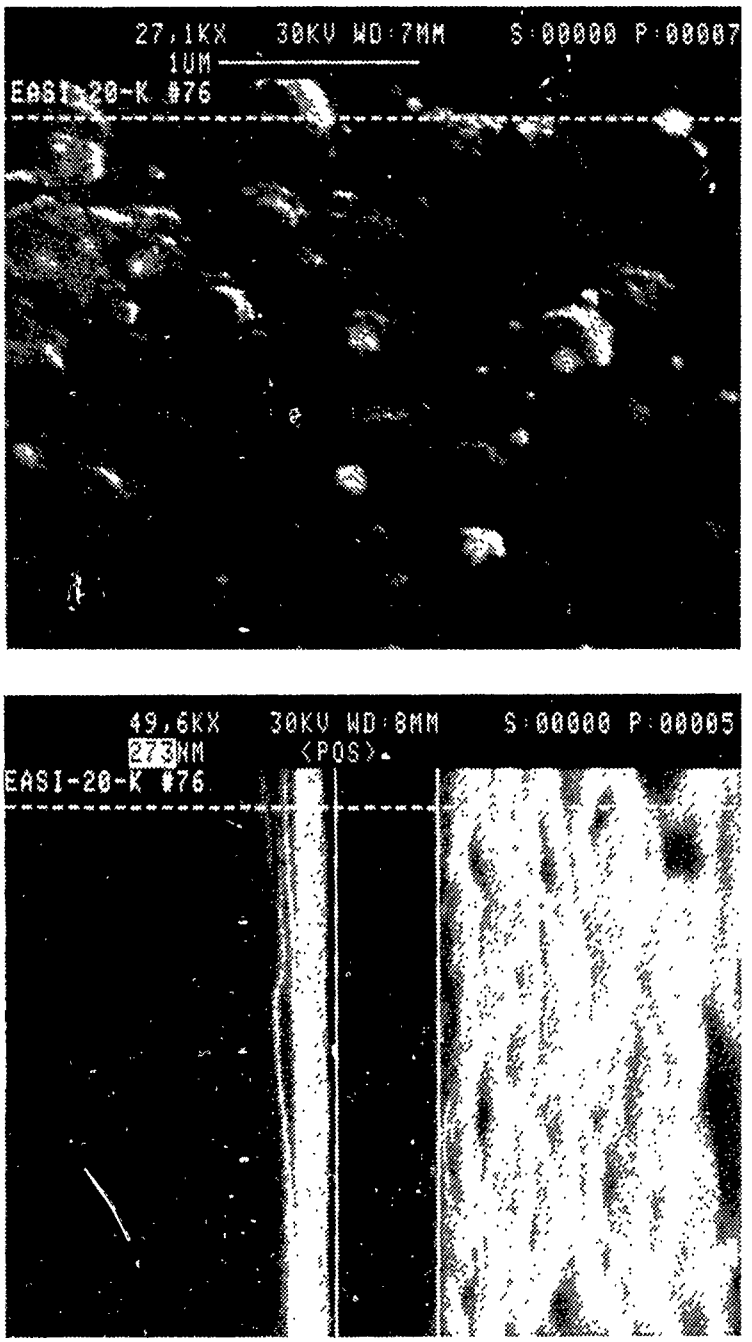

Figure 218. Cauliflower growth of EASI-20-K, Sample No. 76 (also see Figure 215); parallel white borders indicate film thickness.

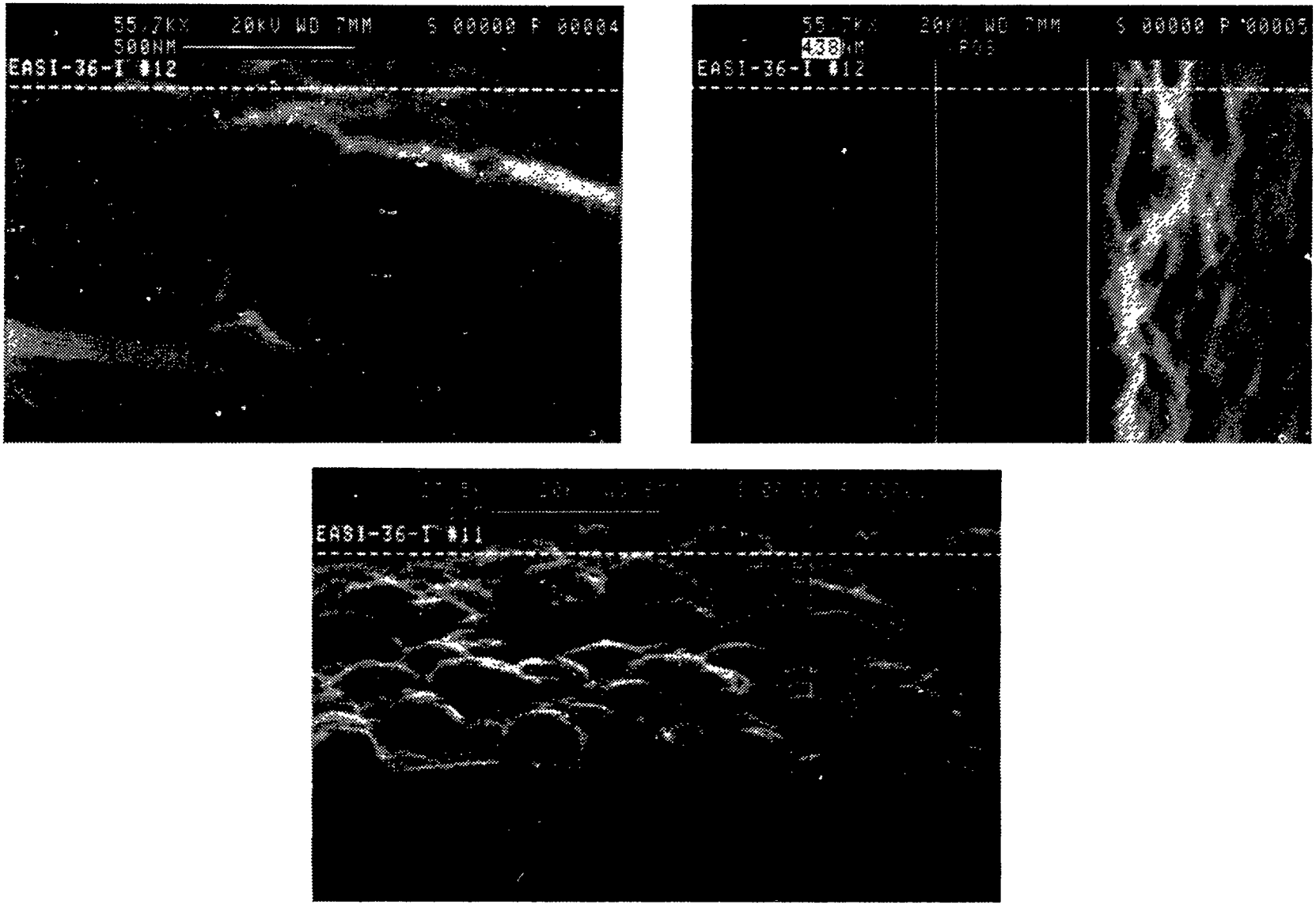

Figure 219. Nodular coning of a thicker EASI-36-I, Sample No. 11 (also see Figure 215); parallel white borders indicate film thickness.

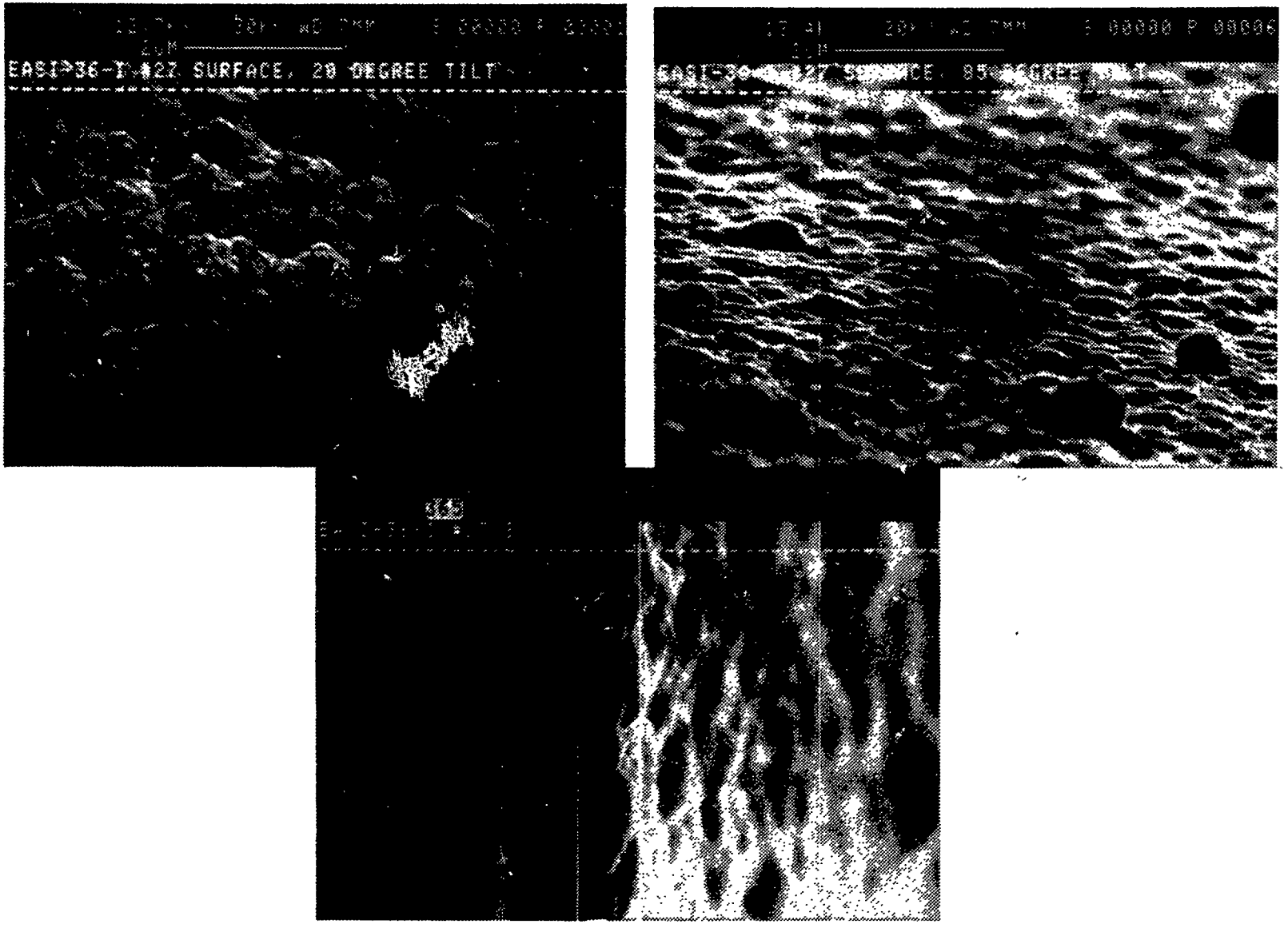

Figure 220. High and low tilt angle SEM photomicrographs of cauliflowered, ~400 nm thick CVD diamond film, EASI-36-I, Sample No. 27 (also see Figure 215); parallel white borders indicate film thickness.

Figure 221. The faceted appearance of EASI-36-I, Sample No. 27 (same as Figure 220), under ultrahigh (53,200 x) SEM magnification, typical of {111} texturing.

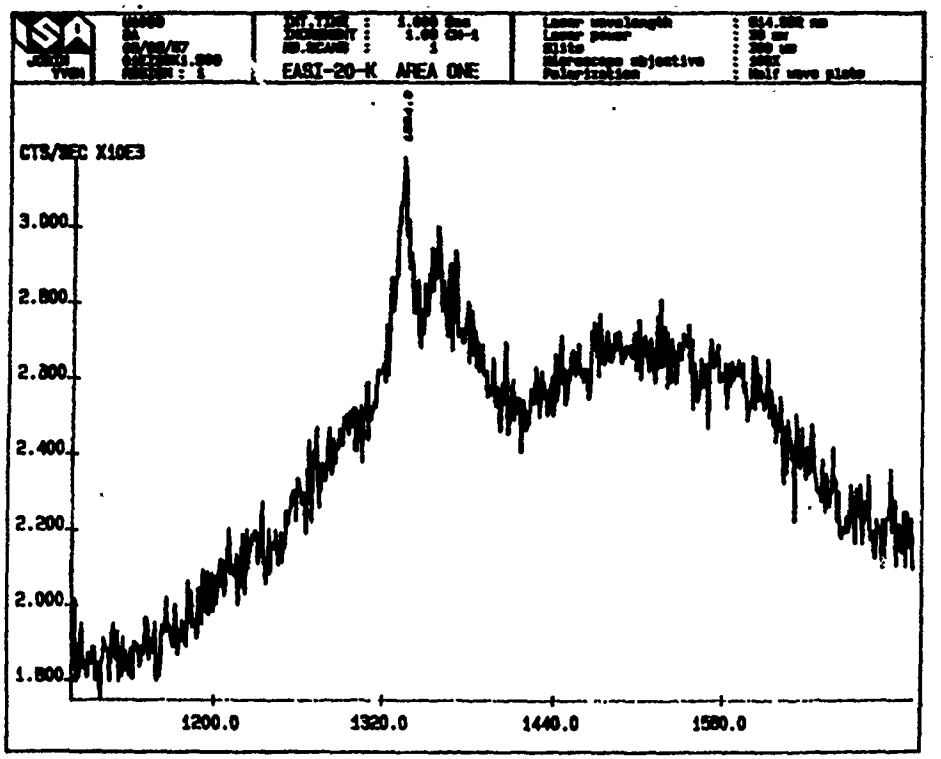

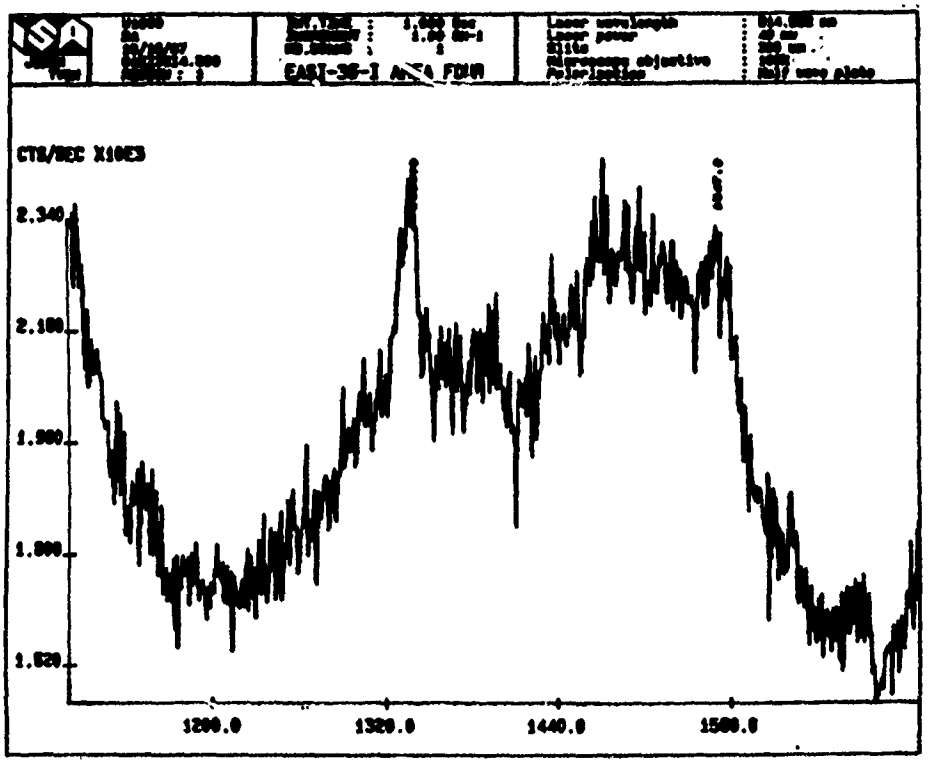

Figure 222. Raman spectra of (a) EASI-20-K film portion, showing characteristic sp^3 diamond peak (1331-1335 cm^{-1}) and mixed $sp^2 - sp^3$ bonding (1340-1360 and 1490-1580 cm^{-1}) on Sample No. 64 (see Figure 215); and (b) EASI-36-I film portion (Sample No. 33, see Figure 215), showing the same 1331 cm^{-1} sp^3 diamond peak and a complex $sp^2 - sp^3$ peaks in the 1490-1520 cm^{-1} range.

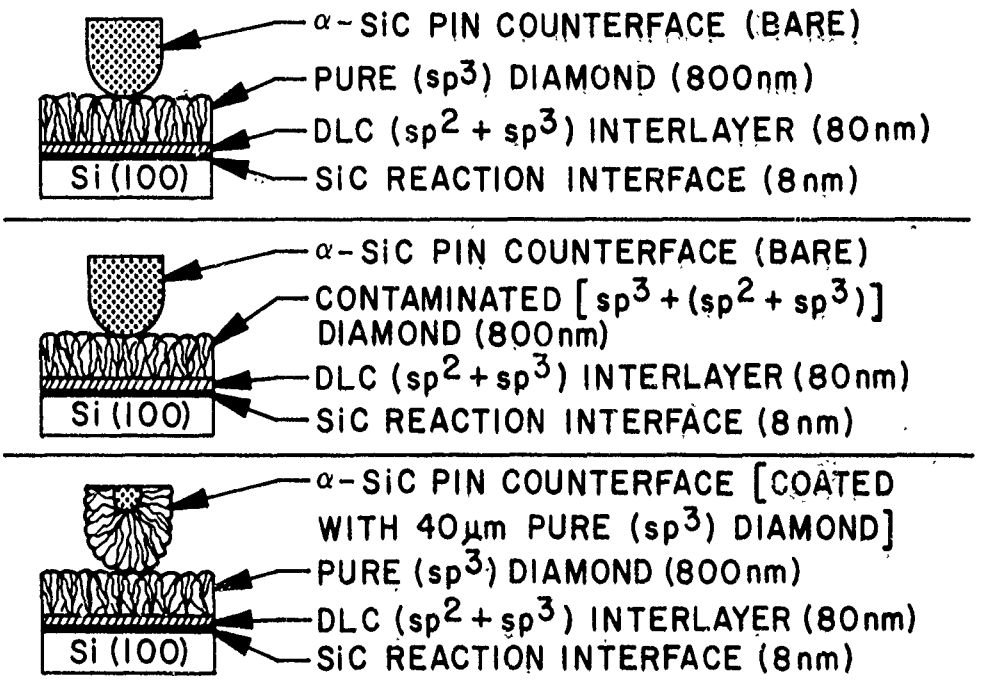

Figure 223. Schematics of test combinations for first round of SEM tribotests.

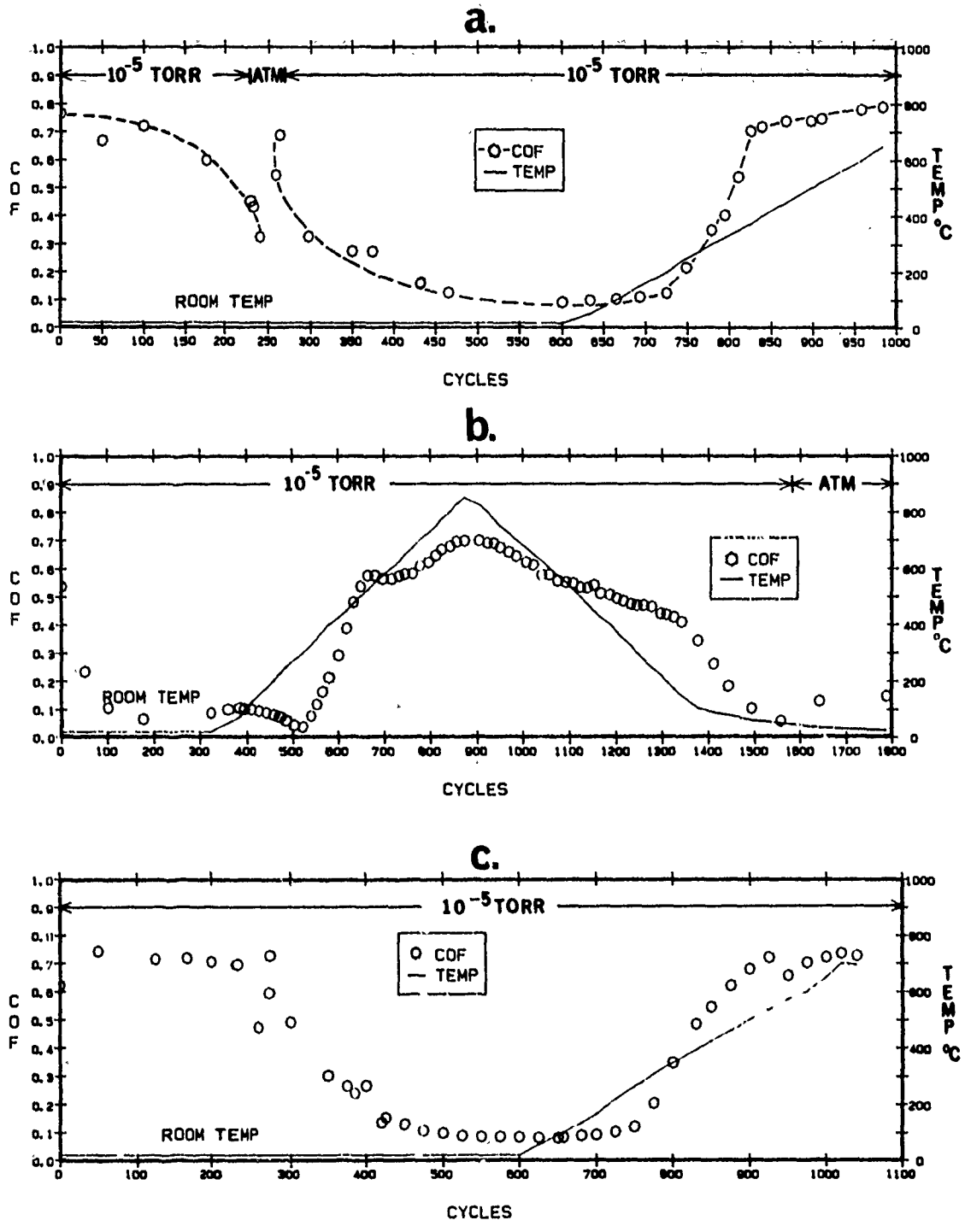

Figure 224. Coefficients of kinetic friction (COF) of (a), (b), "sp^3" vs. α-SiC and (c) "$sp^2 + sp^3$" vs. α-SiC, as a function of temperature, in 1.33 x 10^{-3} Pa = 1 x 10^{-5} torr vacuum.

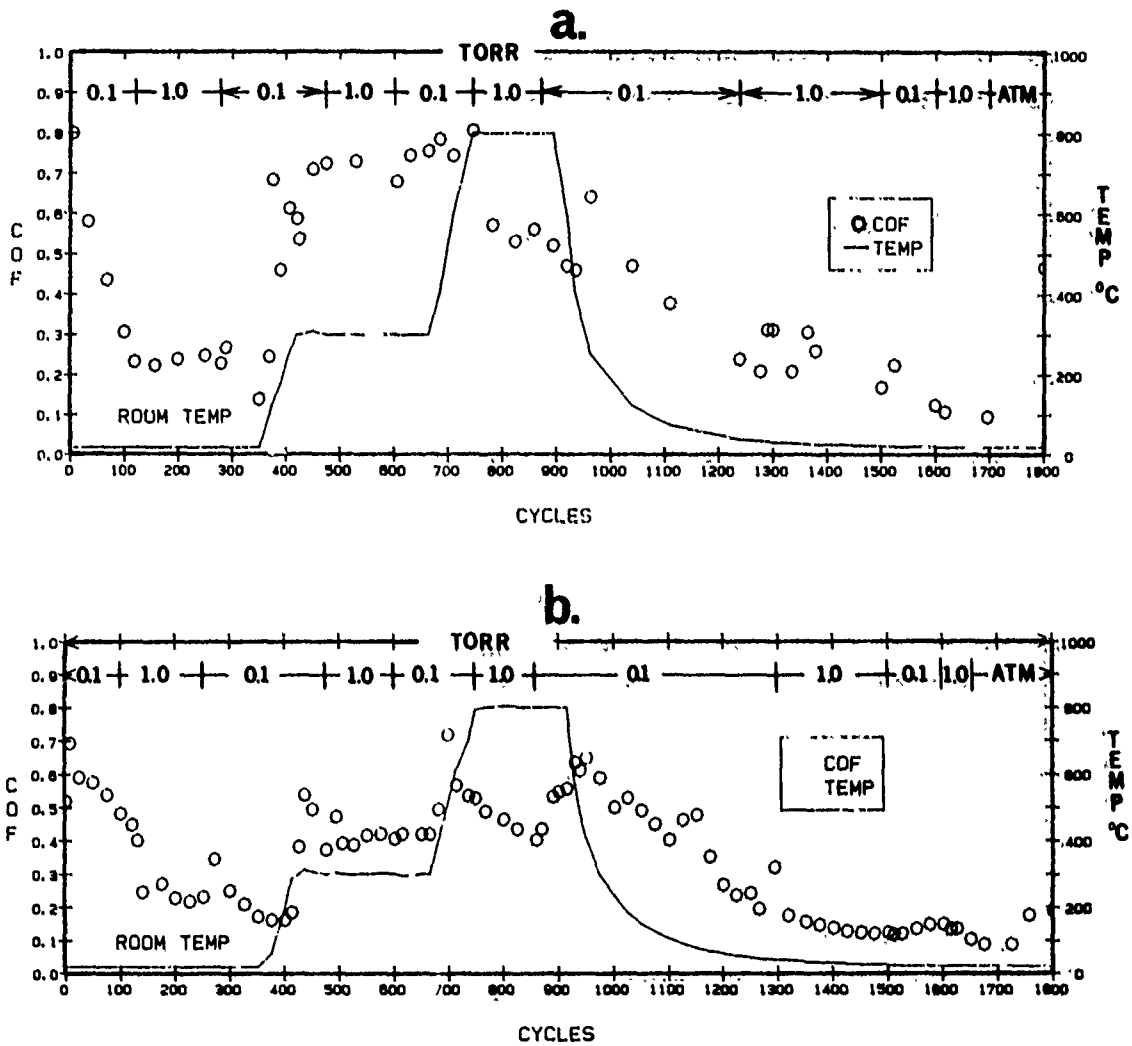

Figure 225. Coefficients of friction (COF) of (a) "sp^3" vs. α-SiC and (b) "$sp^2 + sp^3$" vs. α-SiC, as a function of P_{air}, at various temperatures.

generation of dangling bonds at the frictional interface. The high friction at 850°C persisted until cool-down, at which time the friction gradually dropped to its previously attained, low values as the dangling bonds were eliminated by gas (e.g., hydrogen) re-sorption. In some cases, the thin diamond film delaminated from the Si(100) substrate, under the high friction forces.

In P_{air} (Figure 225), the starting friction was high again, dropping to a value higher than the minimum reached in vacuum, at R.T. On heating, the COF increased here also, with some evidence of graphitization of diamond (or oxidation of the α-SiC) at the highest temperatures. Regardless of diamond purity, more graphite and/or silicon oxide must have been generated before 850°C to 900°C and the friction is somewhat reduced. On cooling, more of these relatively "lubricious" layers are removed than generated and the COF increases.

The α-SiC versus "sp^3" and "$sp^2 + sp^3$" film tribotests qualitatively indicated that the volume wear rate ($\dot{V}$) of the sp^2-bonding contaminated films, as a function of sliding distance and standard heating protocol, was higher than that of the purer diamond counterpart. The "$sp^2 + sp^3$" layers also tended to delaminate from the silicon substrate with greater ease. The less-pure diamond films caused higher wear of the mating α-SiC pin tip ($\dot{V}_{SiC}$ vs. "sp^3" = 2.65×10^{-14} $m^3/N \cdot m$; $\dot{V}_{SiC}$ vs. "$sp^2 + sp^3$" = 7.76×10^{-4} $m^3/N \cdot m$). This unexpected finding was attributed to increased generation and entrapment of fine, diamond wear debris between the frictional surfaces.

The highly faceted and very thick (~40 μm) "sp^3" layer on the α-SiC pin repeatedly and almost immediately removed the much thinner "sp^3" on film from the Si(100) substrate. The sliding-distance-normalized wear volume of the "sp^3" on the real area of the coated α-SiC pin's contact here was in the 10^{-17} $m^3/N \cdot m$ range, about three orders of magnitude lower than $\dot{V}$ of bare α-SiC sliding against the pure diamond films.

In view of the emerging importance of XTL β-SiC, sintered-poly-XTL α-SiC and other ceramic substrates for polycrystalline CVD diamond films, Crystallume's Statement-of-Work for their second phase of research was amended in August 1988 by including the following samples:

1. At least one SEM triboflat consisting of a XTL β-SiC, single crystal film deposited on Si(111), a substrate provided through the courtesy of Professor R. F. Davis (North Carolina State University) and Dr. Max Yoder (ONR); diamond film thickness = 1.0 to 2.0 μm.

2. No more than 10 each triboflats and 4 each tribopins fabricated from sinter-HIP and fully HIP ESK α-SiC; diamond film thickness = 1.0 to 2.0 μm.

3. One (1) each, 4 inch diameter, 0.5 inch thick, graphite fiber reinforced glass matrix composite billet (HAC-GLAS-13-2), coated with polished, polycrystalline β-SiC; during coating of this disc, at least 2 each sintered α-SiC triboflats and 1 each XTL β-SiC-coated Si(111) triboflat to be coated along with the disc, to serve double duty as thickness samples as well as friction and wear specimens; diamond film thickness ≅ 10 μm.

This round of diamond application by Crystallume was aimed to:

1. Determine the wear life of relatively thin films deposited on a substrate of poor adherence (sapphire) and good adherence (α-SiC), and examine the effectiveness of interface "primer" coatings or pretreatments to enhance the adhesion of the diamond films. Under ideal circumstances, ceramic bearing parts coated with diamond should contain the thinnest layers necessary to achieve the desired wear resistance. Thin layers reduce coating deposition times and lower process costs. Furthermore, the characteristically fine-cauliflowered surface of certain diamond films may have a high enough surface finish, at least in the case of thin layers and for certain applications (e.g., as substrates for solid lubricant films, and certain commercial applications requiring lower tolerances, such as drill bits, mining tools, etc.), not to require any post-deposition polishing.
2. Examine our ability to polish the thicker (~ 10 μm) diamond films to determine (a) the finest (i.e., highest) diamond film finish attainable using conventional (i.e., diamond-with-diamond powder) polishing techniques, and (b) any friction and wear changes which may be attributed to an initially lower diamond surface roughness (i.e., higher finish).
3. Generate at least some preliminary information as to our capability to (a) coat a prototype mirror substrate disc fabricated from a ceramic composite with an evenly thick and adherent diamond film, and (b) polish the coating to finishes and thicknesses useful to an optical engineer.
4. Provide diamond-on-sapphire and diamond-on-α-SiC triboflats and at least one diamond-on-α-SiC tribopin with unpolished and thick polished diamond surfaces for fluorination by Prof. John Margrave (Rice University, Houston, TX). The goal was to investigate the usefulness of a fluorinated diamond overlayer to (a) reduce friction and wear of diamond in a wide environmental regime, and (b) provide added protection to optical surfaces, without degrading optical performance.

In order to achieve the best film adhesion to the various substrates, Crystallume employed their technique of interposing a controlled diamond-like-carbon (DLC) interlayer between the substrates and the pure diamond film. In the case of sapphire, a thin titanium interlayer (a carbide-former) was interposed between the sapphire and diamond to enhance adhesion.

3.5.1.2 Diamond-on-Sapphire. As reported by Crystallume in APPENDIX CC, four, CVD diamond-coated XTL sapphire wafers containing the thin, sputtered Ti (adhesion-enhancing) interlayer were cut into approximately 40 each 7 mm x 5 mm SEM tribometer flats. The four wafers were representative of four separate coating runs, as described in Table 39. We, at Hughes, complemented Crystallume's analysis in APPENDIX CC by visual, optical and SEM examination to determine film coverage, integrity and thickness prior to tribotesting. Many of our conclusions have been derived from parallels drawn from the previous scrutiny of the diamond-on-silicon systems:

Table 39. Thin CVD diamond films on sapphire wafers (from Appendix CC).

Sample Number	CH_4 Concentration (Volume %)	Film Thickness (Å)	Deposition Temperature (°C)
P-1-Q-9	0.5	3000	725
9-S-4	0.3	7500	725
9-S-5	0.5	7000	550
9-S-6	0.5	2000	550

- Sample P-1-Q-9 (Table 39)

  The triboflats cut from this wafer were visually somewhat similar to the diamond/silicon samples in that the coating was grayish and had distinct specular and nonspecular regions. We chose the samples which were primarily specular and showed color fringes. From past experience, these areas tend to be more continuous and finer-grained. The SEM photographs show that the films were continuous and had a typical cauliflower structure with a film thickness of approximately 470 nm (1.5 times more than reported by Crystallume). We also noted that the samples from this wafer, unlike two of the other wafers, were opaque.

  The Raman spectrum included in Crystallume's report has sharp peaks at both 1330 and 1500 wave numbers (cm^{-1}), indicating a combination diamond/diamond like (DLC) coating, a result of the high methane deposition concentration. Our findings, with the exception of the film thicknesses, are in line with those reported by Crystallume.

- Sample 9-S-4 (Table 39)

  Again, our conclusions are similar to Crystallume's: as a result of the lower methane deposition concentration for this wafer, lower nucleation density resulted in poor film coverage and the formation of large, discrete crystallites. As we would expect of a low methane concentration deposition, the Raman spectrum indicates that the crystallites are diamond and not diamond-like. The crystallites are approximately 750 nm in height, but since these are not continuous films, it is misleading to quote this dimension as a film thickness.

- Samples 9-S-5/9-S-6 (Table 39)

  These two wafers are discussed jointly, because the findings were similar. From the SEM photographs, ours and Crystallume's, we saw no visual indication of a diamond/DLC film of any degree. The surfaces exhibited neither the typical cauliflowered or faceted structure we usually see. To add credence to this finding, the samples were primarily transparent, with only a very thin, dark film on the surface. The film may have been the titanium intermediate layer, or some sort of organic contamination which we saw on many of the other samples. The Raman spectrum does not have peaks at either the diamond or DLC wave numbers, again indicating that there was no diamond/DLC film deposited. As a consequence, the film thickness data reported by Crystallume are highly questionable.

Based on these results, the following conclusions may be drawn:

1. High temperature depositions (725°C) produced patchy diamond growth (discontinuous films) when coupled with low methane concentration, and continuous diamond/DLC films when coupled with high methane concentrations. We found no visual trace of films on the two wafers coated at the lower, 550°C temperature.

2. The high temperature, low methane concentration deposition produced discontinuous diamond films made up of large, discrete-cauliflower-structured crystallites.

3. The high temperature, high methane concentration deposition produced continuous diamond/DLC films made up of small-grained, cauliflower-structured crystallites.

4. We did not observe any films with the faceted structure that we previously saw on some of the other substrate/diamond combinations.

5. Samples from the low temperature (550°C) depositions should not be (and were not) considered for friction and wear tests.

6. As found before with XTL silicon substrates, the sp^3/sp^2 bonding ratio in the diamond films remained to be a function of the CH_4/H_2 ratio in the gas mix of the plasma.

In general, diamond deposition on sapphire, using a sputtered titanium interlayer, was not shown to be either encouraging or well-controlled. The poor nucleation, coalescence, growth and relatively poor quality of diamond on bare sapphire are well-known; the lack of substantial improvements as a function of the (possibly oxidized) titanium "primer" (originally intended as a carbide-forming, nucleation layer) needs to be further elucidated.

SEM tribotests with diamond-coated, XTL (sapphire) triboflats sliding against a sinter-HIP ESK α-SiC pin under the conventional (50 g = 0.49 N) load indicated that the thin diamond film was removed with an even greater ease from sapphire as it was removed previously from XTL silicon. However, the diamond film lasted just long enough during one of the tests to (a) show the characteristic friction reduction on desorption of oxygen and moisture from the diamond surface in vacuum, at room temperature, and (b) an increase in friction on desorption of hydrogen at elevated temperatures. A more detailed account of these results was presented at the Fourth Annual SDIO/IST-ONR Diamond Technology Initiative Symposium (Arlington, VA, July 11-13, 1989), see (270).

3.5.1.3 Diamond-on-α/β-SiC. The first round of diamond deposition onto α- and β-SiC is also described in APPENDIX CC (see Table 40 for specimen description). The findings may be summarized as follows:

1. The results of diamond deposition on poly-XTL α-SiC are extremely encouraging. The 1 to 2 μm thick films are of high quality and the throwing power of the process was sufficient to deposit the films uniformly on not only the SEM triboflats, but on the hemispherically-tipped SEM tribopins also (see Figure 226). Deposition onto the curved surfaces did, however, require the construction of a special reactor.

2. On epitaxially grown, XTL β-SiC films deposited on n-type Si(111), diamond films nucleated with great difficulty. There appears to be a much larger barrier to nucleation on as-deposited XTL β-SiC than on polished, poly-XTL a-SiC. The fine, small particle size diamond crystallites remain discretely distributed on the β-SiC surface and do not coalesce into a continuous film. Scratching the β-SiC surface does, however, produce profuse nucleation and coalescence at the scratch sites.

3. Nucleation on both XTL β-SiC and the poly-XTL α-SiC was found to be a function of methane pressure (higher pressure = faster nucleation).

Table 40. Thin CVD diamond films on sinter-HIP/HIP ESK α-SiC and XTL β-SiC films on Si(111) SEM triboflats, and on sinter-HIP/HIP ESK α-SiC SEM tribopins (from APPENDIX CC).

Material	Surface treatment	Methane concentration	Film Thickness
Polycrystalline silicon carbide triboflats	Selected samples were etched in HF and HNO_3	0.3%	Typically 1 - 2 μM
Polycrystalline silicon carbide tribopins	"	"	"
CVD single crystal silicon carbide on single crystal silicon	"	"	"

Diamond on Silicon Carbide

13-Y-7 - 3 Triboflats

13-Y-6 - 1 Triboflat

3-I-10 - 3 Tribopins

13-Y-6 - 1 Tribopin

Diamond on Single Crystal Silicon Carbide

3-I-10 - 4 single crystal silicon carbide Triboflats

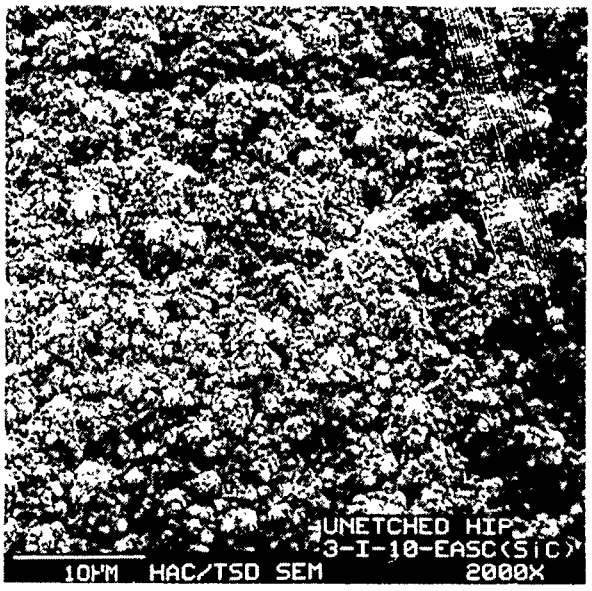

Figure 226. Appearance and surface topography of a HIP α-SiC tribopin coated with ~1.5 μm CVD diamond film; SEM photomicrographs at various magnifications.

3.5.1.3.2 Diamond-on-Polycrystalline α-SiC. SEM tribotests with ~ 1.5 μm diamond on both the ESK α-SiC pins and flats sliding against each other showed that the adhesion of diamond to the DLC-primed α-SiC is best among all the ceramic substrates examined so far. The previously discussed, characteristic friction trends manifested themselves here, as before (17), see the discussion below.

A total of five tests were performed on one coated α-SiC flat with two coated α-SiC pins. Pin No. 1 was used to complete two vacuum (1.33×10^{-3} Pa) tests on separate wear paths (Test No. 1 and No. 2); Pin No. 2 was slid over two additional wear paths, again in vacuum (Test No. 3 and No. 4). Then, Pin No. 1 was reused for the third time, over the last track of the flat (Test No. 5) in 13.3 Pa partial pressure of air (P_{air}).

The four vacuum tests basically consisted of sliding the flat against its respective pin in 1.33×10^{-3} Pa (1×10^{-5} torr) on a given wear path for 600 cycles, at room temperature (R.T.). Between 600 and ~1200 cycles the temperature of the flat was ramped more or less linearly to 850°C, followed by a monotonic decrease to near R.T. At ~40°C, usually reached in 200+ cycles, the chamber was vented to the atmosphere and sliding was continued in air for an additional 100 to 200 cycles. The entire apparatus was fully cooled to R.T., then the flat was moved sideways under the pin to an unworn region. A second test was repeated with the same pin.

Finally, the previously used Pin No. 1 was reassembled in its original position, and a fifth (and final) test was run on the same flat: the same thermal profile was followed here, but now in 13.3 Pa (1×10^{-1} torr) P_{air}.

3.5.1.3.2.1 The Effects of Hydrogen Desorption and Adsorbate Resorption on the Friction of Poly-XTL Diamond in Vacuum. The vacuum friction data on the four experiments are shown in Figure 227. At the onset of sliding, there appeared to be a pronounced run-in effect: the f_k (COF) was reduced from ~0.4 to near 0.1 as room temperature sliding began. On heating, a monotonic increase in COF occurred in every case. This increase caused peeling of the coating from the flat in the respective scars of Pin No. 1/ Test No. 1 (Figure 227a) and Pin No. 2/Test No. 2 (Figure 227d). Although the limited number of tests does not permit much speculation, delamination occurred irrespective of the average starting stress of each test, i.e., whether the pin was new or used once in a particular case. It appears that there had been some real variation in adhesion from scar site to scar site, the magnitude of the starting average stress between the pin tip and the flat notwithstanding. Where the diamond delaminated, changing the sliding couple from diamond vs. diamond to α-SiC vs. diamond, the friction trends were comparable to previous data (17) with a bare α-SiC pin sliding against an adherent, DC-PACVD diamond film on Si(100), in vacuum (see Figure 224). On heating (and desorption) the friction increased, on cooling (and adsorbate resorption) the friction decreased. The comparison indicates that once the diamond coating delaminates from either the pin or the flat, the α-SiC vs. diamond contact behavior becomes very similar.

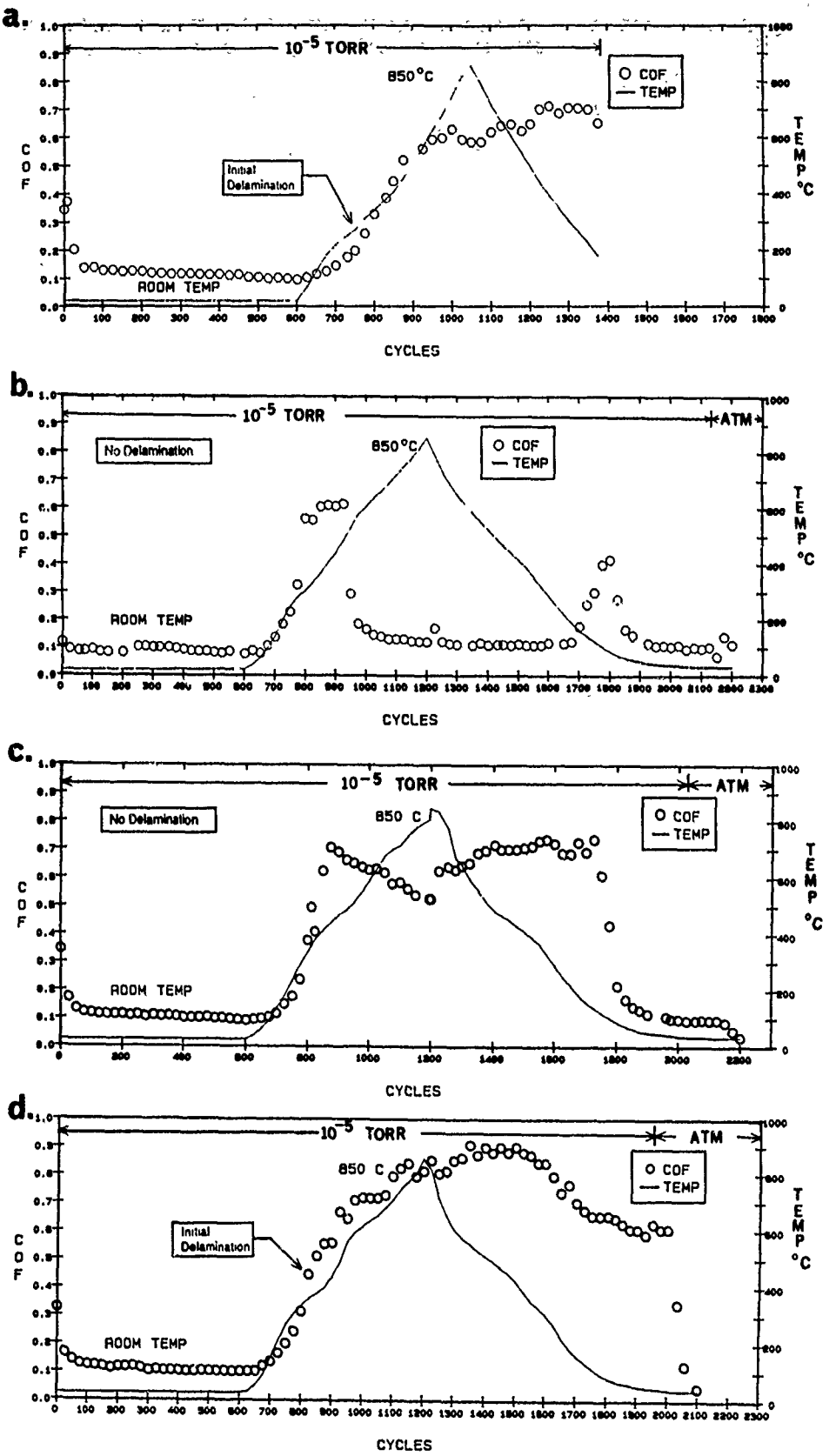

Figure 227. Coefficients of friction (COF) of diamond vs. diamond in 1.33×10^{-3} Pa (1×10^{-5} torr), at various temperatures: (a) Pin No. 1/Test No. 1 (Wear Track No. 1); (b) Pin No. 1/ Test No. 2 (Wear Track No. 2); (c) Pin No. 2/Test No. 1 (Wear Track No. 3); and (d) Pin No. 2/Test No. 2 (Wear Track No. 4).

With the undelaminated film tests (Figure 227b and 227c) the data in Figure 227c also followed the same trend as was previously observed with the α-SiC vs. diamond couple (see Figure 224): increasing friction on heating, decreasing friction on cooling. At the highest temperatures, the clearly discernible dip in the coefficients of friction in Figure 227c may be attributed to some graphitization. Before ~ 850°C, more graphite is generated than removed, and the friction is reduced. On cooling, more graphite is removed than generated and the friction increased, essentially exposing pure diamond underneath, just as previously observed with the diamond vs. α-SiC, in Figure 225. This type of friction behavior may be explained by the hydrogen desorption-resorption hypothesis brought forth by Pepper and Goddard, superimposed by the possibility of graphitization. We can only speculate that hydrogen became preferentially resorbed onto the diamond surface on further cooling, instead of other benign (i.e., low-friction-producing) species present in the vacuum chamber at 1.33×10^{-3} Pa.

In Figure 227b, however, the friction trend previously observed in Figure 227c was contrasted by two unusually large and distinct maxima in COF: one at ~ 400°C on heating, and one at ~ 100°C on cooling. Between these peaks, the f_k became uncharacteristically small with a slight but distinct middle peak at 850°C. This unusual trend was remarkably similar (but not identical) to the one previously observed with the thick (40 μm) DC-PACVD film-coated α-SiC tribopin oscillating against a thin (0.8 μm) DC-PACVD-film-coated Si (100) flat described in 3.5.1.1. This flat suffered early delamination of diamond in the SEM tribometer [see Figure 228, taken from (17)]. Therefore, the de-facto combination yielding the three, well-defined COF maxima in Figure 228 essentially constituted a diamond coating on the pin sliding against a XTL silicon flat with some diamond/silicon wear debris present. We believe that these unusual friction trends represent a heretofore unobserved footprint of diamond and silicon surface reconstruction, as discussed in the following section.

3.5.1.3.2.2 The Effects of Reconstruction on the Friction of Poly-XTL Diamond and Si (100) Surfaces in Vacuum. Some experimental evidence has been presented here to show that unoccupied orbitals on diamond surfaces will lead to high friction. These dangling bonds may be terminated with certain adsorbates (e.g., hydrogen) to reduce the adhesion and thus the friction.

There is a growing body of information in the literature that reconstruction of diamond surfaces also eliminates dangling bonds. Lurie and Wilson's early work (271) was followed by Pandey (272), Pate (273) and Kubiak, et al (274, 275, 276) in showing that the (1 x 1) unit cells of hydrogen-stabilized (111) and (100) diamond planes undergo reconstruction to a (2 x 1) structure on desorption of hydrogen in vacuum. The dangling bonds collapse into dimerized, π–bonded surface chains first proposed by Pandey (272).

Electron-stimulated and thermal desorption of hydrogen from the (111) surfaces in vacuum revealed the onset of dangling bond generation in the temperature range of 587° to 900°C. Reconstruction started at around 100°C (273,274). The reconstruction to the (2 x 1) domains was not completed until considerable annealing near that temperature provided the necessary activation energy (274). After

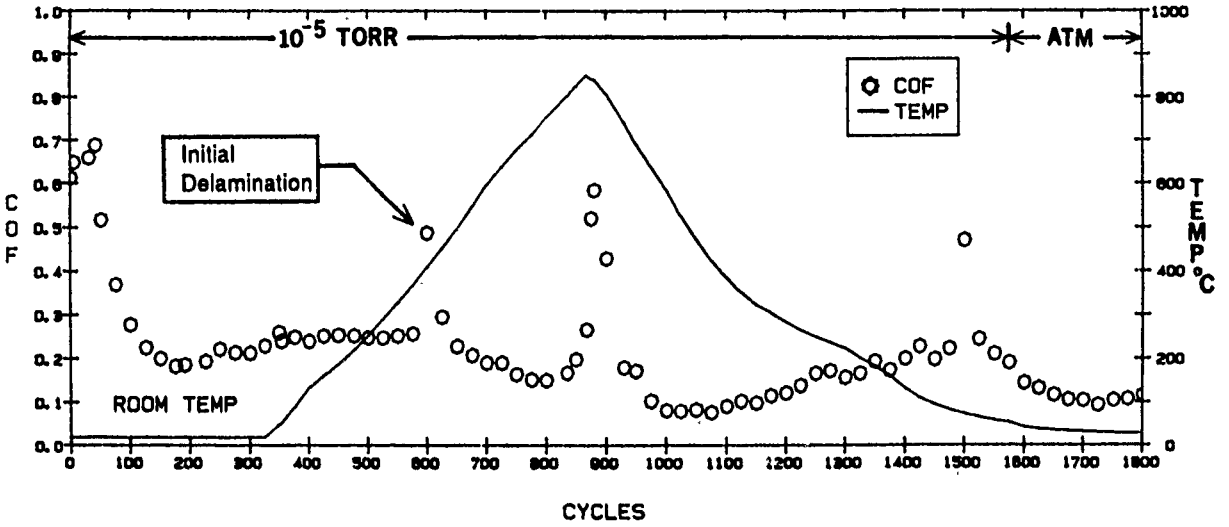

Figure 228. Coefficients of friction (COF) of diamond-on-α-SiC pin vs. diamond-on-Si(100) in 1.33 x 10^{-3} Pa (1 x 10^{-5} torr), at various temperatures, before and after diamond film delamination from the Si(100) flat (17).

reconstruction, the surfaces were hydrogen-free (273). On the C(100), hydrogen also desorbed at ~ 950°C, followed by alteration to the (2 x 1) reconstruction symmetry starting at 1077°C. Here, unlike the C(111), chemisorbed hydrogen coexisted with the (2 x 1) domains over a broad range of temperatures. The C-H or H-C-H groups exposed on the surfaces appeared to be either as an integral part of the (2 x 1) structure or as a coexisting phase. The monohydride model was more consistent with the experimental data (276).

It is suggested that the unusual reduction in the friction of poly-XTL diamond at high temperatures, in vacuum (Figure 227b) as well as a similar reduction in the friction of Si(100) vs. diamond in Figure 228 may be attributed to reconstruction of the respective surfaces. It is also suggested that the large difference in the respective magnitude of the middle friction peak at ~ 850°C in the referenced figures is attributed to (a) the presence of as-grown or wear-exposed C(100) planes on the surface and, consequently, some mono- or dihydride bonds remaining there (note that reconstruction of the C(111) leaves no dangling bonds behind), and (b) the difference in the strength of the monohydride Si-H and C-H bonds typically remaining behind in the altered domains, after reconstruction to the (2 x 1) arrays had been completed.

As previous mentioned, the surface texture of the cauliflowered DC-PACVD films is predominantly but not exclusively {111}. This actually means that a mixture of exposed (100), (110) and (111) planes are present on the surface to some proportions. Most of them, however, consist of the {111} facets of the square-based pyramids growing on top of the square (100) planes. This growth mechanism is responsible for a pyramid-type and prism-edge-like, pseudo (100) diamond surface depicted in Figure 229. When the tips and edges wear off the pin or the flat (as in Figure 230), then the exposed surface planes will be richer in C(100).

During SEM tribometry, there are three different kinds of energy input to these aggregate, mostly C(111) and C(100) surfaces:

1. Breaking of C-C and C-H bonds by tangential shear, mechanical action and asperity flash temperature generation.
2. Thermal desorption of hydrogen by resistance heating of the flat.
3. Hydrogen adsorbate desorption by the impingement of the electron beam.

The combination of these three factors acting simultaneously is more effective in creating dangling bonds than thermal desorption alone. Thermal desorption is normally observed within well-defined temperature ranges. In our cases, there is an immediate increase in COF at the onset of heating, electron bombardment and sliding in vacuum. This COF increase continues until enough of these bonds are generated to cause their collapse into the (2 x 1) configuration on further heating [i.e. supply the activation energy found necessary by Hamza, et al, see (274)], even though the mesh vectors within the randomly exposed crystal facets on the triboflat may not show any long-range, azimuthal order. It is

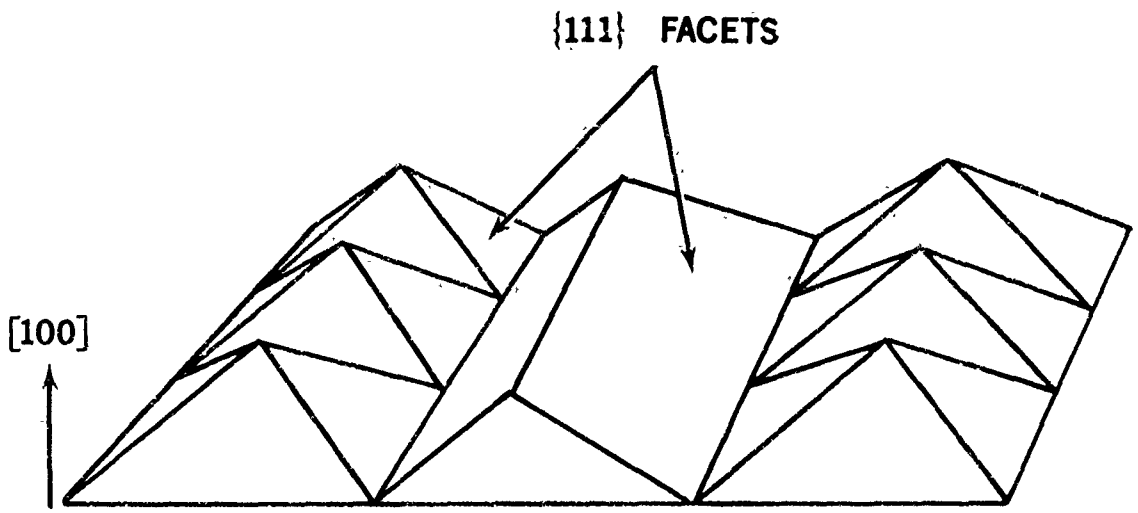

Figure 229. Mixed pyramidal and prism-edge model of (111) planes of diamond comprising pseudo-(100) surfaces, forming the preferentially {111} textured surface.

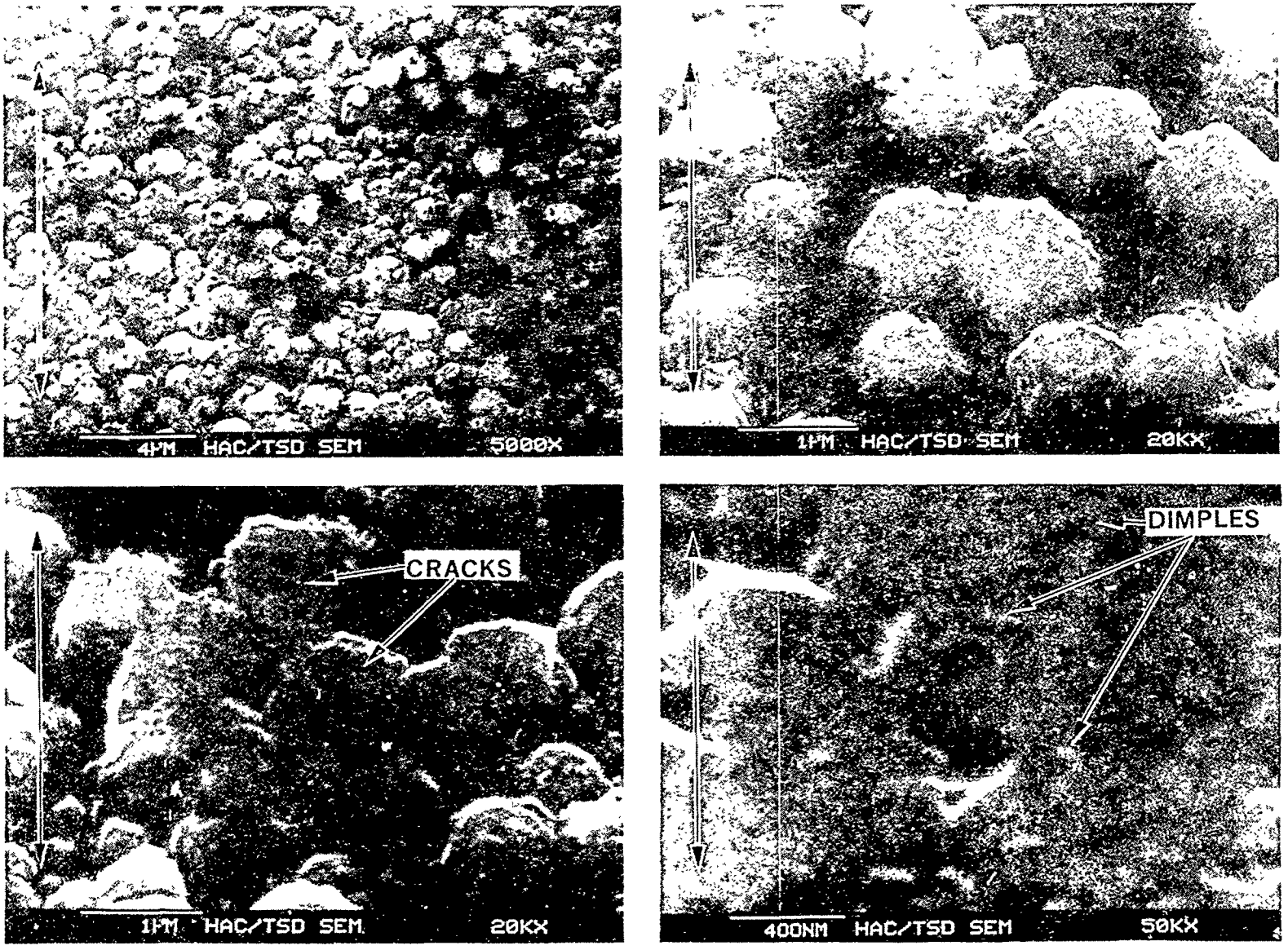

Figure 230. Post-test appearance of the worn, but undelaminated diamond film on the triboflat, in the wear track associated with Figure 227b, double-headed arrows indicate direction of oscillatory sliding.

important to understand that a poly-XTL diamond pin vs. Si(100) flat, as well as a poly-XTL diamond-covered pin vs. a poly-XTL diamond-covered flat represent similarly behaving contacts, because the reconstruction mechanism of silicon is nearly identical to that of the sliding-exposed diamond crystallites due to the similarities in chemical bonding and crystal structure (20, 277, 278). The main differences should lie (a) in the C(111)/C(100) ratio on the worn diamond surfaces, as contrasted with the Si (100) wear plane, and (b) in the lower energy of the carbon orbitals and the consequently higher bond strength of C-H over that of Si-H (279).

These bond strength differences are also believed to be the cause of the large disparity in the respective 850°C friction peak sizes in Figure 227b and Figure 228. On the reconstructed surfaces of the worn (111)/ (100) diamond and the worn Si(100) the atoms pair up in adjacent rows to form the (2 x 1) array of dimers. This results in hydrogen-saturated or ruptured (dangling) monohydride bonds left standing where the reconstructed (100) surfaces are exposed. Under the combined input energies to which the sliding surfaces are subjected, the stronger C-H bond is broken only under more energetic excitation than the Si-H equivalent. As a consequence, a smaller number of dangling bonds will form on poly-XTL diamond with some (100) character than on Si (100), at equal energy inputs. We speculate that if we heated the diamond flat higher than 850°C in Figure 227f, the friction maximum at that (highest) temperature would have been higher.

The break-up of the reconstructed bonds on cooling and the resulting third and final friction peaks in Figure 227b and Figure 228 are more difficult to speculate upon. It takes activation energy to effect reconstruction and continuously provided thermal energy to keep the rubbed surface reconstructed, because the bonds are strained. The (a) sudden loss of reconstruction and the simultaneous reappearance of dangling bonds where heating is diminished, but sliding is maintained, followed by (b) their rapid saturation with hydrogen or other adsorbate(s) constitute the basis for the most reasonable explanation for the final friction maxima on cooling.

The relative influence of graphitization over reconstruction and the consequent degree of friction reduction differences appears to be a complex phenomenon. The conditions under which one predominates over the other are yet to be determined. More work is needed, both with XTL diamond facets and poly-XTL diamond films, to confirm the proposed frictional effects of reconstruction.

3.5.1.3.2.3 The Friction of Poly-XTL Diamond in Partial Pressures of Air. In 13.3 Pa P_{air} the friction of diamond is slightly higher at R.T. but is significantly lower than in vacuum once the flat begins to be heated (Figure 231). Although a stepwide increase in COF as a function of progressively higher temperatures is discernible, the magnitude of increase is substantially smaller than that of theundelaminated film in vacuum (Figure 227c). It is hypothesized that the generation of gaseous combustion products (CO and CO_2), combined with the well-known enhancement of graphitization by the presence of oxygen (280) are quite effective in reducing COF. Here, this reduction was generally more precipitous than with the diamond vs. bare α-SiC couples in Figure 225.

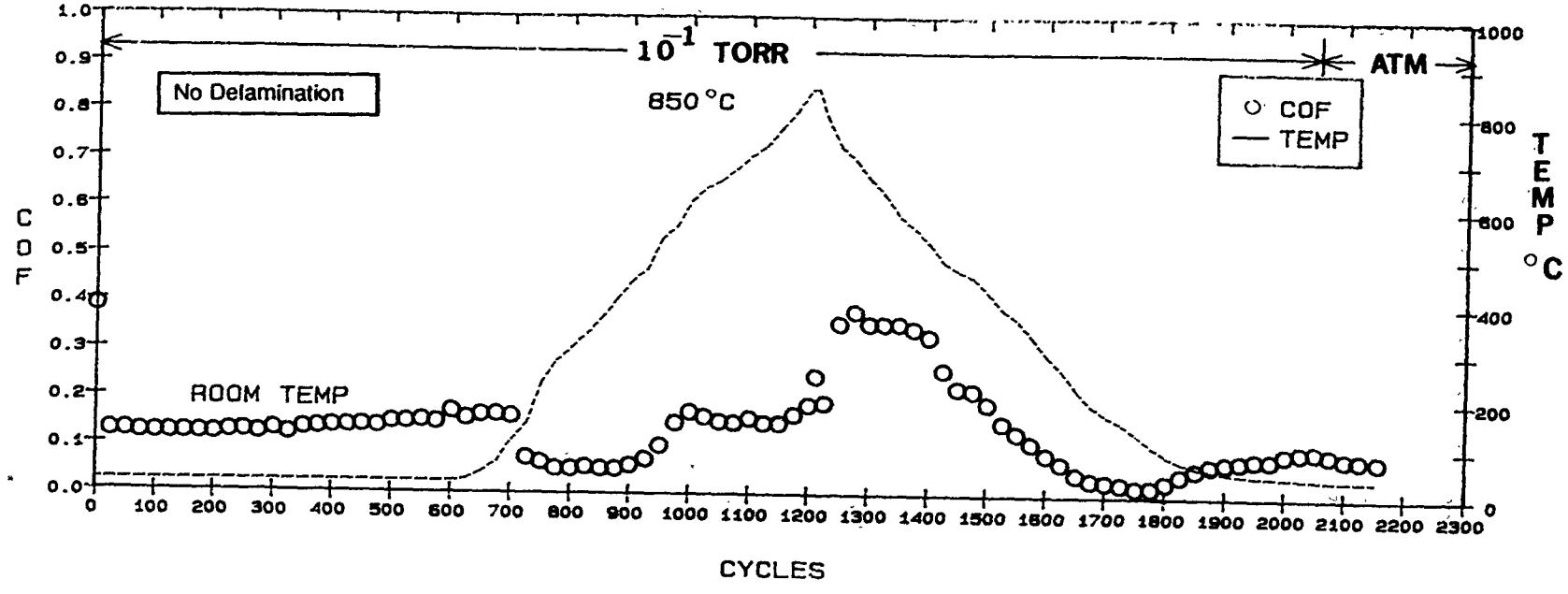

DIA0071

Figure 231. Coefficients of friction (COF) of diamond versus diamond in 13.3 Pa (1 x 10^{-1} torr) P_{air}, at various temperatures; Pin No. 1/Test No. 3 (Wear Track No. 5).

3.5.1.3.2.4 The Wear of Poly-XTL Diamond Films in Various Environments. The average volume wear rates of bare α-SiC and diamond removed from the pin tips (Figure 232) are included in Table 42. These rates are only rough estimates for the following reasons:

1. The wear rates are representative of partly room temperature and partly higher temperature sliding.
2. Although the reported wear rate is normalized to the applied load, as the pin tip wear scar increases the average stress decreases. Therefore, the wear rates reported are averages of the pin versus flat stresses ranging from 6.9 GPa+ to those representative of 50g (0.49N) divided by the apparent areas of contact.
3. The wear scar on a diamond-coated α-SiC pin tip is not a perfect circle. Therefore, the removed volume of diamond is not a perfect spherical segment. While the volume loss associated with Figure 227c is the closest to the ideal, those of Figure 227a and Figure 227b are less precise, see Figure 232. The calculations were based on average wear scar diameters. Note that the double wear scar represents three tests: one scar was formed after (a) two vacuum tests (Pin No. 1/Test No. 1 and Test No. 2), where the pin was reused without dissembly, and (b) the single test in P_{air}, where Pin No. 1 was reassembled for the final experiment, sliding on the last remaining wear track on the flat (Pin No. 1/Test No. 3). Since repositioning the pin to slide exactly over the previously generated scar on the tip was not possible due to some inevitable (albeit small) misalignment, a second wear scar was generated on the same tip. This scar is associated with the P_{air} test alone and was employed to estimate the respective wear rate in Table 42.

Where the diamond film did delaminate, the film appeared to part at the diamond/α-SiC interface (Figure 233). Some of the cross-hatched marks left behind by the α-SiC flat's polishing process are still discernible. Since pits are present on the polished surface of even highly consolidated HIP α-SiC, it is difficult to determine whether any additional pits were formed by tribotesting alone. The nature of the cauliflowered morphology of the diamond coating is also depicted here with some cross-sectional clarity.

The worn but still-adherent film on the flat (and on the pin) resembled the mesa-like appearance of the highest cauliflower mounds worn planar by the sliding action (for the appearance of the worn flat, see Figure 230). Examination of this figure indicates why estimation of volume wear rates based on wear scars of the flat would be unusually difficult. Summing the worn cauliflower tips accurately would be a formidable (if at all possible) undertaking. Estimating volume loss from the miniscule weight losses would have involved an equally large measure of error. Note that the wear of the cauliflowered tips on the flat appeared the same as that reported for the pin tips in (17).

Encouraged by the above data, the objective of Crystallume's final phase of program participation was to deposit <u>thick</u> diamond films on a variety of silicon carbide substrates, characterize the films and deliver the coated parts for further Hughes scrutiny. Table 41 (taken from APPENDIX DD) describes the type of substrates coated.

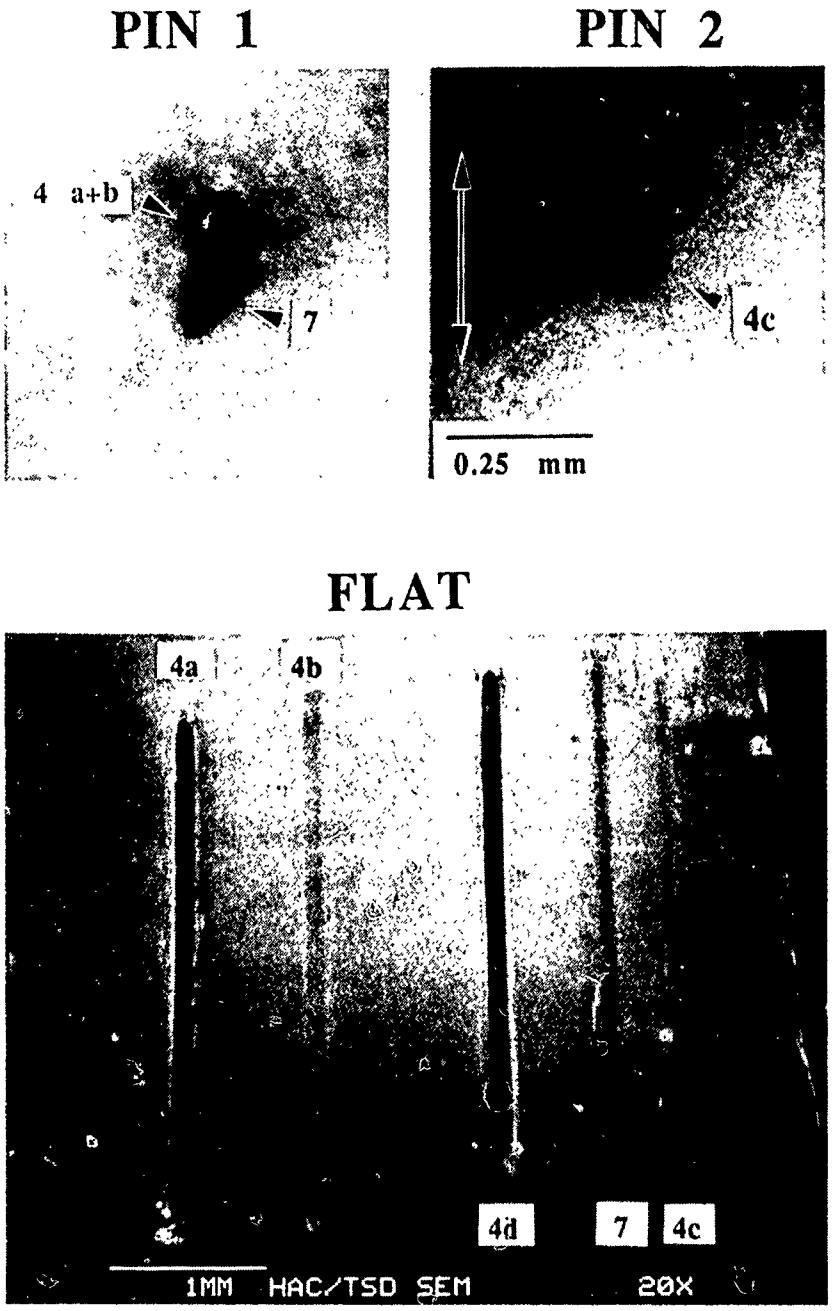

Figure 232. Post-test SEM photomicrograph of the five wear tracks referred to in Figure 227 and Figure 231, along with optical photomicrographs of the pin tip wear scars employed to calculate the wear rate of diamond in vacuum and in P_{air} (Table 41); double-headed arrow indicates direction of oscillatory sliding.

Table 41. The wear rate of α-SiC and diamond versus diamond in various environments.

Pin	Flat	Pin Wear Rate ($m^3/n \cdot m$)	Pressure (Pa)
1.5 μm "sp^3" film on α-SiC	1.5 μm "sp^3" film on α-SiC	4.27×10^{-16}	1.33×10^{-3}
1.5 μm "sp^3" film on α-SiC	1.5 μm "sp^3" film on α-SiC	9.50×10^{-16}	13.3
Bare α-SiC	0.8 μm "sp^3" film on Si(100)	2.65×10^{-14}	1.33×10^{-3}

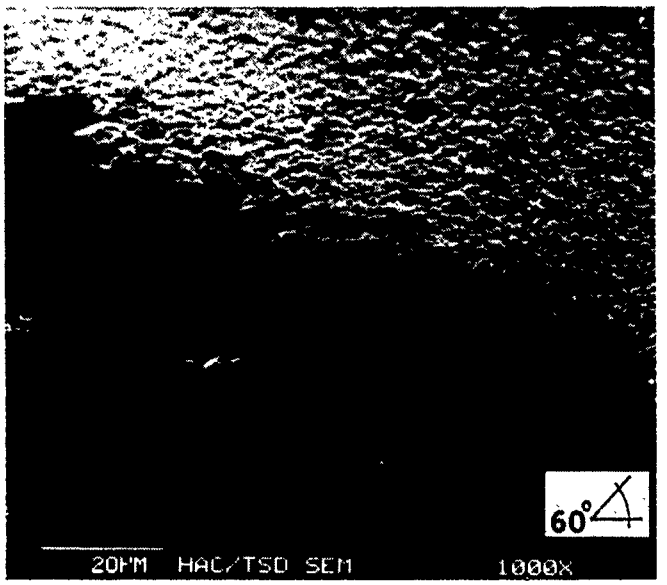

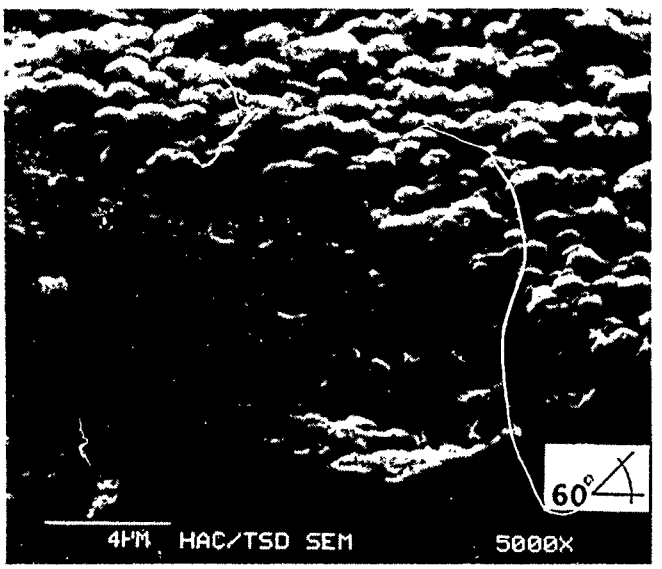

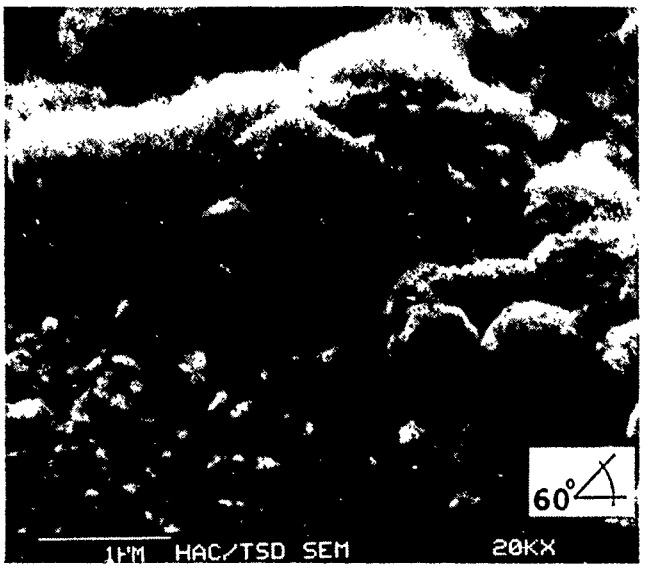

Figure 233. Post-test SEM photomicrographs of the edge of the wear track associated with Figure 227a (also see Figure 232), showing interfacial delamination of the diamond film from its α-SiC substrate.

Table 42. Thick CVD diamond films on sinter-HIP/HIP ESK α-SiC SEM triboflats and tribopins, on XTL β-SiC films, on Si(111) SEM triboflats and on HAC-GLAS billet coated with polished CVD β-SiC (polycrystalline) film (from APPENDIX DD).

Substrate	Comments
Single crystal β–SiC on single crystal silicon	Thin diamond films have been difficult to nucleate on single crystal SiC. Thick film growth has been found to be effective.
Sintered α– Silicon Carbide triboflats	Triboflats previously coated with thin (1-2 μM) diamond films were returned to Crystallume for depositing thick diamond films on the reverse side of the flats. One etched and one unetched HIP sample, respectively, were subjected to thick film deposition.
3 in. diameter, ~ 0.5 in thick, graphite fiber reinforced glass matrix composite billet (HAC-GLAS-13-2) coated with polished, polycrystalline β-SiC.	β-SiC film on the billet was extremely non uniform and discolored.
Single crystal silicon troboflat for thickness calibration	Following diamond deposition the silicon sample was cut in half for accurate film thickness measurement.

3.5.2 Large Area Deposition and Polishability of Thick Films

The main objectives of this round of experiments consisted of the following:

1. Determine Crystallume's ability to evenly deposit an ~10 μm thick, pure diamond coating on a 7.8 cm (3 in.) dia., 1.3 cm (0.5 in.) thick poly-XTL (CVD) β-SiC-coated and polished ceramic composite disc. This disc is a prototype specimen of an advanced, high energy laser mirror substrate.
2. Deposit the same, thick diamond film on two (2 ea) α-SiC SEM triboflats and several thickness control specimen flats placed on the periphery of the composite disc.
3. Attempt to polish the coated mirror substrate and the triboflats to a reasonably high surface finish by using conventional diamond polishing techniques.
4. Examine the diamond coating before and after polishing for (a) morphological defects (by optical/SEM photomicrography, (b) film purity in terms of sp^3/sp^2 bonding ratios and interfilm stresses (by Raman spectroscopy); (c) elemental impurities (by EDX), and (d) surface roughness, film thickness and surface height variations (by stylus profilometry).
5. Evaluate the chemical and broad spectral range optical properties of free-standing, (0.5 – 8 μm thick) diamond windows commercially sold by Crystallume as X-ray windows used for SEM/EDX analyses.

3.5.2.1 Mirror Substrate Coating and Polishing. The evaluation of the laser mirror substrate disc before and after the diamond coating (the first four objectives) is described in APPENDICES EE, FF and GG. The summary of the findings is as follows (also see Table 42):

1. The diamond film thickness was close to 9 ± 0.9 μm.
2. The film was relatively free of sp^2 (graphite-like) bonded species, but it did contain a considerable amount of Si contamination. Since previous work on coating α/β-SiC with diamond did not show any Si content in the film, it appears that Si species from the lithium-aluminum silicate substrate are sputtered into the plasma and redeposited on the growing diamond films.
3. The surface morphology of the diamond ranged from cauliflowered (in the center of the disc, at the gas inlet of the reactor) to faceted (at the edge of the disc).
4. The diamond film nucleated on, and adhered to, both the polished β-SiC and to areas where the original β-SiC coating was completely polished off at the edges prior to diamond deposition. The tips of the graphite fibers and the lithium-aluminum silicate matrix were fully exposed at these areas. In fact, the adhesion of the as-deposited diamond film was so good everywhere that the diamond-powder-charged polishing cloth was ripped to shreds as polishing of the disc surface first began.
5. During diamond growth, the crack network in the polished β-SiC film substrate served as nucleation sites for cracks which propagated into the diamond film. These and other substrate

defects heavily influenced the structural integrity and topography of the as-deposited diamond film.

6. Both the Raman peak shift (from the characteristic 1333 cm^{-1} to a strong one at 1330 cm^{-1}) and the chipping of the film at certain (small) areas, combined with the observation of both intergranular and transgranular fracture in the diamond film at the cracks, indicated high interfilm stresses. Note that the thermal mismatch between the components ($\Delta\alpha_{x-y} = 0.65 \times 10^{6} \cdot °C^{-1}$) is small, but not negligible.

7. The surface roughness of the diamond film was ~0.35 μm (~14 μin) rms in the as-deposited condition and ~0.23 μm (~9 μin) rms after polishing. About a 1 μm thick diamond layer was removed during the process.

In essence, to develop an optimum diamond film in terms of defect-free morphology, the predeposited surface of the substrate must meet or exceed the final mirror finish requirements. Because of the size limitations of this particular (DC-plasma-assisted) deposition method, the surface area must be kept to a minimum. The outer limit of the diameter is four inches, noting that the variation in film thickness is ±10 percent even for the best possible growth conditions.

The mirror's substrate material, processing and diamond coating must be developed with several considerations in mind. In addition to the inherent requirements necessary for high energy laser mirrors, the interface surface must provide the optimum nucleation and growth conditions. The deposition variables must produce the best quality films in terms of morphology (whether faceted or cauliflowered), crystallite size, and chemical structure. Many of these characteristics cannot be controlled carefully enough at this time. Additionally, the size requirements of the mirrors push the DC-plasma-assisted deposition method to its limit. The long (~10 days) deposition time also indicates the need for a growth method which is more efficient.

These findings were reported at a University of Arizona Optical Sciences Department Diamond Initiative Planning Meeting held on February 23, 1989, Tucson, AZ, with WRDC, SDIO, University of Arizona, S-Cubed, Crystallume and Hughes representatives in attendance (see APPENDIX GG).

3.5.2.2 Diamond Windows. The first major product line from Crystallume is a 0.5 μm thick, ~6 mm dia., free-standing diamond window capable of transmitting low energy X-rays during SEM/EDX, down through the element B. Early versions of these windows consisted of diamond deposited by DC-plasma CVD on a XTL Si wafer, followed by chemical etching of the Si away from the diamond layer. This leaves a roughly circular, free-standing (actually, silicon-frame-supported) window behind.

Three of these early X-ray windows were examined at Hughes by SEM and optical photomicrography, combined with FTIR analysis. One of the windows became broken during handling, giving us an opportunity to photograph the free-standing film on-edge.

As shown in Figure 234, the broken window contains clear and hazy areas. Higher magnification shots in Figure 235 and 236 indicate that the clear areas are almost all DLC films. The hazy ones contain a DLC underlayer, with nucleated and coalescing diamond crystallites growing on top. In reflected light,

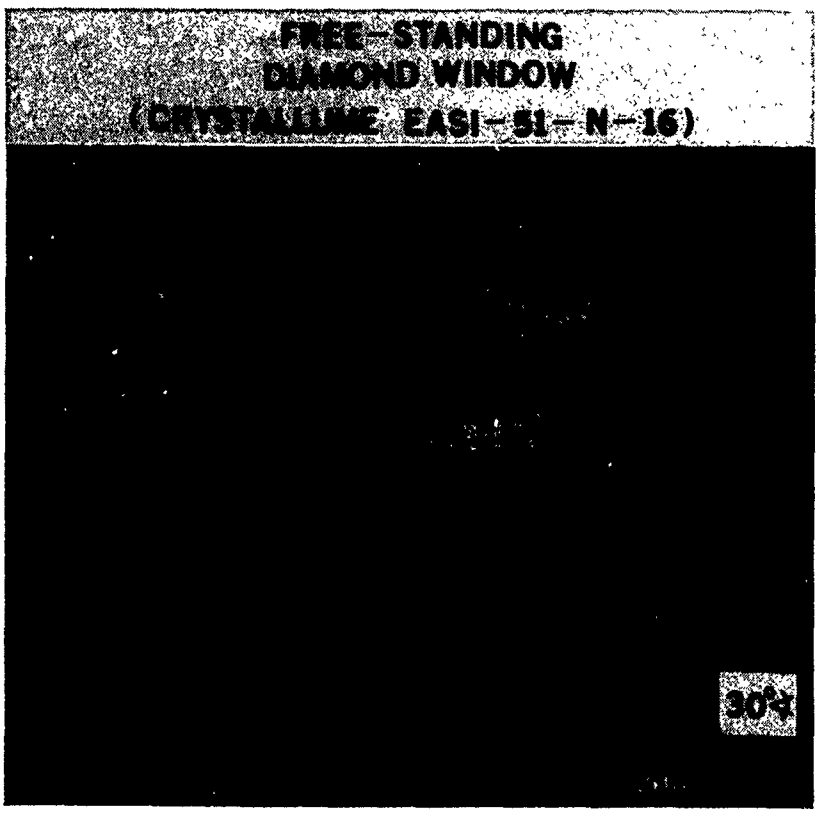

Figure 234. Low magnification, shallow-angle SEM photomicrograph of Crystallume's broken X-ray window; indicated areas are clear or hazy in terms of visual transparency.

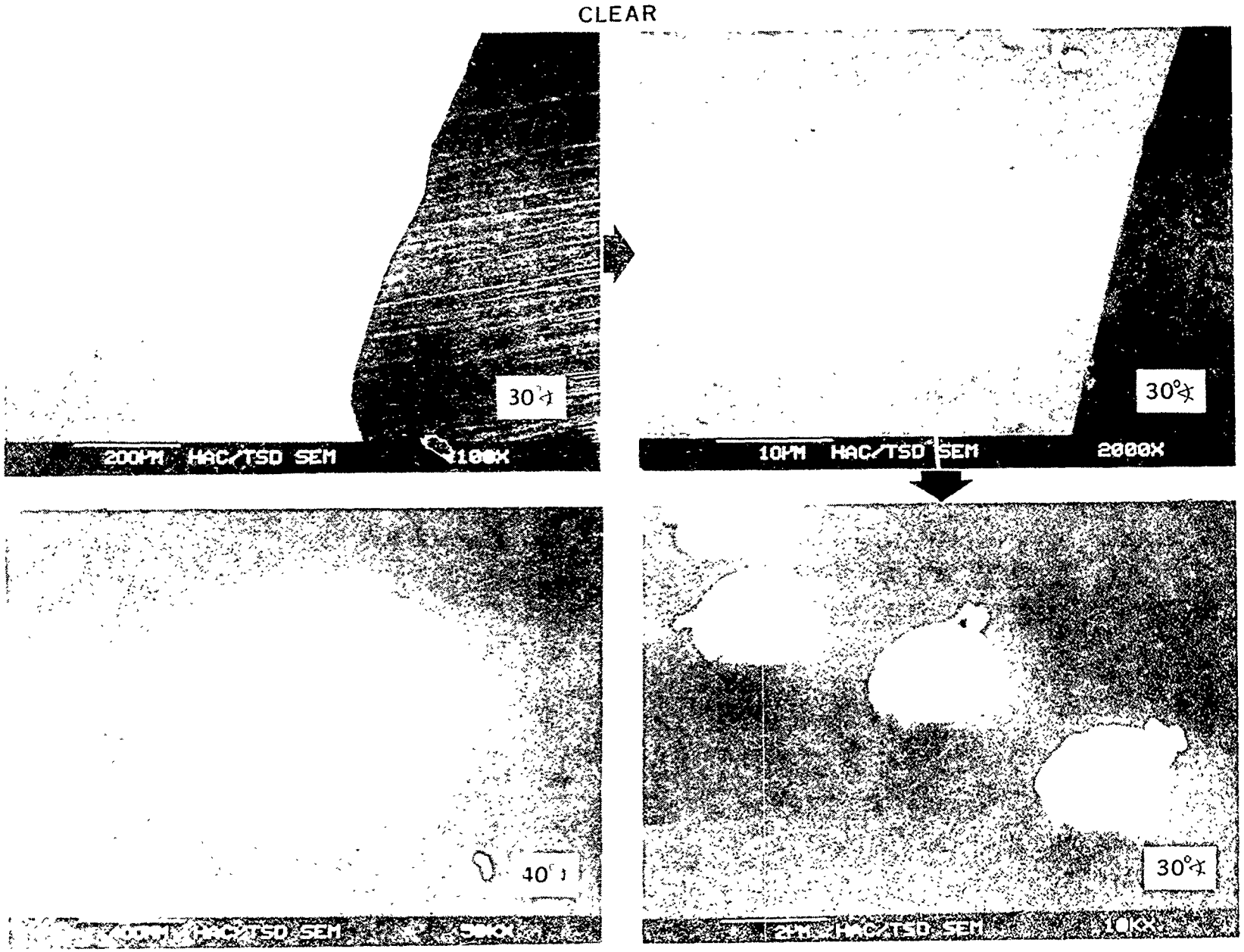

Figure 235 High magnification SE[illegible]ographs of Crystallume [illegible]oken X-ray wind[illegible] and clear area; note poor [illegible]rop-like diamond crystalli[illegible]n DLC underl[illegible]

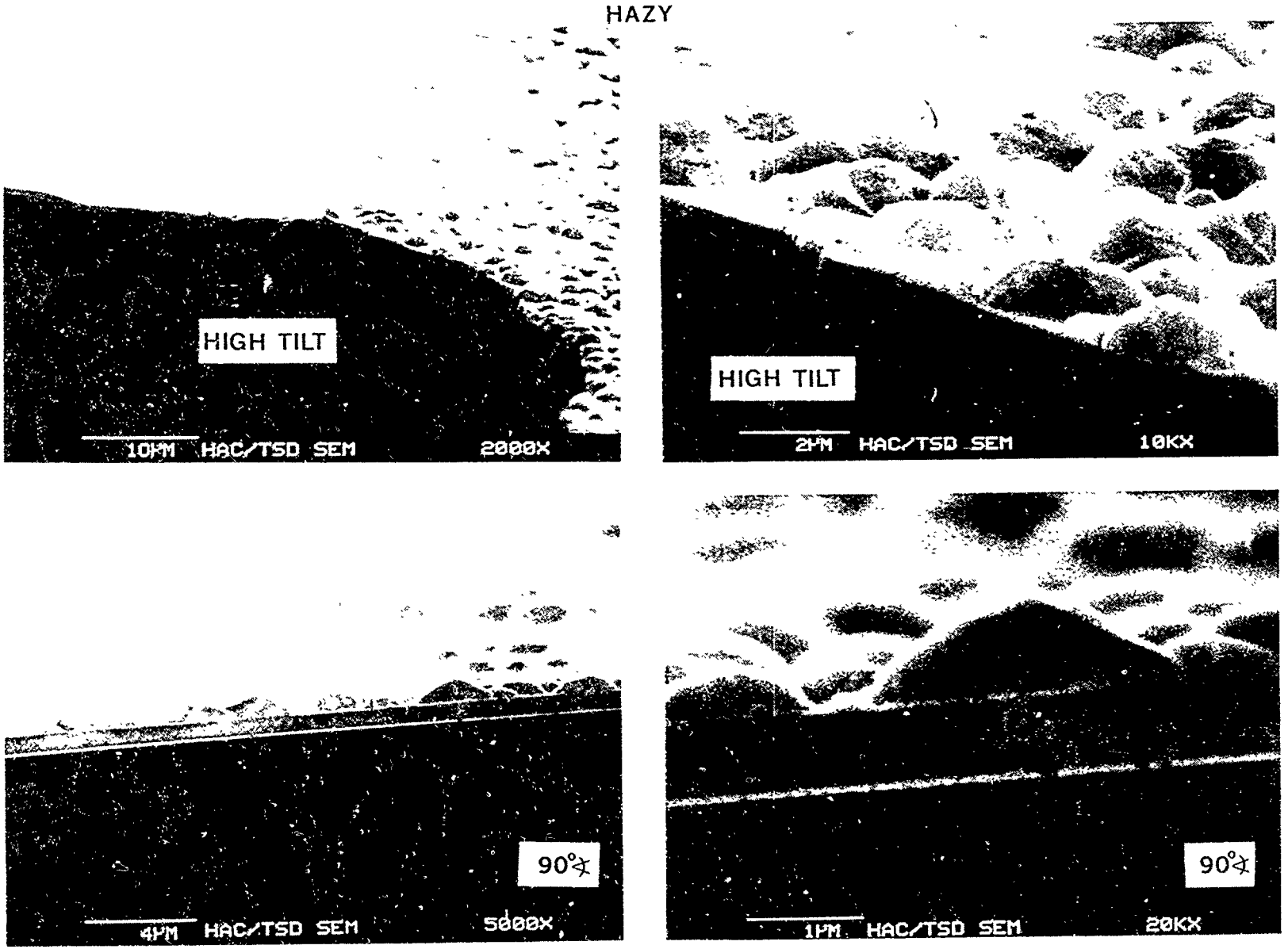

Figure 236. High magnification SEM photomicrographs of Crystallume's broken X-ray window, at a hazy area; note better, but still incomplete nucleation and coverage of more faceted diamond crystallites on the DLC underlayer.

the DLC side is shiny, the diamond side is hazy; the DLC layer faithfully contours the high, specular surface finish of the XTL Si substrate, while the reflection from the faceted diamond crystallites is somewhat diffuse. EDX of the DLC layer revealed a considerable amount of Si, especially at the Si/DLC interface.

Color Polaroid photos were also taken with a Leitz Metalloplan (an incident-light, large-field microscope) of Crystallume Window Sample No., EASI-51-N-15 (opaque) and EASI-51-N-16 (clear). These photomicrographs are included here in the black-and-white form as Figures 237 and 238. Both sets of photos indicate a large number of small, submicron and micron-size inclusions and the evidence of some voids. The various colors observed in the original photos were attributed to film-thickness-difference-caused optical phenomena (e.g., color changes determined by the appropriate fringes of equal chromatic order).

One interesting observation was the wrinkled appearance of the free-standing, diamond film enclosed and housed by the Si chip frame. Inasmuch as the thermal expansion match is poor and, consequently, diamond-on-Si is under 2.8 to 5.5 GPa (400 to 800,000 psi) compressive stress under certain deposition conditions, a wrinkled film should be expected after separating the diamond from its Si backing.

After photomicrography, the films depicted in Figures 237 and 238 were examined in the transmission mode by FTIR for any organic contamination.

The Hughes FTS-40 FTIR instrument is several orders of magnitude more sensitive than conventional infrared spectrometers. Some contaminants, weighing as little as ten picograms (1 picogram = 10^{-12} gram) can be detected with the FTS-40. A 50 μm particle or a fiber as thin as 20 μm can be easily analyzed. The optical/infrared microscope allows the examination of particles as small as 15 μm. This microscope has an adjustable aperture, and therefore a sample can be centered in the optical path. Then, without being moved, the sample is interrogated by replacing the visible light with the infrared beam. Both reflectance and transmission test modes are available. At this time, measurements on opaque bearing surfaces are limited to specular reflection, at near-normal light incidence only.

The FTIR data indicated no organic contamination in the CVD diamond layers, because no evidence of C-H, C-O or C-F bonds was present. Even though two of the diamond film samples were hazy, they were very transparent to the infrared beam.

More recently, a greatly improved version of the X-ray window, with a thick (6-8 μm) and very pure diamond film, encased in a steel washer frame was subjected to broad spectral range optical examination. The Cary 2300 spectrophometer (UV/VIS/NIR) and the FTS-40 FTIR instrument (mid-IR range extended to 22 μm) were used in the analyses. In both cases, the large window area allowed large slit heights and, therefore, more than adequate beam energies to produce spectra with good signal-to-noise ratios.

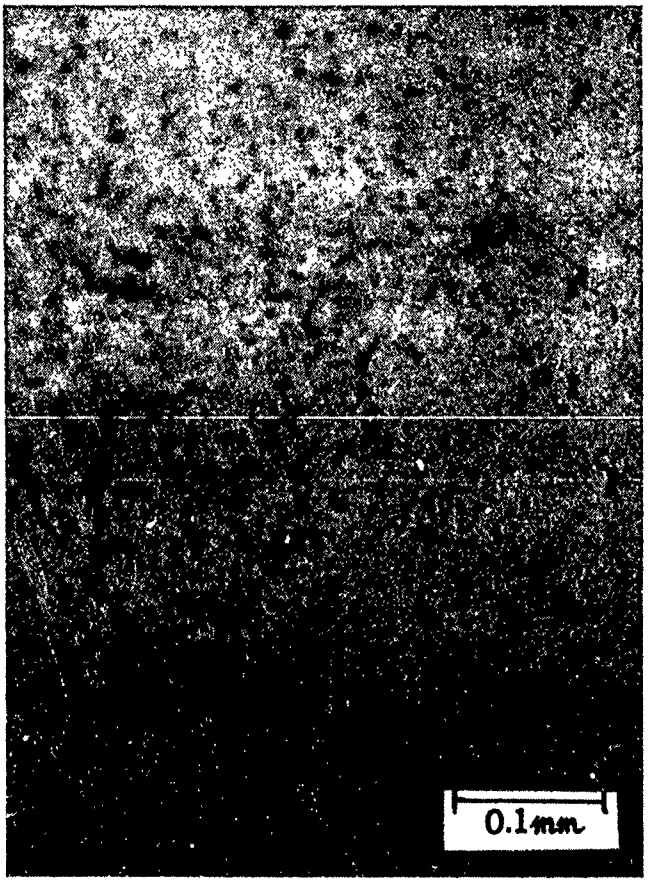

Figure 237. Optical photomicrograph of one of Crystallume's unbroken, hazy X-ray windows, at 200x magnification.

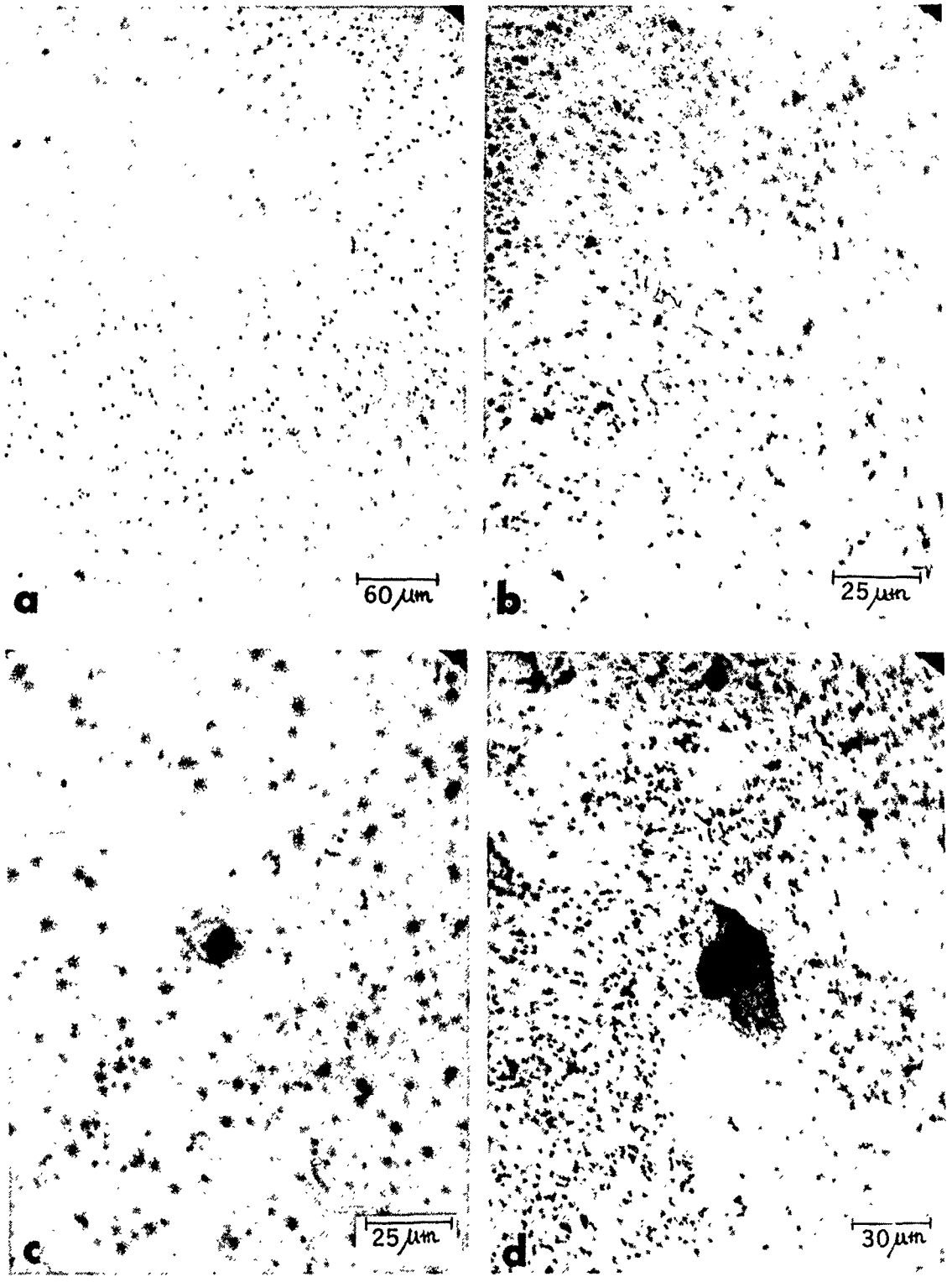

Figure 238 Optical photomicrographs of Crystallume's unbroken, clear X-ray window, at various magnifications (a = 250X; b = 625X; c = 500X; d = 625X, under reflected light).

The film heavily absorbed in the UV region and considerably in the visible range, but the IR transmittance was superbly high (see Figure 239 and APPENDIX HH). Note that the absorbance is the negative $\log_{10}$ of transmittance.

3.5.3 Fluorination of CVD Diamond Films

3.5.3.1 Deposition Studies. Following up the research Professor John Margrave and co-workers (Rice University, Houston, TX) started on fluorinating diamond powder (see APPENDIX II), their effort continued using diamond films and slabs as specimens. Their most recent data were presented at the 1988 MRS Fall Meeting's Tribology Symposium S (18).

As described in (18), in addition to diamond powders, XTL diamonds (slabs and naturally occurring stones), and CVD diamond films were fluorinated via direct fluorination and plasma techniques at a variety of temperatures and reaction times. Infrared, ESCA (XPS), and mass spectrometric studies verified that the diamond surfaces are altered by fluorination and that fluorine is attached to the surface to some degree. Based on spectra obtained using the FTIR techniques of DRIFTS and STR, the fluorine appears to have an effect on the diamond surfaces at relatively low temperatures and in short reaction times by the removal of surface contaminants. A relatively high temperature (600°C) or long reaction time at slightly lower temperatures is needed, however, to attach a significant number of fluorine atoms onto the diamond surface. Once fluorinated, the diamonds show enhanced resistance to oxidation. The outward appearance of the diamonds remains unchanged even at fluorination temperatures nearing 800°C.

One very significant observation was that ESCA verified the presence of both oxygen and fluorine on the diamond surface. By comparing peak areas relative to carbon, one concludes that approximately 3.5 percent of the diamond surface in this sample is covered by fluorine. In other ESCA work, it was seen that the relative amount of oxygen decreases linearly with the increase in fluorine. This suggests that hydrogen directly bonded to carbon may not be as prominent on the diamond surface as previously believed, since H should preferentially be attacked by the fluorine relative to oxygen to evolve very stable HF. In that case, there would be no observable decrease of oxygen as the fluorine content increased. Also, there was no evidence of any C-H stretching frequencies around 2900 cm^{-1} in any of the IR spectra, unless the diamond was treated with H_2 in some fashion. The data suggest that oxygen is the most predominant species on an untreated diamond surface. This finding is extremely significant, especially in view of the high friction of CVD diamond films in air, at room temperature. It is suspected that the oxidized diamond surface attracts moisture to a certain extent by hydrogen bonding (and/or another binding mechanism).

It is noteworthy that in the case of graphite, the oxidation products are CO and CO_2 (gases) and graphite oxide (a solid). Leong et al (29) described graphite oxide as a solid, one of the two known covalent compounds of graphite. The materials demonstrates high stability at normal temperatures because of its covalency. No definite stoichiometry can be assigned to it, however, an idealized formula of $C_8O_2(OH)_2$ has been postulated. The covalent C-O-C bonds are like ether linkages. They suggest

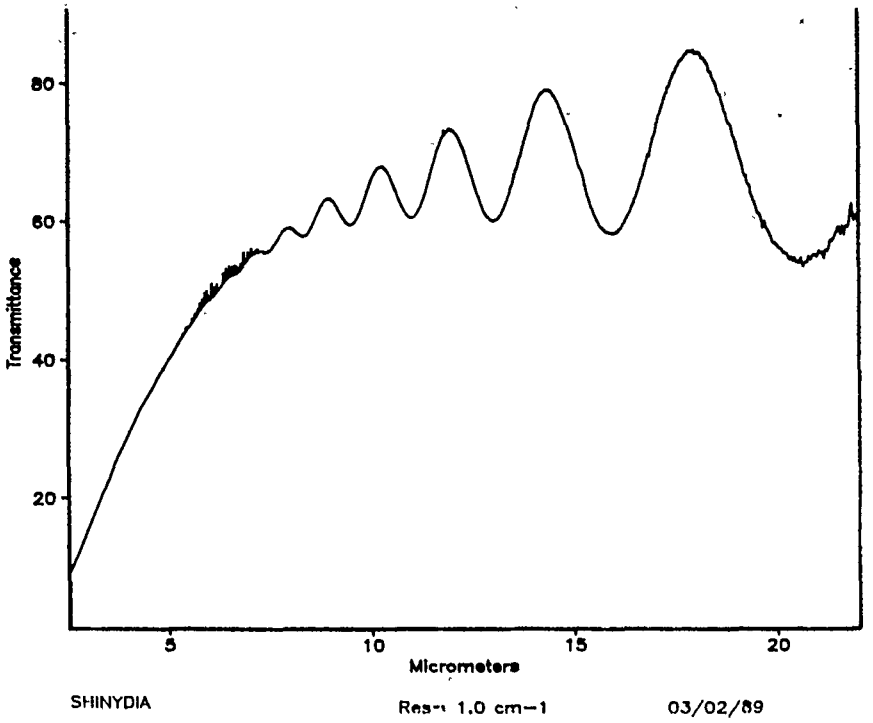

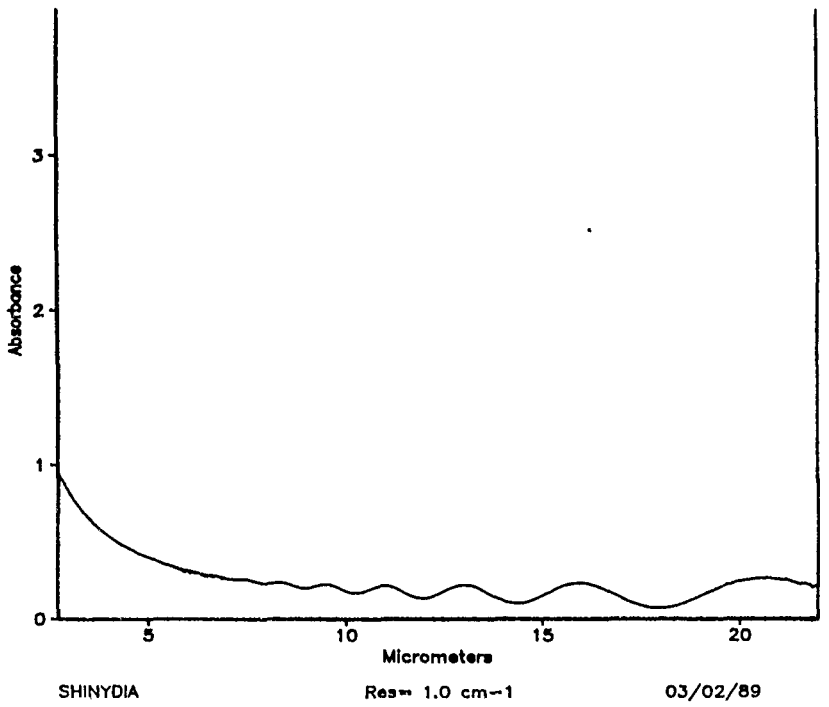

Figure 239. IR transmittance and absorbance of Crystallume's 6-8 μm thick X-ray window.

puckering of the carbon layers and through a keto-enol tautomerism tend to preserve the otherwise planar-hexagonal network of graphite. There are no equivalent data on the suggested stoichiometry of "diamond oxide," although some differences are suspected. Previous Hughes/Marchem, Inc. research (38) indicated that the fluorination of graphite fiber weaves is a first order reaction, eventually converting all fibers to the white powder $CF_{1.1}$ (graphite fluoride), see Figure 240. Yet, program research indicated that the fluorination of the diamond's surface is a higher order reaction, because the "fluoro-skin" is self-protective and remains thin during continued fluorination. The high reactivity of the graphite edge sites versus the lower reactivity of the preferentially formed and inert (111) diamond habit planes on most CVD diamond films may be the most probable, underlying difference in the fluoridation and oxidation of both materials. Unfortunately, no literature data could be found on the subject of "diamond-oxide-hydroxide" stability, under tribotest conditions.

In view of the main objective of diamond fluorination, i.e., tribooxidative stabilization of a CVD diamond film surface in a wide environmental regime, another P.O. was written for Prof. Margrave to fluorinate a total of no less than 10 each additional samples provided by Hughes Aircraft Company, consisting of:

1. 7 mm x 5 mm x ~1 mm, bare Si(100) and XTL sapphire flats primer-coated with 100 μm titanium interlayer and both types of flats further coated with 0.5 – 1.0 μm thick, poly-XTL diamond film on one 7 mm x 5 mm side only. It was of interest to see if any reduced-friction "fluoro-skin" could postpone delamination of the diamond film normally adhering very poorly to sapphire.
2. 7 mm x 5 mm x 2 mm, sintered α-SiC flats coated with ~1.5 μm thick, poly-XTL diamond film on the polished 7 mm x 5 mm side only. These samples were intended to provide direct comparison with the as-deposited, but as yet unfluorinated samples.
3. 7 mm x 5 mm x 2 mm, sintered α-SiC flats coated with ~1.5 μm thick, poly-XTL diamond film on the polished 7 mm x 5 mm side and ~10 μm thick diamond film on the ground 7 mm x 5 mm side. Here, the thick diamond film was polished to allow the examination of polished-unfluorinated and polished-fluorinated thick films against similarly treated tribopins (see 4 below).
4. 2 mm dia., 10 mm long, hemispherically tipped sintered α-SiC pins coated on the tip with ~1.5 μm and 10 μm thick and unpolished, poly-XTL diamond films; and
5. At least one (1) each, ~10 mm dia., free-standing poly-XTL diamond window. It is of interest to see if fluorination would affect, in any significant way, the wide wavelength range transmission of the diamond film.

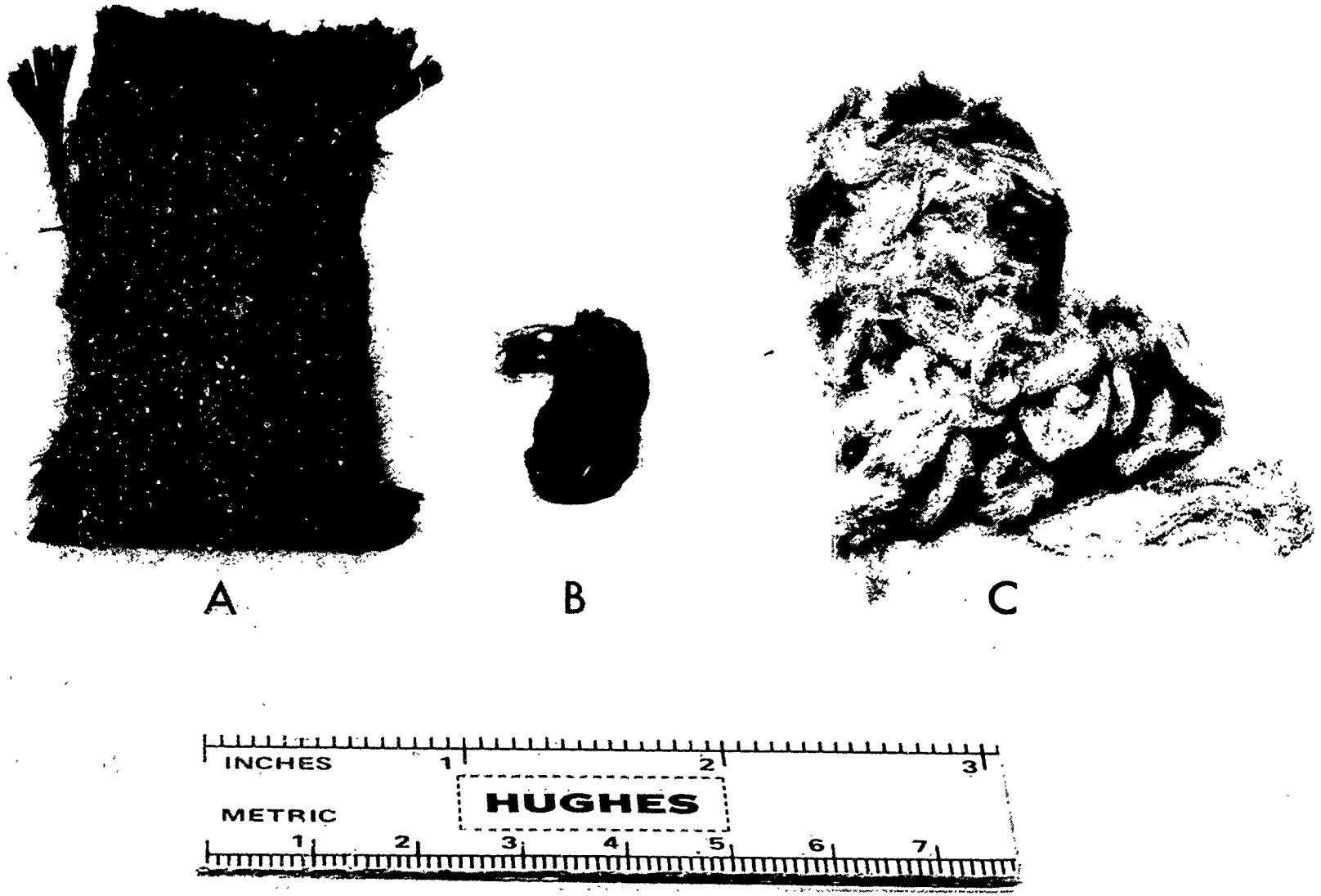

Figure 240. The fluorination of graphite fiber weaves; (a) original weave; (b) after brief reaction, and (c) halfway to complete decomposition (reaction) to graphite fluoride ($CF_{1.1}$).

3.5.3.2 SEM Tribometry of Fluorinated Diamond. Basically, Prof. Margrave and his coworkers used three different types of fluorination techniques:

- direct, high temperature fluorination in F_2 gas; 340° to 530°C, 4 to 8 hours.
- UV-assisted fluorination, with 10 percent F_2 in He; 2 hours.
- plasma fluorination in 5 to 10 percent CF_4 in Ar plasma, 1 to 3 hours.

The first observations which were made on opening the package from Rice University immediately indicated the harmful effects of fluorination (see Figure 241). The extensive delamination of the films from the triboflats, with only a few exceptions, was an indication of interface attack by fluorine through microcracks and pinholes in the film. Most of the pin tip coatings suffered from microcracking after fluorination, although gross and catastrophic delamination could not be observed.

The SEM tribometer tests were performed in a conventional manner (normal load = 50 g = 0.49 N; oscillatory speed 4.66 $mm \cdot s^{-1}$, 1.33 x 10^{-3} Pa = 1 x 10^{-5} torr, or 13.3 Pa = 0.1 torr), with up-and-down ramping the temperature, as before (850°C maximum).

After a few preliminary experiments with the diamond film-coated sapphire flat (near-immediate delamination at R.T.), it was decided to complete the first two out of the three, still relatively intact specimen combinations described in Table 43. Prior to the tribotests, extensive XPS (ESCA) analysis of one unpolished and the other polished 5 mm x 7 mm sides of an α-SiC diamond triboflat was completed. We looked for the characteristic C and F binding energy shifts, which might indicate PTFE-like $[-(CF_2)_n-]$ bonding between the diamond substrate and fluorine. Note that the binding energy of carbon (C1s) under such circumstances would be just below 292 eV; the equivalent energy of fluorine (F1s) is close to 689 eV.

XPS of the unpolished side (Figures 242, 243, 244 and the summary Table 44) revealed that the fluorine was, at best, only chemisorbed on the surface, with no evidence of $-(CF_2)_n-$ like bonding. The meager 8.9 percent F concentration on the surface dropped to 3.82 percent after a 15 second Ar ion etch, indicating ready desorption. There was some minimal shift of the binding energy peaks to higher eV values after Ar etching, possibly some additional C-F bonding induced by the ion-etching process itself. The data in Table 44 show some Al, Si and Na contamination (from glassware?); the oxygen content is low.

The XPS results on the polished side of the same triboflat confirm the substantive lack of reaction between C and F (Figures 245 through 248 and Table 45). However, as shown by the data in Table 45, there are some significant differences caused apparently by the polishing of diamond prior to fluorination.

1. Fluorine was present in greater concentration on the polished side (11.87 percent) than on the unpolished side (8.9 percent). A 15 second ion etch lowered the polished-side F content to 10.69 percent, while the unpolished side's F content went as low as 3.82 percent. A second 15 second ion etch only incrementally lowered the fluorine content to 9.19 percent, on the polished

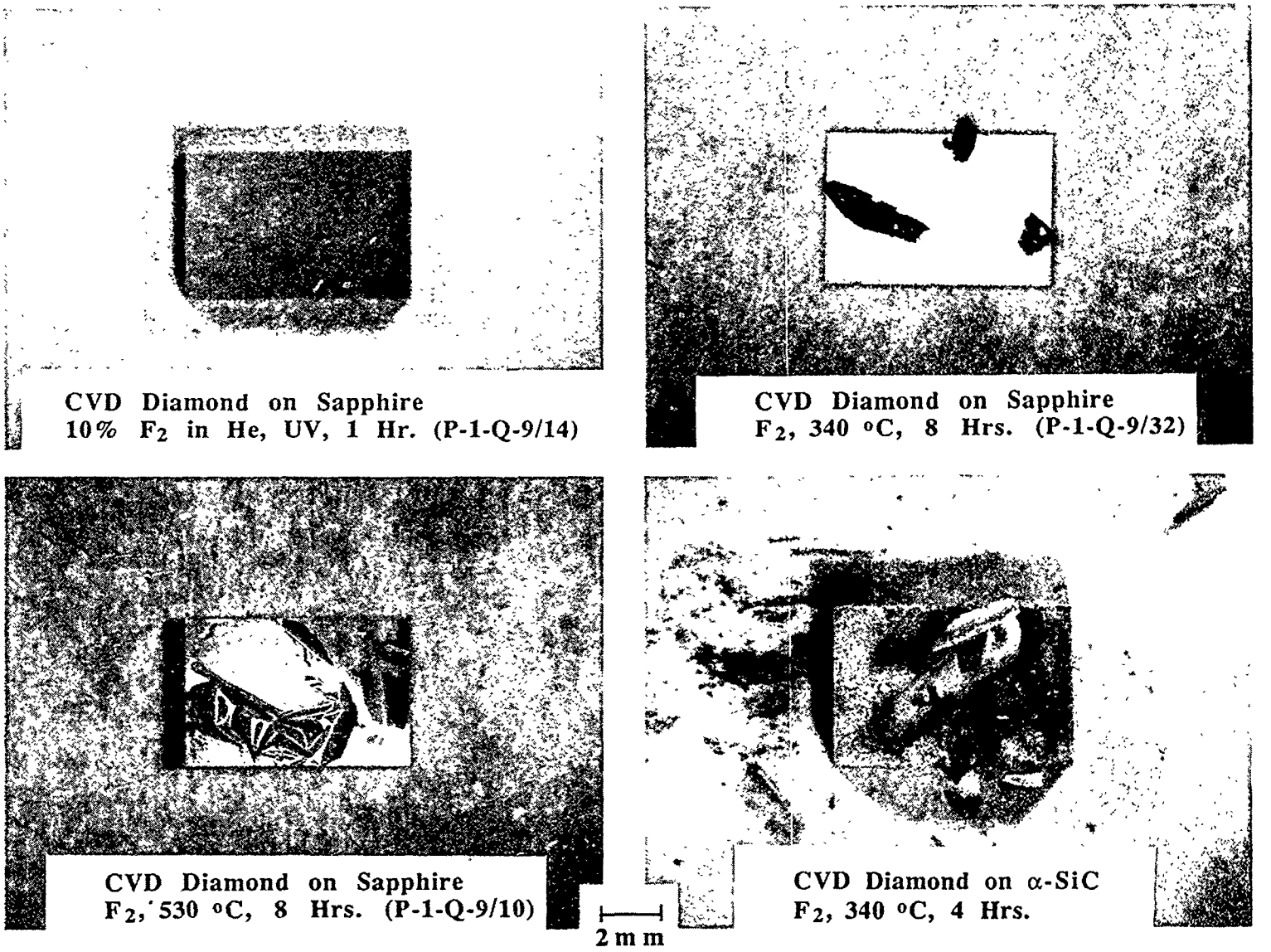

Figure 241. The appearance of fluorinated, poly-XTL CVD diamond films on sapphire and poly-XTL α-SiC substrates.

Table 43. Fluorination parameters of poly-XTL CVD diamond film-coated, ceramic SEM tribometer specimens.

FLAT	PIN
DC-CVD Dia. on Si (100) **10% CF_4, Ar Plasma, 3 hr.**	DC-CVD Dia. on α-SiC **F_2, 350 °C, 4 hr.**
DC-CVD Dia. on α-SiC (polished) **10% F_2 in He, UV, 1 hr.**	MW-CVD Dia on α-SiC **10% F_2 in He, UV, 2 hr.**
DC-CVD Dia. on α-SiC **10% F_2 in He, UV, 2 hr.**	MW-CVD DIA on α-SiC **10% F_2 in He, UV, 2 hr.**

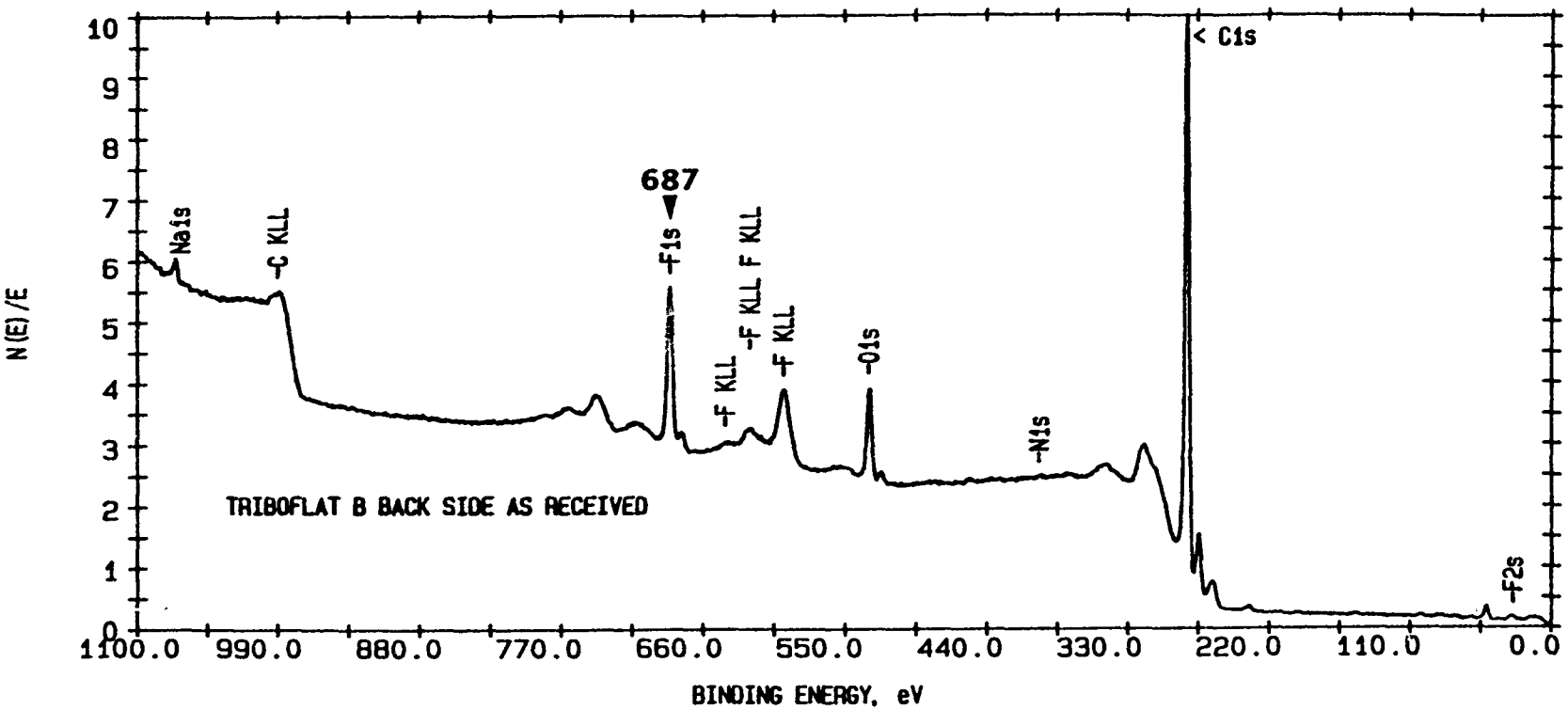

ESCA SURVEY 8/23/89 ANGLE= 45 deg ACQ TIME=19.82 min
FILE: DIAMOND14 TRIBOFLAT B--ETCHED HIP
SCALE FACTOR= 13.905 k c/s, OFFSET= 1.042 k c/s PASS ENERGY=178.950 eV mg 400 W

Figure 242. XPS spectrum of fluorinated diamond (unpolished) on α-SiC triboflat (see Table 43).

CURVE FIT	AREA	POSITION	HEIGHT	% TOTAL AREA	ATOMIC CONCENTRATION
1	130067	284.50	73900	74.1	61.2
2	33381	285.20	14318	19.0	15.7
3	12112	287.01	5195	6.9	5.7

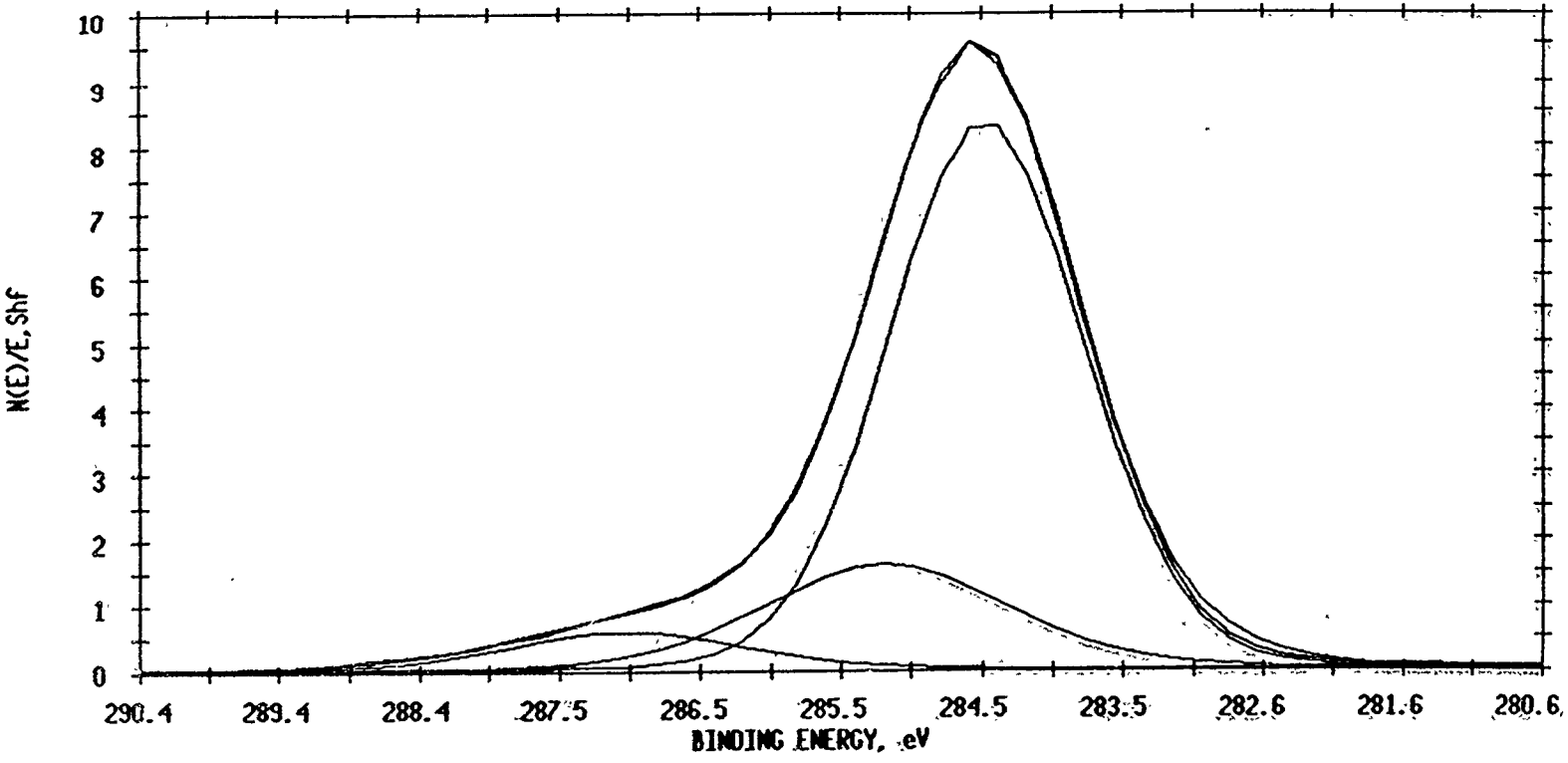

Figure 243. XPS curve-fit for carbon (same specimen as in Figure 242).

CURVE FIT	AREA	POSITION	HEIGHT	% TOTAL AREA	ATOMIC CONCENTRATION
1	110398	284.50	47352	73.1	67.4
2	31488	285.20	14791	20.8	19.2
3	9140	287.34	4293	6.1	5.6

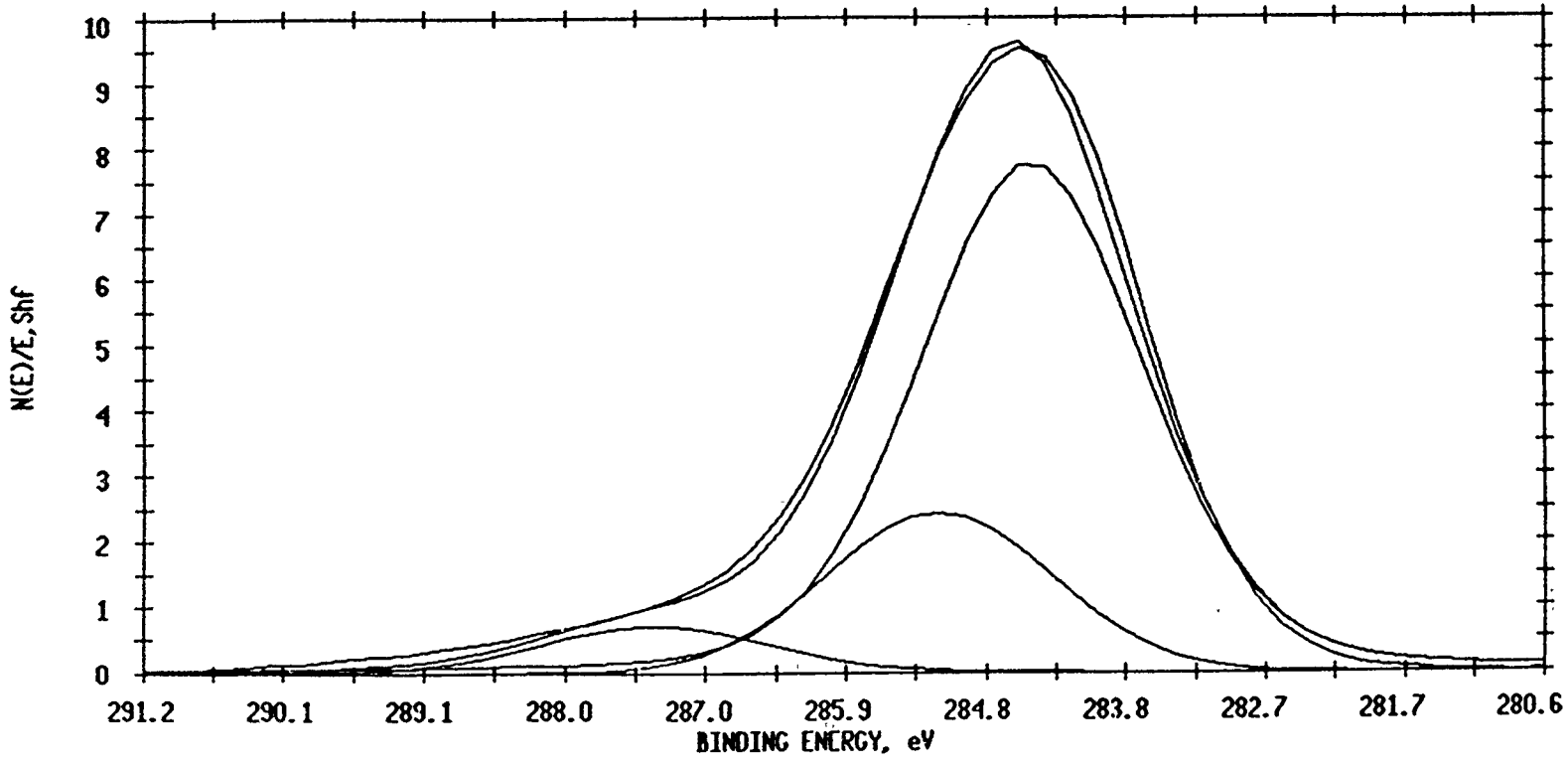

Figure 244. XPS curve-fit for carbon, after a 15 sec. Ar ion etch (same specimen as in Figures 242 and 243).

Table 44. Atomic concentration table for the unpolished diamond-on-SiC triboflat side (see Figures 242, 243, and 244), by XPS.

Element	As Received			1 x 15 Sec Etch
	Area (cts-eV/s)	Sensitivity Factor	Concentration (%)	Concentration (%)
C1s	275,071	0.296	82.63	92.19
N1s	1,184	0.477	0.22	
O1s	55,498	0.711	6.94	1.86
F1s	100,103	1.000	8.90	3.82
Al2p	594	0.234	0.23	0.30
Si2p	1,536	0.339	0.40	0.56
Na1s	12,796	1.685	0.68	1.28

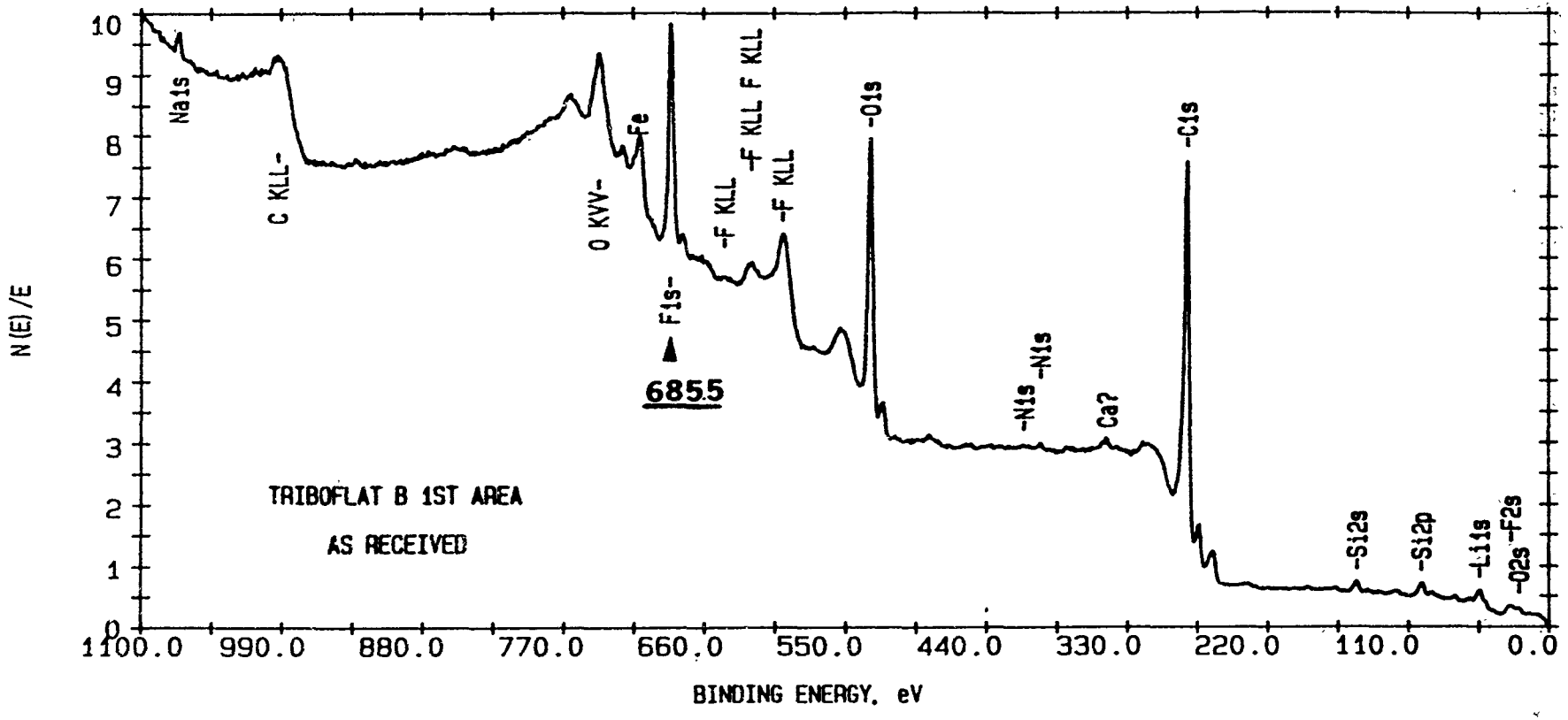

ESCA SURVEY 8/23/89 ANGLE= 45 deg ACQ TIME=19.82 min
FILE: DIAMOND8 TRIBOFLAT B--ETCHED HIP
SCALE FACTOR= 12.008 k c/s, OFFSET= 1.932 k c/s PASS ENERGY=178.950 eV mg 400 W

Figure 245. XPS spectrum of fluorinated diamond (polished) on α-SiC triboflat (see Table 43).

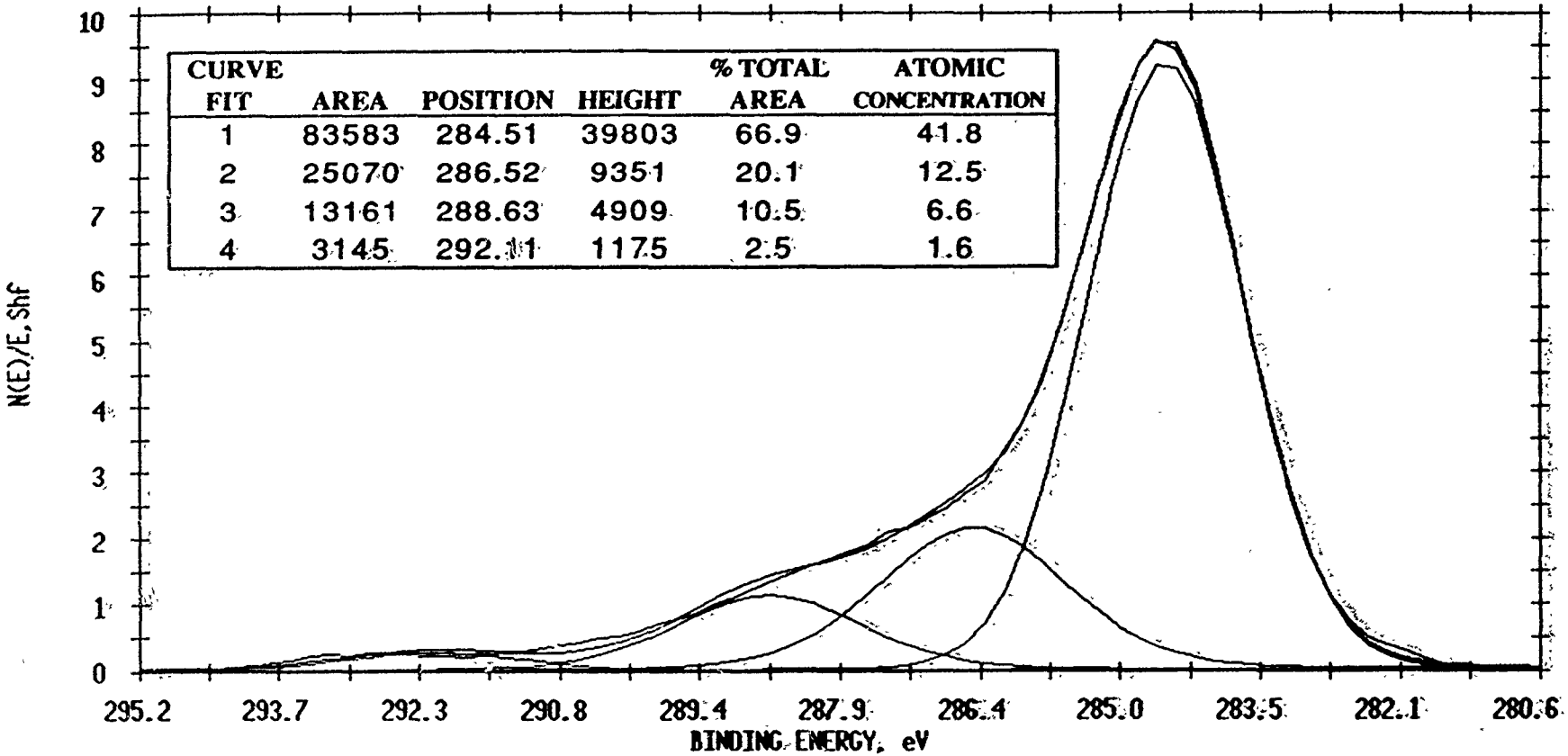

Figure 246. XPS curve-fit for carbon (same specimen as in Figure 245).

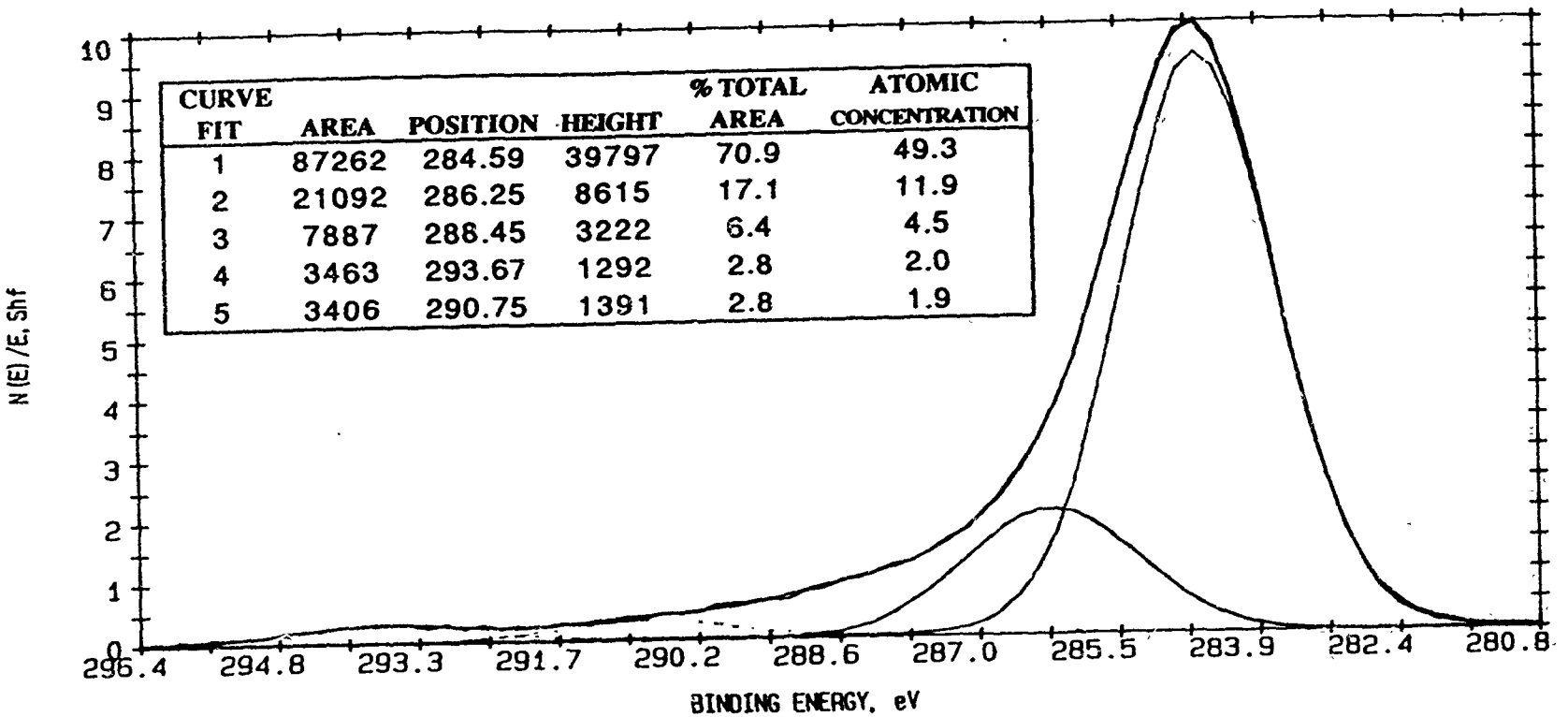

CURVE FIT	AREA	POSITION	HEIGHT	% TOTAL AREA	ATOMIC CONCENTRATION
1	87262	284.59	39797	70.9	49.3
2	21092	286.25	8615	17.1	11.9
3	7887	288.45	3222	6.4	4.5
4	3463	293.67	1292	2.8	2.0
5	3406	290.75	1391	2.8	1.9

ESCA CURVE FIT 8/23/89 ANGLE= 45 deg ACQ TIME=2.52 min
FILE: Curve_Fit TRIBOFLAT B--ETCHED HIP
SCALE FACTOR= 4.204 k c/s, OFFSET= 0.000 k c/s PASS ENERGY= 71.550 eV mg 400 W

Figure 247. XPS curve-fit for carbon, after a 1x15 sec. Ar ion etch (same specimen as in Figure s245 and 246).

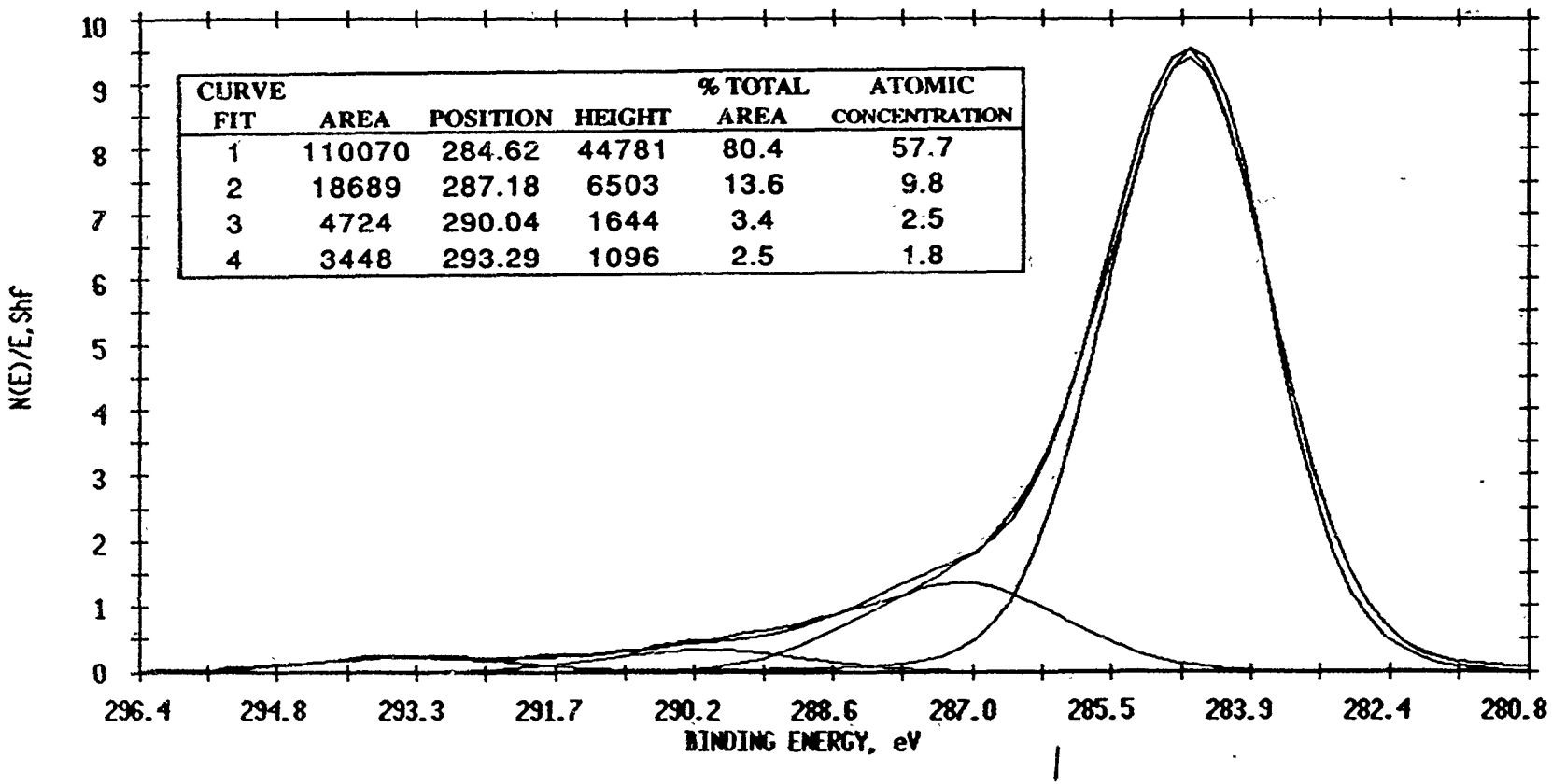

Figure 248. XPS curve-fit for carbon, after a 2x15 sec. Ar ion etch (same specimen as in Figures 245 and 246).

Table 45. Atomic concentration table for the polished diamond-on-SiC triboflat side (see Figures 245 through 248), by XPS.

Element	As Received			1 x 15 Sec Etch	2 x 15 Sec Etch
	Area (cts-eV/s)	Sensitivity Factor	Concentration (%)	Concentration (%)	Concentration (%)
C1s	178,375	0.296	62.44	69.59	71.80
N1s	2,200	0.477	0.48	0.26	0.28
O1s	137,283	0.711	20.01	9.29	8.01
F1s	114,523	1.000	11.87	10.69	9.19
Si2p	7,019	0.339	2.15	3.26	2.95
Fe2p3	46,666	1.971	2.45	5.43	4.60
Na1s	9,956	1.685	0.61	1.48	1.40
				Al2p	1.14
				Ca2p	0.63

side. Here, the oxygen content of the surface was also far greater (20.01 percent) than that of the unpolished surface (6.94 percent). The argon ions removed oxygen more efficiently than fluorine. One may attribute the larger F and O content of the surface to activation by polishing.

2. The cast iron polishing plate transferred some Fe to the diamond, the residue of which (e.g., iron oxides) must have penetrated the microcracks (see increase in Fe content on Ar etching). Sodium, Si, Ca and Na contamination was also present here, as before.

Fluorine's unwillingness to react with the diamond surface has been recently substantiated by Freedman and Stinespring's research (280). They fluorinated diamond (100) substrates with atomic (F) and molecular (F_2) fluorine in ultrahigh vacuum and found that (a) atomic fluorine reacts with an initial accommodation coefficient of 0.25 ± 0.1 at 300K, resulting in a saturation coverage of ~3/4 of a monolayer stable to 700K without desorption, and (b) molecular fluorine reacts even slower, with a saturation coverage of less than 1/5 monolayer, even at the exposure temperatures as high as 700 K. These fluorine-containing diamond surfaces showed no loss of fluorine after exposure to beams of H_2 and O_2 at temperatures between 300 K and 700 K.

A priori, even before the SEM tribotests, one would have doubts about the wear resistance of the extremely thin, fluorinated layers at elevated temperatures. As shown by Hauge, et al (18), the bond strength of fluorine to carbon was only incrementally higher than that of hydrogen during thermal description studies.

The SEM tribometer data in Figure 249 substantiated the expected results. The response of COF to heating in vacuum and in P_{air} here is the same as that of unfluorinated (i.e., largely and essentially hydrogenated) diamond in Figures 224, 225 and 227. Interestingly, however, the equilibrium R.T. COF of the fluorinated polished diamond was the lowest (at or substantially below 0.1) before the onset of heating. This phenomenon is partially attributed to the influence of Coulomb friction, which is manifested by the climbing of the asperities on one surface over those of the counterface. This means that the significant roughness and morphology differences between poly-XTL, CVD diamond films as a result of different deposition techniques and parameters substrate type, preparation etc. should heavily influence COF. For example, recent tribometry revealed (281) that rough diamond surfaces produced COF values up to an order of magnitude greater than smooth ones, when sliding against various solids, in air.

On heating, the COF of fluorinated diamond also increases, presumably due to the progressive desorption of fluorine (and residual hydrogen) and the simultaneous generation of dangling bonds. However, due to the high-COF-caused delamination of the diamond from the flat at the high temperatures (see Figure 250), this combination became again, as in Figure 227a and d, diamond versus α-SiC during both tests in Figure 249.

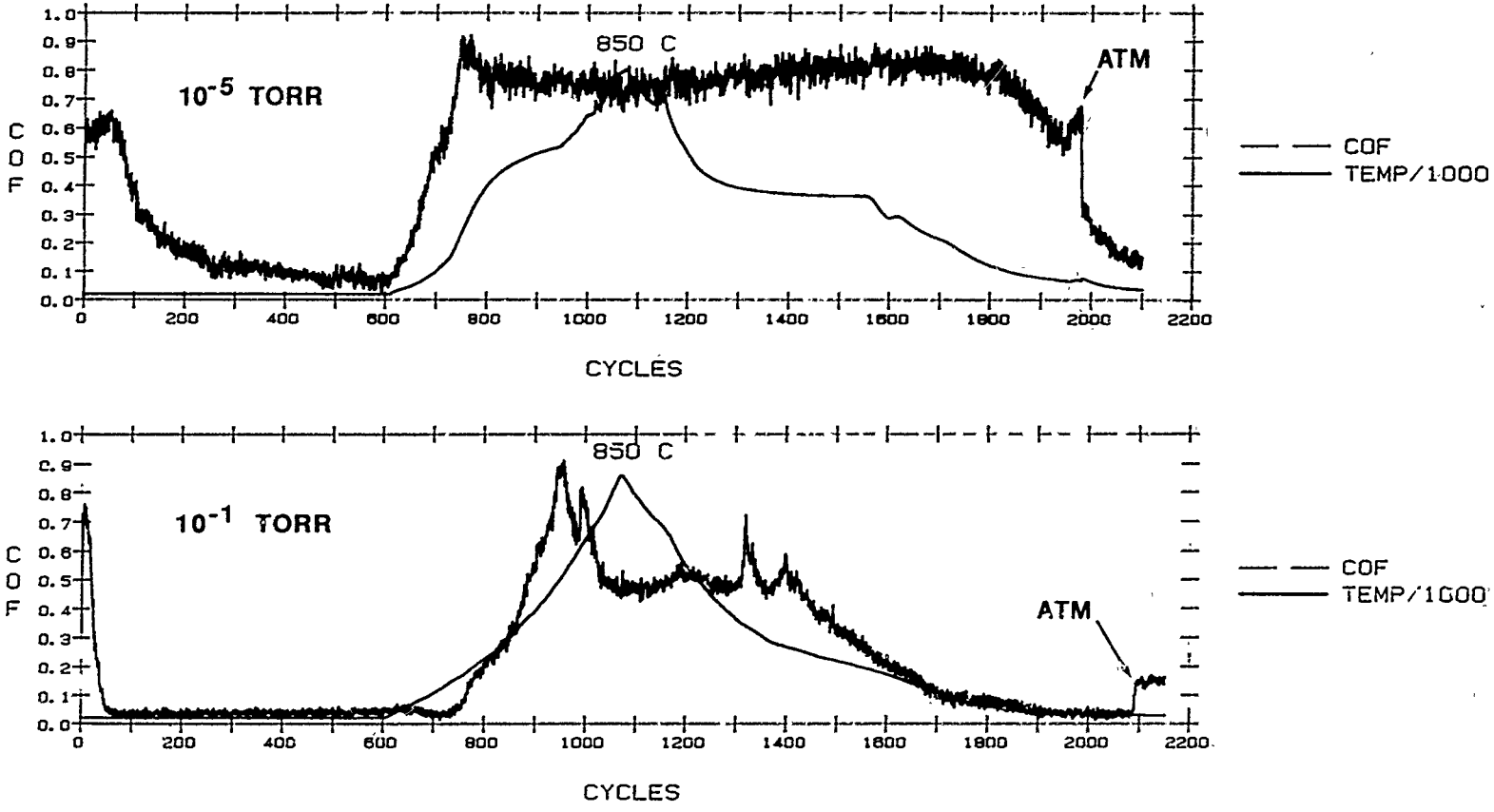

Figure 249. Coefficients of friction (COF) of fluorinated-unpolished diamond on α-SiC pin vs. fluorinated-polished diamond on α-SiC flat, in 1.33×10^{-3} Pa = 1×10^{-5} torr vacuum and in 13.3 Pa = 0.1 torr P_{air}, at various temperatures.

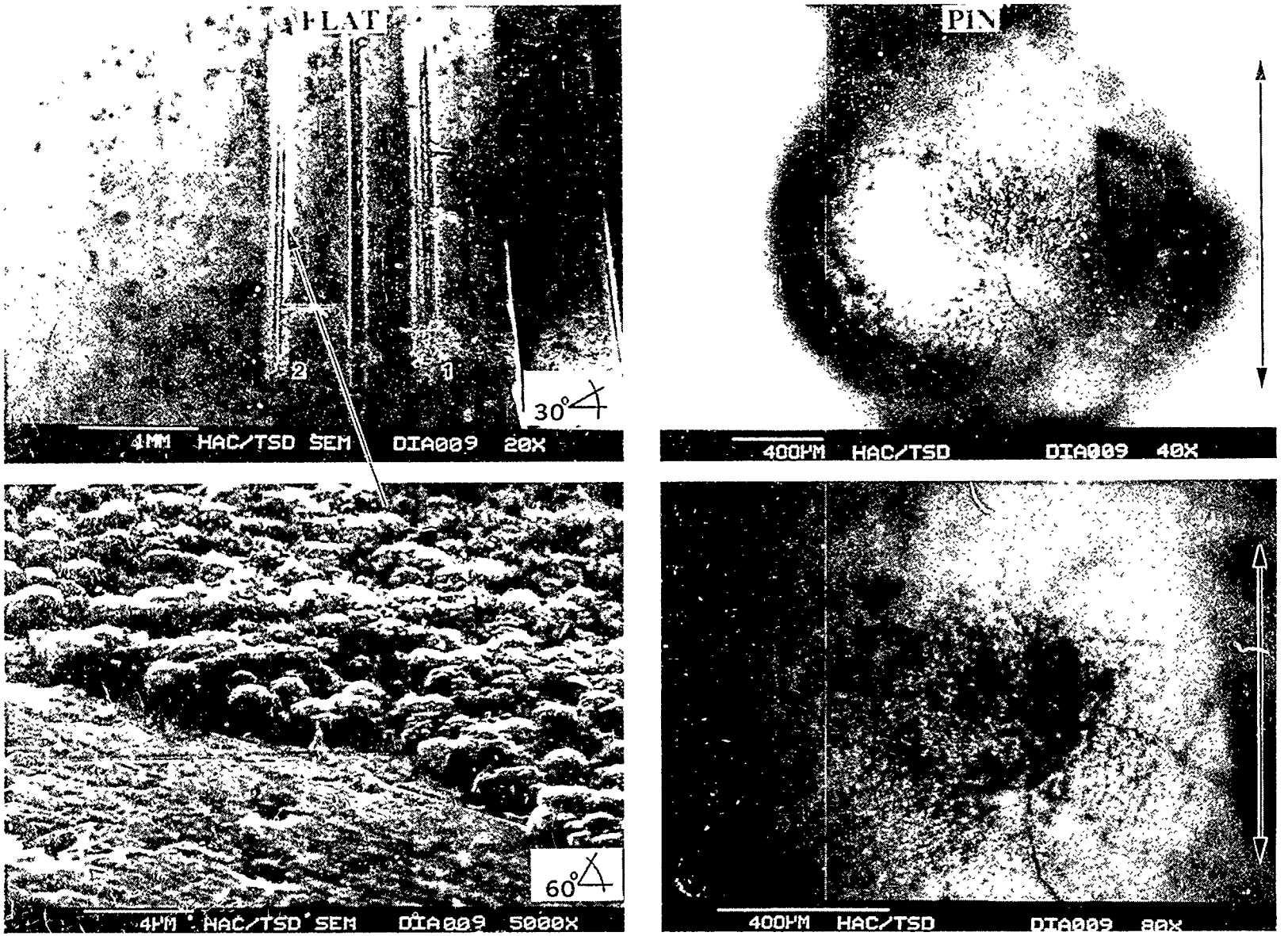

Figure 250 The appearance of the used SEM tribometer counterfaces at various SEM magnifications, associated with the tests described in Figure 249; double headed arrow indicates direction of oscillation

The SEM phogomicrographs of the cracked but not delaminated (fluorinated-unpolished) diamond on the tip of the α-SiC pin indicated that the fluorination process may have indeed weakened the interface, via the cracks. Since (a) reactive ion etching of SiC thin films in fluorinated gas plasmas showed no evidence of chemical reaction between fluorine and carbon (281), and (b) both atomic and molecular fluorine etches sp^2-bonded carbon components in diamond to a point of being able to achieve thermal CVD of diamond using CF_4 and F_2 without having to resort to plasma generation (282), the best explanation for diamond film delamination from the various ceramic substrates is based on fluorine attack of the DLC-like interlayer, through cracks and pinholes in the film.

The COF results on fluorinated-unpolished 1.5 μm diamond on the α-SiC pin versus fluorinated-unpolished 0.8 μm diamond on the Si(100) flat corroborated the previous results, see Test No. 1 and 2 in Figure 251. The R.T. equilibrium COF stabilized around 0.1. However, even at this low friction, the diamond film delaminated during Test No. 1 (see Figure 252). The point of delamination there occurred near 300 cycles (by video observations), indicating that the smooth Si (fluorinated?) substrate exhibited lower friction than the rougher, diamond surface.

During the heated Test No. 2, the diamond began to peel around the 300th cycle also, followed by a COF increase characteristic to dehydrogenated (i.e., dangling bond-containing) diamond or silicon.

The outstanding tribological behavior of the fluorinated diamond film, at elevated temperatures from the onset of sliding, was most surprising (see Test No. 3 in Figure 251). The COF was maintained at ~0.13, and the diamond film did not delaminate until the tribosystem was cooled at ~1560 cycles (note drastic increase in COF).

The overall data indicate that fluorination of CVD diamond films has not been effective to reduce and maintain COF in a wide environmental range, or to increase the wear life of the diamond layers.

3.5.4 Overall Conclusions and Recommended Future Work

The wide environmental range tribological behavior of poly-XTL diamond films deposited by DC- and MW-PACVD was examined by SEM tribometry. In the absence of in-situ surface analytical capability, the test data were interpreted on the basis of a large body of information collected from the literature, and the causes of the observed friction trends and wear behavior differences were speculated upon accordingly.

Our data appear to confirm Pepper's and Goddard's hypothesis in that the adhesion and friction of the respective couples are mainly controlled by the surface chemistry of the exposed crystallites (grains). Desorption of gases (mainly hydrogen) upon heating and rubbing under the electron beam, in vacuum , create dangling bonds on the surfaces. The same happens with single crystals of the respective materials sheared tantentially. If these bonds did not reconstruct or were not satisfied (capped) by hydrogen or

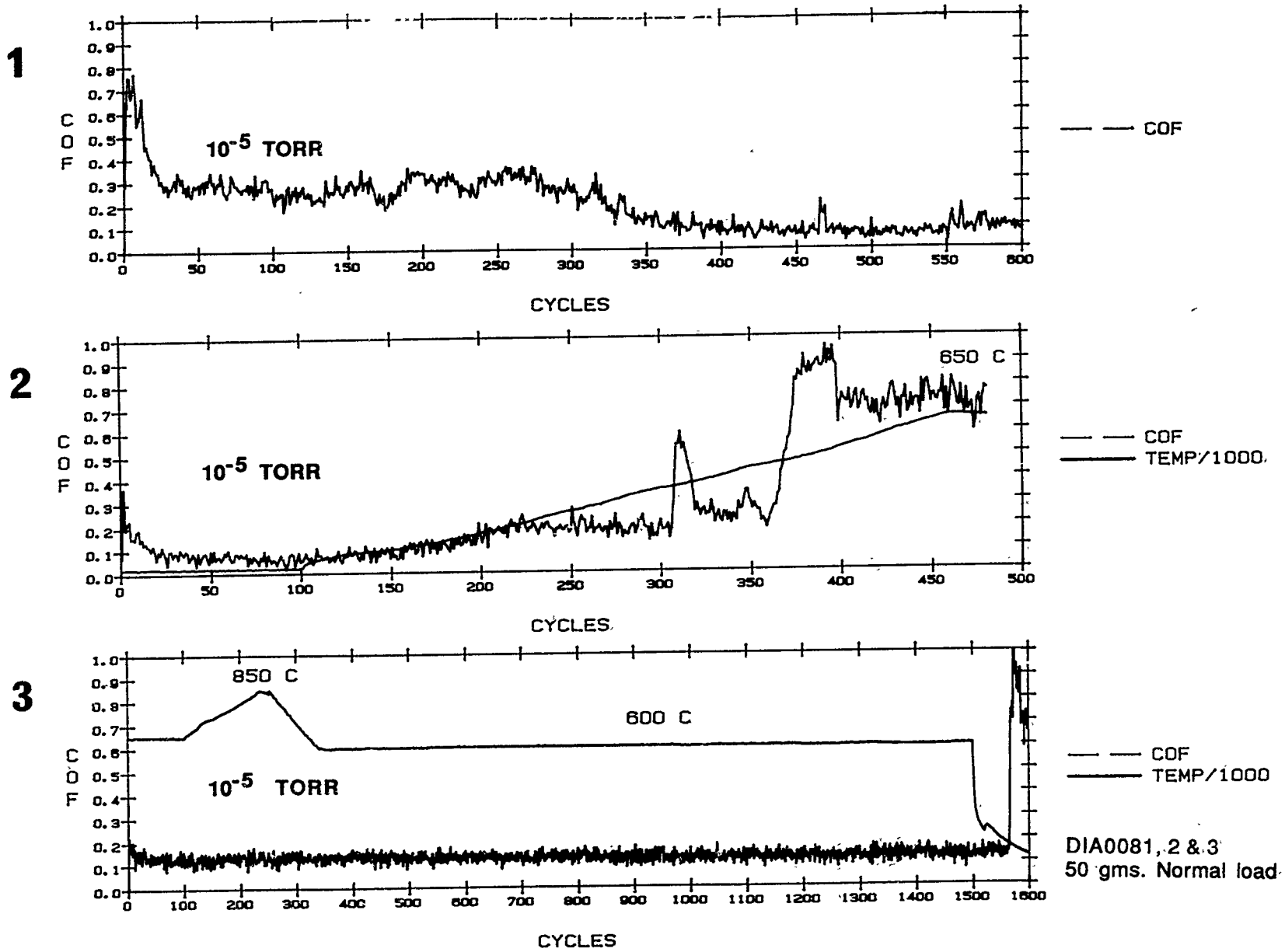

Figure 251. Coefficients of friction (COF) of fluorinated-unpolished diamond on α-SiC pin versus fluorinated-unpolished diamond on Si(100) flat, in 1.33 x 10^{-3} Pa = 1 x 10^{-5} torr vacuum, at various temperatures.

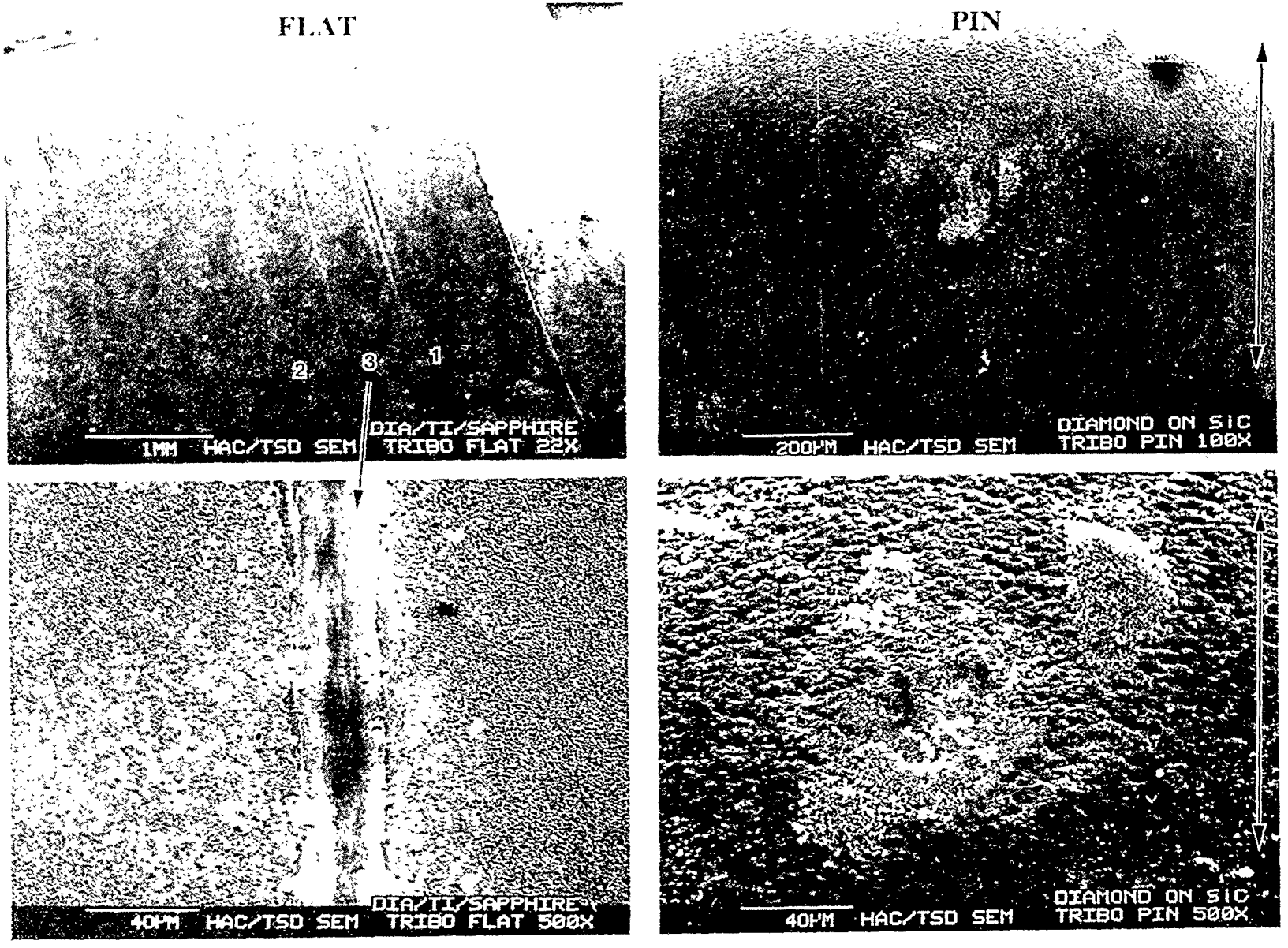

Figure 252 The appearance of the used SEM tribometer counterfaces at various SEM magnifications, associated with the tests described in Figure 251; double headed arrow indicates direction of oscillation.

another benign adsorbate, then they interact with the sliding counterface to generate high ($f_k \equiv 0.8$) friction forces. Enhanced resorption of such adsorbates (e.g., on cooling the tribosystem in the relatively hydrogen-rich atmosphere of the turbomolecular-pumped SEM tribometer) annihilates unreconstructed dangling bonds, lowering the friction to $f_k \equiv 0.1$. The friction trends also indicate that at high temperatures, in vacuum, the friction may also become reduced by graphitization and by bond reconstruction on the sliding surfaces. Reconstruction of the Si(100) appears to be equally effective in reducing the adhesive interaction between itself and its sliding counterface at high temperatures, except where the remaining C-H and Si-H bonds on the exposed facets begin to break and form friction-increasing dangling bonds at ~850°C and higher. The equivalent rupture of the lesser number and higher strength C-H bonds there is negligible, and probably depends on the proportion of the (100) facets progressively exposed by wear.

In P_{air} and at high temperatures, the friction of poly-XTL diamond is substantially lower than in vacuum. The generation of gaseous and solid oxidation products, combined with the temperature-shear-oxygen-induced phase transformation to graphite, lead to lower surface shear strength and reduced friction.

Wear of the diamond films in the wide temperature range characteristic to the present test procedure is assumed to be directly proportional to (a) the friction forces (higher friction, higher wear or even delamination) and to (b) the atmosphere of sliding (more oxidation, higher wear). The wear rates of pure, poly-XTL diamond against itself varied from ~4×10^{-16} $m^3/N \cdot m$ in 1.33×10^{-3} Pa vacuum to ~1×10^{-15} $m^3/N \cdot m$ in 1.13 Pa P_{air}. The corresponding wear rate of the softer α-SiC versus diamond is ~3×10^{-14} $m^3/N \cdot m$ in 1.33×10^{-3} Pa environment.

Fluorination of the CVD diamond films was unsuccessful in lowering the coefficient of friction or lengthening of the films' wear lives due to the attack of the substrate-diamond interface by the fluorine gas, through the pinholes and cracks in the layers, and a lack of substantive reaction between C and F on the sliding surfaces.

The data in this report represent the first step in a systematic study to determine the tribological fundamentals governing the utility of poly-XTL diamond coatings for friction and wear applications. The results point to additional work needed to resolve the following critical issues, especially with ceramic substrates in mind:

1. Surface activation methods must be found to enhance the adhesion of diamond to the largely inert (covalent-bonded) ceramics, such as α-SiC and Si_3N_4.

2. Deposition methods capable of producing fine, microcrystalline coatings, which need minimal (if any) polishing, must be developed for precision moving mechanical assemblies. Certain crystallographic texturing on the surface may be preferable to others.

3. Since some polishing of the diamond films will probably be needed anyway, chemical or ion-etching methods must replace the expensive and time-consuming technique of mechanically polishing diamond with diamond. These techniques must be suitable for close-tolerance, non-planar surfaces, such as balls and races of rolling element bearings.

4. While lubricating diamond-coated surfaces with oils and greases is trivially obvious, using diamond bare or solid lubricated for extreme environment applications is not. The presence of dangling bonds on the diamond surface may serve to enhance adhesion of mating solid lubricant films, provided that the film interfaces themselves are property tailored.

A great deal of additional research must be performed before CVD diamond film technology can fully take its rightful place as the one providing the ultimate in friction and wear reduction. Our overall impressions as to the world-wide research on poly-XTL diamond films are as follows:

1. The current CVD films and those to be prepared in the near future are (and will be) disordered-polycrystalline, exhibiting a very high number of stacking faults, microtwins and other defects (approximately $10^{13}/cm^2$). While these attributes are acceptable (and in certain respects, desirable) for mechanical/tribological and some optical applications, they preclude those applications in electronics where well-controlled, near-perfect XTLs are needed. Yet, the major emphasis in the U.S. appears to be on doping-related electronic uses. With respect to key thermal properties, note than even sintered (polycrystalline) diamond has a thermal conductivity of 4-5 $W \cdot cm^{-1} \cdot K^{-1}$, exceeding the value of some of the best AlN XTLs grown to date in the U.S. (3.9 $W \cdot cm^{-1} \cdot K^{-1}$). Consequently, even the disordered films could be employed as improved static or tribological heat sinks (e.g., heat sinks in electronics, or as in-situ-abrasive-resistant surfaces able to conduct flash-temperature-generated heat away from the contact zone).

2. The Japanese are already capitalizing on the commercial usage of the excellent mechanical properties of even the currently manufactured, not-quite-perfect CVD films. Typical uses are for highly abrasion-resistant machine tools (diamond-coated Co-WC for aluminum and superalloy machining) and diamond-coated alumina and titanium speaker cones for higher fidelity sound (taking advantage of the highest Young's modulus of diamond). Why couldn't we do the same?

3. Further improvements in the mechanical properties or abrasion resistance of polycrystalline CVD films can be more readily achieved and would be more immediately useful than growing monocrystalline films on suitable substrates, or growing large monolithic XTLs for doping or heat sink applications. At the same time, all research along these lines would contribute to learning how to eventually deposit thin, XTL diamond films on the same or analogous substrates. Thus, electronic applications would also be achieved in the shortest possible time, especially if these films could be grown sufficiently thick, more rapidly, without stress or defects.

4.0 CONCLUSIONS

The goals, structure and highlights of a recently completed multiyear/multinational research program are described. The main driving force behind this effort was the aim to advance the technology base so engineers can successfully and confidently design, build and operate solid lubricated ceramic tribocomponents in extreme environments. Specially designed friction and wear testers were employed to perform well-defined model experiments on single crystal and polycrystalline ceramics and solid lubricants. The research led to discoveries such as (1) a lubricious oxide with the shear strength of MoS_2 in vacuum, (2) CVD diamond films with low friction and extraordinarily low wear, (3) intercalated graphites with high tribothermal resistance in vacuum and in air, and (4) a wear equation for Si_3N_4 ceramics. The fundamental nature of the research was exemplified by ab-initio predictions of the friction coefficient of single crystal (111) diamond sliding against its mating $(\bar{1}\bar{1}\bar{1})$ diamond plane, and molecular dynamics calculations on single crystal CaF_2 and BaF_2 (111) $[\bar{1}0]$ interface shear forces. The test equipment developed for completing the model experiments included an Auger/ESCA tribometer capable of unidirectional and oscillatory sliding at room temperature, a SEM tribometer designed for oscillatory sliding to 1000°C in vacuum and in partial pressures of reactive gasses, an 850°C+ dual-rubshoe friction and wear tester employing a rolling contact fatigue rod as one of the sliding specimens, and 850°C+ friction/traction apparatus capable of operating to extraordinarily high PV limits.

The fundamental nature of the research notwithstanding, the main goals were directed towards finding potential solutions and applications useful to practicing tribologists and lubrication engineers.

The theoretical and experimental discoveries have already been instrumental to kindling interest among academicians in microscopic modeling of tribocontracts. Our results also generated wide-spread interest in the U.S. in constructing a variety of microscopic/macroscopic tribometers equipped with modern in-situ surface analytical instrumentation. The advent of increased utilization of such friction and wear testers challenges the ingenuity of experimentalists and theoreticians alike to confirm or modify predictions or to generate new ones.

The program results established use limits for environmentally stable ceramic substrates, surface-modifying hard coatings and pinpointed the most difficult tasks facing extreme environment tribologists today: (a) providing adhesion of solid lubricants to ceramics at least as good as that to metallic alloys, and (b) mitigating the overall degradation of solid lubricated ceramic in adverse thermal and atmospheric environments. The breadth and extent of the efforts by our international work team have provided vastly improved insights to solving these problems, established the feasibility of solid lubrication useful ceramic bearing hardware and laid out the pattern of solid lubrication research for years to come.

5.0 REFERENCES

1. L. L. Fehrenbacher, and I. C. Oelrich, "Opportunities in Future Military Tribology Research and Development," IDA Paper P-1805, Nov. 1984.
2. L. L. Fehrenbacher, "Tribology Research & Development Needs of Advanced Military Systems," Proc. Int. Conf. on Engineered Materials for Advanced Friction and Wear Applications, 1-3 March 1988, Gaitersburg, MD, pp. 169-179 (1988).
3. M. N. Gardos, "Solid Lubrication of Ceramic and Superalloy Surfaces of High Temperatures," invited paper published in Proc. DARPA Workshop on Tribology Fundamentals - Needs and Future Directions, 12-13 December 1984, Institute for Defense Analyses, Alexandria, VA, NTIS-PB85-176246.
4. M. N. Gardos, "On Ceramic Tribology," Lubrication Engineering, 44, pp. 400-407 (1988).
5. P. D. Fleischauer, S. V. Didziulis, and P. A. Bertrand, "Structure and Composition Effects on the Solid Lubrication of Ceramic Surfaces," Final Report, DARPA Order No. 5708, The Aerospace Corporation, 1990.
6. P. A. Bertrand, "Orientation of RF-Sputtered MoS_2 Films," J. Mat. Res., 4, pp. 180-184 (1989).
7. S. V. Didziulis, P. D. Fleischauer, B. L. Soriano and M. N. Gardos, "Chemical and Tribological Studies of MoS_2 Films on SiC Substrates," Surf. & Coat. Technol., 43/44, pp 652-662 (1990).
8. ibid, R. N. Bolster, "Preparation, Analysis and Tribological Behavior of IBAD MoS_2 Films," (in press).
9. H. Kuwano and K. Kagai, "Friction Reducing Coatings by Dual Fast Atom Beam Technique," J. Vac. Sci. Technol. A4, pp. 2993-2996 (1986).
10. I. L. Singer and J. H. Wandass, "Ion-beam Alloying of Ceramics at High Temperatures," in Structure-Property Relationships in Surface Modified Ceramics, Ed. C. J. McHargue, Kluwer Academic Publishers, pp. 199-208, 1989.
11. R. N. Bolster, et al, "Tribological Behavior of TiN Films Deposited by High Energy Ion Beam Assisted Deposition," Surf. & Coat. Technol., 36, pp. 781-790 (1988).
12. M. N. Gardos, "The Tribooxidative Behavior of Rutile-Forming Substrates," Mat. Res. Soc. Symp. Proc. Vol. 140, New Materials Approaches to Tribology: Theory and Applications, Eds. L. E. Pope, L. L. Fehrenbacher and W. O. Winer, pp. 325-338 (1989).
13. M. N. Gardos, "The Effect of Anion Vacancies on the Tribological Properties of Rutile (TiO_{2-x})," STLE Tribology Trans., 31, pp. 427-436 (1988), also see discussions in STLE Tribology Trans. 32, pp. 30-31 (1989).
14. M. N. Gardos, H. S. Hong and W. O. Winer, "The Effect of Anion Vacancies on the Tribological Properties of Rutile (TiO_{2-x}), Part II: Experimental Evidence," STLE Tribology Trans., 32, pp. 209-220 (1990).
15. H. Hong and W. O. Winer, "A Fundamental Tribological Study of Ti/Al_2O_3 Contact in Sliding Wear," Trans. ASME, J. of Tribology, 111, pp. 504-509 (1989).

16. H. S. Hong and W. O. Winer, "A Tribological Study of Mo/Al_2O_3 in Sliding Contact," Mat. Res. Soc. Symp. Proc. Vol. 140, New Materials Approaches to Tribology: Theory and Applications, Eds. L. E. Pope, L. L. Fehrenbacher and W. O. Winer, pp. 301-308 (1989).

17. M. N. Gardos and K. V. Ravi, "Tribological Behavior of CVD Diamond Films," Proc. First Int. Symp. on Diamond and Diamond-Like Films, The Electrochem. Soc. Proc. Vol. 89-12, pp. 475-493 (1989); also see M. N. Gardos and B. L. Soriano, "The Effect of Environment on Tribological Properties of Polycrystalline Diamond Films," 5, pp. 2599-2609 (1990).

18. D. E. Hauge, R. H. Hauge and J. L. Margrave, "Fluorinated Diamond Films, Slabs and Grit," Mat. Res. Soc. Symp. Proc. Vol. 140, New Materials Approaches to Tribology: Theory and Applications, Eds. L. E. Pope, L. L. Fehrenbacher and W. O. Winer, pp. 351-356 (1989).

19. D. A. Levin, et al, "Assessment of Fundamentals in Materials Science:, Volume I; Volume II: Appendices," IDA Memorandum Report M-542, Final Report, DARPA Procurement No. MDA 903-84-C-0031, Institute for Defense Analyses, Alexandria, VA, Dec. 1988.

20. W. A. Goddard, III, and T. C. McGill, "Study of Surfaces and Interfaces using Quantum Chemistry Techniques," J. Vac. Sci. Technol., 16, pp. 1308-1217 (1979).

21. K. H. Johnson and S. V. Pepper, "Molecular-Orbital Model for Metal-Sapphire Interfacial Strength," J. Appl. Phys., 53, pp. 6634-6637 (1982).

22. W. A. Goddard, III, "Theoretical Chemistry Comes Alive," Eng. & Sci. (Caltech), XLIX, pp. 2-8 (1985).

23. S. V. Pepper, "Effect of Electronic Structure of the Diamond Surface on the Strength of the Diamond-Metal Interface," J. Vac. Sci. Technol., 20, pp. 643-646 (1982).

24. H. Mishina and D.H. Buckley, NASA TP-2405, Dec. 1984.

25. B. Stepien, C. Jedrzejek and R. E. Allen, "Dangling-Bond Resonances and Intrinsic Schottky Barriers," Solid State Commun., 69, pp. 647-650 (1989).

26. L. S. Plano, S. Yokota and K. V. Ravi, "Oxidation of DC PECVD Diamond Films," Proc. First Int. Conf. on Diamond and Diamond-Like Films, The Electrochem. Soc. Proc. Vol. 89-12, pp. 380-392 (1989).

27. J. M. Thomas, "Adsorbability of Diamond Surfaces," in Properties of Diamond, Ed. J. E. Field, Academic Press, London, 1979; also see J. M. Thomas and E. L. Evans, "Surface Chemistry of Diamond," Diamond Research, 1975.

28. J. O. Hansen, et al, "A Tensiometric Study of Diamond (111) and (110) Faces," J. Coll. and Interface Sci., 130, pp. 347-258 (1989); also see: T. E. Derry, C.C.P. Madiba and J.P.F. Sellschop, "Oxygen and Hydrogen on the Surface of Diamond," Nucl. Instrum. & Methods in Phys. Res., 718, pp. 559-562 (1983).

29. K. Leong, W. C. Forsman and F. L. Vogel, "Conversion of Carbon-Graphite Fibers to Fibers of Graphite Oxide," Mat. Sci. Eng., 64, pp. 148-155 (1984).

30. M.W. Ribarsky and U. Landman, "Dynamical Simulations of Stress, Strain and Finite Deformations," Phys. Rev., B38, pp. 9522-9537 (1988).

31. U. Landman, " Molecular Dynamics Simulations in Materials Science and Condensed Matter Physics," in Computer Simulations Studies in Condensed Matter Physics: Recent Developments, Eds. D. P. Landau, K. K. Mon, and H.-B. Schuttler, Springer, Berlin, 1988.

32. U. Landman, W. D. Leudtke, and M. W. Ribarsky, "Micromechanics and Microdynamics via Atomistic Simulations," Mat. Res. Soc. Symp. Proc. Vol. 140, New Materials Approaches to Tribology: Theory and Applications, Eds. L. E. Pope, L. L. Fehrenbacher, and W. O. Winer, pp. 101-117 (1989).

33. M. Robinson and D. M. Cripe, "Growth of Laser-Quality Rare-Earth Fluoride Single Crystals in a Dynamic Hydrogen Fluoride Atmosphere," J. Appl. Phys., 37, pp. 2072-2074 (1966).

34. R. C. Pastor and M. Robinson, "Solid Solution Single Crystals: (1-x) HoF_3 • $xErF_3$," Mat. Res. Bull., 9, pp. 449-453 (1974).

35. R. C. Pastor and A. C. Pastor, "Crystal Growth in a Reactive Atmosphere," Mater. Res. Bull., 10, pp. 117-124 (1975).

36. R. C. Pastor and M. Robinson, "Crystal Growth of Alkaline Earth Fluorides in a Reactive Atmosphere: Part III," Mater. Res. Bull., 11, pp. 1327-1334 (1976).

37. M. Robinson, "Processing and Purification Techniques of Heavy Metal Fluoride Glass (HMFG)," J. Cryst. Growth, 75, pp. 184-194 (1986).

38. M. N. Gardos and C. R. Meeks, "Solid Lubricated Rolling Element Bearings, Part I: Gyro Bearings and the Associated Solid Lubricants Research, Volume 1: Summary" and "Part II: Turbine Bearings and the Associated Solid Lubricants Research, Volume 1: Summary," AFWAL-TR-83-4129, Final Report, Hughes Aircraft Company, El Segundo, CA, February 1984.

39. C. R. Meeks, and K. Ng, "The Dynamics of Ball Separators in Ball Bearings - Part I: Analysis," ASLE Trans., 28, pp. 277-287 (1985).

40. C. R. Meeks, "The Dynamic of Ball Separators in Ball Bearings - Part II: Results of Optimization Study," ASLE Trans., 28, pp. 288-295.

41. C. R. Meeks and A. N. Tran, "Ball Bearing Dynamics Analysis Computer Program - SEPDYN, Dynamics Volume 1," WRDC-TR-89-2059, Final Report, Avcon, Inc./Hughes Aircraft Co., August 1989; also see C. R. Meeks and A. Tran, "Ball Bearing Dynamic Analysis Computer Methods - Part 1: Analysis," STLE Tribology Trans., [32, (in press)].

42. N. Gane and F. P. Bowden, "Microdeformation of Solids," J. Appl. Phys., 39, pp. 1432-1435 (1968).

43. W. A. Glaeser, "The Use of Surface Analysis Techniques in the Study of Wear," Wear, 100, pp. 477-487 (1984).

44. K. Kato, et al, "Three Dimensional Shape Effect on Abrasive Wear," Trans ASME, J. Tribology, 108, pp. 346-351 (1986).

45. W. Holzhauer and S. J. Calabrese, "Modification of SEM for In-Situ, Liquid-Lubricated Sliding Studies," ASLE Trans., 30, pp. 302-309 (1987).

46. W. Holzhauer and F. F. Ling, "In-Situ SEM Study of Boundary Lubricated Contacts," STLE Tribology Trans., 31, pp. 359-368 (1988).

47 Y. Talmon, et al, "Cold-Stage Microcopy System for Fast Frozen Liquids," Rev. Sci. Instrum., 50, pp. 698-704 (1979).

48. H. Seifert, "Liquid Helium Cooled Sample Stage for Scanning Electron Microscope," Cryogenics, 22, pp. 657-660 (1982).

49. R. P. Huebener, "Scanning Electron Microscopy at Very Low Temperatures," in Advances in Electronics and Electron Physics, Vol. 780, Ed. P. W. Hawkes, Academic Press, Inc., pp. 1-75 (1988).

50. A. Begelinger and A. W. J. de Gee, "Synopsis of the Results from an International Cooperative Wear Program," Lubr. Eng., 26, pp. 256-263 (1970).

51. H. Czichos, Tribology - A Systems Approach to the Science and Technology of Friction, Lubrication and Wear, Elsevier, 1978.

52. M. Godet, "Extrapolation in Tribology, "Wear, 77, pp. 29-44 (1982).

53. D. Tabor and W. O. Winer, "Silicone Fluids: Their Action as Boundary Lubricants," ASLE Trans., 8, pp. 69-77 (1965).

54. J. O. Smith, et al "Stresses due to Tangential and Normal Loads on an Elastic Solid with Application to Some Contact Stress Problems," J. Appl. Mech., 20, p. 157 (1953).

55. J. E. Merwin and K. L. Johnson, "Analysis of Plastic Deformation in Rolling Contact," Proc. Inst. Mech. Eng., Appl. Mech. Group Paper p. 25/63, 1963.

56. T. G. Johns, et al, "Engineering Analysis of Stresses in Railroad Rail, Phase I," Battelle Columbus Laboratories, FRA Contract DOT-TSC-1038, June 1977.

57. J. W. Kannel and J. L. Tevaarwerk, "Subsurface Stress Evaluations Under Rolling/Sliding Contacts," paper presented at the ASME/ASLE Joint Lubr. Conf., Hartford, CT, Oct. 18-20, 1983, ASME Paper No. 83-Lub-18.

58. D. Glover, "A Ball-Rod Rolling Contact Fatigue Tester," in Rolling Contact Fatigue Testing of Bearing Steels, ASTM STP 771, Ed. J.J.C. Hoo, pp. 107-125 (1982).

59. J. J. McLaughlin, "Alternate Ceramic Materials for Roller Bearings - Final Report," Contract No. N00019-81-C-02894, Teledyne CAE, Toledo, OH, March 1984.

60. J. F. Dill, et al "Rolling Contact Fatigue Evaluation of Hard-coated Bearing Steels," ASLE Proc. 3rd. Int. Conf. on Solid Lubr., Aug. 7-10, 1984, Denver, CO, ASLE SP-14, pp. 230-241 (1984).

61. L. Fiderer, "Unique Friction and Wear Tester for Fundamental Tribology Research," in Selection and Use of Wear Tests for Ceramics," ASTM STP 1010, Eds. C.S. Yust, and R. G. Bayer, pp. 24-42 (1988).

62. D. C. Cranmer, "Friction and Wear Properties of Monolithic Silicon-Based Ceramics," J. Mat. Sci., 20, pp. 2029-20378 (1985).

63. Y. S. Touloukian and D. P. DeWitt, Thermal Radiation Properties - Nonmetallic Solids, Vol. 8, IFI/Plenum Publ. Corp., NY, 1972.

64. D. D. Elleman, J. L. Allen and M. C. Lee, "Laser Pyrometer for Spot Temperature Measurements," NASA Tech. Briefs, Sept. 1988, p. 48.

65. T. F. J. Quinn, "The Division of Heat Surface Temperatures at Sliding Steel Interfaces and Their Relation to Oxidational Wear," ASLE Trans., 21, pp. 78-86 (1978).

66. K. R. Mecklenburg, "The Effect of Wear on the Compressive Stress in the Sphere-on-Plane Configuration," ASLE Trans., pp. 149-157 (1974).

67. S. L. Rice, H. Nowotny and S. F. Wayne, "The Role of Specimen Stiffness in Sliding and Impact," Wear, 77, pp. 13-28 (1982).

68. S. L. Rice, H. Nowotny and S. F. Wayne, "Specimen Material Reversal on Pin-on-disc Tribotesting," Wear, 88, pp. 85-92 (1983).

69. R. J. Conant, S. L. Rice, and R. Solecki, "Influence of Aspect Ratio on the Interface Pressure Distribution on Cylindrical Wear Specimens," Wear, 93, pp. 101-110 (1984).

70. T. Sakurai, "Recent Research on Tribology in Japan," Wear, 100, pp. 543-560 (1984).

71. B. Gecim and W. O. Winer, "Steady Temperature in a Rotating Cylinder Subject to Surface Heating and Convective Cooling," Trans. ASME, J. of Tribology, 106, pp. 120-127 (1984).

72. B. Gecim and W. O. Winer, "Steady Temperatures in a Rotating Cylinder - Some Variations in the Geometry and Thermal Boundary Conditions," Trans. ASME, J. of Tribology, 108, pp. 446-454 (1986).

73. J. A. Griffioen, S. Bair and W. O. Winer, "Infrared Surface Temperature Measurements in a Sliding Ceramic-Ceramic Contact," Proc. Leeds-Lyon Symp., Ed. D. Dowson, C. M. Taylor, M. Godet and D. Berthe, Paper IX, Sept. 1985.

74. T. F. J. Quinn and W. O. Winer, "The Thermal Aspects of Oxidational Wear," Wear, 102, pp. 67-80 (1985).

75. T. F. J. Quinn and W. O. Winer, "An Experimental Study of the "Hot-Spots" Occurring during the Oxidational Wear of Tool Steel on Sapphire," Trans. ASME, J. Tribol., 109, pp. 315-320 (1987).

76. G. S. Whiston, "An Analytical Model of Two-Dimensional Impact/Sliding Response to Harmonic Excitation," J. of Sound and Vibration, 86 pp. 557-562 (1938).

77. J. T. Oden and J. A. C. Martins, "Models and Computational Methods for Dynamic Friction Phenomena," Computer Methods in Applied Mech. and Eng., 52, pp. 257-634 (1985).

78. W. A. Rakowski, "The Establishment of Friction Standards - A Suggestion," Wear, 76, pp. 349-351 (1982).

79. M. C. Shaw, "Dimensional Analysis for Wear Systems," Wear, 43, pp. 263-266 (1977).

80. ASME Wear Control Handbook, Eds. M. B. Peterson and W. O. Winer, The American Society of Mechanical Engineers, New York, NY 1980.

81. P. J. Blau, "The Units of Wear - Revisited," Lubr. Eng., 45, pp. 609-614 (1989).

82. S. C. Lim and M. F. Ashby, "Wear Mechanism Maps," Acta Metall, 35, Overview No. 55 (1987).

83. J. F. Dill, "Extreme Measures - Tribological Testing in Hostile Environments," Lubr. Eng., 44, pp. 1004-1009 (1988).

84. J. Kraus, J. J. Blench and S. G. Braun , "In-Situ Determination of Rolling Bearing Stiffness and Damping by Modal Analysis," Trans. ASME, J. Vibration, Acoustics, Stress and Reliability in Design, 109, pp. 235-240 (1987).

85. T. Harris, Rolling Bearing Analysis, John Wiley & Sons, 1966, pp. 424-434.

86. L. O. Hewko, "Contact Traction and Creep of Lubricated Cylindrical Rolling Elements at Very High Surface Speeds," ASLE Trans., 12, pp. 151-161 (1969); also see Hewko's discussion of E. N. Diaconescu, G. D. Kerrison and P. B. Macpherson, "A New Machine for Studying the Effects of Sliding and Traction on the Fatigue Life of Point Contacts," ASLE Trans. 18, pp. 239-248 (1975).

87. L. D. Wedeven, R. A. Pallini and N. C. Miller, "Tribological Examination of Unlubricated and Graphite Lubricated Silicon Nitride Under Traction Stress," Proc. Int. Conf. Wear of Mater., Ed. K. Ludema, Apr. 5-9, 1987, ASME, pp. 333-347.

88. R. A. Pallini and L. D. Wedeven, "Traction Characteristics of Graphite Lubricants at High Temperature," STLE Tribology Trans., 31, pp. 289-295 (1988).

89. S. A. Barber and J. W. Kannel, "A Technique in the Evaluation of Thin, Solid Film Lubricants Under Combined Rolling and Sliding," ASLE Trans., 26, pp. 487-491 (1983).

90. S. A. Barber, J. W. Kannel, "Solid Lubricated Turbine Bearings: Part IV - Transfer Mechanisms for Solid Film Bearing Lubrication," Proc. 3rd. Int. Conf. on Solid Lubrication, ASLE SP-14, pp. 275-281 (1984).

91. J. A. Jefferis and K. L. Johnson, "Sliding Friction Between Lubricated Rollers," Proc. Inst. Mech. Engrs. London, Vol. 182, Part 1, 1967-68.

92. K. L. Johnson and R. Cameron, "Shear Behaviour of EHD Oil Films at High Rolling Contact Pressures," Proc. Instn. Mech. Engrs. London, Vol. 182, Part 1, 1967-68.

93. K. L. Johnson and J. L. Tevaarwerk, "Shear Behaviour of EHD Oil Films," Proc. Roy. Soc. London, Series A, 356, pp. 215-236 (1977).

94. J. A. Powell, "Silicon Carbide & Progress in Crystal Growth," Mat. Res. Soc. Symp. Proc. Vol. 97, pp. 159-170 (1987).

95. P. Liew and R. F. Davis, "Epitaxial Growth and Characterization of ß-SiC Thin Films," J. Electrochem. Soc: Solid-State Science and Technology, 132, p. 642 (1985).

96. N. W. Jepps and T. F. Page, "Progress in Crystal Growth and Characterization," Vol. 7, Ed. P. Krishna, pp. 259-308, Pergamon Press, NY, 1983.

97. K. Hunold and H. Reh, "High Performance Ceramics, II, Materials: Silicon Carbide (SiC), an Old Acquaintance," Interceram., No. 1, pp. 35-39 (1988).

98. R. C. Marshall, J. W. Faust and C. E. Ryan, (Eds.), "Silicon Carbide-1973," Proc. 3rd. Int. Conf. on SiC, Florida, University of South Carolina Press, 1973.

99. M. G. S. Naylor and T. F. Page, "Microhardness, Friction and Wear of SiC and Si_3N_4 Materials as a Function of Load, Temperature and Environment," Third Annual Tech. Report. US Army ERO Grant No. DA-ERO-G-010, Dept. of Metall. and Mat. Sci., U. of Cambridge, Pembroke St., Cambridge, England.

100. K. Miyoshi and D. H. Buckley, "Adhesion and Friction of Single-Crystal Diamond in Contact with Transition Metals," Appl. Surf. Sci., 6, pp. 161-172 (1980).

101. K. Miyoshi and D. H. Buckley, "XPS, AES and Friction Studies of Single-Crystal Silicon Carbide," Appl. Surf. Sci., 6, pp. 357-376 (1982).

102. K. Miyoshi, D. H. Buckley and M. Srinivasan, "Tribological Properties of Sintered Polycrystalline and Single Crystal Silicon Carbide," Ceram Bull., 62, 494-500 (1983).

103. L. Muehlhoff, W. J. Choyke, M. J. Bozack and J. T. Yates, Jr., "Comparative Electron Spectroscopic Studies of Surface Segregation on SiC (0001) and SiC ($000\bar{1}$)," J. Appl. Phys., 60, pp. 2842-2853 (1986).

104. C. Cm. Wu, R. W. Rice, D. Johnson, and B. A. Platt, "Grain Size Dependence of Wear in Ceramics," Ceram. Eng. Sci. Proc., 6 (7-8), pp. 995-1011 (1985).

105. V. Tvergaard and J. W. Hutchinson, "Microcracking in Ceramics Induced by Thermal Expansion or Elastic Anisotropy," J. Am. Cer. Soc., 71(3), pp. 157-166 (1988).

106. C. Cm. Wu, R. W. Rice, B. A. Platt and S. Carrle, "Wear and Microstructure of SiC Ceramics," Ceram. Eng. Sci. Proc., 6(7-8), pp. 1023-1039 (1985).

107. F. B. Knudsen, "Dependence of Mechanical Strength of Brittle Polycrystalline Specimens on Porosity and Grain Size," J. Am. Cer. Soc., 42(8), pp. 376-387 (1959).

108. D. C. Cranmer, R. E. Tressler and R. C. Bradt, "Surface Finish Effects and Strength-Grain Size Relation in SiC," J. Am. Cer. Soc., 60(5-6), pp. 230-232 (1977).

109. R. H. Smoak and E. H. Kraft, "Sintered Alpha Silicon Carbide: Some Aspects of the Microstructure - Strength Relationship," paper presented at the Fall Meeting of the Am. Cer. Soc., Sept. 27, 1977, Hyannis, MA, The Carborundum Co., Niagara Falls, N.Y., Carborundum Form A 11,011, 1977.

110. O. O. Ajayi and K. C. Ludema, "Surface Damage of Structural Ceramics: Implications for Wear Modeling," Proc. Int. Conf. Wear of Materials (Ed. K. Ludema), Apr. 5-9, 1987, Houston, TX, ASME, Vol. 1, pp. 349-360.

111. J. Breznak, E. Breval and N. H. Macmillan, "Sliding Friction and Wear of Structural Ceramics, Part 1: Room Temperature Behavior," J. Mat. Sci., 20, pp. 4657-4680 (1985).

112. K. L. More, C. H. Carter, Jr., J. Bentley, W. H. Wadlin, L. LaVanier and R. F. Davis, "Occurrence and Distribution of Boron-Containing Phases in Sintered α-Silicon Carbide," J. Am. Cer. Soc., 69(9), pp. 659-698 (1986).

113. Y. Tajima and W. D. Kingery, "Grain-Boundary Segregation in Aluminum-Doped Silicon Carbide," J. Mater. Sci., 17, pp. 2289-2297 (1982).

114. R. Browning, J. L. Smialek and N. S. Jacobson, "Multielement Mapping of α-SiC by Scanning Auger Microscopy," Adv. Ceram. Mat., 2(4), pp. 773-779 (1987).

115. C. V. Thompson, "Secondary Grain Growth in Thin Films of Semiconductors: Theoretical Aspects," J. Appl. Phys., 58(2), pp. 763-772 (1985).

116. H. Sato, N. Otsuka, G. L. Liedl and S. Mansour, "Formation of Elongated Particles in ß-SiC Compacts," Mat. Lett., 4(3), pp. 136-144 (1986).

117. V. M. Bermudez, "Growth and Structure of Aluminum Films on (001) Silicon Carbide," J. Appl. Phys., 63(10), pp. 4951-4959 (1988).

118. K. Hunold, "Sinterung and Heissisostatische Nachverdichtung von Siliciumcarbid," Proc. Sinter/HIP Symp. "Technische Keramik," Dec. 2-3, 1987, Hagen, W. Germany.

119. R. Oberacker, A. Kühne and F. Thümmler, "Einsatzmöglichkeiten für die Sinter-HIP-Technik bei der Herstellung keramischer Hochleistungswerkstoffe," Powder Metall. Int., 19, pp. 43-50 (1987).

120. K. Hunold, "Heissisostatiches Verdichten von SiC," Powder Metall. Int., 16(5), pp. 236-238 (1984).

121. K. Hunold, "Heissisostatiches Verdichten von SiC," Powder Metall. Int., 17(2), pp. 91-93 (1985).

122. L. J. Lindberg, "Elevated Temperature Durability of Ceramic Materials," paper presented at the AIAA/ASME/SAE/ASEE 24th Joint Propulsion Conf., July 11-13, 1988, Boston, MA, Paper No. A1AA-88-3055.

123. K. T. Faber and A. G. Evans, "Crack Deflection Processes, Part I: Theory, Part II: Experiments," Acta Metall., 31,565, 577, (1983).

124. T. A. Ramanarayanan, R. Ayer, R. Petkovic-Luton and D. P. Leta, "The Influence of Yttrium on Oxide Scale Growth and Adherence," Oxid. Metals, 29 (5-6), pp. 455-472 (1988).

125. J. Karch and H. Gleiter, "Ceramics Ductile at Low Temperature," Nature, 330, pp. 556-558 (1987).

126. W. R. Cannon and T. G. Langdon, "Review, Creep of Ceramics, Part 2: An Examination of Flow Mechanisms," J. Mat. Sci., 23, pp. 1-20 (1988).

127. M. Miyake, "Oxidation-enhanced Diffusion of Ion-implanted Boron in Silicon in Extrinsic Conditions," J. Appl. Phys., 57(6), pp. 1861-1868 (1985).

128. G. Charitat and A. Martinex, "Boron Segregation at Si-SiO_2 Interface During Neutral Anneals," J. Appl. Phys. 55(8), pp. 2869-2873 (1984).

129. J. R. Smyth and D. W. Richerson, "High Temperature Dynamic-Contact Behavior of Sintered Alpha Silicon Carbide," Proc. 7th. Ann. Conf. Composites and Advanced Ceramic Materials, Jan. 16-19, 1983, Cocoa Beach, FL. Am. Cer. Soc., pp. 663-673 (1983).

130. K. Shobu, T. Watanabe, Y. Enomoto, K. Umeda and Y. Tsuya, "Frictional Properties of Sintered TiN-TiB_2 and Ti(CN)-TiB_2 Ceramics at High Temperature," J. Am. Cer. Soc., 70, pp. C103-C104 (1987).

131. R. H. Stulen and R. Bastasz, "Surface Segregation of Boron in Nitrogen-Strengthened Stainless Steel," J. Vac. Sci. Technol., 16(3), pp. 940-945 (1979); also see K. Nii and K. Yoshihara, "Surface Precipitation and Its Application to Coatings," J. Mater. Eng., pp. 41-50 (1987).

132. M. N. Gardos, "Determination of Tribological Fundamentals of Solid Lubricated Ceramics, Volume 1: Summary," Second Semiannual Report for the period 1 May 1986 through 31 October 1986, Contract No. F33615-85-C-5087, Hughes Aircraft Co., El Segundo, CA 90245, 15 November 1986.

133. C. DellaCorte, "Tribological Properties of Alumina-boriasilicate Fabric," paper presented at the ASME/STLE Tribology Conference, Oct. 16-19, 1988, Baltimore, MD,. STLE Preprint No. 88-TC-3E-1.

134. V. A. Lavrenkno, A. P. Pomytkin, P. S. Kislj and B. L. Grabchuk, "Kinetics of High-Temperature Oxidation of Boron Carbide in Oxygen," Oxid. Metal, 10(2), pp. 85-95 (1976).

135. B. M. DeKoven and P. L. Hagans, "The Coefficient of Friction between Boron Carbide (B_4C) Surfaces in Air and Ultrahigh Vacuum (UHV)," Mat. Res. Soc. Symp. Proc. Vol. 140, New Materials Approaches to Tribology: Theory and Applications, Eds. L. E. Pope, L. L. Fehrenbacher and W. O. Winer, pp. 357-362 (1989).

136. T. Hirai, K. Neihara and T. Goto, "Oxidation of CVD Si_3N_4 at 1550°C to 1650°C," J. Am. Cer. Soc., 63 (7-8), pp. 419-424 (1980).

137. J. Schlichting and K. Schwetz, "Oxidation Behavior of Sintered α-Silicon Carbide," Proc. 10th CVD Plansee Seminar, June 1-5, 1981, Reutte, Asutria, pp. 487-495.

138. I. Ogawa, K. Kobayashi and S. Nishikawa, "Oxidation Resistance of Carbon-Ceramics Composite Materials Sintered from Ground Powder Mixtures of Raw Coke and Ceramics," J. Mat. Sci., 23, pp. 1363-1367 (1988).

139. D. Lange, "Verschleissfeste Werkstoffe auf Borcarbidbasis," Report No. KfK4009, Institute fur Material-und Festkörperforschung, Kernforschungszentrum Karlsruhe, W. Germany, Dec. 1985.

140. J. A. Costello and R. E. Tressler, "Oxidation Kinetics of Hot-Pressed and Sintered α-SiC," J. Am. Cer. Soc., 64, pp. 327-331 (1981).

141. ibid, "Oxidation Kinetics of Silicon Carbide Crystals and Ceramics: I, In Dry Oxygen," 69, pp. 674-681 (1986).

142. K. A. Blakely and P. T. B. Shaffer, "Oxidation-Resistant B_4C/SiC-A Carbon Neutron Absorbing Material," Cer. Bull., 69, pp. 192-195 (1990).

143. L. G. Podobeda, A. K. Tsapuk and A. D. Burov, "Oxidation of Boron Nitride Under Nonisothermal Conditions," Poroshkovaya Metallurgiya (Soviet Powder Metallurgy), 9(165), pp. 44-47 (1976).

144. S. C. Singhal and F. F. Lange, "Effect of Alumina Content on the Oxidation of Hot-Pressed Silicon Carbide," J. Am. Cer. Soc., 58, pp. 433-435 (1975).

145. E. G. Michel, J. E. Orgeta, E. M. Oellig, M. C. Asensio, J. Ferron and R. Miranda, "Early Stages of the Alkali-Metal-Promoted Oxidation of Silicon," Phys. Rev. B., 38, pp. 13,399-13,406 (1988).

146. I. J. Fritz, "Elastic Properties of a Lithia-Alumina-Silica Glass-Ceramic at High Pressure," J. Appl. Phys., 49, pp. 4423-4426 (1978).

147. K. I. Kondo, S. Iio and A. Sawaoka, "Nonlinear Pressure Dependence of the Elastic Moduli of Fused Quartz Up to 3 GPa," J. Appl. Phys., 52, pp. 2826-2831 (1981).

148. M. P. Brassington, Tu. Hailing, A. J. Miller and G. A. Saunders, "Elastic Constants of a Fluorozirconate Glass," Mat. Res. Bull., 16, pp. 613-621 (1981).

149. S. Hart, "The Elastic Moduli of Tellurite Glasses," J. Mat. Sci., 18, pp. 1264-1266 (1983).

150. R. M. Hazen and L. W. Finger, "Crystals at High Pressure," Sci. Amer., 252, pp. 110-118 (1985).

151. F. Lin, T. Marieb, A. Morrone and S. Nutt, "Thermal Oxidation of Al_2O_3-SiC Whisker Composites: Mechanisms and Kinetics," Mat. Res. Soc. Symp. Proc. Vol. 120, pp. 323-332 (1988).

152. F. D. Jue and T. Y. Chen, "Thermomechanical Cracking in Layered Media from Moving Friction Load," Trans. ASME, J. of Tribology, 106, pp. 513-518 (1984).

153. F. D. Jue and J. C. Liu, "Parameters Affecting Thermomechanical Cracking in Coated Media Due to High-Speed Friction Load," paper presented at the ASLE/ASME Tribology Conference, San Antonio, TX, Oct. 5-8, 1987; ASME Preprint No. 87-Trib-22.

154. S. J. Bennison and B. R. Lawn, "Role of Interfacial Grain-Bridging Sliding Friction in the Crack-Resistance and Strength Properties of Nontransforming Ceramics," Acta Metall., 37, pp. 2659-2671 (1989).

155. R. F. Davis and C. H. Carter, "Kinetics and Mechanisms of Primary and Steady State Creep in B- and Al-containing Alpha Silicon Carbide," ARO-23025, Final Report, North Carolina State Univ., July 1989.

156. B. R. Lawn and D. B. Marshall, "Indentation Fractography: A Measure of Brittleness," J. Res. Nat. Bureau Stds., 89(6), pp. 435-451, Nov. - Dec. 1984.

157. Yiu-Wing Mai and B. R. Lawn, "Crack Stability and Toughness Characteristics in Brittle Materials," published in Ann. Rev. Mat. Sci., 1986.

158. E. E. Gdoutos and G. Drakos, "Crack Initiation and Growth in Contact Problems," Theoretical and Appl. Fract. Mech, 3, pp. 227-232 (1985).

159. R. S. Vecchio and R. W. Hertzberg, "A Rationale for the "Apparent Anomalous" Growth Behavior of Short Fatigue Cracks," Eng. Fract. Mech., 22 (6), pp. 1049-1060 (1985).

160. T. Fett and D. Munz, "Determination of Crack Growth Parameter N in Ceramics under Creep Conditions," J. Testing and Eval., 13, pp. 143-151 (1985).

161. D. B. Marshall and A. G. Evans, "Measurement of Adherence of Residually Stressed Thin Films by Indentation. I: Mechanics of Interface Determination; II: Experiments with ZnO/Si," J. Appl. Phys., 56(10), pp. 2632-2644 (1984).

162. T. A. Grzybowski and A. L. Ruoff, "New Method of Determining the Onset of Ring Cracking," Rev. Sci. Instrum., 54(3), p. 357 (1983).

163. J. W. Lucek, et al, "Severe Environmental Testing of Silicon Nitride," Final Report, Contract NASC N00019-77-C-0551, Norbon Co., Worchester, Mass., Nov. 1979.

164. J. W. Kannel and T. L. Merriman, "Evaluation of Subsurface Stresses in the Vicinity of an Inclusion," ASLE Proc. 3rd. Int. Conf. on Solid Lubr., ASLE SP-14, p. 66 (1984).

165. P. Tsai and W. H. Chen, "Finite Element Analysis of Elastoplastic Contact Problems with Friction," AIAA J., 24(2), pp. 344-346 (1986).

166. H. C. Sin and N. P. Suh, "Subsurface Crack Progagation due to Surface Traction in Sliding Wear," MIT Industrial Liaison Program Report 5-40-82, Project No. 1.45.019, (1983).

167. S. S. Chiang and A. G. Evans, "Influence of a Tangential Force on the Fracture of Two Contacting Elastic Bodies," J. Am. Cer. Soc. 66(1), pp. 4-10 (1983).

168. B. R. Lawn, S. M. Wiederhorn and D. E. Roberts, "Effects of Sliding Friction Forces on the Strength of Brittle Materials," J. Mat. Sci., 19, pp. 2561-2569 (1984).

169. T. C. Chivers and S. C. Gorderlier, "Fretting Fatigue and Contact Conditions: A Rational Explanation of Palliative Behavior," Proc. Inst. Mech. Eng., Part C - Mech. Eng. Sci, 199 (C4), pp. 325-337 (1985).

170. A. G. Evans and E. A. Charles, "Fracture Toughness Determination by Indentation," J. Am. Cer. Soc., 59, pp. 371-372 91976).

171. A. G. Evans and T. R. Wilshaw, "Quasi-Static Solid Particle Damage in Brittle Solids - I. Observations, Analysis and Implications," Acta Metall. 24, pp. 939-956 (1976).

172. J. G. Baldoni, S. F. Wayne and S. T. Buljan, "Cutting Tool Materials: Measurement Properties - Wear Resistance Relationships," ASLE Trans., 29, pp. 347-352 (1986).

173. S. T. Buljan and S. F. Wayne, "Wear and Design of Ceramic Cutting Tool Materials," Wear, 133, pp. 309-321 (1989).

174. H. P. Kirchner and E. D. Isaacson, "Residual Stresses in Hot-Pressed Si_3N_4 Grooved by Single-Point Grinding," J. Am. Cer. Soc., 65, pp. 55-60 (1982).

175. T. Ohji, S. Sakai, M. Ito, Y. Yamauchi, W. Kanematsu and S. Ito, "Tensile Strength Properties of Hot-Pressed Silicon Nitride," Proc. 30th Jap. Cong. on Mat. Res., Kyoto, Japan, Sept. 1986, pp. 201-206.

176. B. Thomas, D. West, W. W. West, Jr. and K. Wyckoff, "Effect of Machining Parameters on the Surface Finish and Strength of Hot-Pressed Silicon Nitride," Powder Metall. Int. 20, pp. 39-44 (1988).

177. H. R. Baumgartner and W. M. Wheildon, "Rolling Contact Fatigue Performance of Hot-Pressed Silicon Nitride Versus Surface Preparation Techniques," paper presented at the "Symposium on Surfaces and Interfaces of Glass and Ceramics," N. Y. S. College of Ceramics, Alfred University, Alfred, N.Y., Aug. 27-29, 1973, Norton Co. Reprint Form 5216.

178. H. Takebayashi and K. Ueda, "Rolling Contact Fatigue of Ceramics and Effects of Defects in Material," Koyo Seiko Co., Ltd. Engineering Report No. 130R.

179. K. C. Ludema, "Engineering Progress and Cultural Problems in Tribology," Lubr. Eng., 44, pp. 500-509 (1988).

180. E. Rabinowicz, "Penetration Hardness and Toughness Indicators of Wear Resistance," MIT Industrial Liaison Program Report No. 2-40-88, Massachusetts Institute of Technology, Cambridge, MA, 1988.

181. N. P. Suh and H. C. Sin, "On Prediction of Wear Coefficients in Sliding Wear," ASLE Trans., 26, pp. 360-366 (1983).

182. K. S. Mazdiyashni and R. Ruh, "High/Low Modulus Si_3N_4-BN Composite for Improved Electrical and Thermal Shock Behavior," J. Am. Cer. Soc., 64, pp. 415-418 (1981).

183. K. Niihara, L. D. Bentsen, D. P. H. Hasselman and K. S. Mazdiyashni, "Anisotropy Effects in the Thermal Diffusivity of Si_3N_4 - BN Composites," Am. Cer. Soc. Comm., 61, pp. C117-C118 (1981).

184. Personal communications with D. R. Petrak, 16 Oc. 1985; data from Babcock & Wilcox Report RDD:84:3247-01:01 (1984).

185. T. M. Shaw, O. L. Krivanek and G. Thomas, "Glass-Free Grain Boundaries in BeSiN Ceramics," J. Am. Cer. Soc., 62, pp. 305-306 (1979).

186. D. Bonnell, "Development of Structure in Silicon Nitride Grain Boundaries," in Ceramic Microstructures '86: Role of Interfaces, Proc. Int. Mat. Symp., Berkeley, CA, July 28-31, 1986, Plenum Press, NY, pp. 877-882.

187. G. M. Crosbie, J. M. Nicholson and E. D. Stiles, "Sintering Factors for a Dry-Milled Silicon Nitride-Yttria-Alumina Composition," Cer. Bull., 68, pp. 1202-1206 (1989); also see W. E. Lee and G. E. Hilmas, "Microstructural Changes in ß-Silicon Nitride Grains upon Crystallizing the Grain-Boundary Glass," J. Am. Ceram. Soc., 872, pp. 1931-1937 (1989).

188. E. Butler, R. J. Lumby and A. Szweda, "SYALON Ceramics for High Temperature Engines; An Illustration of Grain Boundary Engineering," Proc. Int. Symp. on Ceramic Components for Engines, Japan, 1983, pp. 159-169.

189. M. N. Gardos, "Determination of Tribological Fundamentals of Solid Lubricated Ceramics, Part II: Formulation of Improved Tribomaterials for Advanced Cryogenic Turbopump Applications," Second Semiannual Report for the period 01 November 1987 to 31 May 1988, Contract F33615-85-C-5087, Hughes Aircraft Company, El Segundo, CA; also see Third Semiannual Report 01 June 1988 to 28 February 1989.

190. P. Sutor, "Ceramic Frictional Studies," AFWAL-TR-84-4053, Midwest Research Institute, Kansas City, MO, 01 March 1984.

191. D. J. Joyner and D. M. Hercules, "Chemical Bonding and Electronic Structure of B_2O_3, H_3BO_3, and BN: An ESCA, Auger, SIMS, and XPS Study," J. Chem. Phys. 72, pp. 1095-1108 (1980).

192. F. Bassini and G. P. Parravicini, Electronic States and Optical Transitions in Solids, Int. Ser. Monographs in the Sci. of Solid State, Vol. 8, Pergamon Press Ltd., Oxford, 1975.

193. A. Catellani, M. Posternak, A. Baldereschi, H. J. F. Jansen and A. J. Freeman, "Electronic Interlayer States in Hexagonal Boron Nitride," Phys. Rev. B., 32, pp. 6997-6999 (1985).

194. G. L. Doll, J. S. Speck, G. Dresselhaus, M.S. Dresselhaus, K. Nakamura and S. I. Tanuma, "Intercalation of Hexagonal Boron Nitride with Potassium," J. Appl. Phys. 66, pp. 2554-2558 (1989).

195. G W. Rowe, "Some Observations on the Frictional Behavior of Boron Nitride and of Graphite," Wear, 3, pp. 275-285 (1960).

196. D. H. Buckley, "Friction and Transfer Behavior of Pyrolytic Boron Nitride in Contact with Various Metals," ASLE Trans. 21, pp. 118-124 (1978).

197. C. Schiritzer, Technology Update ("Uses for BN Coatings Vary"), Cer. Bull., 69, P. 56 (1990).

198. T. Pieczenka, J. Frydrych and S. Stolarz, "Interactions Occurring Between Nickel and Boron Nitride," Powder Metall. Int., 19, pp. 24-28 (19878).

199. E. Rabinowicz, and M. Imai, "Frictional Properties of Pyrolytic Boron Nitride and Graphite," Wear, 7, pp. 298-300 (1964).

200. K. Miyoshi, D. H. Buckley, S. A. Alterovitz, J. J. Pouych, and D. C. Liu, "Adhesion, Friction and Deformation on Ion-Beam-Deposited Boron Nitride Films," Proc. Inst. Mech. Eng., London, Paper C222/87, pp. 621-628 (1987).

201. K. Miyoshi, D. H. Buckley, J. J. Pouch, S. A. Alterovitz and H. E. Sliney, "Mechanical Strength and Tribological Behavior of Ion-Beam-Deposited Boron Nitride Films on Non-Metallic Substrates," Surf. Coat. & Technol., 33, pp. 221-233 (1987).

202. J. J. Pouch, S. A. Alterovitz, K. Miyoshi and J. D. Warner, "Boron Nitride: Composition, Optical Properties and Mechanical Behavior," MRS Symp. Proc. Vol. 93, pp. 323-328 (1987).

203. J. Hirvonen and W. Halverson, "Self-Lubricating-Diamond-Like Coatings Deposition," WRDC-TR-89-4119, Spire Corp. Bedford, MA, Dec. 1989.

204. "Pyrolytic Boron Nitride," Atomergic Chemetals Corp., Product Bulletin, Plainview, N. Y.

205. "Combat® Boron Nitride," Carborundum Technical Bulletin A-14, 011, Sept. 1984.

206. T. Matsuda, H. Nakae and T. Hirai, "Density and Deposition Rate of Chemical-Vapour-Deposited Boron Nitride," J. Mat. Sci., 23, pp. 509-514.

207. L. G. Podobeda, A. K. Tsapuk and A. D. Buravov, "Oxidation of Boron Nitride Under Nonisothermal Conditions," Poroshkovaya Metallurgiya (Soviet Powder Metallurgy), 9, pp. 44-47 (1976).

208. Handbook of Chemistry and Physics, 64th Ed., CRC Press, 1983-1984.

209. A. Y. Liu, R. M. Wentzcovitch and M. L. Cohen, "Atomic Arrangement and Electronic Structure of BC_2N," Mat. Res. Soc. Symp. Extended Abstracts EA-16, pp. 137-140 (1989).

210. ibid, A. W. Moore, S. L. Strong, G. L. Doll and M. S. Dresselhaus, "Physical Properties of Co-deposited C-BN Composites," pp. 141-144 (1989).

211. M. N. Gardos, "On the Elastic Constants of Thin Solid Lubricant Films," Proc. 16th Leeds-Lyon Symp. on Tribology (Mechanics of Coatings), Sept. 5-8, 1989, Lyon, France, Elsevier, pp.3-13.

212. J. R. Jones and G. W. Hoover, "Abrasiveness of MoS_2 in Bonded Solid Lubricants," ASLE Trans., 14, pp. 55-61 (1971).

213. M. N. Gardos, "The Synergistic Effects of Graphite on the Friction and Wear of MoS_2 Films in Air," STLE Tribology Trans., 31, pp. 214-227 (1987).

214. J. Gänsheimer, "Lubrication by Solids," paper presented at the Seminar on Friction, Lubrication and Wear, Lucerne, Switzerland, Sept. 18, 1959; Alpha-Molykote Corp. Special Print 445.

215. Y. Ikeda, H. Ito, T. Mizuno, K. Amioka and G. Matsumoto, "Sublimation Behavior of Molybdenum Oxides," High Temp. Sci,, 16, pp. 1-22 (1983).

216. B. M. Nirsa, L. V. Saveleva, and V. I. Reharskij, "Thermal Oxidation of Molybdenum Trisulfide," Neorganicheskie Materialy (Sov. Inorganic Materials), 21, pp. 375-377 (1985).

217. G. Ramadorai, M. E. Wadsworth, and C. K. Hansen, "The Kinetics of Molybdenum Dioxide Oxidation," Met. Trans. B, 6, pp. 579-584 (1975).

218. A. A. Zaitsev, N. A. Korotkov and E. M. Lazarev, "Oxidation of Molybdenum and Molybdenum-Tungsten Alloys," Metallovedenie i Temicheskaya Obrabotka Metallov (Sov. Metal Science and Heat Treatment), 18(10), ppl. 34-38 (1976).

219. B. M. Zykov, D. S. Ikonnikov and V. K. Tskhakaya, "Oxidation of the (110) Face of a Molybdenum Single Crystal," Sov. Phys. Sol. State, 19, pp. 2144-2147 (1977).

220. G. M. Raynaud, "The High Temperature (T = 1000K) Oxidation of Molybdenum," J. Mat. Sci. Lett., 3, pp. 965-967 (1984).

221. M. Matsunaga, T. Homma and A. Tanaka, "Investigation of Vapor Adsorption on Molybdenum Disulfide Surfaces by Auger Electron Spectroscopy," ASLE Trans., 25, pp. 323-328 (1982).

222. M. Matsunaga and T. Nakagawa, "Frictional Behavior of Various Kinds of Molybdenum Disulfide," Proc. 2nd. Int. Conf. on Solid Lubr., ASLLE SPP-6, pp. 45-50 (1978).

223. R. D. Kremith et al, "Solid Lubricant Coatings Applied by Plasma Spray," Cer. Bull., 47, pp. 813-818 (1968).

224. R. P. Burns, D. E. Pierce, H. M. Dauplaise, K. A. Gabriel and L. J. Mizerka, "Evaluation of Solid Lubricants: Temperature Prorammed Desorption of MoS_2 on Molybdenum," MTL-TR-88-36, U. Of Illinois at Chicago, Nov. 1988.

225. H. Oshima, et al, "Electronic Properties of Carbon Fibers Intercalated with Copper Chloride," Jap. J. Appl. Phys., 23 (1), pp. 40-43 (1984).

226. A. A. Conte, Jr., "Graphite Intercalation Compounds as Solid Lubricants," ASLE Trans., 26, p. 26 (1983).

227. L. C. Lipp and H. Stern, "Effect of Radiation and Additives on Graphite Lubricants for High Temperature Applications," in Bearing and Seal Design in Nuclear Power Machinery, ASME Proc. Symp. Lubr. in Nucl. Appl., June 5-7, 1967, Miami Beach, FL, pp. 288-303.

228. N. Akuzawa, et al, "Stability of Potassium-Graphite Intercalation Compounds in an Oxygen Atmosphere," Synthetic Metals, 7, pp. 57-63 (1983).

229. B. S. Elman, et al, "Stoichiometric Determination of $SbCl_5$- Graphite Intercalation Compounds Using Rutherford Backscattering Spectrometry," J. Appl. Phys. 55(4), pp. 894-898 (1984).

230. H. Kamimura, "Graphite Intercalation Compounds," Physics Today, 40, pp. 64-71, Dec. 1987.

231. G. J. L. Griffin, "Orientation Effects in Filled Plastic Bearing Materials," ASLE Trans., 15, p. 171 (1972).

232. W. S. Coblenz and D. Lewis III, "In Situ Reaction of B_2O_3 with AlN and/or Si_3N_4 to Form BN-toughened Composites," J. Am. Ceram. Soc., 71, pp. 1080-85 (1988).

233. P.C.S. Hayfield, "Electrode Material, Electrode and Electrochemical Cell," U.S. Patent No. 4,422,913, December 17, 1983.

234. R. L. Clarke and S. K. Harnsberger, "New Electrically Conductive Ceramic — A Fundamental Advance in Electrode Technology," Amer. Laboratory, (News Ed.), June 1988.

235. L. A. Bursill, "An Electron Microscope Study of the FeO-Fe_2O_3-TiO_2 system and of the Nature of Iron-Doped Rutile," J. Sol. State Chem., 10, pp. 72-94 (1974).

236. M. G. Blanchin, L. A. Bursill, and D. J. Smith, "Precipitation Phenomenon in Non-Stoichiometric Oxides I. Pairs of Crystallographic Shear Planes in Reduced Rutiles," Proc. Roy. Soc. Lond. A., 391, pp. 351-372 (1984).

237. L. H. Edelson, "Sintering of Monosized Titania," M. S. Thesis, U. C. Berkeley, 1986.

238. "Ceramic Source '90," Vol. 5, Am. Cer. Soc., Inc., Table 100, p. 315 (1989).

239. S. S. Kim, K. Kato, K. Hokkirigawa, and H. Abé, "Wear Mechanism of Ceramic Materials in Dry Rolling Friction," Trans. ASME, J. of Tribology, 108, pp. 522-526 (1986).

240. S. G. Saxe, M. J. Messerly, B. Bovard, L. De Sandre, F. J. Van Milligen and H. A. Macleod, "Ion Bombardment-induced Retarded Moisture Adsorption in Optical Thin Films," Appl. Opt., 23(20), pp. 3633-3637 (1984).

241. C. M. Kennemore and V. J. Gibson, "Ion Beam Processing for Coating MgF_2 onto Ambient Temperature Substrates," Appl. Opt., 23(20), pp. 3608-3611 (1984).

242. J. D. Targrove, J. P. Lehan, L. J. Lingg, H. A. Macleod, J. A. Leavitt, and L. C. McIntyre, Jr., "Ion-assisted Deposition of Lanthanum Fluoride Thin Films," Appl. Opt., 26(17), pp. 3733-3737 (1987).

243. J. R. McNeil, A. C. Barron, S. R. Wilson and W. C. Herrman, Jr., "Ion-assisted Deposition of Optical Thin Films: Low Energy vs. High Energy Bombardment," Appl. Opt., 23(4), pp. 552-559 (1984).

244. J. R. McNeil, G. A. Al-Jumaily, K. C. Jungling, A. C. Barron, "Properties of TiO_2 and SiO_2 Thin Films Deposited using Ion Assisted Deposition," Appl. Opt., 24(4), pp. 486-489 (1985).

245. G. A. Al-Jumaily, J. J. McNally, J. R. McNeil, and W. C. Hermann, Jr., "Effect of Ion Assisted Deposition on Optical Scatter and Surface Microstructure of Thin Films," J. Vac. Sci. Technol., A3(3), pp. 651-655 (1985).

246. Anon. "Scientists Deposit Superconducting Thin Films on Silicon, SiO_2 and Sapphire," Semicond. Int. 11, pp. 13-15, (1988).

247. M. Gurvitch and A. T. Fiory, "Preparation and Substrate Reactions of Superconducting Y-Ba-Cu-O Films," Appl. Phys. Lett., 51(13), pp. 1027-1029 (1987).

248. H. Koinuma, M. Kawasaki, T. Hashimoto, S. Nagata, K. Kitazawa, K. Fueiki, K. Masubuchi, and M. Kudo, "Some Problems in the Preparation of Superconducting Oxide Films on Ceramic Substrates," Jap. J. Appl. Phys., 26(5), pp. L763-L765 (1987).

249. M. J. Cima, J. S. Schneider and S. C. Peterson, "Reaction of $Ba_2YCu_3O_{6.9}$ Films with Yttria-Stabilized Zirconia Substrates," Appl. Phys. Lett., 53(8), pp. 710-712 (1988).

250. R. N. Bolster, I. L. Singer, R. A. Kant, B. D. Sartwell, and C. R. Gossett, "Tribological Behavior of TiN Films Deposited by High Energy Ion-Beam-Assisted Deposition," Surf. Coatings & Technol., 36, pp. 781-790 (1988).

251. R. W. Fathauer, and L. J. Schowalter, "Surface Morphology of Epitaxial CaF_2 Films on Si Substrates," Appl. Phys. Lett., 45, pp. 519-521 (1984).

252. I. Granet, Modern Materials Science, Reston Publ. Co. (Prentice-Hall), Reston, VA, 1980, pp. 134, 136-137.

253. H. Czichos, Tribology — A Systems Approach to the Science and Technology of Friction, Lubrication, and Wear, Elsevier, Amsterdam, 1987.

254. M. B. Peterson, and W. O. Winer (Eds.), Wear Control Handbook, American Society of Mechanical Engineers (ASME), 1990, p. 1320.

255. D. L. Deadmore, and H. E. Sliney, "Hardness of CaF_2 and BaF_2 Solid Lubricants at 25 to 670°C," NASA-TM-88979, March 1987.

256. A. A. Urusovskaya, and V. G. Govorkov, "Influence of Impurities on the Plastic Deformation of CaF_2 Single Crystals," Sov. Phys. Crystallography, 10, pp. 437-441 (1966).

257. P. F. Becher, and S. W. Freiman, "Crack Propagation in Alkaline-Earth Fluorides," J. Appl. Phys., 49, pp. 3779-3783 (1978).

258. W. L. Phillips, Jr., "Deformation and Fracture Process in Calcium Fluoride Single Crystals," J. Am. Cer. Soc., 44, pp. 499-506 (1961).

259. G. E. Dieter, Mechanical Metallurgy, McGraw-Hill Book Co., N.Y., 1986, p. 81.

260. J. J. Gilman, "Direct Measurement of the Surface Energies of Crystals," J. Appl. Phys. 31, pp. 2208-2218 (1960).

261. K. Weiss and J. M. Phillips, "Calculated Specific Surface Energy of Molybdenite," Phys. Rev. B., 14, pp. 5392-5395 (1976).

262. M. N. Gardos, "On the Elastic Constants of Thin Solid Lubricant Films," Proc. 16th Leeds-Lyon Symp. on Tribology (Mechanics of Coatings), Sept. 5-8, 1989, Lyon, France, Elsevier, Trib. Series 17, 1990, pp. 3-13.

263. J. M. Karanikas, R. Sooryakuma, and J. M. Phillips, "Dispersion of Elastic Waves in Supported CaF_2 Films," J. Appl. Phys., 65, pp. 3407-3409 (1989).

264. P. W. Sullivan, R. F. C. Farrow, and G. R. Jones, "Insulating Epitaxial Films of BaF_2, CaF_2 and $Ba_x Ca_{1-x} F_2$ Grown by MBE on InP Substrates," J. Cryst. Growth, 60, pp. 403-413 (1982).

265. S. Hart, "The Acoustic Soft Mode in Barium Fluoride," So. Afr. J. Phys., 4, pp. 103-105 (1981).

266. C. A. Brookes, V. R. Howes, and A. R. Parry, "Multiple Slip in Diamond due to a Nominal Contact Pressure of 10 GPa at 1,000°C," Nature, 332, pp. 139-141 (1988).

267. B. G. Hyde, "Crystallographic Shear Relations between the Structure Types α-VO_3, CaF_2, La_2O_3 and NaCl and a Correlation of Some Lanthanide and Actinide Oxide Structures," Acta Cryst., A27, p. 617 (1971).

268. H. E. Sliney, T. N. Strom, and G. P. Allen, "Fluoride Solid Lubricants for Extreme Temperatures and Corrosive Environments," ASLE Trans., 8, pp. 307-322 (1965).

269. M. N. Gardos, "Some Topographical and Tribological Characteristics of a CaF_2/BaF_2 Eutectic-Containing Porous Nichrome Alloy Self-Lubricating Composite," ASLE Trans., 18, pp. 175-186 (1975).

270. M. N. Gardos, and B. L. Soriano, "Tribological Behavior of CVD Diamond Films Deposited on Selected Ceramic Substrates," Proc. 4th Ann. SDIO/IST-ONR Dia. Tech. Initiative Symp., July 11-13, 1989, Crystal City, VA Paper Th 5 (Extended Abstract).

271. P. G. Lurie and J. M Wilson, "The Diamond Surface, I. The Structure of the Clean Surface and the Interaction with Gases and Metal," Surf. Sci., 65, pp. 453-475 (1977).

272. K. C. Pandey, "New Dimerized-Chain Model for the Reconstruction of the Diamond (111)-(2x1) Surface," Phys. Rev. B., 25, pp. 4338-4341 (1982).

273. B. B. Pate, "The Diamond Surface: Atomic and Electronic Structure," Surf. Sci., 165, pp. 83-142 (1986).

274. A. V. Hamza, G. D. Kubiak, and R. H. Stulen, "The Role of Hydrogen on the Diamond C(111)-(2x1) Reconstruction," Surf. Sci., 206, pp. L833-L845 (1988).

275. G. D. Kubiak, and K. W. Kolasinski, "Normally Unoccupied States on C(111) (Diamond) (2x1): Support for a Relaxed π-Bonded Chain Model," Phys. Rev. B., 39, pp. 1381-1384 (1989).

276. G. D. Kubiak, A. V. Hamza, and R. H. Stulen, "Hydrogen Chemisorption and the (2x1) Reconstruction on Natural Diamond (100) Surfaces," Proc. Fourth Ann. SDIO/IST-ONR Dia. Tech. Initiative Symp., July 11-13, 1989, Crystal City, VA, Paper W9.

277. C. H. Seager, and P.M. Lenahan, "Optical Absorption and Dangling Bonds in Damaged Silicon," J. Appl. Phys., 58, pp. 2709-2712 (1985).

278. C. H. Seager, P. M. Lenahan, K. L. Brower, and R. E. Mikawa, "Dangling Bonds and the Urbach Tail in Silicon," J. Appl. Phys. 48, pp. 2704-2708 (1985).

279. Handbook of Chem. & Phys., 53rd Ed., The Chem. Rubber Co., Cleveland, OH, 1972-1973, p. F-183.

280. A. Freedman and C. D. Stinespring, "Fluorination of Diamond (100) by Atomic and Molecular Beams," Appl. Phys. Lett., 57, pp. 1194-1196 (1990).

281. P. W. S. Oh, and A. J. Steckl, "Reactive Ion Etching of SiC Thin Films by Mixtures of Fluorinated Gases and Oxygen," Interim Tech. Report, INTEL Corp. (Santa Clara, CA) and U. of Cincinnati (Cincinnati, OH), UC-TR-19/JECS-89-04-135, 1989.

282. R. A. Rudder, J. B. Posthill, and R. J. Markunas, "Thermal CVD of Homoepitaxial Diamond Using CF_4 and F_2," Electr. Lett., 25, pp. 1220-1221 (1989).

U.S. Government Printing Office 648-127